

**UCLA**

**UCLA Electronic Theses and Dissertations**

**Title**

Characterizing Seismic Performance of Levees on Peaty Organic Soils from Case Histories and Simulations

**Permalink**

<https://escholarship.org/uc/item/2wg7b13s>

**Author**

Tsai, Yi Tyan

**Publication Date**

2018

Peer reviewed|Thesis/dissertation

UNIVERSITY OF CALIFORNIA

Los Angeles

Characterizing Seismic Performance of Levees on Peaty Organic Soils from  
Case Histories and Simulations

A dissertation submitted in partial satisfaction of  
the requirements for the degree of Doctor of Philosophy  
in Civil Engineering

by

Yi Tyan Tsai

2018

© Copyright by

Yi Tyan Tsai

2018

## ABSTRACT OF THE DISSERTATION

### Characterizing Seismic Performance of Levees on Peaty Organic Soils from Case Histories and Simulations

by

Yi Tyan Tsai

Doctor of Philosophy in Civil Engineering

University of California, Los Angeles, 2018

Professor Scott Joseph Brandenburg, Co-Chair

Professor Jonathan Paul Stewart, Co-Chair

Levee systems along Kushiro and Tokachi Rivers in Hokkaido, Japan, rest on significant deposits of peat and organic soils in downstream regions. Both levee systems were subjected to strong shaking during the 1993 **M** 7.6 Kushiro-oki and 2003 **M** 8.2 Tokachi-oki earthquakes. Local levee staff with the Japan Ministry of Land, Infrastructure, and Tourism (MLIT) performed thorough inspections of the full length of these levee systems after both events, which documented the location and severity of damages. This record of field performance presents a valuable dataset for investigating the factors that given rise to different levels of seismic performance. To my knowledge, this is the only such data set world-wide of levee performance when founded on peaty organic soils and subjected to strong earthquake shaking.

A crucial requirement for an investigation of the seismic performance of these levee systems is to understand the levels of seismic shaking they experienced. This is accomplished using a Kriging routine that operates on event-adjusted residuals between observed ground motions from local recording stations and ground motion models. Two ground motion models are considered, with some accommodations made to the path and site components of the ground motion models.

The site response component of the ground motion models is not able to capture the effect of the local geologies in the downstream regions, where the soft peat and organic soils are outside of the range present in global site databases. Accordingly, a regional site amplification model is developed using recordings from the downstream portion of the Tokachi River system in combination with nonlinear ground response analyses (GRA) with representative profiles. The profiles are based on information from the literature, local field offices, and a subsurface exploration program conducted as part of this research using the spectral analysis of surface waves (SASW) method and ambient noise measurements at 21 sites. The fundamental site period is estimated from the horizontal to vertical spectra ratio (HVSr) of the ambient noise and used as a predictive parameter for the empirical site response model. Dispersion curves are inverted to obtain shear wave velocity profiles for GRA and estimates of  $V_{S30}$  along the levees. The empirical amplification is higher and exhibits less nonlinearity than the amplification model derived from simulations. The regional model is used in place of the ergodic site terms in the ground motion models for predicting PGA at the levee segments with similar foundation conditions.

Seismic levee fragility is expressed as the probability of exceeding a damage level given the peak ground acceleration. The levee system is discretised into 50 m segments, each of which is assigned damage levels based on crack depth, crack width and subsidence from the MLIT reconnaissance.

Around a third of the 9,768 levee segments have peat within the foundations. Within the levee systems examined, levees on peat are found to be significantly more fragile than levees on inorganic soils.

Detailed analyses were performed for ten cross sections along the Tokachi River where strong motion recordings on the levees are available for the 2003 earthquake. Typical geotechnical performance assessment methods (liquefaction susceptibility, triggering, and consequence) are applied to examine the degree to which the observed field performance can be predicted. 2-D limit equilibrium models are constructed to evaluate slope displacements from Newmark analysis. A composite prediction framework considering both liquefaction severity indices and slope displacements is proposed to account for damage from multiple failure mechanisms and the consequence of liquefaction in the foundation and/or body of the levee.

The dissertation of Yi Tyan Tsai is approved.

Henry Burton

Robert Kayen

An Yin

Scott Joseph Brandenburg, Committee Co-Chair

Jonathan Paul Stewart, Committee Co-Chair

University of California, Los Angeles

2018

# TABLE OF CONTENTS

<b>ABSTRACT OF THE DISSERTATION.....</b>	<b>ii</b>
<b>TABLE OF CONTENTS .....</b>	<b>vi</b>
<b>LIST OF FIGURES .....</b>	<b>ix</b>
<b>LIST OF TABLES .....</b>	<b>xviii</b>
<b>ACKNOWLEDGEMENTS .....</b>	<b>xix</b>
<b>CURRICULUM VITA .....</b>	<b>xxii</b>
<b>1 INTRODUCTION .....</b>	<b>1</b>
<b>2 STUDY REGION AND DATASET.....</b>	<b>4</b>
2.1 Regional Geology and Construction History .....	4
2.2 Earthquake Recordings.....	5
2.3 Site Characterization.....	8
2.4 Damage Documentation .....	12
<b>3 GEOPHYSICAL SITE INVESTIGATION.....</b>	<b>15</b>
3.1 Introduction .....	15
3.2 Ambient Noise Recordings And Site Period.....	17
3.3 Spectral Analysis of Surface Waves .....	21
<b>4 DETAILED ANALYSIS OF LEVEE SECTIONS.....</b>	<b>28</b>
4.1 Introduction .....	28
4.2 Ground Motions During the 2003 Tokachi-oki Earthquake .....	28
4.1 Subsurface Conditions and Observations.....	37
4.1.1 Section 2 - Tokachi River left bank.....	40
4.1.2 Section 5 - Tokachi River right bank.....	43
4.1.3 Section 7 - Tokachi River left bank.....	46
4.1.4 Section 8 - Tokachi River left bank.....	48



4.1.5	Section 9 and 10 - Gyushubetsu River .....	51
4.1.6	Section 11 - Gyushubetsu River left bank .....	55
4.1.7	Section 12 - Satsusakubetsu River right bank .....	58
4.1.8	Sections 13 and 14 - Satsubunnai River .....	62
4.2	Analysis of Levee Cross Sections.....	66
4.2.1	Strength loss mechanisms .....	67
4.2.2	Liquefaction Severity Indices.....	68
4.2.3	Initial material strengths.....	72
4.2.4	Residual strengths .....	73
4.2.5	Slope stability and Newmark displacements .....	77
4.2.6	Example LPI calculations and model construction.....	79
4.3	Combined Damage Assessment.....	82
4.3.1	Cross section 7 .....	89
4.3.2	Cross section 11 .....	90
4.3.3	Cross section 13 .....	92
4.4	Summary .....	93
<b>5</b>	<b>REGIONAL LINEAR SITE AMPLIFICATION MODEL FOR SOFT PEAT SITES 95</b>	
5.1	Introduction .....	95
5.2	Data Sources.....	97
5.2.1	Ground Motions and Related Metadata.....	97
5.3	Ground Motion Data Analysis.....	102
5.3.1	Event terms and region terms.....	102
5.3.2	Site terms .....	117
5.3.3	H/V spectral ratios from pre-event noise and application to site amplification. 120	
5.4	Model Development .....	123
5.4.1	Mean amplification .....	123
5.4.2	Aleatory variability model and Model bias .....	127
5.4.3	Nonlinearity .....	131
5.5	Model Comparison .....	135
5.6	Limitations .....	139

<b>6</b>	<b>NONLINEAR RESPONSE OF SOFT ORGANIC SOIL SITES .....</b>	<b>140</b>
6.1	Site Characterization.....	140
6.1.1	Soil classification and index properties .....	141
6.1.2	Shear strength .....	143
6.1.3	Shear wave velocity profiles .....	144
6.1.4	Modulus reduction and damping curves.....	147
6.2	Input Motions .....	153
6.3	Ground Response Analysis.....	155
6.3.1	Initial results and damping adjustments .....	156
6.4	Summary .....	163
<b>7</b>	<b>DEVELOPMENT OF FRAGILITY FUNCTIONS.....</b>	<b>165</b>
7.1	Introduction .....	165
7.2	Damage Data .....	166
7.3	Ground Motion Distribution .....	167
7.4	Fragility Function .....	172
7.5	Summary and Discussion .....	181
<b>8</b>	<b>CONCLUSION AND RECOMMENDATIONS.....</b>	<b>182</b>
8.1	Conclusions .....	182
8.2	Recommendations for Future Research .....	183
	<b>APPENDIX A: HVSR, SASW ARRAY SETUP AND DISPERSION CURVES .....</b>	<b>185</b>
	<b>APPENDIX B: LIQUEFACTION SEVERITY INDICES AND 2-D MODELS .....</b>	<b>250</b>
	<b>REFERENCES.....</b>	<b>303</b>

# LIST OF FIGURES

Figure 2.1. The fault plane and the focal mechanisms for the 1993 Kushiro-oki (top) and the 2003 Tokachi-oki (bottom) earthquake..... 7

Figure 2.2. Longitudinal cross section along Kushiro River from the river mouth to 15 km (left), and 30-50 km (right). A consistent layer of peat (purple) is present under the levees in the downstream region and tapers out around 38 km upstream..... 10

Figure 2.3 Longitudinal cross section along Tokachi River from the river mouth to 20 km. A consistent layer of peat (purple) is present under the levees. .... 11

Figure 2.4 Distribution of damage levels for segments with peat or inorganic foundation material for both earthquakes. .... 13

Figure 2.5 Photographs after the 1993 and 2003 earthquakes showing the various damage levels. (a) Level 1, with minor cracking and no subsidence, (b) Level 2, with 20-30 cm of subsidence and cracks on the exterior face (c) Level 3, with subsidence of over 30 cm and (d) Level 4, with 60-225 cm of subsidence and 6 m wide cracks (KDCCO 1994, 2004)..... 14

Figure 3.1 Test sites along Kushiro River are concentrated within the downstream basin, where peat deposits are present. Ambient noise measurements are performed close to SASW tests..... 16

Figure 3.2 Test sites along Tokachi River. A local network of recording stations installed on the levees and are prioritized for testing. .... 17

Figure 3.3 Ambient vibrations recorded at 1050HK site (top). Shorter segments are selected to exclude transient excitations. The H/V spectra ratio is computed for each windowed interval and the averaged spectra shown by the solid black line with a distinct peak around 1.2 Hz (bottom)..... 20

Figure 3.4 The mass shakers for generating harmonic stepped waves (top left) and the seismometer (top right). The spacing between the seismometers are changed after each sweep by the mass shakers (bottom)..... 23

Figure 3.5 Experimental dispersion curves obtained from two adjacent SASW tests, a) is in the free-field and the individual curves are overlapping, b) is on the levee crest and the data is scattered with multiple modes. .... 24

Figure 4.1 Sensor position and orientation at each ODCD strong motion station with respect to the levee. (Personal communication T. Sato).....	29
Figure 4.2 Time histories and response spectra at Toitokki station (TTK). .....	31
Figure 4.3 Time histories and response spectra at Rabirai station (RB).....	32
Figure 4.4 Time histories and response spectra at Horooka station (HK). .....	33
Figure 4.5 Time histories and response spectra at Reisakubetsu station (RSB). .....	34
Figure 4.6 Time histories and response spectra at Gyushubetsu station (GSB). .....	35
Figure 4.7 Time histories and response spectra at Higashiinaho station (HNH). .....	36
Figure 4.8 Downstream region of Tokachi River with strong motion recording stations and post-earthquake investigations performed after the 2003 Tokachi-oki earthquake. ....	38
Figure 4.9 Vicinity map and subsurface investigation for Section 2.....	41
Figure 4.10 (a) Extensive cracking on access road and sand boils visible in some of the cracks at Section 2. (b) Plan view showing distribution of longitudinal cracks on levee crest. ....	42
Figure 4.11 Vicinity map and subsurface investigation for Section 5.....	44
Figure 4.12 (a) Severe localized damage at Section 5 on the land-side slope, with deep cracks at the land-side edge of the access road on the levee crest. (b) Plan view of longitudinal cracks observed. ....	45
Figure 4.13 Vicinity map and subsurface investigation for Section 7.....	47
Figure 4.14 Cracks and differential settlement on the crest access road at Section 7.....	48
Figure 4.15 Vicinity map and subsurface investigation for Section 8.....	49
Figure 4.16 Cracking on the crest (top) and land-side slope (bottom left) at Section 8. Sand boils on crest access road downstream (bottom right). ....	50
Figure 4.17 Vicinity map for Sections 9 and 10. ....	52
Figure 4.18 Subsurface investigation for Section 9. ....	53

Figure 4.19 Cracking on the access road on the levee crest at Section 9 with slip and settlement on the land-side slope. ....	53
Figure 4.20 Subsurface investigation for Section 10. ....	54
Figure 4.21 Cracking of the roadway on the levee crest accompanied by slip on the slope at Section 10. ....	54
Figure 4.22 Vicinity map and subsurface investigation at section 11. ....	56
Figure 4.23 Extensive subsidence and collapse of the levee at Section 11. ....	57
Figure 4.24 Mapped surface of excavation at Section 11, showing fill placement history and failure geometry. The fill placed in 1956 (S31) likely liquefied during the earthquake. ....	57
Figure 4.25 Vicinity map and subsurface investigation at Section 12. ....	59
Figure 4.26 Damage at Section 12, cracks on the roadway on the levee crest (top left). Slip and displacement of the land-side slope towards the levee toe (top right, bottom). ....	60
Figure 4.27 Mapped surface of the excavation at section 12 showing fill placement history and failure geometry. Fill placed in 1959 (S34) and 1960 (S35) composed of coarse sands with gravels is deemed to be susceptible to liquefaction. ....	61
Figure 4.28 Vicinity map for Sections 13 and 14 on the subsidiary Satsubunnai River. ....	63
Figure 4.29 Subsurface investigation for Section 13. ....	64
Figure 4.30 Subsurface investigation for Section 14. ....	64
Figure 4.31 Cracks on the roadway on the levee crest at Section 14 from slip on land-side slope. ....	65
Figure 4.32 Shallow layers are weighted more in the $LPI_{ISH}$ than LPI procedure (Maurer et al., 2015). ....	70
Figure 4.33 Undrained strength ratio decreasing with pore pressure ratio for Akita peat (Yasuhara, 1994). ....	77

Figure 4.34 Liquefaction indices calculated from SPT and CPT through the crest at section 11. Susceptibility is based on material classification and ground water level from boring log. ....	80
Figure 4.35 2-D model of section 11 showing yield acceleration for slope failure towards the river-side with pre-earthquake material properties.....	81
Figure 4.36 2-D model of section 11 showing slope failure towards the river-side with liquefied strength in saturated fill with softened strength in clay and peat.....	82
Figure 4.37 Liquefaction severity indices at each cross section based on all SPTs and CPTs shows a range of values. Cross sections with the same damage level are offset in the x-axis for visualization. ....	83
Figure 4.38 Flowchart for selecting representative value of liquefaction severity index from multiple borings at a cross section. ....	85
Figure 4.39 Relationships between maximum shear strain during cyclic loading (left) and volumetric strain following liquefaction (right) with factor of safety. Both tend towards zero as factor of safety exceeds 2.0 (Yoshimine et al., 2006) .....	86
Figure 4.40 Damage levels predicted with only $LPI_{ISH}$ or Newmark displacements tend to underestimate at high damage levels.....	87
Figure 4.41 Predicted damage levels based on both Newmark displacements and $LPI_{ish}$ minimizes under prediction for high damage levels and are generally within one damage level of the observed performance. ....	88
Figure 4.42 Flow failure predicted on land-side slope through liquefied levee fill ( $FS < 1.0$ ). The uncertainty in the extent of the liquefiable fill greatly influence the damage level predicted. ....	89
Figure 4.43 Reduced strength in the liquefiable zone at the base of the levee destabilized the levee. The factor of safety (top) and yield acceleration (bottom) are greatly lowered, with Newmark sliding block predicting large displacements. ....	91
Figure 4.44 Liquefaction triggering is predicted in the saturated sand layer directly below the levee but leads to over-estimation of damage. Possible explanation is partial saturation in the upper layers during the earthquake. ....	92

Figure 5.1 Histograms of $V_{S30}$ for sites in NGA-West2 database (top, Seyhan and Stewart, 2014) and NGA-Subduction database (bottom, Ahdi et al. 2017).....	95
Figure 5.2 Recording stations on levees in the downstream region of Tokachi. ....	97
Figure 5.3 Focal mechanisms of events in NGA-subduction databases that have produced recordings at the ODCD stations. ....	98
Figure 5.4 Recordings for Event 6 (2011 Tohoku earthquake), showing stations used in this study (green), stations not considered on basis of distance cutoff criteria developed in the NGA-Subduction project (pink), stations not considered due to their location in the backarc region of Japan (blue), and ODCD stations (red).....	100
Figure 5.5 Histograms of median-component peak accelerations at ODCD stations for Events 1-9 and Event 10, with the latter having significantly higher intensity.....	101
Figure 5.6 Variation of total residuals with distance for Events 1 and 3. Event 3 shows a negative trend with distance at short periods.....	104
Figure 5.7 Variation of total residuals with distance for Events 4 and 5. Event 4 shows a negative trend with distance at short periods.....	105
Figure 5.8 Variation of total residuals with distance for Event 6 and 7. Event 7 shows a strong negative trend with distance for Honshu stations (green) and a positive trend for Hokkaido stations (black) at short periods.....	106
Figure 5.9 Variation of total residuals with distance for Events 8 and 9.....	107
Figure 5.10 Event terms across periods for the eight events recorded by the ODCD stations.....	109
Figure 5.11 Within-event residuals for all eight events. Trends with distance differ between Honshu and Hokkaido stations and is most apparent at short periods. ....	110
Figure 5.12 Region terms for Hokkaido and Honshu stations for events from South or North region. ....	111
Figure 5.13(a) Trend of region-corrected within-event residuals with closest distance for all data. Distance range for ODCD stations are marked out. ....	115
Figure 5.14(b) Trend of region-corrected within-event residuals with closest distance for North events only. Distance range for ODCD stations are marked out. ....	116

Figure 5.15(c) Trend of region-corrected within-event residuals with closest distance for South events only. Distance ranges for ODCD stations are marked.....	116
Figure 5.16 Region-adjusted within event residuals (top) and estimated site response (bottom) for the seven Obihiro stations .....	119
Figure 5.17 Comparison of H/V spectral ratios (data and fit) with observed total site response.....	122
Figure 5.18 Relationship between peak in H/V spectra ( $f_{peak}$ ) and peak in PSA site amplification ( $f_0$ ). Linear regression provides $f_0 = 1.379f_{peak} - 0.485$ (frequencies in Hz). .....	122
Figure 5.19 Fit of model to observed amplification with model coefficients from site-specific optimization.....	124
Figure 5.20 Relationship between peak in H/V spectra ( $f_{peak}$ ) and peak in Mexican hat fitting function of site response ( $f_p$ ). .....	125
Figure 5.21 Fit of model to observed amplification when model coefficients are taken from regional average model.....	126
Figure 5.22 Relationship between peak in H/V spectra ( $f_{peak}$ ) and peak in Mexican hat fitting function of site response ( $f_p$ ). .....	127
Figure 5.23 Comparison of site-to-site standard deviations from Obihiro stations (this study) and Japan average from Al Atik (2015).....	129
Figure 5.24 Comparison of single station standard deviations from Obihiro stations (this study) and KiK-net database from Rodriguez-Marek et al (2011). .....	130
Figure 5.25 Comparison of single station and site-to-site standard deviation terms for the two forms of the proposed site amplification model. ....	130
Figure 5.26 Comparison of model bias for the ergodic model of Zhao et al. (2016a, 2016b) and the Zhao et al. model combined with the two proposed region-specific site amplification models. ....	131
Figure 5.27 Boxplots of soil surface shear strain index $I\gamma_S$ for Event 1-9 and Event 10. Strains from Event 10 is significantly higher and nonlinear behavior is anticipated. ....	132
Figure 5.28 Event term for Event 10 compared to Event 1-9.....	133



Figure 5.29 Region adjusted within event residuals for data recorded at ODCD stations versus reference site $PGA^r$ (Site Class 2).....	134
Figure 5.30 Within event residuals (event terms corrected) of ODCD stations by Abrahamson’s model.....	136
Figure 5.31 Within event residuals for ODCD stations using recordings from Events 1-9 and Aea18 model with its ergodic site term.....	138
Figure 5.32 Within event residuals for ODCD stations by using recordings from Events 1-9 and Aea18 model with the regional site term developed in this chapter. ....	138
Figure 6.1 Large number of borings are available along the Kushiro levees in downstream marshland and are used to assignment of material properties and MRD relationships. The pair of collocated suspension log (PS-2) and SASW test (1056HK) is used to develop shear wave velocity profiles for the GRA in <i>DEEPSOIL</i> . ....	142
Figure 6.2 Suspension logs and SASW investigations in the downstream region Tokachi River used to develop shear wave velocity profiles. Stratigraphy from nearby borings and CPTs provides soil type for assignment of material properties and MRD relationships. ....	143
Figure 6.3 Processed shear wave velocity profiles from downhole suspension logging in Tokachi and Kushiro. The logs were presented in this smoothed form by the Hokkaido River Disaster Prevention Research Center and the Kushiro Development and Construction Office. ....	145
Figure 6.4 Representative shear wave velocity profiles with combining surface wave measurements and suspension logs.....	146
Figure 6.5 Modulus reduction and damping curves from cyclic torsional shear tests on samples of sandy silt (S-1), silty clay (C-1, C-2) and peat (P-1, P-2). Modulus reduction in peats is more gradual with higher damping at small strains (Tokimatsu and Sekiguchi, 2006).....	149
Figure 6.6 MRD curves for Shinotsu peat from Hokkaido (Hayashi et al. 2018), peat from the Niigata region (Tokimatsu and Sekiguchi 2006), and a mean model prediction for organic soils by Kishida et al. (2009).....	151

Figure 6.7 Comparison of the Darendeli (2001) modulus reduction and damping curves for clays of variability plasticity to tests on highly organic clays for the Hokkaido region (Hayashi et al., 2018).....	152
Figure 6.8 $V_S$ profiles for strong motion recording station HKD094 (left) and TKCH11 (right) with to be compatible with the base of the modeled soil column. ....	154
Figure 6.9 GRA results and fitted nonlinear amplification model. Amplification for Tokachi profile is systematically higher for Kushiro, particularly at periods between 0.5-1.0 s.....	157
Figure 6.10 Normalized amplification highlighting the effects of nonlinearity. ....	159
Figure 6.11 Comparison of nonlinear amplification functions based on data and ground response analysis. At short periods, the simulation results fall outside the 95% confidence interval from data. ....	160
Figure 6.12 $f_2$ derived from data and GRA smoothed across periods. The GRA are performed with MRD curves for clays based on Hayashi et al. (2018) and Darendeli (2001), with the latter showing more nonlinearity.....	161
Figure 6.13 Amplification functions for peat sites from this study compared with GRA by Terronez (2017) and Kishida et al. (2009). Empirically derived site amplification function shows more linear amplification and lower nonlinearity than the simulations. ....	163
Figure 7.1 Distribution of $V_{S30}$ at strong motion stations that recorded the 1993 (left) and 2003 (right) events compared to distribution of $V_{S30}$ measured at the levees. Site conditions at levees are generally softer than at the recording stations and at the lower limit of empirical site amplification models.....	168
Figure 7.2 Within-event residuals with respect to Zea16 GMM in the forearc region for 2003 earthquake. ....	171
Figure 7.3 Region-specific amplification models are applied in the highlighted areas along the Tokachi (left) and Kushiro (right) Rivers. These areas have thick soft sediments and site response that differs from the ergodic model.....	172
Figure 7.4 Fragility functions for occurrence of any damage conditioned on PGA. Segments on peat has higher probability of damage than segments on inorganics when subjected to the same PGA.....	176

Figure 7.5 Empirical fragility data points and fitted fragility functions for varying damage levels. Fitting performed with $\beta$ variable (dashed lines) and fixed (solid lines).....	178
Figure 7.6 Fragility functions for levee segments founded on peaty foundation materials as derived using ground motion estimates from the modified Aea18 and Zea16 GMMs. .....	179
Figure 7.7 Comparison of fragility curves for probability of any damage level (DL>0) as evaluated for Hokkaido levees (this study) and Shinano River levees (Kwak et al. 2016). .....	180

## LIST OF TABLES

Table 2.1 Active strong motion recording stations from each network.....	6
Table 2.2 Damage level assignment .....	13
Table 3.1 Fundamental frequencies estimated from HVSR.....	21
Table 3.2 SASW test sites and data.....	25
Table 4.1 Recording stations near levees during 2003 Tokachi-Oki earthquake .....	30
Table 4.2 Location and performance of selected levee sections .....	39
Table 4.3 Susceptibility based on soil classification.....	68
Table 4.4 Fines correction recommended for estimating residual strengths.....	75
Table 4.5 Damage level thresholds for $LPI_{ISH}$ and Newmark displacements .....	87
Table 5.1 Metadata of ODCD stations .....	98
Table 5.2 Metadata for the nine considered earthquakes .....	99
Table 5.3 F-test for significance of region effects for both sources and sites.....	113
Table 5.4 F-test for significance of region effects for both sources and sites.....	114
Table 5.5 F-test for significance of region effects for both sources and sites.....	114
Table 5.6 Model coefficients obtained by fitting Eq. (5.13) .....	124
Table 6.1 Laboratory tests along left bank of Kushiro River .....	141
Table 6.2 PGA and scaling for input ground motion used for analysis.....	154
Table 6.3 Values of $f_2$ regressed from empirical data and GRA with different MRD relationship...	161
Table 7.1 Analysis methods and data employed (Porter et al., 2007) .....	167
Table 7.2 Mean and standard deviation of lognormal CDFs for PGA-based fragility curves .....	177

## ACKNOWLEDGEMENTS

This project was funded by the Department of Water Resources under Contract No. 4600010406. Any opinions, findings, conclusions and recommendations expressed here are those of the author and do not necessarily reflect the views of the DWR. The Department of Civil and Environmental Engineering at UCLA supported me through fellowships and teaching apprenticeships, the latter of which provided a wonderful opportunity to interact with the undergraduate students.

This dissertation came to fruition through the guidance and help rendered by numerous individuals in all imaginable shapes and forms. A small fraction of which is described here:

I am deeply indebted to Professor Atsushi Mikami from Tokai University for procuring the reconnaissance reports and requesting permission for the field investigation, as well as Takashi Sato from the Civil Engineering Research Institute for obtaining the recordings from the Obihiro stations. I also acknowledge the National Research Institute for Earth Science and Disaster Prevention (NIED), Ministry of Land, Infrastructure, Transportation and Tourism (MLIT) and Japanese Meteorological Agency (JMA) for making their data readily available online.

Much gratitude to my committee, whose expertise spans the breadth of geology to structural engineering, for their thoughtful and challenging feedback. I owe my initial interest in geology to Professor An Yin for mistakenly letting me into his Yosemite Fiat Lux, and greatly enjoyed our discussions as well as the endless supply of tea. The geophysical investigation performed in Japan would have been impossible without Professor Robert Kayen, whose experience with the testing procedures and unflappable calm make the field work a pleasure. Thank you for bringing me to places I have never been, working on things I have never done.

I also won the advisor lottery – twice! Scott Brandenburg and Jonathan Stewart are extraordinary educators and exemplary advisors. Their dedication to detail and commitment to each student while juggling numerous other responsibilities is inspiring and humbling. Thanks Jon for opening up your home and hosting us for various celebrations and holidays – I now have a rudimentary understanding of American football and know to stay away from eggnog. Thanks Scott for always having your door open to questions big and small, and believing in me through all the rough patches. It was a distinct privilege to work with and learn from both of you.

A large portion of my doctorate work transpired within the collaborative environment of the geotechnical family at UCLA. I was blessed with several “older siblings” who were always happy to help, thank you Dong Youp for starting me off on the project and sharing several ; Mandro for sharing your teaching notes; Paolo and Margo for their excellent life advice and graciously hosting me in Italy, I look back very fondly on that trip. Special thanks to Sean, who did most of the heavy lifting (literally) for the geophysical field work, and Pengfei with the statistical analysis for the linear site response model. I am also grateful to have the mutual support of Sean and Grace as we wrapped up our dissertations together. And Ben, Sam, Ali, Kioumas, Claudia, Victor, Yang Yang and Ebuka for your companionship and insights.

I am also grateful for help from the departmental staff, Reba, Ben and Jesse, with all manners of paperwork and requirements. I am particularly grateful for Jesse Dieker - from lending a listening ear to wheeling over extra pizza to our office, you went far above and beyond to serve the students.

Beyond my academic circle, I am incredibly thankful to spend many normal days with my housemates, Alice, Maggie<sup>2</sup>, Devin, Jennifer and Joanna; Prisca for all our remote study sessions, Grace<sup>2</sup> for all the prayers and Susan for understanding my Ph.D struggles and listening to me practice for my major presentations.

Finally, the uttermost appreciation goes to my family – my Dad for giving me a firm foundation in the sciences and encouraging me to study abroad, my sister for balancing me and cheering me on. Xiaoguma for warmly welcoming me whenever I am back. Even though the distance and time difference are a challenge, your unwavering support made it possible for me to finish this marathon.

## CURRICULUM VITA

2012	B.S. in Civil and Environmental Engineering, University of California - Los Angeles
2013	M.S. in Civil Engineering, University of California - Los Angeles
2014-2018	Graduate Research Assistant, Department of Civil and Environmental Engineering University of California - Los Angeles
2015	Teaching Assistant, Samueli School of Engineering, University of California - Los Angeles
2016-2018	Teaching Assistant, Department of Civil and Environmental Engineering University of California - Los Angeles

### Publications

- Brandenberg, S. Stewart, J., Shafiee, A., Tsai, Y.T., Wang, P and Mikami, A. (2018). "Seismic Deformation Potential of Peaty Organic Soils Underlying Delta Levees", Project Report for California Department of Water Resources, Civil & Environmental Engineering Dept., UCLA.
- Tsai, Y.T., Brandenberg, S., Kayen, R., Mikami, A. Sato, T., Stewart, J. (2017) "Dataset for Empirical Assessment of Seismic Performance for Levees Founded on Peaty Organic Soils", 6<sup>th</sup> International Symposium on Geotechnical Safety and Risk, Denver, CO. Geo-Risk 2017.
- Tsai, Y.T., Brandenberg, S., Stewart, J., (2016) "Estimating Ground Motions for Levees Founded Upon Soft Soils," Proc. Association of State Dam Safety Officials Annual Conference, Philadelphia.

### Presentations

- Tsai, Y.T., Brandenberg, S.J., "Case Studies of the Seismic Performance of Levee Segments on Peat Foundation Soil", Dam Safety 2018, Seattle, September 2018
- Tsai, Y.T., Brandenberg, S.J., Stewart, J.P. "Developing fragility functions for levees on peat from case histories", Le Val Lund Student Symposium - Lifeline Infrastructure and Community Resilience, California Institute of Technology, April 2017.
- Tsai, Y.T., Kayen, R.E., "Site characterization using non-invasive surface wave tests in Hokkaido, Japan", Bremen University, Germany, March 2017
- Tsai, Y.T., "Seismic vulnerability of levee systems", Temple University, September 2016



# 1 INTRODUCTION

Levees are earthen embankments elevated from the surrounding land. They can occur naturally from deposition during flood events, or can be constructed as infrastructure to protect coastal or riverside communities during high water events. Earthquakes pose a serious hazard to levees in seismically active regions, since they are frequently founded on loose alluvial deposits with shallow groundwater, and are therefore prone to liquefaction and softening from cyclic loading. This is concerning for the San Francisco Bay-Delta region in California, where the levees continuously impound water and rest on peaty foundation soils, the seismic response of which is poorly understood.

This study aims to characterize the seismic performance of levees by developing empirical fragility functions from field performance data and by performing geotechnical analysis of individual levee cross sections with well-understood ground motion demands and field performance. Following a similar approach to that introduced by Kwak et al. (2016) for the Shinano River levees, fragility functions are developed for four damage states conditioned on ground motion intensity using a combined data set from the Kushiro and Tokachi levee systems in Hokkaido. Both systems have portions of the levee system founded on peaty organic soils, as well as the occurrence of widespread and well-documented levee failures during the 1993 Kushiro-oki and 2003 Tokachi-oki earthquakes (Sasaki 2009).

The dissertation contains 6 main body chapters and progresses through the dataset development to the final fragility function development in the following manner:

Chapter 2 introduces the study region and summarizes the dataset collected, which includes geology, subsurface conditions, soil properties within and beneath the levees. The two earthquakes considered, ground motion recordings, and station information are also presented. Documentation of observed

damage and conversion to damage levels are described. Based on the dataset assembled, shear wave velocity profiles are identified to be lacking, and Chapter 3 summarizes the geophysical site investigations performed and the interpretation of the data collected with the spectral analysis of surface waves (SASW) method and ambient noise measurements to obtain additional shear wave velocity profiles and to estimate site frequencies. The site investigation revealed an additional local network of seismic stations directly on the levees in Obihiro, and subsequent collaboration with the network administrators secured additional recordings.

Chapter 4 describes the analysis performed for ten levee cross sections close to Obihiro recording stations for the 2003 Tokachi-oki earthquake. Damage severity predicted using liquefaction severity indices, as well as slope stability and deformation analyses, are compared with observed performance. The section analyses provide insight on the mechanisms driving the failure, and complement the fragility functions by providing insights to the behaviors observed.

Recognizing differences in site amplification within the downstream areas relative to predictions of ergodic site response models, Chapter 5 and 6 describe the development of site amplification functions specific to the downstream region. Chapter 5 discusses the derivation of the site amplification function empirically by examining recordings from the Obihiro stations on the levees. I provided the recordings and station properties, and Pengfei Wang performed the statistical analysis to develop the site amplification function from the within-event residuals. Chapter 6 lays out the development of representative soil profiles and ground response analysis that were performed in *DEEPSOIL* to constrain the nonlinear behavior at strong shaking. The work in Chapter 5 is previously unpublished and included here for completeness for comparison with the simulation-based site amplification functions.

In Chapter 7, the shaking intensity, represented by the PGA at the levee sites, is estimated using a combination of ground motion models and Kriging of the residuals. The resulting dataset consists of 9,768 segments for each of the events, with around a third having peat in the foundation. Failure probability and median demands are developed from binned data, and a lognormal cumulative distribution function is fitted for varying damage levels, which comprises the recommended fragility function. Comparison within the same systems show that levees on peat are much more fragile than those on inorganic soils.

Finally, Chapter 8 summarizes the findings from the work and provides recommendations for future research.

## 2 STUDY REGION AND DATASET

### 2.1 REGIONAL GEOLOGY AND CONSTRUCTION HISTORY

The environment in Hokkaido is favorable for peat formation, and prior investigations have found continuous peat deposits in the downstream region. We focused on two levee systems along the Kushiro and Tokachi Rivers on the eastern coast of Hokkaido, Japan. These levees have experienced strong shaking from large magnitude subduction earthquakes occurring directly offshore. The Hokkaido Development Bureau (HDB), under the Ministry of Land, Infrastructure, Transportation and Tourism (MLIT), manages both systems through local offices.

The Kushiro River originates from Lake Kussharo, flowing south for 154 km through several towns and Kushiro City before discharging into the Pacific Ocean. The first levees were constructed in response to the devastating flood in 1920, with expansions and upgrades continuing until 1981. The original levees were trapezoidal and around half the height of the current levees. Expansions were made in stages through a combination of raising the levee height and widening the levee on the landward side, while retaining the original levees at the core. The current levees are benched and have a 1V:2H slope, with a crest elevation of around 9 m, crest width of 8 m and a base width of around 45-50 m in the downstream sections (Sasaki, 2009). The levees can be broadly divided into two continuous stretches: within the first 15km through Kushiro City and surrounding the Kushiro Marsh, and between 38 to 75 km along the towns of Shibecha and Teshikaga, totaling around 74 km of levees. Levees are absent between these two stretches as the neighboring areas are mostly uninhabited and surrounded by hills that naturally confine the river flow.

The Tokachi River originates from the Taisetsu Mountains and has a length of 156 km. Unlike the Kushiro River which is mostly linear, many subsidiary rivers join the Tokachi River in the Tokachi

Plains and the flood plain consists of alluvial fans and stream terraces. The steep gradient between the surrounding mountains and the plains contribute to frequent flooding. A flood control plan was established in 1918 and initial levees are constructed along the Tokachi, Otohuke, Sastunai and Urahoro Rivers. The levees along the main Tokachi River were significantly broadened in the early 2000s to remedy settlements due to the soft peaty organic soils. The peat extend to a depth of 2-6 m and are underlain by alluvial deposits of sandy, silty and clayey sediments. Under the levees, the peat layer is typically 0.5-1.0 m thinner than in the free-field. Penetration resistance measured during CPTs and SPTs, as well as shear wave velocities are low in the area. Relatively firm material, likely Pleistocene in age, is located at greater depths generally around 35-40 m.

The levees are delineated based on satellite imagery and the flood control maps compiled by the Geospatial Information Authority of Japan (2009). Levees designated as temporary on the official maps are not included as they may not be inspected after earthquakes.

## **2.2 EARTHQUAKE RECORDINGS**

Two large magnitude earthquakes are selected based on the extensive damage that was observed, the availability of detailed damage documentation, and a wide spectrum of shaking intensities along the levee systems. Both occurred off the eastern coast of Hokkaido. The 1993 **M** 7.6 Kushiro-oki earthquake occurred on January, 15, 1993, and is an intra-slab earthquake with a hypocentral depth of 107 km. The geometry and the slip distribution of the fault plane for Kushiro-oki was obtained from the inversion of near-field strong ground motion records and aftershock distribution (Ide & Minoru 1996). Substantial lengths of levees were damaged in both system, though the more severe damage is confined to Kushiro. The 2003 **M** 8.2 Tokachi-oki earthquake occurred on September, 26, 2003, and is an inter-slab earthquake, with a hypocentral depth of 23.3 km. The finite fault model is inverted

using a combination of ground motion records and geodetic data by Koketsu et al. (2004). The hypocenter was located offshore and further south, and mainly damaged levees along the Tokachi River. Figure 2.1 shows the hypocenter, focal mechanism, slip distribution and surface projection of the finite fault planes for both events.

Ground motion recordings are obtained from the Japan Meteorological Agency (JMA), Port and Airport Research Institute (PARI), and National Research Institute for Earth Science and Disaster Prevention (NIED) and the Hokkaido Development Bureau (HDB). The NIED maintains two strong-motion seismograph networks – the Kyoshin Network (K-NET) and the Kiban Kyoshin Network (KiK-net) (NIED, 2015) and has stations deployed at approximately 20 km intervals throughout Japan. The network was established after 1995, hence limited recordings are available for the 1993 event. Obihiro Development and Construction Department (ODCD), which is a local branch of the Hokkaido Regional Development Bureau (HDB) under MLIT maintains a local network on the levees in the downstream region of Tokachi River. This is particularly valuable and discussed in more detail in Chapter 4. The number of stations active during the two earthquakes are listed in Table 2.1 for each network.

Table 2.1 Active strong motion recording stations from each network

<b>Network</b>	<b>1993 Kushiro-oki</b>	<b>2003 Tokachi-oki</b>
JMA	20	55
PARI	13	9
NIED	-	553
HDB (WISE)	15	120
ODCD	-	6
<b>Total</b>	<b>48</b>	<b>737</b>

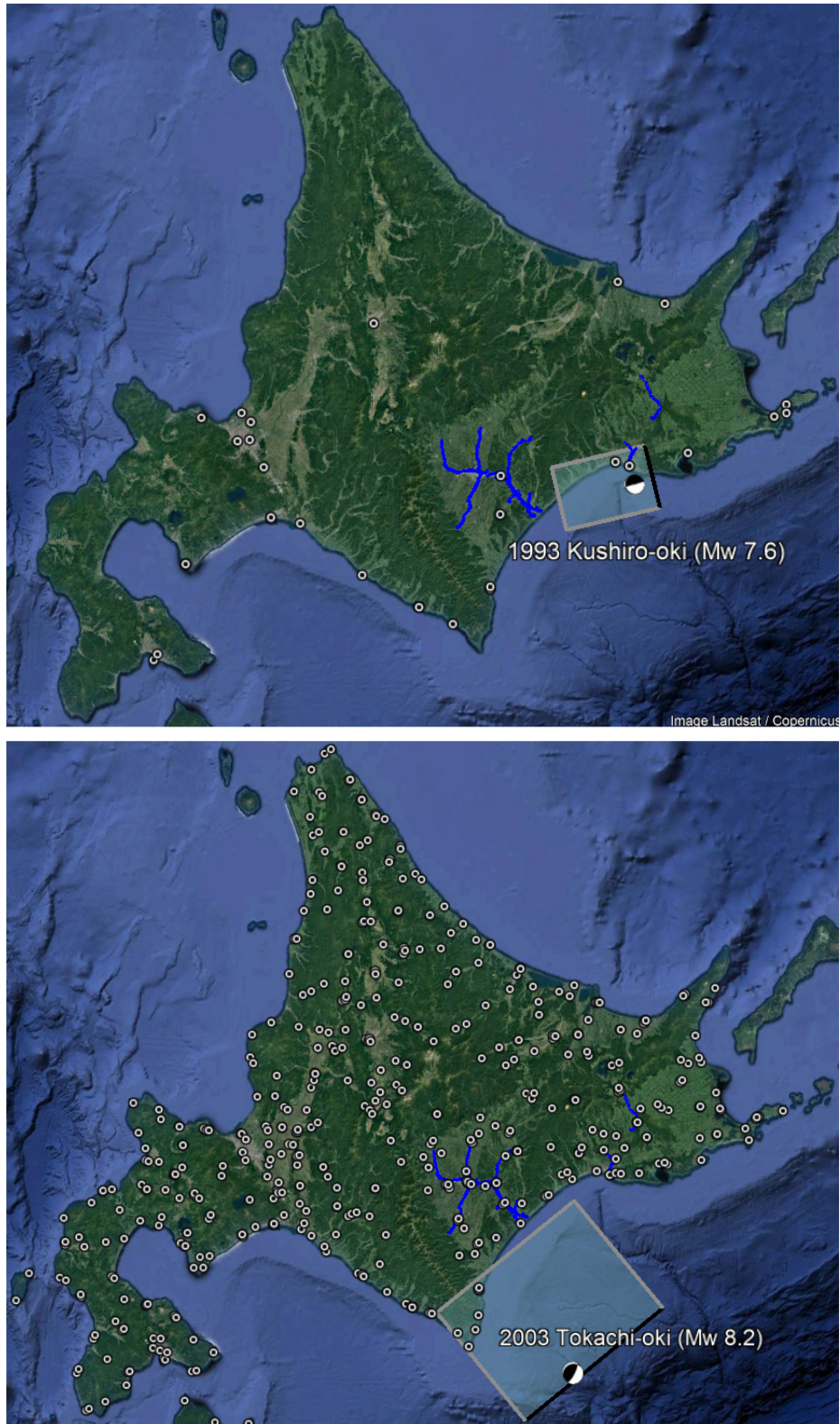


Figure 2.1. The fault plane and the focal mechanisms for the 1993 Kushiro-oki (top) and the 2003 Tokachi-oki (bottom) earthquake.

Site condition at the stations, typically represented by the time-averaged shear-wave velocity in the upper 30 m ( $V_{S30}$ ), is of interest for site response considerations. The degree of site characterization varies among the networks, with NIED stations possessing the most complete data, which includes P and S-wave velocity profiles from downhole measurements, SPT blow counts, soil type and bulk density. For stations without measured velocity profiles,  $V_{S30}$  is estimated from the geomorphology, elevation, slope and distance to hill/mountains at the station location (Wakamatsu & Matsuoka 2011). With assistance from T. Kishida, all recordings are filtered and corrected following standard PEER procedures.

## **2.3 SITE CHARACTERIZATION**

Geotechnical data collected during routine site investigations include Cone Penetration Tests (CPTs), boring logs with Standard Penetration Tests (SPTs), and index laboratory tests on retrieved samples for soil classification purposes. Ground water levels are reported when encountered in borings, and is an important parameter for considering liquefaction susceptibility.

For the Kushiro River, subsurface information is obtained from borings and geotechnical investigations performed by the Kushiro Development and Construction Office (KDCO) for design and maintenance. Additional site investigations performed at damaged sections to evaluate suitable repair measures are also collected (KDCO, 1994). These include open-cuts and excavation pits for investigating cracks and deformation, during which soil samples are also retrieved for testing and stratigraphy of underlying layers are noted. A total of 181 borings were performed between 1980 and 2004 along Kushiro River, with the majority located in the downstream region close to Kushiro City and Kushiro Marsh. The graphical representations of the borings and an interpreted cross-section are available in an AutoCAD file, from which individual logs are extracted and digitized. Each boring is identified by the year and



the order of the investigation (i.e., S56-16 refers to the 16<sup>th</sup> boring performed in 1981), and includes groundwater depth, raw blow counts from standard penetration tests (SPT), and soil classification. The drilling method and sampler used for the borings are not specified. Figure 2.2 shows the cross section along the levees from the river mouth to around 50 km upstream. Peat, abbreviated as A<sub>p</sub> and colored purple, is present throughout the downstream region and tapers out at around 38 km upstream. Beyond that, the foundation material consists mostly of Holocene alluvial sand or gravel deposits.

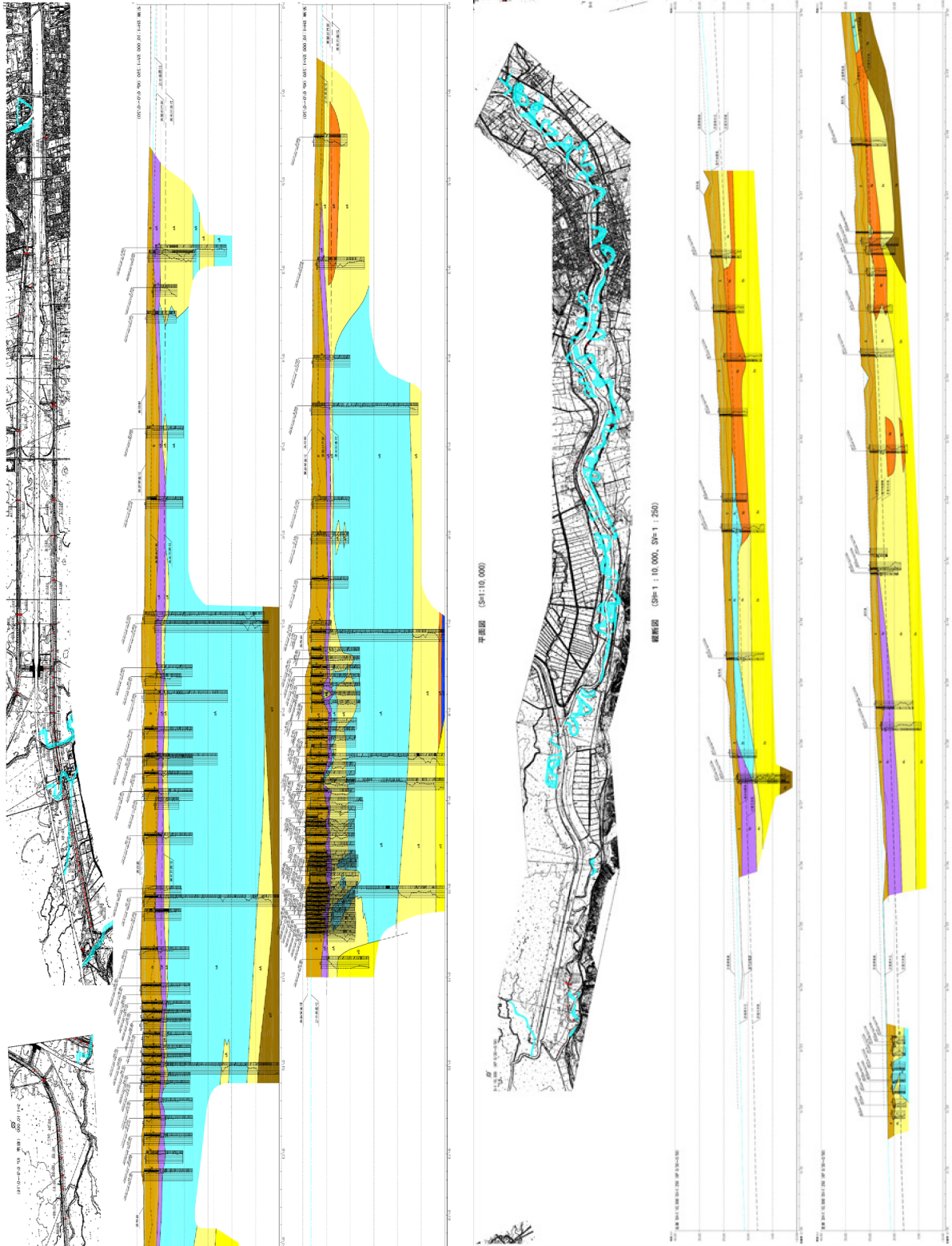


Figure 2.2. Longitudinal cross section along Kushiro River from the river mouth to 15 km (left), and 30-50 km (right). A consistent layer of peat (purple) is present under the levees in the downstream region and tapers out around 38 km upstream.

For Tokachi, the original field reports for at 21 sites investigated after the 2003 Tokachi-oki earthquake were available and includes layer descriptions according to the Japanese soil classification system, layer boundary depths, groundwater depths, raw SPT blow counts and CPT cone tip resistance. The SPTs are accompanied by stratigraphy description and soil type classified based on the composition by weight, with the major fraction exceeding 50%, the secondary fraction exceeding 15%, and the minor fraction between 5 - 15%. Thick peat deposits are present in the downstream region of Tokachi, ranging from 1-6 m. The ground water levels tend to be elevated within the levees in the downstream region.

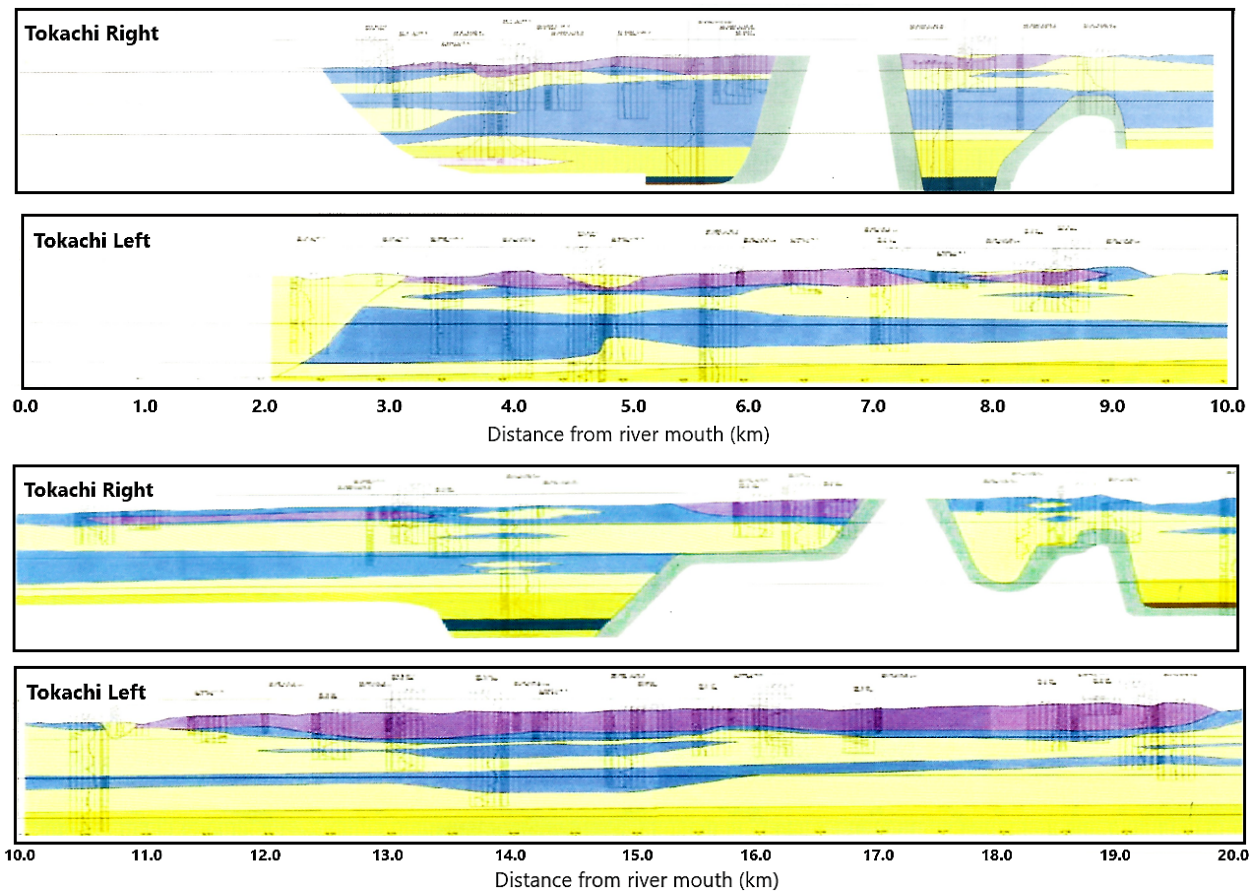


Figure 2.3 Longitudinal cross section along Tokachi River from the river mouth to 20 km. A consistent layer of peat (purple) is present under the levees.

## 2.4 DAMAGE DOCUMENTATION

After a strong seismic event, levees along major rivers are inspected by teams from the regional HDB offices. During the post-event reconnaissance, engineers visually inspect the entire length of the levees, documenting any signs of distress. The entire levee system is inspected and is a crucial detail indicating 1) segments without reported damage are confirmed null cases rather than unobserved performance, and 2) the performance data collected is not biased towards sections with distress. Levee sections with damage are noted, and accompanied by measurements of subsidence, differential settlement, and crack depth and width where applicable. Evidence of liquefaction, such as sand boils, are also noted where present. The information is collected from reports published by the Kushiro Development and Construction Office (KDCO) (1994, 2004), Civil Engineering Research Institute (CERI) (1993), and the Hokkaido River Disaster Prevention Research Center (2004, 2005).

The levees are discretized into 50 m segments as the basic unit. The performance, soil properties, and seismic demand is assumed to be constant within a segment. The occurrence of lack of damage for each segment is established from the reconnaissance reports, starting from the most general description of damage at the sectional level. Sections span tens to a few hundred meters, across which the range of crest settlement, width and depth of cracks, subsidence and differential settlement are given. All segments within the section are interpreted as damaged. This is followed by localized measurements based on cross-section surveys and plan views of crack distribution, as well as crack dimensions inferred from photographs. The local description supersedes the general descriptions. Levee segments without any observations are interpreted as having no damage.

The descriptions from the reconnaissance reports are mapped to damage levels (DL) indicative of overall performance based the metrics summarized in Table 2.2 (Kwak et al., 2016). If multiple observations are available and correspond to different damage levels, the most severe level is assigned.

The same scheme is adopted to allow meaningful comparison between the fragility function derived from the two studies. Figure 2.4 shows the distribution of damage levels for levees with and without peat in the foundations. Levees with peat foundations were shaken more strongly than levees on inorganic soil further upstream (and further from the earthquake source), therefore Figure 2.4 alone is inadequate to assess the relative fragility of levees on peat compared with levees on inorganic soil. The ground shaking level must also be considered. Figure 2.5 shows photographs for perspective on the severity of each damage level (KDCO, 1994).

Table 2.2 Damage level assignment

Damage Level	Crack depth (cm)	Crack width (cm)	Subsidence (cm)	Description
0	0	0	0	No damage reported
1	0-100	0-10	0-10	Slight damage, small cracks
2	100-200	10-50	10-30	Moderate damage, cracks or small lateral spreading
3	200-300	50-100	30-100	Severe damage, lateral spreading
4	> 300	> 100	> 100	Levee collapse

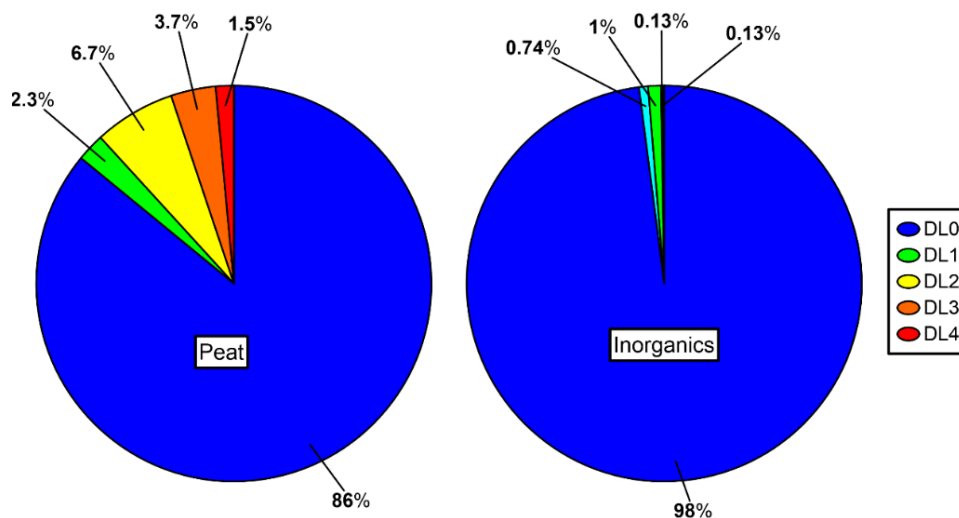


Figure 2.4 Distribution of damage levels for segments with peat or inorganic foundation material for both earthquakes.



Figure 2.5 Photographs after the 1993 and 2003 earthquakes showing the various damage levels. (a) Level 1, with minor cracking and no subsidence, (b) Level 2, with 20-30 cm of subsidence and cracks on the exterior face (c) Level 3, with subsidence of over 30 cm and (d) Level 4, with 60-225 cm of subsidence and 6 m wide cracks (KDCO 1994, 2004).

## 3 GEOPHYSICAL SITE INVESTIGATION

### 3.1 INTRODUCTION

Measurements of shear wave velocity at the levees are not routinely performed in Japan, but is crucial for performing site-specific ground response analysis. In addition, the effect of shallow soil layers on earthquake ground motions is typically represented by the time-averaged shear wave velocity in the upper 30 meters ( $V_{S30}$ ) in Ground Motion Models (GMMs). Professor Robert Kayen, Sean Ahdi and I performed geophysical measurements at 21 sites along Kushiro and Tokachi Rivers from 20 June to 4 July 2016. We focused on the downstream regions where peat is expected based on prior subsurface investigations and geology maps, and with the following considerations:

- Availability of nearby borings to provide stratigraphy information to guide inversion of dispersion curves to obtain shear wave velocity ( $V_s$ ) profiles;
- Prioritizing strong motion stations near/on levees without prior site characterization;
- Adequate spatial coverage representing full range of observed damage from both earthquakes.

We collected ambient noise for developing horizontal-to-vertical (H/V) spectral ratios to estimate site period, and spectral analysis of surface waves (SASW) measurements for developing dispersion curves for inversion. Original plans included drilling and sampling at the levee sites, but permissions could not be secured, and geophysical investigation is performed instead. A total of 23 ambient vibration measurements were made, with 10 along Kushiro River and the 13 along Tokachi River. A total of 21 SASW tests were conducted, with 10 along Kushiro River and the remaining 11 along Tokachi River. The SASW test and ambient noise recordings would ideally be co-located, but due to time constraints, they were performed concurrently. Each test location have a pair of ambient noise and SASW test,

except for 1048HK and 1049HK where two ambient noise measurements were made. The tests are spaced apart by 200-300 m to minimize the disturbance from footsteps and machinery from the SASW testing on the recordings. The test sites are shown in Figure 3.1 and 3.2.

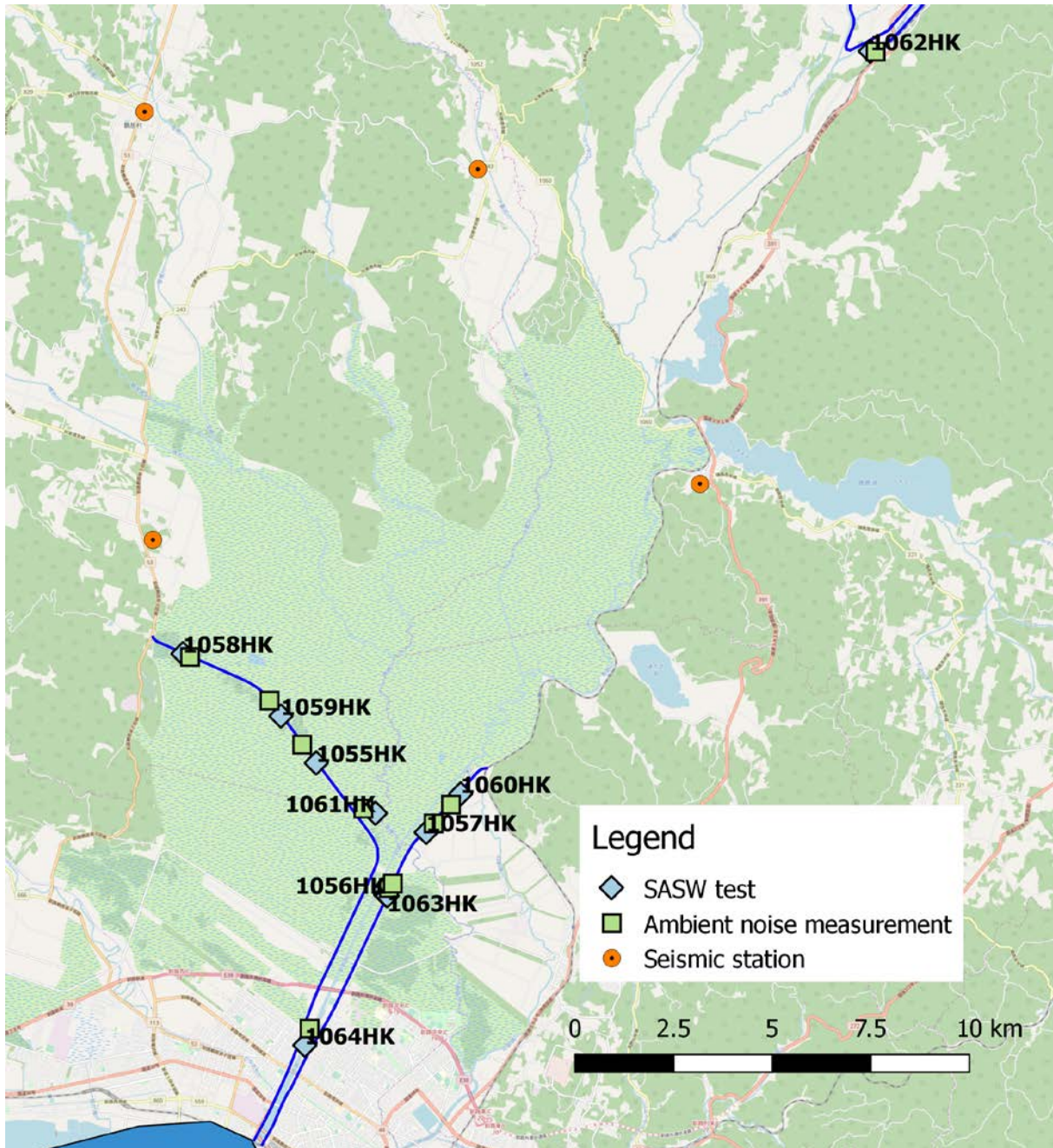


Figure 3.1 Test sites along Kushiro River are concentrated within the downstream basin, where peat deposits are present. Ambient noise measurements are performed close to SASW tests.



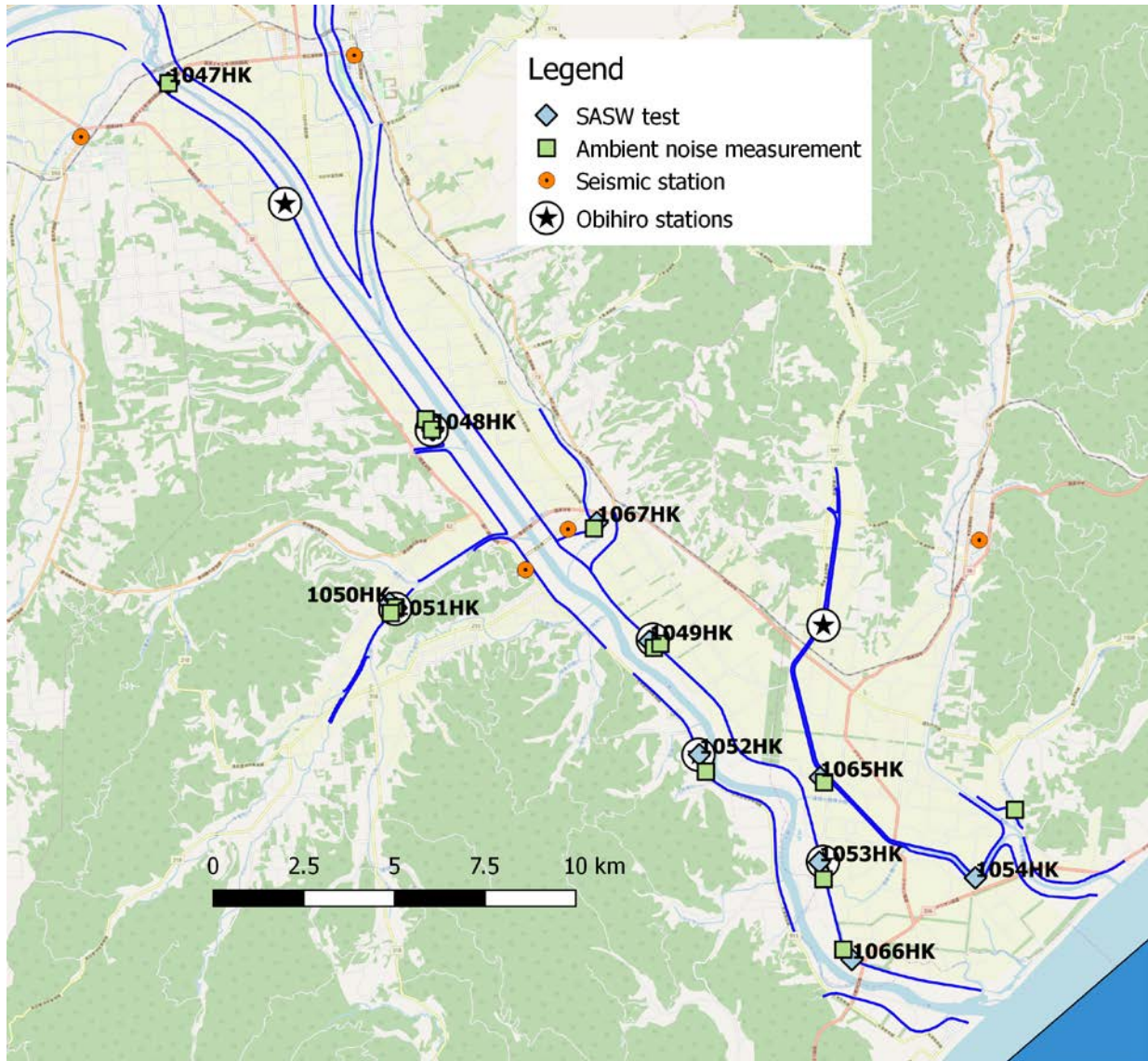


Figure 3.2 Test sites along Tokachi River. A local network of recording stations installed on the levees and are prioritized for testing.

### 3.2 AMBIENT NOISE RECORDINGS AND SITE PERIOD

The principal motivation for considering H/V spectral ratios is to identify the site period and possible resonance effects in the site amplification. The ambient vibrations were recorded using a triaxial seismometer and a Trimble REF TEK 130 data acquisition unit, and each record lasts between 60-120 minutes. The frequency at which the fundamental-mode resonance occurs in the site response ( $f_{peak}$ ) is

estimated from the peaks in plots of H/V spectral ratio against frequency. Shorter windows within the main record are selected to exclude transient signals (e.g., footsteps, passing vehicles and wind) in the open-source program Geopsy ([www.geopsy.org](http://www.geopsy.org)). Figure 3.3 shows ambient vibrations recorded at site 1050HK. Fourier spectra are computed for each time window and subsequently averaged.  $f_{peak}$  at each site are summarized in Table 3.1 and are generally lower along the Kushiro River than along the Tokachi River. The plots of the HV spectra and selected  $f_{peak}$  are presented in Appendix A. The peak frequency is used as a predictive variable for a region-specific ergodic site amplification model in Chapter 5.

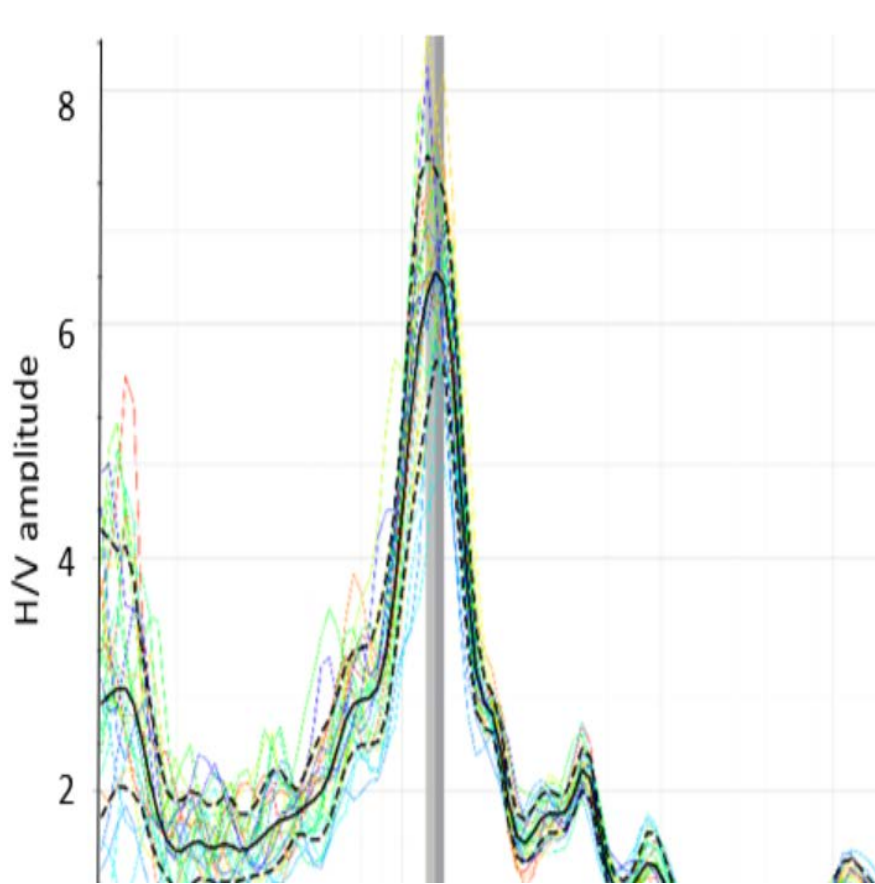
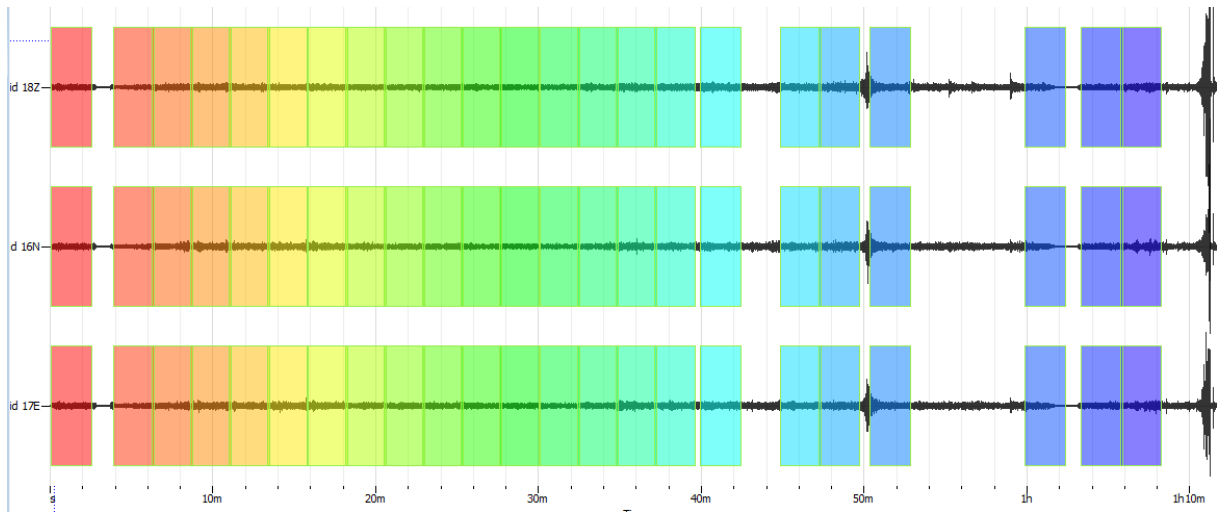


Figure 3.3 Ambient vibrations recorded at 1050HK site (top). Shorter segments are selected to exclude transient excitations. The H/V spectra ratio is computed for each windowed interval and the averaged spectra shown by the solid black line with a distinct peak around 1.2 Hz (bottom).

Table 3.1 Fundamental frequencies estimated from HVSR

Test Site	River	Date	Latitude	Longitude	Position	$f_0$ (Hz)
1047HK	Tokachi	6/25/2016	42.921	143.386	Riverside	0.27
1048HK-a	Tokachi	6/26/2016	42.839	143.472	Landside	1.50
1048HK-b	Tokachi	6/26/2016	42.836	143.474	Landside	1.60
1049HK-a	Tokachi	6/26/2016	42.782	143.549	Riverside	1.54
1049HK-b	Tokachi	6/26/2016	42.783	143.551	Landside	1.66
1050HK	Ushi	6/27/2016	42.792	143.462	Landside	1.19
1051HK	Ushi	6/27/2016	42.791	143.461	Crest	1.18
1052HK	Tokachi	6/27/2016	42.751	143.567	Riverside	1.08
1053HK	Tokachi	6/28/2016	42.725	143.606	Crest	0.87
1054HK	Uraoro	6/28/2016	42.742	143.671	Landside	2.30
1055HK	Kushiro	6/29/2016	43.089	144.374	Landside	0.32
1056HK	Kushiro	6/29/2016	43.057	144.401	Riverside	0.49
1057HK	Kushiro	6/29/2016	43.071	144.415	Landside	0.49
1058HK	Kushiro	6/30/2016	43.109	144.339	Landside	1.24
1059HK	Kushiro	6/30/2016	43.099	144.364	Landside	0.29
1060HK	Kushiro	6/30/2016	43.076	144.420	Landside	0.50
1061HK	Kushiro	7/1/2016	43.075	144.393	Marsh	0.39
1062HK	Kushiro	7/1/2016	43.247	144.552	Riverside	1.25
1063HK	Kushiro	7/2/2016	43.058	144.402	Crest	0.49
1064HK	Kushiro	7/2/2016	43.025	144.376	Riverside	0.59
1065HK	Shita	7/3/2016	42.749	143.607	Landside	1.75
1066HK	Tokachi	7/3/2016	42.708	143.613	Riverside	0.97

### 3.3 SPECTRAL ANALYSIS OF SURFACE WAVES

The SASW test measures surface wave dispersion data of near-surface layers, which is then inverted to profile the subsurface conditions. An active continuous swept-sine wave source is used with a notch-filter, which allows control over the frequencies generated and improves signal to noise ratio (Kayen et al. 2004). Our test setup consists of an electro-mechanical harmonic shaker driven by a signal

generator and two uniaxial seismometers arranged in a linear array. The instruments and the setup are pictured in Figure 3.4.

During each run, the shaker sweeps through a range of frequencies in stepped increments for a set number of cycles. The wavelength range of the dispersion curve was constrained by the source receiver and the inter-receiver distances. The frequency range and step size for each run depend on the thickness and stiffness of the underlying soil layers. A thick, soft soil layer requires lower frequencies to produce waves with sufficiently long wavelengths to penetrate and image it. The separation of the seismometers is increased after each run. Portions of the data with low coherence (low signal to noise ratio) is masked, and the phase angle between the seismometers is determined from the cross-power spectrum. The Rayleigh wave velocity through the underlying soil is given by:

$$V_R = f \times \frac{2\pi}{\phi} \times s \quad (3.1)$$

where  $f$  is the frequency of the shaker,  $\phi$  is the unwrapped, cumulative phase angle in radians, and  $s$  is the separation distance between the sensors. This is performed at all frequencies for each sensor separation.



Figure 3.4 The mass shakers for generating harmonic stepped waves (top left) and the seismometer (top right). The spacing between the seismometers are changed after each sweep by the mass shakers (bottom).

Ideally the individual dispersion curve for a single sensor spacing would overlap with curves for other sensor spacings to form a single composite curve as shown in Figure 3.5a. A few sites have scattered, non-overlapping curves as seen in Figure 3.5b, which may arise from unusual subsurface conditions present at the test site. Several of the ill-behaved test are measured on the levee crest where the presence of the stiffer levee material over the softer underlying peat may result in higher modes in the dispersion curve data. 11 sites have excellent data, and 5 sites have a subset of the measurements at select separations that are excluded. The remaining 5 sites have very scattered data and a composite curve cannot be reasonably fitted. Table 3.2 summarizes the test locations, with site photos and dispersion curves presented in Appendix A.

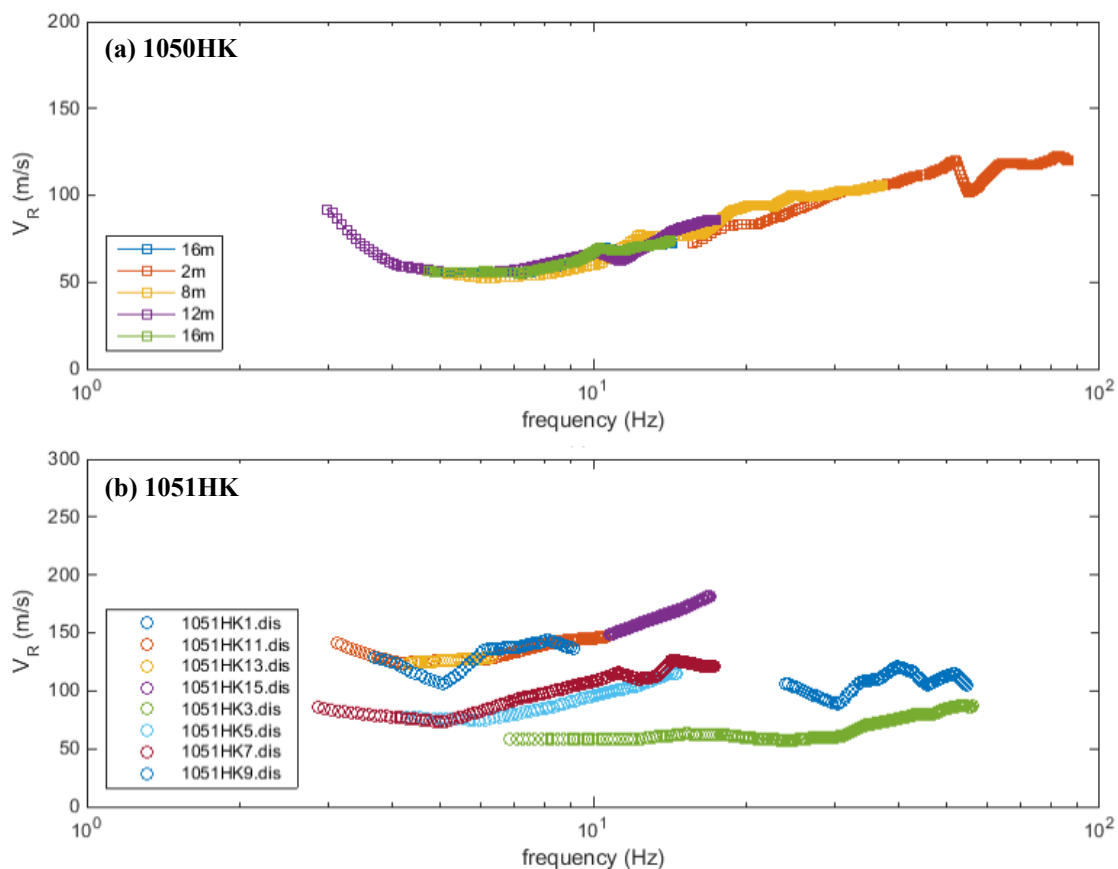


Figure 3.5 Experimental dispersion curves obtained from two adjacent SASW tests, a) is in the free-field and the individual curves are overlapping, b) is on the levee crest and the data is scattered with multiple modes.

Table 3.2 SASW test sites and data

Test Site	River	Position	Latitude	Longitude	Data Quality <sup>(a)</sup>	Nearest Boring <sup>(b)</sup>
1047HK	Tokachi	Riverside	42.9214	143.3857	Bad	-
1048HK	Tokachi	Crest	42.8359	143.4747	Bad	B-12-1
1049HK	Tokachi	Riverside	42.7837	143.5477	Excellent	B-2-2
1050HK	Ushi	Landside	42.7932	143.4602	Excellent	B-11-2
1051HK	Ushi	Crest	42.7920	143.4623	Excellent	B-11-1
1052HK	Tokachi	Crest	42.7557	143.5645	Excellent	B-5-1
1053HK	Tokachi	Riverside	42.7291	143.6049	Excellent	P-7-5
1054HK	Urahoro	Landside	42.7252	143.6575	Excellent	P-17-2
1055HK	Kushiro	Landside	43.0852	144.3782	Bad	H4-28
1056HK	Kushiro	Riverside	43.0553	144.3998	Excellent	H5-1
1057HK	Kushiro	Landside	43.0695	144.4124	Good	H2-72
1058HK	Kushiro	Landside	43.1100	144.3367	Good	H5-77
1059HK	Kushiro	Landside	43.0959	144.3672	Excellent	H5-69
1060HK	Kushiro	Landside	43.0782	144.4231	Excellent	H5-33
1061HK	Kushiro	Marsh	43.0738	144.3966	Excellent	H5-56
1062HK	Kushiro	Riverside	43.2467	144.5506	Good	H13-4
1063HK	Kushiro	Crest	43.0550	144.4003	Bad	H5-1
1064HK	Kushiro	Riverside	43.0210	144.3746	Good	H11-1
1065HK	Shita	Landside	42.7500	143.6052	Bad	P-20-2
1066HK	Tokachi	Riverside	42.7050	143.6159	Excellent	P-7-5
1067HK	Tokachi	Riverside	42.8130	143.5300	Good	P-14-2

<sup>(a)</sup>Condition of the composite experimental dispersion curve; "bad" denotes cases where the individual curves cannot be reasonably combined into a single curve and inversion is not performed.

<sup>(b)</sup>SPTs with stratigraphic information used to guide inversion.

The experimental dispersion curves are inverted to obtain the shear-wave velocity profiles, with layering constrained by the stratigraphy of neighboring borings. Robert Kayen applied the direct simplified inversion method (SIM) to obtain the  $V_s$  profiles (Pelekis and Athanasopoulos, 2011). The SIM directly inverts the surface wave dispersion data by considering the shape (i.e., slope, curvature) of the dispersion curve, and a penetration depth coefficient which is a function of the Poisson's ratio.



For 1050HK and 1056HK, the inversion is also performed using the Geopsy program. The approach differs from the SIM method in that a suite of trial layered earth models are generated and their resulting dispersion curves are compared with the experimental dispersion data. The forward computations for each trial earth model are based on the work originally developed by Thomson (1950) and Haskell (1953) and later modified by Dunkin (1965) and Knopoff (1964). A dispersion misfit value is computed for each trial model (Wathelet et al. 2004), and the "best" profile with the lowest misfit is selected.

The resulting  $V_s$  profiles are used to define soil profiles for ground response analysis in Chapter 6 and to estimate the time averaged shear wave velocity in the upper 30 m,  $V_{S30}$ , along the levees.  $V_{S30}$  is commonly used to represent site condition, and is calculated as,

$$V_{S30} = \frac{30}{\sum \frac{h_i}{V_{s,i}}} \quad (3.2)$$

where  $h_i$  and  $V_{s,i}$  are the thickness and shear wave velocity of the  $i^{\text{th}}$  layer, to a depth of 30 m. The profiles at the majority of the sites tested extended to depths less than 30 m as the shear wave velocities in the surficial layers are low. For those cases, extrapolation to  $V_{S30}$  is based on Midorikawa and Nogi (2015):

$$\log(V_{S30}) = c_0 + c_1 \log(V_{SZ}) + c_2 \log(V_s(z_p)) \quad (3.3)$$

where  $z_p$  is the profile depth,  $V_s(z_p)$  is the  $V_s$  at the base of the profile, and  $V_{SZ}$  is the time-average shear wave velocity to depth  $z_p$ .

The inversion procedures utilized only considered the fundamental mode of propagation. 3-D effective mode forward analysis may be more appropriate given the inversely dispersive velocity structure present at some of the sites, particularly where measurements are performed atop the levees. The

uncertainties of inverting the dispersion curves are not addressed in this study but recognized as an important consideration.  $V_{S30}$  is an averaged parameter and is likely stable, but as discussed in Chapter 6, the amplification characteristic of a soil column is sensitive to the boundaries and impedance contrasts in the  $V_S$  profile.

## **4 DETAILED ANALYSIS OF LEVEE SECTIONS**

### **4.1 INTRODUCTION**

A local network of strong motion stations located on levees implemented in Obihiro recorded ground motions during the 2003 **M** 8.2 Tokachi-oki earthquake. Japanese engineers provided detailed observations of levee damage induced by this event, and performed a total of 22 site investigations at various locations along the levees. The combination of ground motion measurements, detailed subsurface information, and observations of levee damage make this an unprecedented set of case histories.

In this chapter, typical methods of levee performance assessment (liquefaction susceptibility, triggering, and consequence) are applied to 10 selected levee cross sections having good performance and varying severity of damage. Recorded ground motions are presented first, followed by subsurface conditions and observations of damage. I analyzed the slope stability of the levee sections and estimated slope displacements for a rigid sliding block with the 2D limit equilibrium analysis software SLIDE (Rocscience, 2017). Liquefaction severity indices and Newmark displacements are considered in conjunction to predict a representative damage level and compared to the observed performance.

### **4.2 GROUND MOTIONS DURING THE 2003 TOKACHI-OKI EARTHQUAKE**

The Obihiro Development and Construction Department (ODCD) maintains a local network of seven strong motion recording stations to assess potential for damage and plan emergency responses after earthquakes. Each station has a pair of triaxial sensors on the crest and at the land-side toe of the levee, with the horizontal components oriented parallel and perpendicular to the levees as diagramed in Figure 4.1. The levees are within the active channel and sited on recent soft alluvial deposits, the  $V_{S30}$  are low.

Two additional stations were in the vicinity of the levees further inland. Details of the fault and rupture for the 2003 Tokachi-oki earthquake are described in Section 2.2. All recordings were filtered and processed according to PEER standards. The RoTD50 peak accelerations from the horizontal channels are summarized in Table 4.1 with the site properties of the stations. These recordings provide estimates of ground shaking intensities, as well as time histories to be used with the subsurface investigations to assess performance at nearby levee segments. The time series and acceleration response spectra for each station are shown in Figures 4.2-4.7. In general, the motion at the levee crest was higher than that at the levee toe, and the peak in the acceleration response spectrum on the crest tended to occur at an oscillator longer than or equal to that at the toe.

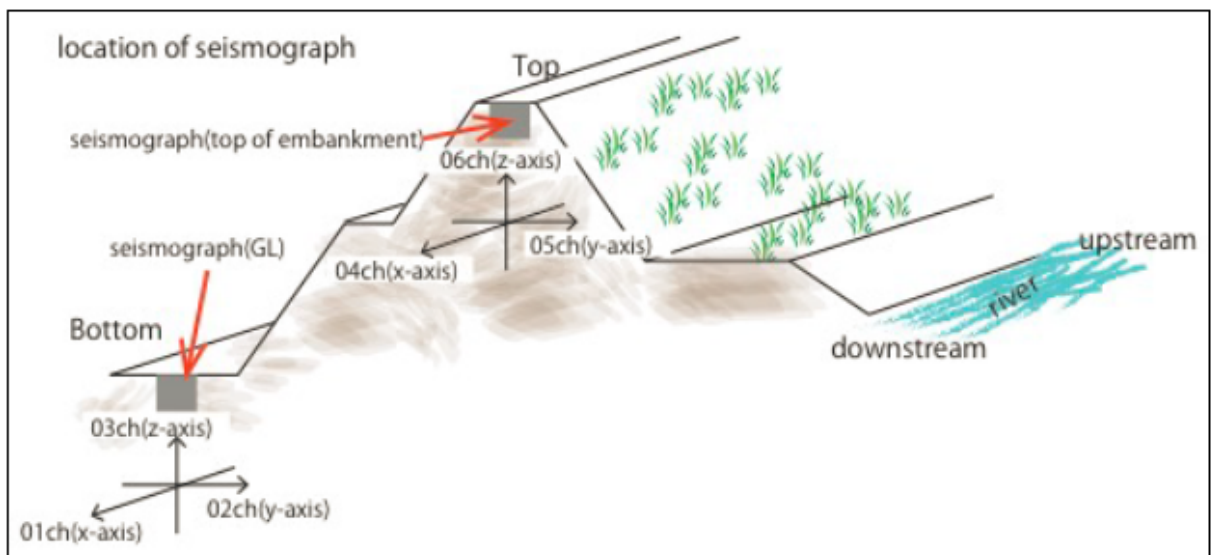


Figure 4.1 Sensor position and orientation at each ODCD strong motion station with respect to the levee. (Personal communication T. Sato).

Table 4.1 Recording stations near levees during 2003 Tokachi-Oki earthquake

Station Name	Station Code	Owner/ Network	Location		V <sub>S30</sub> (m/s)	PGA (g)		Liquefaction evidence <sup>(c)</sup>
			Lon (deg)	Lat (deg)		Toe	Crest	
Toitokki	TTK	ODCD	143.6043	42.7281	117.2 <sup>(a)</sup>	0.648	0.481	Yes
Rabirai	RB	ODCD	143.5642	42.7556	150.5 <sup>(a)</sup>	0.431	0.416	Yes
Horooka	HK	ODCD	143.5489	42.7841	102.2 <sup>(a)</sup>	0.350	0.602	No
Reisakubetsu	RSB	ODCD	143.4744	42.8359	181.4 <sup>(a)</sup>	0.668	0.706	No
Gyushubetsu	GSB	ODCD	143.4622	42.7921	130.8 <sup>(a)</sup>	0.307	0.498	Yes
Higashiinaho	HNH	ODCD	143.6063	42.7876	211.5 <sup>(b)</sup>	0.656	0.541	No
-	TKCH07	NIED	143.5203	42.8114	140.1 <sup>(b)</sup>	0.371	NA	No
-	51563	JMA	143.5060	42.8014	302.2 <sup>(b)</sup>	0.550	NA	No

<sup>(a)</sup>From Vs profile inverted from SASW testing, extrapolated to 30 m where necessary

<sup>(b)</sup>Estimated from geomorphology and slope proxy based on Wakamatsu and Matsuoka (2013)

<sup>(c)</sup>Reported from the reconnaissance survey

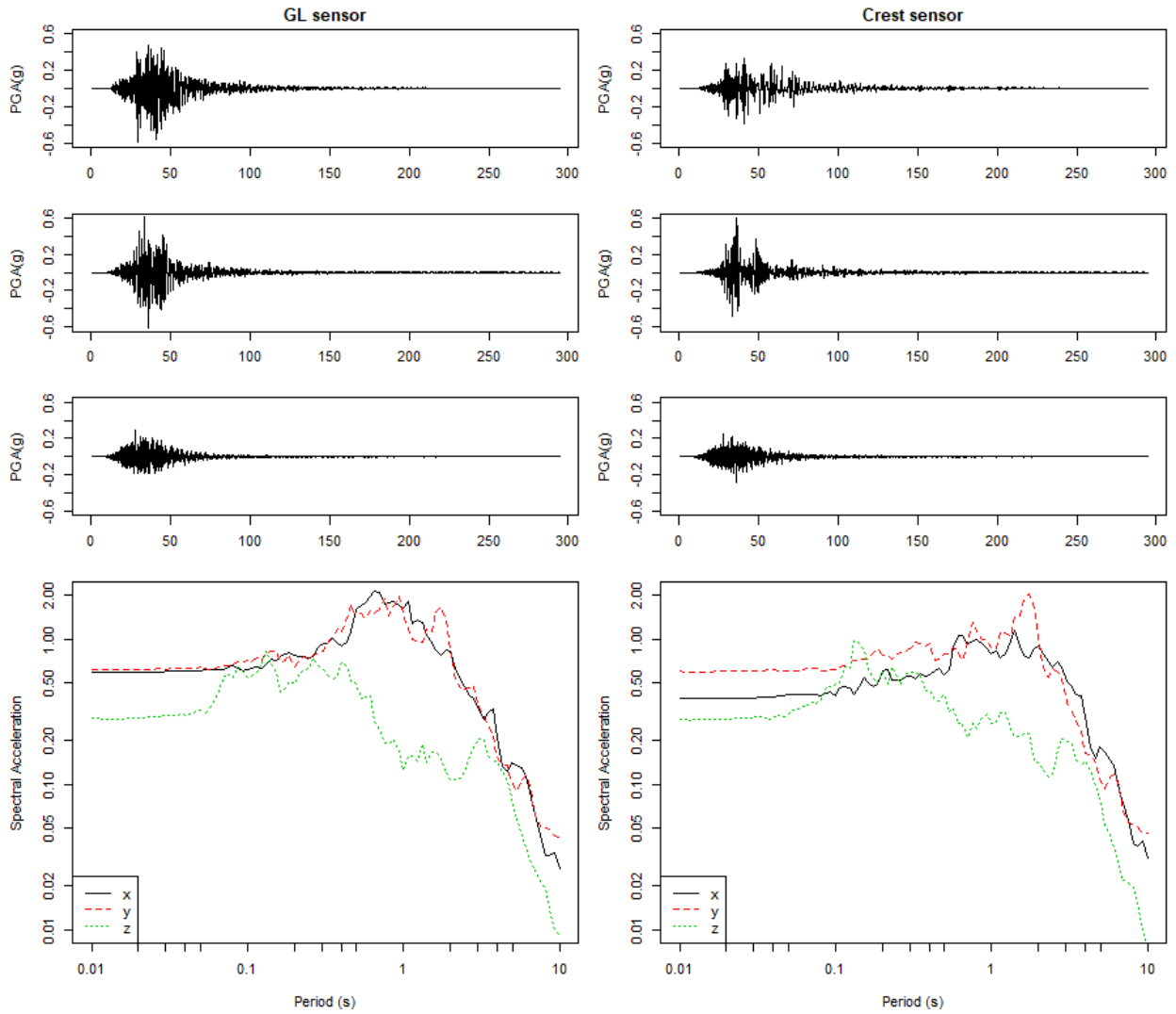


Figure 4.2 Time histories and response spectra at Toitokki station (TTK).

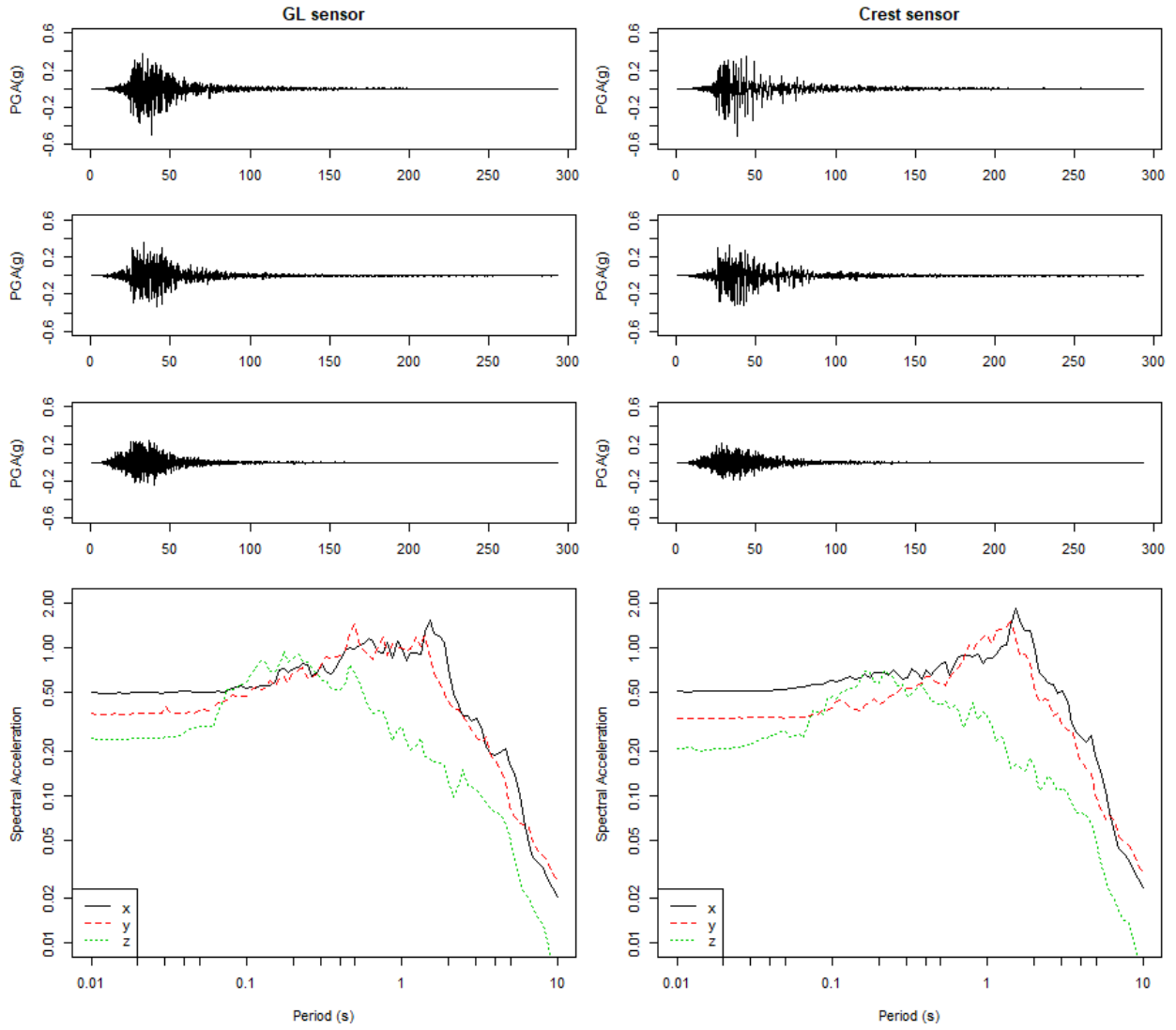


Figure 4.3 Time histories and response spectra at Rabirai station (RB).

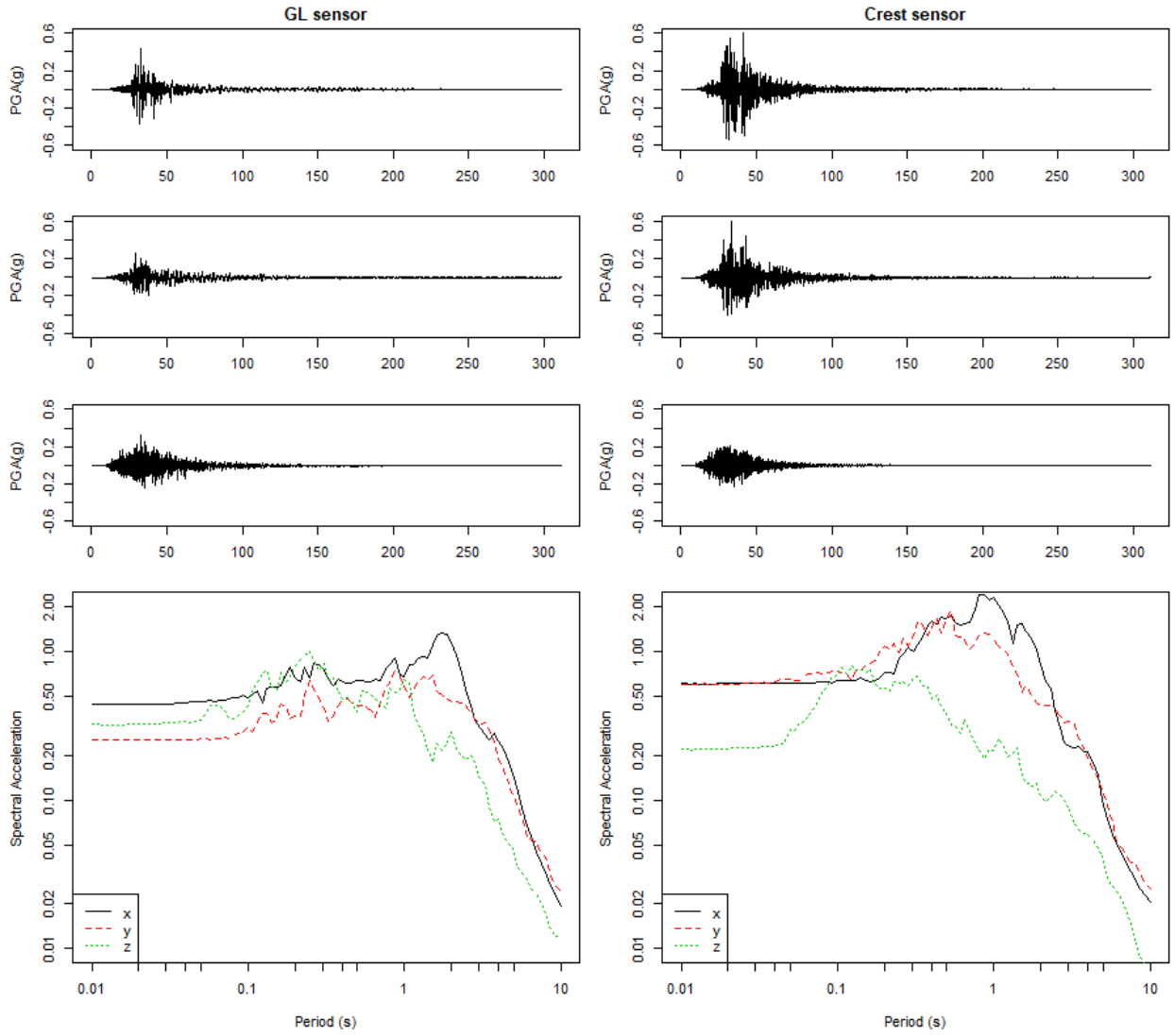


Figure 4.4 Time histories and response spectra at Horooka station (HK).



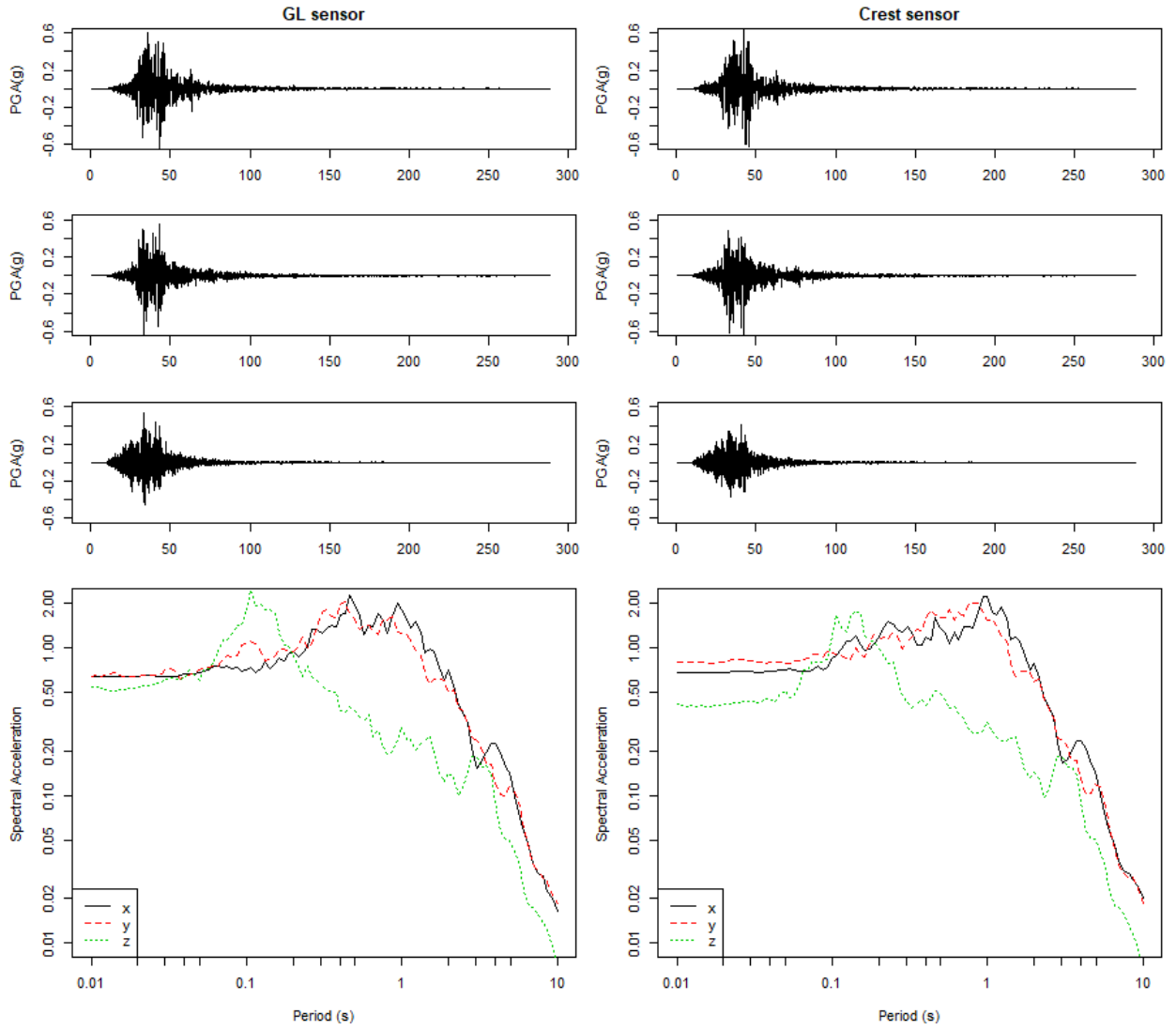


Figure 4.5 Time histories and response spectra at Reisakubetsu station (RSB).

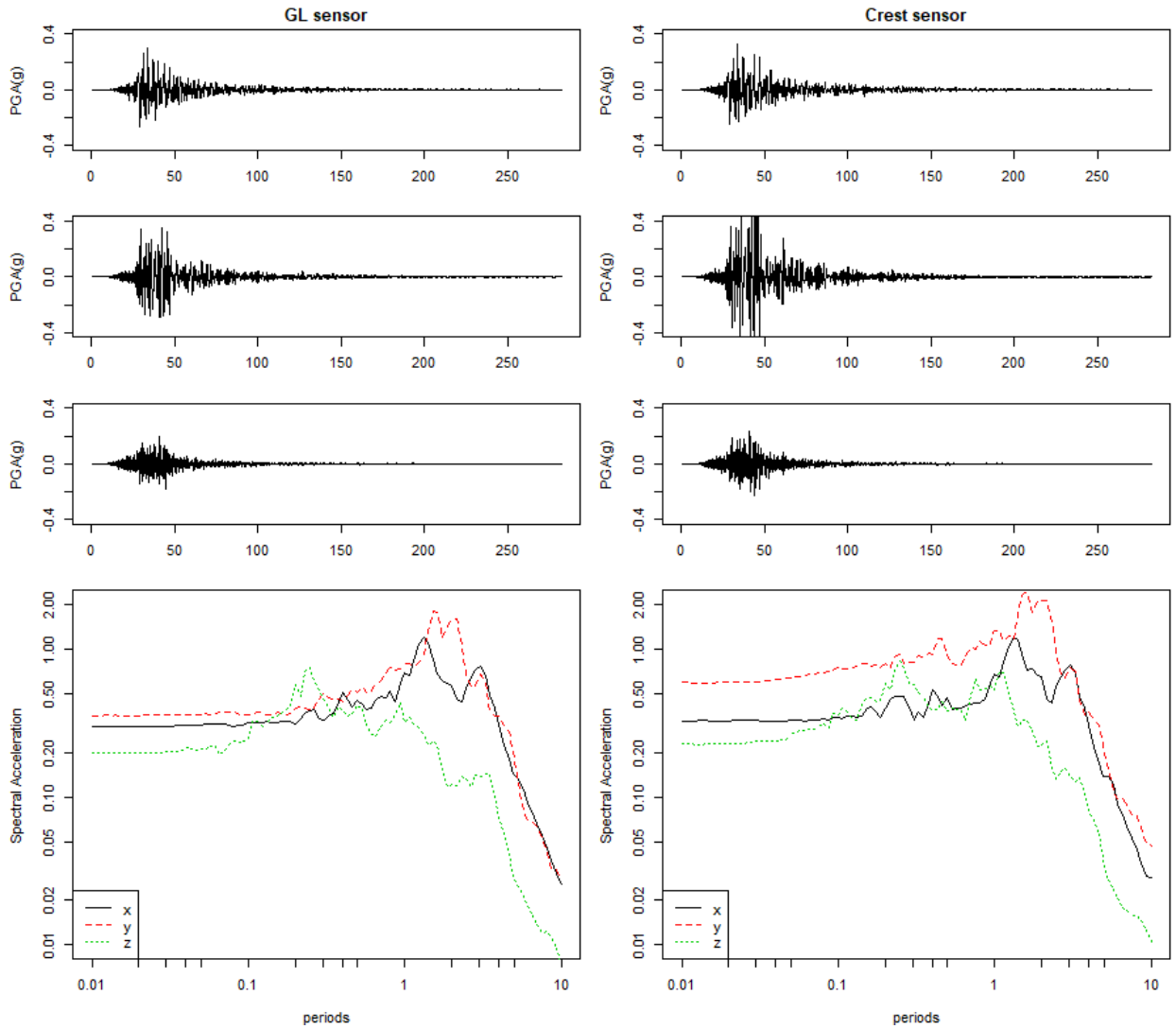


Figure 4.6 Time histories and response spectra at Gyushubetsu station (GSB).

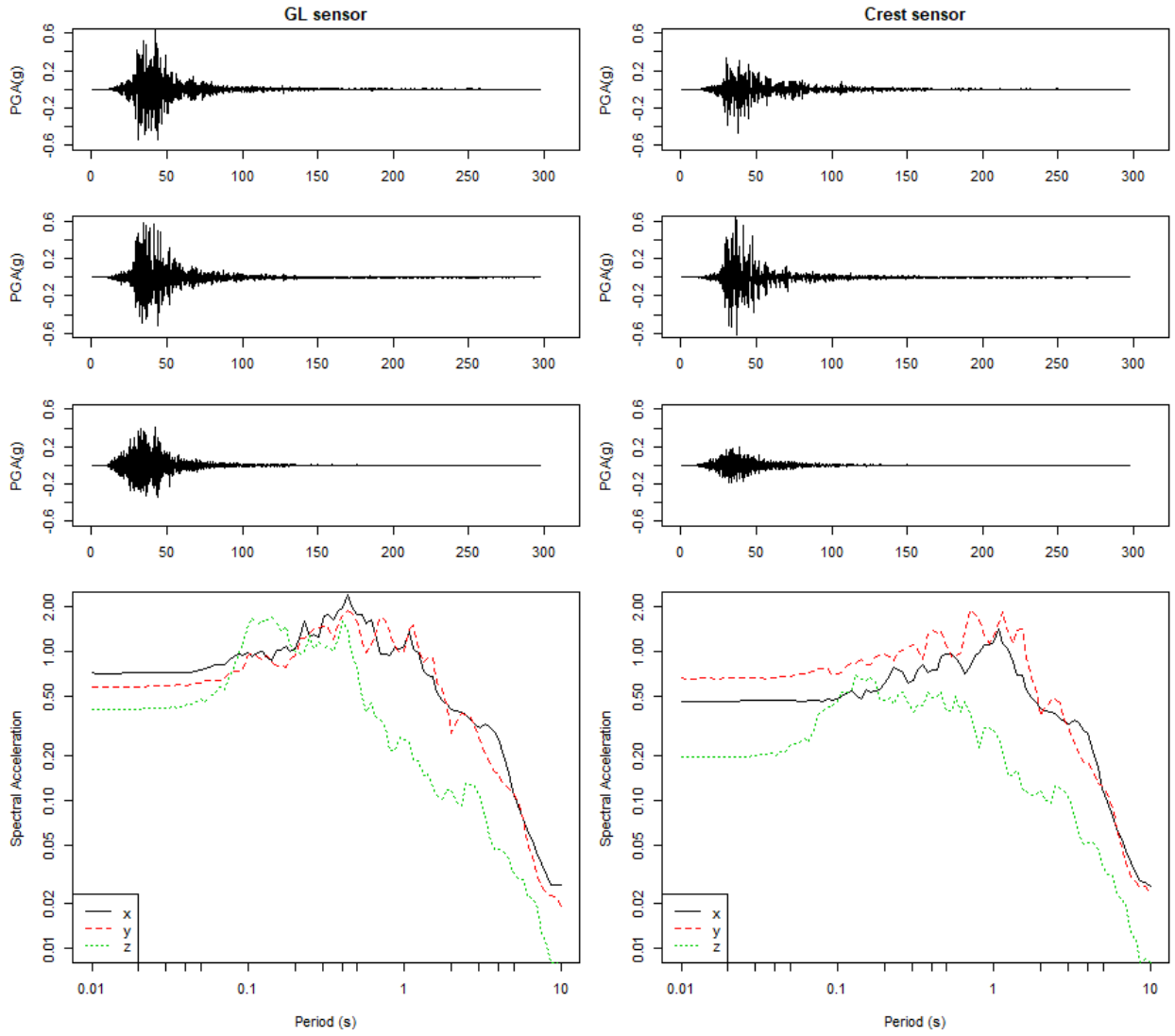


Figure 4.7 Time histories and response spectra at Higashiinaho station (HNH).

### **4.3 SUBSURFACE CONDITIONS AND OBSERVATIONS**

Immediately after the 2003 Tokachi-oki earthquake, engineers from local management agencies visually inspected all levee systems along the major rivers in the region. Visible damage was reported and accompanied by measurements of subsidence, differential settlement and cracks and evidence of liquefaction (e.g., sand boils) were encountered (Hokkaido River Disaster Prevention Research Center, 2004). The engineers did not explicitly report undamaged levees. However, since all of the levees were inspected, a lack of reported damage is interpreted as evidence of a lack of damage. Besides the initial inspection, additional detailed investigations were conducted at 22 locations in the months following the earthquake, as shown in Figure 4.8, concentrating on the downstream region. The investigations included Standard Penetration Tests (SPTs), Cone Penetration Tests (CPTs), open excavations and laboratory testing to study the failure mechanisms and evaluate the performance of the existing structure, and to inform subsequent repair efforts.

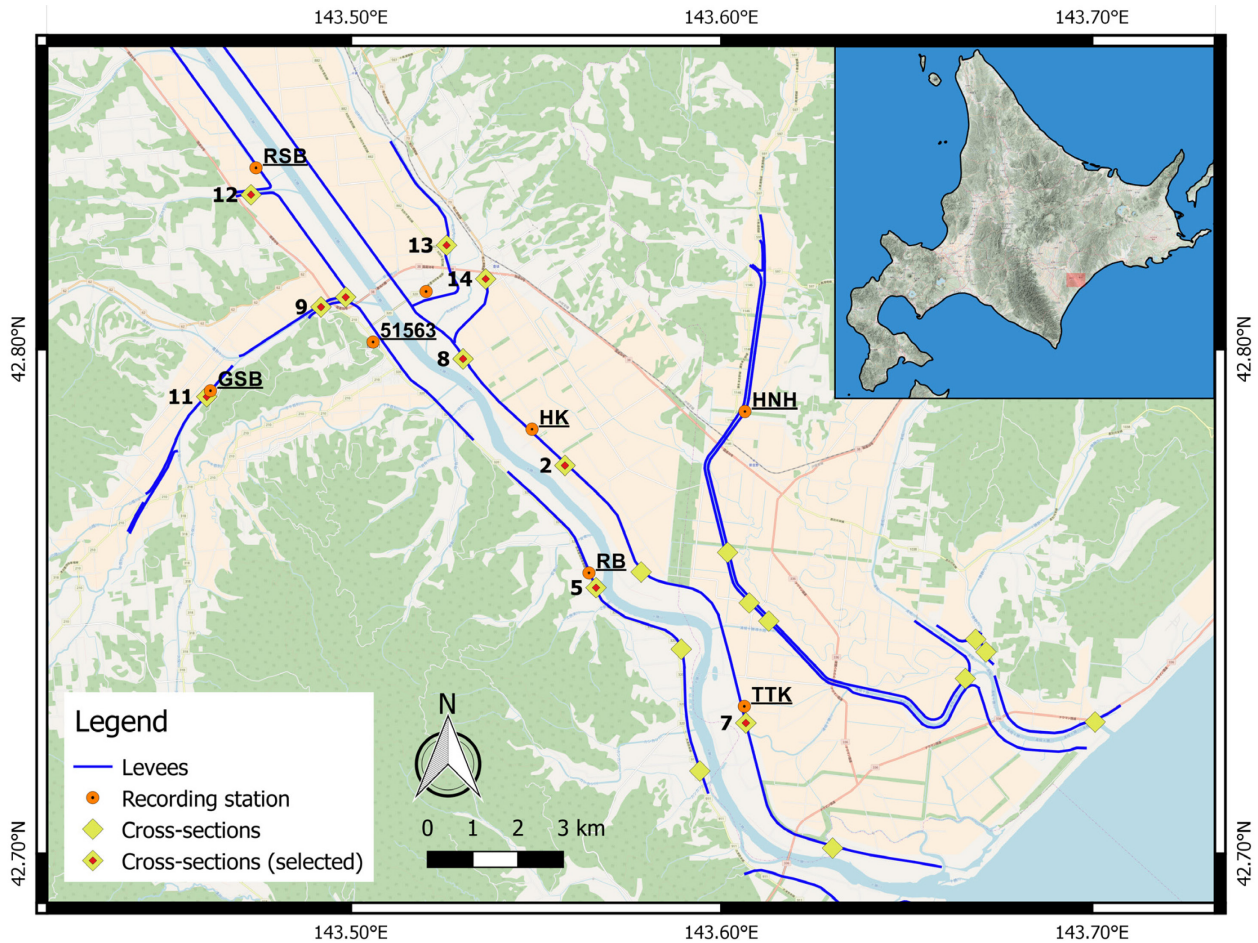


Figure 4.8 Downstream region of Tokachi River with strong motion recording stations and post-earthquake investigations performed after the 2003 Tokachi-oki earthquake.

We selected 10 sites that were near the ODCD recording stations for detailed analysis. These sites exhibited varying levels of damage, and numbering of the sections here follows the numbering from the reconnaissance investigation for consistency. Sites 2, 5, 7, 8 are along the main Tokachi River, and levees rest atop a thick peat layer. The levees along the Tokachi River are broad and gently sloped, with side slopes of around 1:4 to 1:6. They were expanded in the late 1990s to reduce problems associated with subsidence on the soft peat soils and provide a larger cross-section to prevent loss of water retention capabilities should failure occur. Sites 9 -14 are along the tributary streams, with thinner peat soils beneath the levees and the steeper side slopes around 1:2.5 to 1:3. The location and performance at each site is summarized in Table 4.2.

Table 4.2 Location and performance of selected levee sections

Section	Location		Nearest station	Crack dimension		Subsidence (cm)	Damage Level	Liquefaction evidence
	Lon (deg)	Lat (deg)		Width (cm)	Depth (cm)			
2	143.558	42.777	HK	120-140	75-120	30-70	4	Yes
5	143.566	42.753	RB	285	80	-	3	Yes
7	143.607	42.726	TTK	120	30	-	2	None
8	143.531	42.798	TKCH07	120-195	25-50	40	3	Yes
9	143.492	42.808	51563	130	80	-	3	Yes
10	143.498	42.810	51563	200	270	Large (~50)	4	Yes
11	143.461	42.791	GSB	105	74	220	4	Yes
12	143.473	42.831	RSB	~50	~100	50-70	3	Yes
13	143.526	42.820	TKCH07	0	0	0	0	None
14	143.537	42.814	TKCH07	110	~60	-	3	None

### **4.3.1 Section 2 - Tokachi River left bank**

Section 2 is located around 16 km upstream of the river mouth and 300 m from the active channel. The closest station is HK, located on the levee around 1000 m upstream from Section 2 (Figure 4.9). The levee was constructed in stages, with the core placed in the 1950s and composed mainly of clean sands with small amounts of gravels and silts. The levee section was broadened in the late 1990s on the land-side, using fill with a higher fines content classifying as silty sands to silts. Groundwater was encountered within the levee fill during site investigations after the earthquake.

The levee is underlain by a laterally continuous peat layer about 3 to 4 m thick. The blow count ranges from 1-5 and is highest below the levee crest. The peat transitions into a thin clay layer (Ac) of around 1 m thick. Below that, the sand content increases with depth, and is mainly clean sands (As) at 10 m below the free-field ground surface. The resistance also picks up rapidly in this layer.

The segment was severely damaged with extensive longitudinal cracks on the crest. Crack depths and widths up to 140 cm and 120 cm were observed, with sand boils visible in and around the cracks on the access road on the levee crest (Figure 4.10). Subsidence of 30-70 cm and settlement were observed on the land-side portion of the levee.

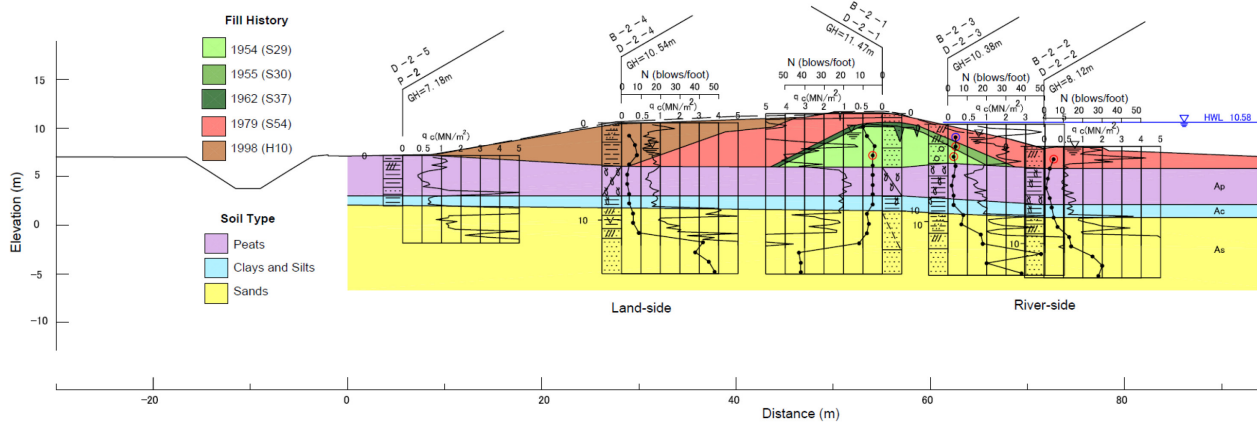
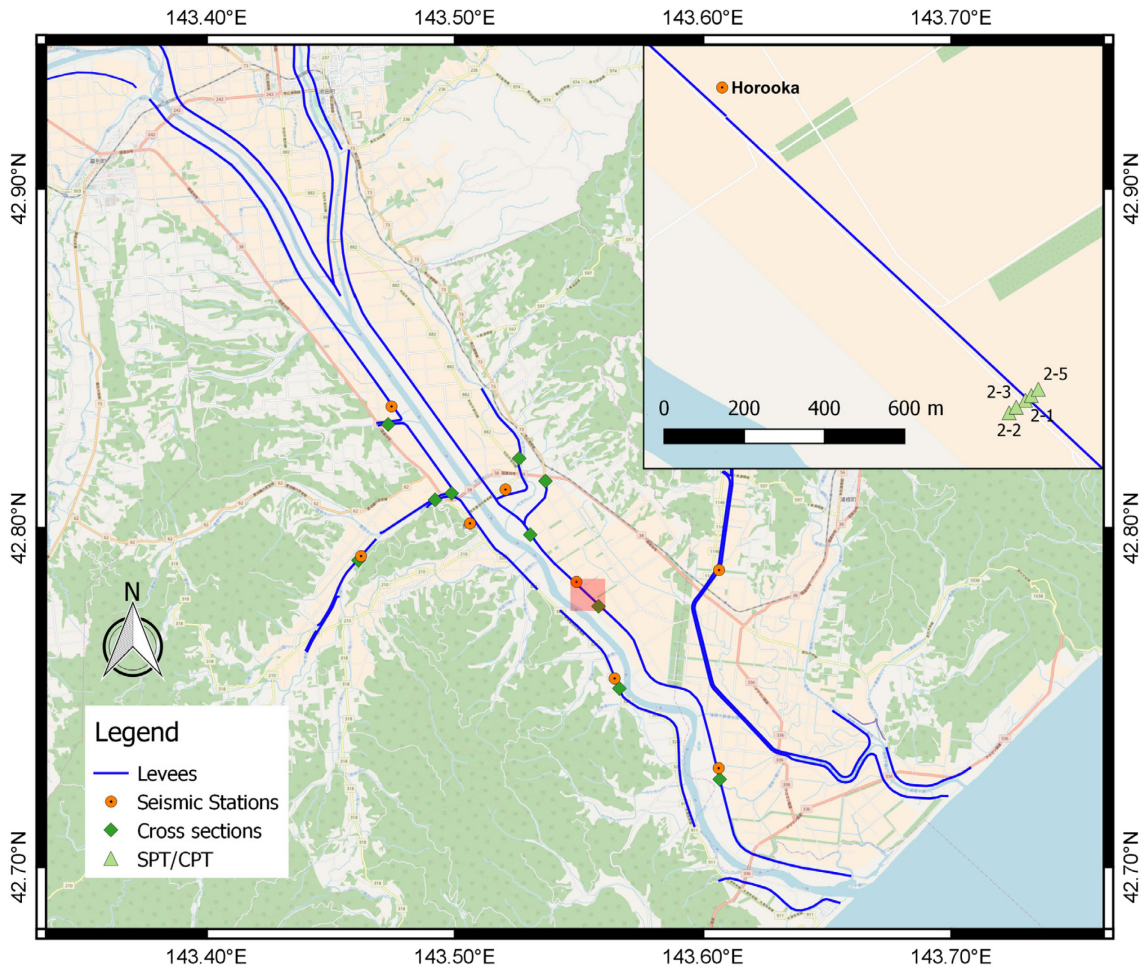


Figure 4.9 Vicinity map and subsurface investigation for Section 2.



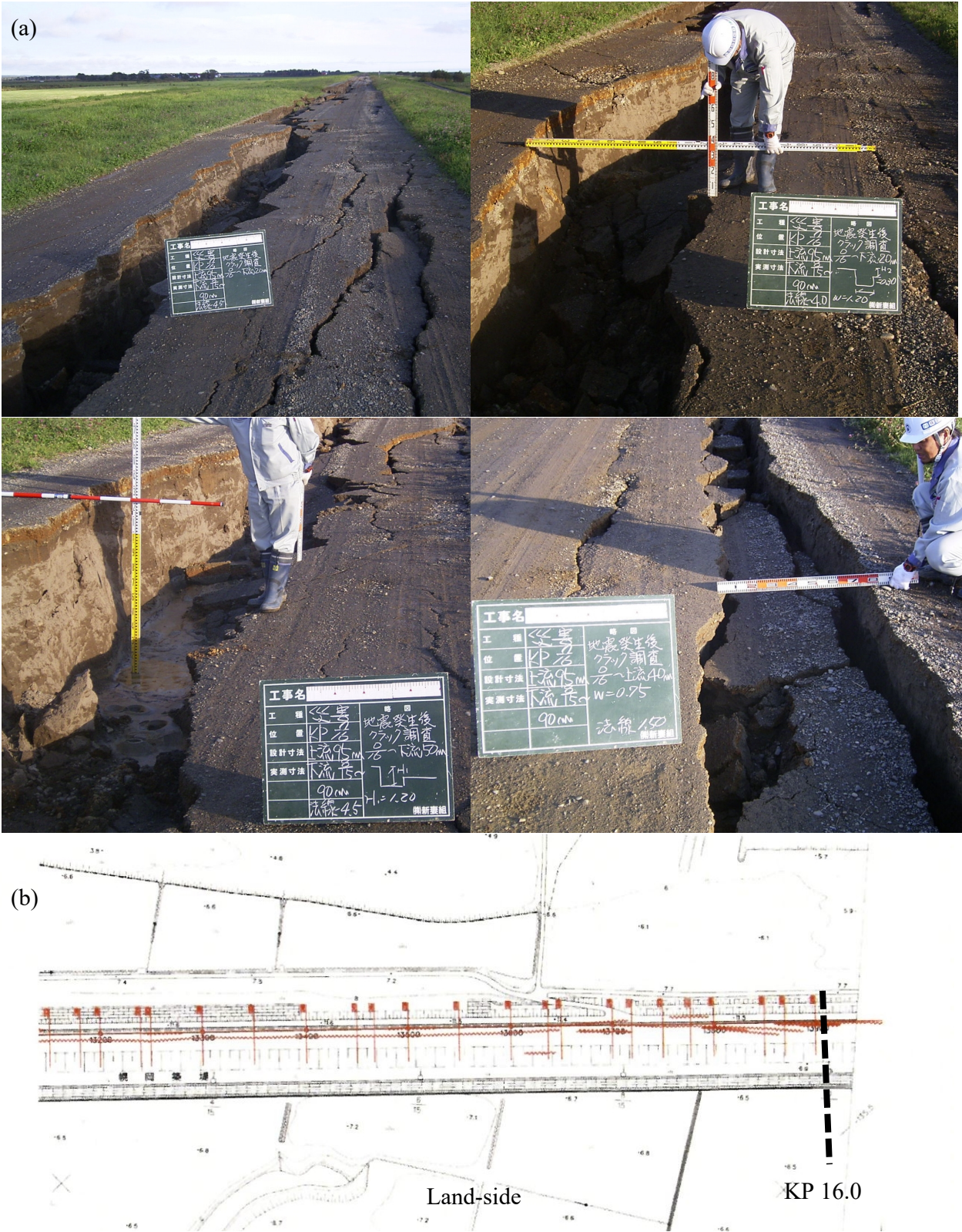


Figure 4.10 (a) Extensive cracking on access road and sand boils visible in some of the cracks at Section 2. (b) Plan view showing distribution of longitudinal cracks on levee crest.

### **4.3.2 Section 5 - Tokachi River right bank**

Section 5 is located on the outer bend around 100 m from the river channel and around 13.2 km from the river mouth. The RB station is located on the levee on the same side of the river, around 400 m upstream. The original levee was constructed in 1965-1966 with clean sands containing small amounts of gravels. The levee was subsequently expanded towards the river in 1989 using sandy fill containing low to moderate amounts of silt. The water level is elevated in the levee body, likely from several precipitation events earlier in the month.

A continuous layer of peat and organic clays underlies the levee, around 5 m thick on the land-side and thinning to around 2 m on the river-side. The material transitions to sand below the organic layer, with a clayey seam on the land-side tapering out under the levee crest. The blow count ranges between 10-20 in the sandy layer and is lower in zones with higher fines content.

A short segment of the levee was severely damaged, with longitudinal cracks, settlement and slumping on the land-side slope only (Figure 4.12). Displacement was not observed in the free-field peat away from the levee, suggesting that the failure is contained within the body of the levee.

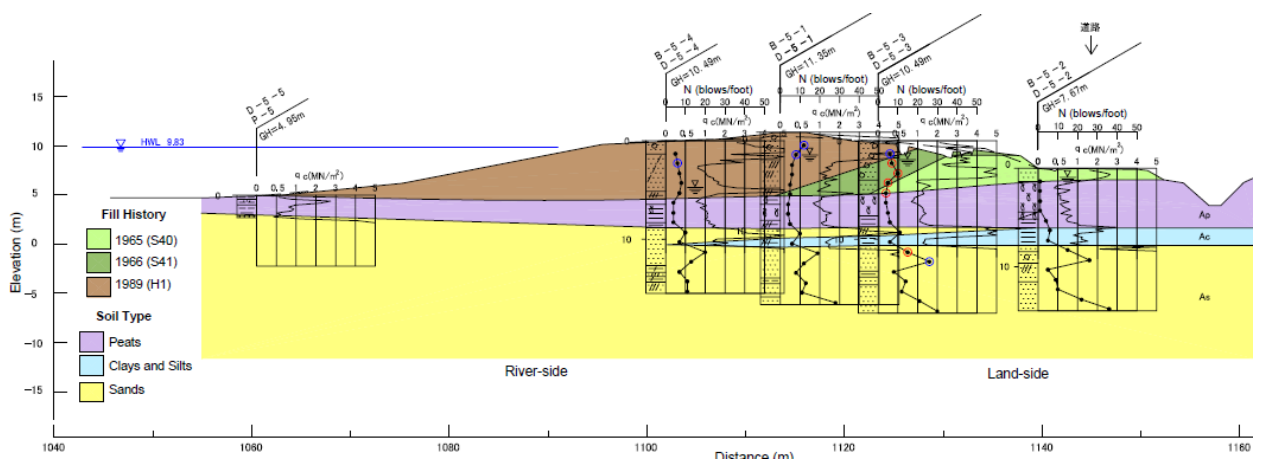
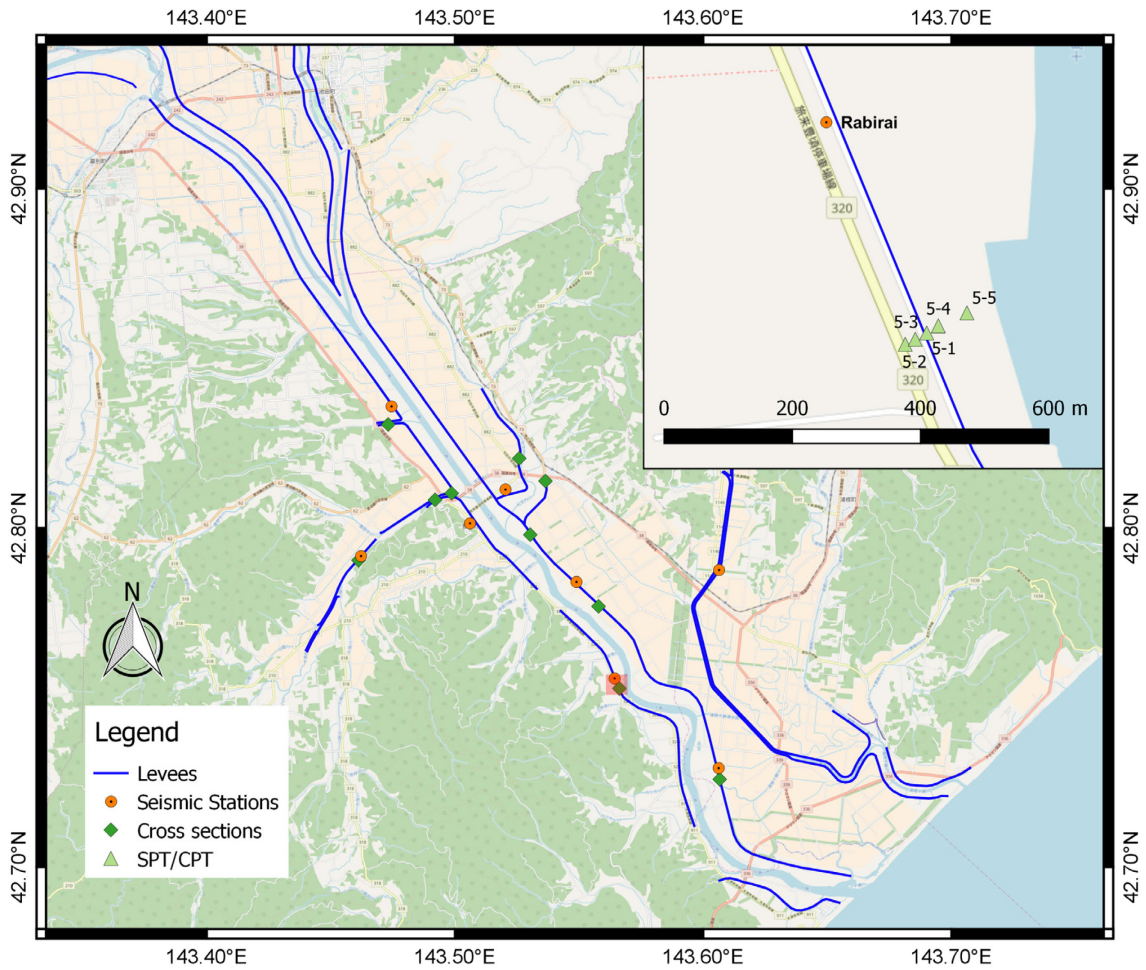


Figure 4.11 Vicinity map and subsurface investigation for Section 5.

(a)



(b)

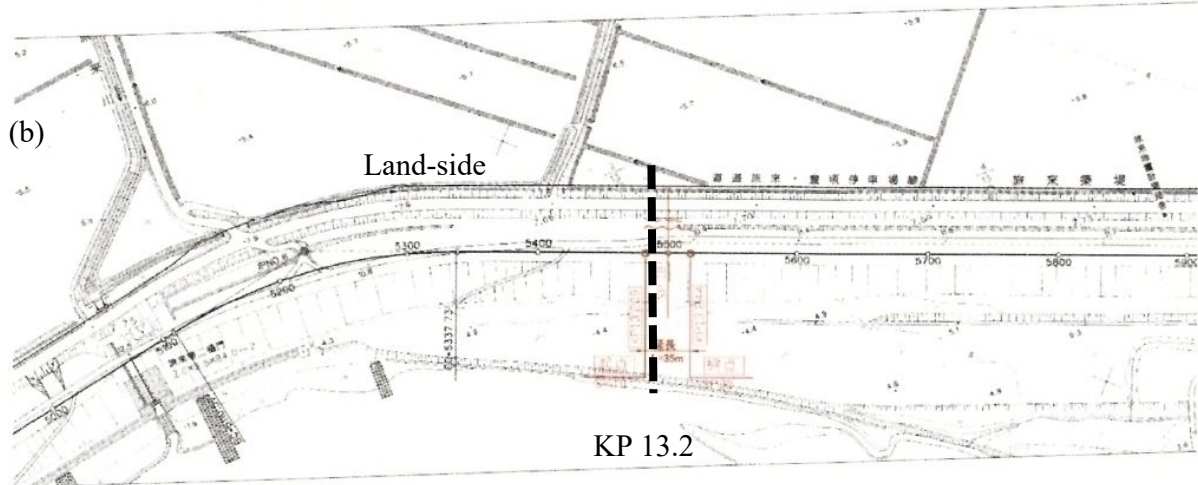


Figure 4.12 (a) Severe localized damage at Section 5 on the land-side slope, with deep cracks at the land-side edge of the access road on the levee crest. (b) Plan view of longitudinal cracks observed.

### **4.3.3 Section 7 - Tokachi River left bank**

Section 7 is around 700 m inland from the river channel and 8.6 km from the river mouth. TTK is the closest station around 400 m upstream and on the same side of the river (Figure 4.13). The land-side portion of the levee is mainly sand with minor amounts of gravels. The silt content is higher on the upper and riverside portion of the levee. The construction history of the levee here is unknown, but expected to be similar to neighboring sections where the initial sandy core is expanded in phases. The ground water is elevated within the levee body.

A continuous peat layer (Ap) around 4 m thick underlies the levee and extends out into the free-field, with blow counts of 1-3. Under the peat is a thin silty sand layer (As1), followed by a silty layer (Ac), which finally transitions into stiffer, relatively clean sands at around 10 m below the free-field surface.

The section suffered moderate damage from displacement of the land-side slope, concentrated mostly within a 50 m stretch of the levee. Cracks up to 120 cm deep and 30 cm wide are observed on the crest access road (Figure 4.14). Evidence of liquefaction was not observed at this location.

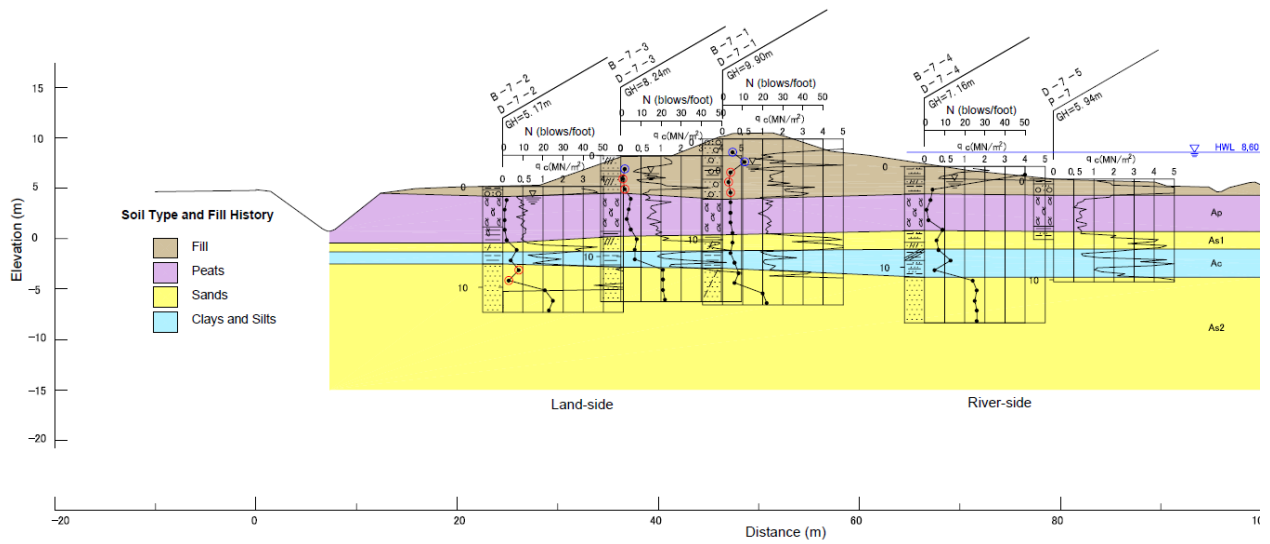
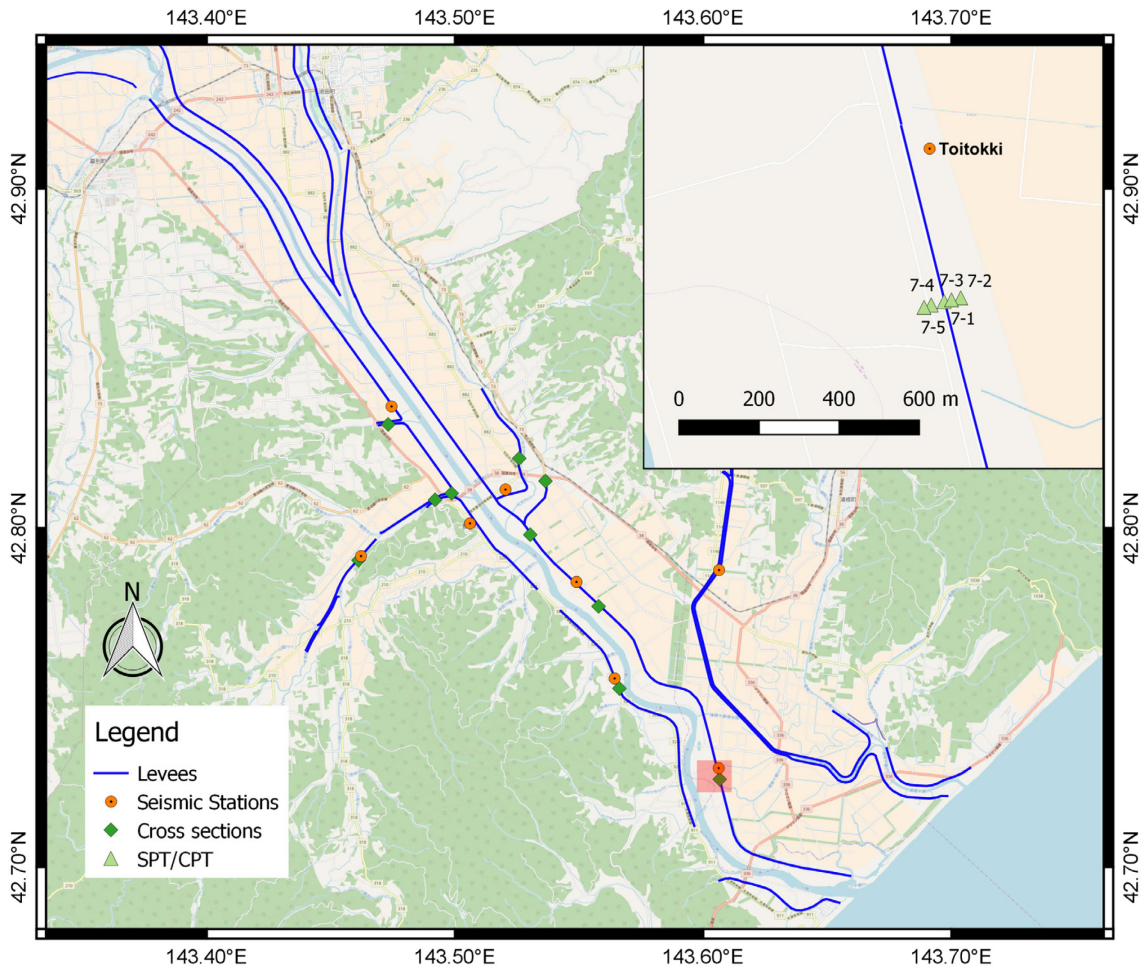


Figure 4.13 Vicinity map and subsurface investigation for Section 7.

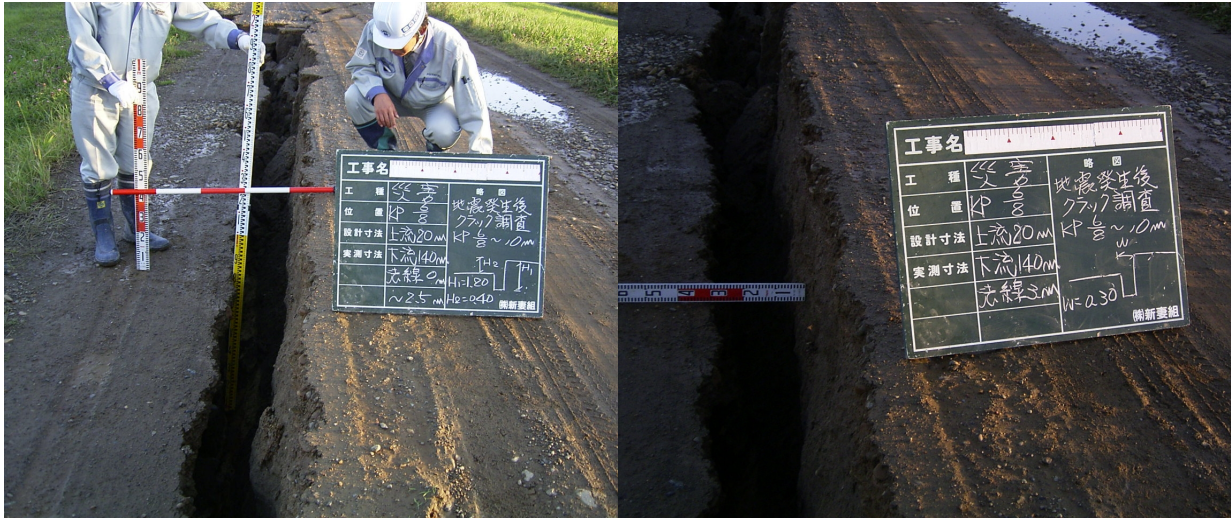


Figure 4.14 Cracks and differential settlement on the crest access road at Section 7.

#### 4.3.4 Section 8 - Tokachi River left bank

Section 8 is located near the intersection of the Tokachi River and Satsubunnai River, around 19.2 km upstream from the river mouth. The nearby stations are TKCH07 and 51563, both located upstream and off the levee in the free-field (Figure 4.15). The core of the current levee was placed in 1952 and expanded on both slopes in two phases to create gentler slopes while maintaining the original crest. The original fill was predominantly sand with minor amounts of silt. The 1978 fill has higher fines content, and prior testing shows some plasticity. The fill placed in 1996 has high fines content and significant plasticity in the upper zones, transitioning to lower fines in the lower portion. The ground water is elevated within the levee.

Directly underneath the fill is an interbedded layer of peat and clay (Ap), with visible peat fibers, around 5-6 m thick. The material is very soft, with blow counts around 2-3 in the free-field and increasing to around 5 under the levee. The organic content decreases with depth and transitions to a 1-2 m thick layer of clayey silts (Ac1), followed by a sandy layer with low to moderate fines content (As1), which tapers from about 4 m on the riverside, to around 0.5 m on the land-side.

Subsidence up to 40 cm was present over a broad region of the levee, and cracks around 120-195 cm deep and 25-50 cm wide were reported. Sand boils were observed on the access road on the levee crest. Cracking and settlement are concentrated near the crest, likely resulting from liquefaction and settlement of the older fill material.

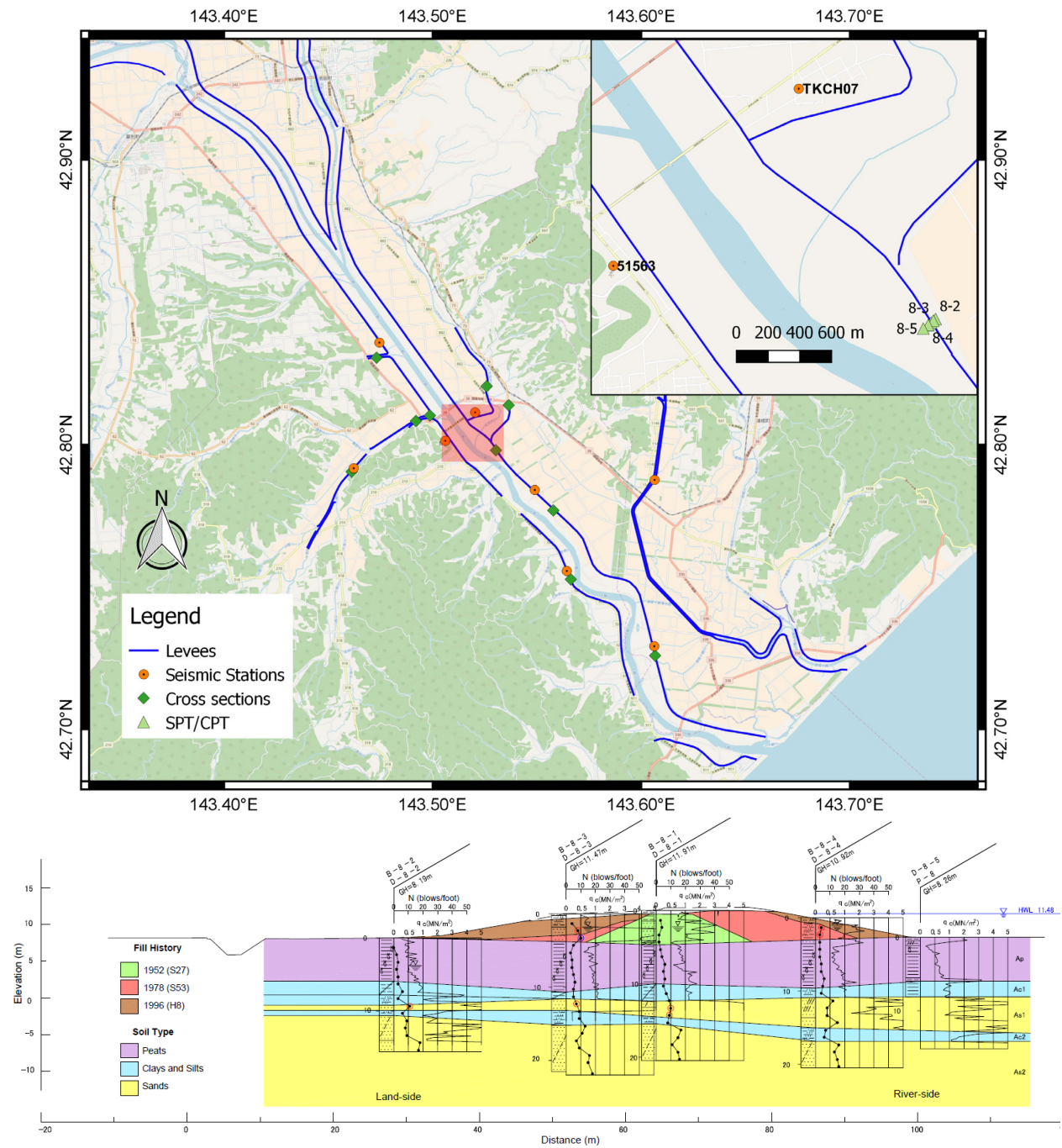


Figure 4.15 Vicinity map and subsurface investigation for Section 8.





Figure 4.16 Cracking on the crest (top) and land-side slope (bottom left) at Section 8. Sand boils on crest access road downstream (bottom right).

### 4.3.5 Section 9 and 10 - Gyushubetsu River

The Gyushubetsu River joins the Tokachi River on the right bank around 21 km upstream from the river mouth. Sections 9 and 10 are located close to the intersection, on the right and left bank respectively. The nearest station is 51563 located downstream along the Tokachi River (Figure 4.17).

The original date of construction is unknown for both locations. Section 9 was enlarged in 1972 to have a higher crest elevation. The fill is composed of sand and gravelly sand, and the ground water is elevated within the levee. The levee has settled around 1 m into the underlying peat layer (Ap), which is about 2 m thick directly beneath the crest and 3-5 m thick in the free-field. A 2 m continuous clay layer (Ac) lies immediately below the peat layer, and transitions into sands (As) with fines content decreasing with depth (Figure 4.18).

The section is moderately damaged, with cracks up to 130 cm deep and 80 cm wide on the access road on the levee, and settlement of the levee crest and the land-side slope (Figure 4.19).

Section 10 underwent 2 major expansion in 1961 and 1980 on the land-side slope (Figure 4.20). The earlier fill was predominantly sand with minor amounts of silt. The fill placed in 1980 contained moderate amount of silts with small amounts of gravels. A layer of peat and organic clay (Ap, Ac1) lies directly below the levee, with the organic content highest near the surface. Below the material alternates from silty sands (As1) to sandy silts (Ac2), and back to silty sands (As2) with fines content decreasing with depth. Layers with higher sand content are reflected by increased cone tip resistance.

The section was severely damaged; cracks up to 200 cm deep and 270 cm wide were observed on the roadway on the levee crest. The slope slid and budged outwards, and was accompanied by subsidence of the levee crest. (Figure 4.21).

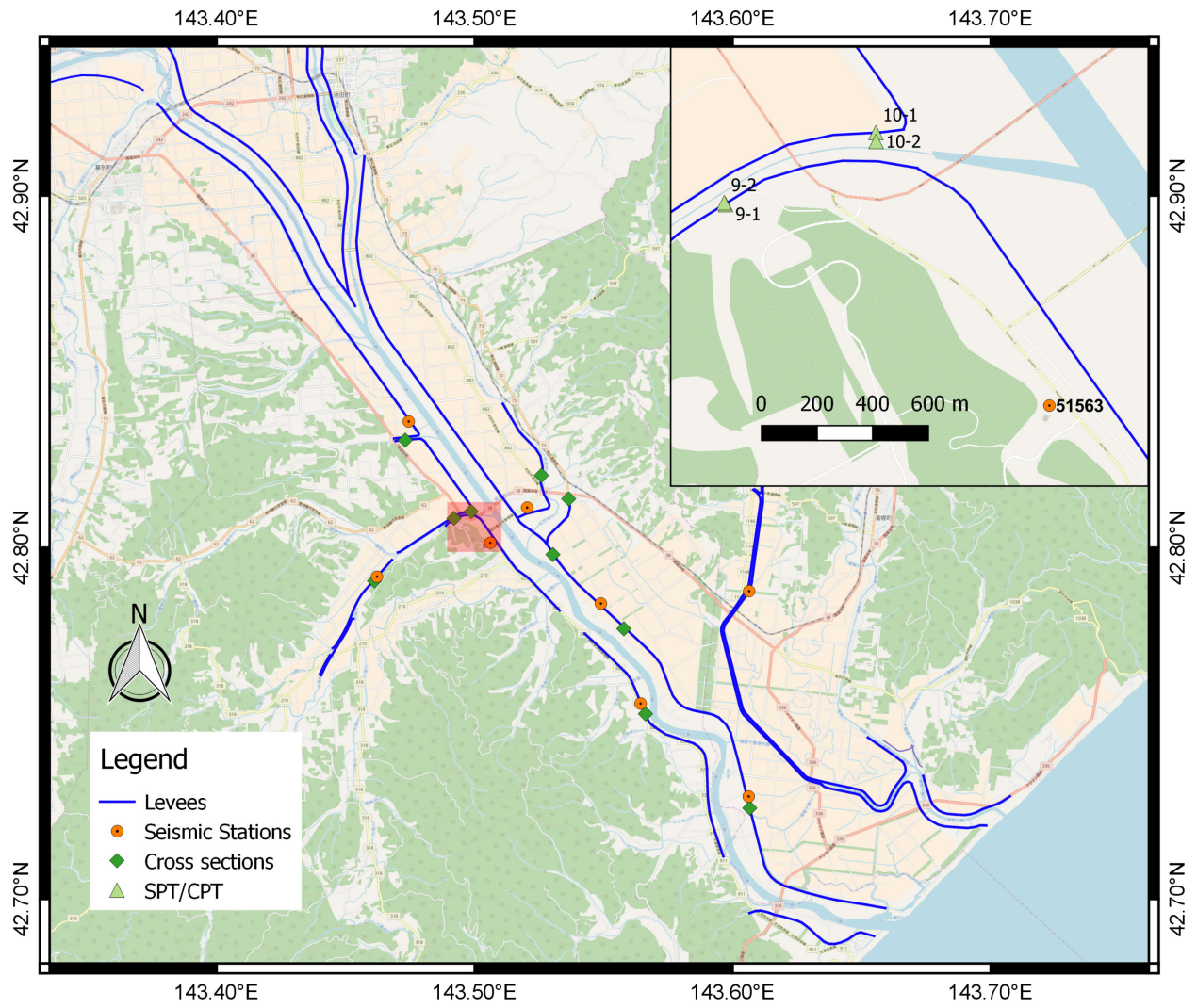


Figure 4.17 Vicinity map for Sections 9 and 10.

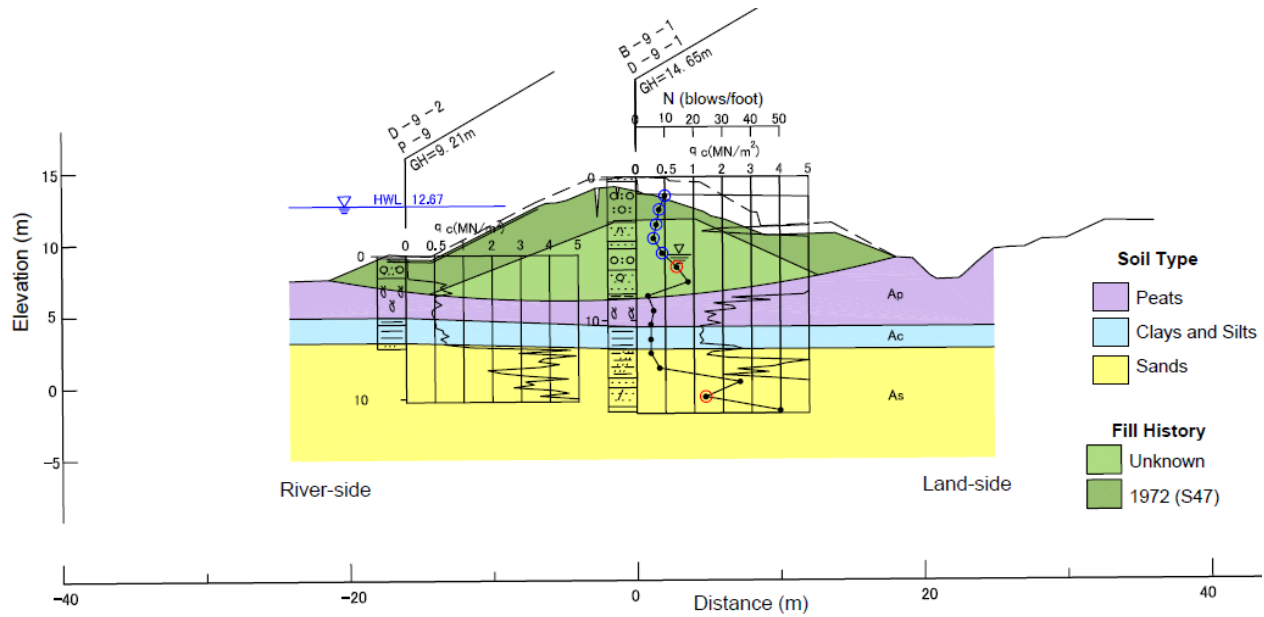


Figure 4.18 Subsurface investigation for Section 9.

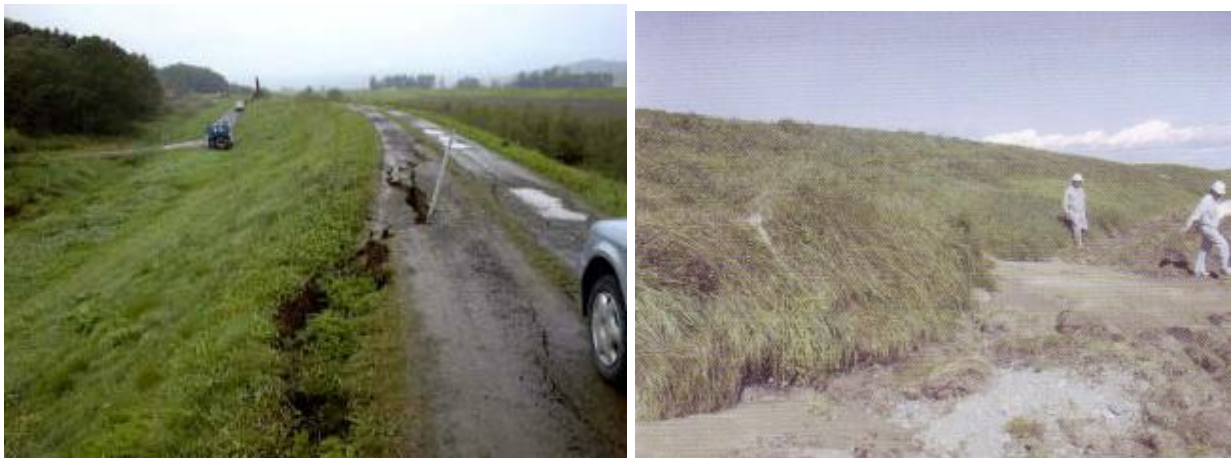


Figure 4.19 Cracking on the access road on the levee crest at Section 9 with slip and settlement on the land-side slope.

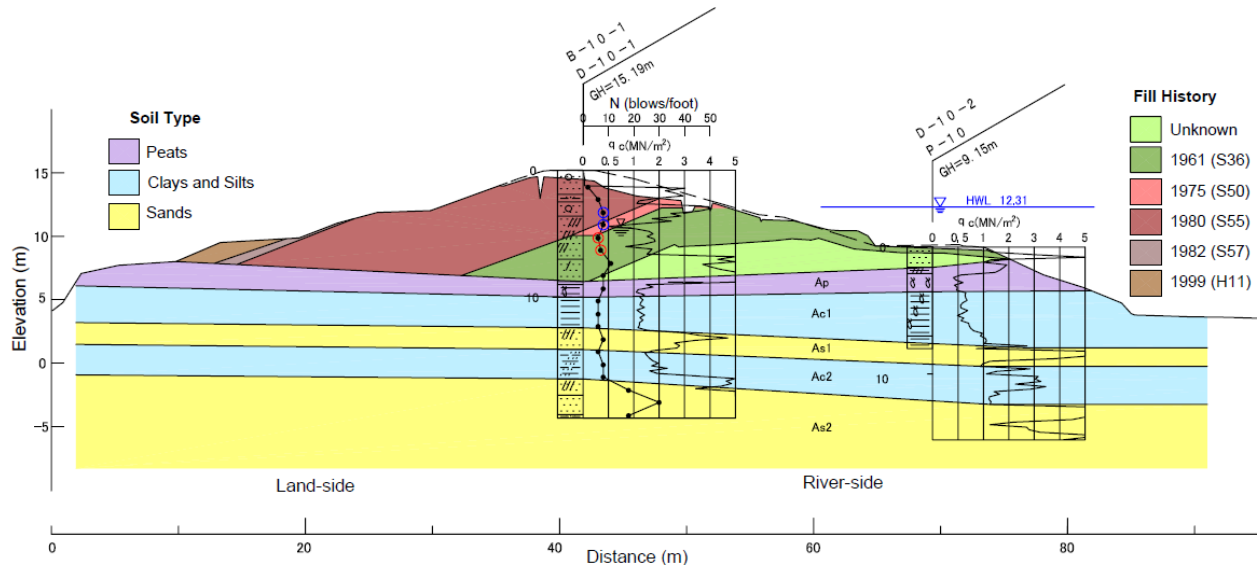


Figure 4.20 Subsurface investigation for Section 10.



Figure 4.21 Cracking of the roadway on the levee crest accompanied by slip on the slope at Section 10.

#### **4.3.6 Section 11 - Gyushubetsu River left bank**

The Gyushubetsu River joins the Tokachi River on the right bank around 21 km upstream of the river mouth. The cross section is located around 4.0 km from the intersection, and the closest station is GSB on the levee around 100 m downstream (Figure 4.22). The oldest portion of the levee is predominantly peat, with layers of fine sand. The construction date is unknown and is likely unengineered fill. The fill placed in 1956 is tested and found to consist of fine to medium sand with 20% gravels of 5-10 mm and some silts. The subsequent expansion of the levee involved sandy soil with minor amounts of gravels. Ground water level is elevated within the levee fill.

The levee rests directly on peaty soils (Ap) around 5 m thick in the free-field, with the levee fill settling around 2 m into the peat. A thick clay layer (Ac) underlies the peat, before transitioning into coarser material (As) at 20 m

The section suffered extensive damage, with crack widths of 60-270 cm and crack depth up to 200 cm. The levee subsided up to 3 m at the crest and essentially collapsed. (Figure 4.23). Complete replacement was necessary, and the location of the site investigation was opportunely excavated and mapped during the restoration process (Figure 4.24). Sand boils and ejecta could not be identified definitively due to the severe damage. The deformation pattern of the fill layers suggests loss of bearing capacity in the submerged portion, leading to instability and collapse of the levee. Laboratory tests on retrieved samples identified the fill placed in 1956 (S31) to be primary composed of coarse sands, with minor gravels and minimal fines, to be susceptible to liquefaction. The drainage ditch on the land-side toe of the levee was intact, and the failure through the peat layer is unlikely.

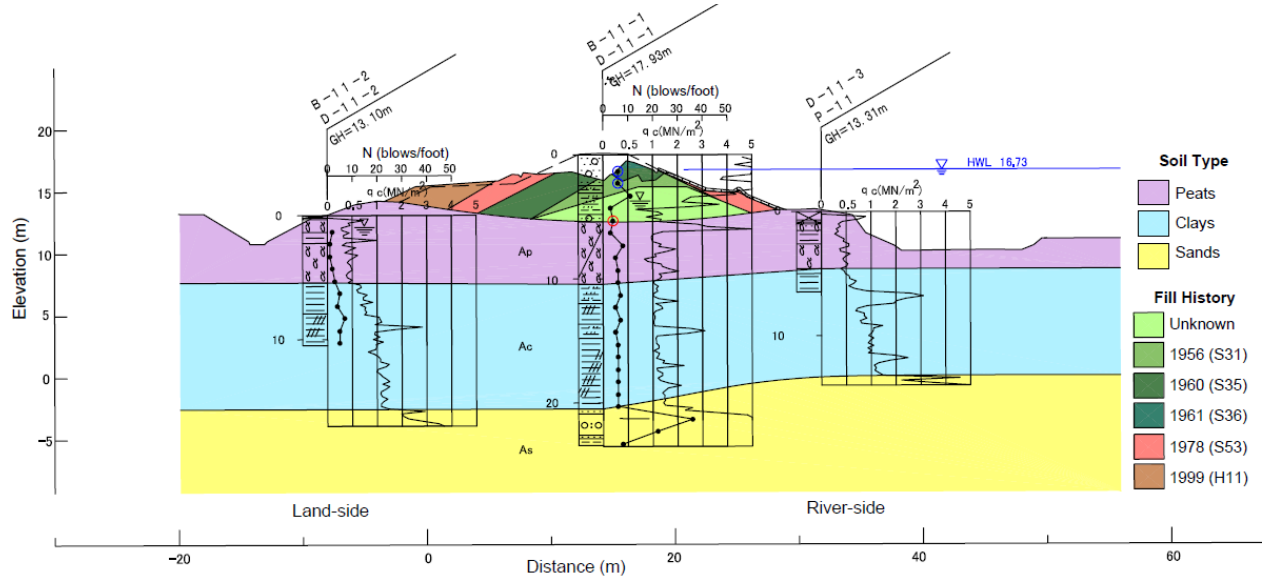
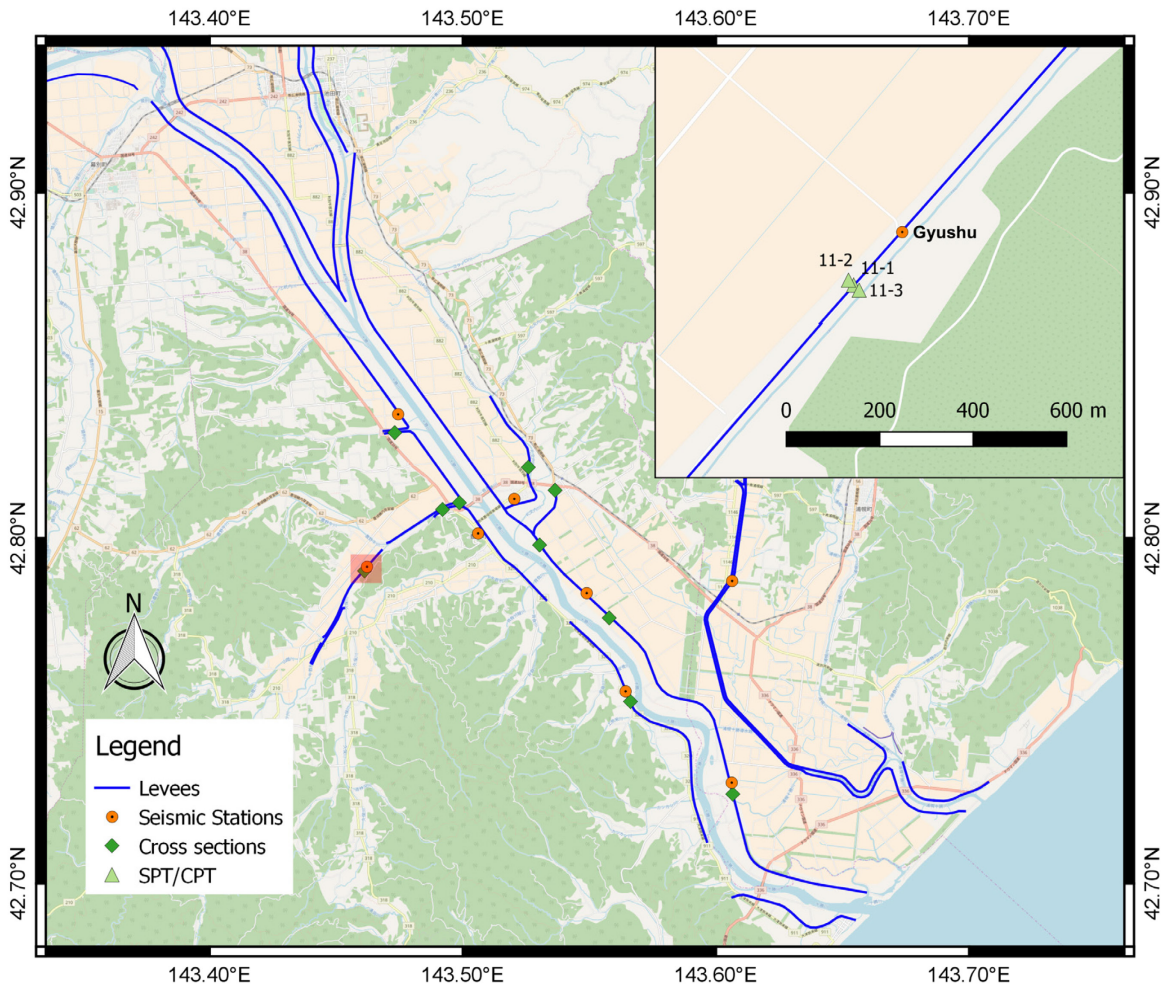


Figure 4.22 Vicinity map and subsurface investigation at section 11.





#### **4.3.7 Section 12 - Satsusakubetsu River right bank**

The Satsusakubetsu River joins the Tokachi River on the right bank around 24.6 km upstream of the river mouth. The cross section is around 500 m from the intersection and the closest station is RSK, located around 500 m upstream on the levees on the right bank of Tokachi River (Figure 4.25). The levee was initially constructed in the 1959 and 1960, and subsequently expanded in 1975. The levee fill consists mainly of sandy gravels, with average blow count of about 5. The CPT at the crest terminated near the base of the levee, which is likely early due to contact with gravel. Ground water was encountered at the base of the levee at the top of the peat layer, which is unusually low compared to other locations.

The levee rests on top of a peat layer (Ap) around 4 m thick, with seams of sand and silts (As1) in the free-field away from the levee. A sandy layer (As2) of variable thickness underlies the peat layer, and is followed by a sandy silt layer (Ac) that decreases in fines to be predominately sands deeper into the profile (As3). The sandy layers are observed to have higher cone tip resistance that is not readily reflected in the blow counts.

The levees were heavily damaged, crest subsidence was estimated to be around 50-70 cm and accompanied by cracks up to 100 cm wide and 50 cm deep with cracks with width and depth up to 80 cm and 100 cm and crest subsidence around 50 cm (Figure 4.26). The Sand boils and additional cracks around 5 cm wide and 50 cm deep were observed on the slope.

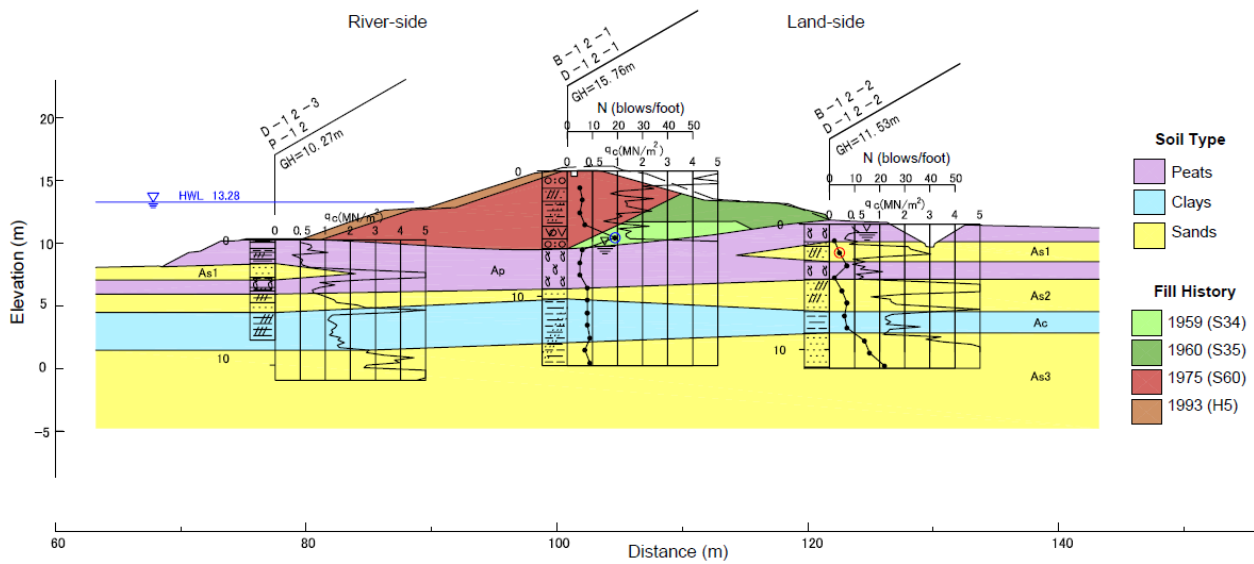
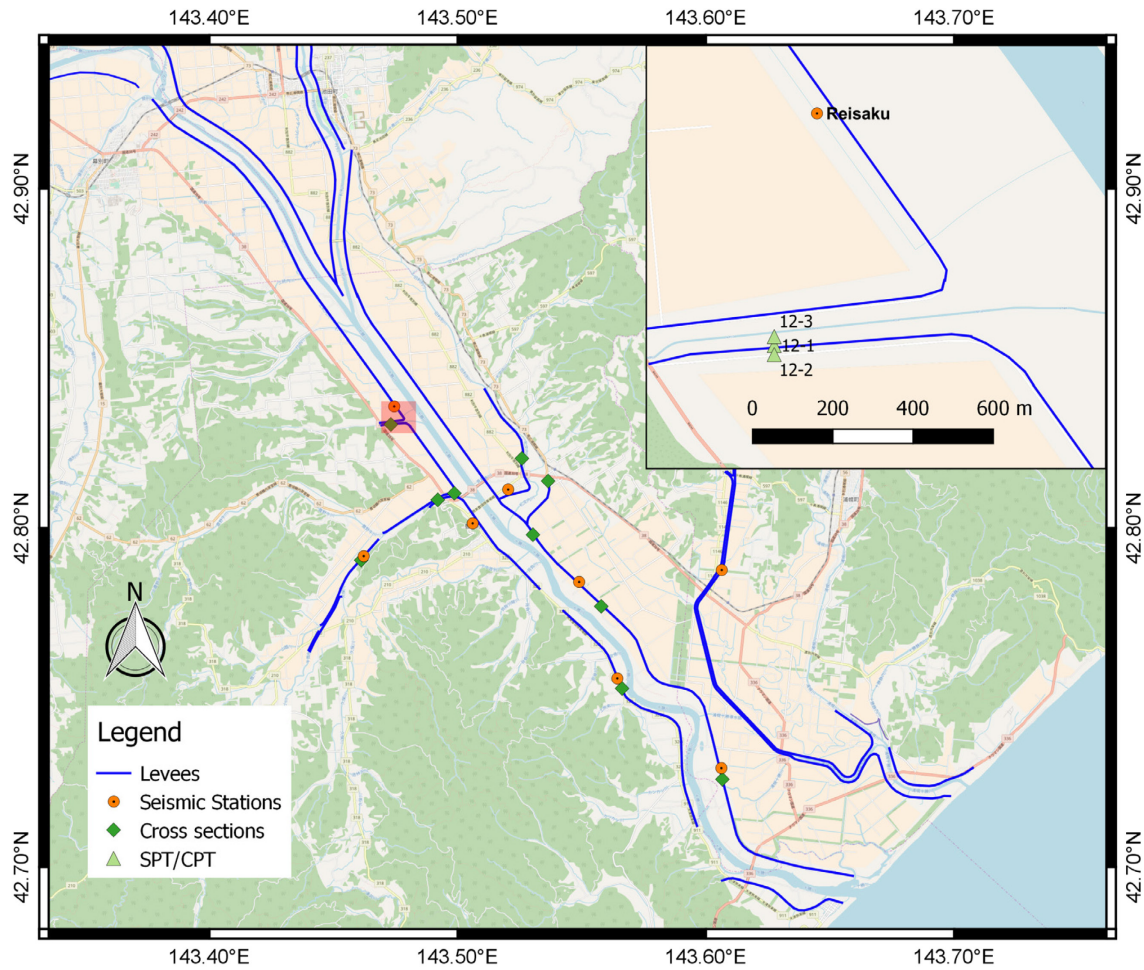


Figure 4.25 Vicinity map and subsurface investigation at Section 12.



Figure 4.26 Damage at Section 12, cracks on the roadway on the levee crest (top left). Slip and displacement of the land-side slope towards the levee toe (top right, bottom).

During the restoration process, the section where the SPTs and CPTs were advanced was excavated and mapped (Figure 4.27). Laboratory tests identified the fill placed in 1959 (S34) and 1960 (S35) to be primarily composed of coarse sands, with gravels mixed in and minimal fines, to be susceptible to liquefaction. Ground water was encountered around 2 m from the base of the levee fill. Deformation in the foundation was not observed and slip through the peat layer was deemed unlikely.

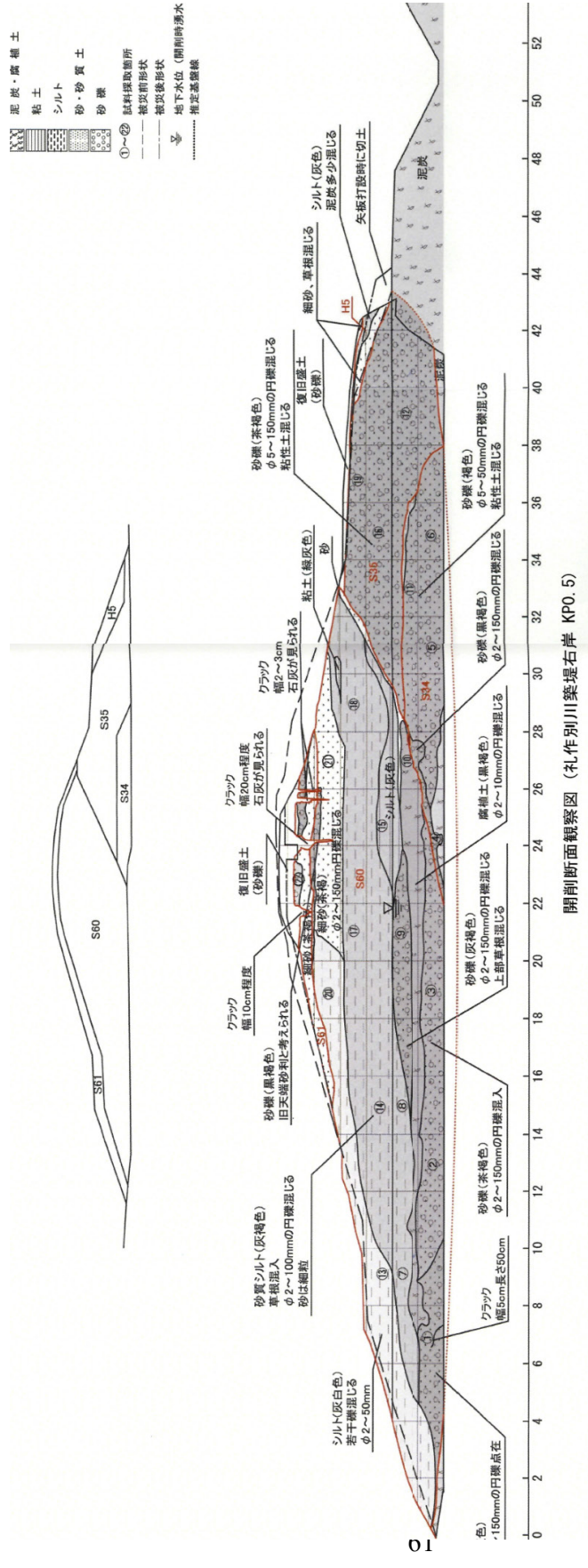


Figure 4.27 Mapped surface of the excavation at section 12 showing fill placement history and failure geometry. Fill placed in 1959 (S34) and 1960 (S35) composed of coarse sands with gravels is deemed to be susceptible to liquefaction.

#### 4.3.8 Sections 13 and 14 - Satsubunnai River

The Satsubunnai River is a subsidiary stream and joins the Tokachi River around 20 km upstream from the river mouth. Section 13 is on the right bank around 1.7 km upstream of the intersection and is close to the river channel. Section 14 is on the left bank around 0.9 km upstream from the intersection, with a setback of around 400 m from the river channel. The closest station is TKCH07, located further upstream and inland off the right bank, shown in Figure 4.28 together with the two sections.

At section 13, both the fill and the foundation contain mainly sands; peats and clays are absent at this location (Figure 4.29). The upper layer of sand (As1) contains minor amounts of silt beneath the levee, increasing in fines content towards the land-side toe. Directly beneath that is around 5 m of clean sands, interbedded with silts at larger depth (As2). Ground water was encountered around 1 m below the free-field surface and the levee fill is unsaturated. No damage was observed at this section, though severe cracking and settlement at the crest was observed around 100 m downstream

At section 14, the levee is underlain by around 2 m of peat (Ap) followed by around 1 m of clay (Ac1) (Figure 4.30). A highly interbedded sandy layer (As1) is sandwiched between the upper and lower clayey layers (Ac2). The lower sand layer (As2) is much stiffer, as reflected by the rapid increase in blow counts and cone tip resistance. The ground water table is within the peat layer, around 1 m below the free-field surface, and the levee fill is unsaturated.

The section experienced extensive cracking and warping of the paved roadway on the crest, with settlement and slip on the land-side slope. Cracks around 110 cm deep and 60 cm wide, and differential settlement over 30 cm of the levee slope from the edge of the asphalt roadway (Figure 4.31).

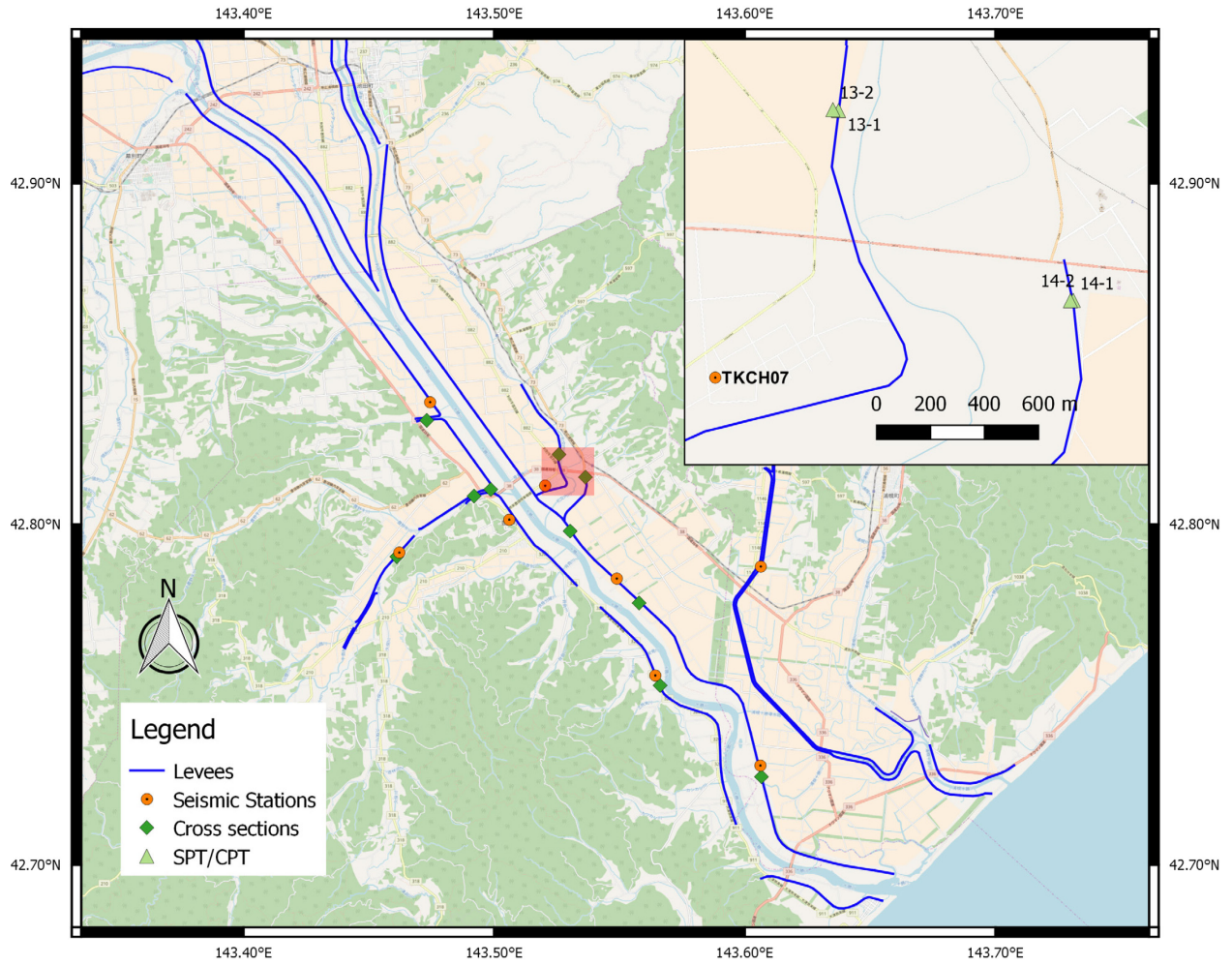


Figure 4.28 Vicinity map for Sections 13 and 14 on the subsidiary Satsubunnai River.

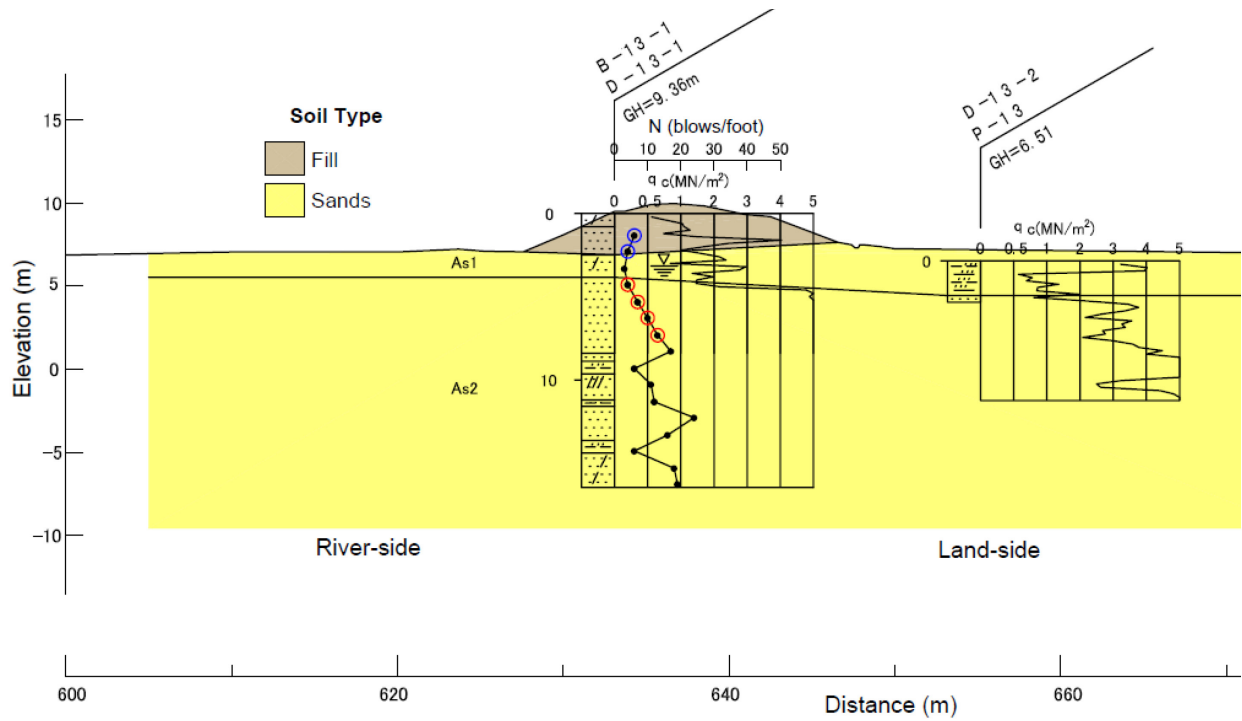


Figure 4.29 Subsurface investigation for Section 13.

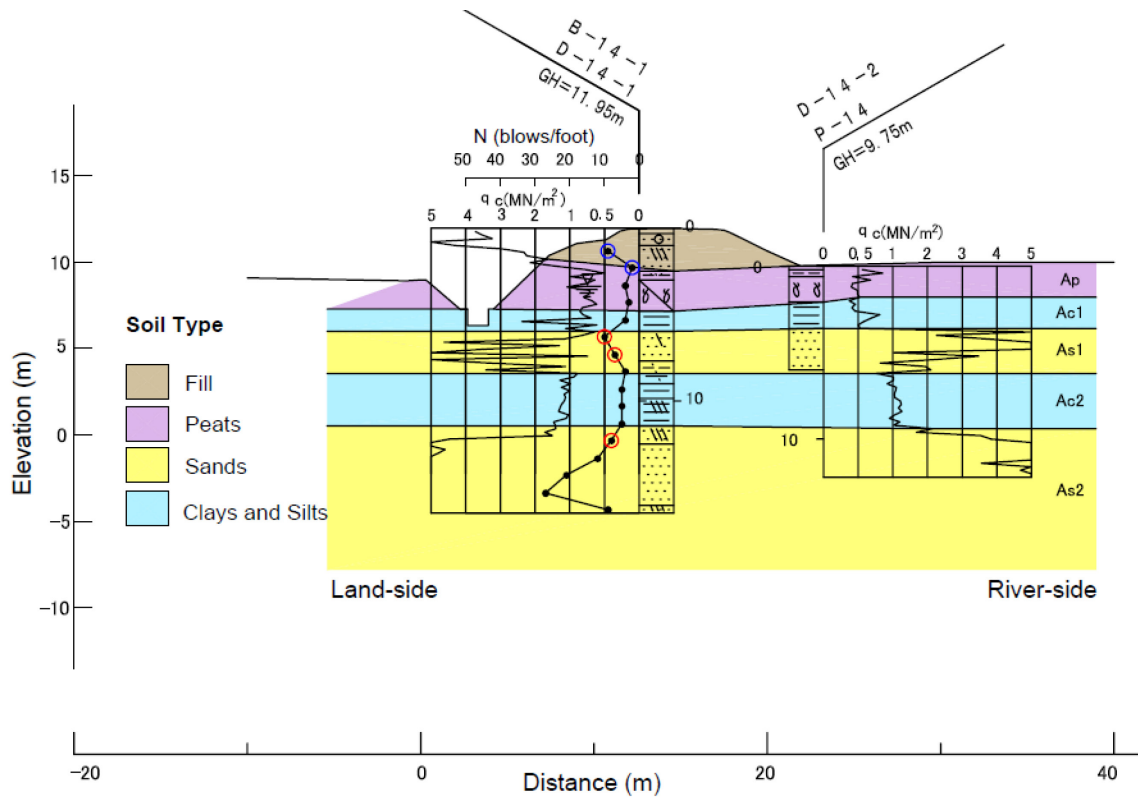


Figure 4.30 Subsurface investigation for Section 14.



Figure 4.31 Cracks on the roadway on the levee crest at Section 14 from slip on land-side slope.



## 4.4 ANALYSIS OF LEVEE CROSS SECTIONS

Damage to the levees presented above was caused by liquefaction, bearing capacity failure in the soft underlying peat, or a combination of both. This section presents an analysis procedure for predicting these effects. The analysis procedure utilizes liquefaction severity indices with slope stability and Newmark displacements. Liquefaction severity indices integrate liquefaction potential in some manner over depth, and are therefore more severe for thick liquefiable layers. They have been shown to correlate reasonably well with liquefaction damage observations. However, they are performed for a single boring, and do not inherently capture lateral variability. Slope stability simulations combined with Newmark sliding block analyses provide a better assessment of lateral continuity of weak zones, but this approach is relatively insensitive to the thickness of liquefiable or weak layers. The two approaches are therefore viewed as complementary, and the aggregate damage potential is defined as a function of both analyses.

The analysis procedure is outlined below:

- 1) Determine liquefaction susceptibility of material present and evaluate the cyclic resistance;
- 2) For the given seismic loading, determine factor of safety against liquefaction or cyclic softening. If strength loss is likely, apply the appropriate procedures to evaluate residual strengths;
- 3) Compute liquefaction severity indices for each SPT and CPT profile;
- 4) Compute FS, yield accelerations and Newmark displacements for each cross section;
- 5) Combine the results from Steps 3 and 4 to assign an aggregate damage level.

The aggregate damage levels from Step 5 above are then compared with observed levee damage.

#### 4.4.1 Strength loss mechanisms

Assessing liquefaction susceptibility is the critical step to the process of characterizing soil behavior under cyclic loading. Liquefaction triggering procedures should be used to assess soils determined to be susceptible to liquefaction, whereas cyclic softening procedures should be applied to fine-grained soils deemed too clay-rich to liquefy. The estimated resistance is then compared with the anticipated seismic demands the soil to determine if significant loss of strength and/or large strains are expected. In current geotechnical engineering practice, susceptibility is typically evaluated through the soil's index properties, such as gradation, liquid limit (LL) and plasticity index (PI), that characterize the composition and properties of the soil mixture. Bray and Sancio (2006) consider both PI and LL, with material with  $PI < 12$  and  $LL > 0.85$  as susceptible,  $PI > 18$  as not liquefiable, but can have large strength loss and strains, and intermediate PI with  $LL > 0.8$  to be moderately susceptible. Boulanger and Idriss (2006) focused on differentiating between sand-like and clay-like behavior to select the appropriate procedure for characterize the behavior of fine-grained soils, and recommend soils with  $PI \geq 7$  are clay-like, and with  $PI < 7$  are sand-like.

The classification from the boring logs is used to estimate liquefaction susceptibility. The Japanese soil classification adopts a three letter code based the following scheme (JHPC, 2005):

- 1) The first letter represents soil type of the major fraction, which  $> 50\%$  of the dry soil is composed of by weight;
- 2) The second letter represents the minor fraction, which 15-50% of the dry soil is composed of by weight;
- 3) The third letter represents a minority fraction, which 5-15% of the dry soil is composed of by weight. It is preceded by a dash to distinguish it from the letter for the minor fraction. (e.g., S-M)

The letters for each soil type is similar to the Unified Soil Classification System (USCS), with G for gravels, S for sands, M for silts, C for clays. Less common materials present here are peat (P) and traces of volcanic ash (V). Under this system, a material classified as "SM-G" would be a silty sand with traces of gravel, with the silt and gravel content not exceeding 50% and 15% respectively. Alternatively, "S" would indicate relatively clean sands, with no other soil type comprising more than 5% (if present). In addition, index tests on samples from the two excavated sections showed levee fill with major fraction of silt to have high PI ( $\geq 7$ ). Based on the classification scheme, the strength loss mechanisms employed in subsequent analysis is given in Table 4.3 based on the soil classification.

Table 4.3 Susceptibility based on soil classification

Group	Soil Classification	Description	Cyclic Strength Loss Mechanism
1	S, SM, SM-G, S-G, S-M, SV	Clean sands, sand with minor mixtures, silty sands, gravelly sands,	Liquefaction
2	M, MC, MS, M-C, M-G, M-S C, CM, C-M, C-S P, PC, PM, P-C, P-G	Silts, clays and peats	Cyclic softening
3	G, GS, V	Gravels and volcanic soils	None

#### 4.4.2 Liquefaction Severity Indices

Surface manifestation of liquefaction depends on both loading intensity and site conditions (e.g., depth of liquefiable layers, thickness of non-liquefiable crust, lateral continuity), requires liquefaction to be triggered in a stratum that is sufficiently thick and shallow, such that the excess pore pressure will exit at the ground surface. Liquefaction severity indices combine liquefaction triggering with site characteristics to assess the occurrence and severity of surficial manifestation, which is linked to the

potential for liquefaction induced damage. Four indices are considered for estimating cross-section performance, as summarized below. For consistency across different indices,  $FS_{liq}$  and  $D_R$  are computed using either the blow counts or cone tip resistance following the procedures in Boulanger and Idriss (2012 and 2016).

The Liquefaction Potential Index (LPI) proposed by Iwasaki et al. (1978) integrates the factor of safety against liquefaction triggering ( $FS_{liq}$ ) after applying a weighting function that decreases with depth. All else being equal, liquefaction of a shallower layer yields a higher LPI, reflecting that the shallowest layers in a profile most strongly influence surface manifestation and damage. Based on the 55 case histories from Japan examined, severe liquefaction is expected for  $LPI > 15$ , and not expected for  $LPI < 5$ .

$$LPI = \int_0^{20\ m} F \times w(z) dz \quad (4.1)$$

$$F = \begin{cases} 1 - FS, & \text{if } FS \leq 1 \\ 0, & \text{if } FS > 1 \end{cases} \quad (4.2)$$

$$w(z) = 10 - 0.5z \quad (4.3)$$

Maurer et al. (2015) extended the LPI framework to incorporate the suppressive effects of non-liquefiable crusts presented by Ishihara (1985), and incorporated case histories from a global dataset (e.g., the 1989 Loma Prieta (USA), 1994 Northridge (USA), 1999 Kocaeli (Turkey), 1999 Chi-Chi (Taiwan), 2010 Darfield (New Zealand), and 2011 Christchurch (New Zealand) earthquakes). The updated Ishihara-inspired index,  $LPI_{ISH}$ , employs a power law depth weighting function.

$$LPI_{ISH} = \int_0^{20} F_1 \times \frac{25.56}{z} dz \quad (4.4)$$

where

$$F_1 = \begin{cases} 1 - FS, & \text{if } FS \leq 1 \cap H_1 \times m(FS) \leq 3 \\ 0, & \text{if } FS > 1 \end{cases} \quad (4.5)$$

$$m(FS) = \exp\left(\frac{5}{25.56(1 - FS)}\right) - 1$$

$H_1$  is the thickness of the non-liquefiable crust and is estimated as the surface to the top of the first susceptible layer. The authors recommend a minimum of 0.4 m for shallow ground water cases. As shown in Figure 4.32, the upper 3 m of the profile is weighted more than in LPI's linear depth weighting function.  $LPI_{ISH}$  shares the same performance thresholds as LPI.

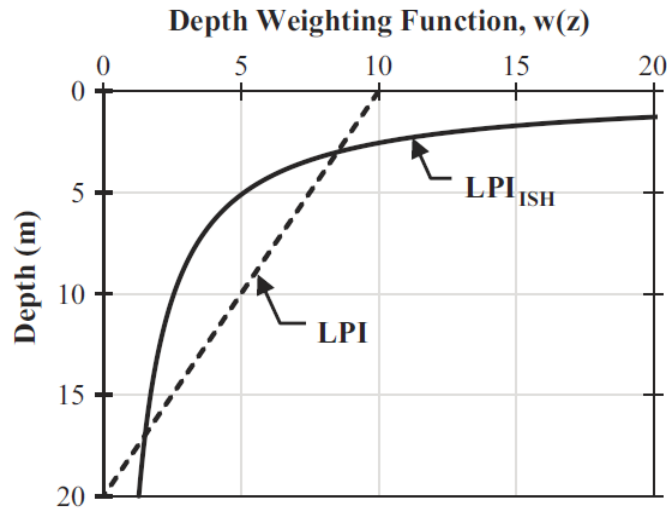


Figure 4.32 Shallow layers are weighted more in the  $LPI_{ISH}$  than LPI procedure (Maurer et al., 2015).

Van Ballegooy et al. (2014) examined over 11,500 CPT profiles and liquefaction manifestation during the Canterbury earthquake sequence in New Zealand. The Liquefaction Severity Number (LSN) estimates the potential ground surface settlement by integrating one-dimensional reconsolidation strains over the upper 20 m of the profile,

$$LSN = 10 \int_0^{20 \text{ m}} \frac{\epsilon_v}{z} dz \quad (4.6)$$

where  $z$  is the depth below the ground surface in meters and  $\epsilon_v$  is the post-liquefaction volumetric strains (%), which can be correlated to relative density ( $D_R$ ) and  $FS_{liq}$  (e.g., Yoshimine et al., 2006). Severe liquefaction is expected where  $LSN > 40$ , and minimal to no manifestation is expected where  $LSN < 20$ , with moderate to severe manifestation where  $20 \leq LSN \leq 40$ .

The Lateral Displacement Index (LDI) by Zhang et al., (2004) presents a potential maximum lateral displacement at the ground surface by considering the cyclic shear strains mobilized over the profile,

$$LDI = \int_0^{z_{max}} \gamma_{max} dz \quad (4.7)$$

where  $z_{max}$  is the depth below all potentially liquefiable material with  $FS < 2$ . The limiting shear strain,  $\gamma_{lim}$ , is based on Idriss and Boulanger (2008) and restricted to 0.5% to avoid a single loose measurement dominating the estimated strains. The mobilized shear strains in each liquefiable layer is based on correlations with  $FS_{liq}$  and shear strains observed in lab tests by Ishihara and Yoshimine (1992).

$$\gamma_{max} = \begin{cases} 0, & FS \geq 2 \\ \gamma_{lim}, & FS \leq F_\alpha \\ \min\left(\gamma_{lim}, 0.035 \times (1 - F_\alpha) \left(\frac{2 - FS}{FS - FS_\alpha}\right)\right) & otherwise \end{cases} \quad (4.8)$$

$$F_\alpha = 0.032 + 4.7D_R - 6.1 (D_R)^2 \quad (4.9)$$

$$\gamma_{lim} = 1.859(1.1 - D_R)^3 \leq 0.5 \quad (4.10)$$

### 4.4.3 Initial material strengths

Material below the ground water table is assumed to be saturated and the undrained strength is used for seismic analysis of fine-grained soils and coarse-grained soils deemed susceptible to liquefaction. Coarse-grained material above the water table is assumed to be unsaturated and drained strength parameters are used. Fine-grained material above the water table is assumed to be saturated due to capillary rise, and undrained strength is used. Coarse-grained material below the water table (e.g., gravels without a low-permeability capping layer) are assigned drained strength parameters. Soil properties such as relative density, peak friction angle, and undrained shear strength are estimated for a given unit.

For sandy soils, shear strength is defined with the friction angle,  $\phi'$ , correlated with penetration resistance from SPT or CPT (e.g., Hatanaka and Uchida (1996)), or as a sum of the critical state friction angle and the difference between peak and critical state friction angle ( $\phi' - \phi_c$ ) (Bolton 1986). The difference can be related to the relative dilatancy index, which is a function of the relative density and mean effective stresses for the material.

$$\phi' = \phi'_c + 3I_R \quad (4.11)$$

$$I_R = D_R(10 - \log \sigma'_m) - 1 \quad (4.12)$$

$$\text{Mean effective stress, } \sigma'_m = \frac{1 + 2K_0}{3} \times \sigma'_v \quad (4.13)$$

$$K_0 = 1 - \sin \phi' \quad (4.14)$$

where  $\phi'_c$  is a function of minerology and ranges between 32-40°, and is typically taken to be 32° or quartz sands. Relative densities are correlated from SPT or CPT based on Idriss and Boulanger (2008):

$$D_R = \sqrt{\frac{(N_1)_{60,cs}}{46}} \quad (4.15)$$

$$D_R = 0.478 q_{c1Ncs}^{0.264} - 1.063 \quad (4.16)$$

$$21 \leq q_{c1Ncs} \leq 254 \quad (4.17)$$

For cohesive soils, the undrained shear strength ( $S_u$ ) is correlated to in-situ measurements from the cone tip resistance,  $q_c$  and an empirical cone factor ( $N_k$ ) as:

$$S_u = \frac{q_c - \sigma_{vo}}{N_k} \quad (4.18)$$

$N_k$  of 15 and 12 are selected for clays and silts (Lunne et al, 1985). For peat,  $N_k$  is estimated to range from 20 - 25 from CPTs and direct simple shear tests on peat samples from Sherman Island, California (Shafiee 2016), and 21 for peats in Hokkaido (Hayashi and Hayashi 1991). The latter is adopted since the testing program involved samples from multiple river systems in Hokkaido having similar depositional environment, and are more representative of peat along the Tokachi River. For typical monotonic undrained shear strength tests, Stewart et al. (2014) suggests a 20-40% increase to account for rate effects as loading during from earthquake is much faster. The strain rates for the CPTs pushed are unknown and strength adjustments are not applied.

#### 4.4.4 Residual strengths

Considering the effects of strength loss, liquefied strengths for susceptible layers with  $FS_{liq} < 1$  are estimated using relationships proposed by Olson and Stark (2002), Idriss and Boulanger (2007) and Kramer and Wang (2015). Both SPT and CPT based approaches are utilized measurements for susceptible material with  $FS_{liq} < 1$  during the 2003 earthquake. Estimated residual strength is capped at  $\sigma'_v \tan \phi'$  at shallow depths, such that the drained shear strength of the material is not exceeded.



Olson and Stark (2002) and Idriss and Boulanger (2007) proposes relationships for normalized residual strength estimated using both SPT and CPT data. Olson and Stark (2002) back analyzed thirty liquefaction flow failures to estimate residual shear strengths,

$$\frac{S_u(liq)}{\sigma'_{v0}} = 0.03 + 0.0075(N_1)_{60} \quad N_1 \leq 12 \quad (4.19)$$

$$\frac{S_u(liq)}{\sigma'_{v0}} = 0.03 + 0.0143(q_{c1}) \quad q_{c1} \leq 6.5MPa \quad (4.20)$$

$$q_{c1} = q_c \left( \frac{1.8}{0.8 + \frac{\sigma'_{v0}}{p_a}} \right) \quad (4.21)$$

The ratios ranges from 0.24 to 0.30. For both CPT and SPT correlations, the standard deviation is 0.025, with  $\pm 0.030$  for the upper and lower bounds.

Idriss and Boulanger (2007) adopts a fines correction factor based on Seed (1987), summarized in Table 4.4, which is distinct from the fines correction in liquefaction triggering analysis. Effects of void redistribution are considered where the formation of a water film may further reduce the shear strength. For the sites considered here, a low permeability capping layer is absent from the levee fill and the foundation, so void redistribution effects are ignored. Additionally, the blow counts are within the liquefiable layers are generally below 10, and the recommended curves for the two cases are mostly overlapping. Given the above, void redistribution effects are not expected to be significant and the residual strength ratio is estimated as follows,

$$\frac{S_r}{\sigma'_{v0}} = \exp\left(\frac{(N_1)_{60-sr}}{16} + \left(\frac{(N_1)_{60-sr} - 16}{21.2}\right)^3 - 3.0\right) \times \left(1 + \exp\left(\frac{(N_1)_{60-sr}}{2.4} - 6.6\right)\right) \quad (4.21)$$

$$\frac{S_r}{\sigma'_{v0}} = \exp\left(\frac{q_{c1N-Sr}}{24.5} - \left(\frac{q_{c1N-Sr}}{61.7}\right)^2 + \left(\frac{q_{c1N-Sr}}{106}\right)^3 - 4.42\right) \times \left(1 + \exp\left(\frac{q_{c1N-Sr}}{11.1} - 9.82\right)\right) \quad (4.22)$$

Table 4.4 Fines correction recommended for estimating residual strengths

<b>Fines Content</b>	$\Delta(N_1)_{60-Sr}$	$\Delta q_{c1N-Sr}$
10	1	10
25	2	25
50	4	45
75	5	55

Lastly, Kramer and Wang (2015) directly relates residual strength to penetration resistance and effective stresses instead of a normalized strength ratio,

$$\ln(S_r) = -8.444 + 0.109(N_1)_{60} + 5.379(\sigma'_{v0})^{0.1} \quad (atm) \quad (4.23)$$

Cyclic failure of clay-like soils are assessed with a framework similar to liquefaction in sands. The cyclic resistance of the soil is compared to the estimated cyclic stress imposed by the earthquake, and where the factor of safety ( $FS = \frac{CRR}{CSR}$ ) is below 1, cyclic failure where large deformation develop are likely (exceeding 3% strain). To account for effect of number of cycles on resistance, scaling related to earthquake magnitude is developed, the MSF for clays is much flatter for clays than sands, and is close to unity for the  $M_w$  8.2 Tokachi-oki earthquake considered.

$$MSF = 1.12 \exp\left(-\frac{M_w}{4}\right) + 0.828 = 0.957 \quad (4.24)$$

The cyclic strength of clay-like soils can be obtained either directly from cyclic laboratory testing, or correlated to monotonic undrained shear strength ( $s_u$ ) with empirical factors to account for rate and direction effects (Boulanger & Idriss 2007). The undrained shear strength may be measured in the field (e.g., vane shear, CPT), from laboratory testing, or estimated based on normalization with stress history.

Boulanger and Idriss (2007) recommended taking cyclic strength ratio  $\left(\frac{\tau_{cyc}}{s_u}\right) = 0.83$  for natural deposits of clay-like fine grained soils ( $PI > 7$ ) for any OCR, and the cyclic resistance ratio (CRR) for normally consolidated soils to be  $\frac{\tau_{cyc}}{\sigma'_{vc}} = 0.18$  for two dimensional cyclic loading with 30 equivalent cycles. Later works suggest that the ratio may be dependent on PI, and suggest a transition of cyclic strength ratio from 0.611 at  $PI = 10$  to 0.8 at  $PI > 18$  (Eslami 2017).

$$CRR_{M=7.5} = \frac{\tau_{cyc}}{\sigma'_{vc}} = \left(\frac{\tau_{cyc}}{s_u}\right) \left(\frac{s_u}{\sigma'_{vc}}\right) \quad (4.25)$$

Cyclic loading in cohesive soils tend reduce the undrained shear strength and stiffness, especially in sensitive soils. Normally consolidated clays that are cyclically sheared sufficiently to achieve cyclic softening have been observed to have pore pressure ratios within the range 0.30 to 0.80, which develop for shear strain amplitudes varying from 1 to 9.5% (Boulanger and Idriss 2006; Dahl et al. 2014). Excess pore pressure ratio is lower than sands even at large strains, and drastic reduction of strength at the level experienced during liquefaction of granular material is unlikely. The extent of strength loss in claylike soils from cyclic softening depends on the magnitude of seismically-induced shear strains, OCR and sensitivity of the soil.

Testing performed by Yasuhara (1994) on Akita peat showed post-cyclic undrained shear strength to be a function of the excess pore pressure at the end of cyclic loading (Figure 4.33). Shafiee (2016) performed undrained monotonic tests after cyclic strain controlled loading on Sherman Island peat, and observed an average 25% reduction in the undrained shear strengths from 15 cycles of loading and reaching shear strains around 10% and pore pressure ratios around 0.37. The strength reduction is larger for Sherman Island peat than Akita peat with a similar the pore pressure ratio.

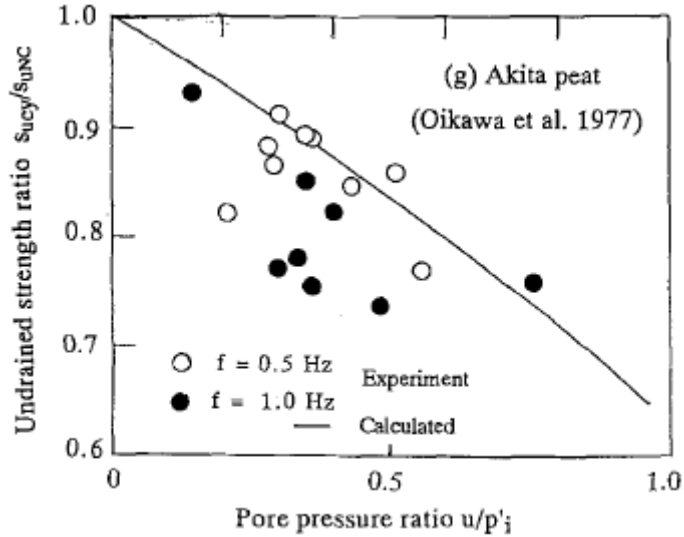


Figure 4.33 Undrained strength ratio decreasing with pore pressure ratio for Akita peat (Yasuhara, 1994).

An alternative metric to consider is the shear strain developed during cyclic loading. The ultimate undrained shear strength of a saturated soil is governed by the void ratio and soil fabric, therefore if the cyclic loading has not altered the void ratio or the soil structure, the undrained strength at large strains will remain the same. As the cyclic strain amplitude approaches the strain level of failure for monotonic loading, the soil structure is being altered and the monotonic strength decreases. Using the FS as an indicator of potential levels of strains for the applied cyclic load, minor strains are expected for high FS (i.e.,  $FS \geq 1.5$ ) and cyclic softening is not expected. For small strains ( $1.0 < FS < 1.5$ ) and moderate strains, the monotonic undrained shear strength is reduced by 10% and 20% respectively to account for cyclic softening.

#### 4.4.5 Slope stability and Newmark displacements

The model geometry is defined using the pre-earthquake dimensions from the cross-sections; the material properties and layering are based on the penetration resistance and soil classification from the boring logs. If multiple estimates of material strengths are available within the same material unit, the 33<sup>rd</sup> percentile value was assigned as an equivalent uniform property, which produces displacements

in reasonable agreement with dynamic simulations using stochastic models that consider spatially-correlated variable subsurface properties (Montgomery & Boulanger 2017). In addition, a unit may be subdivided to reflect lateral and vertical transitions in material strengths. This is most prevailing in the peat layers, where the resistance under the levee crest is significantly higher than in the free-field from consolidation under the additional stresses from the levee fill, as well as the higher confining stresses. For cohesive materials, tension cracks are accounted for and the depth of cracking is given by  $z_{cr} = \frac{2c'}{\gamma\sqrt{K_a}}$  for  $c-\phi$  material, and as  $z_{cr} = \frac{2s_u}{\gamma}$  for undrained conditions (Duncan et al., 2014). Cohesion is assumed to be low in predominantly sandy material in the levee fill, though from the deep cracks observed in the reconnaissance, the fines content is likely sufficient to develop some cohesion. Without further testing, higher cohesion is not adopted since the deeper tension cracks is balanced by a higher strength within the material. The sensitivity of the analysis to cohesion assumed and the corresponding crack depth will be considered in a future study.

Stability analyses were performed in *SLIDE* considering failure of both slope faces with initial material strengths and subsequently with reduced strength where liquefaction or cyclic softening is predicted. For the non-circular failure surfaces considered, Spencer and Morgenstern-Price methods of slices are utilized because both methods satisfy force and moment equilibrium. The resulting factor of safety (FS), yield accelerations ( $a_y$ ) and displacements are largely similar for a given section, and Spencer's method is used in subsequent analyses. All levees are stable under static conditions and generally  $FS \geq 1.5$  for the initial material properties estimated in Section 4.4.3. The minimum horizontal pseudo-static seismic load that will destabilize the slope ( $FS \leq 1.0$ ) is computed for both orientations and taken as the yield acceleration. The analysis is repeated with strength reductions to include the effects of liquefaction and cyclic softening. Flow failure are expected where  $FS < 1.0$ , indicating the levee is unstable and large displacements are expected. For sections where  $FS > 1.0$ , rigid sliding block

analyses are used to predict seismic displacement potential of slopes (Newmark 1965), by assuming accumulation of displacement whenever the yield acceleration is exceeded by the earthquake acceleration. The levee perpendicular component of the recording from the nearest station (Table 4.2) is used for each cross section.

#### **4.4.6 Example LPI calculations and model construction**

The analysis is demonstrated with section 11, which had extensive damage during the earthquake (Section 4.3.6). The bottom of the levee fill is predominantly sand, with trace amounts of gravel and susceptible to liquefaction. CPT and SPT measurements through the levee crest is shown in Figure 4.34, with measurements in susceptible layers highlighted. Appendix B contains the plots for each profile. The shallower susceptible layer corresponds to the saturated fill. The thick layer of peat and clay directly under the levee fill is not liquefiable, followed by a thick layer of dense sand that is susceptible but has high penetration resistance. The cyclic resistance ratio is estimated from the normalized and fines corrected tip resistance and blow counts, which is compared to the cyclic stress ratio estimated from the PGA measured at the ground level sensor at the GSB station. The FS against liquefaction is significantly lower than 1.0, and triggering of liquefaction is expected. The dense sand layer is beyond the 20 m considered, and only the saturated portion of the levee fill contributes to the indices. The process is repeated for profiles on either side of the levee toe.

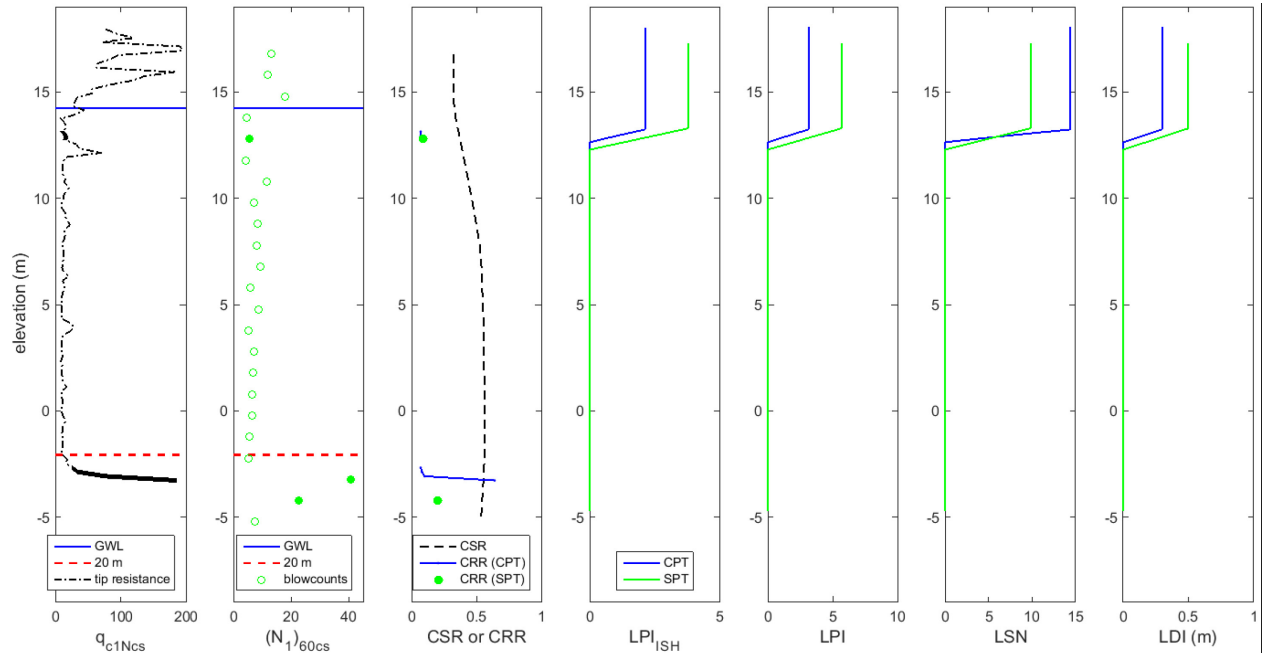


Figure 4.34 Liquefaction indices calculated from SPT and CPT through the crest at section 11. Susceptibility is based on material classification and ground water level from boring log.

For the 2-D slope stability model, the shear strength of levee fill and the dense sand are defined with the Mohr-Coulomb model using friction angles estimated from blow counts. For the peat and clay layers, the undrained shear strengths for the peat and clay layers are correlated from the cone tip resistance. The tip resistance is typically higher under the crest than in the free-field within the same strata, and reflects the higher stresses and consolidation from the placement of the levee fill. The resistance may also differ between the land-side and river-side, and is typical for the broad levees (spanning 60-80m at the base) along the main Tokachi River. For section 11, shear strength is similar between the two sides and an averaged value is assigned, as shown Figure 4.36 by the symmetric color coded material assignment. Materials with comparable classification are given similar colors, with lighter shades corresponding to lower strengths.

With the initial material properties, the static factor of safety is 1.81 and 1.72, with yield acceleration of 0.23 g and 0.22 g for the riverside and land-side respectively. Moderate displacements of 25 cm and 35 cm are estimated.

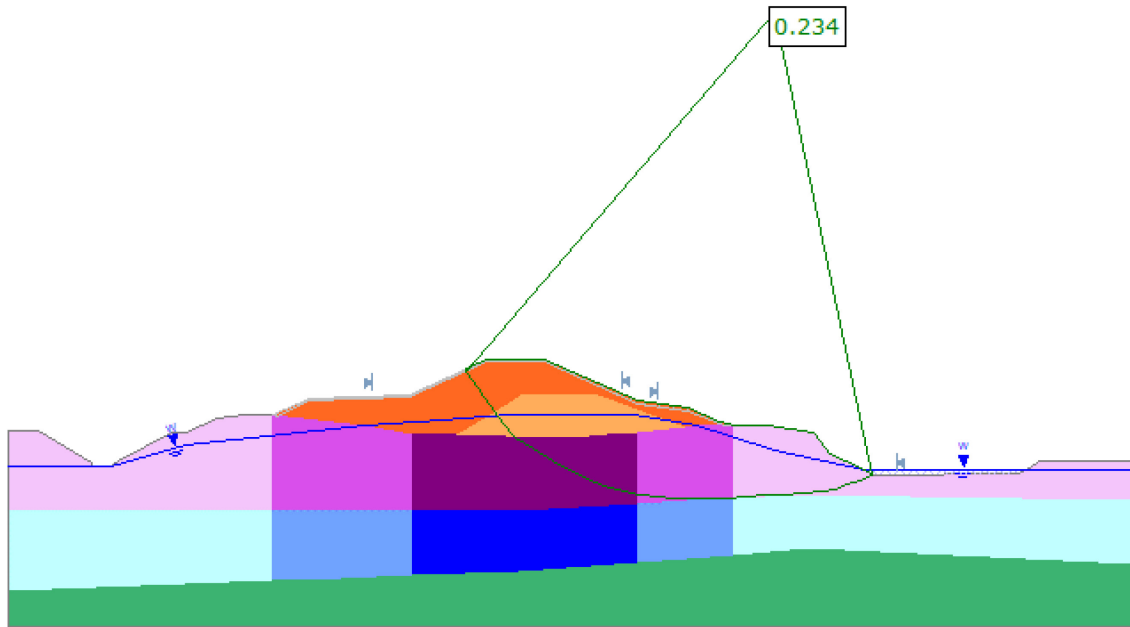


Figure 4.35 2-D model of section 11 showing yield acceleration for slope failure towards the river-side with pre-earthquake material properties.

The next step is to consider the influence of cyclic loading on material strengths. The potential for cyclic softening is assessed for the peat and clay layers. The FS exceeds 1.5 in the peat underneath the levee and the clay layers, and the initial strength is retained. For the free-field peat, FS is between 1.0 and 1.5 for the free-field peat and the undrained strength is reduced by 10%. Liquefaction is expected in the saturated levee fill in the levee. Judging by the construction history and samples taken during the open excavation, this corresponds to fill placed in 1956 and liquefied strength is assigned. With the strength reductions, FS falls to 1.01 and 1.60 for the river-side and land-side slopes. The river-side slope shown in Figure 4.36 is essentially on the verge of a flow failure and very low yield acceleration of 0.002 g is obtained. The calculated Newmark displacements is around 20 m, which indicating large



movements are expected, but is not physically meaningful since the rigid block assumption would be violated prior to achieving movement of that magnitude.

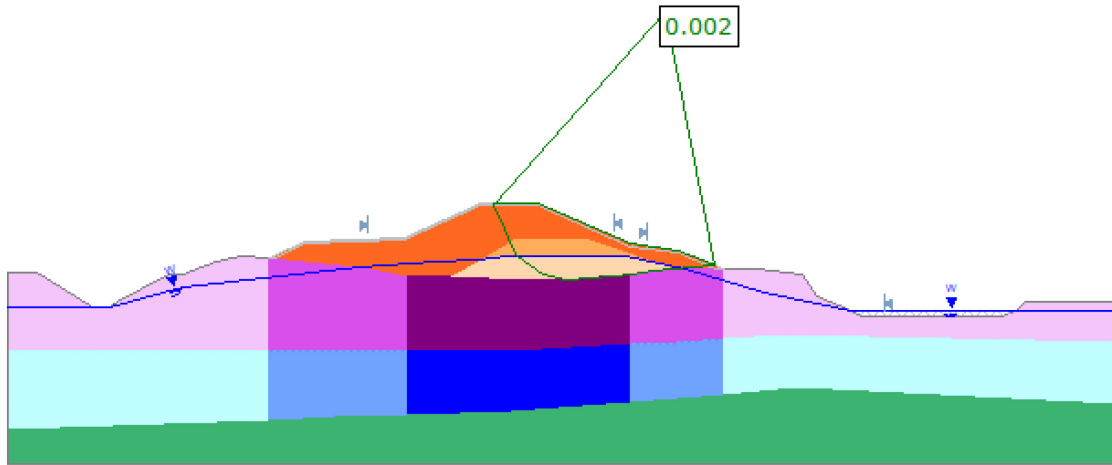


Figure 4.36 2-D model of section 11 showing slope failure towards the river-side with liquefied strength in saturated fill with softened strength in clay and peat.

Appendix B contains plots of the calculations for the liquefaction indices for each profile, as well as the *SLIDE* models showing the critical failure surfaces and the relevant material properties for each section.

## 4.5 COMBINED DAMAGE ASSESSMENT

The following section describes the framework for incorporating both liquefaction indices and Newmark displacements into damage level prediction for levee cross sections. Representative values for both metrics and thresholds for damage level are first determined individually, and combined to capture the potential effects from different failure mechanisms.

Multiple SPT or CPT are present at different locations on the levee and the resulting indices represents the local condition which generally vary across the levee. Figure 4.38 shows values from profiles at each cross section together with the original thresholds for minor, moderate and severe liquefaction

manifestation (Ishihara, 1985; Maurer et al., 2015; Van Ballegooy et al., 2014). The results for the sections are offset in the x-axis for visualization (i.e., DL 4 was observed for sections 2, 10 and 11). From the post-earthquake geometry and deformation patterns observed, it appear the shallower layers within or directly below the levees have more contribution than the deeper liquefiable layers to damage. As LPI weighs the contribution of the liquefiable strata linearly with depth, and LDI does not explicitly account for depth of the liquefiable layer, both tend to overestimate severity, with the majority of the values lying above the severe manifestation boundary. The power-law weighting used in  $LPI_{ISH}$  and LSN capture the observed performance better. These two indices are strongly correlated, and utilizing both is therefore unnecessary.  $LPI_{ISH}$  is adopted in subsequent analysis because it incorporates a broader dataset and includes the mitigating influence of a non-liquefiable crust.

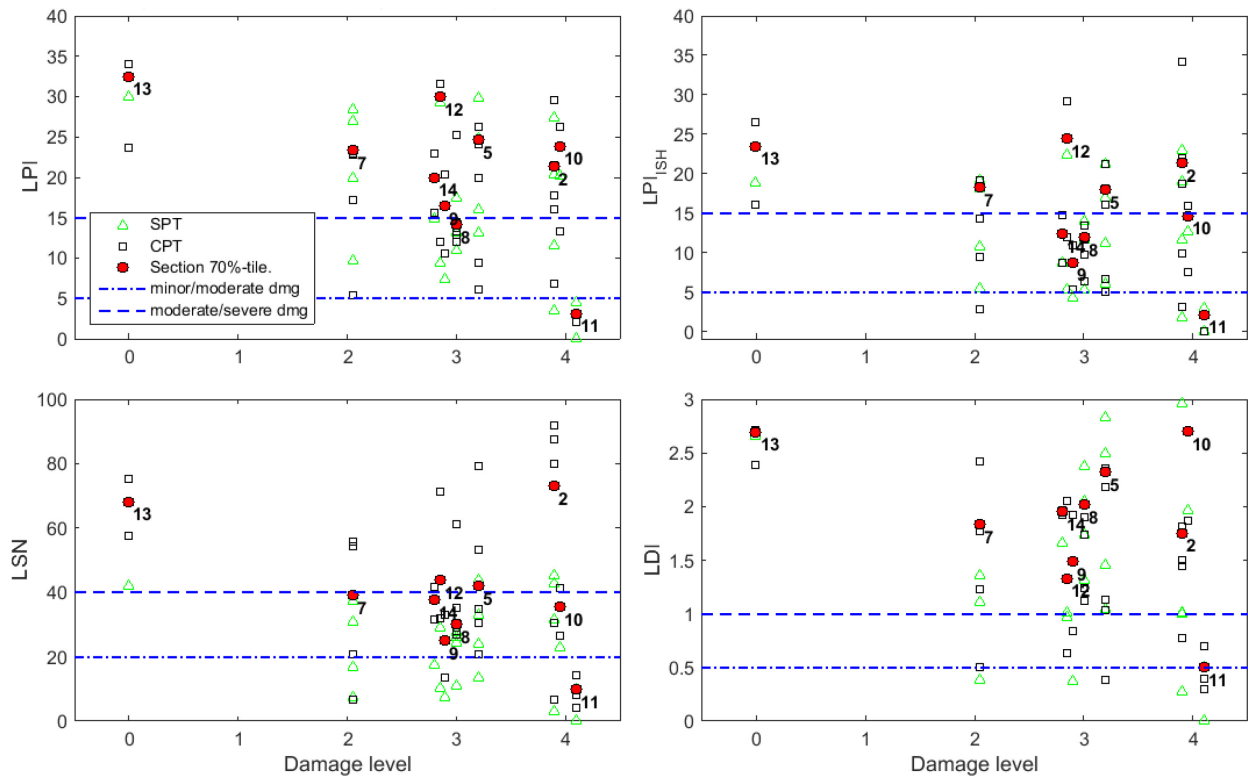


Figure 4.37 Liquefaction severity indices at each cross section based on all SPTs and CPTs shows a range of values. Cross sections with the same damage level are offset in the x-axis for visualization.

The liquefaction indices are computed along a vertical boring log or CPT profile, and therefore do not inherently capture the effects of lateral variability. When multiple liquefaction indices are computed for a levee cross-section, a decision must be made regarding how to combine them into an aggregate liquefaction index for assessing levee damage. In this case, the 70<sup>th</sup> percentile  $LPI_{ISH}$  value is selected as representative of the levee, which emphasize the effects of loose regions in the fill or foundation on the overall performance at a levee section. Additionally, based on the deformation patterns observed in the photographs and open excavation of damaged levee segments, liquefaction within the fill is likely more damaging than within the foundation due to the static driving shear stresses present within the levee. For composite failures with liquefaction predicted in both the fill and foundation, indices from the profiles through the levee are assigned double weight when computing the 70<sup>th</sup> percentile. The process to select a representative  $LPI_{ISH}$  value for the different scenarios is summarized in Figure 4.38.

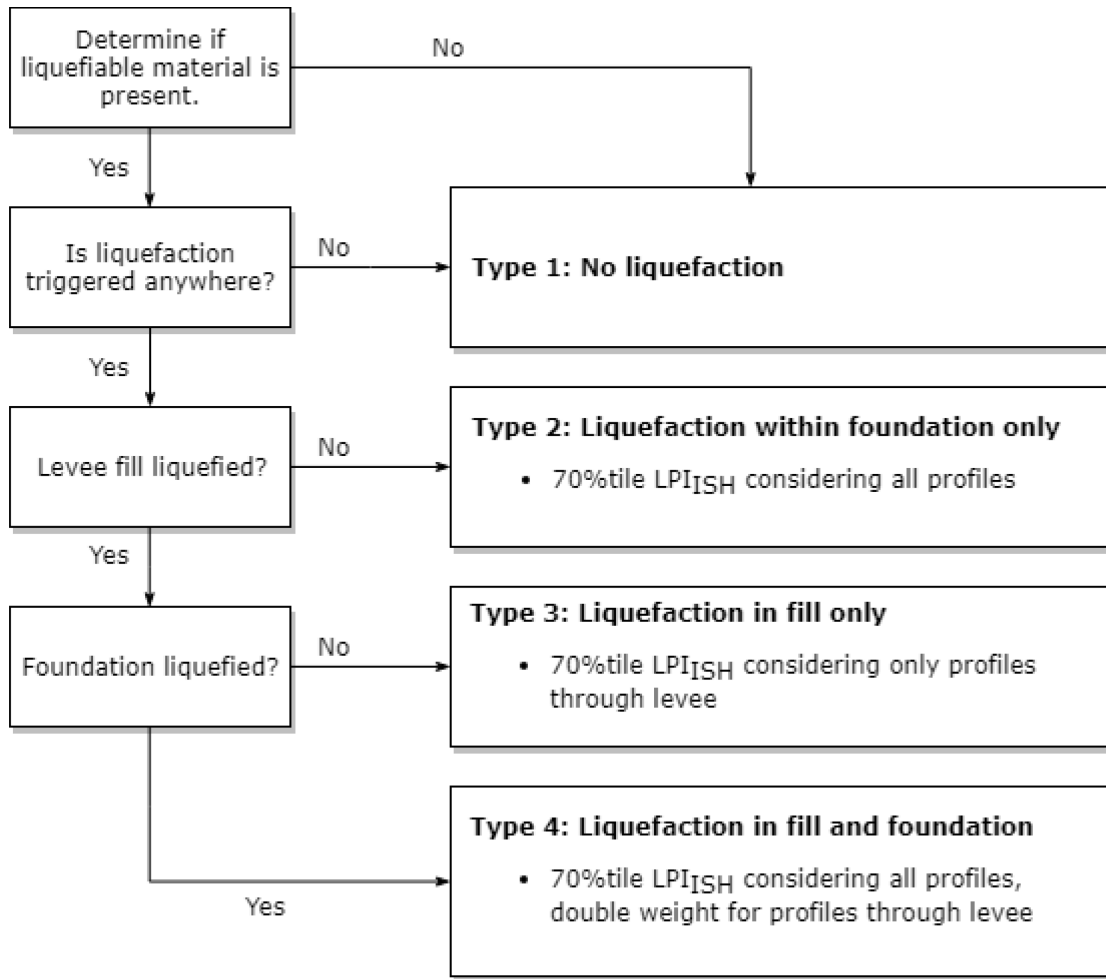


Figure 4.38 Flowchart for selecting representative value of liquefaction severity index from multiple borings at a cross section.

For slope stability, the displacements computed with fully liquefied strengths represent an upper bound estimate, since several loading cycles may be necessary to induce liquefaction. Both shear strains and volumetric strains are diminished greatly FS exceeds 1.0, and are approximately zero with  $FS \geq 2.0$  (Figure 4.39).

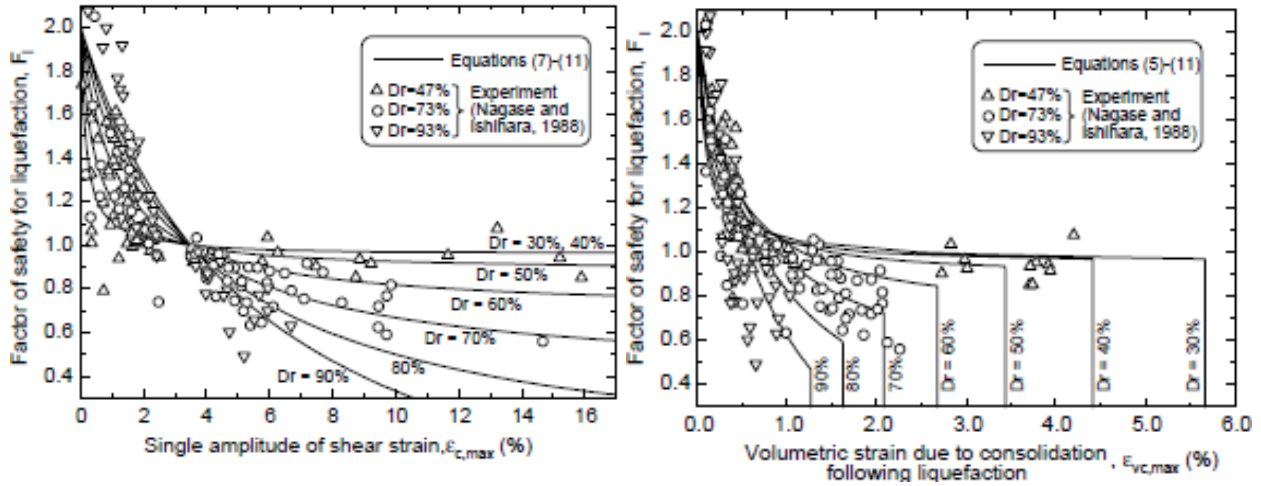


Figure 4.39 Relationships between maximum shear strain during cyclic loading (left) and volumetric strain following liquefaction (right) with factor of safety. Both tend towards zero as factor of safety exceeds 2.0 (Yoshimine et al., 2006)

The computed Newmark displacements from the initial and residual strengths are interpolated linearly based on Eq. (4.26), using the average FS within the liquefied strata that the critical failure surface passes through. In the limiting case where the material liquefied at the start of shaking ( $FS = 0$ ), the full deformation assuming with the liquefied strengths would be expected.

$$\Delta_{interpolated} = \begin{cases} \Delta_{pre-EQ} + \frac{2 - FS_{critical}}{2} (\Delta_{post EQ} - \Delta_{pre-EQ}), & FS \leq 2.0 \\ \Delta_{pre-EQ}, & FS > 2.0 \end{cases} \quad (4.26)$$

The damaged levels are predicted separately for the representative  $LPI_{ISH}$  and interpolated Newmark displacements. The  $LPI_{ISH}$  thresholds for surface manifestation severity recommended by Maurer et al. (2015b) performs well and is applied with a minor modification of subdividing the "severe liquefaction" category into damage levels 3 and 4. The thresholds for Newmark displacements are initially selected to be consistent with the subsidence criteria used to define the damage levels, then subsequently revised to reflect the overall higher range of displacements obtained from the analysis. The difference may arise from the rigid body assumption being violated as the levee deforms at large

displacement to a configuration with lower driving shear stresses and higher yield acceleration. The thresholds are summarized in Table 4.5.

Table 4.5 Damage level thresholds for  $LPI_{ISH}$  and Newmark displacements

Damage Level	$LPI_{ISH}$	Newmark Displacements
0	<1	<10
1	1-5	10-30
2	5-13	30-100
3	13-20	100-200
4	>20	>200

Having established a selection protocol for representative values, the resulting damage level predicted are compared with observations based on a single index and shown in Figure 4.40. Using only  $LPI_{ish}$ , predicted damage level shows fair amount of scatter and is significantly under predicting for section 11. Considering only Newmark, damage level is under predicted for sections 9 and 10, and over predicted for section 13.

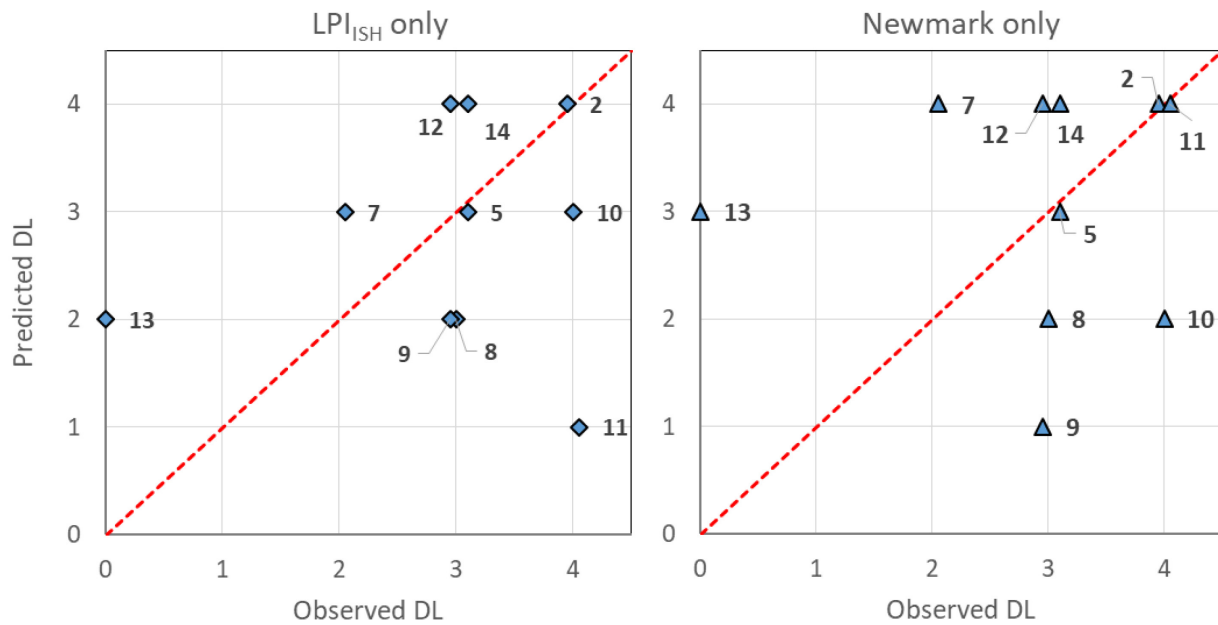


Figure 4.40 Damage levels predicted with only  $LPI_{ISH}$  or Newmark displacements tend to underestimate at high damage levels.

With the view that the two metrics are complementary and account for different causes of levee damage, a combined damage level is assigned as the more severe predicted damage level from the two methods, and is assigned to the cross section and shown in Figure 4.41. With the exception of sections 7 and 13, the damage level predicted with the combined index is within one level's difference from the observed performance. In particular, underestimation previously observed for sections 9, 10 and 11 are remedied by considering both metrics together. The combined damage assessment is therefore superior to either the liquefaction displacement index method or the Newmark sliding block method on its own.

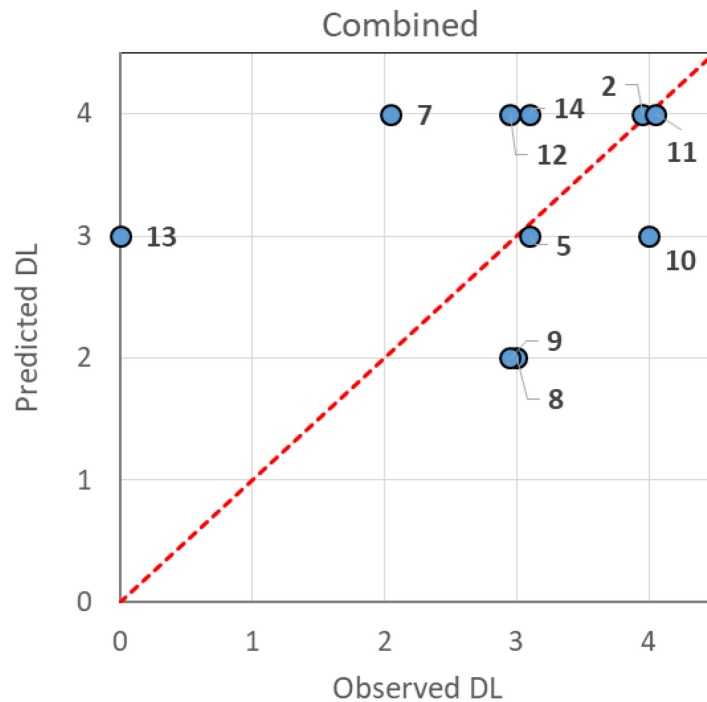


Figure 4.41 Predicted damage levels based on both Newmark displacements and  $LPI_{ish}$  minimizes under prediction for high damage levels and are generally within one damage level of the observed performance.

While the combined index improves the prediction at higher damage levels, over prediction for the lower damage levels is observed. In the following, example cases are discussed for a section where the combined index worked well, and for sections where damage was over-predicted.

### 4.5.1 Cross section 7

Damage level 2 was observed at cross section 7, whereas LPI<sub>ISH</sub> predicts damage level 3 and Newmark sliding block predicts damage level 4 due to a flow failure. This section explores possible reasons for the over-predictions.

Unlike other sections, the detailed construction history was unavailable at this location. Judging from the distinctive benched geometry and the cross sections of nearby segments, the levee likely started as a smaller structure and was subsequently expanded out towards the river. The oldest fill typically has low fines content and is susceptible to liquefaction. This zone is defined to be under the landside bench based on soil classification from the boring logs. The critical failure surface with  $FS < 1.0$  is shown in Figure 4.42 and passes through the liquefied levee fill.

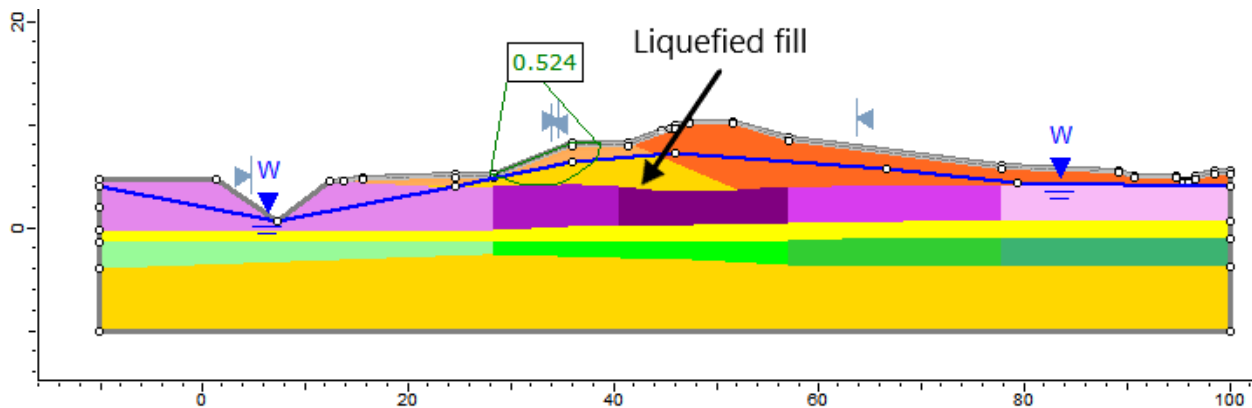


Figure 4.42 Flow failure predicted on land-side slope through liquefied levee fill ( $FS < 1.0$ ). The uncertainty in the extent of the liquefiable fill greatly influence the damage level predicted.

However, there is some uncertainty regarding the spatial extent of materials susceptible to liquefaction. The upper layers in the liquefiable zone contains moderate amount of silt, but the plasticity characteristics of the silt are not known. The silt may render the sand non-susceptible to liquefaction. In addition, the position of the groundwater table within the levee is known only at certain positions in the cross section at the time the boring logs were performed. It is possible that the groundwater table



was deeper within the predicted failure region. Both of these factors could contribute to an over-prediction of the spatial extent of liquefied soils, and therefore an over-prediction of damage.

#### **4.5.2 Cross section 11**

The levee section suffered extensive subsidence and deformation and required complete replacement after the earthquake. Newmark sliding block predicts damage level 4 and is in agreement with the observations, while  $LPI_{ISH}$  predicts damage level 1 and drastically underestimates the damage. This section explains the reasons for the significant difference in predictions, and highlights the benefits of accounting for complex damage mechanisms through applying multiple indices.

A thick non-liquefiable crust of peat and clay is present at this location. The sandy, saturated zone near the base of the levee and the silty sand layer below the clay is susceptible to liquefaction. The deeper sand layer expected to have minor influence given its greater depth and higher plasticity.

The liquefiable fill material is encountered in the SPT and CPT through the crest, but not in the investigations near the levee toe.  $LPI_{ISH}$  for the individual profiles ranges from 2-3 and unanimously predicts minor surficial manifestation. However the liquefied zone corresponds to the oldest levee fill and extends over most of the base on the river side. The reduced shear strength within this zone destabilizes the levee, and the critical surface now passes through the liquefied fill as shown in Figure 4.43. The FS for river side slope is barely above 1.0 which indicates the levee is on the verge of flow failure. Yield acceleration is similarly greatly reduced, and the Newmark displacements predicts several meters of movement.

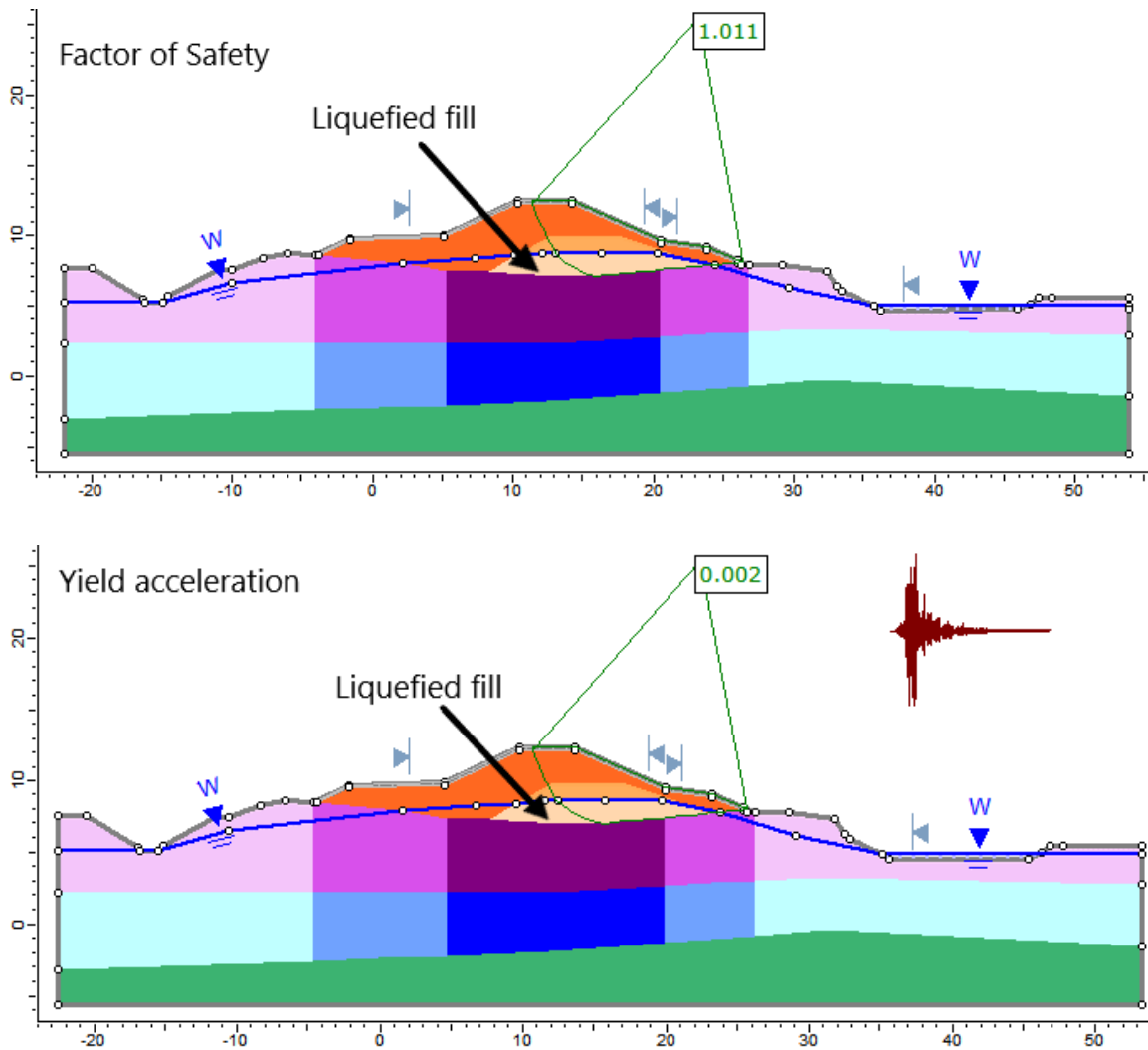


Figure 4.43 Reduced strength in the liquefiable zone at the base of the levee destabilized the levee. The factor of safety (top) and yield acceleration (bottom) are greatly lowered, with Newmark sliding block predicting large displacements.

Liquefaction indices considers a 1D soil column and cannot directly account for 2D effects such as lateral continuity and instability from existing shear stresses. For cross section 11, the damage due to a thin but laterally extensive liquefiable layer is greatly underestimated. Complementing the damage assessment with a 2D limit equilibrium slope stability analysis allows the potential instability to be identified from the location of the critical surface, low FS and high Newmark displacements.

### 4.5.3 Cross section 13

No visible damage was observed at cross section 7 despite  $LPI_{ISH}$  and Newmark sliding block predicting damage levels 2 and 3 (moderate to severe damage). This section discuss possible reasons for the over-prediction by both indices.

The subsurface conditions is relatively simple, with the levee resting directly on a thick layer of sand. The ground water is below the levee fill, but sufficiently shallow that surface manifestation through the unsaturated crust is expected if the underlying sand layer liquefies. The upper 0.5-1.0 m contains minor to moderate amounts of silt, below which the material transitions to clean sands. Liquefaction is predicted to be triggered in the saturated sand layer and lowers both the FS and yield acceleration. The slope is stable, but large displacements up to 2.4 m is predicted by the Newmark sliding block.

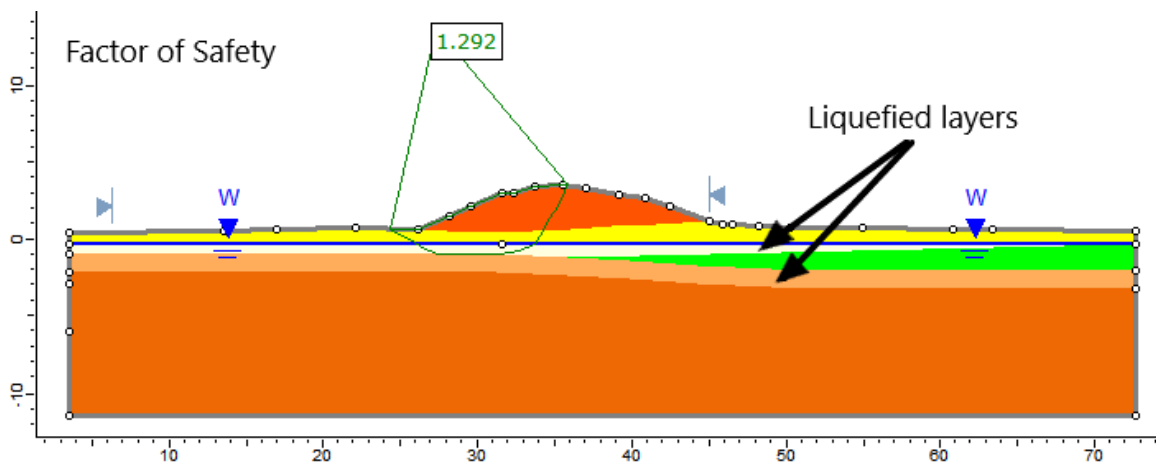


Figure 4.44 Liquefaction triggering is predicted in the saturated sand layer directly below the levee but leads to over-estimation of damage. Possible explanation is partial saturation in the upper layers during the earthquake.

Considering the lack of visible damage, liquefaction was likely not triggered in the surficial sand layers during the earthquake. Given the presence of the thick layer of clean sand with low blow counts which is clearly susceptible, incomplete saturation is the most plausible explanation for the absence of liquefaction. The ground water level is only measured at the crest for this location, therefore the depth

in the free field carries significant uncertainty. In addition, fluctuations in the ground water level may result in the shallower layers not being fully saturated. This case shows that the damage assessment is highly sensitive to the assessment of the liquefaction susceptibility and triggering.

## **4.6 SUMMARY**

Geotechnical engineering assessments are performed for 10 levee cross sections to predict damage severity and compared to the performance observed following the 2003 Tokachi-oki earthquake. Ground motion intensities and acceleration time histories are obtained from recording stations sited on the levees, which greatly reduce the uncertainty associated with estimating the seismic demand. Liquefaction severity indices, 2D slope stability and Newmark displacements are considered in combination to produce an overall damage level. The selection of a representative value for liquefaction severity indices associated with multiple investigations at a cross section is presented based on position of the liquefiable region to approximately account for effects of lateral continuity and static shear stress within the levee that is not directly captured by the 1-D analysis. The combined assessment accounts for different failure mechanisms and reduces under prediction seen with application of a single index, especially for higher damage levels.

The actual failure of the levee is highly complex and only partially represented in the simplified assessment. The deviation between predicted and observed damage severity may arise from a combination of factors, significant ones being (1) errors in determining liquefaction susceptibility solely based on soil classification available; (2) differences in ground water level present during the earthquake and measured during the site investigation, (3) differences in PGA between recording station and levee section; and (4) other contributing mechanisms, such as secondary consolidation of the underlying peat, that are not considered. Analysis of additional cross sections with lower damage

levels would be beneficial to ascertain if the suggested approach tend to over predict and make any necessary adjustments.

# 5 REGIONAL LINEAR SITE AMPLIFICATION MODEL FOR SOFT PEAT SITES

## 5.1 INTRODUCTION

The application of ergodic site terms in ground motion models (GMMs) to regions having very soft, peaty organic soils carries large epistemic uncertainty. One substantial driver of this uncertainty is the low time-averaged shear wave velocities in the upper 30 m ( $V_{S30}$ ) at these sites. Figure 5.1 shows the distribution of  $V_{S30}$  for stations in the NGA-West2 and NGA-Subduction databases. The peat sites in the downstream regions have  $V_{S30}$  around 100-200 m/s, and are on the lower limit of the dataset used to derive the ergodic models.

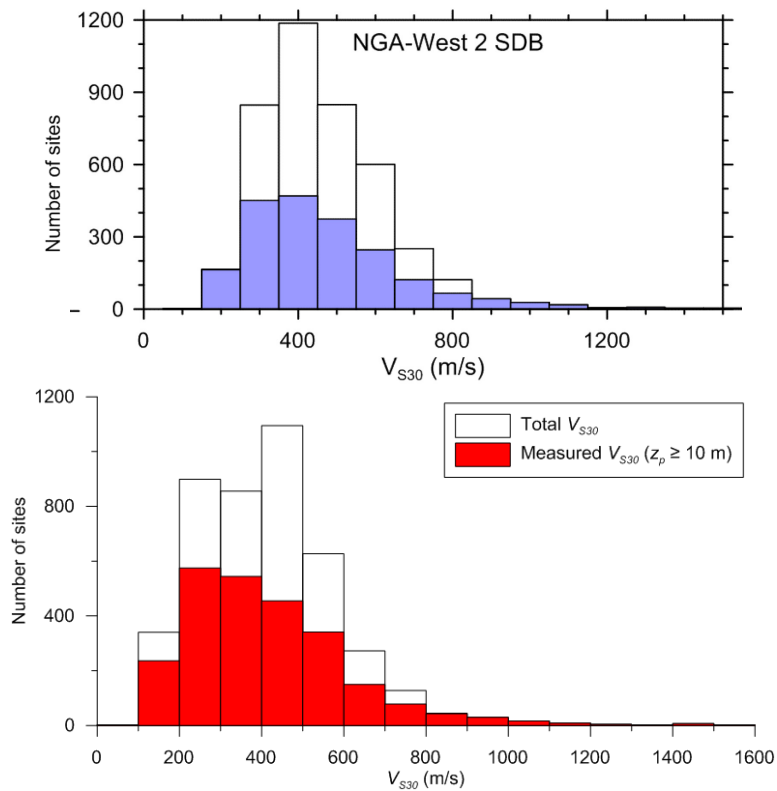


Figure 5.1 Histograms of  $V_{S30}$  for sites in NGA-West2 database (top, Seyhan and Stewart, 2014) and NGA-Subduction database (bottom, Ahdi et al. 2017).

In addition, as soft peats usually overlie relatively firm, inorganic soils at depth, the steep velocity gradients within the site profile that can give rise to more pronounced impedance and resonance effects than would be typical at non-peat sites. Such effects produce site response transfer functions with strong peaks at one or more site frequencies. These features of site response cannot be captured by  $V_{S30}$ -based models as used in typical GMMs, although they could potentially be captured by a model that combines  $V_{S30}$ -scaling terms with site resonance terms that take the peak frequency ( $f_{\text{peak}}$ ) as a site parameter (e.g., Kwak et al., 2017; Hassani and Atkinson, 2018a and 2018b).

As a result, the ergodic site terms in current GMMs for subduction earthquakes in Japan, whether based on  $V_{S30}$  (Abrahamson et al. 2016, 2018) or site class (Zhao et al. 2016a and 2016b), are expected to have bias and large uncertainty when applied to peaty organic soil sites in Hokkaido. The objective in this study is to improve ground motion estimates by developing region-specific ergodic site amplification models derived from non-ergodic site responses at recordings sites. In other words, we seek to gain insights into the features of local site response from non-ergodic analyses, including impedance and resonance effects, and then to build a more generic (local but ergodic) model from those results.

The approach taken in this chapter is to develop a linear site amplification model using recordings with relatively low amplitudes, where significant nonlinear effects are not expected. We subsequently examine nonlinear effects through residuals analysis using data from one event that produced relatively strong shaking. Nonlinear effects are further investigated using ground response analysis in Chapter 6.

## 5.2 DATA SOURCES

The region-specific analysis performed in this study applies to the portion of the Tokachi River in Hokkaido, Japan passing through peaty organic soil layers that extend roughly from the river mouth to 50 km upstream of the river mouth, as shown in Figure 5.2. This region contains seven instruments owned and operated by the Obihiro Development and Construction Department (ODCD), for which we have processed recordings from nine earthquakes in the NGA-Sub database. This section discusses the data compiled for analysis of non-ergodic site responses at these seven stations.

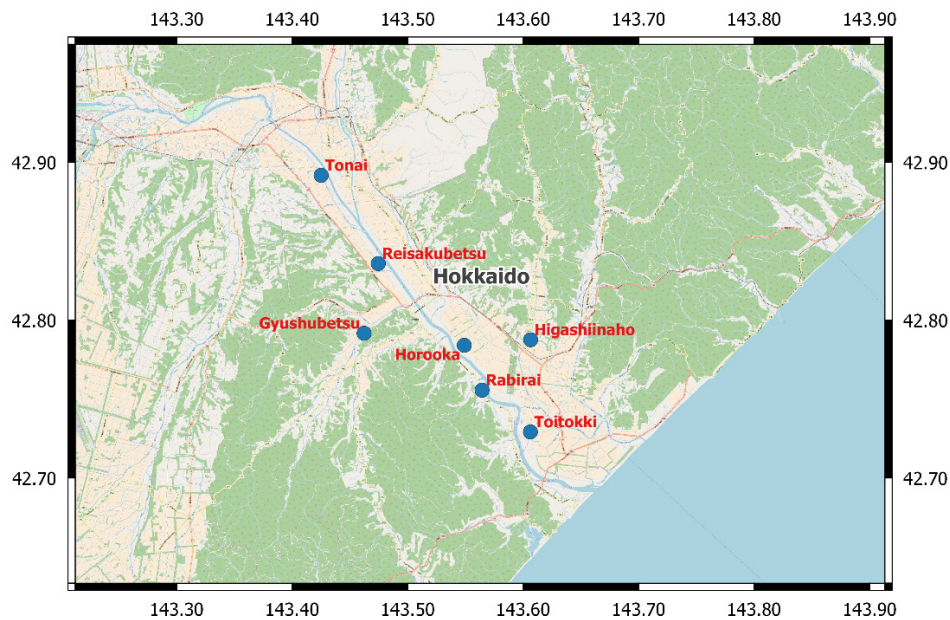


Figure 5.2 Recording stations on levees in the downstream region of Tokachi.

### 5.2.1 Ground Motions and Related Metadata

Table 5.1 provides the metadata for the seven stations in the study region. The station locations were provided by ODCD and the basis for the site information ( $V_{S30}$  and classification) is provided in Section 5.2.2. As shown in Figure 5.2, the stations are distributed evenly with good spatial coverage across the study region.



Table 5.1 Metadata of ODCD stations

Station Name	Longitude	Latitude	$V_{S30}$ (m/s)	$f_{peak}$ (Hz)	Site Class
Gyushubestu	143.4622	42.7921	130.8	1.14	IV
Higashiinaho	143.6063	42.7876	211.5	1.6	III
Horooka	143.5589	42.7841	102.2	1.42	IV
Reisakubetsu	143.4744	42.8359	181.4	1.62	IV
Rabirai	143.5642	42.7556	150.5	1.14	IV
Toitokki	143.6043	42.7281	117.2	0.88	IV
Gyushubestu	143.4622	42.7921	130.8	1.14	IV
Tonai	143.4250	42.8917	181.4	1.50	IV

The stations have recorded 25 earthquakes from 1994 to 2013, of which nine are included in the NGA-Subduction database (Kishida et al. 2017). The event metadata and the number of processed recordings available are summarized in Table 5.2, and the hypocenter locations are shown in Figure 5.3.

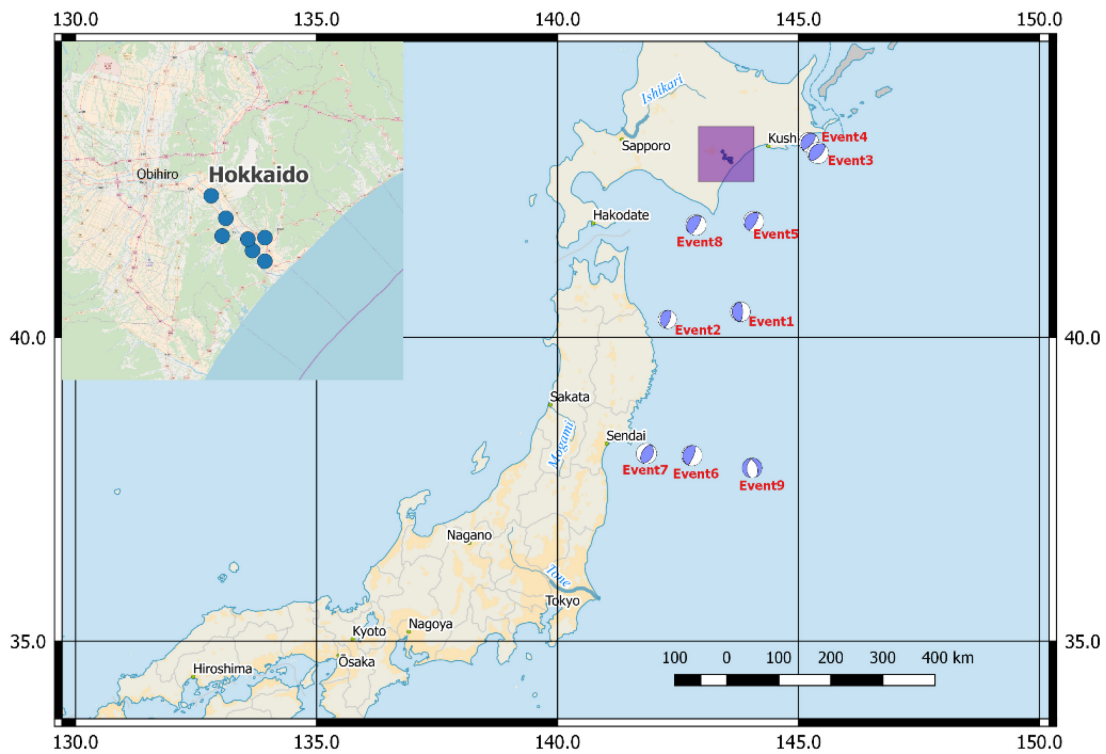


Figure 5.3 Focal mechanisms of events in NGA-subduction databases that have produced recordings at the ODCD stations.

Table 5.2 Metadata for the nine considered earthquakes

Event	Date	$M_w$	Event Type	Longitude Latitude	Hypocenter Depth (km)	NGA-SUB recordings		ODCD Stations
						Total	Used	
1	1994/12/28	7.7	Interface	143.75, 40.43	10	31	10	3
2	1995/01/06	7	Interface	142.31, 40.22	47.8	13	0	3
3	2004/11/28	7	Interface	145.28, 42.95	48.17	378	84	7
4	2004/12/06	6.7	Interface	145.34, 42.85	45.84	204	57	7
5	2008/09/11	6.8	Interface	144.15, 41.78	30.86	407	64	6
6	2011/03/11	9.1	Interface	142.86, 38.10	23.74	1293	698	7
7	2011/04/07	7.1	Slab	141.92, 38.20	65.9	799	445	7
8	2011/11/24	6.2	Interface	142.89, 41.75	43.21	177	57	6
9	2012/12/07	7.3	Slab	144.12, 37.84	52	866	359	7
10	2003/09/25	8.29	Interface	144.09, 41.78	25	302	173	6

Note: All events are subduction earthquakes with reverse faulting

For each event, a subset of the NGA-Sub recordings is used, as illustrated in Figure 5.4 for Event 6 (the 2011 Tohoku earthquake). Stations beyond the maximum limiting distance criteria provided in the NGA-Sub flatfile are shown in pink and stations in the backarc (northwest of the volcanic arc) are in blue, both are excluded and only stations in green are used in the subsequent analysis. Limiting distance criteria is intended to avoid potential bias from recordings with weaker amplitudes failing to trigger the instruments. Stations beyond a maximum distance  $R_{max}$  are excluded. The cutoff distance depends on instrument properties and varies between the networks. In cases where the rupture distances of Obihiro stations are modestly larger than  $R_{max}$ , we extend the NGA-Subduction values of  $R_{max}$  (by no

more than 40%) to include the stations at these distance ranges. Backarc stations are not used because the Obihiro sites of interest in are in the forearc, and our principle interest is source-site wave paths within the forearc. Event 2 is excluded due to deficiency in useable recordings - of the 13 recordings in the NGA-Sub database, nine are removed based on the  $R_{max}$  criteria, and the remaining four have rupture distances much less than those for ODCD stations (113 vs 300 km).

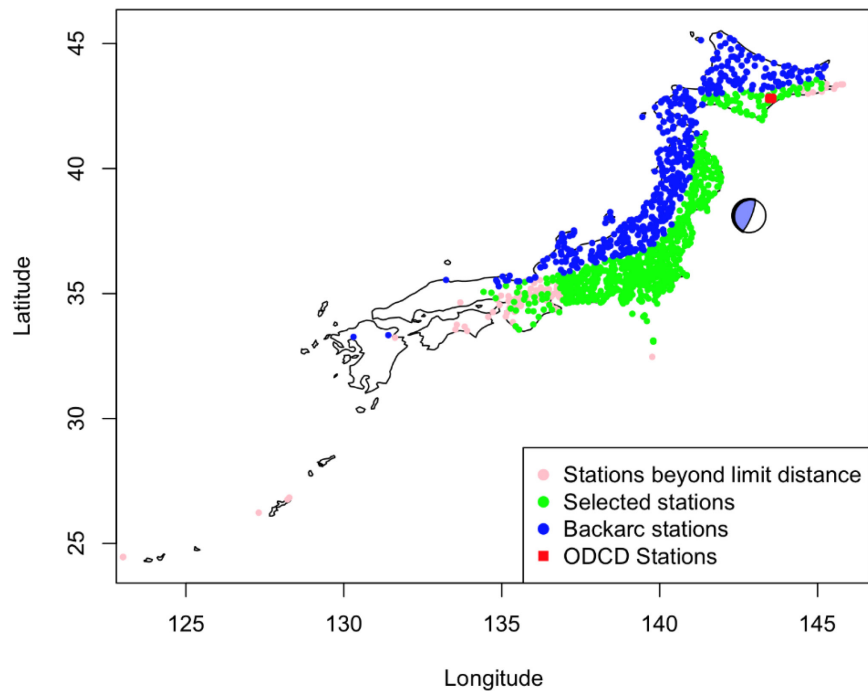


Figure 5.4 Recordings for Event 6 (2011 Tohoku earthquake), showing stations used in this study (green), stations not considered on basis of distance cutoff criteria developed in the NGA-Subduction project (pink), stations not considered due to their location in the backarc region of Japan (blue), and ODCD stations (red).

The recordings at the ODCD stations are not part of the NGA-Subduction database and the raw digital recordings were provided by S. Takashi (personal communication, last update November 10<sup>th</sup>, 2017). The data was processed following PEER procedures (Ancheta et al. 2014), and included instrument correction, application of both high and low pass acausal filters at operator-determined corner frequencies and baseline correction. The median-component intensity measures RotD50 (Boore, 2010)

for peak acceleration, peak velocity, and 5% damped pseudo-spectral accelerations (PSA) are computed from the post-processed recordings with the R package by Wang et al. (2017).

As shown in Figure 5.5, Events 1-9 produced relatively weak motion recordings at the ODCD stations, which are useful for developing the linear component of a regional site amplification model. In contrast, Event 10 (2003 Tokachi-Oki Earthquake) produces appreciably stronger shaking. Accordingly, our approach to model development is to develop a linear model using data from Events 1-9, and then to perform residuals analysis using data from Event 10 to investigate potential nonlinearity effects.

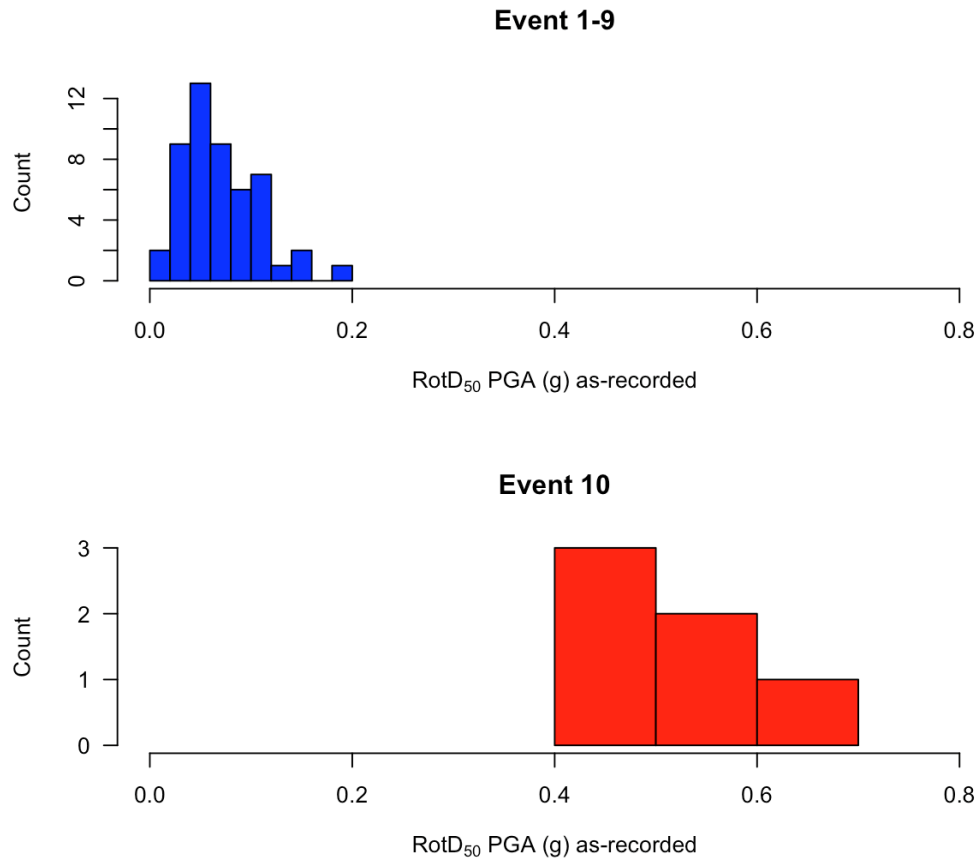


Figure 5.5 Histograms of median-component peak accelerations at ODCD stations for Events 1-9 and Event 10, with the latter having significantly higher intensity.

Development of the linear component of the site amplification function requires recordings of weak motions such that nonlinearity is not expected to have significant influence. The median rock PGA

predicted by the GMM at the stations for each earthquake is used to screen out stronger motions, which is taken as  $PGA_{rock}$  exceeding 0.1 g. Event 1-9 are below this threshold and used to develop the linear component of the site response, while event 10 is set aside to examine the effect of nonlinearity.

### 5.3 GROUND MOTION DATA ANALYSIS

This section presents our analyses of ground motion recordings to support model development, which is presented in Section 5.4. Section 5.3.1 describes analyses that provide region-adjusted, within event residuals for event  $i$  and recording  $j$ ,  $\delta W_{ij}^{reg}$ , at the seven ODCD sites. Non-ergodic site responses are evaluated for each site in Section 5.3.2. Section 5.3.3 describes the analysis of H/V spectral ratios from ground motion recordings at the ODCD instruments; such information supplements the geophysical site exploration presented in Section 5.2.2.

#### 5.3.1 Event terms and region terms

Our approach to data analysis operates on residuals, which are the difference between the natural log of an observation and its prediction from a GMM. Models developed from recordings of subduction earthquakes in Japan by Zhao et al. (2016a and 2016b) (Zea16 herein) is selected. We investigate sensitivity to the GMM by also examining residuals of the data relative to the Abrahamson et al (2018) (Aea18 herein) GMM applied with Japan regionalized path terms (Section 5.5).

Total residuals are computed using the reference GMM as:

$$R_{ij} = \ln(Y_{ij}) - (\mu_{\ln Y})_{ij} \quad (5.1)$$

where  $Y_{ij}$  is the observed RotD50 intensity measure for recording  $j$  from event  $i$ , and  $(\mu_{\ln Y})_{ij}$  is the natural log mean prediction from a GMM for the given magnitude, site-source distance, site condition,

and other parameters used in the model. Non-zero residuals indicate deviation from the observed ground motion from the prediction, and have several potential causes. The ground motions from a given earthquake may be systematically low or high relative to the median prediction from the GMM. Likewise, a particular source-to-site path may have attenuation that is higher or lower than the average rate. As the ultimate goal is to quantify the site response from the residuals, systematic (repeatable) effects related to source or path are removed from the total residuals computed using Eq. (5.1). The remainder of this section addresses the adjustment to the total residuals based on the available data.

Figure 5.6 to 5.9 show total residuals versus rupture distance. Bias in the GMM path term appear as positive or negative trend with distance. Residuals from events 3, 4, and 7 show slopes at short periods, trending up for Hokkaido stations beyond 200 km (Event 3 and 4, periods 0.005 s and 0.08 s) and divergent slopes for Hokkaido stations and Honshu stations beyond about 300 km. We considered adjusting the path term to model these regional differences, but eventually elected to limit the distances to 200 km for Events 3 and 4, and 300 km for Event 7 where the residuals are nearly flat. Trends with distance are not observed for the remaining events.

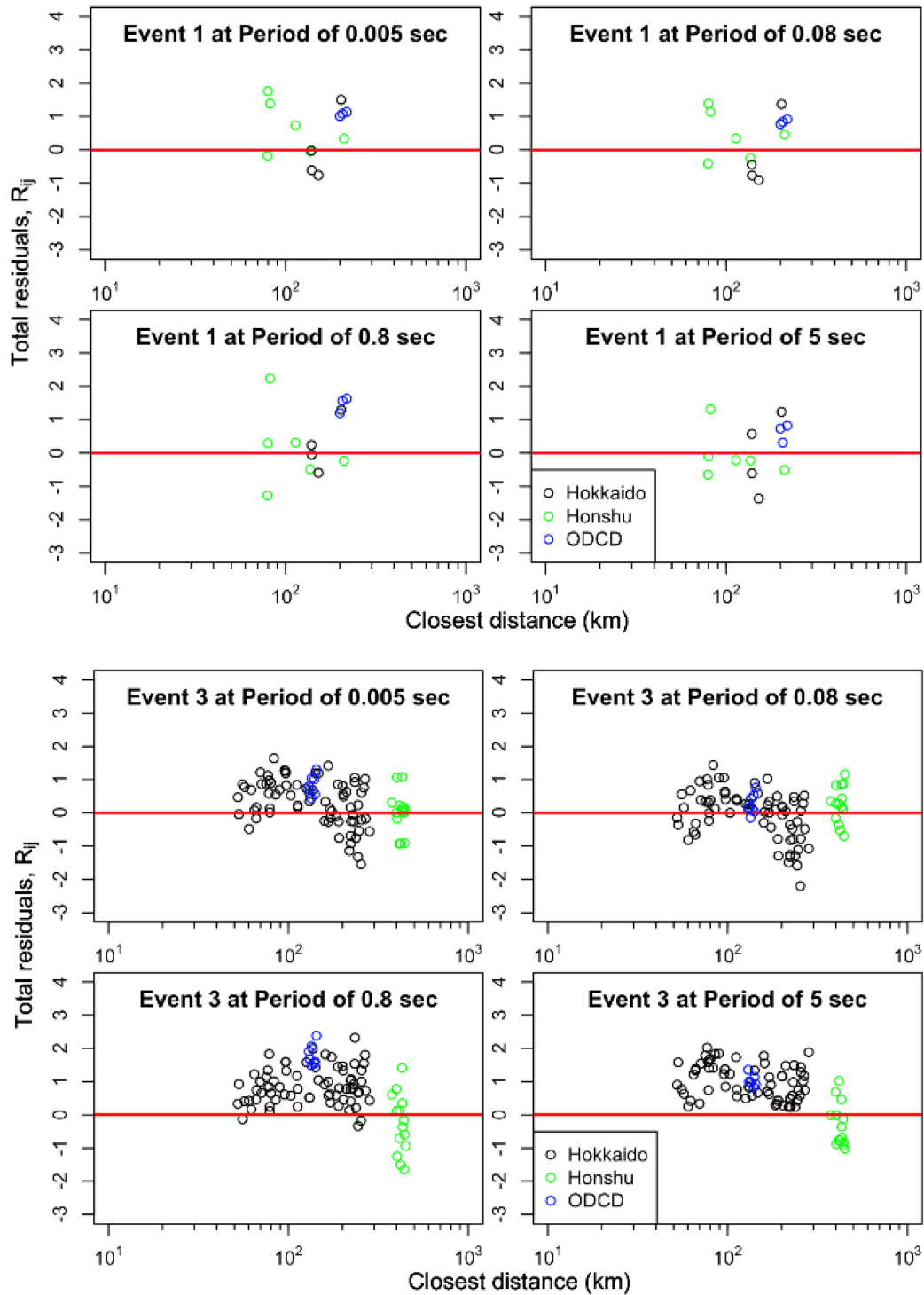


Figure 5.6 Variation of total residuals with distance for Events 1 and 3. Event 3 shows a negative trend with distance at short periods.

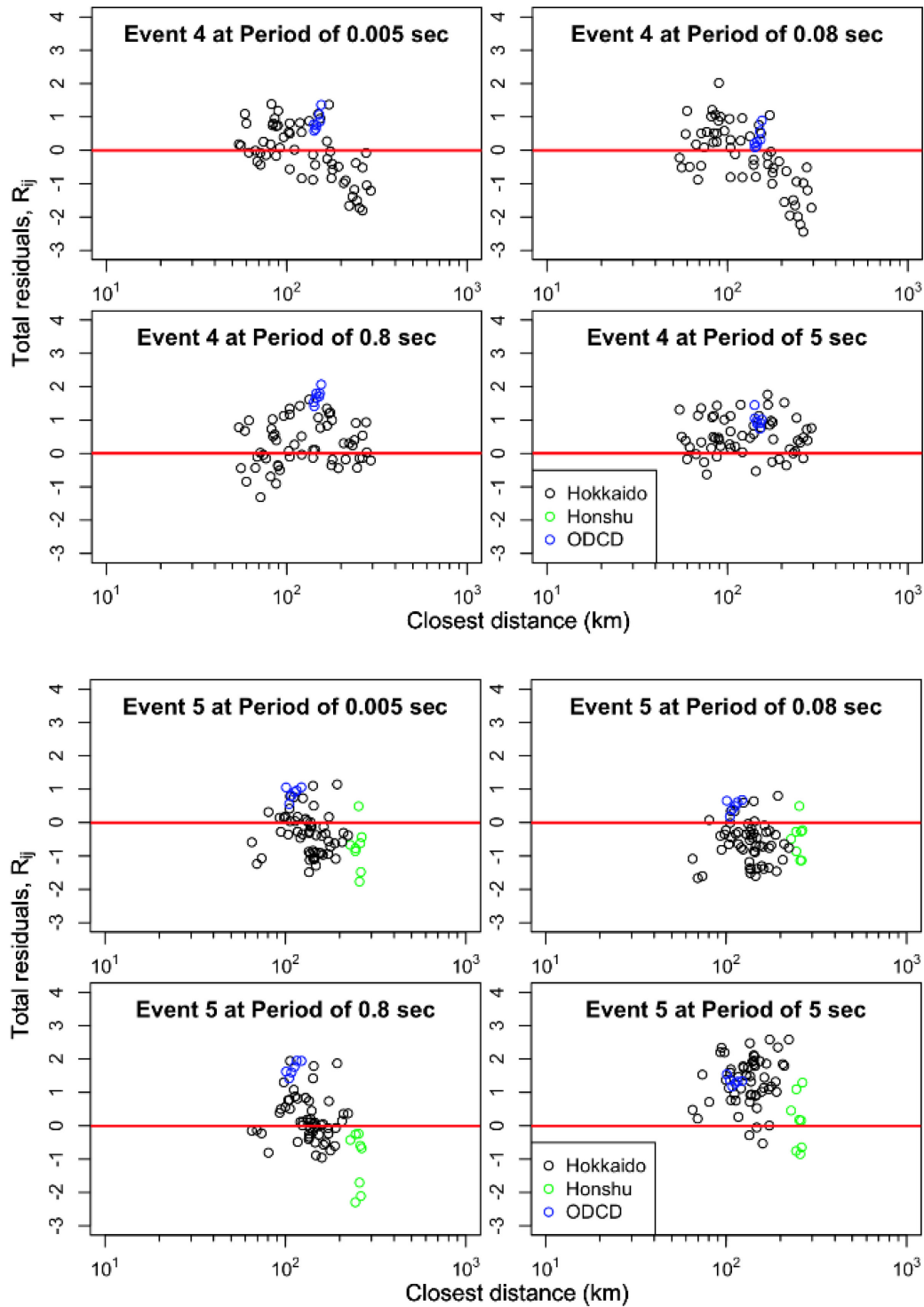


Figure 5.7 Variation of total residuals with distance for Events 4 and 5. Event 4 shows a negative trend with distance at short periods.



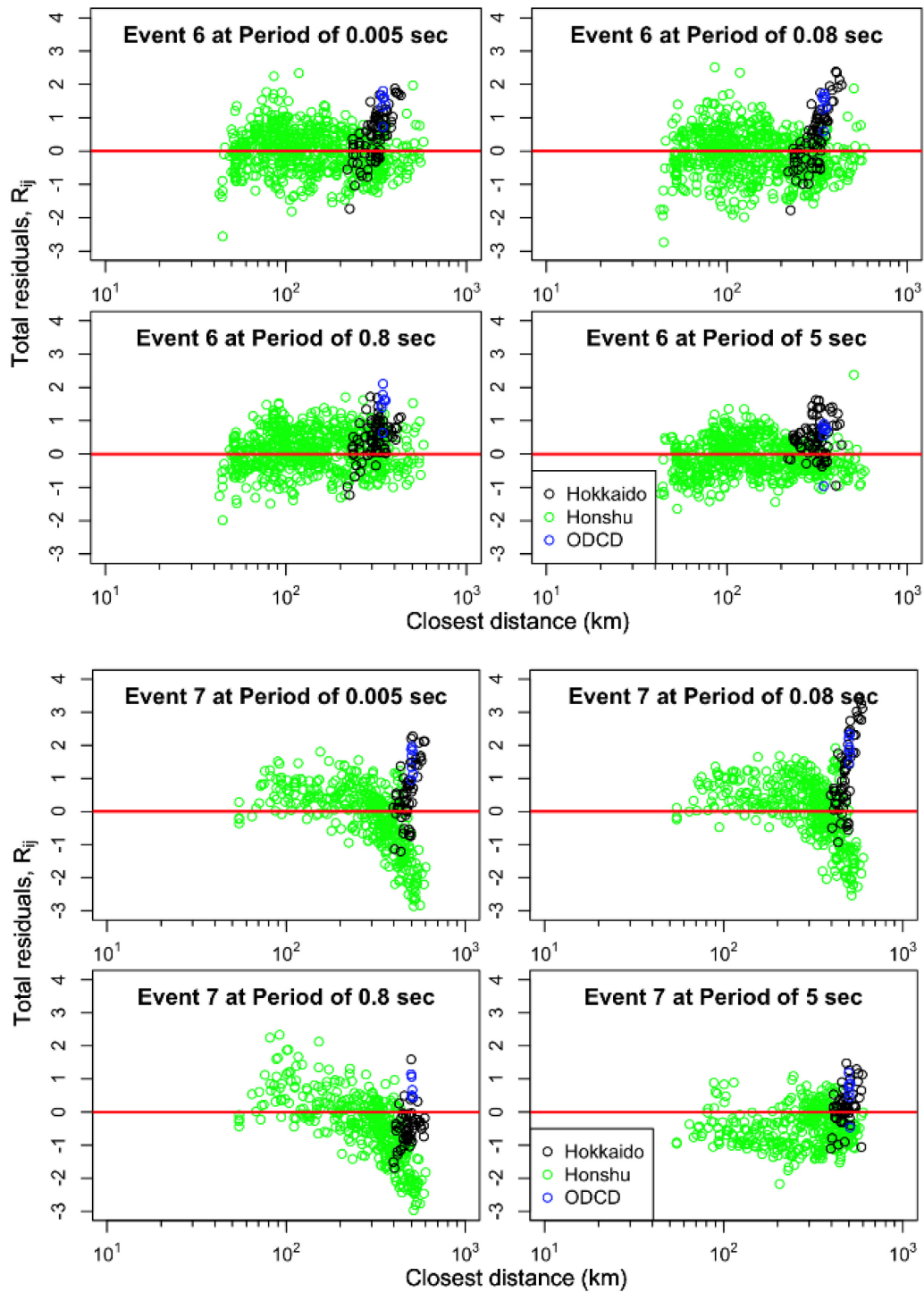


Figure 5.8 Variation of total residuals with distance for Event 6 and 7. Event 7 shows a strong negative trend with distance for Honshu stations (green) and a positive trend for Hokkaido stations (black) at short periods.

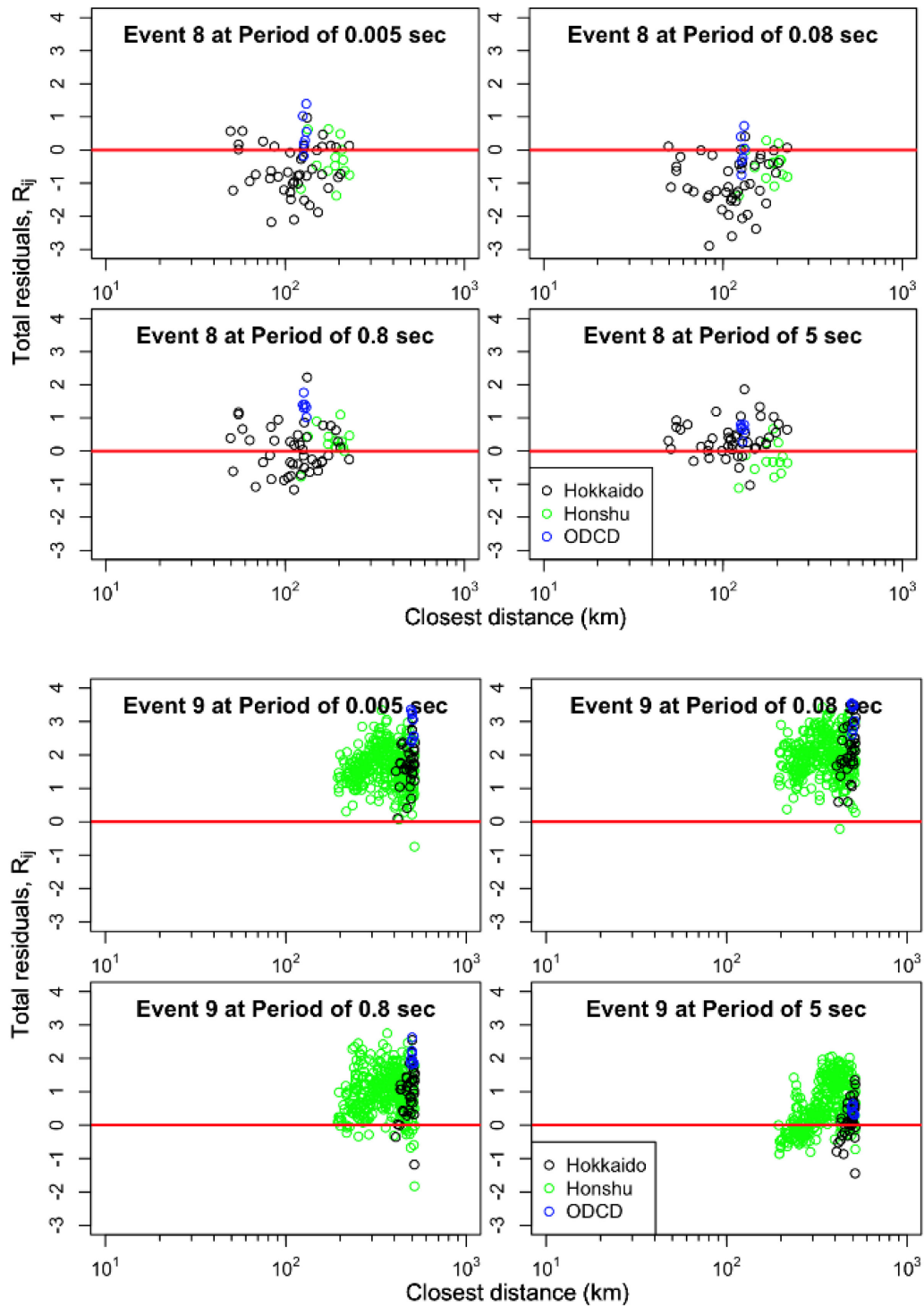


Figure 5.9 Variation of total residuals with distance for Events 8 and 9.

For a given event  $i$ , the event term is taken as the average of the residuals:

$$\eta_{E,i} = \frac{1}{n_i} \sum_{j=1}^{n_i} R_{ij} \quad (5.2)$$

where  $n_i$  is the number of recordings from stations within the range of applicability of the selected GMM for event  $i$ . Eq. (5.2) represents a use of Frequentist statistics, with the other option being a random effects model (Bayesian statistics). We adopt the Frequentist approach so as to provide unbiased estimators for the event terms (Stewart et al. 2017). As described in Section 5.2.1, stations in the backarc and with site-to-source distances beyond maximum limiting distance of NGA-Subduction data are excluded. Data are also excluded beyond the aforementioned limiting distances for Events 3, 4, and 7. The use of Eq. (5.2) implies the GMM is unbiased overall, otherwise a constant term accounting for the model bias (usually denoted as  $c_c$ ) should be added for all events. A model may be biased when applied to data from a different region, since Zea16

Event terms obtained from Eq. (5.2) are shown in Figure 5.9. Most of the event terms are positive, indicating under-prediction by Zea16. The exception is Event 9 with a large positive event term, around 1.5-2.0 for periods less than 0.3 sec.

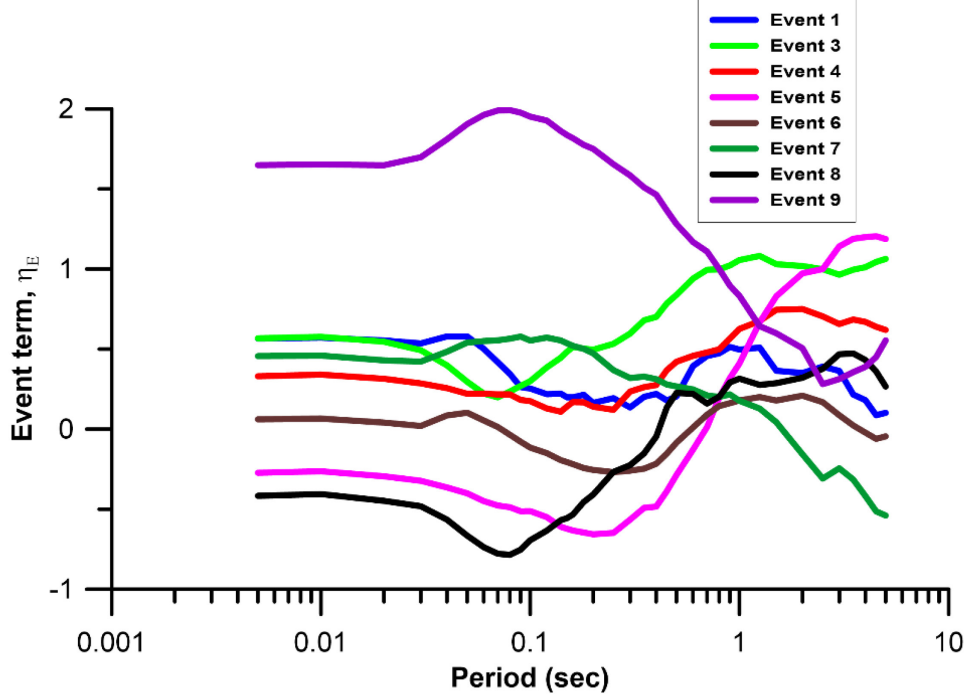


Figure 5.10 Event terms across periods for the eight events recorded by the ODCD stations

Japan is known to have strong regional variations in anelastic attenuation (e.g., Ghofrani and Atkinson, 2011) which can introduce systematic differences in residuals between the forearc and backarc sites. The effects of paths crossing the volcanic front was addressed by excluding backarc stations. Additional regional complexities in the forearc, observed for Events 3, 4 and 7, were addressed with implementing distance cutoffs. The remaining issue considered here is potential effects of travel paths passing between Honshu and Hokkaido (i.e., the rupture near Hokkaido is recorded by a station on Honshu). To investigate this, we first compute the within-event residual as,

$$\delta W_{ij} = R_{ij} - \eta_{Ei} \quad (5.3)$$

which is plotted against distance in Figure 5.10. Honshu stations show a negative trend with distance, while Hokkaido stations shows a positive trend with distance starting around 300 km, and is most apparent for short periods. Since these divergences are a path phenomenon, they should be removed prior to the site term analysis. Accordingly, we separate sources and sites into North (latitude > 39

degrees) and South (latitude < 39 degrees) regions to examine if region terms are necessary when a subset of recordings are in a different region than the earthquake occurs in one region. The North group includes Hokkaido sites and Events 1, 3, 4, 5, and 8. The South group includes Honshu sites and Events 6, 7, and 9.

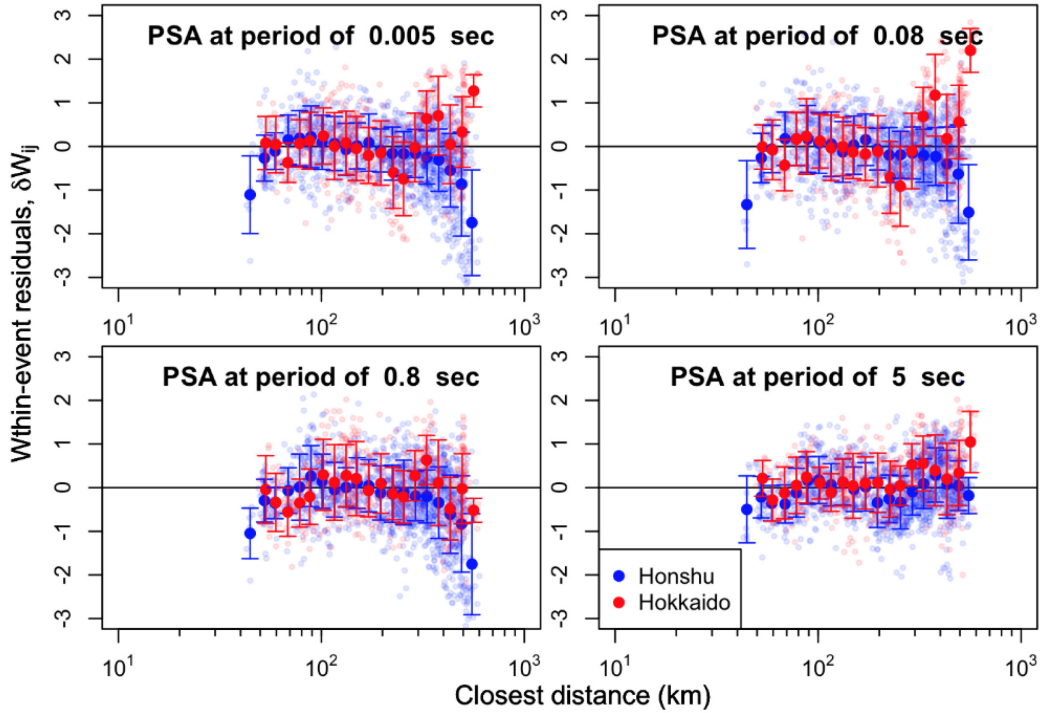


Figure 5.11 Within-event residuals for all eight events. Trends with distance differ between Honshu and Hokkaido stations and is most apparent at short periods.

Region terms for each combination of event and station regions are computed as the average of the within-event residuals,

$$\eta_{reg,l,k} = \frac{1}{n_{l,k}} \sum_{\forall i \in l, \forall j \in k} \delta W_{ij} \quad (5.4)$$

where  $i$  is the event index and  $j$  the recording index respectively, the  $\forall$  symbol in combination with  $\in$  (e.g.,  $\forall i \in l$ ) indicates ‘for any value of  $i$  among the set specified by array  $l$ ’, which sorts the data into source-path groups. We take  $l \in \{0, 1\}$  (i.e.,  $l$  can be 0 or 1) to segregate event regions (0 refers to

South Events and 1 refers to North Events) and  $k \in \{0, 1\}$  to segregate station regions (0 refers to Honshu and 1 refers to Hokkaido). Figure 5.11 plots the region terms over the period range 0.08 sec to 5 sec with their 95% confidence intervals for each source-station regional combination. For cases with source and station in the same region (e.g., Honshu stations recording South region events, index  $l = 0$  and  $k = 0$ ), region terms are relatively small without distinct trend with period. However large biases are present when the indices differ. The highly positive region terms at short periods ( $< 2$  sec) for South events and Hokkaido stations is consistent with the upward (positive) trend in the residuals in Figure 5.10. There is also a large negative bias at long periods for North events recorded by Honshu stations.

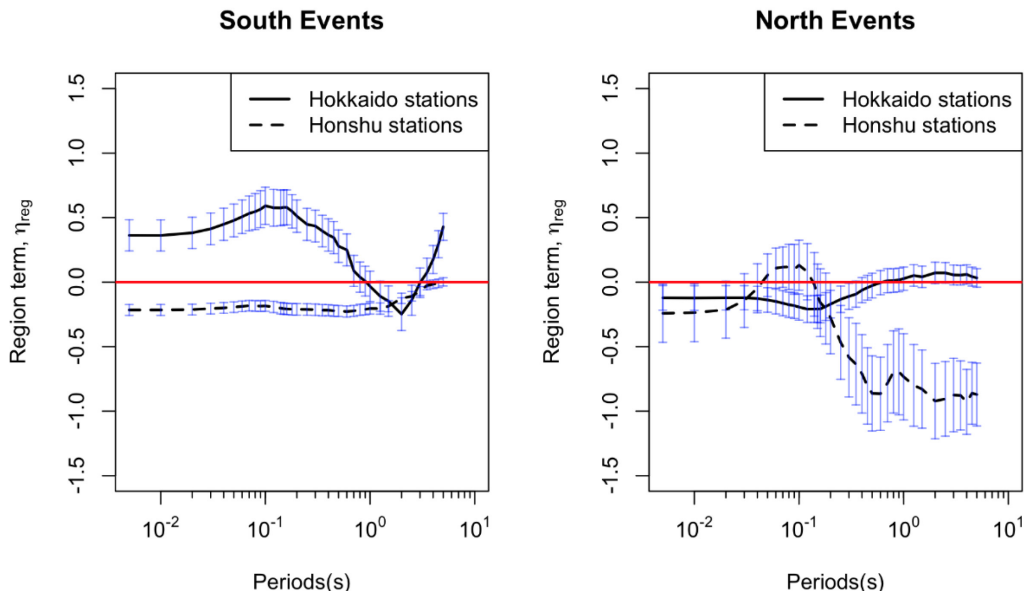


Figure 5.12 Region terms for Hokkaido and Honshu stations for events from South or North region.

The between-island effect is a novel observation, therefore prior to including these regional effects in subsequent analyses, the statistical significance of the distinguishing between the data groups is judged with statistical F test (Cook and Weiberg, 1999). The F test examines whether a data set is better described by a combined single model or a set of sub-models; the combined model would not consider the regional terms, whereas the sub-models would include the four regional combinations. The F statistic is given by,

$$F = \frac{(RSS_f - \sum_{l=0}^1 \sum_{k=0}^1 RSS_{l,k}) / (\sum_{l=0}^1 \sum_{k=0}^1 p_{l,k} - p_f)}{\hat{\sigma}^2} \quad (5.5)$$

where  $RSS_{l,k}$  represents the residuals sum of squares (RSS) of the submodel for the  $l$  event region and  $k$  station region, and  $p$  refers to the number of fitted parameters in the full model and submodels. Since the ‘models’ are simply the means,  $p = 1$  in each case (for combined model and each individual sub-model). The denominator is given by,

$$\hat{\sigma}^2 = \frac{\sum_{l=0}^1 \sum_{k=0}^1 RSS_{l,k}}{\sum_{l=0}^1 \sum_{k=0}^1 (N_{l,k} - p_{l,k})} = \frac{\sum_{l=0}^1 \sum_{k=0}^1 RSS_{l,k}}{\sum_{l=0}^1 \sum_{k=0}^1 df_{l,k}} \quad (5.6)$$

where  $N_{l,k}$  is the number of recordings for the data belonging to source group  $l$  and station group  $k$ ,  $p_{l,k}$  is the number of fitted parameters for that sub-model, and  $df_{l,k} = N_{l,k} - p_{l,k}$  is the degree of freedom for that sub-model. The degree of freedom of the full (combined) model is  $df_f = N - p_f = \sum_{l=0}^1 \sum_{k=0}^1 N_{l,k} - p_f$ . In this case, the summation in Eq. (5.5) and (5.6) unrelated to  $RSS$  are  $(\sum_{l=0}^1 \sum_{k=0}^1 p_{l,k} - p_f) = df_f - \sum_{l=0}^1 \sum_{k=0}^1 df_{l,k} = 3$ , and  $\sum_{l=0}^1 \sum_{k=0}^1 df_{l,k} = 1820$ .

The F statistic is compared to the F distribution to evaluate a significance level ( $p$ ) for the test, where values exceeding a select threshold (i.e.,  $p > 0.05$ ) imply the sub-models are not distinct. The results from F-test for four selected periods are shown in Table 5.3 for the case of one overall combined model in comparison to four sub-models. The F statistic, the minimum value of the F statistic for  $p = 0.05$ , and the significance level are provided. In each case, the testing indicates that the sub-models are distinct and justifies the use of regional terms.

Table 5.3 F-test for significance of region effects for both sources and sites

Period (s)		Full model $f$	Submodels $l = \{0, 1\}$ $k = \{0, 1\}$	F-statistic	F-critical <sub>(3, 1827)</sub> value at significance level $p=0.05$	p-value			
0.005	RSS	1174.09	1081.39	52.00	2.61	0			
	df	1823	1820						
0.08	RSS	1211.89	1102.70	60.07		2.61	0		
	df	1823	1820						
0.80	RSS	1184.04	1102.36	44.95			2.61	0	
	df	1823	1820						
5.00	RSS	724.74	659.52	60.00				2.61	0
	df	1823	1820						

We also consider two additional F tests to examine the difference between Honshu and Hokkaido recordings, considering only data from source region (i.e., only South event data in one set of tests, and only North event data in a second set of tests). In this case, the F-statistic is computed as:

$$F_l = \frac{(RSS_l - \sum_{k=0}^1 RSS_{l,k}) / (\sum_{k=0}^1 p_{l,k} - p_l)}{\hat{\sigma}_l^2} \quad (5.7)$$

where  $l$  is either 0 or 1, and the denominator is,

$$\hat{\sigma}_l^2 = \frac{\sum_{k=0}^1 RSS_{l,k}}{\sum_{k=0}^1 (N_{l,k} - p_{l,k})} = \frac{\sum_{k=0}^1 RSS_{l,k}}{\sum_{k=0}^1 df_{l,k}} \quad (5.8)$$

The combined model for these tests groups Honshu and Hokkaido recordings for a given event group  $l = 0$  or 1, and  $RSS_l$  represents the RSS for that combined model. The results of two F-tests for  $l = 0$  (South Event) and  $l = 1$  (North Event) are given in Table 5.4 and 5.5. For most cases, the testing confirms that the separation of regions for each event group is justified. These exceptions occur at periods where the regional terms in Figure 5.11 are nearly zero (e.g., T=0.08s for North events, where the p-value is 0.35).



Table 5.4 F-test for significance of region effects for both sources and sites

Period (s)		South Event model $l = 0$	Submodels $l = 0$ $k = \{0, 1\}$	F-statistics	F-critical <sub>(1, 1521)</sub> at significance level $p=0.05$	p-value
0.005	RSS	963.59	909.49	90.46	3.85	0
	df	1522	1521			
0.08	RSS	1014.85	928.29	141.83		
	df	1522	1521			
0.80	RSS	931.52	921.12	17.19		
	df	1522	1521			
5.00	RSS	578.81	549.33	81.64		
	df	1522	1521			

Table 5.5 F-test for significance of region effects for both sources and sites

Period (s)		North Event model $l = 1$	Submodels $l = 1$ $k = \{0, 1\}$	F-statistics	F-critical <sub>(1, 299)</sub> at significance level $p=0.05$	p-value
0.005	RSS	172.41	171.90	0.88	3.87	0.35
	df	300	299			
0.08	RSS	177.46	174.41	5.22		
	df	300	299			
0.80	RSS	199.03	181.23	29.36		
	df	300	299			
5.00	RSS	139.12	110.19	78.51		
	df	300	299			

Based on the results seen in Figure 5.11 and the statistical testing, we consider the between-island regional terms significant and incorporated regional terms into the residuals analysis. The region terms to the within-event residuals from Eq. (5.4) as follows:

$$\delta W_{ij}^{reg} = \delta W_{ij} - \eta_{reg,l,k} \quad (5.9)$$

where  $\delta W_{ij}^{reg}$  is the region-adjusted within-event residual.

Figure 5.12 shows the variation with distance of  $\delta W_{ij}^{reg}$  for (a) all data, (b) North events only and (c) South events only. The results in Figure 5.12(a) can be compared to those in Figure 5.10 to see the effect of the regional terms on residuals trends – those trends are slightly reduced but not eliminated. While the residual trends for North events are generally flat, the gradients remain for the much better recorded South events. The vertical lines in Figure 5.12(b) and (c) indicate the distance range of ODCD stations across all events in the respective groups (around 100-200 km for North events, 320-500 km for South events). The residuals trends within these distance ranges are reasonably flat, indicating acceptable performance of the path model with the regional corrections applied. This feature of the data holds even for Hokkaido recordings of South events (Fig. 1.12c). As a result of these findings, our conclusion is that no further adjustments to the path models in Zea16 are needed for the analysis of site terms.

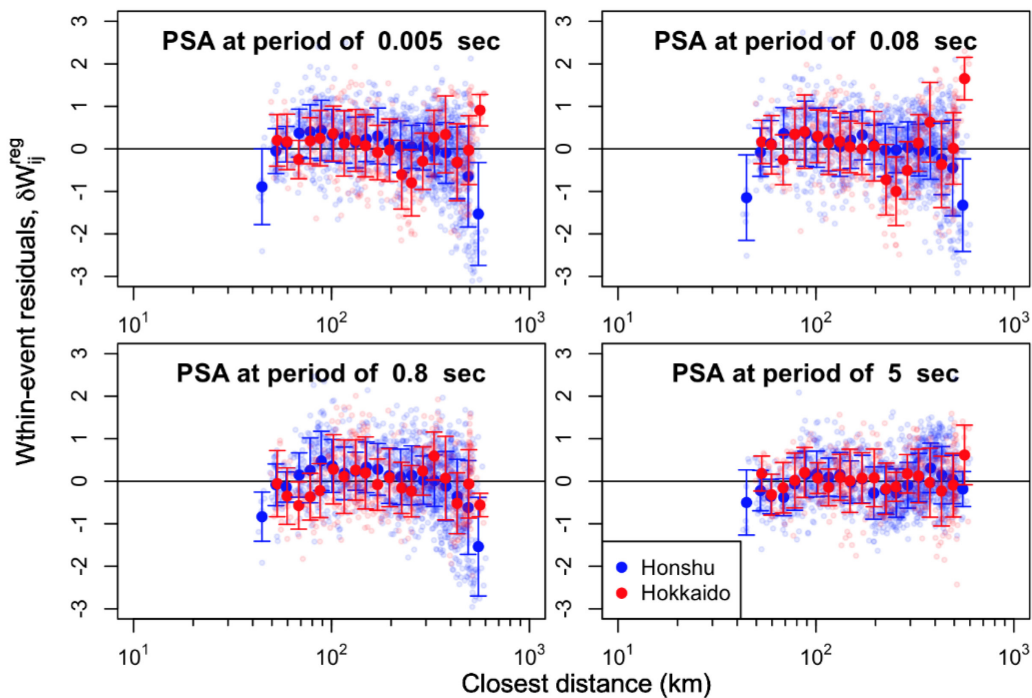


Figure 5.13(a) Trend of region-corrected within-event residuals with closest distance for all data. Distance range for ODCD stations are marked out.

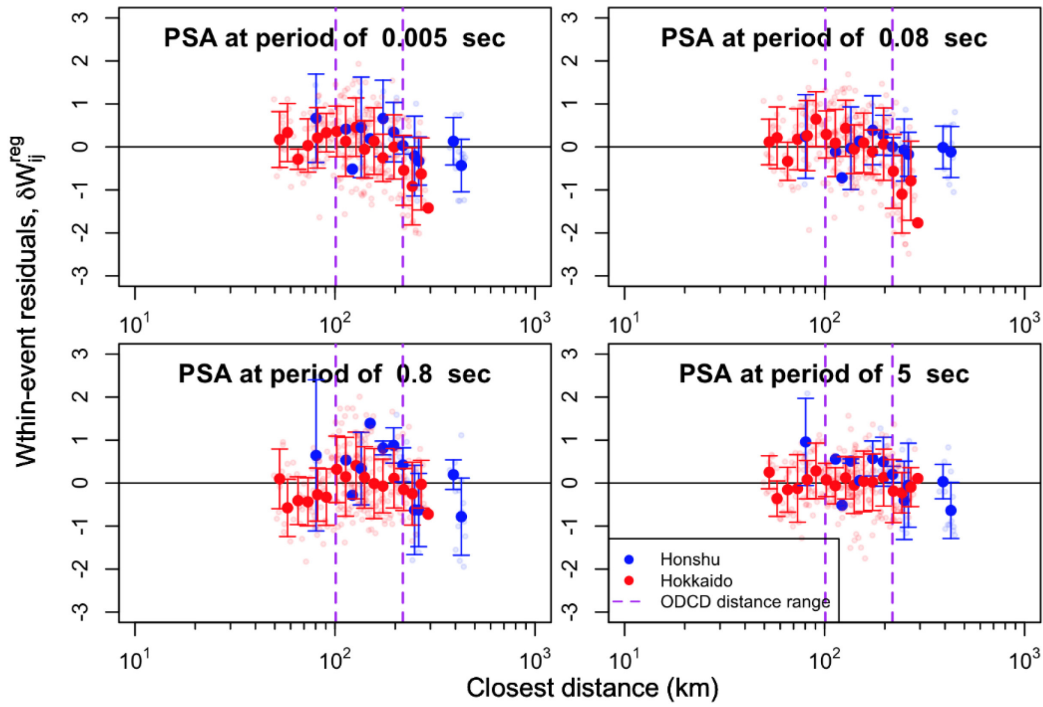


Figure 5.14(b) Trend of region-corrected within-event residuals with closest distance for North events only. Distance range for ODCD stations are marked out.

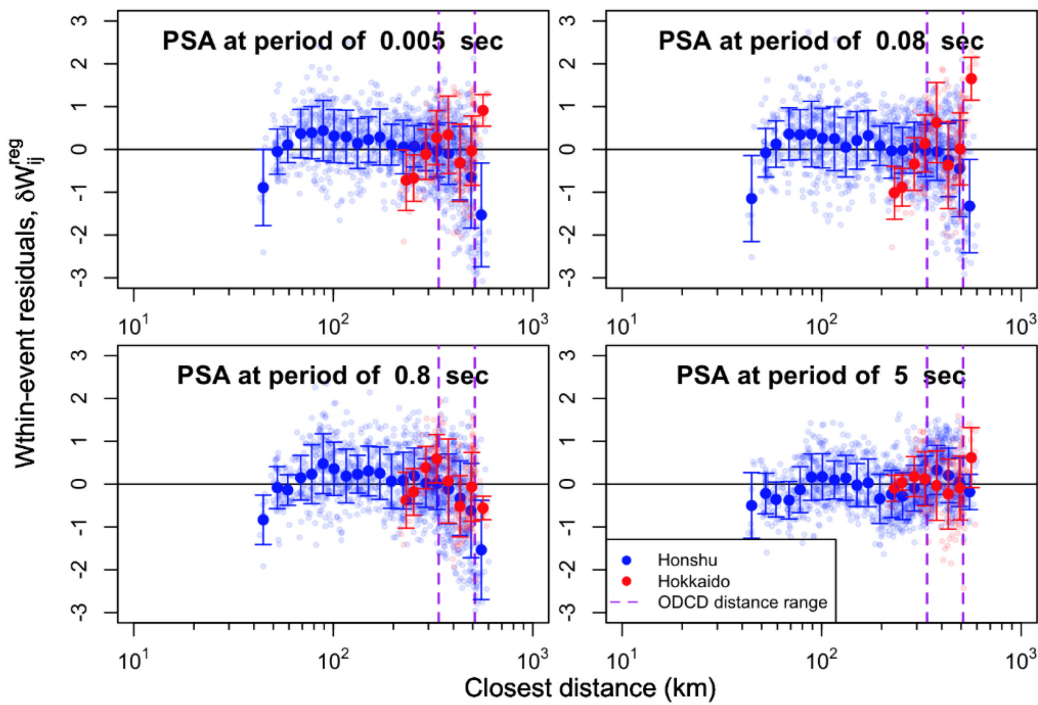


Figure 5.15(c) Trend of region-corrected within-event residuals with closest distance for South events only. Distance ranges for ODCD stations are marked.

### 5.3.2 Site terms

By adjusting residuals for event biases,  $\eta_{E,i}$  and regional biases,  $\eta_{reg,l,k}$ , the remaining region-adjusted within-event residual,  $\delta W_{ij}^{reg}$ , represents errors in the prediction of observed intensity measures from the GMM that can be attributed to the combination of systematic site effects at each station and relative random, event-to-event path errors. If the path errors are indeed random, they would average to zero when summed over many observations. With this in mind, we estimate the effect of site, also called the site term,  $\eta_{S,j}$ , at site  $j$  as follows,

$$\eta_{S,j} = \frac{1}{n_j} \sum_{i=1}^{n_j} \delta W_{ij}^{reg} \quad (5.10)$$

where  $n_j$  is the number of recordings for station  $j$ . As with the event term computation, this represents a frequentist interpretation of the problem statistics.

The site response model assumed to apply for a given intensity measure at a given site is taken as (Stewart et al. 2017):

$$F_S = f_1 + f_2 \ln \left( \frac{x_{IMref} + f_3}{f_3} \right) \quad (5.11)$$

where  $x_{IMref}$  represents the amplitude of shaking for a reference site condition (generally rock) for a particular earthquake at a particular site (expressed as an intensity measure, which is often PGA),  $f_1$  is the coefficient representing linear site response,  $f_2$  represents the slope (generally negative) in amplification- $x_{IMref}$  space for  $x_{IMref} \gg f_3$ , and  $f_3$  represents a transitional value of the reference site intensity measure below which the site response is nearly linear, and above which the trend of amplification with  $x_{IMref}$  is nearly linear in log-log space.

The site term in Eq. (5.10) represents the misfit between the observed site response and the site response predicted by the ergodic model in the GMM. Assuming the ground motions are sufficiently weak that nonlinear response is marginal,  $f_1$  from Eq. (5.11) can be evaluated as,

$$(f_1)_j = \eta_{s,j} + F_{s,j} \quad (5.12)$$

where  $F_{s,j}$  is the ergodic site response as evaluated from the selected model (for the case of the Zhao's GMM, this is a constant value for a given intensity measure for class IV sites).

Figure 5.13 shows for each of the seven sites, the region-adjusted within-event residuals  $\delta W_{ij}^{reg}$  (top) and the total site response (bottom) computed as in Eq. (5.12). Each of the sites exhibits a peaked site response at an apparent site period. For example, at the Toitokki site (dark blue), the first peak site response occurs at a period of about 0.5 sec, and the amplification at that period is approximately  $e^{2.8} \approx 16.4$ . This very high site amplification is likely associated with resonance and impedance effects from the soft upper peat layers relative to deeper, stiffer sediments.

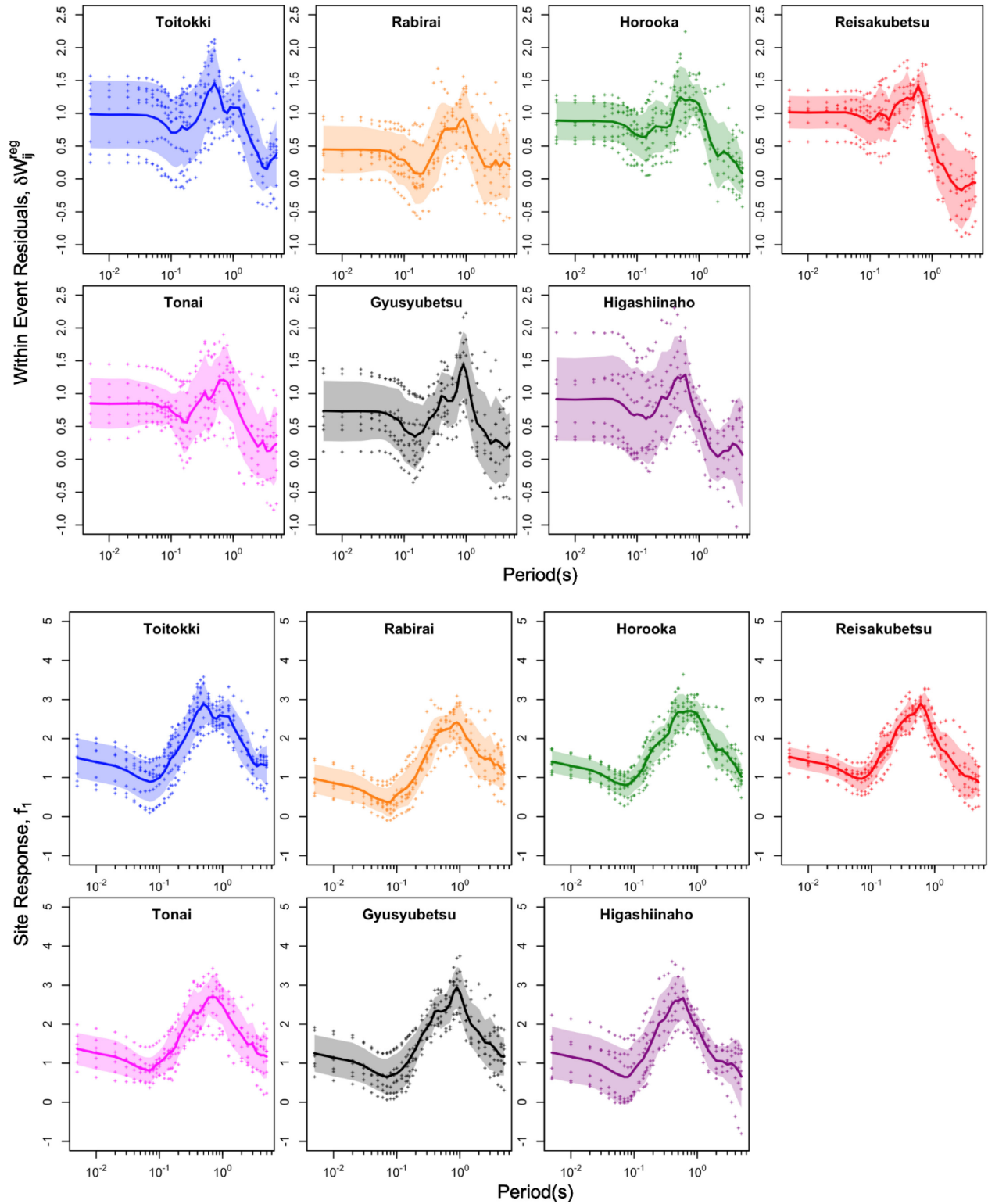


Figure 5.16 Region-adjusted within event residuals (top) and estimated site response (bottom) for the seven Obihiro stations

### 5.3.3 H/V spectral ratios from pre-event noise and application to site amplification

As the sites within the study region exhibit site amplification patterns pointing towards resonance at the site frequency, we sought to use H/V spectral ratios to estimate the frequency of the peak response ( $f_{\text{peak}}$ ). The concept is to use  $f_{\text{peak}}$  as a site parameter to be used in the regional ergodic model. Ambient noise measurements (microtremors) is used to estimate of  $f_{\text{peak}}$  independently from the ground motions. Before proceeding, a point of clarification on notation – frequency  $f_0$  is taken as the frequency of the peak site response as obtained from non-ergodic analysis (Section 5.3.2), which is not an independent variable (it is derived from ground motions, hence it is not independent of those motions), while frequency  $f_{\text{peak}}$  is measured from H/V spectral ratios and hence is an independent site parameter if measured from noise signals. Some prior research has shown that  $f_{\text{peak}}$  is consistent with  $f_0$  for many soil sites (Lermo and Chávez-García. 1993, Lachet et al. 1996, Theodulidis et al. 1996, Bonilla et al. 2002, Kawase et al. 2011, Cadet et al. 2012, and Ghofrani et al. 2013).

Geophysical testing was performed in the vicinity of the Toitokki, Horooka, Rabirai, Reisakubtsu, and Gyushubetsu stations and provided Rayleigh wave dispersion curves and horizontal-to-vertical spectral ratios (HVSr). The  $V_{S30}$  and  $f_{\text{peak}}$  values obtained from these measurements are summarized in Table 5.1. Tests were not performed near Tonai and Higashiinaho stations and here we investigate the use of ground motion signals from the sites to develop H/V spectral ratios, which is the only source of this site attribute for the two sites without measurements. To ensure the selected pre-event signals are mainly noise, we first estimate the p-wave arrival time, and then take preceding portions of the signals for use in analysis. Fourier amplitude spectra (FAS) are computed for both horizontal, as-recorded components and the vertical component. The horizontal FAS is taken as the geometric mean of the two components. The horizontal and vertical FAS are smoothed using the Konno-Ohmachi window

smoothing technique (Konno and Ohmachi, 1998) with parameter  $b = 20$ . Finally, H/V spectra are computed as the ratio of smoothed horizontal FAS to smoothed vertical FAS.

Figure 5.14 shows the resulting H/V spectral ratios in gray (from microtremors where available, for pre-event noise otherwise) for the seven Obihiro stations, with fitted Gaussian pulses in blue (Ghofrani and Atkinson, 2014, Kwak et al. 2017). The  $f_{peak}$  values are established through the pulse fitting procedure and marked with a vertical line. Also shown in Figure 5.17 are the estimated site responses (Eq. 5.12) in red. Sites Toitokki and Rabirai have two H/V peaks, which raises the question of selecting  $f_{peak}$ . This following approach is adopted: (1) if the peaks are of comparable amplitude but distinct in frequency (ratio of the peak frequencies is greater than about 3-5), the lower frequency peak is adopted as  $f_{peak}$ ; (2) if the peaks are of significantly different amplitude (more than a factor of two), the peak with the large amplitude is adopted (this is usually the lower frequency peak); and (3) if the peaks are of comparable amplitude and the frequencies are similar (ratio of the peak frequencies is less than about 3-5), re-fit the Gaussian function to encompass both peaks together. Case 1 applies to the Rabiri site and Case 3 applies to the Toitokki site. Note that adopting this approach provides values of  $f_{peak}$  that are in reasonable accord with  $f_0$ .

Values of  $f_0$  at the peaks of the observed responses are in good agreement with  $f_{peak}$  values, as shown in Figure 1.15. The approach described above for selecting  $f_{peak}$  for sites with two peaks was applied for Toitokki and Rabirai. While the linear regression between the two frequencies does not fall on the 45 degree line, the 95% confidence intervals around the fit include the 45° line. As a result,  $f_{peak}$  can be taken as a suitable estimate of  $f_0$  for the Obihiro sites.



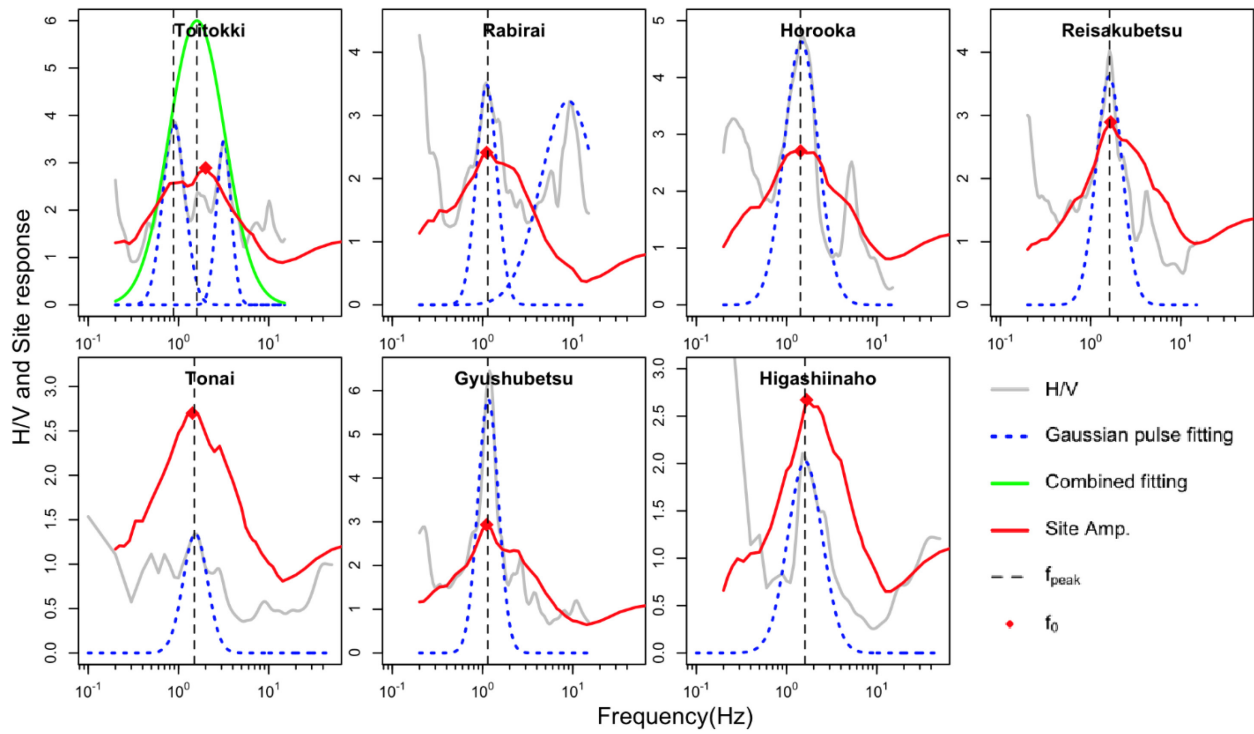


Figure 5.17 Comparison of H/V spectral ratios (data and fit) with observed total site response.

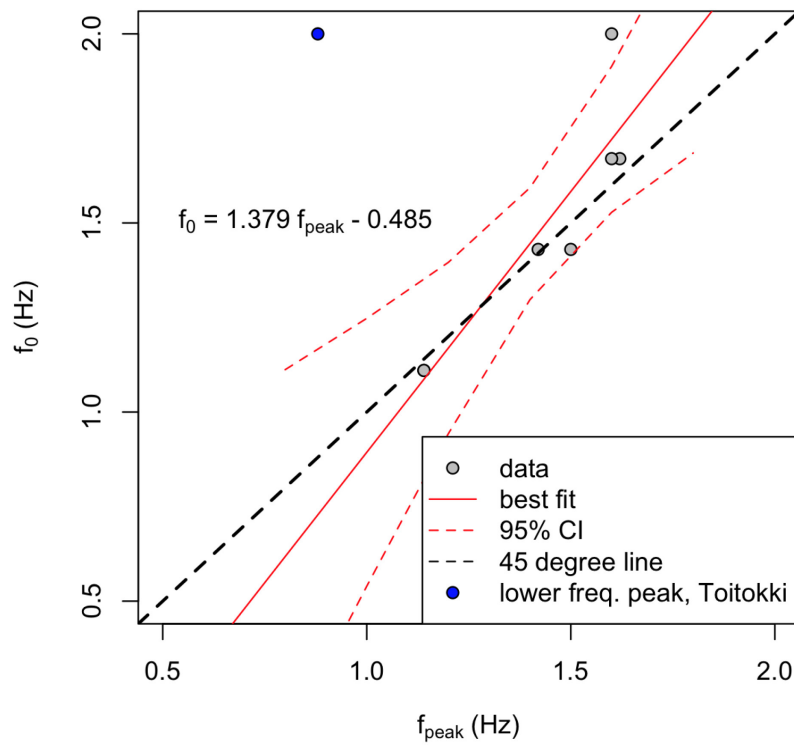


Figure 5.18 Relationship between peak in H/V spectra ( $f_{peak}$ ) and peak in PSA site amplification ( $f_0$ ).  
Linear regression provides  $f_0 = 1.379 f_{peak} - 0.485$  (frequencies in Hz).

## 5.4 MODEL DEVELOPMENT

In this section, we develop a site amplification function that takes  $f_{\text{peak}}$  as input to capture the observed site amplification in an average sense across the seven sites and which presumably would have general applicability across the study region shown in Figure 5.2. We also develop an alternative model in which the only site information is that it is located on peat in the general study region, but  $f_{\text{peak}}$  is unknown.

### 5.4.1 Mean amplification

In order to capture the peaked shape of site amplification observed at the Obihiro sites, we selected a Mexican hat wavelet function (Ryan, 1994). This function is intended to capture site resonance effects that dominate amplification shapes at short to intermediate periods ( $T < 2$  sec). A linear decay function is used at longer periods ( $T > 2$  sec).

The recommended site amplification function for linear conditions is as follows,

$$f_1(T, t_0) = \begin{cases} c_0 + \frac{2c_1}{\sqrt{3c_2}\pi^{1/4}} \left( 1 - \left( \frac{\ln(Tf_p)}{c_2} \right)^2 \right) e^{-\frac{1}{2} \left[ \frac{\ln(Tf_p)}{c_2} \right]^2} & \text{for } T \leq T_{tr} \\ c_3 \ln \left( \frac{T}{T_{tr}} \right) + f_1(T_{tr}, f_p) & \text{for } T > T_{tr} \end{cases} \quad (5.13)$$

where  $c_0$  controls the overall level of site amplification,  $c_1$  scales the amplitude of the hat function,  $c_2$  describes the width of the PSA peak in natural log period space,  $T_{tr} = 2$  sec is the transition period between the Mexican hat and linear functions, and  $c_3$  describes the linear decay of amplification with log period beyond  $T_{tr}$ . Frequency  $f_p$  is the frequency of the peak in the Mexican hat fitting function. Eq. 5.13 fitted to the observed amplification at each site by minimizing the sum square of errors, with the model coefficients are summarized Table 5.6. The fitted functions are plotted in Figure 5.16. For

sites with multi-mode responses, such as the two peaks observed for Toitokki, only the first mode (lower frequency) is captured. Higher modes are not. Due to the unpredictability of higher modes, we have not attempted to capture such modes in the amplification model.

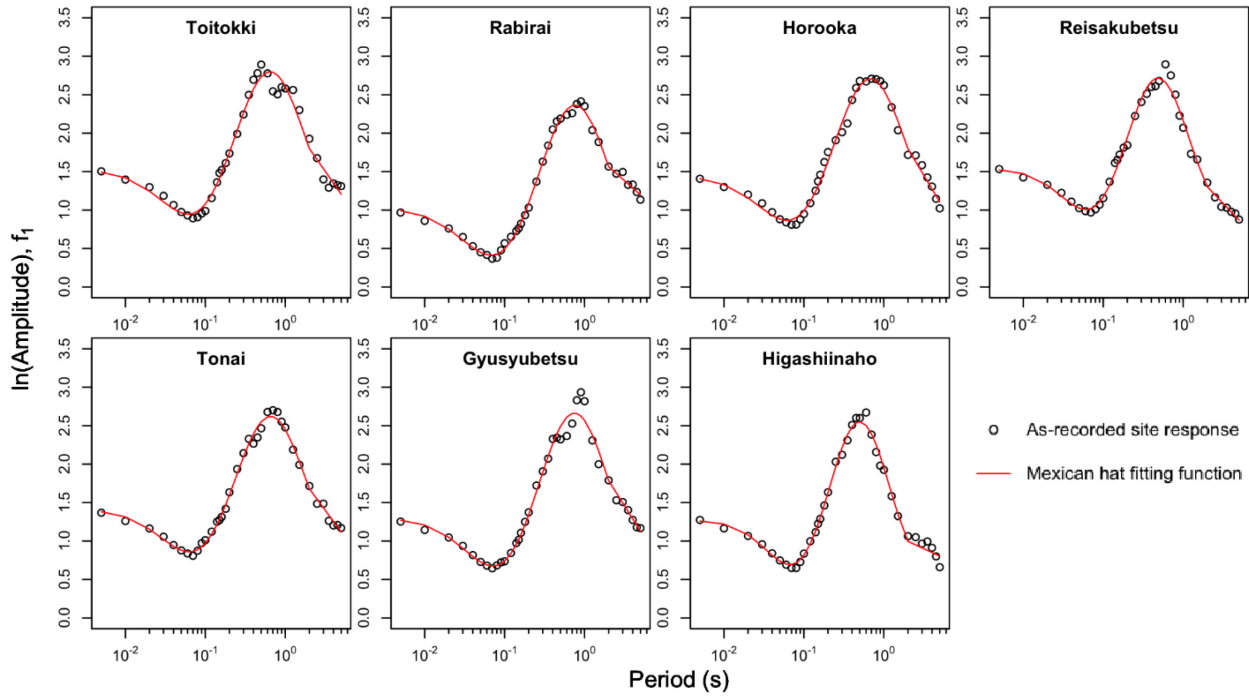


Figure 5.19 Fit of model to observed amplification with model coefficients from site-specific optimization

Table 5.6 Model coefficients obtained by fitting Eq. (5.13)

	Toitokki	Rabirai	Horooka	Reisakubetsu	Tonai	Gyushubetsu	Higashiinaho
$c_0$	1.518	1.015	1.434	1.534	1.403	1.288	1.267
$c_1$	1.724	1.839	1.729	1.496	1.635	1.846	1.597
$c_2$	1.362	1.398	1.387	1.202	1.355	1.358	1.162
$c_3$	-0.647	-0.401	-0.757	-0.475	-0.614	-0.717	-0.210
$f_p$ (Hz)	1.549	1.319	1.480	2.062	1.529	1.343	2.008

To develop the model for sites other than the seven stations in the study region, we examined the relationship between  $f_p$  and  $f_{peak}$  as shown in Figure 5.15. The best fit line is parallel to the 45° line and encompasses it within the 95% confidence interval. The best linear regression relation is  $f_p =$

$1.125f_{\text{peak}} + 0.002$ . As a result, we take  $f_{\text{peak}}$  values as unbiased estimators of  $f_p$  for use in the Mexican hat function. All other coefficients are taken as constant across all sites. The other coefficients were obtained by minimizing the sum of square of errors after specifying  $f_p$  as above, with the resulting values obtained as  $c_0 = 1.341$ ,  $c_1 = 1.703$ ,  $c_2 = 1.413$ , and  $c_3 = -0.849$ . In summary, for the case where  $f_{\text{peak}}$  is known at a site from an H/V spectrum, the regional ergodic site amplification is computed with the above coefficients. The predictions from the general model are compared to data for the seven Obihiro sites in Figure 5.21. The results are generally good with some loss of fidelity relative to the site specific (non-ergodic) fits shown in Figure 5.19.

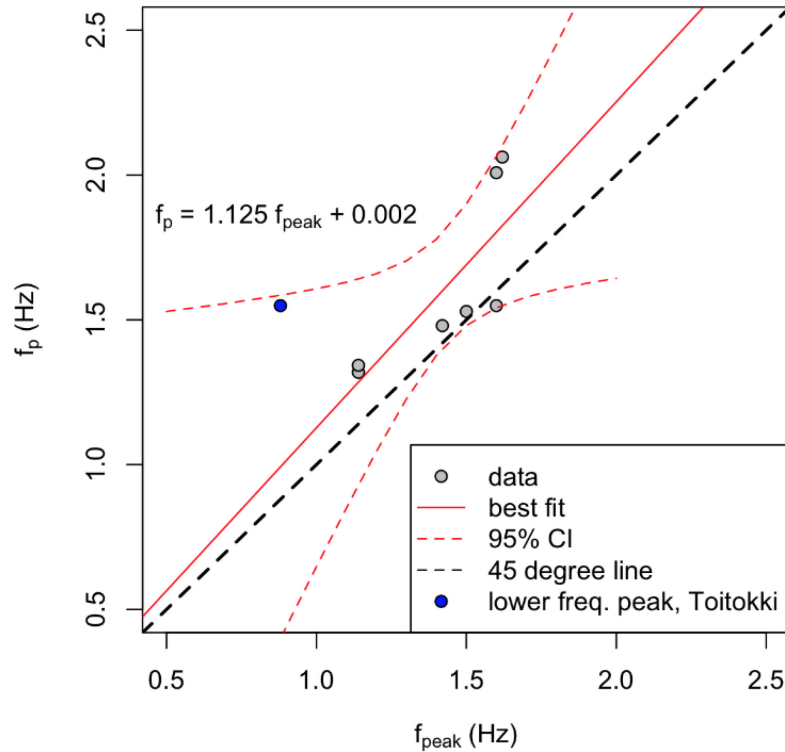


Figure 5.20 Relationship between peak in H/V spectra ( $f_{\text{peak}}$ ) and peak in Mexican hat fitting function of site response ( $f_p$ ).

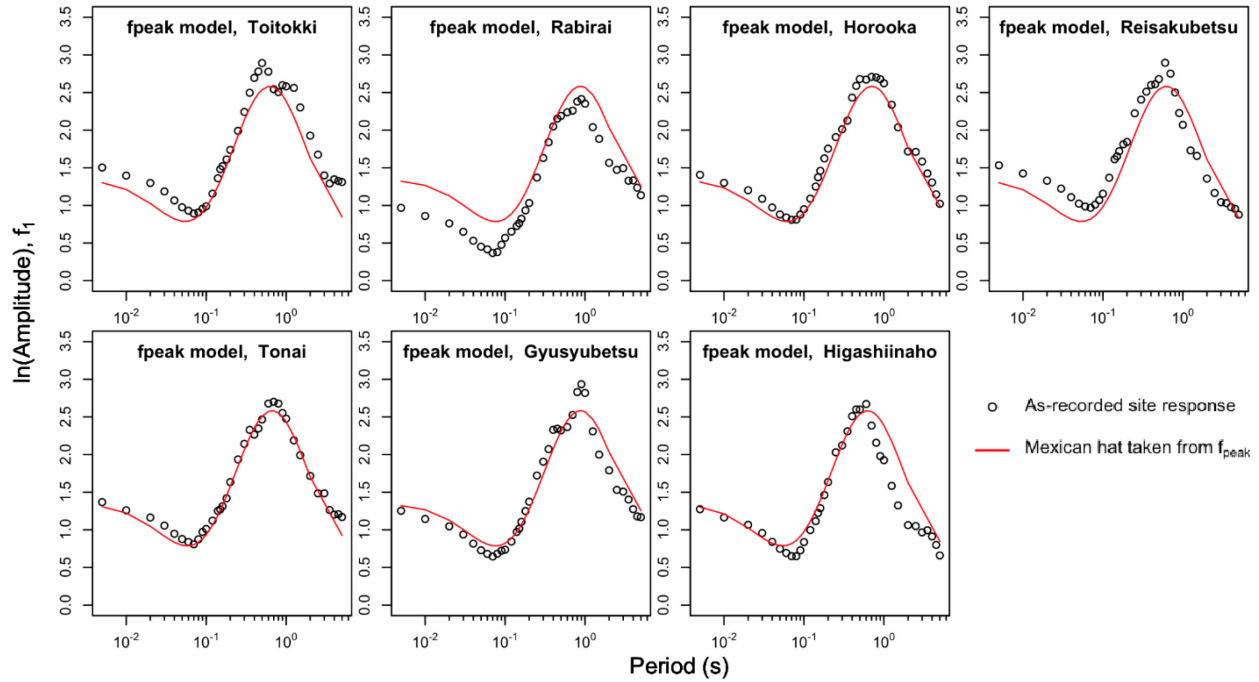


Figure 5.21 Fit of model to observed amplification when model coefficients are taken from regional average model

For the case where  $f_{\text{peak}}$  is unknown, we regressed Eq. (5.13) to the combined data set for all sites to obtain a new set of coefficients as follows:  $c_0 = 1.346$ ,  $c_1 = 1.668$ ,  $c_2 = 1.326$ ,  $c_3 = -0.526$ , and  $f_p = 1.594$  Hz. Note that the  $f_p$  obtained here is a regional average site frequency. By combining all sites, the pulse width and linear decay rate at long periods are both slightly increased. The regional average curve is plotted relative to the observed amplification levels at all Obihiro sites in Figure 5.22.

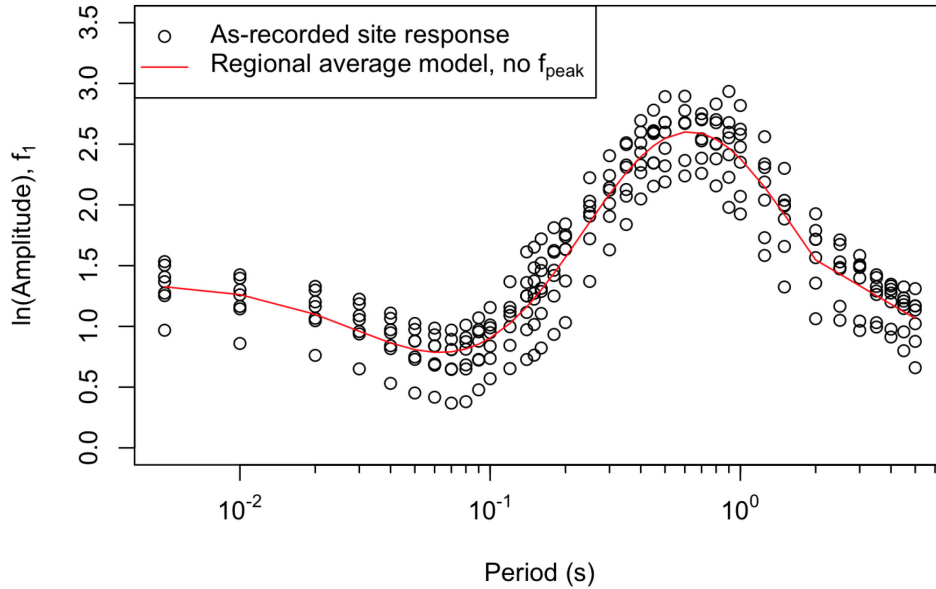


Figure 5.22 Relationship between peak in H/V spectra ( $f_{peak}$ ) and peak in Mexican hat fitting function of site response ( $f_p$ ).

To compare the fitting performance between  $f_{peak}$  model and regional average model, their sums of square error are computed. They are 13.0 for the regional average model and 11.0 for the model that incorporates site-specific  $f_{peak}$  values. Not surprisingly, given the additional site-specific information ( $f_{peak}$ ), the latter model fits the data better.

### 5.4.2 Aleatory variability model and Model bias

The standard deviation terms to use with the proposed site amplification model are  $\tau$  for between-event variability and  $\phi$  for within-event variability. The  $\tau$  model is assumed to be unaffected by the site amplification model described here, and can be taken from GMMs. The  $\phi$  model can be taken from the standard deviation of the within-event residuals obtained through the use of the Zhao's GMM (Zhao et al, 2016a and 2016b) in combination with the proposed site amplification models. To develop this within-event standard deviation model, we compute residuals as in Eq. (5.2), but now using the region-specific site amplification model in lieu of the Zhao's GMM (Zhao et al, 2016a and 2016b) site term.

After subtracting event terms (Eq. (5.3)) and regional terms (Eq. (5.9)), we then partition the within event residual as:

$$\delta W_{ij}^{reg} = c + \eta_{s,j} + \varepsilon_{ij} \quad (5.14)$$

where  $c$  is the model bias,  $\eta_s$  is the site term, and  $\varepsilon_{ij}$  is the remaining residual. The model bias indicates the overall model misfit relative to the data (equivalent to the average of all  $\delta W_{ij}^{reg}$ ). The standard deviation of  $\eta_s$  is denoted the site-to-site dispersion ( $\phi_{s2s}$ ) while the standard deviation of  $\varepsilon_{ij}$  is the single-station within-event dispersion ( $\phi_{ss}$ ).

These standard deviations are shown in Figure 5.23 and 5.24 for the model employing regional average parameters and in Figure 5.25 and 5.26 for the model employing site-specific  $f_{peak}$  values. Arguably, the regional average model could be considered as ergodic because site-specific information is not incorporated, whereas the model incorporating site-specific  $f_{peak}$  values is effectively non-ergodic.

Figure 5.23 shows that the site-to-site dispersion ( $\phi_{s2s}$ ) is approximately 0.2, which is significantly below the average for the entire Japan (from Al Atik, 2015). This is expected given the relatively similar geotechnical conditions within the study region.

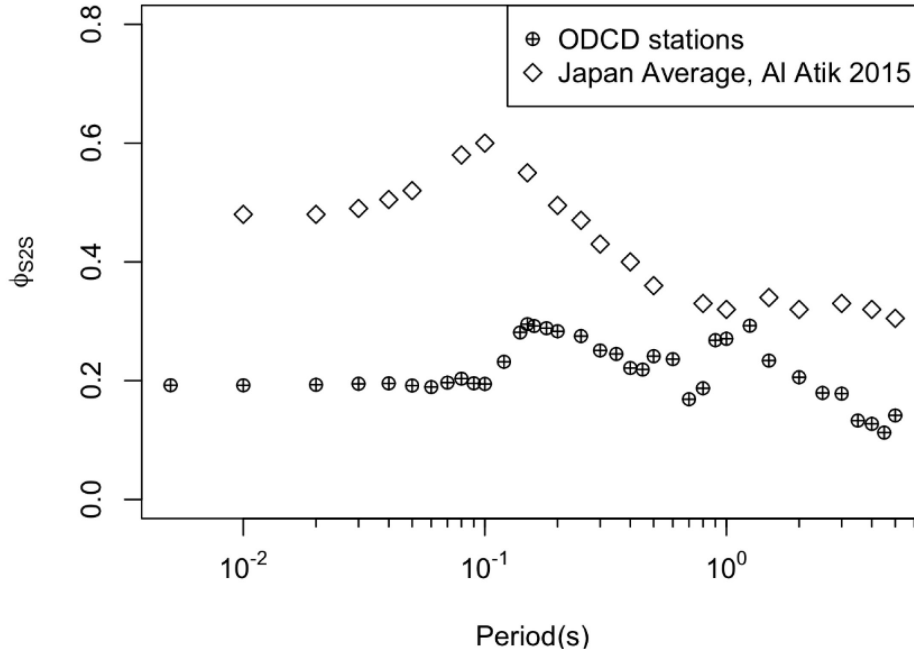


Figure 5.23 Comparison of site-to-site standard deviations from Obihiro stations (this study) and Japan average from Al Atik (2015).

Figure 5.24 shows single-station standard deviations ( $\phi_{ss}$ ), which are remarkably consistent with the Japan average values obtained previously by Rodriguez-Marek et al. (2011). Figure 5.25 compares these two standard deviation terms for the regional average and site specific models. The respective dispersions for the two alternate models are very similar.

Figure 5.26 compares the model bias for the regional average and site specific models, both of which are effectively zero. Also shown for comparative purposes is the bias obtained using the site term in the Zhao's GMM (Zhao et al, 2016a and 2016b), which is very large (indicating under-prediction). The substantial bias of the GMM for the Obihiro sites demonstrates the need for site-specific site factors for these peaty organic soils.



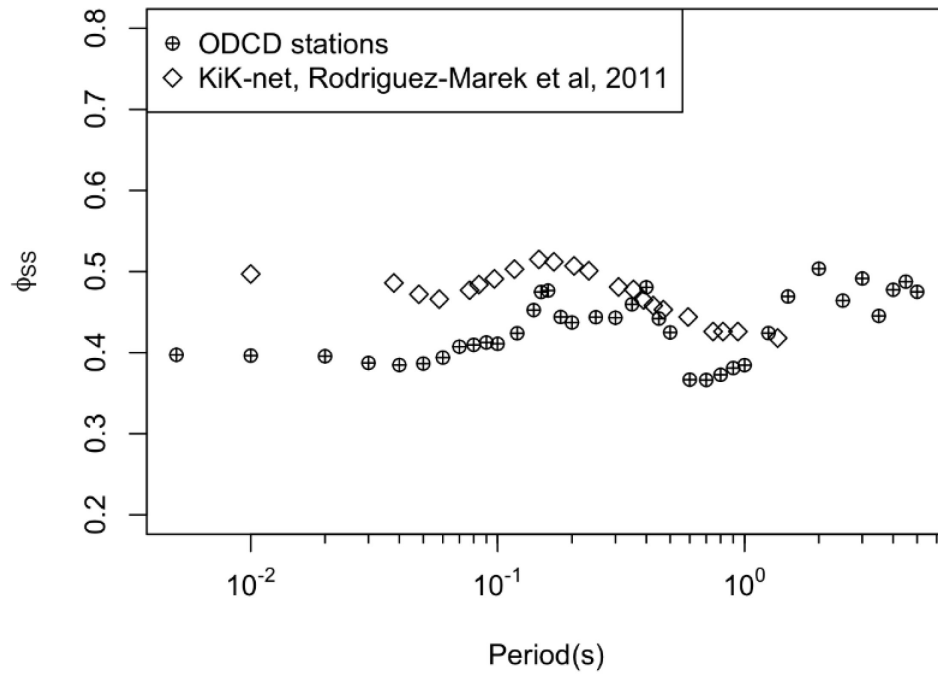


Figure 5.24 Comparison of single station standard deviations from Obihiro stations (this study) and KiK-net database from Rodriguez-Marek et al (2011).

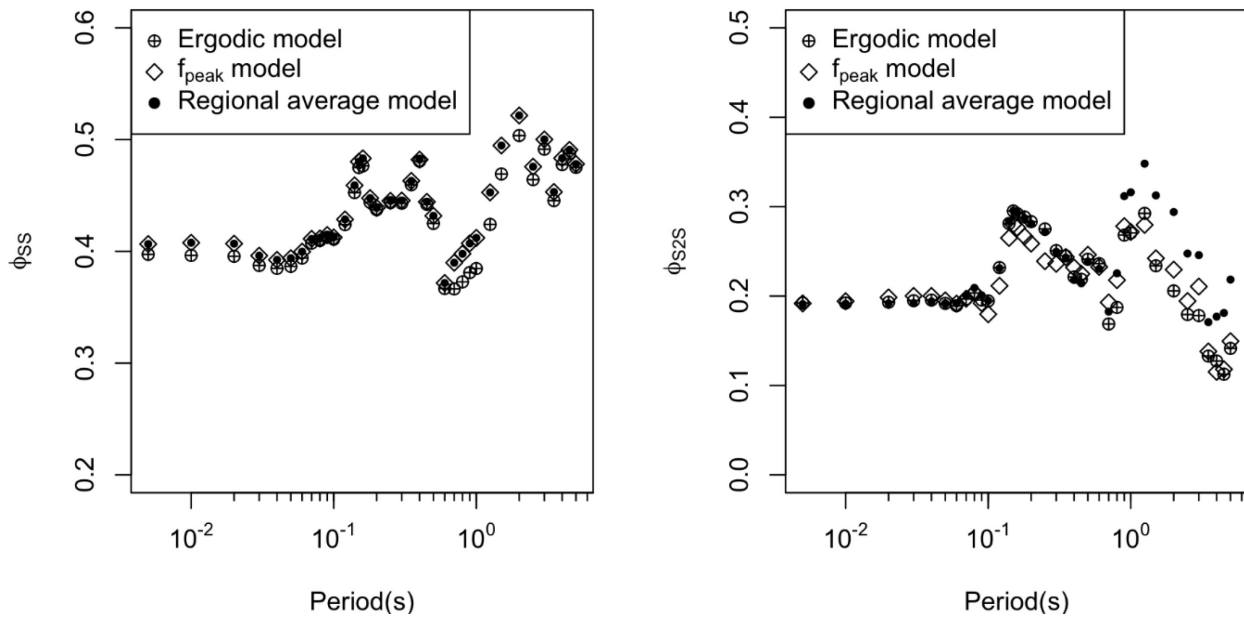


Figure 5.25 Comparison of single station and site-to-site standard deviation terms for the two forms of the proposed site amplification model.

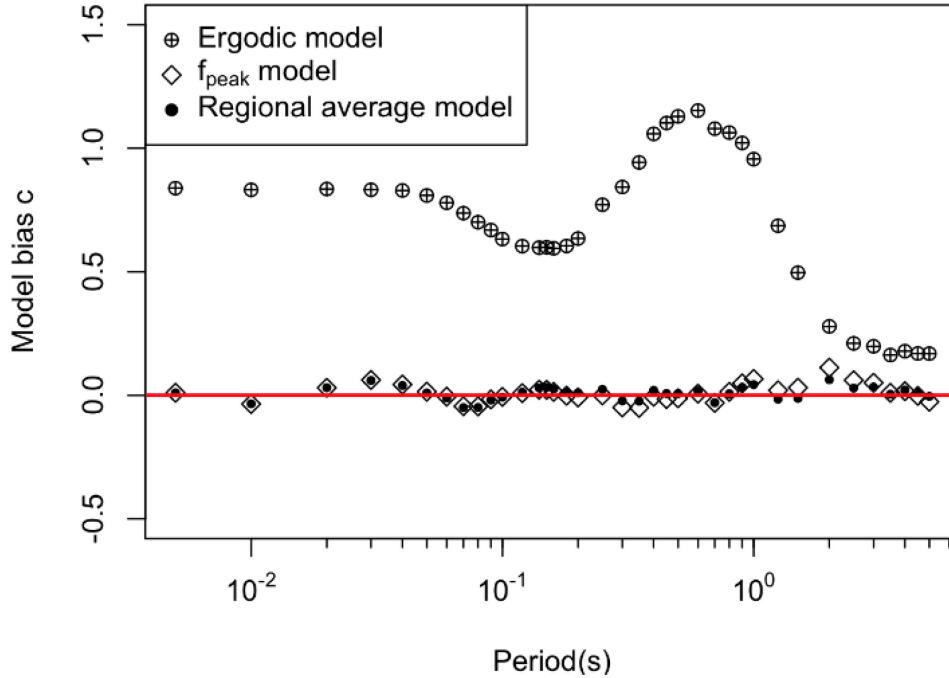


Figure 5.26 Comparison of model bias for the ergodic model of Zhao et al. (2016a, 2016b) and the Zhao et al. model combined with the two proposed region-specific site amplification models.

### 5.4.3 Nonlinearity

The models for mean site response provided in Section 5.4.1 were developed based on relatively weak ground motions from 8 events for linear site amplification. To investigate the potential effects of nonlinearity, we examine model misfits relative to the data from Event 10 (the 2003 Tokachi-Oki Earthquake), which produces significantly stronger ground motions than the other considered events at the ODCD stations (Figure 5.5).

The ratio of PGV to shear wave velocity is often taken as an indicator of nonlinearity (refs), and is considered here to differentiate shaking demands for Event 10 vs the other events considered in model development. Idriss (2016) and Kim et al (2016) adapted this concept to propose a shear strain index ( $I_\gamma$ ) as follows:

$$I_{\gamma} = \frac{PGV^r}{V_{S30}} \quad (5.15)$$

This parameter was used by Kim et al. (2016) to identify conditions where equivalent linear and nonlinear ground response analysis results are comparable ( $I_{\gamma} < 0.03\%$ ) vs those where nonlinear analyses are required (larger  $I_{\gamma}$ ). We could not apply Eq. (5.15) because the reference rock level PGV is unknown. Instead we use the soil surface PGV as follows

$$I_{\gamma}^s = \frac{PGV}{V_{S30}} \quad (5.16)$$

This parameter is used here to differentiate approximate strain demands for the different events. The indices computed here cannot be directly compared to the thresholds recommended by Kim et al (2016). Figure 1.24 compares soil surface strain index from Eq. (5.16) from Events 1-9 to those from Event 10 in the form of box plots. Clearly Event 10 induced much larger strains and nonlinear site response is more likely to be observed.

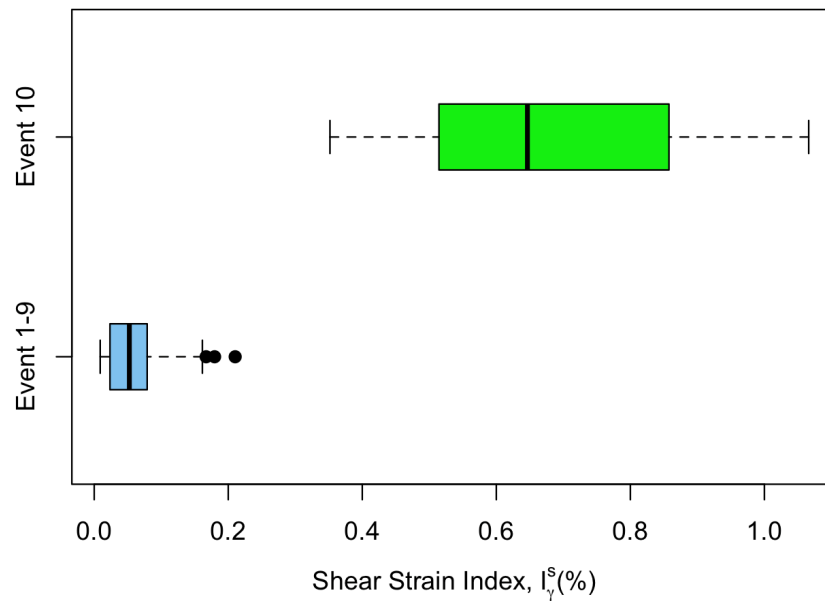


Figure 5.27 Boxplots of soil surface shear strain index  $I_{\gamma}^s$  for Event 1-9 and Event 10. Strains from Event 10 is significantly higher and nonlinear behavior is anticipated.

The analysis of Event 10 follows the process used for other events. Eq. (5.1) is used to compute total residuals, and Eq. (5.2) is used to compute the event terms ( $\eta_{E,10}$ ). Figure 5.28 compares the event terms for Event 10 to the other events considered. In the case of ODCD stations, the GMM used for residuals calculation is modified from the published version,

$$(\mu_{lnY})_{ij} = \mu_{lnY}^r + f_1 \quad (5.16)$$

is where  $\mu_{lnY}^r$  is the mean ground motion prediction for reference rock (i.e., Site Class 1) from Zhao et al. (2016) and  $f_1$  is from Eq. (5.13).

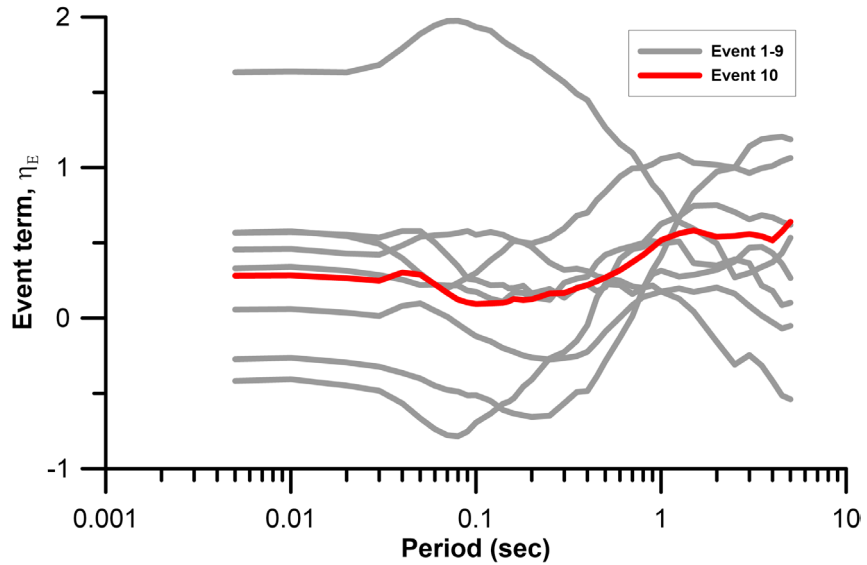


Figure 5.28 Event term for Event 10 compared to Event 1-9.

Region-adjusted within event residuals are computed using Eq. (5.9). Figure 5.29 plots  $\delta W_{ij}^{reg}$  for Event 10 along with those for the other events, using ODCD stations only. The residuals are plotted as a function of  $PGA^r$ , which is the median peak acceleration for the reference site condition from the Zhao GMM for Site Class 2. If the site response from the various events recorded at the ODCD sites is effectively linear, then no trend in  $\delta W_{ij}^{reg}$  would be expected with  $PGA^r$ . This is effectively the case for the Event 1-9 data for each of the intensity measures for which results are shown in Figure 5.29,

with the possible exception of a small upward trend for 5.0 sec PSA. The Event 10 data, however, indicate  $PGA^r$  dependencies that are downward at short periods and upward at 5.0 sec.

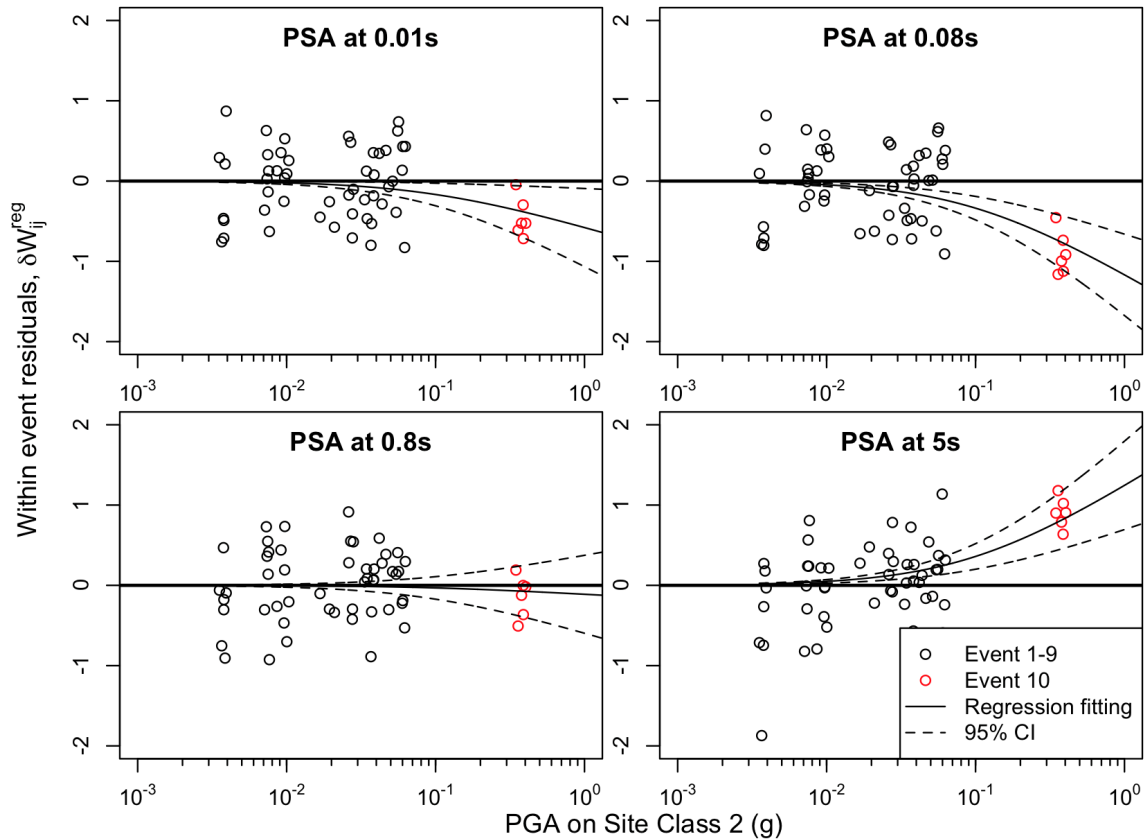


Figure 5.29 Region adjusted within event residuals for data recorded at ODCD stations versus reference site  $PGA^r$  (Site Class 2).

The trends of the results in Figure 5.29 are fitted by regression using the relation in Eq. (5.11) with  $f_1 = 0$  (the setting of  $f_1$  to zero is because of its inclusion in the model used for residuals analysis; Eq. 16) and  $f_3 = 0.1g$  (a typical value). As a result, only parameter  $f_2$  is set by regression. Nonlinearity is evident from curvature in the fit line, and is quantified by  $f_2 \neq 0$ . The downward curvature at short periods is expected, and results from increased damping in sediments as strains increase. The upward trend at long periods is also fairly common. This typically occurs because nonlinearity softens the soil, increasing its fundamental period. Because the elastic (small strain) period is in the range of 1-2 sec,

this softening will bring the soil deposits to resonance at longer periods, which would be reflected by increased long period PSA as indicated by the trend line.

Nonlinear site response for the peaty organic soils encountered along the Kushiro and Tokachi Rivers in Hokkaido is investigated further in Chapter 6 using ground response simulations. The model used to represent nonlinearity in fragility modeling is described there.

## 5.5 MODEL COMPARISON

The model development described previously in this chapter was based on the Zhao (2016) model as the conditioning GMM. The residuals in Eq. (5.1) were computed relative to this model, the event terms in Eq. (5.2), path corrections in Eq. (5.4), and non-ergodic site terms (Eq. 5.10) are relative to this model, and the ergodic component of the regional site response utilizes the site term in this model (Eq. 5.12). Given the pervasive influence of GMM throughout the process, a natural question to ask is whether the site response results would be appreciably different had a different model been selected?

The manner in which the site response effects from Obihiro ground motions are expressed in the development of the regional model is through within-event residuals,  $\delta W$ . Accordingly, the most direct means by which to answer the question of GMM influence is to compare these residuals as computed for multiple models. The Abrahamson et al. (2018) model (hereafter Aea18) was selected for this purpose. To enable comparisons of within-event residuals, event terms were developed for Events 1-9 relative to the Aea18 GMM.

As was described in Section 5.3.1, there are some complicating issues related to path effects when the path from source-to-site travels between islands (Honshu to Hokkaido or vice-versa, which affect  $\delta W$ ). In order to minimize the effects of such complications for this comparison, we compute within-event

residuals for common source – station combinations. Figure 5.30(a) shows for Event 5 (located near Honshu) the correlation of within-event residuals for Honshu stations as computed from both GMMs. The correlation is strong ( $r = 0.86$ ). Figure 5.30(b) shows a similar comparison, but in this case it is for Event 7 (near Hokkaido) and the residuals are for Hokkaido stations. In this case  $r = 0.90$ . The correlations are strong in both cases, and similarly strong correlations were encountered for other events. As a result, we do not expect that the choice of GMM significantly influences the regional site response model developed here.

Figure 5.30(b) shows with green symbols  $\delta W$  for the ODCD stations. The offset from the 1:1 line is due to a reference site incompatibility issue (between the Aea18 GMM and site term), described below.

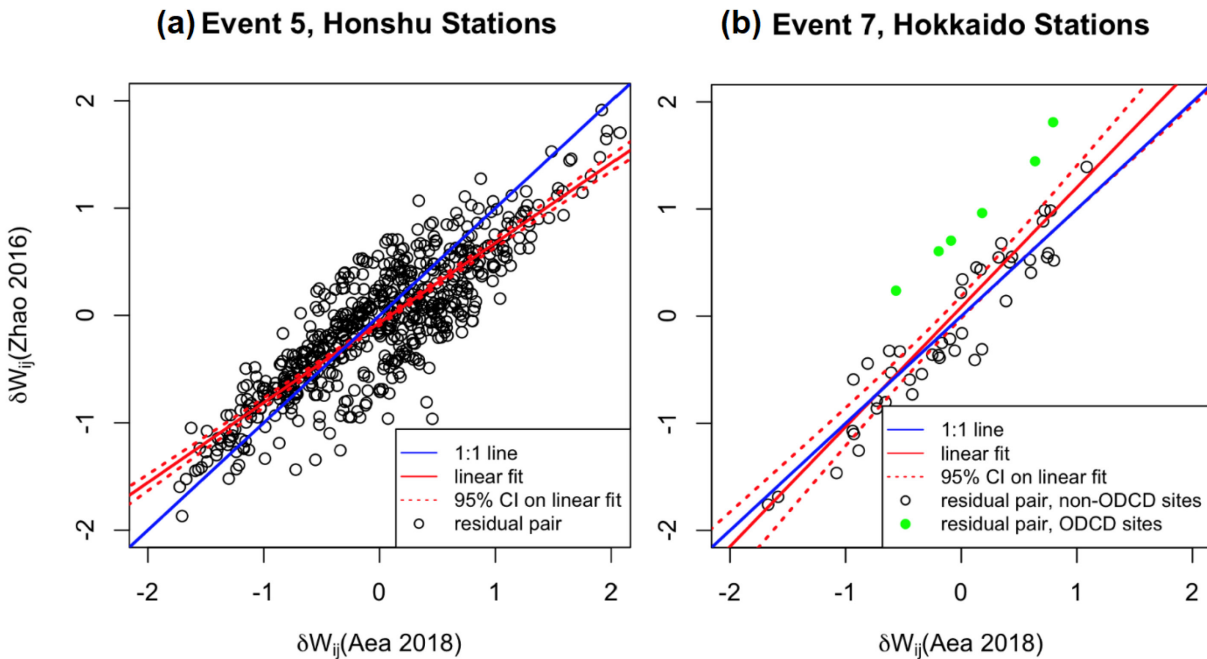


Figure 5.30 Within event residuals (event terms corrected) of ODCD stations by Abrahamson's model.

Next, we investigate the applicability of the regional site amplification model with the Aea18 GMM by specifically examining residuals for ODCD stations. For these sites, total residuals (Eq. 5.1) are computed by combining the Aea18 GMM with site response models (per Eq. 5.16), and then

subsequently correcting total residuals to within-event residuals by removing event terms. In Eq. (5.16),  $\mu_{lnY}^r$  is taken as the Aea18 mean ground motion prediction for an assumed reference site condition of  $V_{S30} = 1.0$  km/s. Two representations of  $f_1$  are used. First, it is taken as the ergodic model in Aea18, with the results in Figure 5.31. Next,  $f_1$  is taken from Eq. (5.13) (regional model), with the result shown in Figure 5.32. No regional path corrections were applied in the use of the Aea18 model, although the Japan-specific anelastic attenuation model was applied.

The results shown in Figure 5.31 with the ergodic site response model indicate substantial underprediction bias (positive residuals), which demonstrates the need for a regional site response model for the Obihiro sites. When the regional model is applied (Figure 5.32), there is clear improvement, with mean residuals being much closer to zero. Some misfit remains, which is a consequence of the assumed reference site condition for the Aea18 model ( $V_{S30} = 1.0$  km/s) being incompatible with the reference condition in the regional model. This is a common issue when combining a site response model with a GMM, and is corrected in forward application through adjustment of the GMM constant term.



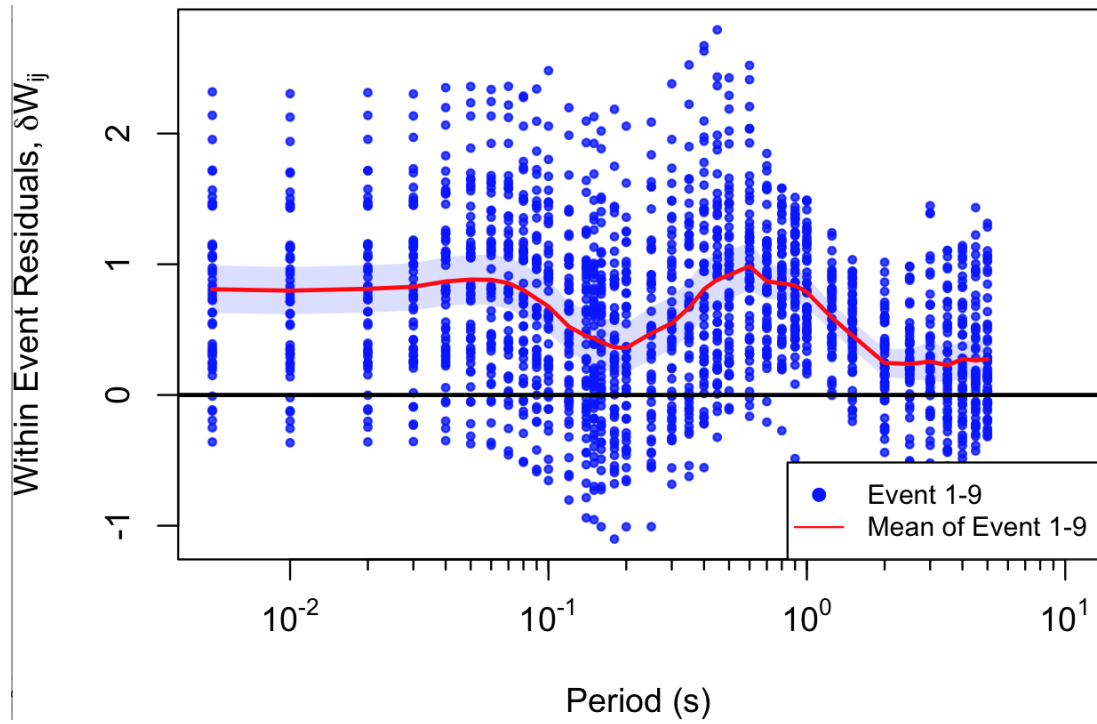


Figure 5.31 Within event residuals for OCDC stations using recordings from Events 1-9 and Aea18 model with its ergodic site term.

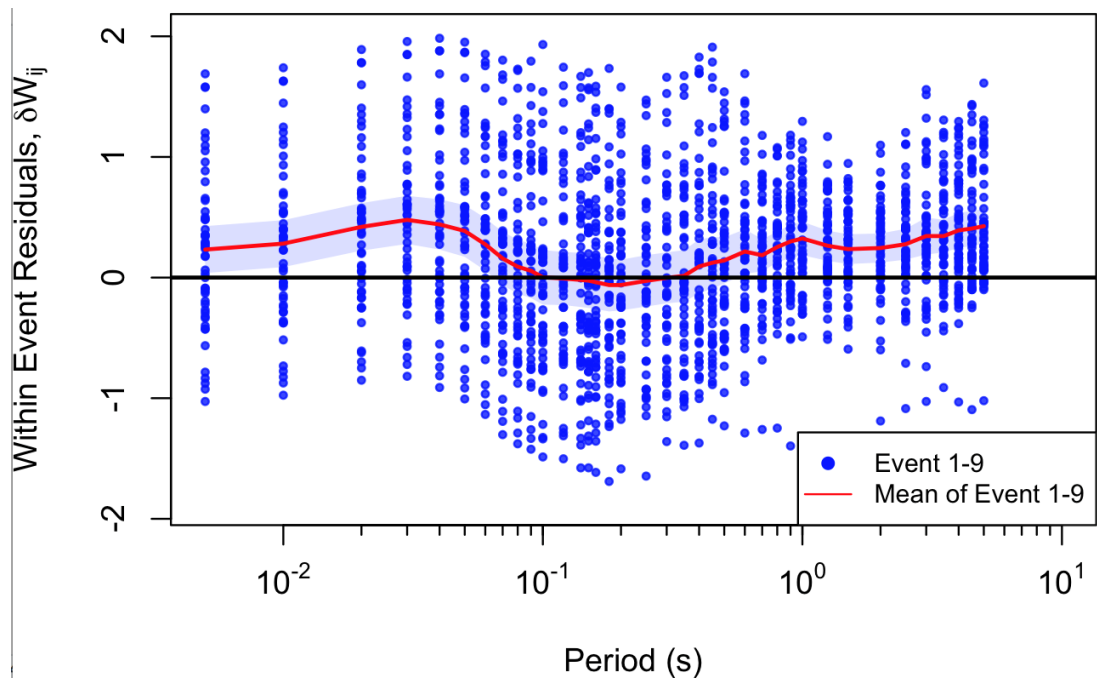


Figure 5.32 Within event residuals for OCDC stations by using recordings from Events 1-9 and Aea18 model with the regional site term developed in this chapter.

## **5.6 LIMITATIONS**

The models for mean site response and within-event standard deviation provided in Section 5.4 apply for the Obihiro area along the Tokachi River, Japan, as shown in Figure 5.2. The model is based on data from seven sites, and could be in error for sites in the study region if they contain peat deposits of significantly different character or thickness. In the absence of validation, it cannot be considered as applicable to peat sites in regions other than Obihiro.

## 6 NONLINEAR RESPONSE OF SOFT ORGANIC SOIL SITES

For a site amplification model to be applicable over a wide range of input parameters (i.e., weak to strong shaking, soft to stiff site conditions), it is often necessary to supplement components of the model constrained by recorded ground motions with additional components constrained at least in part by the results of simulations. In the case of the Obihiro sites, the data limitation is not necessarily related to poorly represented site conditions, but rather to a relative lack of recordings with strong shaking intensities. As a result, the nonlinear behavior is not likely to be adequately constrained by the available data (e.g., the dataset from the Obihiro stations contains only a single high intensity event). This limitation is addressed in this chapter by performing, and interpreting the results of, one-dimensional (1-D) nonlinear ground response analysis (GRA) to propagate motions through a soil column representing the subsurface conditions at the site or region of interest. These simulations are used, along with the available data, to develop the nonlinear component of the Obihiro site amplification model (the linear portion was presented in Chapter 5). The development of the soil profiles and analysis using *DEEPSOIL* v7.0 (Hashash et al. 2016) are presented subsequently. The results are then interpreted to derive nonlinear site amplification coefficients for modeling purposes.

### 6.1 SITE CHARACTERIZATION

The subsurface conditions in the downstream region along Kushiro River and Tokachi River were evaluated by reviewing geotechnical investigations performed by the Kushiro Development and Construction Office and Obihiro Development and Construction Office. Data available from these investigations includes boring logs with Standard Penetration Test (SPT) blow counts, Cone Penetration Tests (CPTs), seismic velocities from suspension logging, laboratory testing of soil samples. The format and quantity of data available differs between the two regions and is presented in

Chapter 2. Shear wave velocities for the surficial layers are supplemented by additional geophysical site characterization performed as part of this study using SASW. The subset of information pertinent to developing the soil profiles are presented here.

### 6.1.1 Soil classification and index properties

A wealth of subsurface information in the form of boring logs with SPT blow counts and laboratory test data is available for the Kushiro area, and includes unit weight, water content, gradation (coefficient of uniformity, mean grain size), density, and organic content. In addition, Atterberg limits, consolidation and unconfined compression tests were performed on cohesive soils and peat. Results from site investigation between KP7.0-11.0 on the left bank is summarized in Table 6.1. The OCR of the silts and clays in Kushiro is estimated to range from 1.2-2.5 based on consolidation tests. Figure 6.1 shows borings and Vs measurements in the downstream region of Kushiro River.

Table 6.1 Laboratory tests along left bank of Kushiro River

Unit	Material	Specific Gravity (Gs)	Natural Water Content (%)	Composition (%)			Liquid Limit	Plastic Limit	Density (g/cm <sup>3</sup> )	Organic Content (%)
				Gravels	Sand	Fines				
Ap	Peat	1.39-1.73	510-830						1.02-1.05	72-85
As	Silty Sand (fine to medium)	2.59-2.67	23-45	0-2	68-86	12-31				
As	Gravelly Sand	2.51	26	26	73	1				
Ac	Silt (sand seams)	2.63	53	0	21	79	47	12	1.64	
Ac	Sandy Silt	2.57-2.61	35-45	0-4	32-45	51-68	42	9	1.72	
Dg	Silty Sand (fine to medium)	2.62-2.63	22	1-3	72-74	23-27				
Dg	Gravelly Sand	3.65-2.72	14	20-29	63-69	5-12				

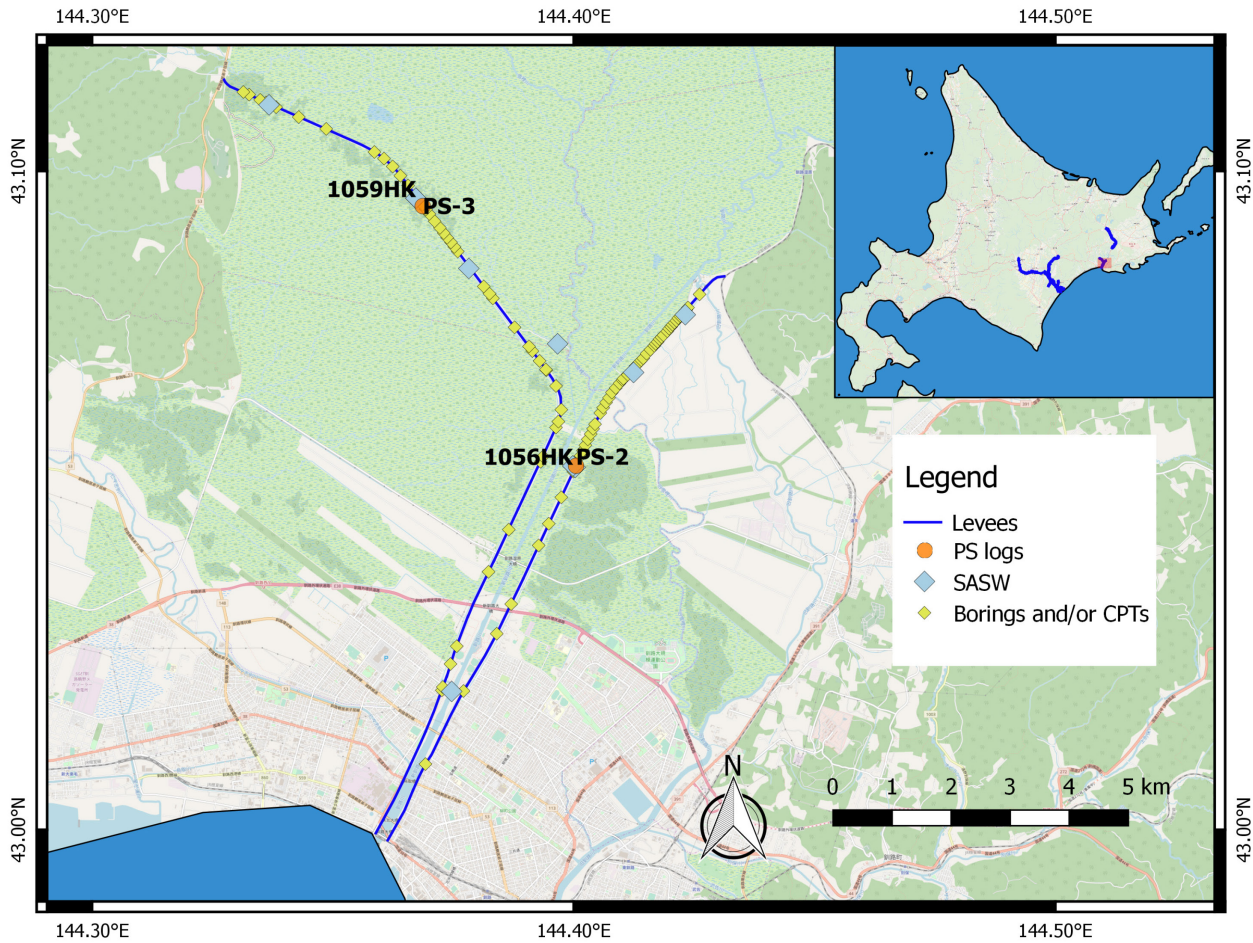


Figure 6.1 Large number of borings are available along the Kushiro levees in downstream marshland and are used to assignment of material properties and MRD relationships. The pair of collocated suspension log (PS-2) and SASW test (1056HK) is used to develop shear wave velocity profiles for the GRA in *DEEPSOIL*.

For the Tokachi region, laboratory tests are limited and the material properties are mostly correlated from soil classification and descriptions from boring logs. Figure 6.2 shows available borings, which are used to estimate the thickness of the soft peat and plastic soils, as well as the depth to firmer material. Plasticity is measured for samples taken from two open excavations performed after the 2003 Tokachi-oki earthquake (section 4.1.6 and 4.1.7); plasticity is assumed to be similar for fill materials sharing the same soil classification and placed during the same time period. The SASW tests are not collocated with the suspension logs as the data was obtained after the geophysical field investigation (Chapter 3) was completed.

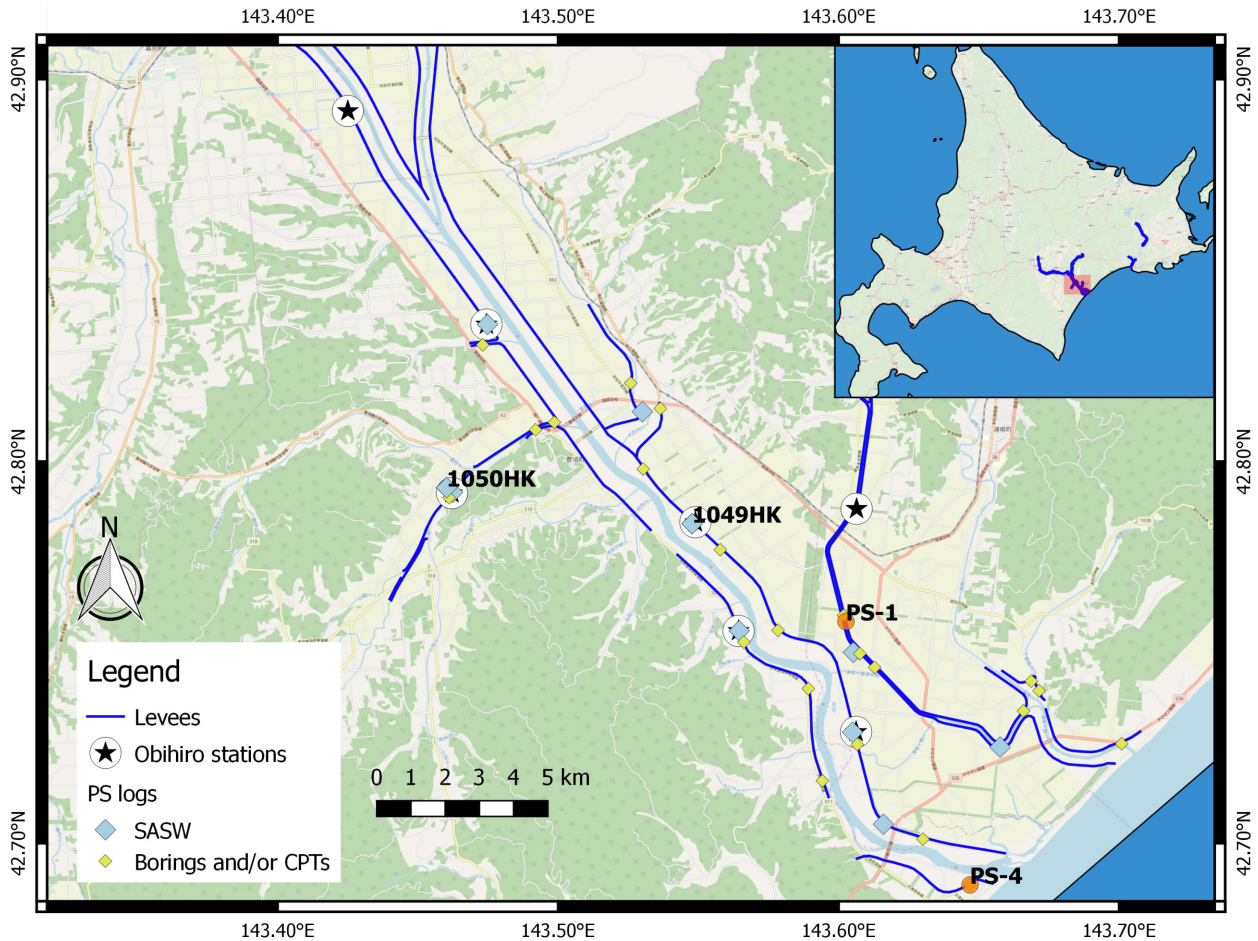


Figure 6.2 Suspension logs and SASW investigations in the downstream region Tokachi River used to develop shear wave velocity profiles. Stratigraphy from nearby borings and CPTs provides soil type for assignment of material properties and MRD relationships.

### 6.1.2 Shear strength

For cohesive soils, the undrained shear strength is applied below the ground water table. In Tokachi, CPTs were co-located or close to SASW test sites. For these sites, the undrained shear strength is evaluated from the cone tip resistance and an empirical cone factor (Section 4.2.3). Based on test data provided in Sheahan et al. (1996), Stewart et al. (2014) suggests 20-40% increase of shear strength to account for rate effects, due to the faster rate of shearing in earthquake loading than in typical laboratory testing. The lower bound value of 20% is adopted. In Kushiro, where CPTs were not

advanced near the SASW test sites, the undrained shear strength ratio was estimated based on strength normalization (Ladd 1991),

$$\frac{S_u}{\sigma'_{v0}} = S \times OCR^m \quad (6.1)$$

Where typical values of  $m$  and  $S$  are 0.8 and 0.2-0.25 respectively. The OCR used in Eq. (6.1) is based on consolidation test results.

For cohesionless material, the peak friction angle was estimated from SPT blow counts in a manner consistent with critical state soil mechanics, with a critical state friction angle of  $32^\circ$  assumed for quartz sand (Negussey et al., 1988). Dilation is also assumed to contribute to friction angle (Section 4.2.3), and the friction angle used for analysis range from  $\phi' = 38 - 41$  deg. The shear strength is estimated as  $\tau_{ff} = \sigma'_v \tan \phi'$ , where  $\sigma'_v$  is the vertical effective stress at the middle of the layer, and  $\phi'$  is the average friction angle for the stratigraphic unit.

### **6.1.3 Shear wave velocity profiles**

Downhole suspension logging was performed in Kushiro and Tokachi by the local River Management Offices. In Kushiro, the logs extend to a depth of 75 m for PS-2 on the left bank, and to 60 m on the right bank for PS-1 (Figure 6.3). Both reached relatively firm material with  $V_s$  exceeding 300m/s at the base of the borehole. Two suspension logs were performed in Tokachi, to depth of 50 m for PS-1 and to 55 m for PS-2; in both cases  $V_s$  exceeds 390 m/s at the base of the boreholes. Each suspension log is accompanied by SPT blow counts and a stratigraphic column. The raw measurements are not provided and the available profiles averaged  $V_s$  over depth intervals corresponding roughly to soil type. Due to the post processing, the resolution of the suspension logs is low. For example, both logs indicate  $V_s \approx 110$  m/s in the upper 9-11 m, which unexpectedly high for peat. It is likely that the profiles contain

softer units near the surface that are not represented due to averaging and smoothing. With the expectation that the soft surficial layers of peat and organic soils will strongly influence the site response, the suspension logs are supplemented with SASW-based profiles.

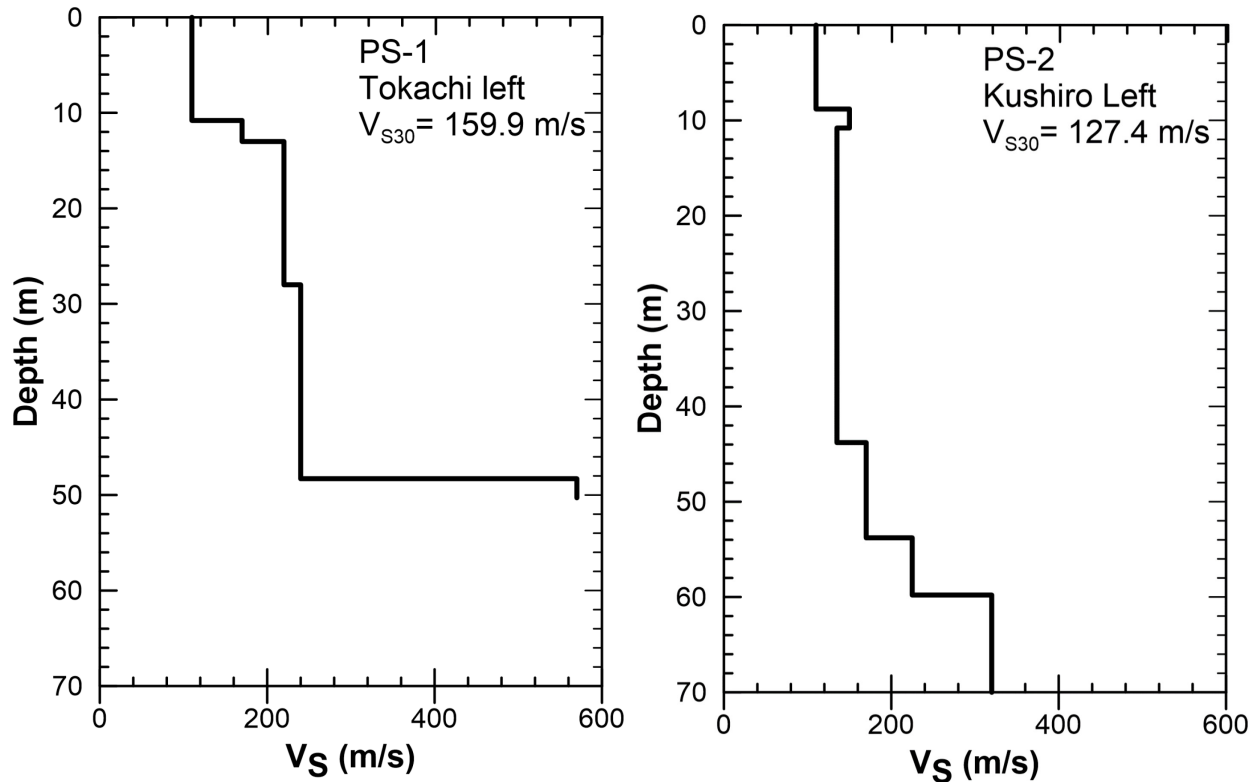


Figure 6.3 Processed shear wave velocity profiles from downhole suspension logging in Tokachi and Kushiro. The logs were presented in this smoothed form by the Hokkaido River Disaster Prevention Research Center and the Kushiro Development and Construction Office.

Two profiles were developed for analysis in the Kushiro and Tokachi regions. For Kushiro, the profiles represent a combination of surface wave data near the ground surface and suspension logging data at greater depth. For Tokachi, the profiles are again based on surface wave data near the surface, but as the SASW was not collocated with a suspension log (the data was made available after the field investigation), the velocities at depth are estimated based on stratigraphy at the SASW site, and velocity gradients in the same material unit based on the suspension logs. Both profiles are extended to sufficient depth such that shear wave velocities of about 300 to 400 m/s are encountered. This reference



condition corresponds to site class II in the Zhao et al. (2016) Ground Motion Models used to develop the empirical site term in Chapter 5. Significant extrapolation would be necessary to extend the profiles to a stiffer reference condition, and would be highly uncertain without any measurements or soil type information at that depth within the study region. Therefore the choice was made to retain a shorter profile. The underlying elastic half-space used for modeling below the seismic velocity profiles has a  $V_s$  compatible with the reference site condition.

The objective in developing these profiles was not to capture the full range of conditions present in the respective study regions, which would be needed for a simulation-based estimate of site response as a whole. Rather, the goal is to define the nonlinear component of site response, which are based on the composite profiles shown in Figure 6.4. Both locations are seen to be inversely dispersive from the SASW.

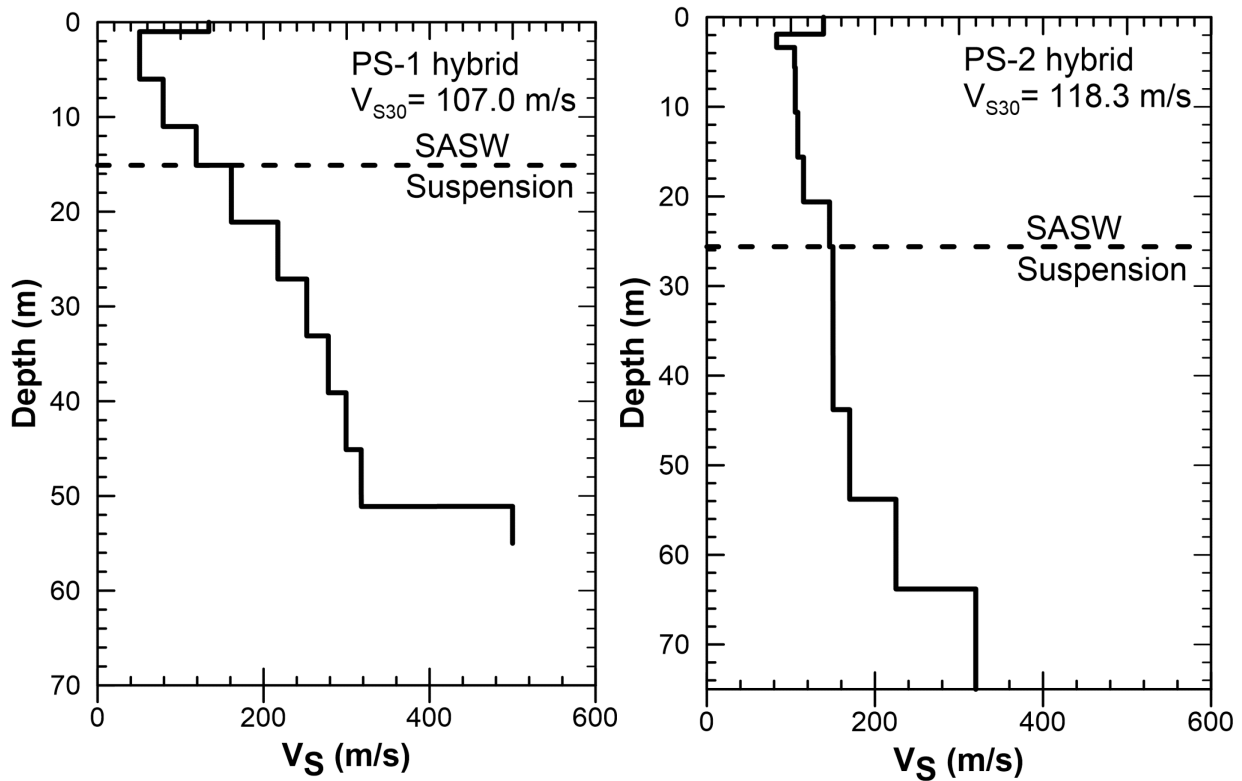


Figure 6.4 Representative shear wave velocity profiles with combining surface wave measurements and suspension logs.

### 6.1.4 Modulus reduction and damping curves

(a) *Available information from literature*

The strain-dependence of shear modulus and material damping ratio are characterized by modulus reduction and damping versus shear strain (MRD) curves. The shear stress-shear strain curve (also known as a backbone curve) is often represented with a hyperbolic function. Upon some rearrangement of this function, the modulus reduction curve can be expressed as,

$$\frac{G(\gamma)}{G_{max}} = \frac{1}{1 + \left(\frac{\gamma}{\gamma_r}\right)^\alpha} \quad (6.2)$$

where the maximum shear modulus is calculated from the shear wave velocity and mass density,

$$G_{max} = \rho V_s^2 \quad (6.3)$$

Empirical modulus reduction curves are derived by regressing laboratory data to obtain  $\gamma_r$ , the pseudo-reference shear strain where the modulus is reduced to half of  $G_{max}$  and  $\alpha$ , which is the curvature coefficient that controls the steepness of the curve near  $\gamma_r$ . Both parameters are dependent on the soil properties (e.g., PI and uniformity coefficient) and mean effective stress. Higher  $\gamma_r$  indicates linear behavior over a larger range of shear strains.

Modulus reduction curves ( $G/G_{max} - \gamma$ ) were developed using empirical models by Darendeli (2001) for both plastic and non-plastic fine-grained soils (clays and silts). The model by Menq (2003) was applied for granular soils. The input parameters are plasticity index ( $PI$ ), overconsolidation ratio ( $OCR$ ), and mean effective stress ( $\sigma'_m$ ) for Darendeli (2001), and the mean grain size ( $D_{50}$ ), coefficient of uniformity ( $C_u$ ), and mean effective stress for Menq (2003). Mean effective stress is related to vertical effective stress ( $\sigma'_v$ ) through,

$$\sigma'_m = \sigma'_v \left( \frac{1 + 2K_0}{3} \right) \quad (6.4)$$

where  $K_0$  is the coefficient of earth pressure at rest, which is estimated as (Jaky, 1948; Mayne and Kulhawy, 1982),

$$K_0 = (1 - \sin \phi) \times OCR^{\sin \phi} \quad (6.5)$$

The properties are taken from testing performed on samples nearby for Kushiro, and estimated from soil classification and descriptions from the boring logs for Tokachi, where detailed information from lab tests is unavailable.

Empirical models for MRD curves in peat are less well established than for more common soil types (clays, silts, sands). However, various investigators have found the dynamic behavior of peat to differ from that of inorganic soils. Tokimatsu and Sekiguchi (2006) examined recordings of the 2004 M 6.6 Niigata-ken Chuetsu earthquake from three nearby stations in Ojiya. Two of the stations are sited on soft surficial soils over stiffer gravel deposits. At the third site, peat is present at depths around 1.5-3.0 m under the K-NET Ojiya station. This peat has  $V_s$  of around 50 m/s, as measured from suspension logging. The ignition loss ( $LI$ ) is around 62% for the tested peat sample ( $LI$  is related to Organic content; ASTM D 2974-00). Cyclic torsional shear tests were conducted on undisturbed hollow specimens to characterize the nonlinear dynamic properties of the surficial soils. The MRD curves presented in Figure 6.5 show this peat material to have high small strain damping (e.g.,  $D_{\min} \approx 3-4\%$ ) and significantly lower nonlinearity (i.e., larger  $\gamma_r$ ) as compared to sands and clays.

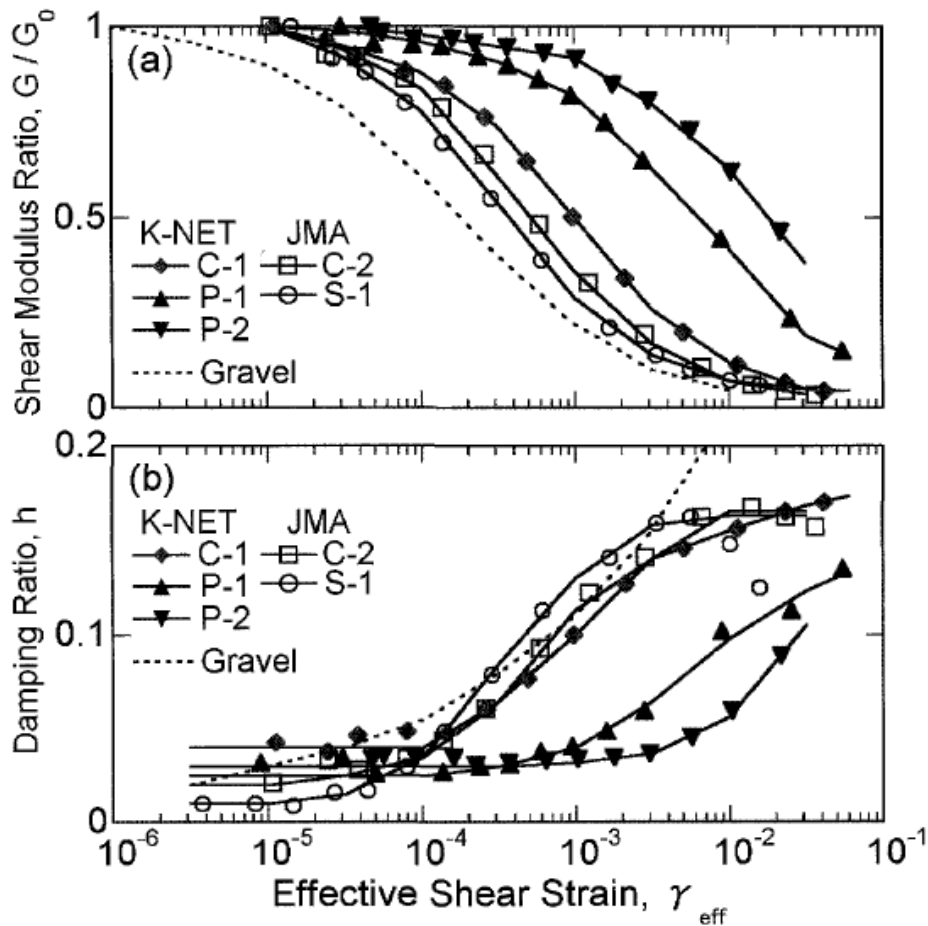


Figure 6.5 Modulus reduction and damping curves from cyclic torsional shear tests on samples of sandy silt (S-1), silty clay (C-1, C-2) and peat (P-1, P-2). Modulus reduction in peats is more gradual with higher damping at small strains (Tokimatsu and Sekiguchi, 2006).

Kishida et al. (2009) developed regression models for the dynamic properties of highly organic soils from a collection of cyclic triaxial and resonant-column/torsional-shear tests. The secant shear modulus ( $G$ ) and damping ratio are dependent on the shear strain amplitude ( $\gamma_c$ ), vertical effective consolidation stresses ( $\sigma'_{vc}$ ) and organic content (OC). Increasing OC and  $\sigma'_{vc}$  increase  $\gamma_r$ , making the soil effectively more linear. The OC-dependence of the behavior is similar to PI-dependence classically observed for clays (Vucetic and Dobry 1991). For highly organic soils, the Kishida et al. (2009) model shows that increasing  $\sigma'_{vc}$  has less effect on the modulus reduction behavior. This feature of the model contrasts

with a strong  $\sigma'_{vc}$  effect that has been observed for some of the same peat materials used to develop the model (Wehling et al. 2003).

Hayashi et al. (2018) performed cyclic torsional tests on undisturbed samples collected from seven sites in Hokkaido. The eight samples of peat and two samples of organic clays encompass a range of physical properties, with ignition loss between 18-95%, and natural water content between 143 and 970%. Relationships for maximum shear modulus, reference strain and maximum damping with ignition loss and confining stresses are derived from test data. The Hardin-Drnevich model is applied to the results, but does not match the observed damping well at small strains.

Figure 6.6 compares MRD curves from the peat from Shinotsu in Ebetsu City tested by Hayashi et al. (2018), two peat specimens near Niigata by Tokimatsu and Sekiguchi (2006), and the general model for organic soil by Kishida et al. (2009) (applied with the OC = 67% and  $\sigma'_v = 45\text{kPa}$ ).  $D_{\min}$  is high and relatively consistent at around 3% for all the materials. Even among the organic peats tested, P-2 shows very linear behavior over a large range of strains. The test data compiled by Hayashi et al. (2018) is used to represent the peat behavior in both Kushiro and Tokachi, since the samples are from Hokkaido, and therefore may be derived from soil units with a similar geologic history to the peats in the study region.

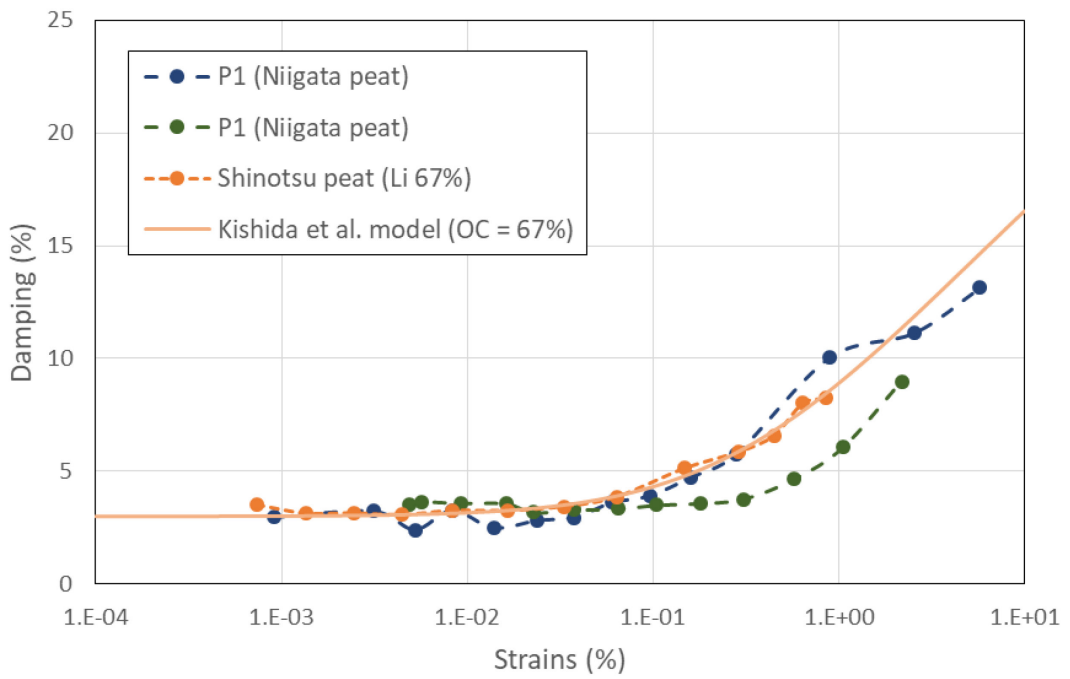
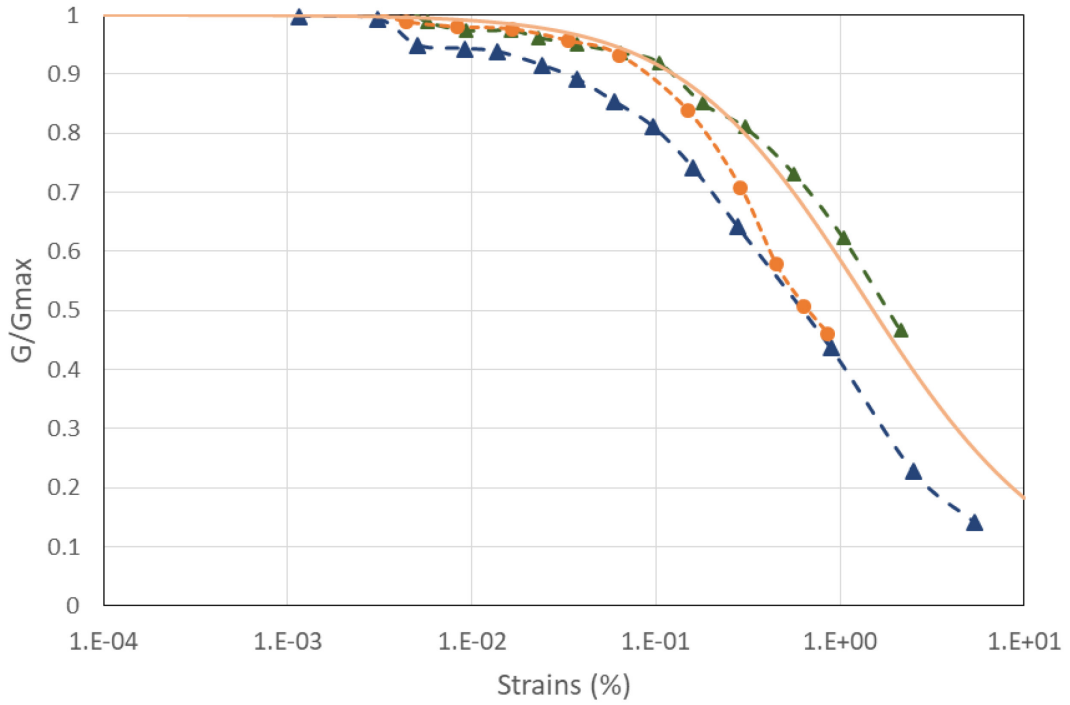


Figure 6.6 MRD curves for Shinotsu peat from Hokkaido (Hayashi et al. 2018), peat from the Niigata region (Tokimatsu and Sekiguchi 2006), and a mean model prediction for organic soils by Kishida et al. (2009).

Figure 6.7 compares MRD curves for organic clays from Hokkaido tested by Hayashi et al. (2018), and the Darendeli (2001) model as applied for clays of variable plasticity. The Hokkaido organic clays lie beyond  $PI = 100$  curves from Darendeli (2001). The Hokkaido materials have very low damping at large strains, but larger  $D_{min}$ . The following section describes the MRD curves selected for analysis.

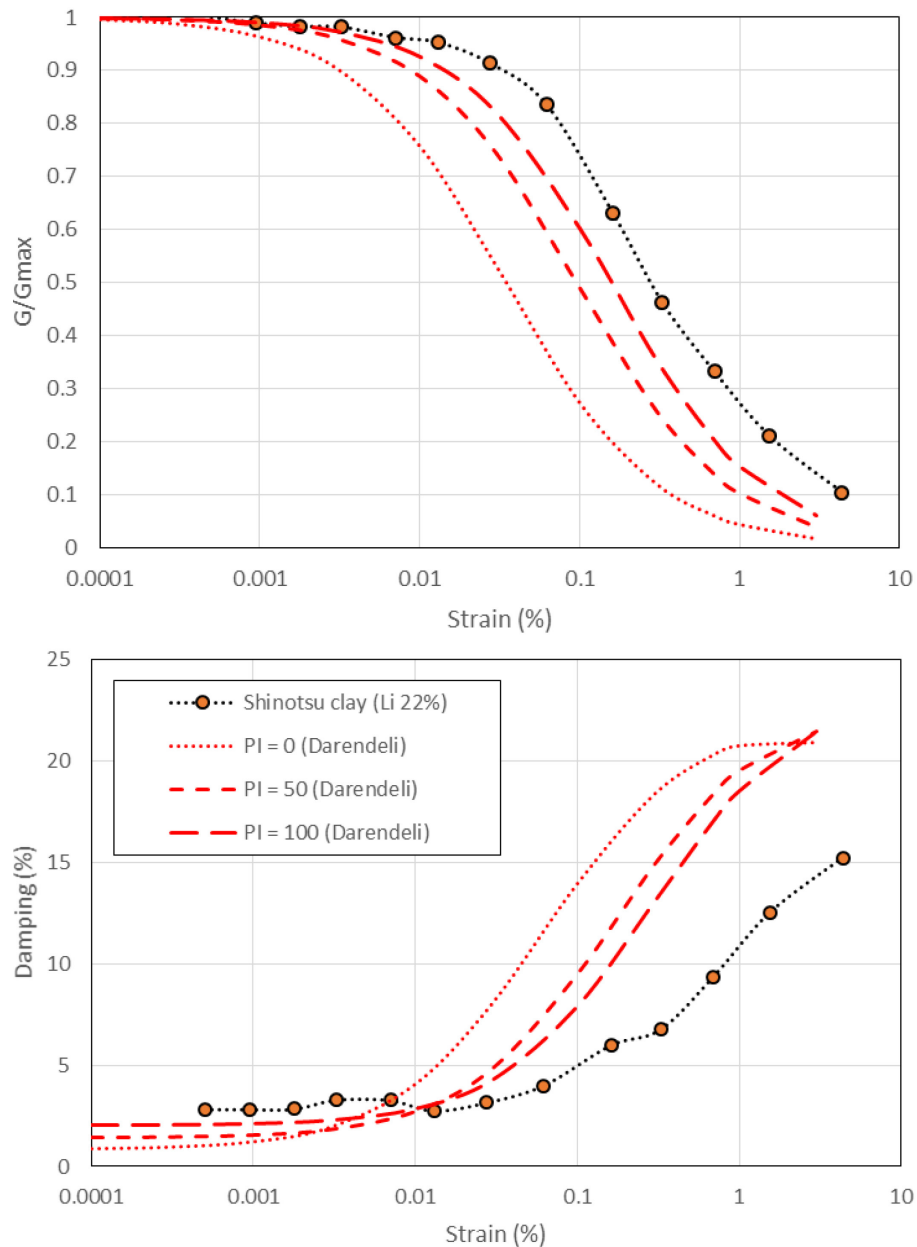


Figure 6.7 Comparison of the Darendeli (2001) modulus reduction and damping curves for clays of variability plasticity to tests on highly organic clays for the Hokkaido region (Hayashi et al., 2018)

*(b) MRD relations considered in analysis*

Two sets of MRD curves were initially selected for analysis. One set consists of the Darendeli (2001) curves, which are used for clay materials with an assumed PI of 50. In this first set of curves, the peat layers are modeled using test data from Hayashi et al. (2018). The second set of MRD curves again uses the Hayashi et al. (2018) data for the peat layers. However, the Hokkaido organic clay curves were used for clays and silts. This has the joint effect of increasing the small strain damping (approximately from around 1% to 4%) and reducing the nonlinearity.

Additional MRD curves are being considered in ongoing analyses to reduce the level of nonlinearity from what is provided by the two sets of curves that were initially considered. This will be considered in future work.

## **6.2 INPUT MOTIONS**

Strong motion recordings from stations at the surface are specified as outcropping motions at the base of the soil profile in DEEPSOIL. Recordings of subduction events at stations having similar site conditions as those at the base of the modeled soil column are therefore preferred. Two stations, HKD094 (K-NET) and TKCH11 (KiK-net), located in the forearc region of Hokkaido (west of the volcanic front) are selected. The  $V_s$  profiles of those sites, as taken from the NIED web site are shown Figure 6.8 (NIED, 2018). The  $V_{s30}$  values for these sites are indicated in the figure (326-459 m/s). In the case of the HKD094 site,  $V_{s30}$  is established using the extrapolation procedure of Midorikawa and Nogi (2015) as the profile is under 30 m in depth. The recordings from eight subduction events are filtered and processed following PEER procedures (Ancheta et al. 2014), and scaled arithmetically to cover a range of shaking intensities. Table 6.2 lists the selected records and the levels of scaling that were applied.



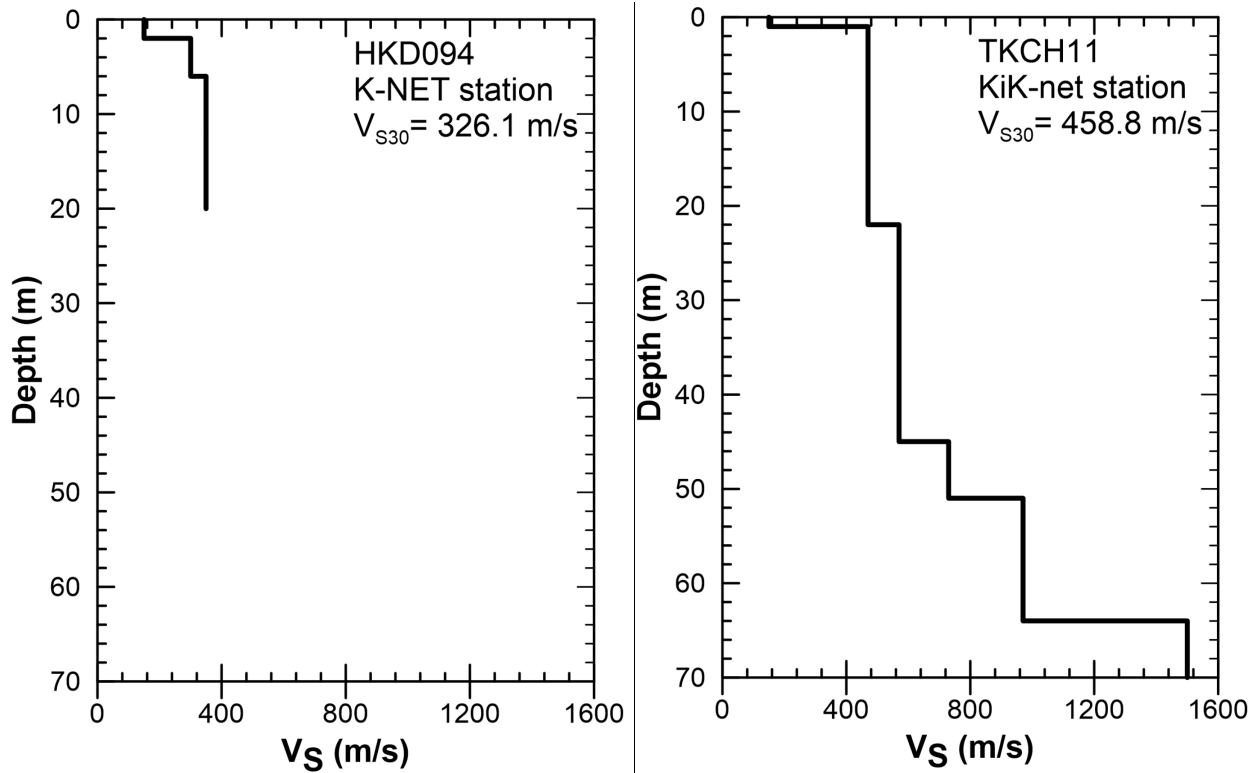


Figure 6.8  $V_s$  profiles for strong motion recording station HKD094 (left) and TKCH11 (right) with to be compatible with the base of the modeled soil column.

Table 6.2 PGA and scaling for input ground motion used for analysis

Station ID	Event	Depth (km)	Magnitude	PGA (g)		Scaling
				NS	EW	
HKD094	10/8/2003	28	5.7	0.0022	0.0022	0.5, 2.0, 3.0, 4.0
HKD094	6/15/1997	99	4.9	0.012	0.013	0.3, 0.5, 3.0
HKD094	8/14/2015	80	5.1	0.02	0.025	0.3, 3.0
HKD094	5/13/1999	104	6.4	0.048	0.05	2.0, 3.0
HKD094	9/26/2003	42	8.0	0.1	0.14	0.3, 0.5, 2.0, 3.0
TKCH11	10/7/2003	28	4.7	0.00065	0.00066	2.0, 3.0, 4.0
TKCH11	9/26/2003	42	5.7	0.23	0.26	0.3, 0.5, 2.0, 3.0
TKCH11	2/2/2013	102	4.9	0.22	0.27	0.3, 0.5, 2.0, 3.0

### 6.3 GROUND RESPONSE ANALYSIS

Nonlinear ground response analyses were performed using DEEPSOIL v7.0 (Hashash et al 2016), with the soil properties and input motions described in Sections 6.1 and 6.2, respectively. Specific information regarding implementation of the target soil properties from Section 6.1 is summarized here:

- Shear strains in the profiles are expected to be large. As a result, the MRD curves need to apply over a wider strain range than is provided by the curves presented in Section 6.1.4. The General Quadratic Hyperbolic (GQ/H) model (Groholski et al. 2016) was used with the MRD curves from Section 6.1.4 at small strains (up to approximately 0.1-0.5%) and the large strain behavior constrained based on the shear strengths estimated in Section 6.1.2.
- Non-Masing rules were used to ensure that the hysteretic damping provided by unload-reload relationships reasonably match the target damping (Phillips and Hashash, 2009).
- As the maximum frequency a layer can propagate is  $f_{max} = V_s/4H$ , the initial layer thicknesses are further subdivided to ensure the maximum frequency that can propagate exceeds 35 Hz. This is particularly important for the soft surficial sediments (e.g., peat), which otherwise could produce artificially low PSA at short periods as a result of numerical filtering of high frequency waves (Kwok et al. 2007; Hashash et al., 2011).

In addition to the nonlinear analysis, linear (visco-elastic) analysis was performed in which modulus reduction does not occur and damping remains at  $D_{min}$  regardless of strain level. This provides an estimate of the linear amplification. Pore pressure generation was not considered in any of the analyses since the majority of the profile contains peat and clays.

### 6.3.1 Initial results and damping adjustments

Linear and non-linear analysis are performed for each input ground motion and each of the profiles. Site amplification at a given spectral period is taken as the ratio between the spectral acceleration at the surface and the input motion, given by,

$$Y = \frac{PSA_{surface}}{PSA_{input}} \quad (6.6)$$

Site amplifications computed in this manner for spectral periods of 0.01, 0.05, 0.1, 0.5, 1.0 and 5.0 s are plotted as a function of the input peak acceleration ( $PGA_r$ ) in Figure 6.9. Results of the linear analyses are plotted along the y-axis ( $PGA_r = 0.001$  g). The simulation results in Figure 6.9 are fitted using the following expression for nonlinear site response (Stewart et al. 2017)

$$f_{site} = f_1 + f_2 \left( \frac{f_3 + PGA_r}{f_3} \right) \quad (6.7)$$

Coefficients for the nonlinear amplification function are obtained by fixing  $f_3$  at 0.1g and then regressing coefficients  $f_1$  and  $f_2$ . The amplification is systematically higher with the Tokachi profile for periods between 0.5-1.0 s. The natural periods of the Tokachi and Kushiro profiles are around 1.5 s and 1.9 s respectively. Hence, the divergence for PSA at 0.5-1.0 s is not likely related to fundamental mode responses. The current interpretation is that the Tokachi profile has a stronger second mode response within this period range. Beyond the site period, GRA are unable to reliably predict site response and it is recommended to estimate the site terms from semi-empirical models (Stewart et al. 2014).

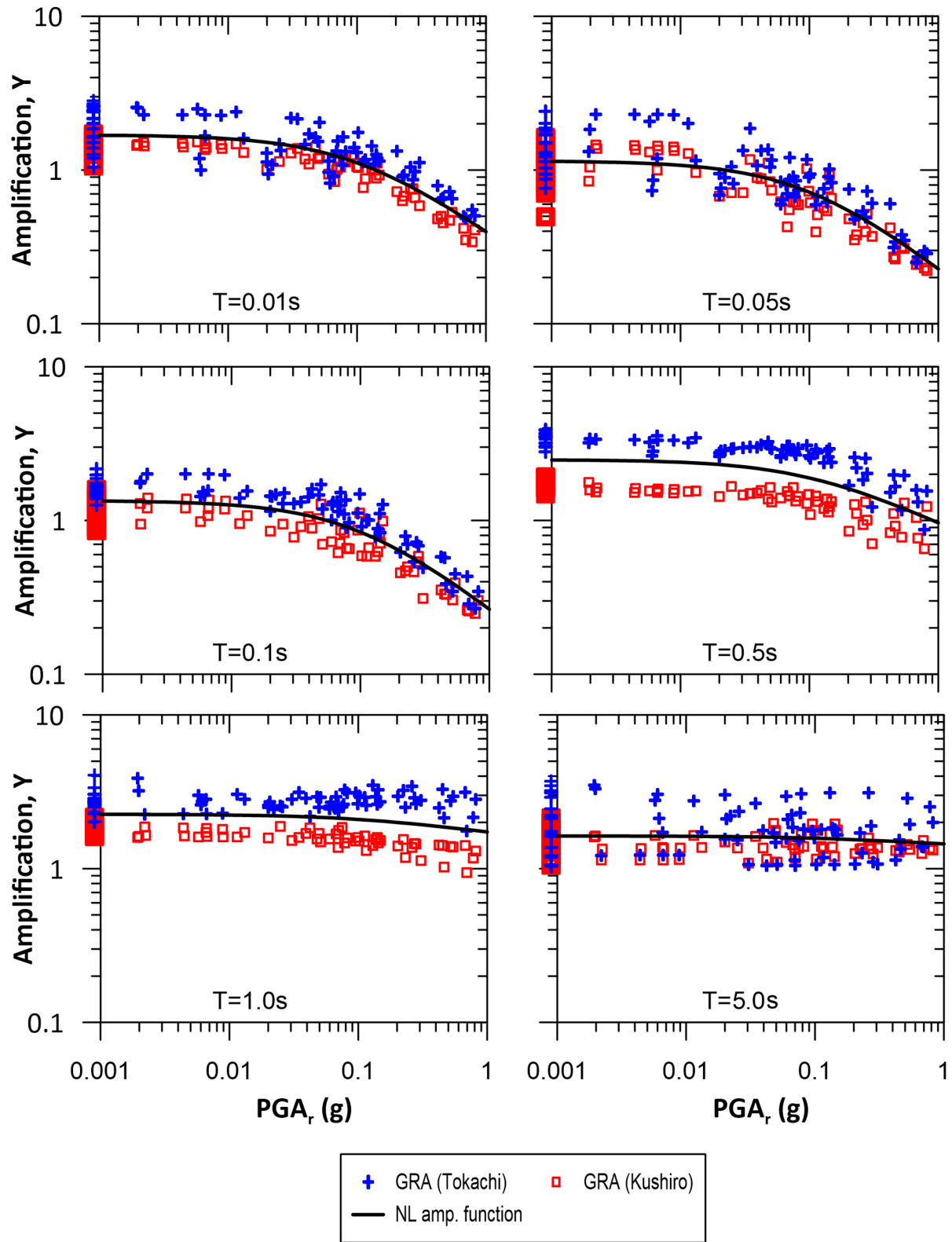


Figure 6.9 GRA results and fitted nonlinear amplification model. Amplification for Tokachi profile is systematically higher for Kushiro, particularly at periods between 0.5-1.0 s.

Since the motivation for performing ground response analyses is to constrain the nonlinear component of the site amplification model (i.e.,  $f_1$  is set separately as given in Chapter 5), the between-motion and between-profile variations among nonlinear amplification results can be largely removed by normalizing nonlinear amplification values ( $Y_{NL}$ ) by their linear amplification counterpart for the same input motion and  $V_s$  profile ( $Y_{lin}$ ),

$$Y_{normalized} = \frac{Y_{NL}}{Y_{lin}} \quad (6.8)$$

Figure 6.10Figure 7.7 shows the normalized amplification values, which have significantly reduced scatter. This data can be fit with a modified form of Eq. 6.8 as follows:

$$f_{NL} = f_2 \left( \frac{f_3 + PGA_r}{f_3} \right) \quad (6.9)$$

This approach avoids the fitted function passing between the two clusters of data points from the different profiles, and leads to more statistically stable estimates of nonlinear parameters  $f_2$  as seen in Figure 6.10.

The analysis is performed for both sets of MRD curves given in Section 6.1.4, which produces different estimates of  $f_2$ . The Hayashi et al. (2018) MRD curves produce less nonlinearity than the Darendeli (2001) curves. Figure 6.11 shows the resulting  $f_{NL}$  functions with empirical data from Section 5.4. The data contain a single event with sufficient shaking intensity to produce nonlinearity, and the empirical fit is shown together with its 95% confidence interval. The functions fitted to the simulated data are lower than the empirical curves, particularly at short periods where they are below the 95% confidence interval.

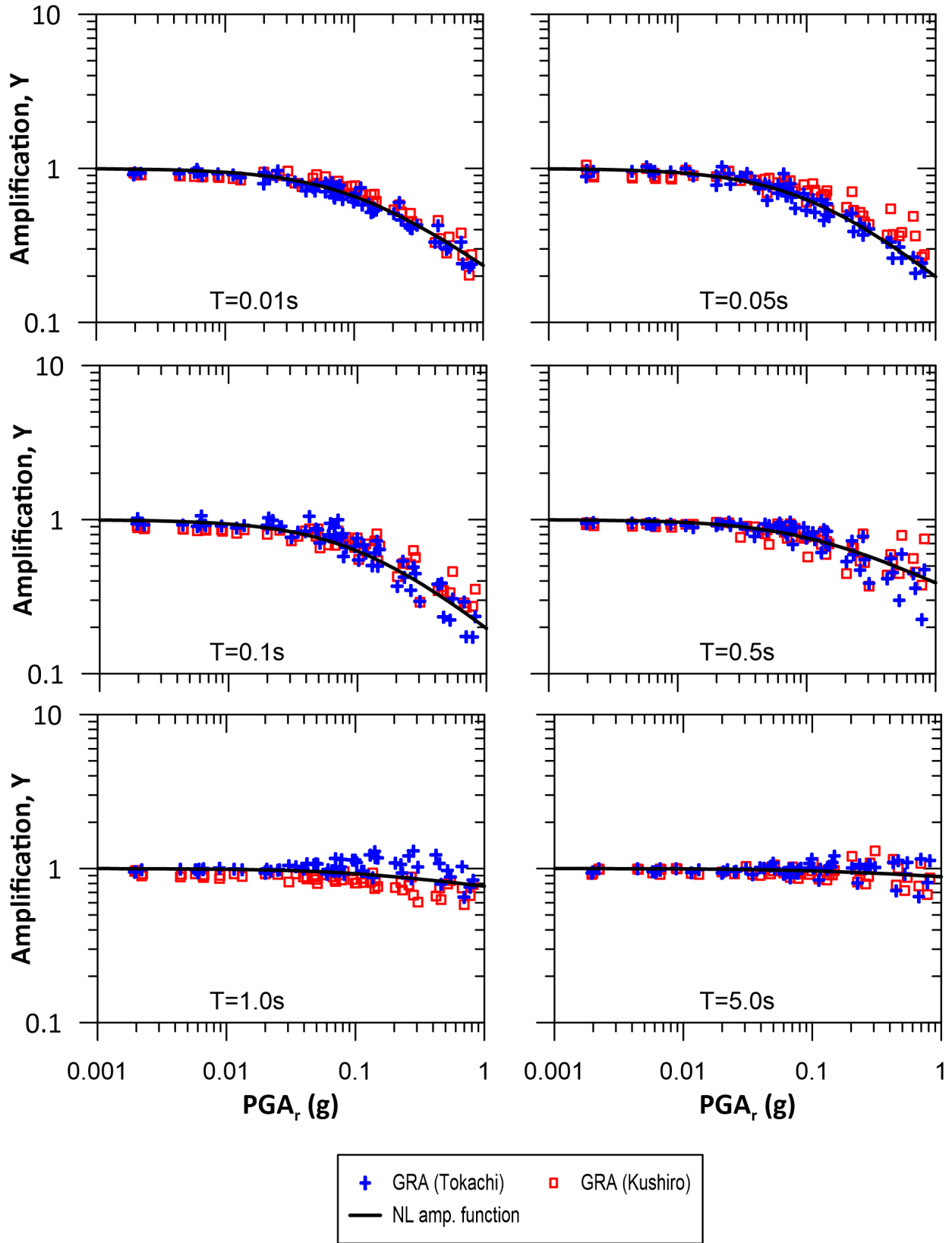


Figure 6.10 Normalized amplification highlighting the effects of nonlinearity.

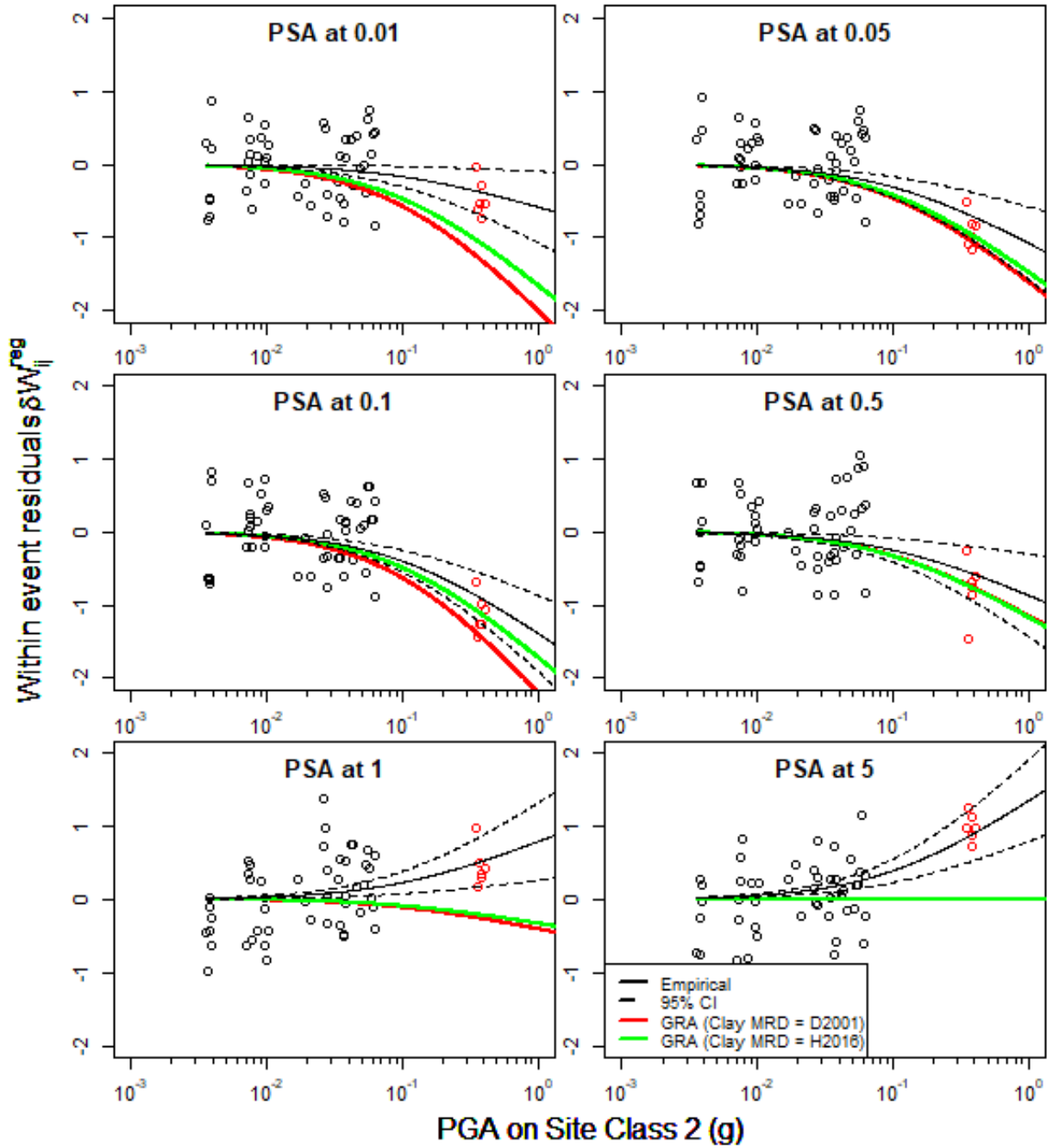


Figure 6.11 Comparison of nonlinear amplification functions based on data and ground response analysis. At short periods, the simulation results fall outside the 95% confidence interval from data.

The nonlinear parameters from all three analyses smoothed across the spectra periods are plotted in Figure 6.12, and values of  $f_2$  are given in Table 6.3 for select periods. More negative  $f_2$  values imply more nonlinearity and stronger deamplification as shaking intensity increases. As noted previously, the empirical data implies lower nonlinearity than the simulations.

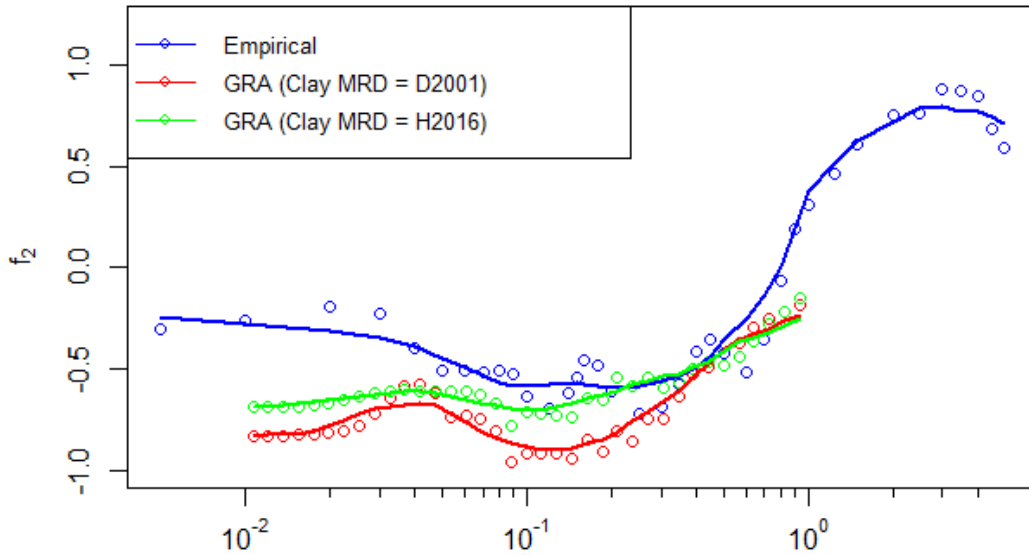


Figure 6.12  $f_2$  derived from data and GRA smoothed across periods. The GRA are performed with MRD curves for clays based on Hayashi et al. (2018) and Darendeli (2001), with the latter showing more nonlinearity.

Table 6.3 Values of  $f_2$  regressed from empirical data and GRA with different MRD relationship.

Period (s)	Nonlinear term $f_2$		
	Empirical	GRA (D01)	GRA (Hea16)
0.01	-0.279	-0.831	-0.687
0.02	-0.317	-0.78	-0.656
0.05	-0.446	-0.701	-0.631
0.1	-0.589	-0.889	-0.71
0.2	-0.591	-0.837	-0.628
0.5	-0.355	-0.42	-0.42
0.9	0.192	-0.239	-0.254
0.01	-0.279	-0.831	-0.687



The amplification functions derived above can be compared to results from two other studies involving sites and profiles with highly organic peat soils. Kishida et al. (2009b) (Kea09) developed a site response model (conceptually similar to Eq. 6.7, but with a different function) for the Sacramento-San Joaquin Delta using 1-D equivalent linear GRA for eighteen soil profiles, all of which contains highly organic soils ranging from 1 to 9 m thick. The dynamic soil properties are defined based on Kishida et al. (2009a). Monte Carlo simulations are used to introduce randomness to the dynamic soil properties. The reference condition is taken as the NERHP site class D based on the  $V_s$  of the dense sand layer below the organic soils. The results are regressed against combinations of parameters, which included PGA on reference site condition,  $M_w$ ,  $S_1$  and  $V_{S10}$ .  $S_1$  is defined as the ratio of  $S_a(1.0)$  and  $S_a(0.2)$ , and is selected to represent spectral shape of the ground motion. Model 3 depends on PGA and  $M_w$  only, and is adopted for comparison.

Terronez (2017) examined two profiles in the Kushiro basin and developed amplification functions using ground response analyses in *DEEPSOIL*. Differences between the analyses performed by Terronez (2017) (T17) and those performed in this study include: 1) the T17  $V_s$  profiles are correlated from blow counts using Kwak et al. (2015) and are not measured, 2) T17 used MRD curves for fine grained soils from Darendeli (2001) and for peat from on Kishida et al. (2009a), and 3) ground motions from crustal strike-slip earthquakes compiled by (Baker et al., 2011) were used. The reference conditions are taken as 450 m/s and 600 m/s for the profiles on the west and east side of the Kushiro basin respectively.

The amplification functions from this study are compared to those recommended by Kea09 (Model 3) and T17 in Figure 6.13 with and without the linear term. The results shown for comparison purposes from this study include the empirical amplification (Chapter 5) and the GRA-based model as derived using Hayashi et al. (2018) MRD curves. While linear terms cannot be directly compared since each

study considered different reference conditions, the empirical linear terms significantly exceed those based on simulations. The data likely contain site effects (e.g., basin effects) that 1-D GRA is unable to capture. Considering only the nonlinear portion of the site response, Kea09 and the empirical model are similar. The GRA-based model for the Hokkaido sites in this study are similar to those from T17, both of which show more nonlinearity than the empirical or Kea09 models.

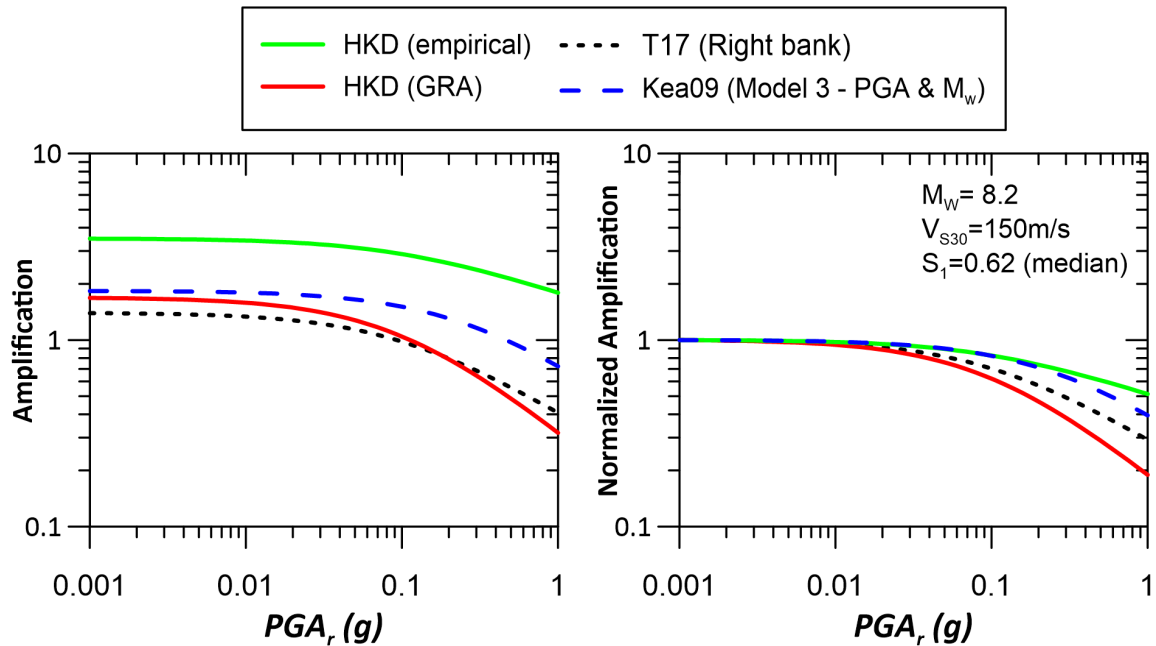


Figure 6.13 Amplification functions for peat sites from this study compared with GRA by Terronez (2017) and Kishida et al. (2009). Empirically derived site amplification function shows more linear amplification and lower nonlinearity than the simulations.

## 6.4 SUMMARY

A site amplification model is developed for the Tokachi and Kushiro regions based on 1-D linear and nonlinear ground response analyses (GRA) with two profiles and a range of input motions. Two sets of MRD relationships are considered for the thick layer of fine grained soils underlying the surficial peat, and the selection of the dynamic properties significantly affects the GRA results. At short periods, the nonlinear term derived from 1-D GRA is more negative and suggests more nonlinearity than is

evident from the data. At longer periods, the nonlinear factor lies within the 95% confidence interval of the values regressed from the data. The GRA would benefit from additional profiles to consider the sensitivity of the results to  $V_s$  and material properties. The empirical site amplification function is adopted for ground motion estimated subsequently. This selection is reinforced by the similarity of the nonlinear model to a previously published model for peaty sites (Kishida et al. 2009b).

## 7 DEVELOPMENT OF FRAGILITY FUNCTIONS

### 7.1 INTRODUCTION

The Pacific Earthquake Engineering Research (PEER) center developed the performance-based earthquake engineering (PBEE) methodology to estimate losses associated with future earthquakes. The average annual rate of exceeding a particular level of the decision variable is obtained through the triple integral (Moehle and Deierlein, 2004),

$$\lambda(DV) = \int_{dm} \int_{edp} \int_{im} G(DV|DM) dG(DM|EDP) dG(EDP|IM) d\lambda(IM) \quad (7.1)$$

The decision variable can be quantities such as repair cost, casualty and downtime which are of interest to stakeholders. The remaining variables in the framework consists of DM, EDP and IM. DM represents a damage measure, such as freeboard loss for a dam or levee, or cracking of a reinforced concrete member. EDP is an engineering demand parameter, such as slope displacement or settlement of a soil structure, or inter-story drift ratio of a building. IM is an intensity measure used to characterize the ground shaking intensity, such as PGA, PGV, or spectral acceleration.  $G(x|y) = P(X > x|Y = y)$  represents the probability of exceeding a given value of X conditioned on Y = y, and  $dG(EDP|IM)$  represents the slope of  $G(x|y)$  with respect to y. A fragility function links the structure performance to loading intensity by providing the probability of exceeding a damage measure as a function of an intensity measure (IM) or engineering design parameter (EDP).

The Delta Risk Management Strategy (DRMS) estimated the risks of levee failure in the California Bay-Delta region using the PBEE methodology. Their seismic levee fragility functions are obtained from Monte Carlo simulations by considering the horizontal levee deformation as a function of the earthquake magnitude and peak ground accelerations, which is combined with a judgment-based

probability of levee breaching conditioned on loss of freeboard. Vorogushyn et al. (2009) developed fragility curves for levees considering other failure mechanisms, such as overtopping, piping, and seepage conditioned on height of water in the channel impounded by the levee and duration of flooding using Monte Carlo simulations. Kwak et al. (2016) considered flood control levees along the Shinano River and developed fragility functions based on field performance during the 2004 M 6.6 Niigata-ken Chuetsu and 2007 M 6.6 Niigata-ken Chuetsu-oki earthquakes. The levees are founded predominantly on sands and gravels with low fines content, and peat is rarely encountered.

For this study, fragility functions are derived empirically from field performance of levees along the Kushiro and Tokachi Rivers. Downstream regions are considered, where peaty organic soils are present in the levee foundations, as well as upstream regions without organic soils in the levee foundations.

## **7.2 DAMAGE DATA**

The damage data comprises information on levee performance, which is observed in post-event reconnaissance, and the imposed loading, which is represented here by a ground motion intensity measure. Table 7.1 summarizes six analysis methods presented by Porter et al. (2007) for synthesizing fragility functions depending on the damage data available. In Table 7.1, IM can be substituted for EDP as the conditioning variable.

For the levee systems and earthquakes considered, the performance of the levee segments are known, and the maximum shaking intensities are estimated, falling under Method B in the above framework. Section 2.4 summarizes available observations along the levees from both earthquakes considered, and the assignment of damage levels based on crack dimensions and subsidence. The maximum demand experienced by the levee segments are characterized by the PGA, and the procedure to estimate PGA along the levees are presented subsequently.

Table 7.1 Analysis methods and data employed (Porter et al., 2007)

<b>Method</b>	<b>Data used</b>
A. Actual failure EDP	All specimens failed at observed values of EDP
B. Bounding EDP	Some specimens failed; maximum EDP for each is known
C. Capable EDP	No specimens failed; maximum EDP for each is known
D. Derived fragility	Fragility functions produced analytically
E. Expert opinion	Expert judgment is used
U. Updating	Enhance existing fragility functions with new method-B data

### 7.3 GROUND MOTION DISTRIBUTION

Shaking intensity is used as the primary demand parameter for levee damage. Ideally ground motion is recorded at the location of interest, however recording stations are sparse relative to the spatial extent of the levees. Spatial interpolation of ground motions from available recording stations is necessary to estimate ground motion at the levee segments. Kriging is a linear interpolation method for estimating a spatially continuous variable from observations at limited locations. Values at locations without observations are solved for by minimizing the mean squared error of prediction based on available observations together with a correlation function. The correlation between two points are described by the semi-variogram, which expresses the semi-variances of the data as a function of separation distance. This reflects the physical phenomenon that two closely located points will have similar ground motions since travel path and site conditions are comparable. Kriging is thus useful for interpolating observed recordings to estimate motions at the locations of interest.

A key assumption inherent to the simple Kriging method is that the variable is generated by a stationary process (variables have a constant mean in space and/or time). Levees are typically founded on alluvial deposits that are softer than the soils outside of the floodplain, where recording stations are usually sited. Figure 7.1 shows the distribution of  $V_{S30}$  at the recording stations and from measurements along

the levees in the downstream region of both river systems. The latter is a combination of existing shear wave velocity profiles from KDCO and ODCO, and the geophysical site investigation presented in Chapter 3. The  $V_{S30}$  at the levees is mostly between 100 - 200 m/s, while it generally exceeds 200 m/s at the stations. Seismic site effects are different at soft and relatively stiff soil sites, thus the systematic differences between site conditions at the recording stations and the levees would be expected to bias interpolated ground motion if Kriging were performed on the ground motions directly. These differences could be especially acute for the present application because of the unusually soft peaty organic soils underlying the levees, which would be expected to produce strong differences from non-peat conditions as encountered at many of the recording stations. Therefore direct interpolations from the stations without accounting for the difference in site response are likely to be inaccurate.

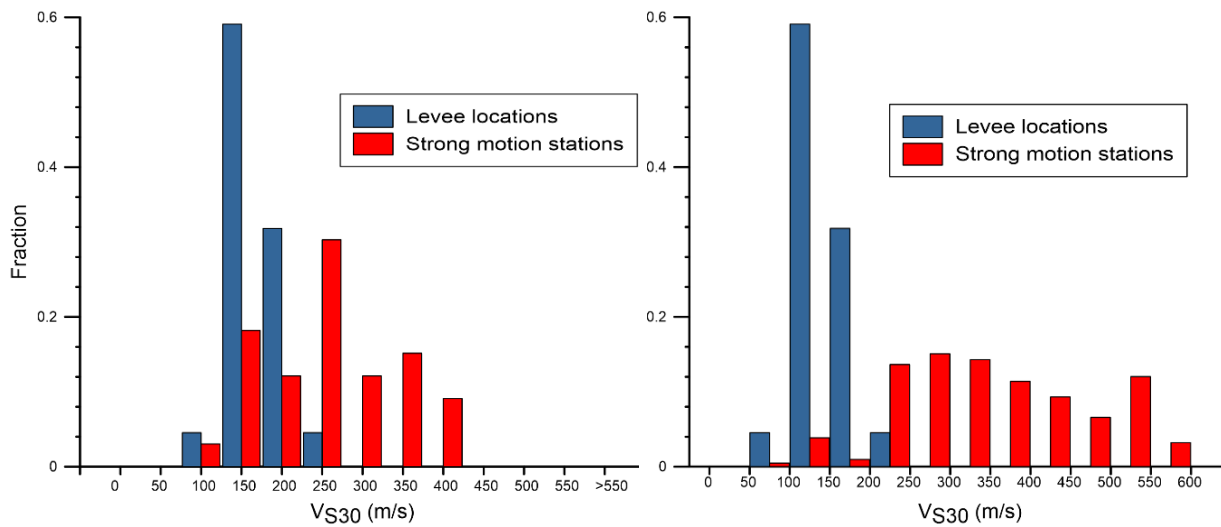


Figure 7.1 Distribution of  $V_{S30}$  at strong motion stations that recorded the 1993 (left) and 2003 (right) events compared to distribution of  $V_{S30}$  measured at the levees. Site conditions at levees are generally softer than at the recording stations and at the lower limit of empirical site amplification models.

Accordingly, spatial interpolation is not performed directly on the measured intensity measures from the stations, but rather on the within-event residuals of a suitable ground motion model (GMM) based on the methodology presented by Kwak et al., (2016). The Kriging method is applied to the within-

event residuals (Eq. 5.4), a spatial map of the deviation from the GMM event-specific median prediction. This approach accounts for the effects of different site conditions across the study region, to the extent that the GMM is able to capture them. The methodology is as follows:

1. Estimate  $V_{S30}$  at recording stations and levees from measured shear wave velocity profiles. If measurements are unavailable, use geomorphic proxies (e.g., Wakamatsu & Matsuoka, 2013) or interpolate from nearby measurements.
2. For earthquake  $i$ , the total residual is the difference between intensity measures from recording  $j$  and the median from the selected GMM for the magnitude, distance, and site conditions at site  $j$  during event  $i$ . The within-event residual subtracts the event term from the total residual, and is computed as:

$$\delta W_{i,j} = \ln(IM_{i,j}^{rec}) - (\mu_{i,j} + \eta_{E,i}) \quad (7.2)$$

Where

- $IM_{i,j}^{rec}$  = intensity measure from recording  $j$
- $\mu_{i,j}$  = GMM median in natural log units
- $\eta_{E,i}$  = event term for earthquake  $i$

3. Apply the Kriging method to obtain a map of the within-event residuals.
4. Compute an estimate of IM at site as:

$$\ln(IM_{i,k}) = \delta W_{i,k}^K + \mu_{i,k} + \eta_{E,i} \quad (7.3)$$

Where

- $\mu_{i,k}$  = GMM median in natural log units for conditions at site  $k$
- $\delta W_{i,k}^K$  = residual at site  $k$  estimated from Kriging

In this approach, the selection of a suitable GMM is critical. GMMs by Abrahamson et al. (2018) and Zhao et al. (2016b, 2016c) are chosen as they are developed from datasets of subduction events with



large proportions of Japanese recordings, and perform well against existing data from Japan as a whole in capturing observed trends such as magnitude saturation and magnitude dependent distance scaling (although local variations in path effects are encountered in Hokkaido that these models do not capture; Section 5.3.1). Both include a  $V_{S30}$ -dependent nonlinear site term, which is critical for the combination of strong shaking and soft sites in the downstream regions during both the 1993 and 2003 earthquakes, where large strains and nonlinearity are anticipated.

Semi-variograms are fitted to describe the spatial correlation of empirical data at short separation distances. These models are used in Kriging to characterize the relative influence of different observations on an interpolated value at a point of interest, with closer stations having stronger correlation and more influence on the resulting estimate (Jayaram and Baker, 2009). The Kriging process only considered stations in the forearc region of Hokkaido Island, as both levee systems are within the forearc. This avoids potential bias from inaccurate modeling of distance attenuation in the backarc and for travel paths between Hokkaido and Honshu (Section 5.3.1). The distribution of interpolated residuals for the 2003 earthquake is shown in Figure 7.2 for the forearc region. The number of recording stations and the coverage is drastically lower for the 1993 event, and the variograms developed from the 2003 event are applied here.

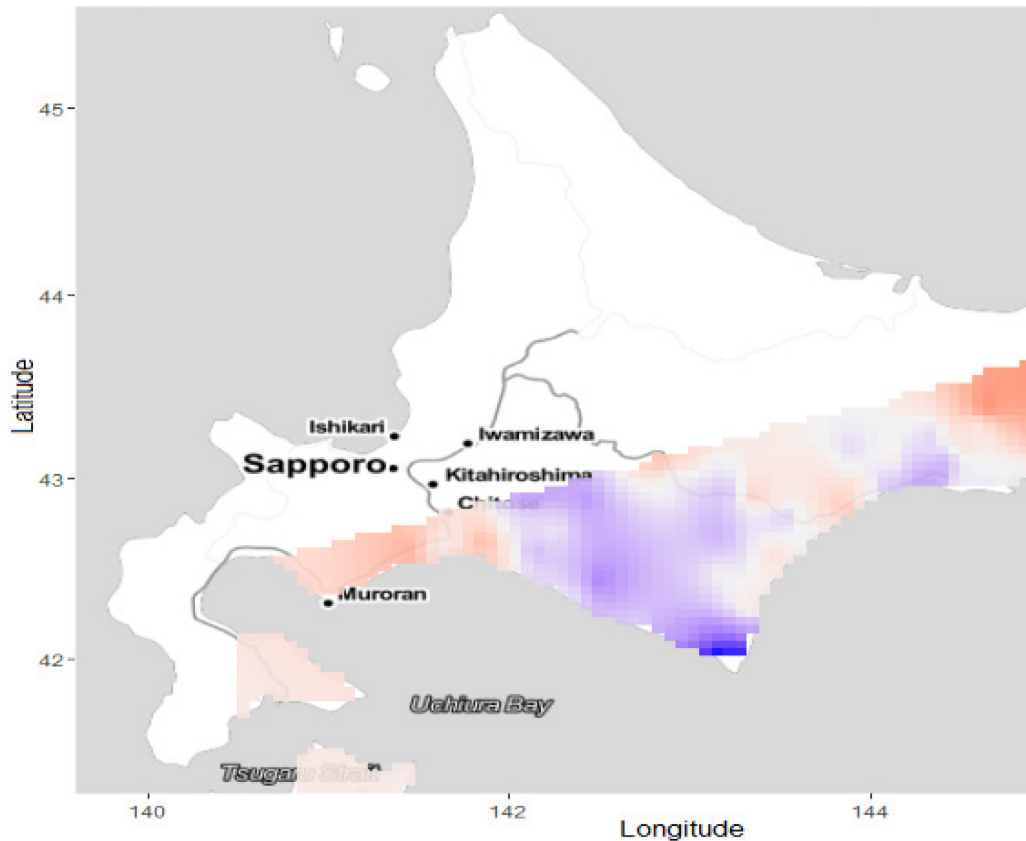


Figure 7.2 Within-event residuals with respect to Zea16 GMM in the forearc region for 2003 earthquake.

The region-specific site amplification models developed from the recordings along the Tokachi River (Chapters 5 and 6) are applied in place of the site terms from the GMMs in the shaded regions shown in Figure 7.3. The Tokachi and Kushiro regions have similar subsurface conditions, which are assumed to be compatible with the site conditions at the Obihiro stations considered in the development of the region-specific model. The organic deposits underlain by thick soft sediments at those sites are not well represented by ergodic site terms in the GMMs. The predictions using the region-specific site terms are assumed to transition linearly to the ergodic prediction over a 5 km zone beyond the edge of the shaded region in Figure 7.3 in order to avoid introducing unrealistic jumps at the edges of the shaded regions.

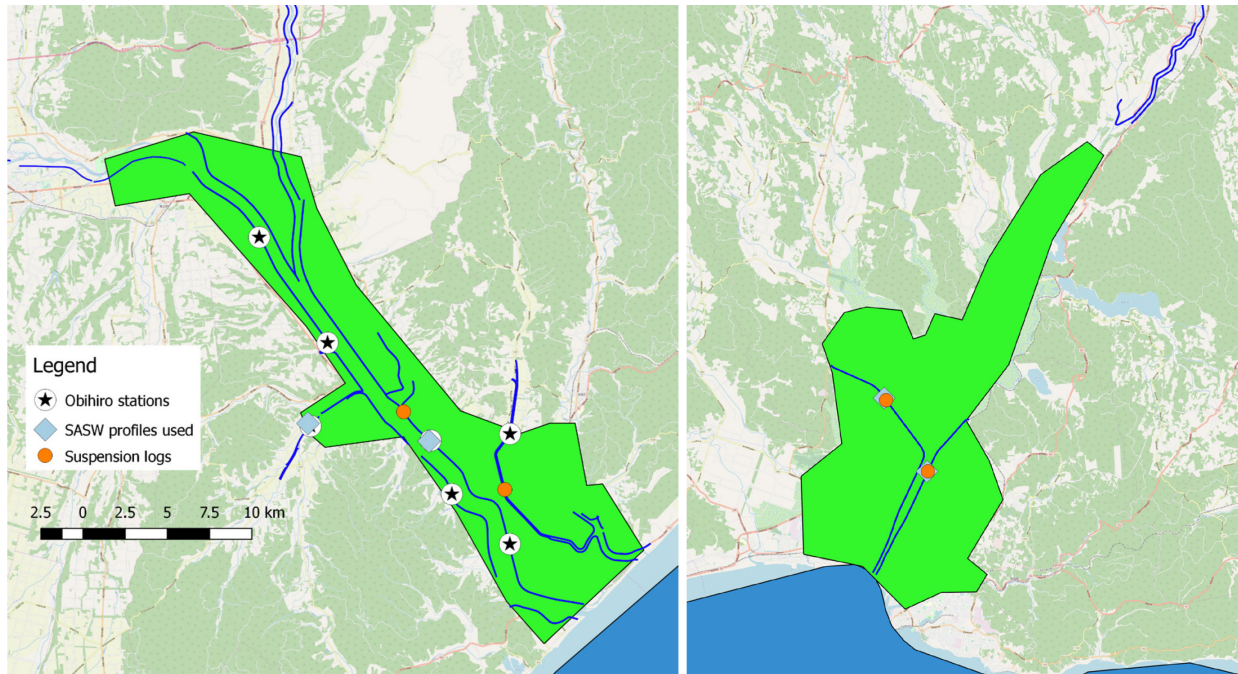


Figure 7.3 Region-specific amplification models are applied in the highlighted areas along the Tokachi (left) and Kushiro (right) Rivers. These areas have thick soft sediments and site response that differs from the ergodic model.

## 7.4 FRAGILITY FUNCTION

The site conditions of the foundation soil beneath the upstream and downstream portions of the levee systems are distinct - the downstream regions have relatively soft soils, including peat, within the foundation materials. In addition, the groundwater level is typically at or above the interface between the peat layer and the levee fill. The saturated sandy soils within the levees are susceptible to liquefaction in many cases, and can result in significant damage, as seen in the section analysis in Chapter 4. The foundation material in the upstream areas consists mainly of granular materials (no peat) with deep groundwater. Based on the difference in hydrological and foundation conditions, levee segments with and without peat in the foundations are separated for the development of fragility data points.

The extent of peat within the foundation was defined from the dense boring logs along the Kushiro levees and from the longitudinal cross section (Figure 2.2). Along the Tokachi levees, borings are limited to the downstream region and the longitudinal cross section only covers the first 20 km from the river mouth of the main Tokachi River (Figure 2.3). The backmarsh category indicated on the engineering geomorphologic classification maps corresponds well with peat occurrence within Kushiro (NIED, 2018). Assuming this correlation also exists at Tokachi, the extent of peat in the upstream portion of the Tokachi levee system and along the tributary branches are assigned according to the surface geomorphology on the engineering geomorphologic classification maps. Each 50 m levee segment is sorted based on their location within the two river systems, with 3,370 of the total 9,768 segments characterized as having peat present in the foundation.

The statistical analysis of fragility is based on grouping observations into bins having consistent estimates of shaking intensity. Porter et al. (2007) recommended selecting the number of bins based on the size of the dataset, taking the total number of bins as the square root of the total number of specimens. This approach is adopted with a modification suggested by Kwak et al. (2016) of the denominator from one to four.

$$m_{bin} = \frac{\sqrt{N_{total}}}{4} \quad (7.4)$$

This reduces the number of required bins, which in turn increase the number of observations per bin, to a level that provides for stable estimates of fragility (probability of damage). The probability of damage for bin  $i$  is computed as the number of failed segments  $n_i$ , divided by the total number of segments  $N_i$ , conditioned on  $pga_i$ , the median PGA for the bin.

$$P_i(DL > dl|PGA = pga_i) = \frac{n_i}{N_i} \quad (7.5)$$

The levees on peat have 21 bins with 320-321 segments each, and levees on inorganic soils have 29 bins with around 436-437 segments each. The slight difference in number of segments is necessary to distribute the segments among the bins required by Eq. (7.4), and has minor effects on the fragility associated with each bin. The damage measure used for the levees is the damage level (DL) determined from the field observations (Section 2.4). Each combination of probability of damage and PGA is taken as a ‘fragility data point’ for the analysis that follows.

A fitting approach with an appropriate functional form is required to produce a fragility function from the empirical fragility data points. The lognormal cumulative distribution function (CDF) is commonly adopted for structural applications (Porter et al., 2007) and has also been applied successfully for fitting levee fragility data (Kwak et al. 2016). The CDF operates between probabilities of zero for demands approaching zero and one for demands approaching infinity, which are realistic bounds. The probability of exceeding a given damage level is given by:

$$P(DL > dl|IM = im) = \Phi\left(\frac{\ln im - \mu_{ln}}{\beta}\right) \quad (7.6)$$

The function is fully defined by the mean ( $\mu_{ln}$ ) and standard deviation ( $\beta$ ) of the distribution, both with clear physical meaning.  $\mu_{ln}$  and  $\beta$  are estimated from the empirical fragility data points using the maximum likelihood estimation (MLE) presented in Baker (2015). The approach seeks to maximize the likelihood function such that the fitted fragility function has the highest probability of producing the observed data.

The probability of  $n$  out of the  $N$  segments in bin  $i$  exceeding a given damage level is given by the binomial distribution,

$$P(n_i \text{ of } N_i \text{ segments with } DL > dl) = \binom{N_i}{n_i} p_i^{n_i} (1 - p_i)^{N_i - n_i} \quad (7.7)$$

where  $p_j$  is the probability of an individual segment will experience a higher damage level when subjected to the shaking intensity (median of the bin), and is represented by lognormal CDF in Eq. (7.6). For all the fragility data points across all the bins, the likelihood of observing the data is given by,

$$L = \prod_{i=1}^M \binom{N_i}{n_j} p_j^{m_j} (1 - p_j)^{M_j - m_j} \quad (7.8)$$

Fragility functions obtained with the MLE for segments experiencing any level of damage ( $DL > 0$ ) are shown in Figure 7.4. Estimated PGAs at segments with organic foundation soils range from 0.18-0.62 g for modified Zea16, and 0.22-0.74 g for modified Aea18 (the ‘modification’ being to the site term, Section 7.3). These differences in PGAs are reflected by higher values of  $\mu_{ln}$  for Aea18 than for Zea16. The probability of any damage occurring reaches around 0.4 at the highest PGA constrained by the data.

The levee segments on inorganic foundations generally experienced lower levels of shaking. The majority of these segments are located in upstream areas, which have longer distances to the fault rupture. At high PGAs (where appreciable damage was observed for levee segments on peaty foundations), the probability of damage is significantly lower. For example, fragilities based on modified Zea16 at  $PGA = 0.6$  g are 0.40 and 0.18, respectively, for levee segments with and without peat in the foundations.

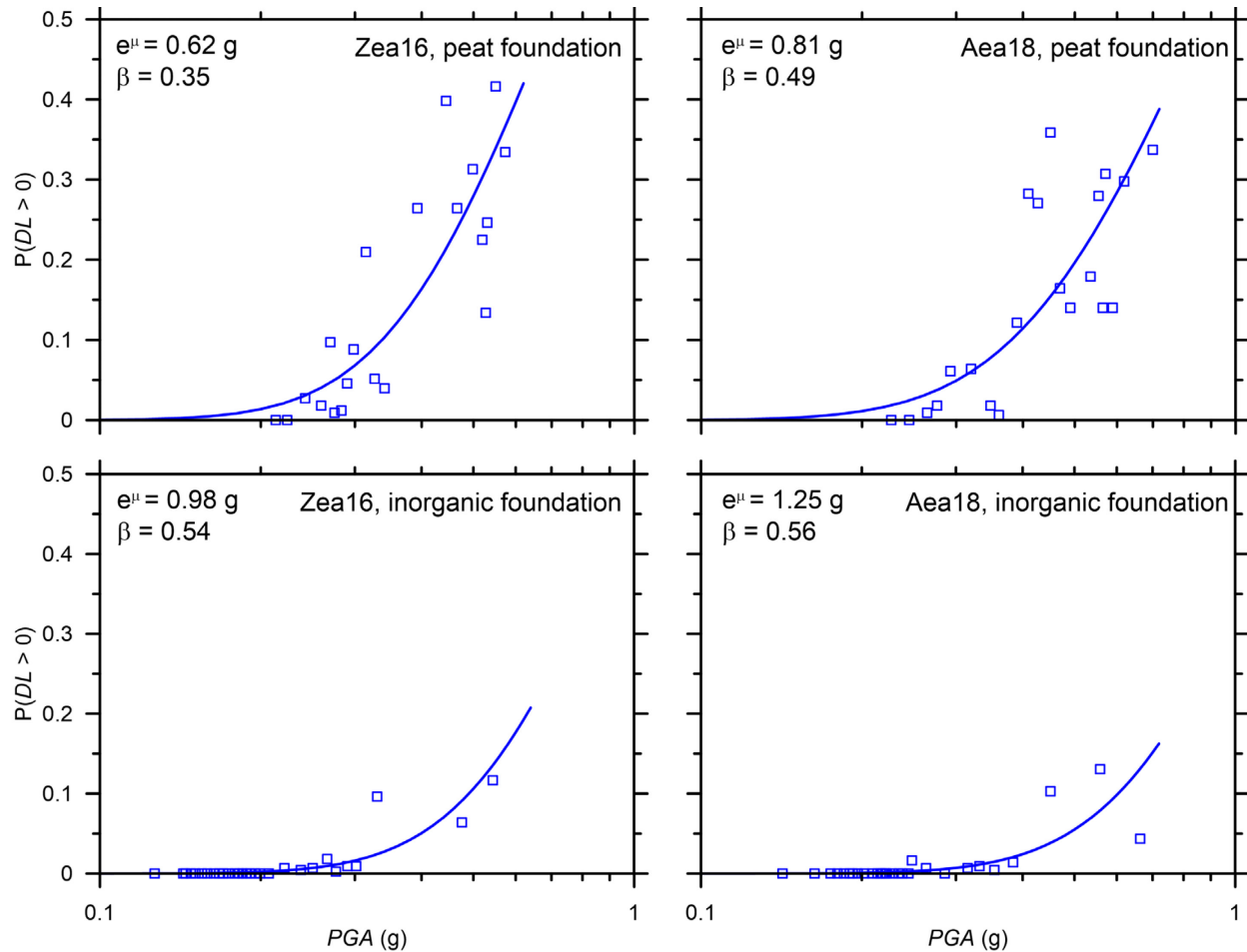


Figure 7.4 Fragility functions for occurrence of any damage conditioned on PGA. Segments on peat has higher probability of damage than segments on inorganics when subjected to the same PGA.

To evaluate fragility functions for higher damage levels, the numerator in Eq. (7.5) is adjusted to consider only segments exceeding the damage level of interest. The fitting is initially performed with both  $\mu_{ln}$  and  $\beta$  as variable parameters, and the resulting fragility functions are shown in Figure 7.5. For fragility data based on PGA estimated with the modified Zea16 GMM, this produced fragility functions that cross at low PGA, implying a higher probability of incurring more severe damage, which is physically unrealistic. Fragility functions for segments on inorganic materials do not have this issue. Kwak et al. (2016) encountered similar difficulties with Shinano river levee data.

To avoid this problem, an alternative approach is applied whereby the data fitting uses a constant  $\beta$  across damage levels. The  $\beta$  used in the fitting is that set from for  $DL > 0$  data. With this constraint applied, the lower probabilities associated with higher damage levels are reflected by an increase in  $\mu_{ln}$ . This ensures that fragility functions for increasing damage levels do not cross. Table 7.2 summarizes the  $\mu_{ln}$  and  $\beta$  parameters fitted with both approaches, and the corresponding log values of the MLE (larger values of likelihood indicate better fits). Fits with and without constraint of  $\beta$  generally produce visually similar fragility curves with comparable likelihood values, and the curves with constrained  $\beta$  are adopted subsequently.

Table 7.2 Mean and standard deviation of lognormal CDFs for PGA-based fragility curves

GMM	Damage Level	Variable $\beta$			Fixed $\beta$		
		$e^\mu$	$\beta$	LL	$e^\mu$	$\beta$	LL
Zea16	DL>0	0.69	0.56	-216.1	0.69	0.56	-216.1
	DL>1	0.82	0.65	-213.2	0.75	0.56	-218.9
	DL>2	0.99	0.54	-192.6	1.03	0.56	-192.9
	DL>3	2.08	0.75	-94.9	1.44	0.56	-97.9
Aea16	DL>0	0.86	0.64	-235.5	0.86	0.64	-235.5
	DL>1	0.98	0.67	-211.3	0.87	0.64	-218.3
	DL>2	1.88	0.87	-174.9	1.17	0.64	-193.0
	DL>3	3.15	0.88	-92.3	1.65	0.64	-99.2



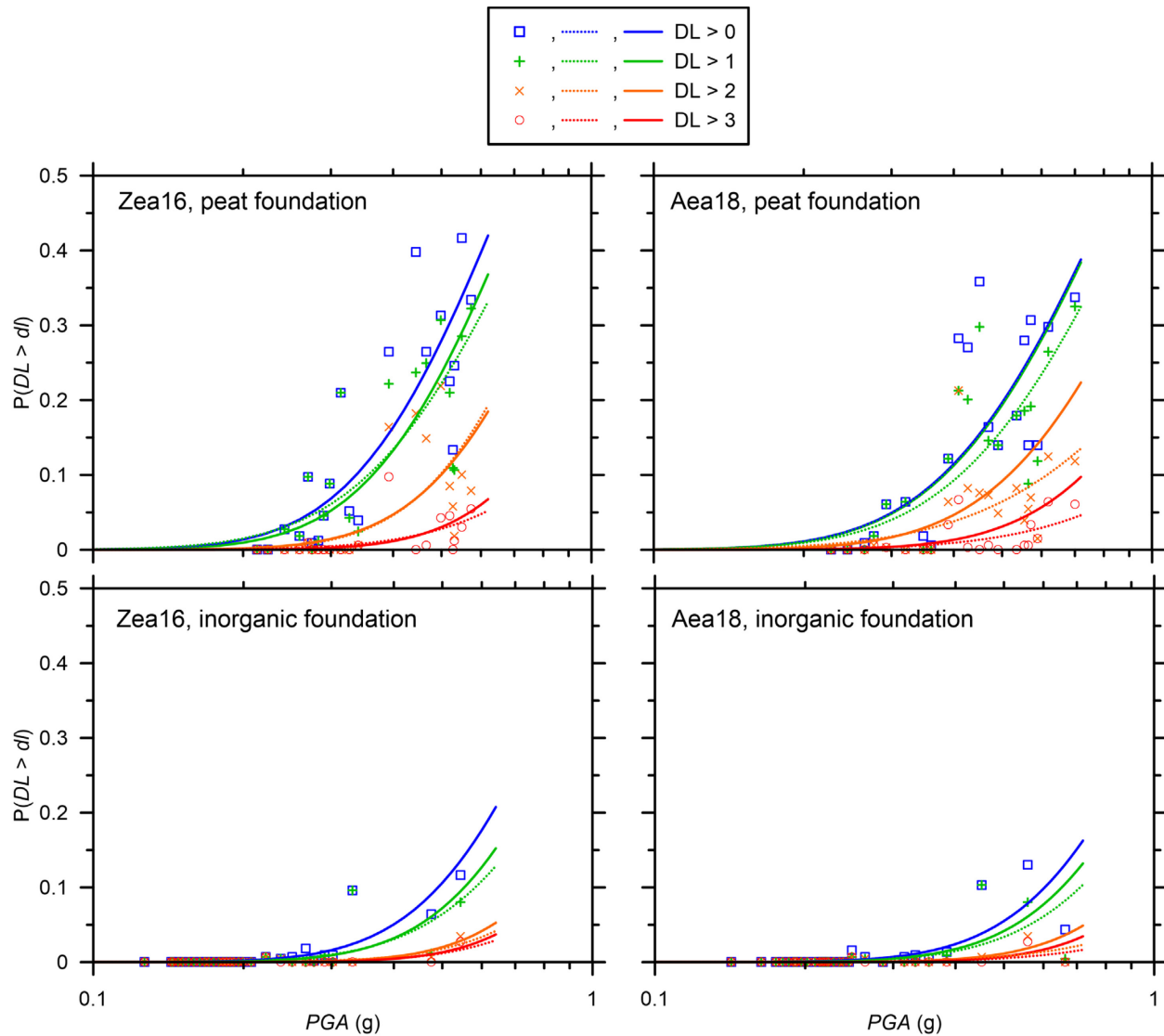


Figure 7.5 Empirical fragility data points and fitted fragility functions for varying damage levels. Fitting performed with  $\beta$  variable (dashed lines) and fixed (solid lines).

Figure 7.6 compares the difference between fragility functions derived using PGA estimated by the modified Zea16 and Aea18 GMMs. These differences reflect epistemic uncertainty associated with the ground motion estimates. The steepness of the fitted functions are governed by  $\beta$  and reflect aleatory variabilities inherent to the data set, which include variable geotechnical conditions along the levee systems and aleatory uncertainties in the ground motion estimates. Lower  $\beta$  indicates reduced dispersion and higher predictive power. The  $\beta$  may be reduced by improving estimates of PGA or by

using an alternative intensity measure that better describes demand (e.g., PGV). Reductions in  $\beta$  could, in principle, be achieved by incorporating levee response into the conditioning parameter by replacing intensity measures with EDPs such as LI and Newmark displacement (which was examined in section analyses, Chapter 4). The latter would require knowledge of the geometry and geotechnical properties of many cross sections along the length of the levees. Since this information is not available at the required levels of resolution, it was not considered in the present work.

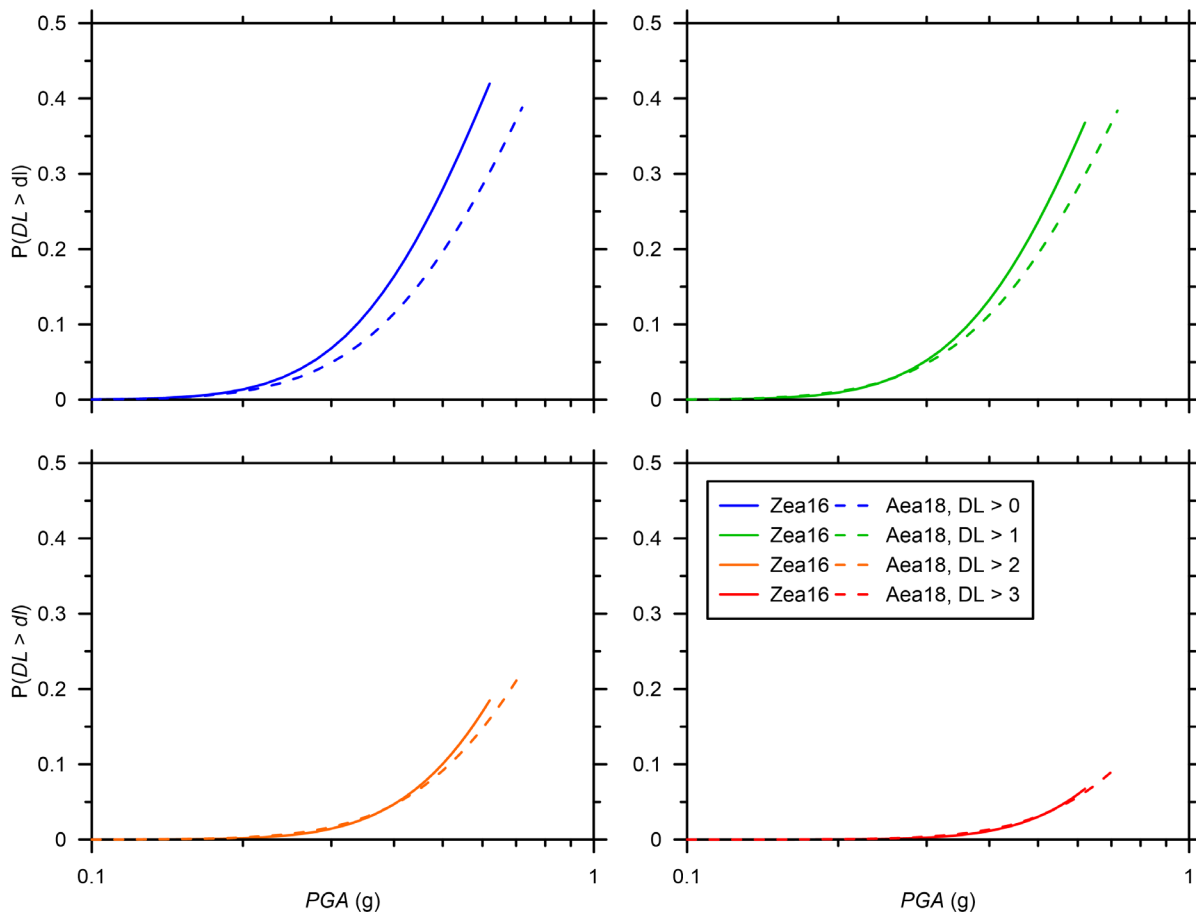


Figure 7.6 Fragility functions for levee segments founded on peaty foundation materials as derived using ground motion estimates from the modified Aea18 and Zea16 GMMs.

Fragility functions derived for the levees in this study (labeled HKD) are compared with those developed for levees along the Shinano River (Kwak et al., 2016) in Figure 7.7. At PGA below 0.27 g,

the probability of damage for the levees on peat is slightly lower. However the probability of damage increases drastically as PGA exceeds 0.30 g.

For levees on inorganic foundations, the Hokkaido levees are less fragile across the range of PGA supported by the data. Possible factors responsible for the observed differences may include differences in the age, mineralogy and depositional environments between the two regions, as well as hydrological differences. Along the Kushiro and Tokachi Rivers, the majority of the levees on inorganic foundations are in upstream areas, where the ground water level is below the levee foundation level. Moreover, these upstream areas along the Kushiro and Tokachi Rivers have relatively high gradients in the stream channels, which tends to produce stiffer and stronger sediments than in low-gradient regions. In contrast, the levees along the Shinano River system includes sections through flood plains, where the ground water level is higher and the gradients are lower. In addition, the type of motion the two systems are subjected to differs, given the Shinano River was shaken by lower magnitude, crustal earthquakes, which are shorter in duration and likely richer in higher frequencies than the subduction events examined for the Hokkaido levees.

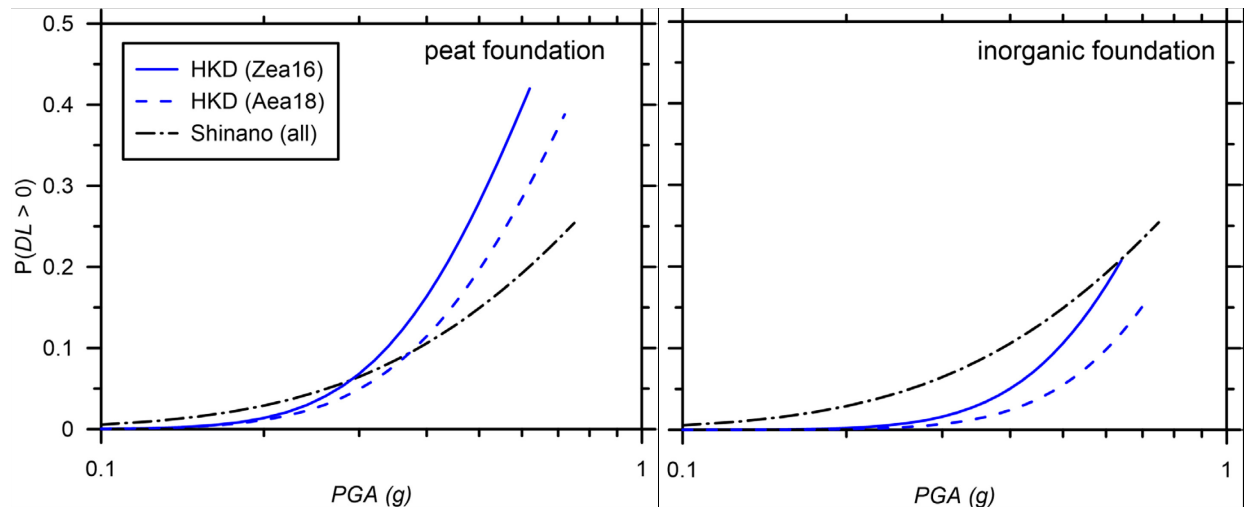


Figure 7.7 Comparison of fragility curves for probability of any damage level ( $DL > 0$ ) as evaluated for Hokkaido levees (this study) and Shinano River levees (Kwak et al. 2016).

## 7.5 SUMMARY AND DISCUSSION

Field performance of levees along the Kushiro River and Tokachi River are combined with estimates of ground motion intensity to provide empirical fragility functions for varying damage levels. For levee segments with peat in the foundation, the fragility is observed to be higher than segments without peat in the foundation within the same river systems in Hokkaido. Compared with fragility functions derived for levees along the Shinano River with inorganic foundation soils, the Hokkaido levees with peat in the foundation have appreciably higher fragility above a threshold PGA of about 0.25 g, as well as a lower  $\beta$  reflected by a steeper curve.

Empirically derived fragility functions reflect ground truth for the complex mechanisms underlying levee damage during an earthquake. Application of the models should be cognizant of the differences and similarities in the conditions of the Hokkaido levees and other levee systems. For instance, levees in the San Francisco Bay-Delta region are constantly impounding water, and would be anticipated to be more susceptible to earthquake damage as a result of the lateral loading and seepage forces from the impounded water as well as a greater degree of saturation of the levee fills, making the soils more susceptible to liquefaction. Given the conditions in the Delta, the fragilities based on the Hokkaido levees would likely present a lower bound of the expected fragility of Delta levees.

Sources of uncertainty associated with the fragility models stem from (1) variations in geotechnical conditions in the levee and foundation materials and (2) aleatory uncertainties in the estimated demand. The damage provided in the reconnaissance reports is relatively objective, and is not considered to be a significant source of uncertainty. Aleatory uncertainties in demand are estimated as part of the Kriging process, and increase with the spacing of ground motion stations. These uncertainties are relatively large for the 1993 Kushiro-oki earthquake (sparse recordings) and smaller for the 2003 Tokachi-oki earthquake.

## 8 CONCLUSION AND RECOMMENDATIONS

### 8.1 CONCLUSIONS

Case histories of the performance of levee systems founded on peat along the Kushiro and Tokachi Rivers during two large magnitude subduction earthquakes are collected and analyzed. Geotechnical analyses are performed at ten location along Tokachi River where the subsurface was characterized and ground motions can be reasonably estimated from nearby recording stations.

Four liquefaction severity indices, as well as slope stability and Newmark-type displacements, are performed to estimate the severity of liquefaction induced damage and levels of permanent slope deformations. Liquefaction susceptibility is based on field classification and testing of samples of materials recovered from trenching across two of the sections. The Newmark displacement analyses are performed using yield accelerations derived from 2-D limit-equilibrium models of the levee cross sections in the computer program SLIDE. The predicted performance is compared with field observations from post-earthquake reconnaissance. The effectiveness of indices that place more weight on shallow layers, such as  $LPI_{ISH}$  and  $LSN$ , are found to perform better. Taking the 70<sup>th</sup> percentile value is recommended when multiple borings and/or CPT profiles are present across a cross section. The rationale for use of a greater than median percentile is that damage is expected to be governed by looser than average pockets of susceptible material within the levee fill or in the foundation. Damage assessment considering both liquefaction indices and Newmark displacements shows improved prediction ability with respect to observed performance.

Fragility functions express the probability of exceeding a damage level (DL) conditioned on an intensity measure. Fragility functions for damage occurrence ( $DL > 0$ ) conditioned on PGA are derived by fitting a lognormal cumulative distribution function (CDF) to damage probabilities estimated

empirically from post-event reconnaissance for the levees along Kushiro and Tokachi Rivers for the two subduction earthquakes considered. The fragility functions for occurrence of any damage,  $P(DL>0)$  are developed for levees with and without peat in the foundations. Levees on peat foundations are significantly more fragile than levees on inorganic soils within the same system.

As part of the process of improving estimates of ground motion intensity at the levees, particularly within the downstream region with soft soils, a region-specific site amplification function is derived. The model is based on non-ergodic site responses at recording stations developed from analysis of recordings on levees within the basin. The empirical analyses are supplemented with results of 1D ground response analysis (GRA) using *DEEPSOIL v7.0*. The empirical linear amplification is high, and may indicate basin effects that are not captured by the 1D analysis. Nonlinearity is stronger in the amplification function derived from the 1D GRA, especially at short periods.

## **8.2 RECOMMENDATIONS FOR FUTURE RESEARCH**

This dissertation research included substantial effort to collect a comprehensive dataset of levee performance during strong shaking and related site characterization to develop empirical fragility functions. Future research recommendations are divided into forward application of the fragility functions, and areas that can be further explored by leveraging the available data.

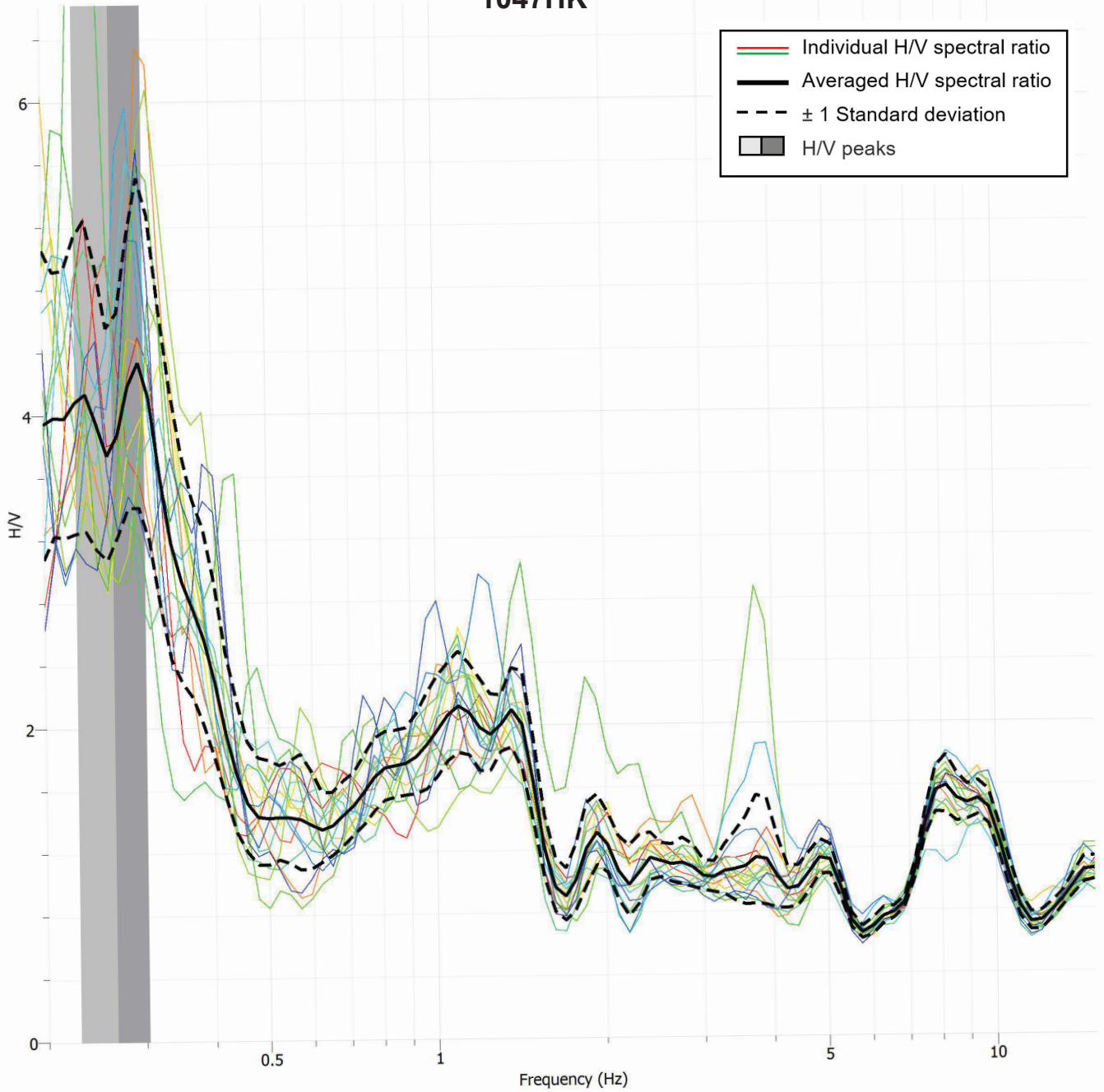
- 1) Risk assessment for the Delta previously used fragility functions based on simulations and expert opinions. While there are differences in the site conditions between the Hokkaido and Delta levees, most notably in the thickness of the peat and the impoundment of water by the latter, an initial reassessment of the seismic hazard using the updated fragility function would be an interesting comparison.

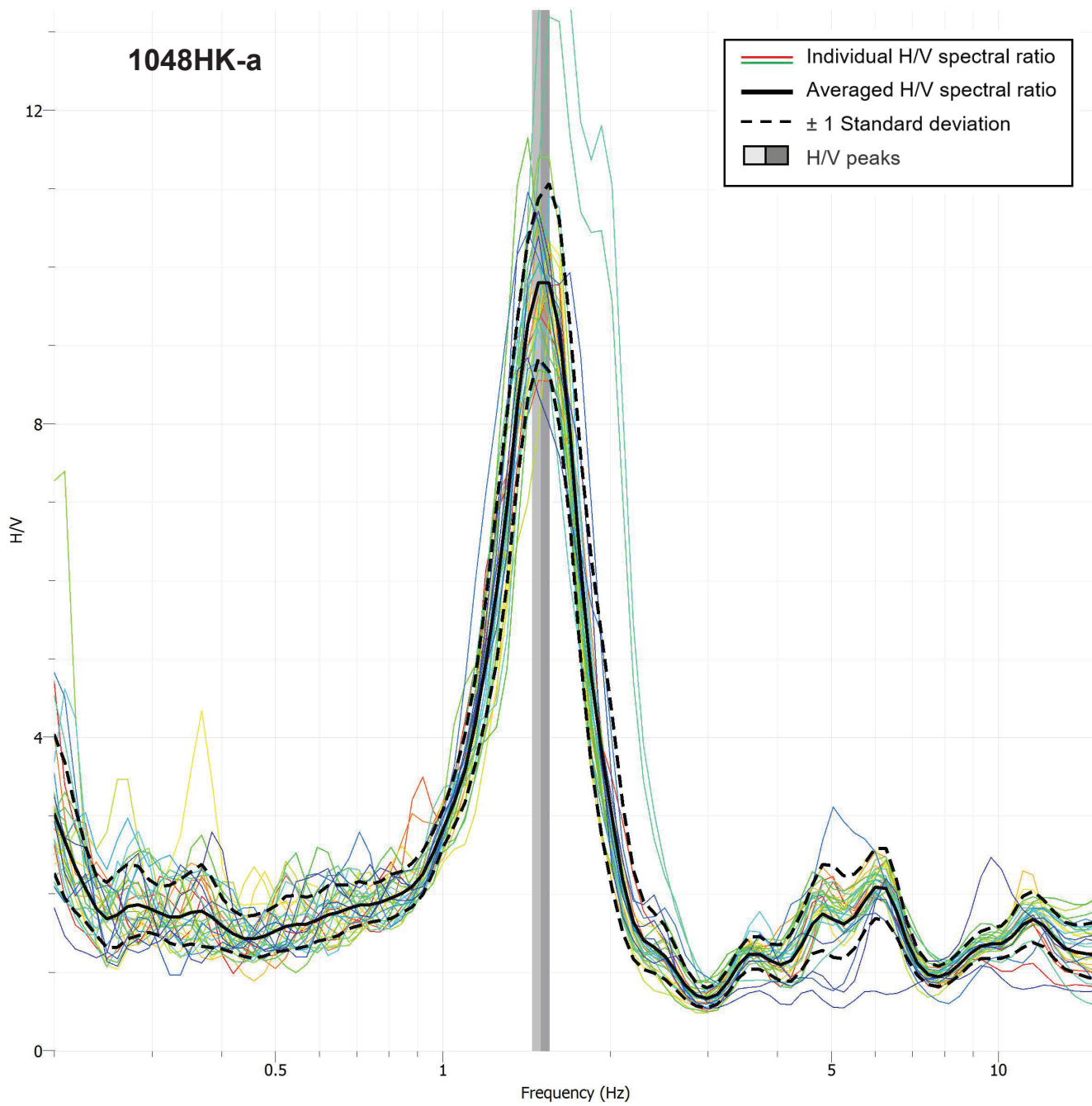
- 2) Probability of failure for the levee as a connected system depends on the spatial correlation of both capacity and demand. Spatial correlation of demand may be estimated using autocorrelation from the segment performance, and compared between the two levee systems and earthquakes.
- 3) The 1D ground response analysis suggests higher nonlinearity than is evident from the empirical data, especially at shorter spectral periods. The differences are not satisfactorily explained with the limited analysis conducted. Additional soil profiles can be developed from the shear wave velocity profiles from the geophysical investigation for both systems, and recordings from the Obihiro stations, especially at higher shaking intensities, could be considered to constrain the empirical nonlinear term.
- 4) PGV has been shown to be a better predictor of levee performance by Kwak et al. (2016). Following the release of additional GMMs from the NGA-SUB project, PGV may replace PGA as the predictor for damage in fragility functions.

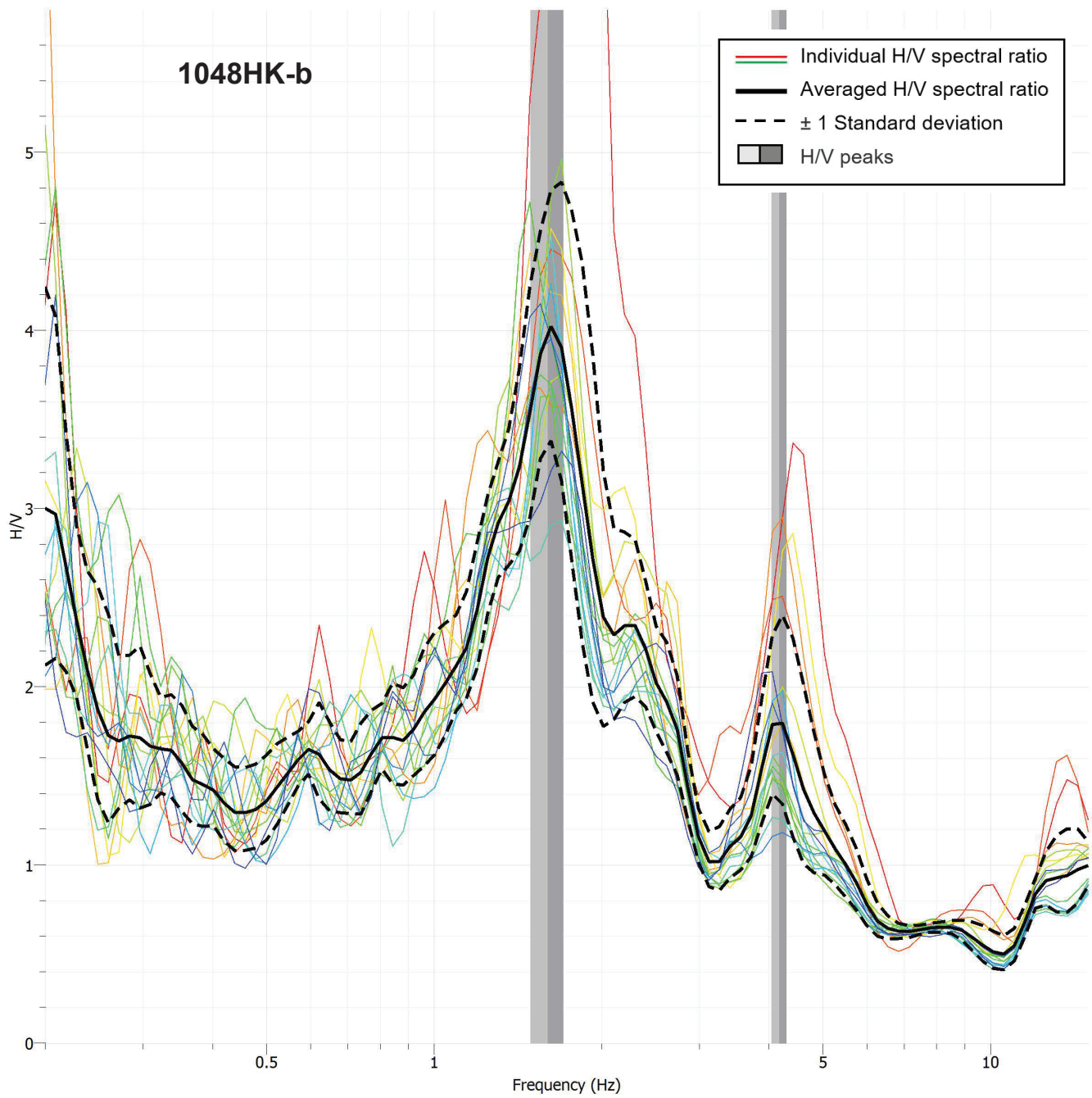
## **APPENDIX A: HVSR, SASW ARRAY SETUP AND DISPERSION CURVES**

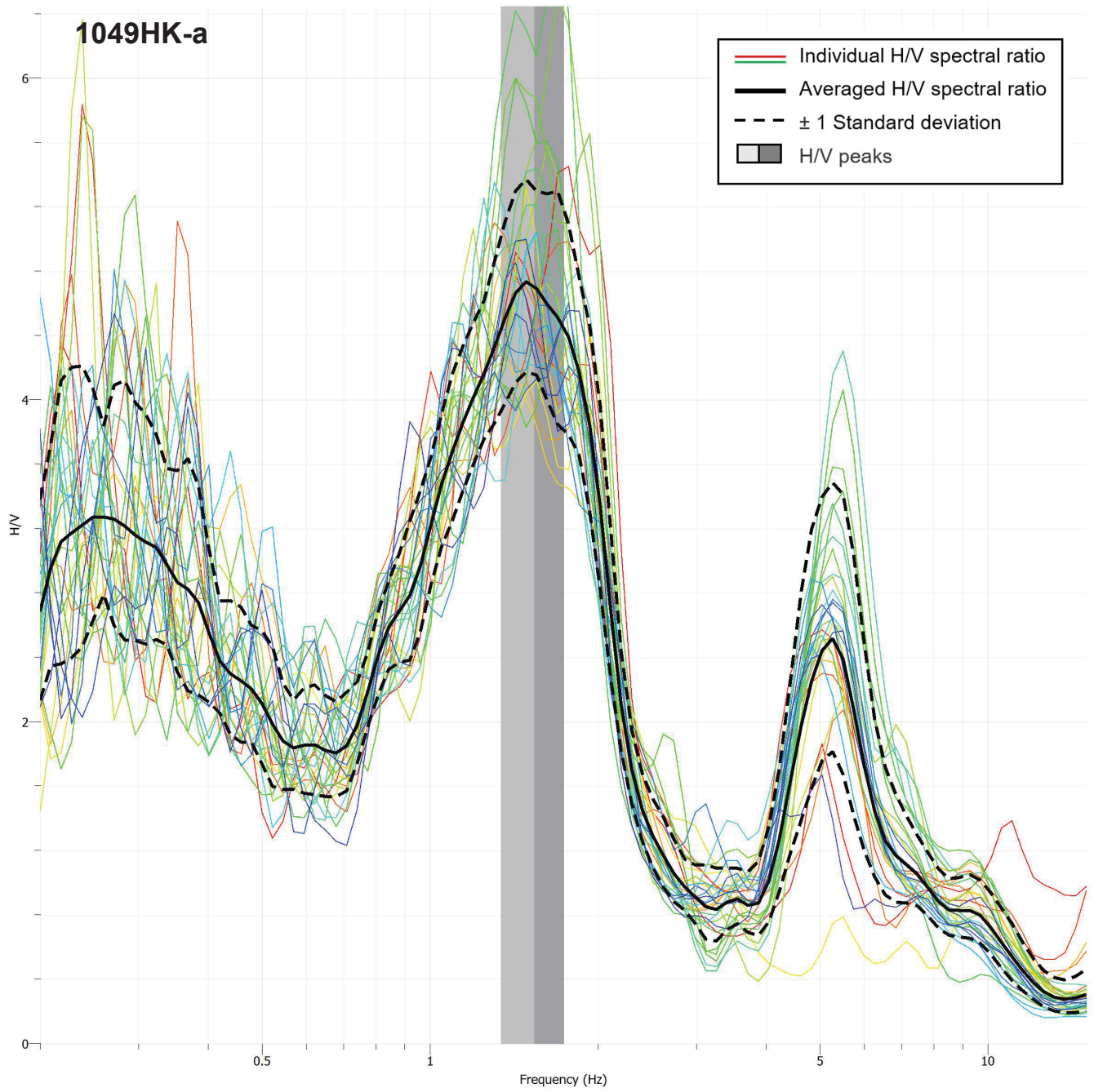


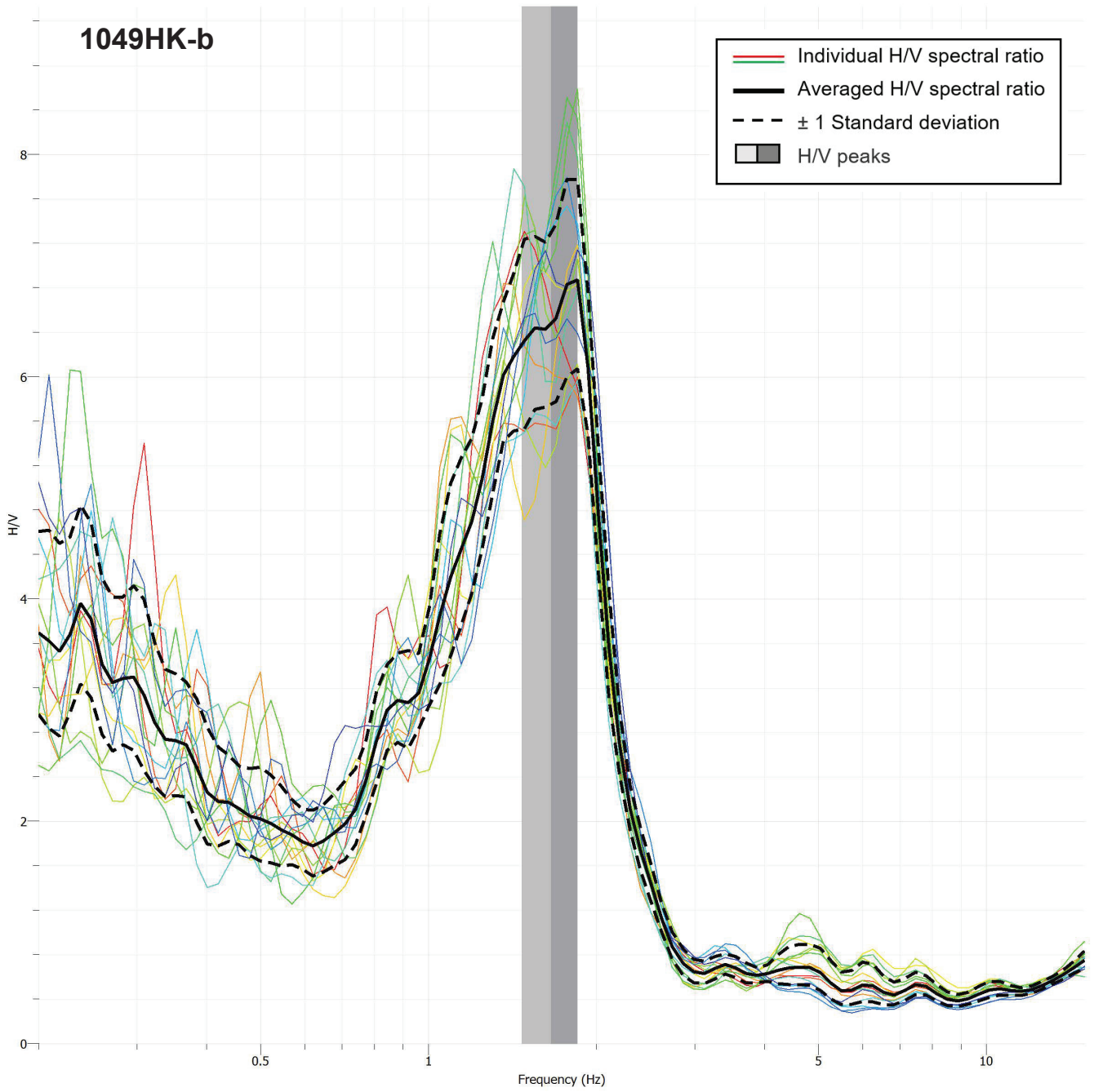
# 1047HK

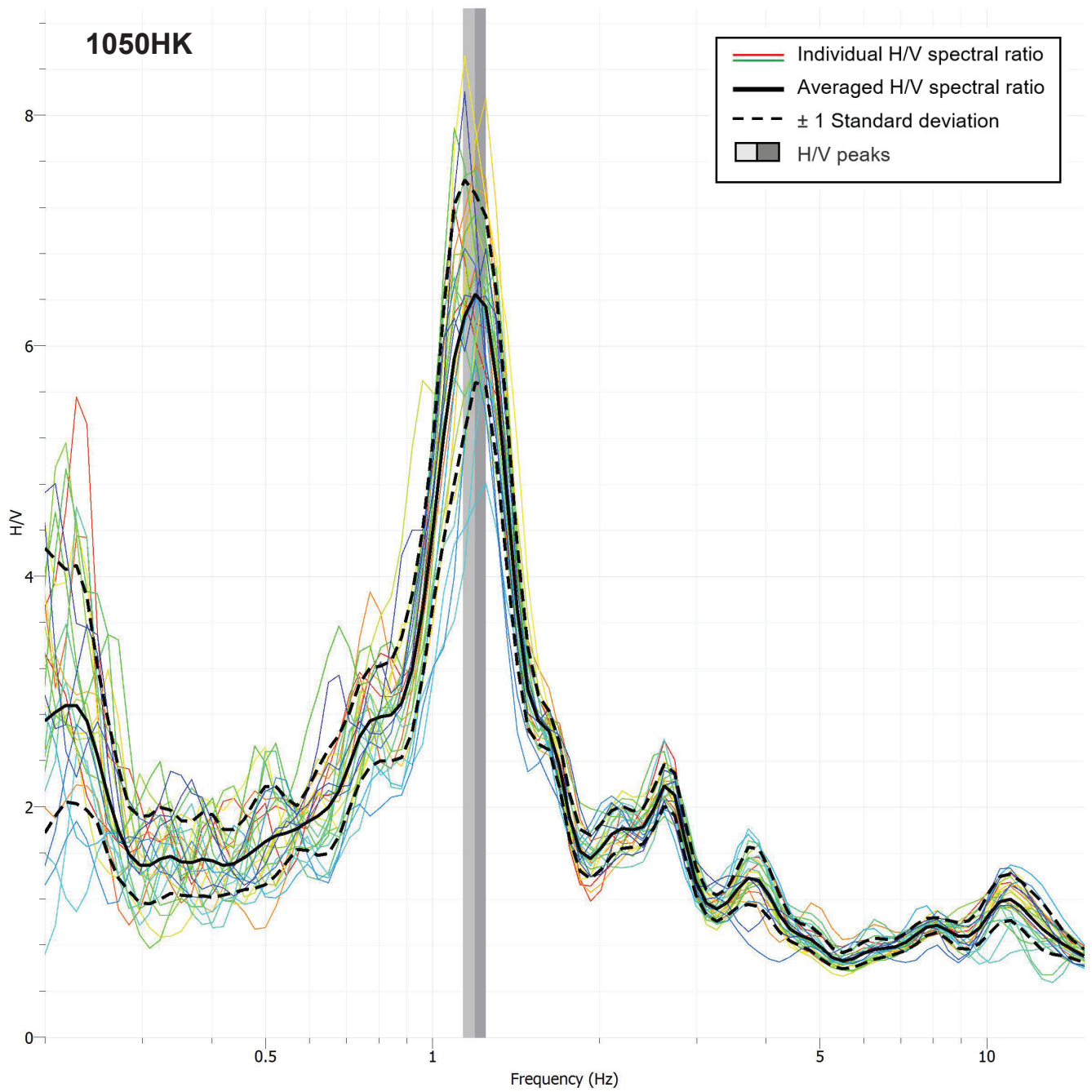


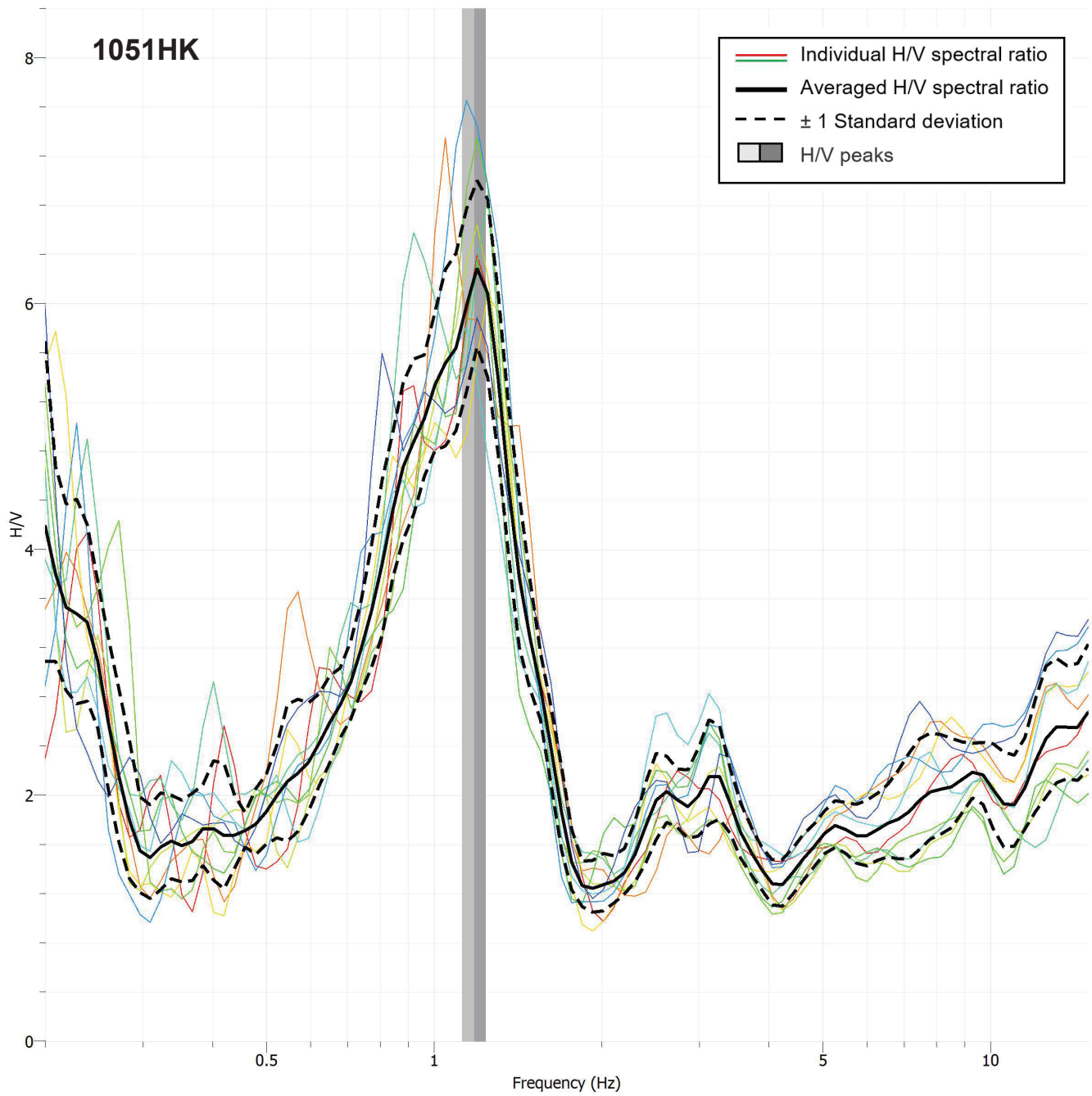


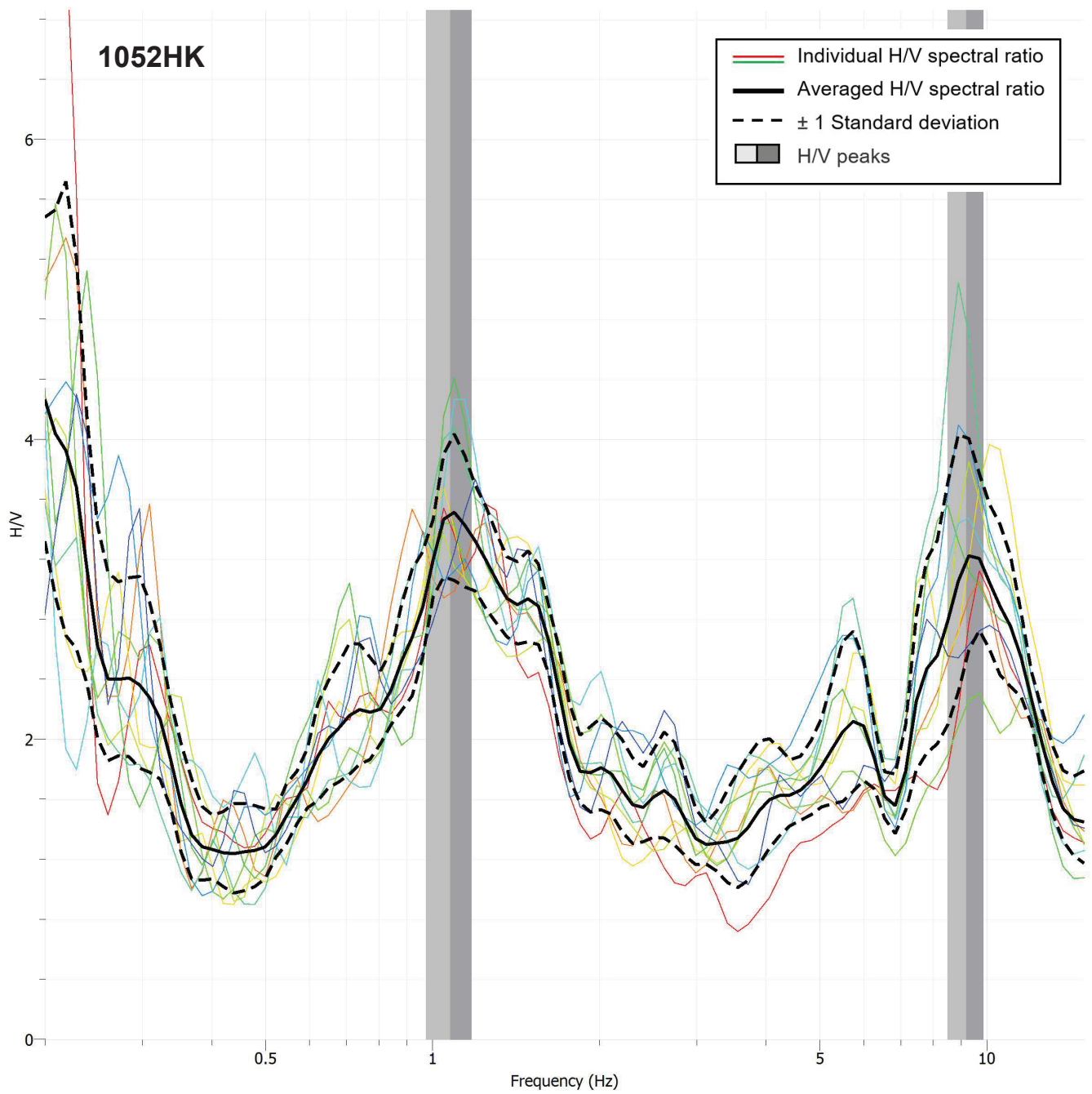




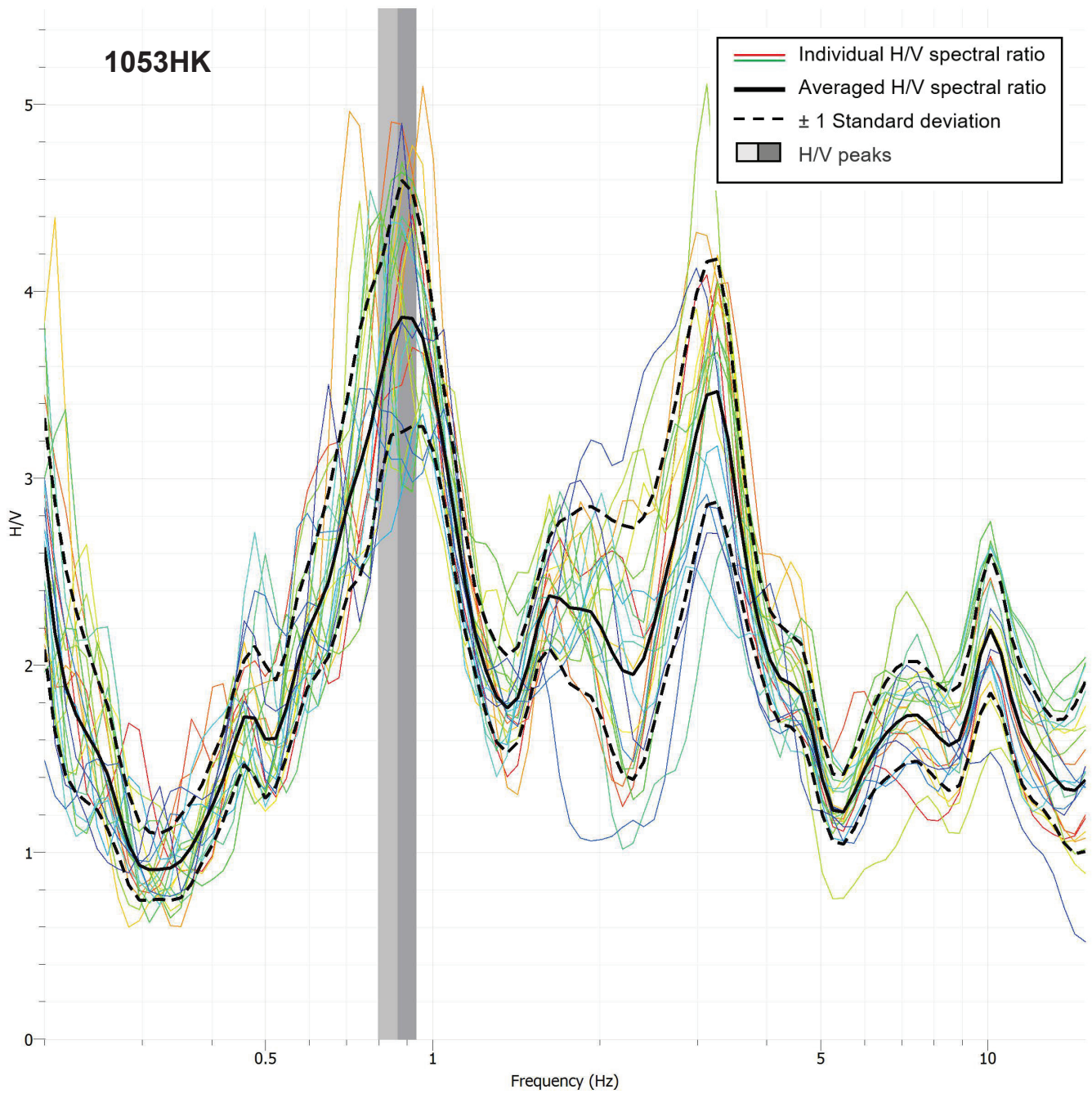


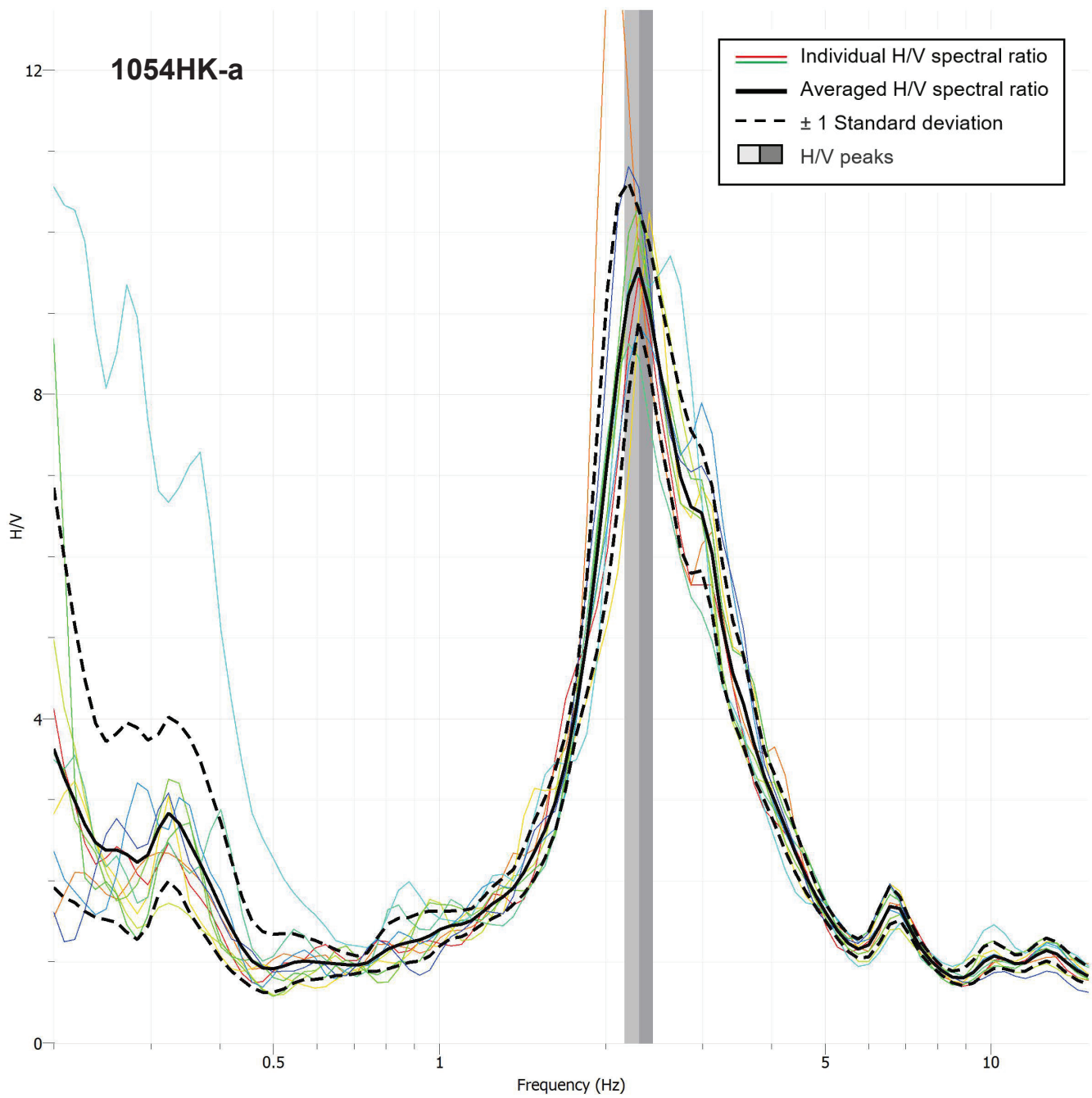




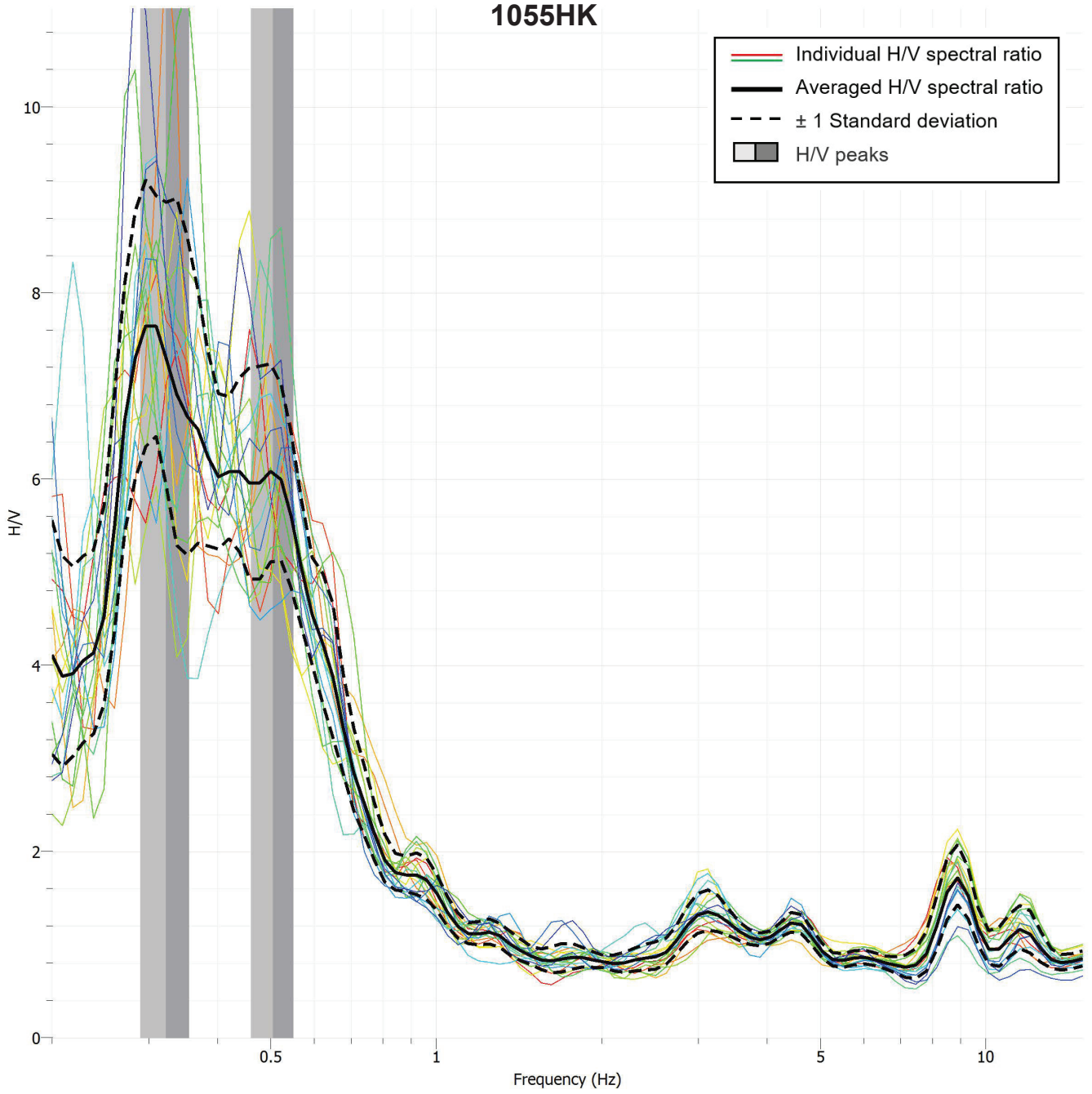




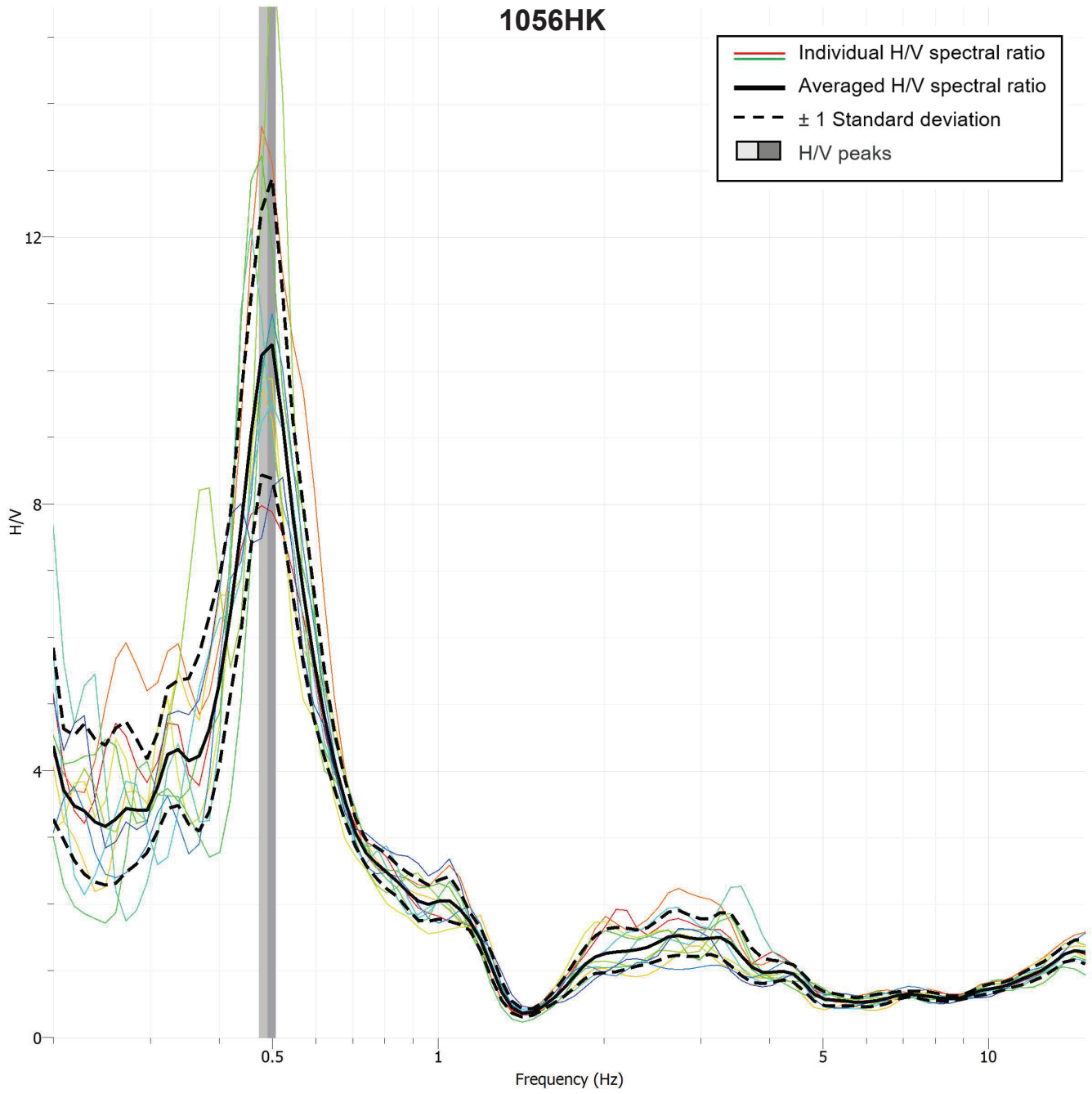


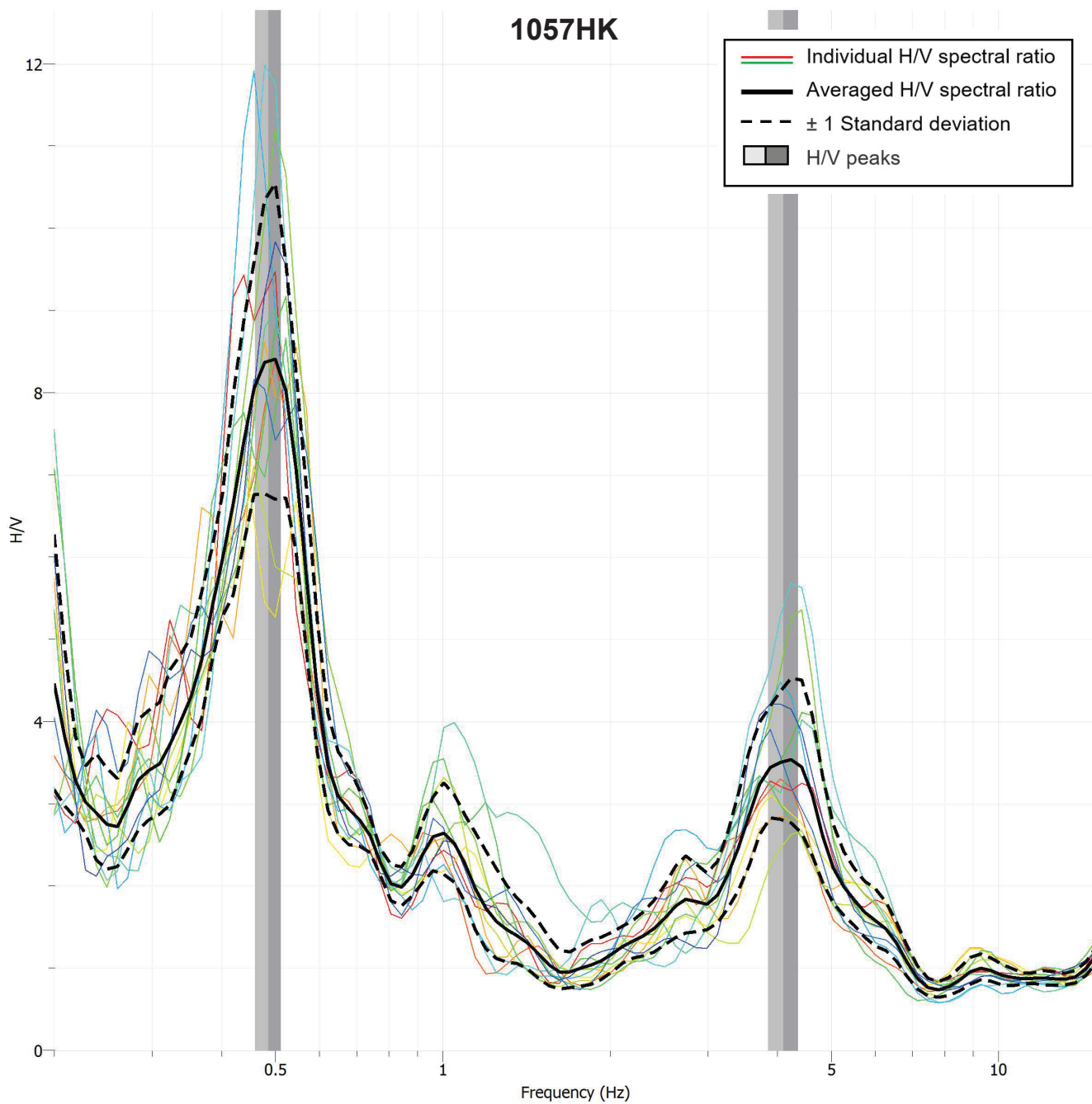


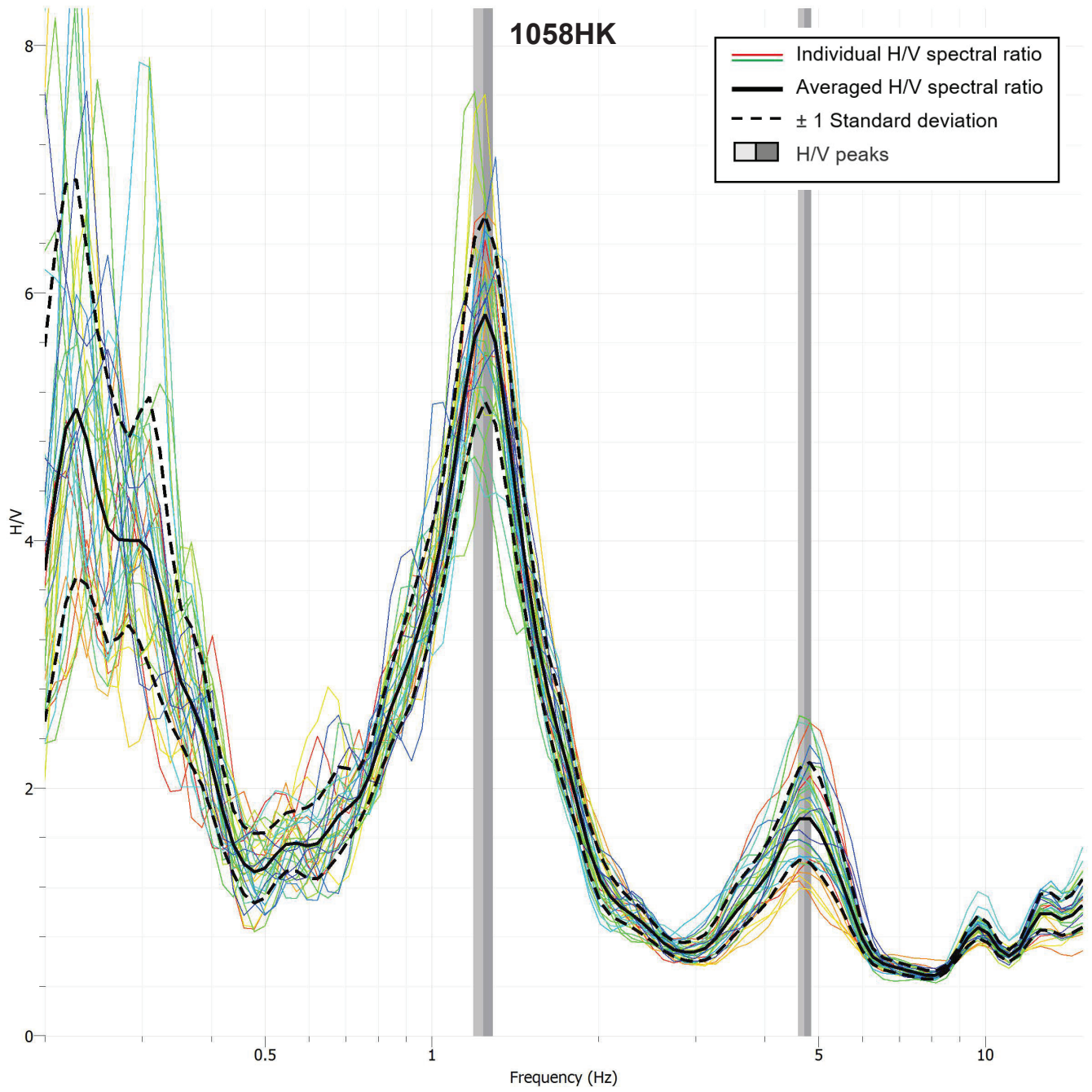
# 1055HK



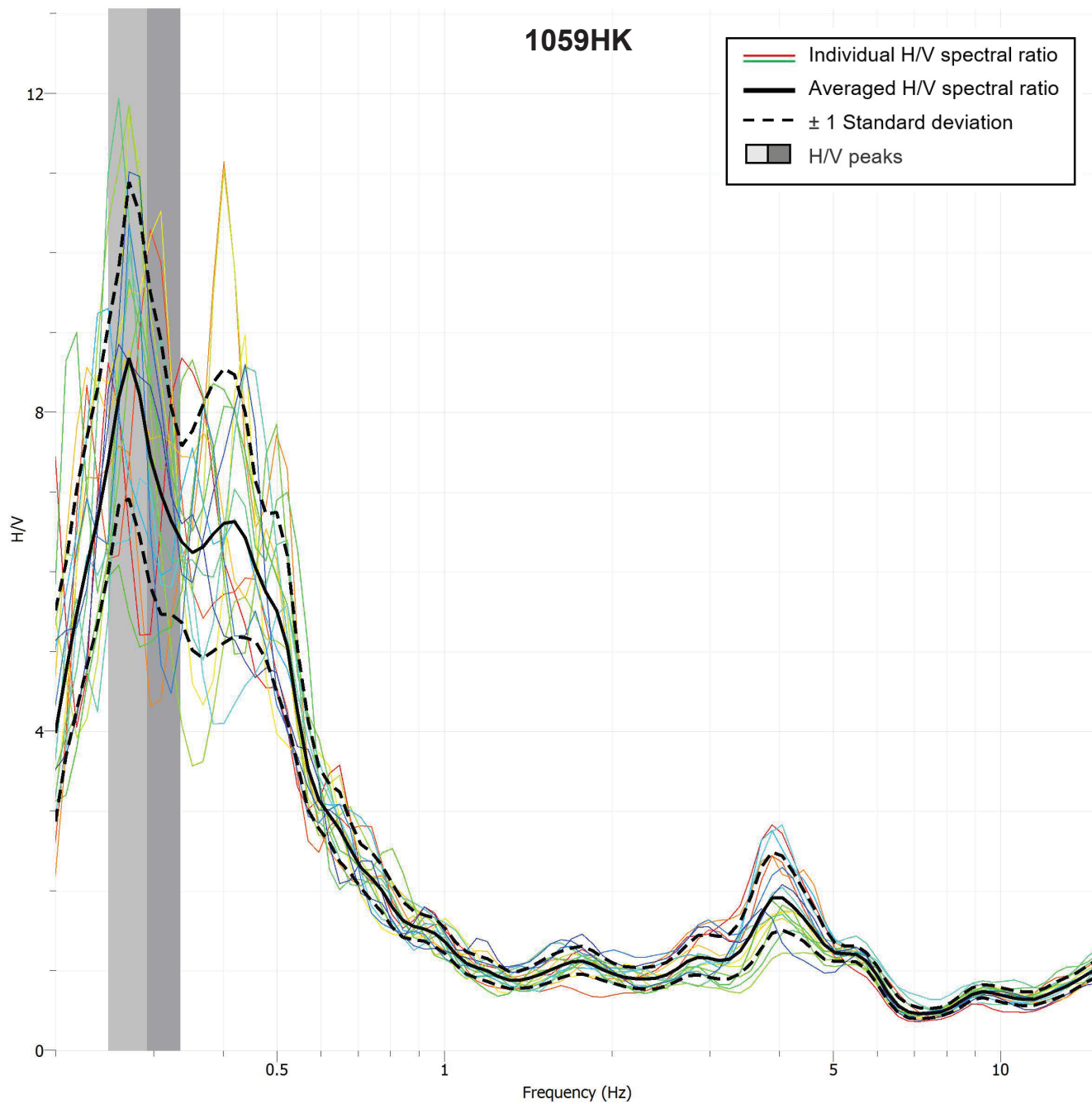
# 1056HK

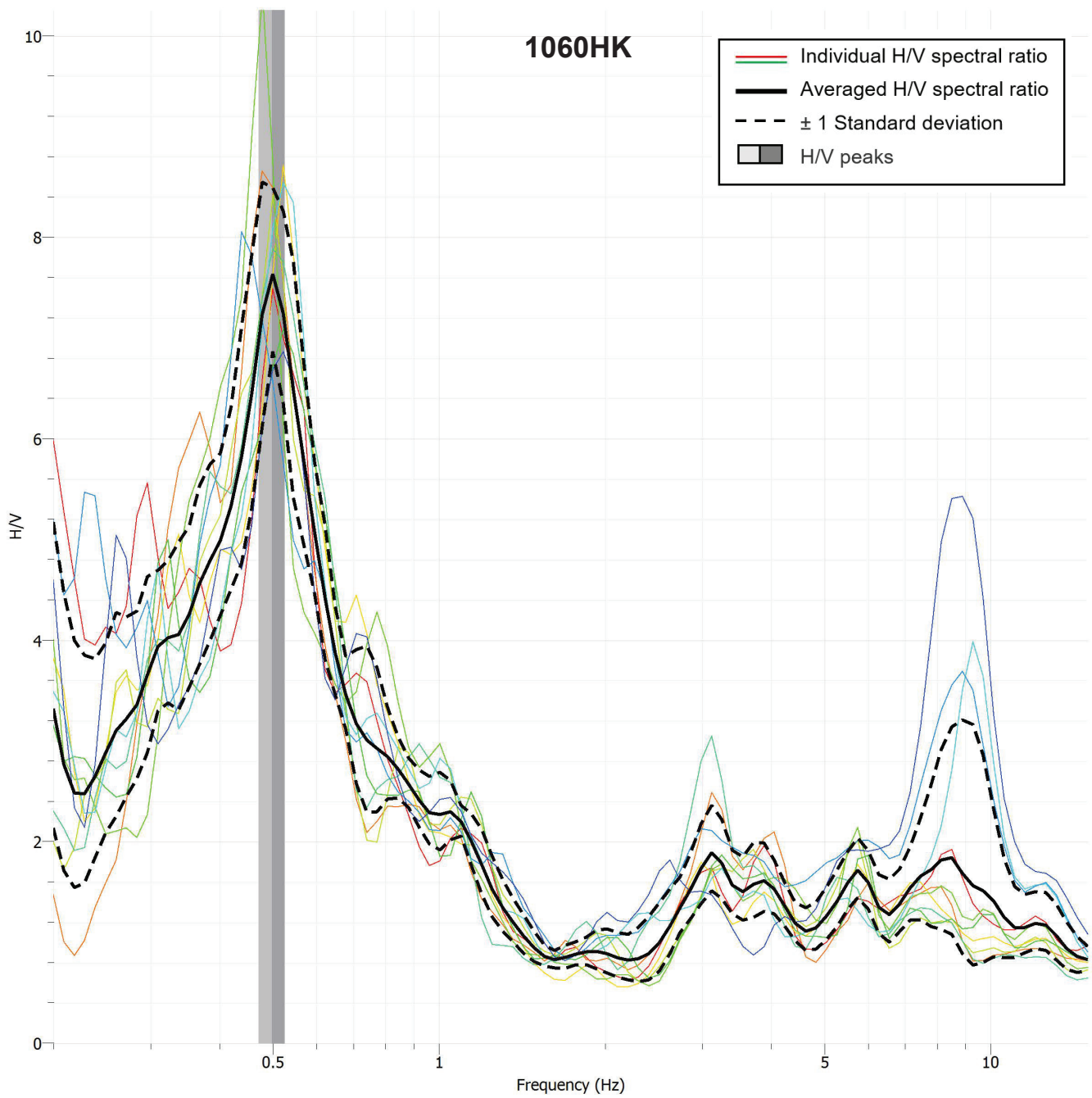




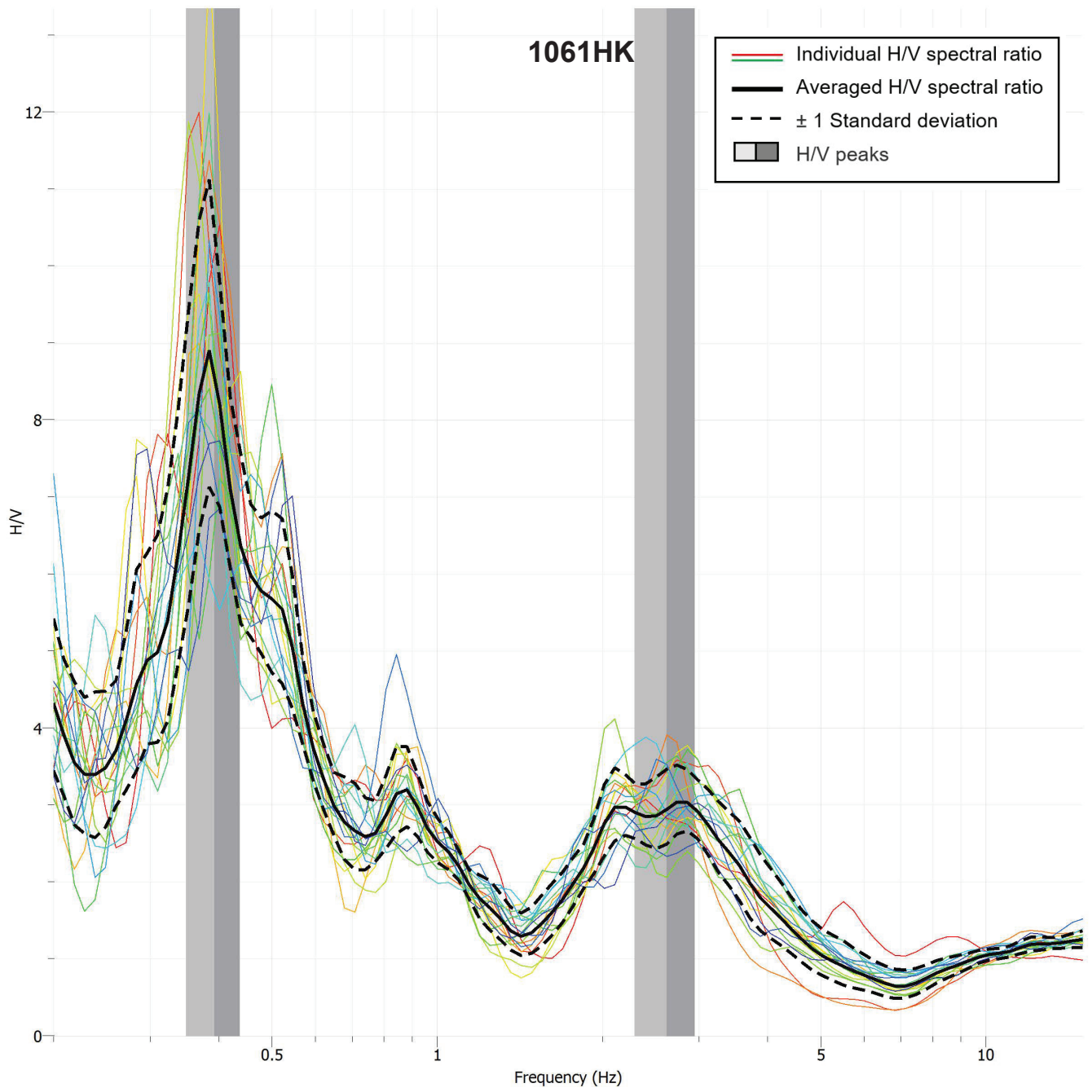


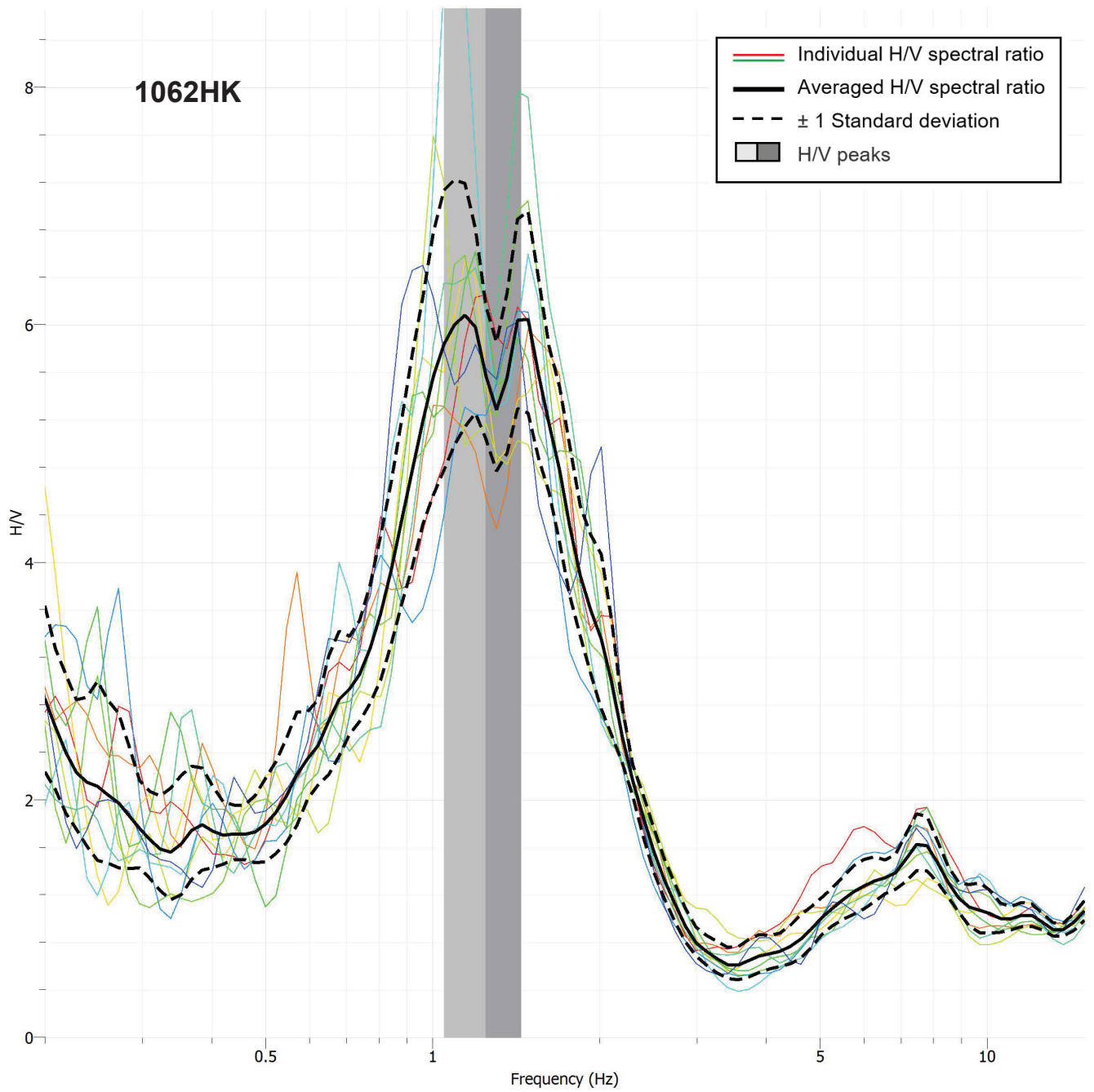
# 1059HK

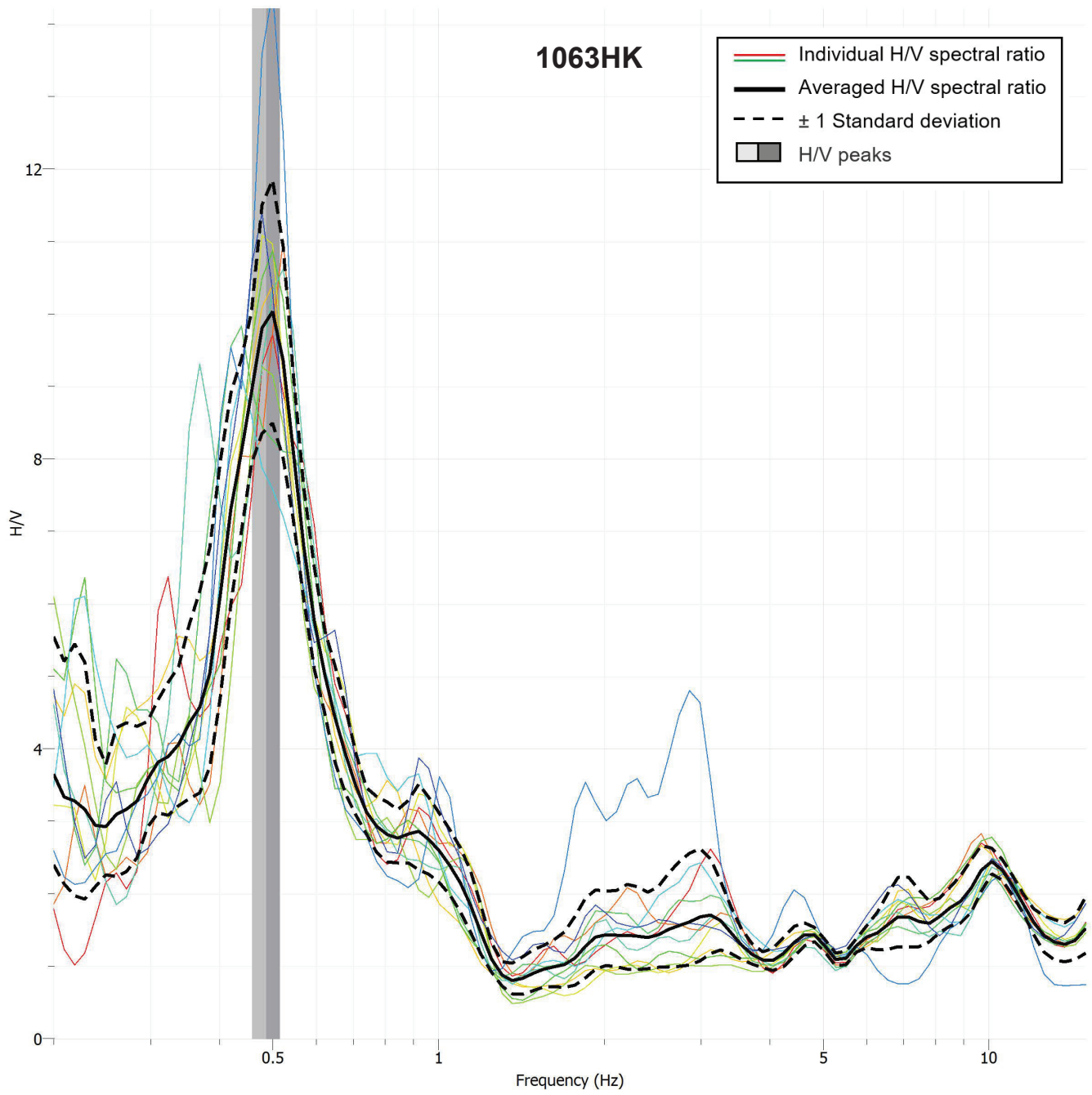


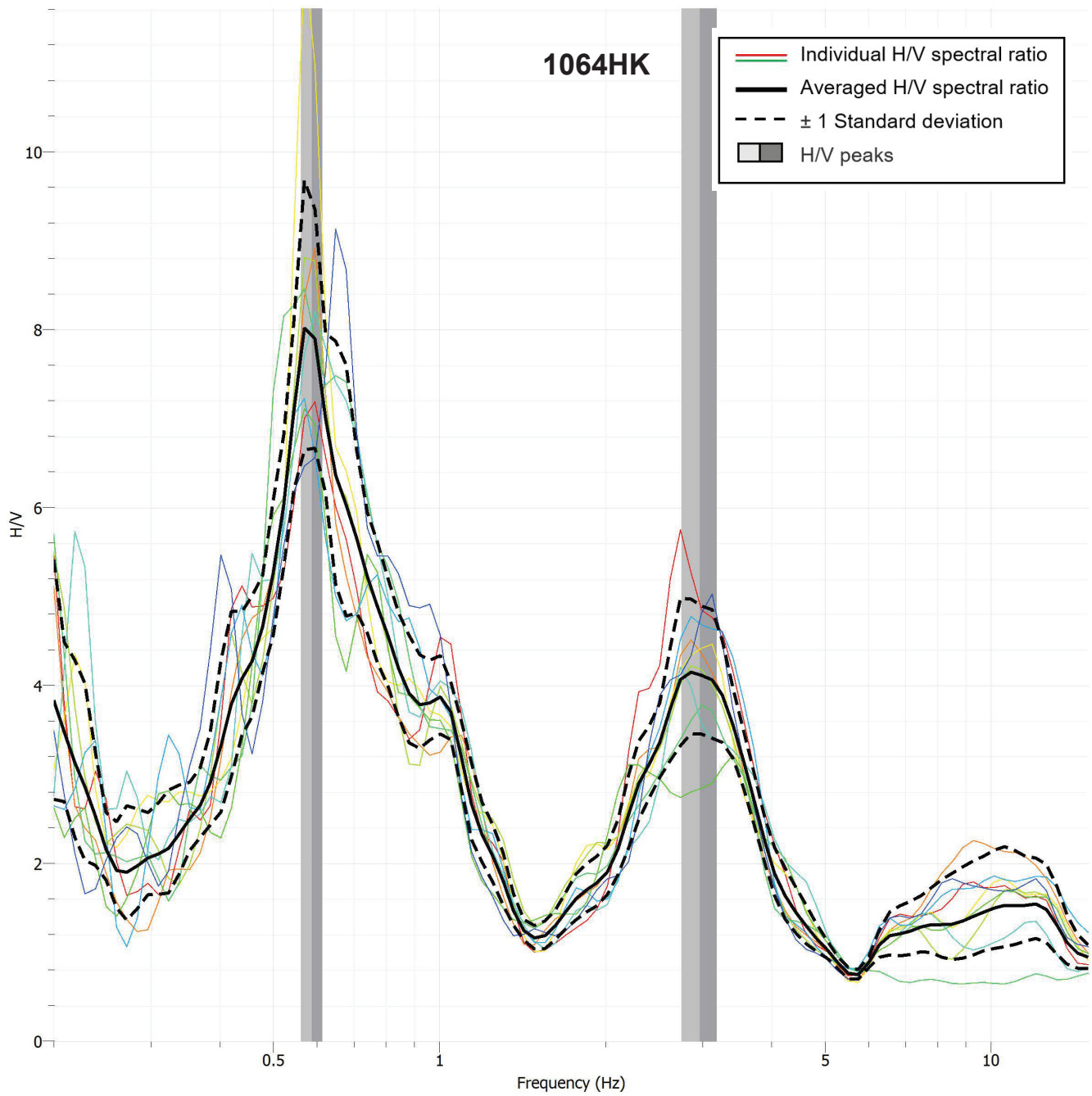


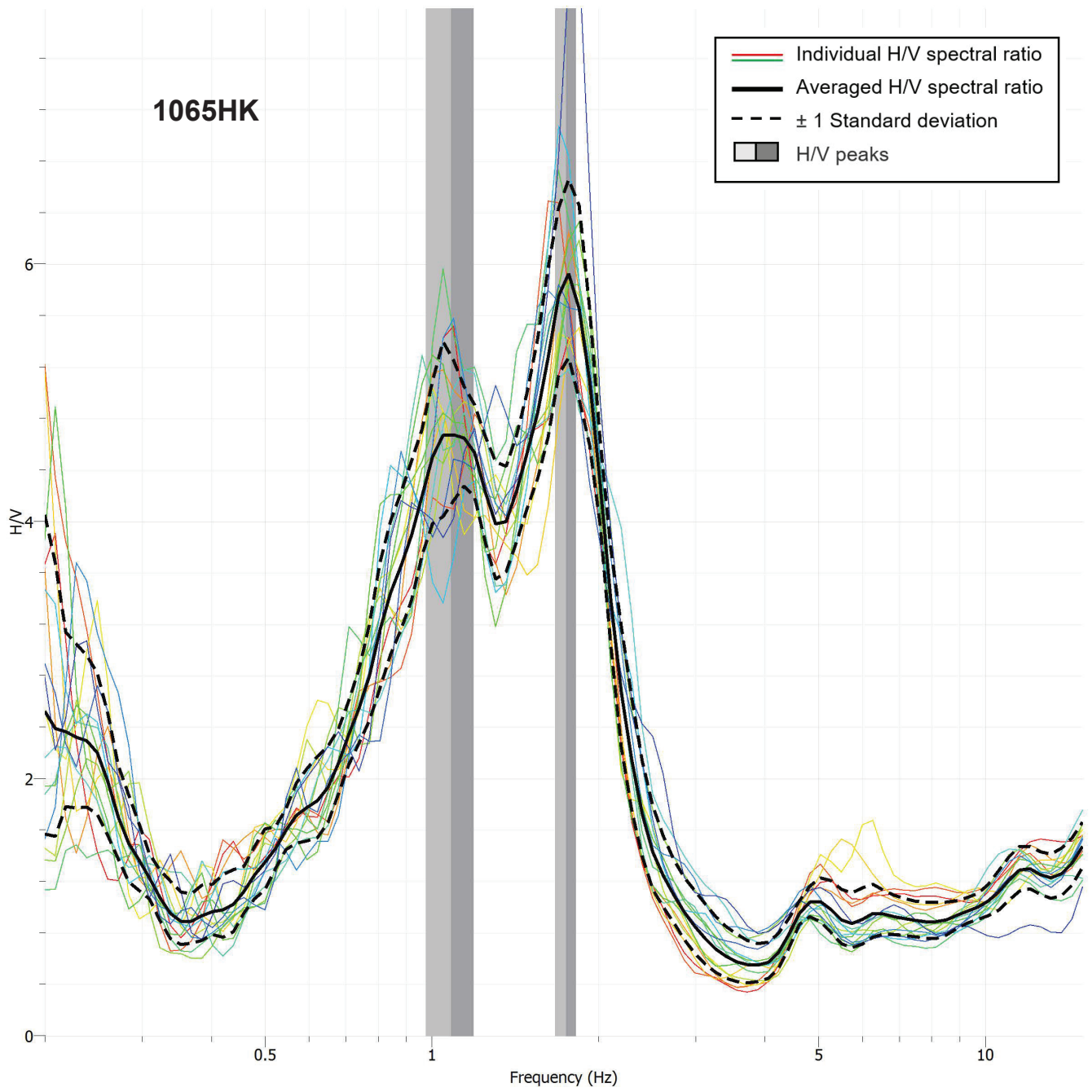


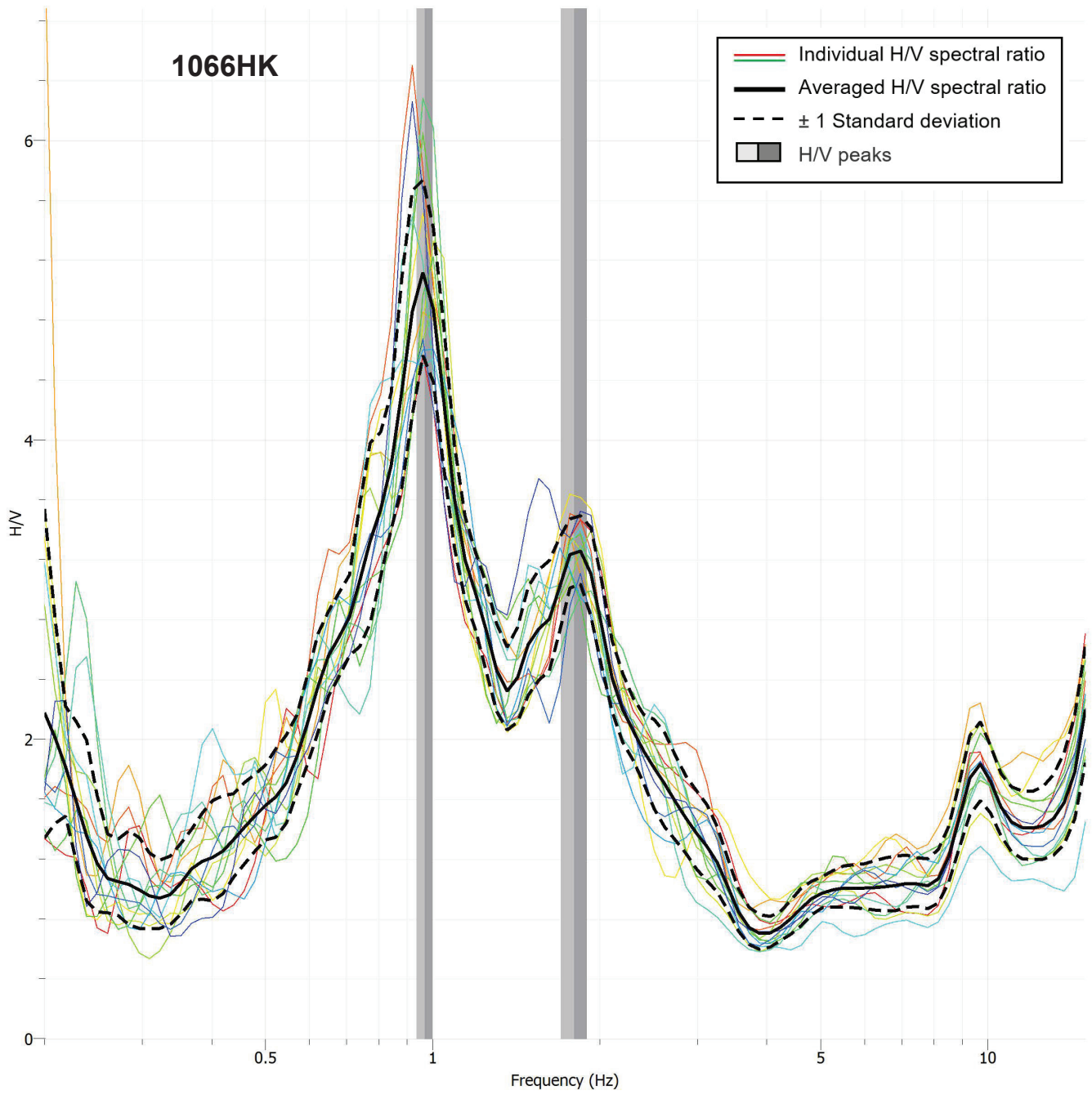


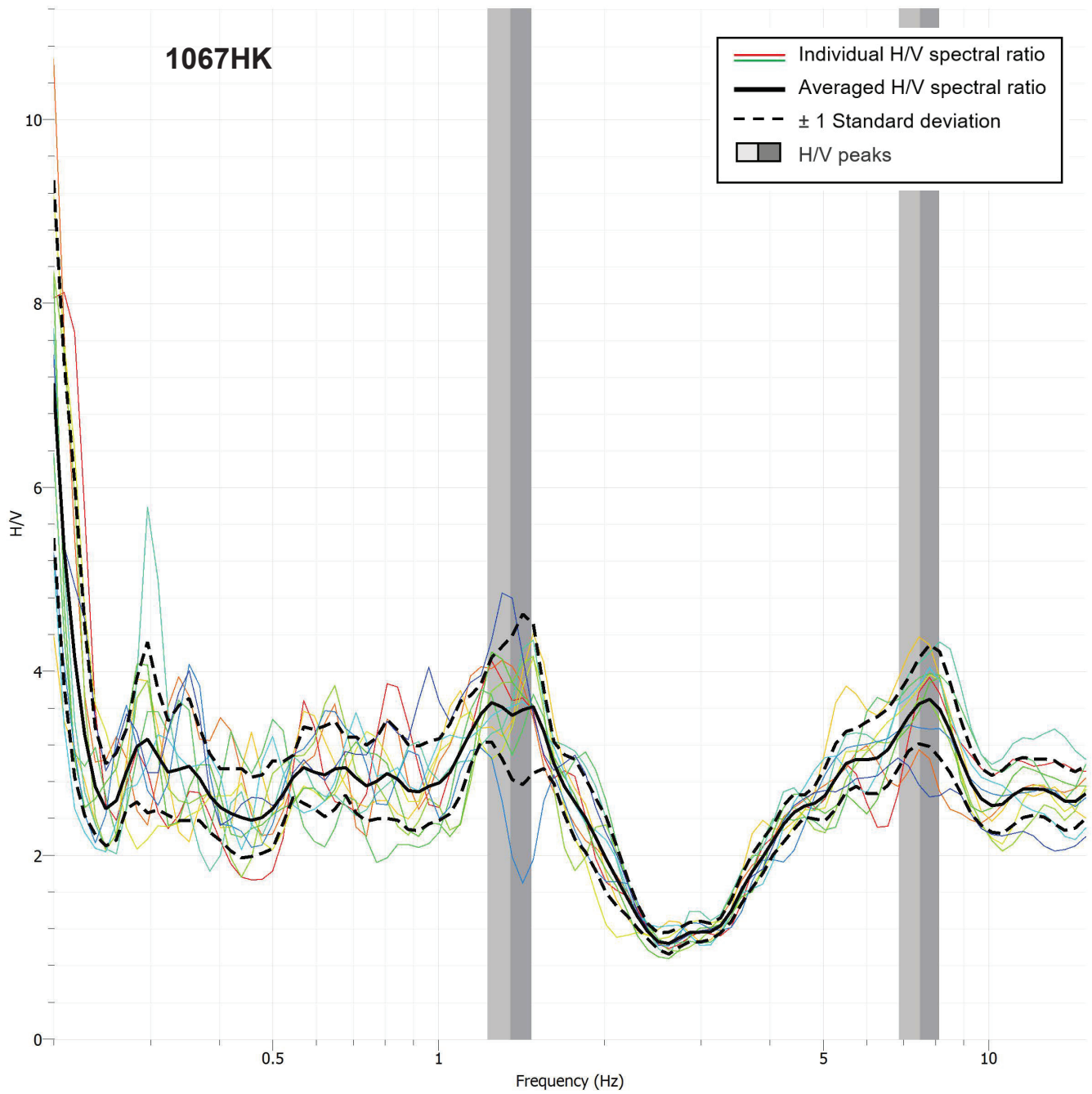


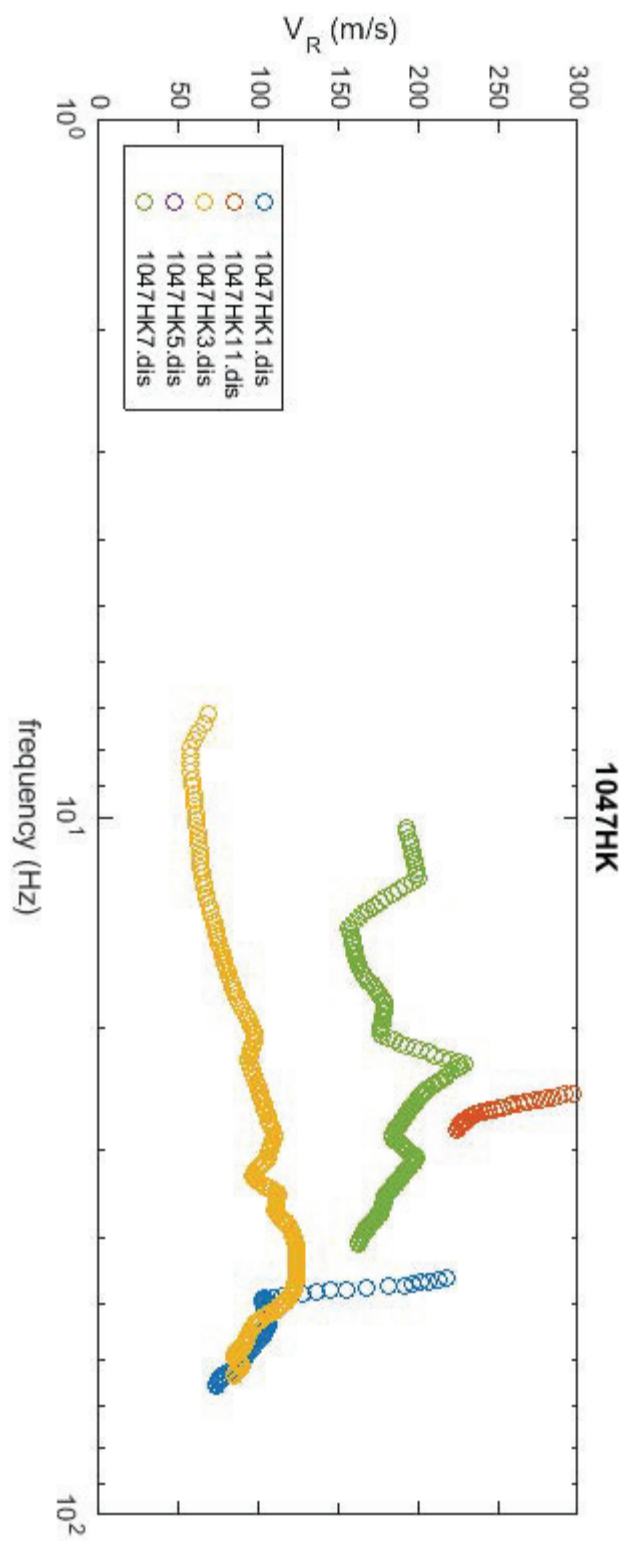
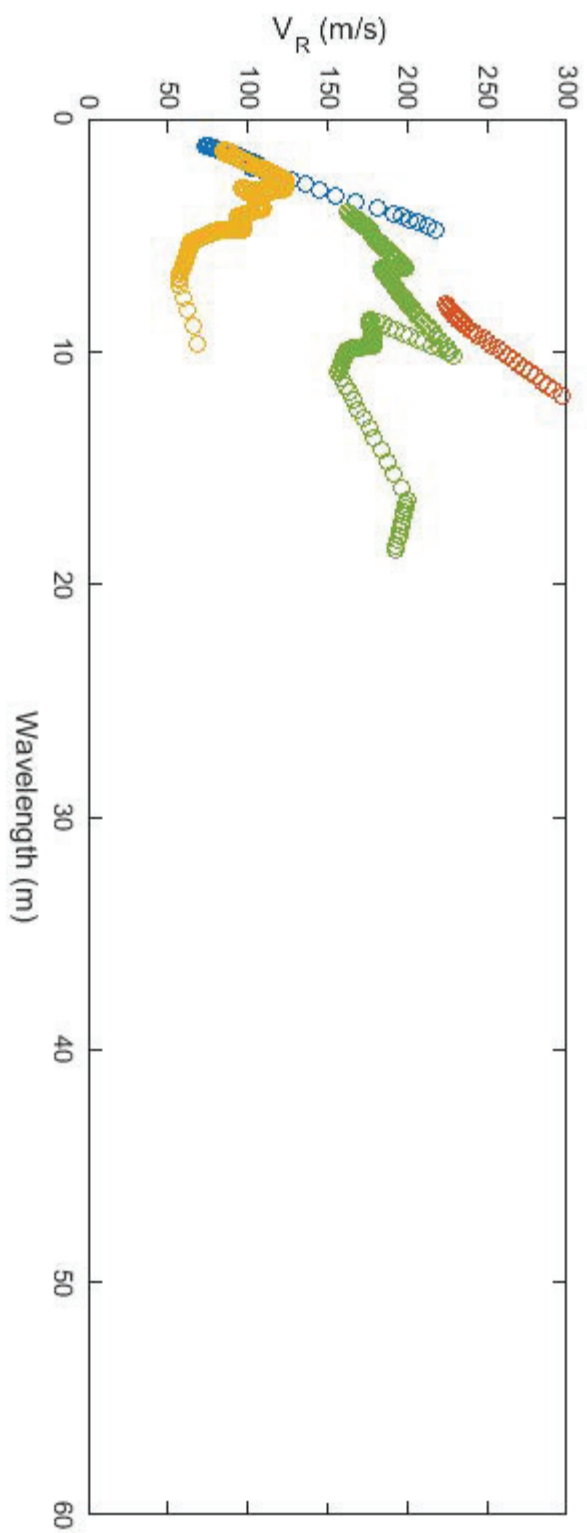




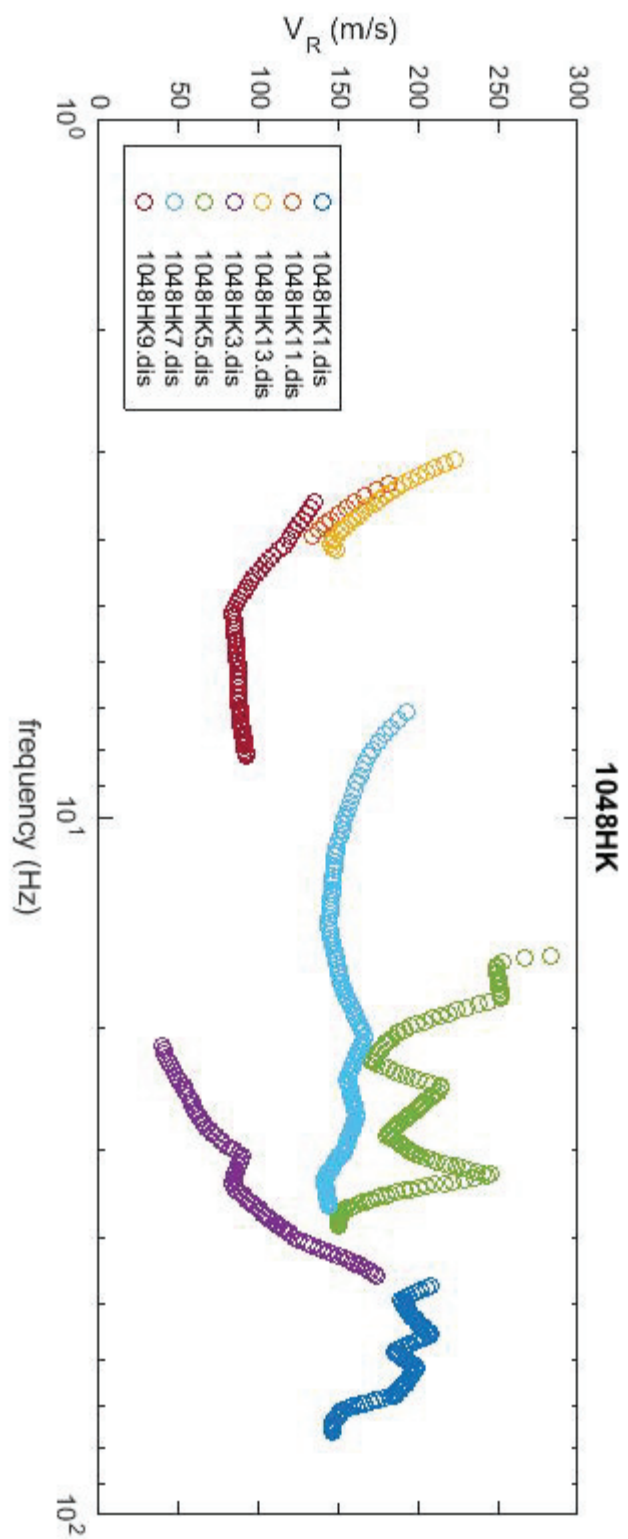
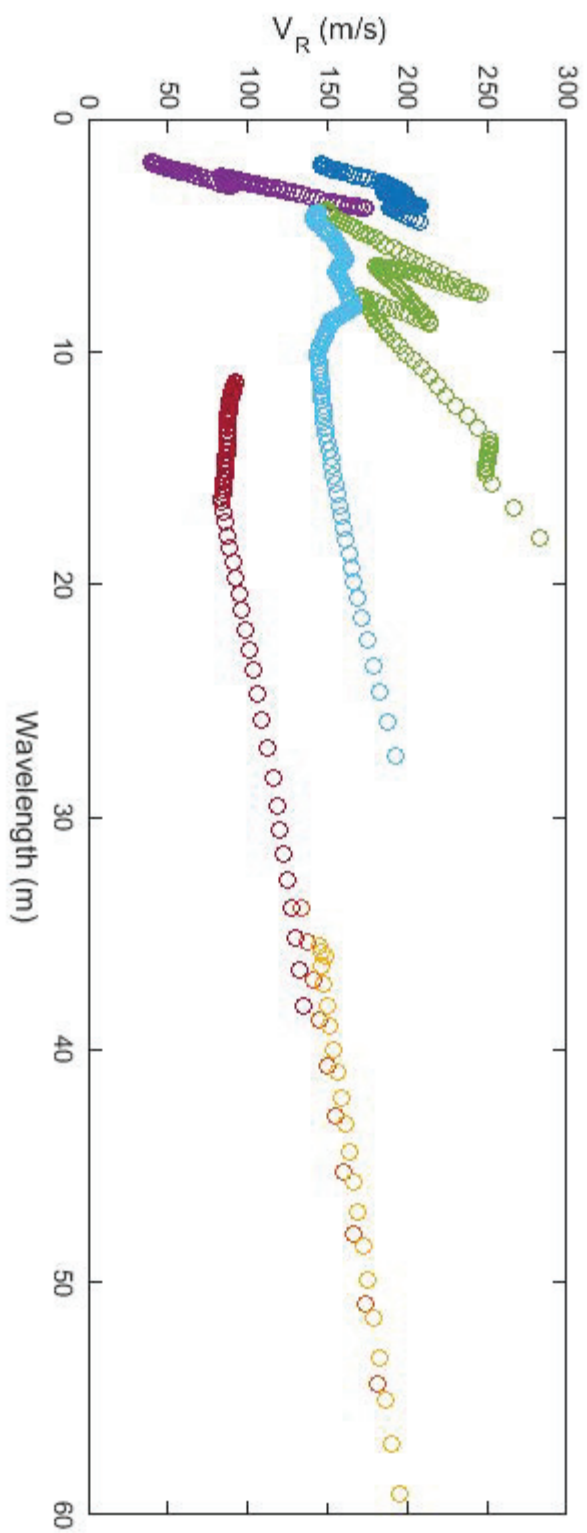


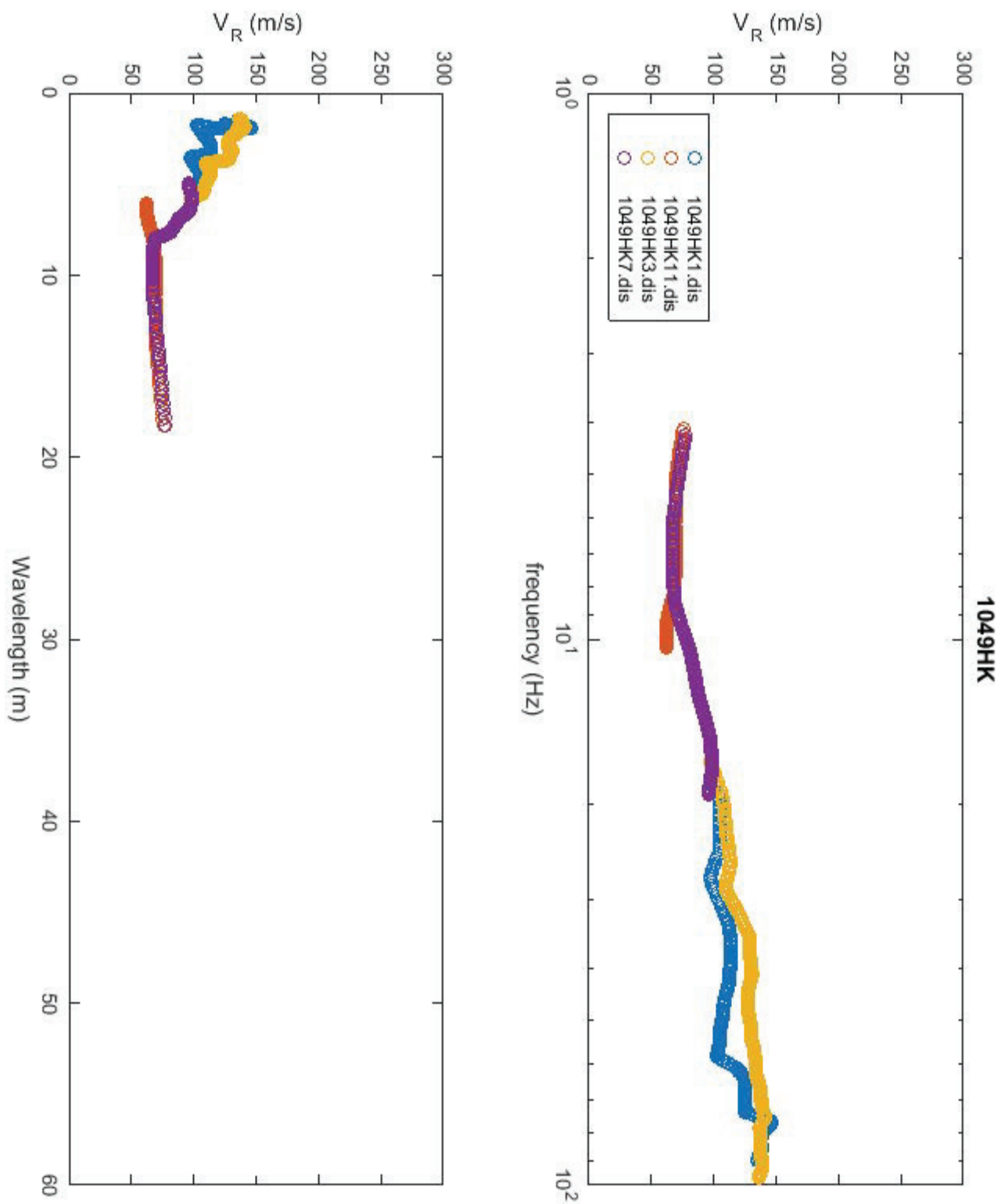


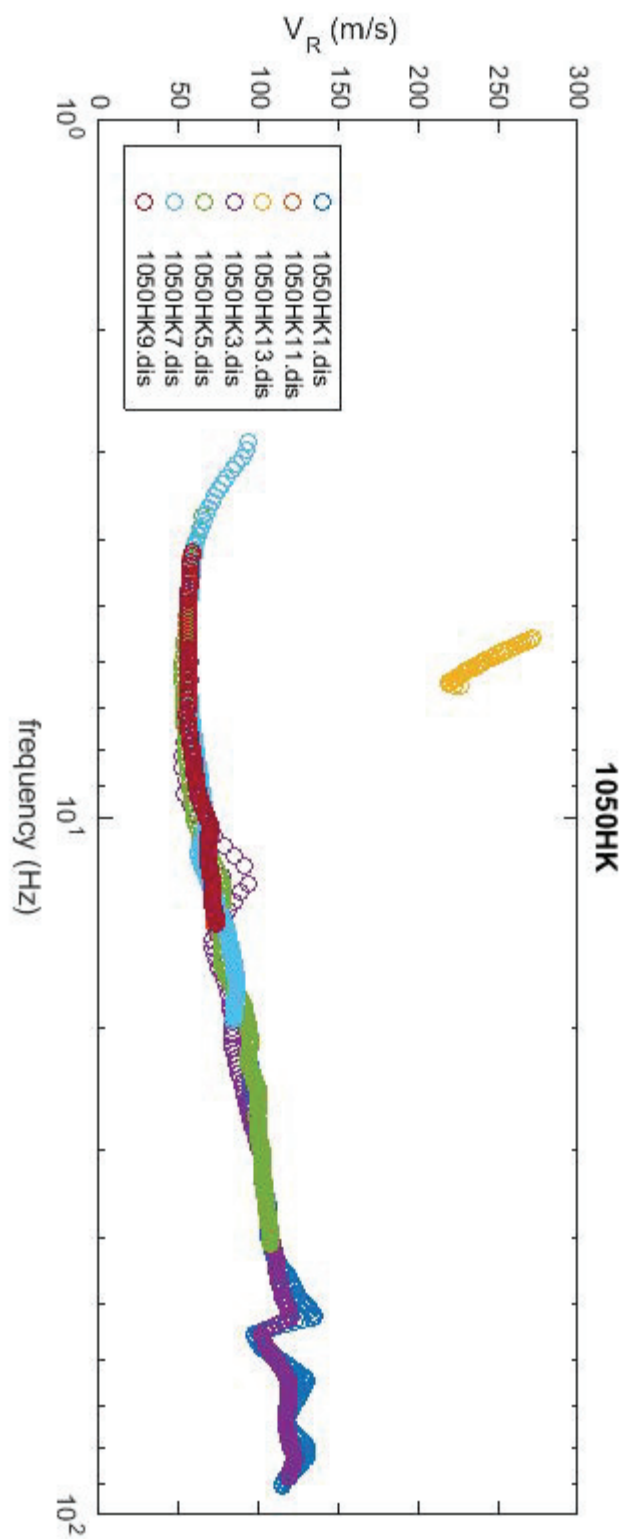
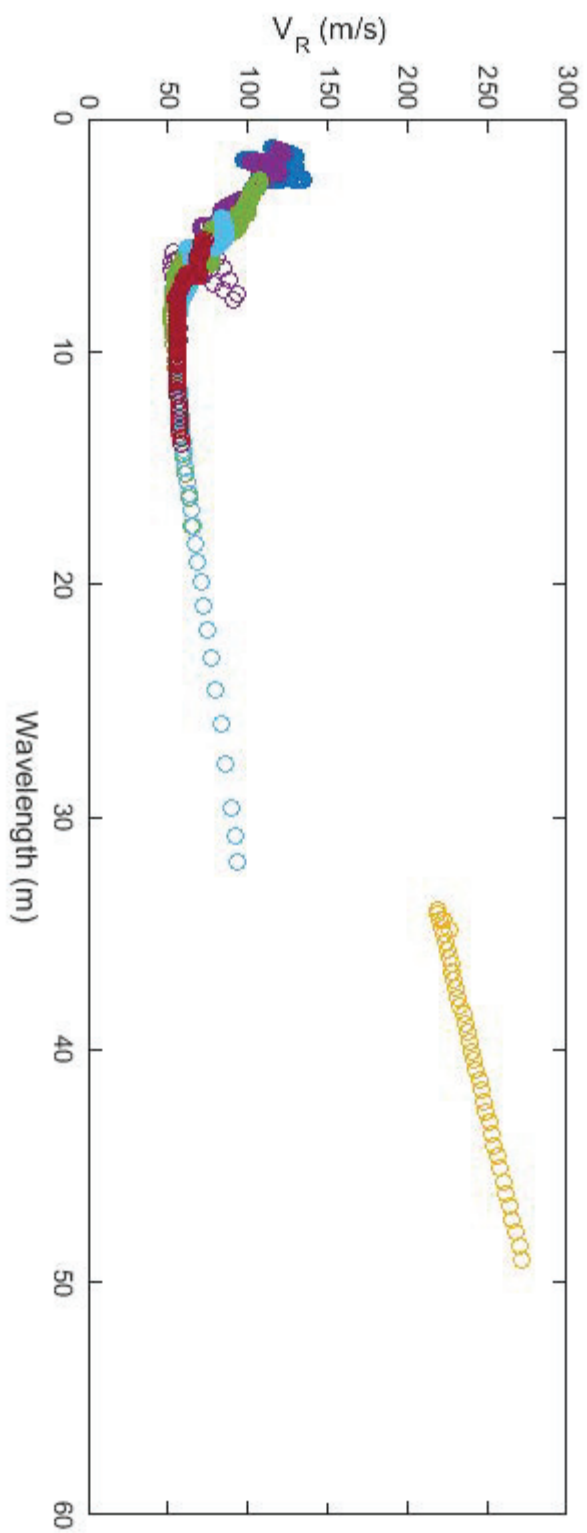


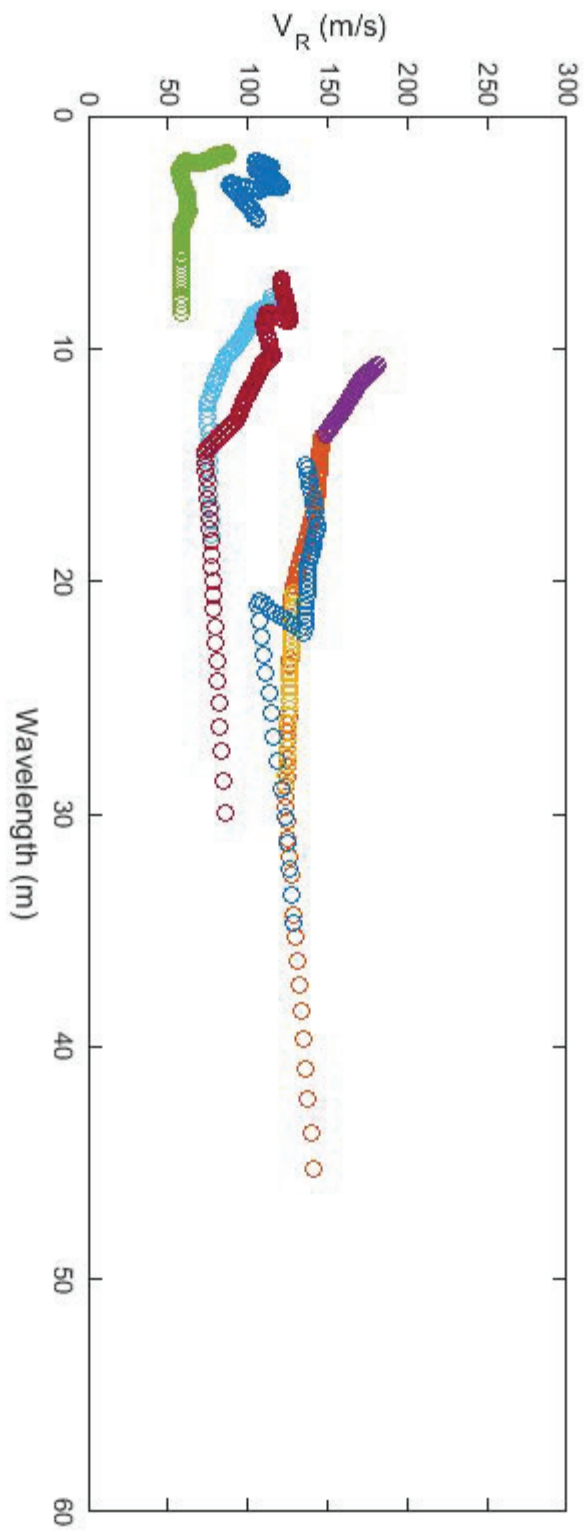
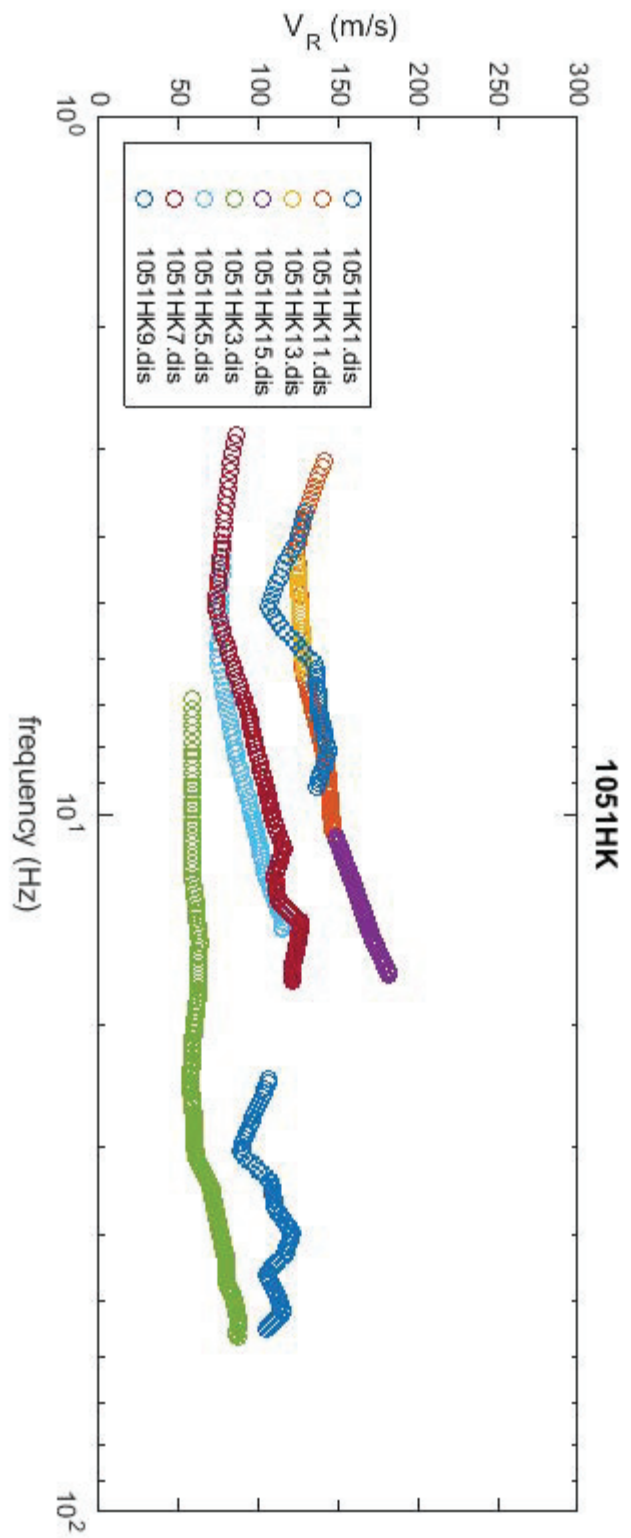


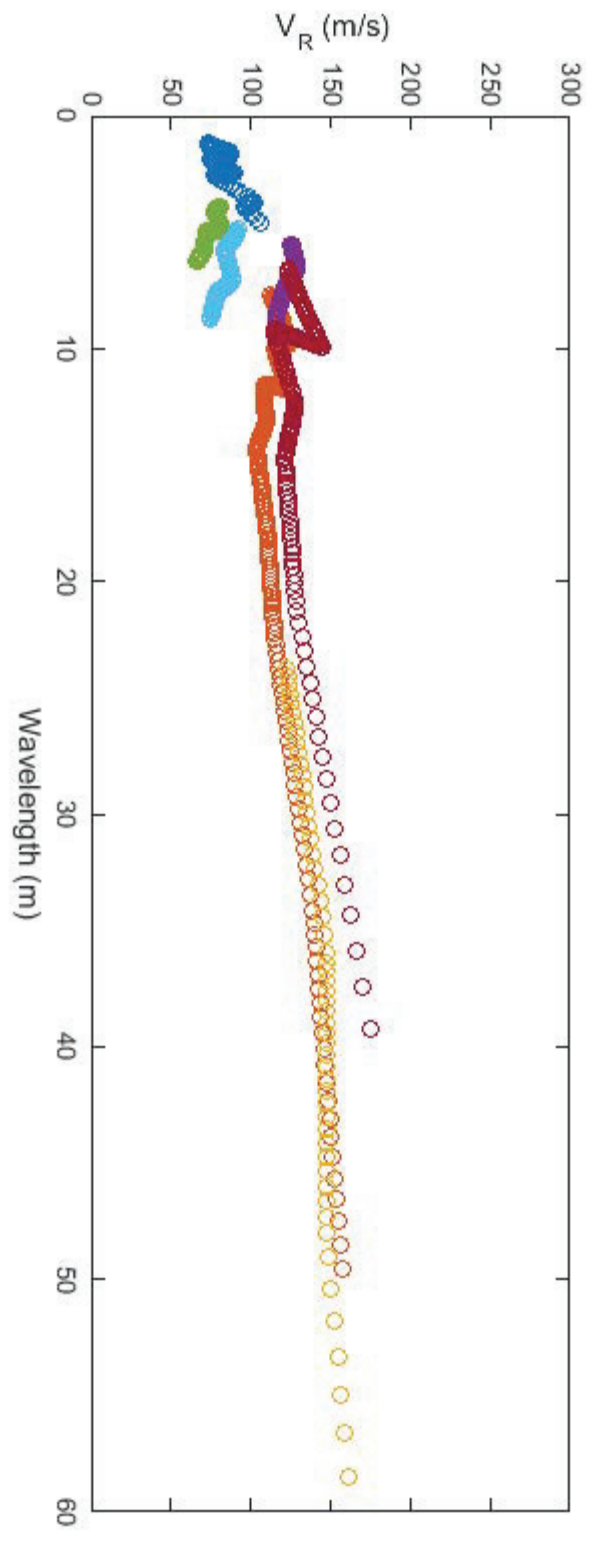
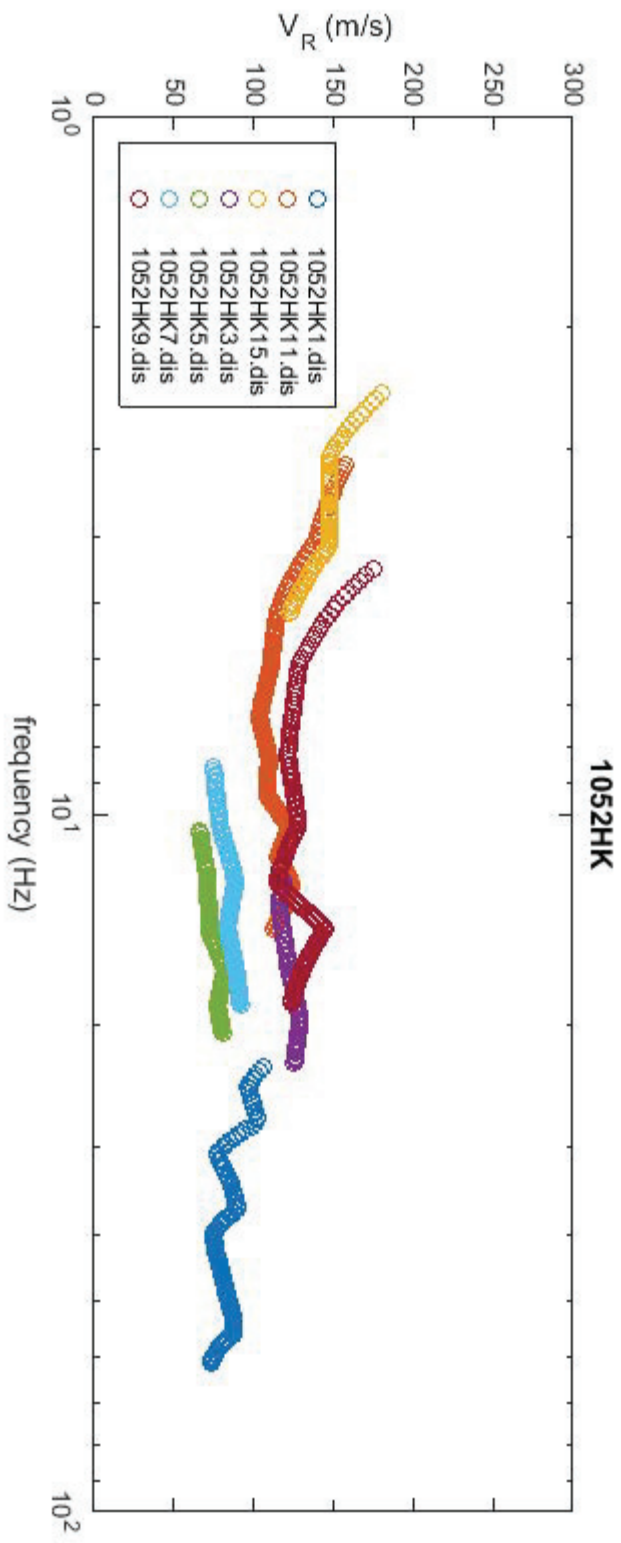


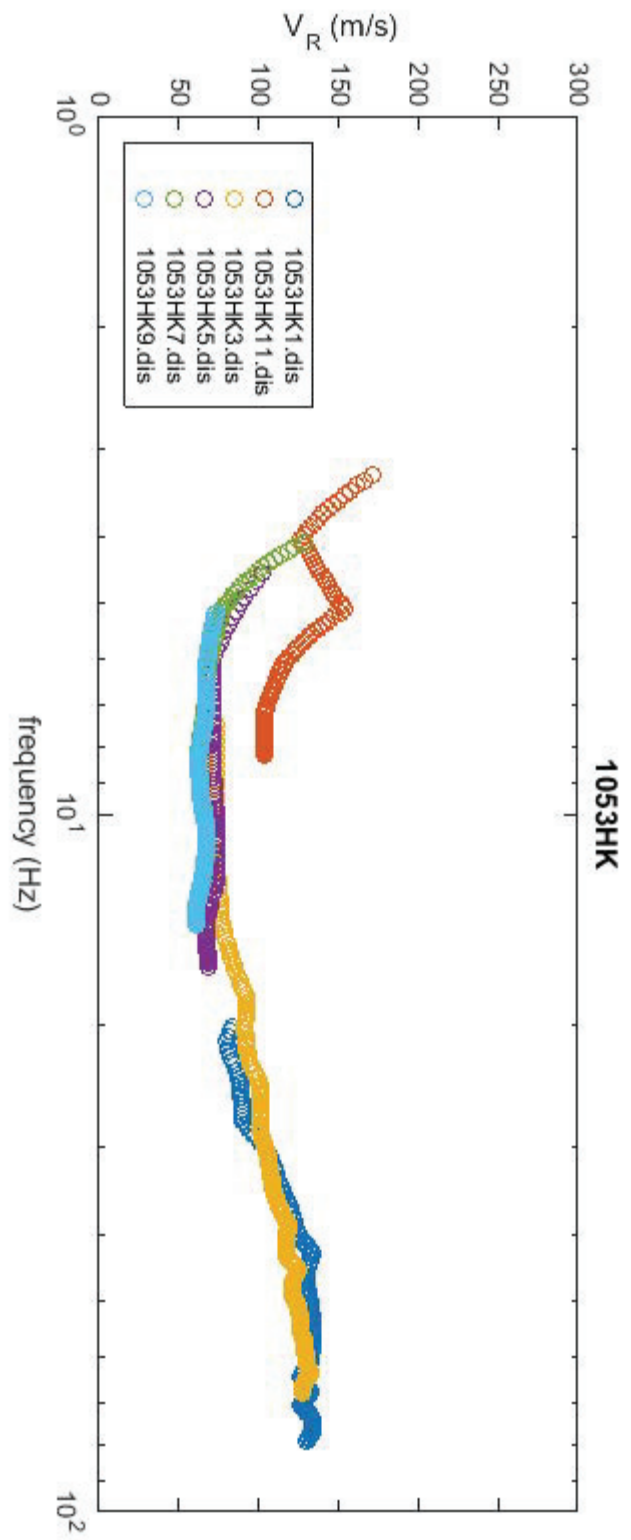
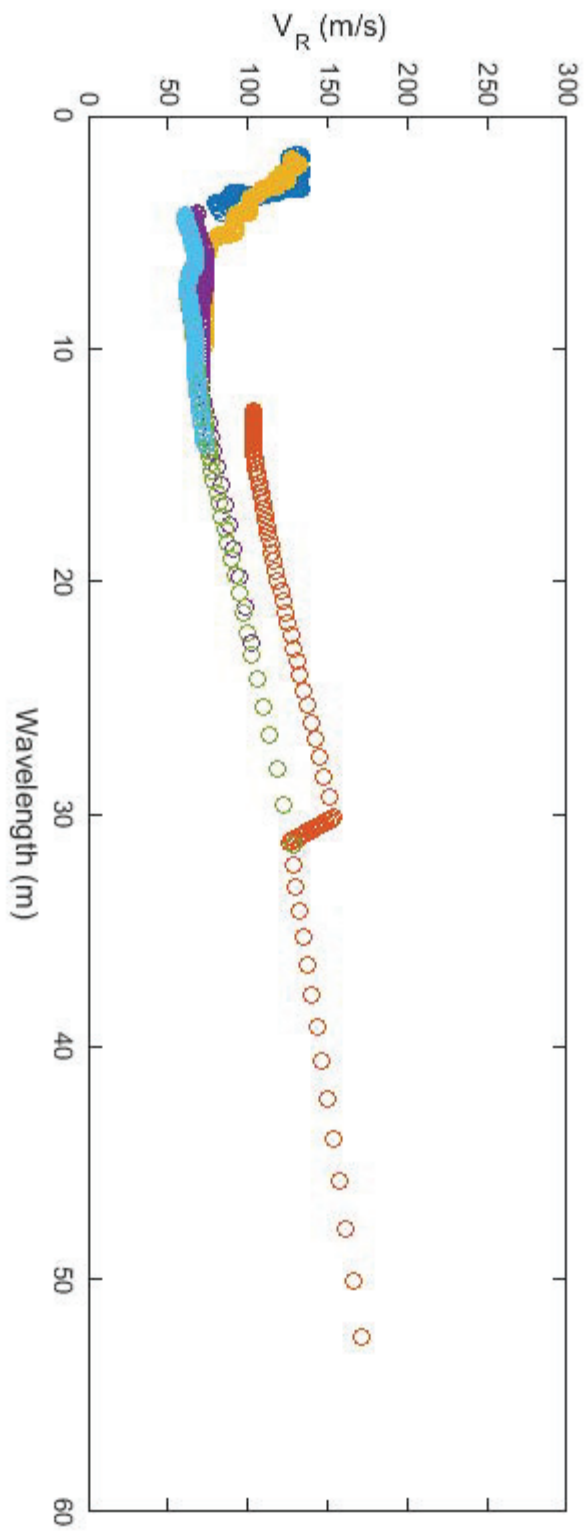


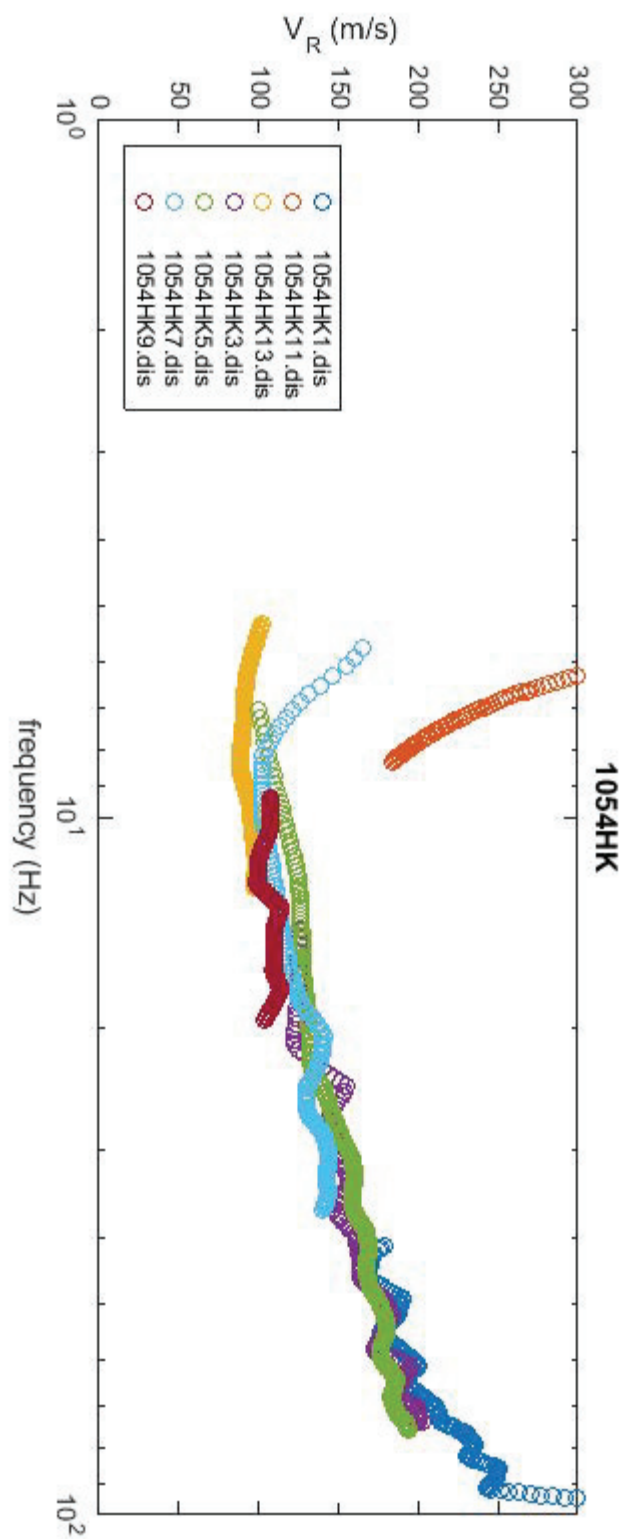
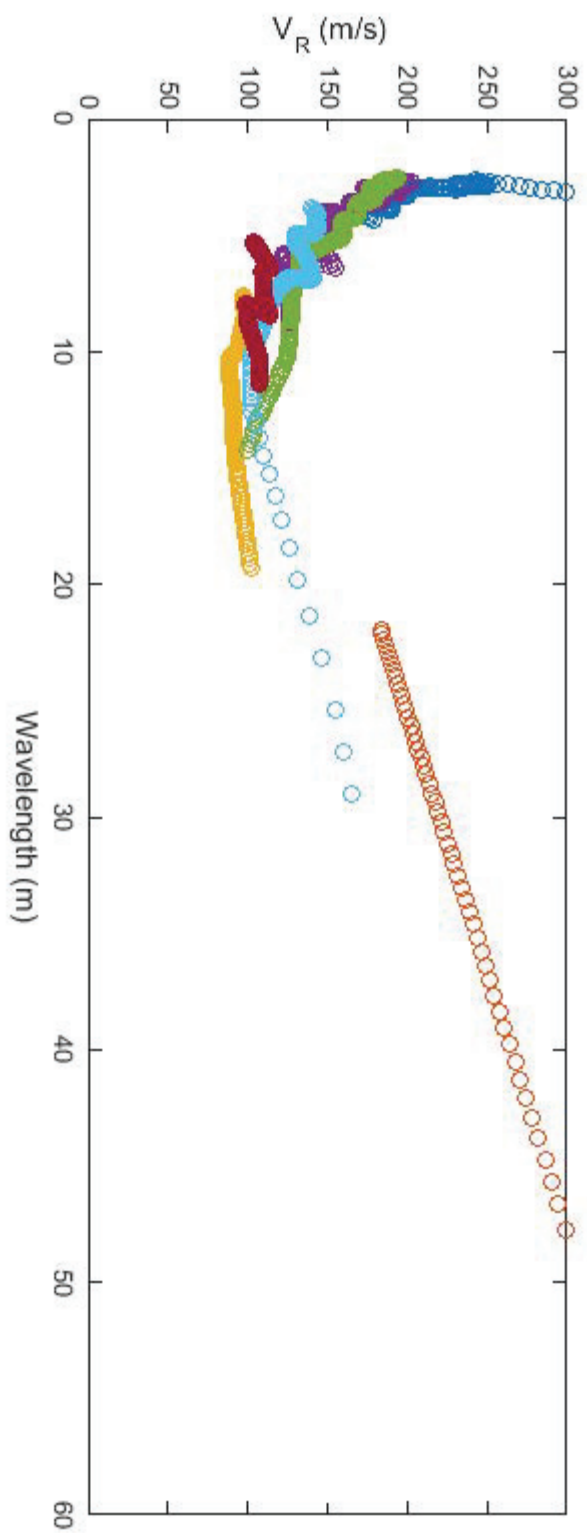


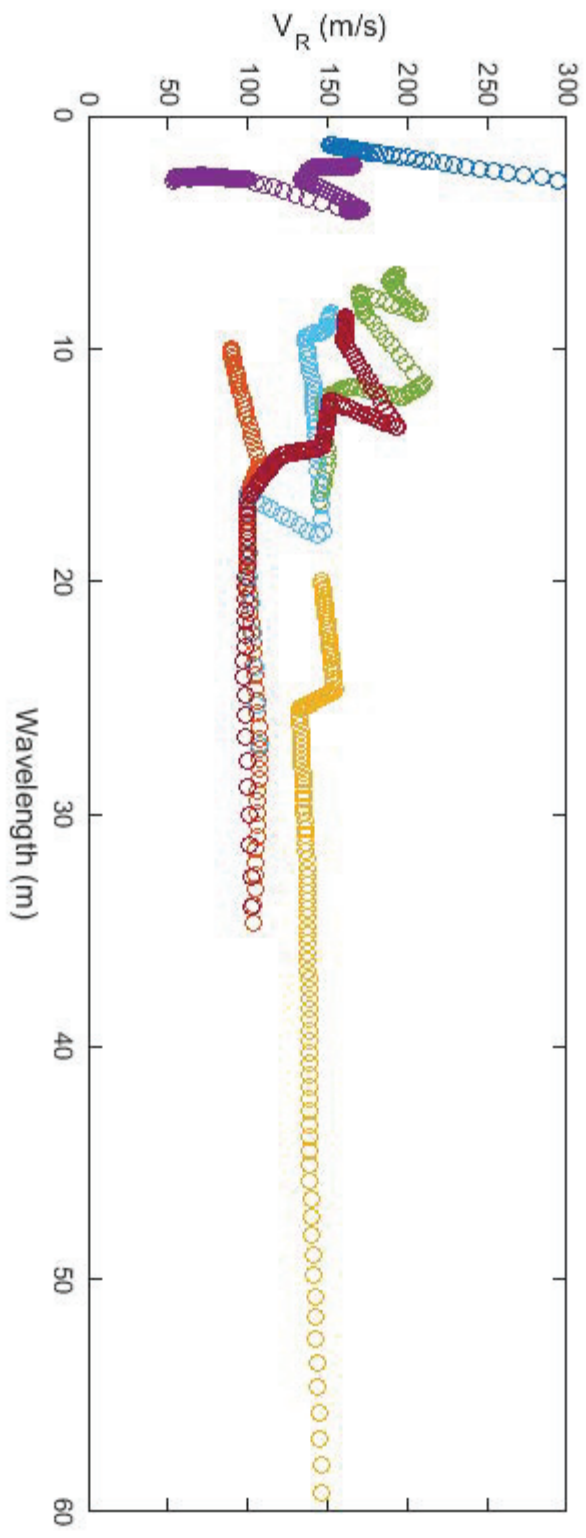
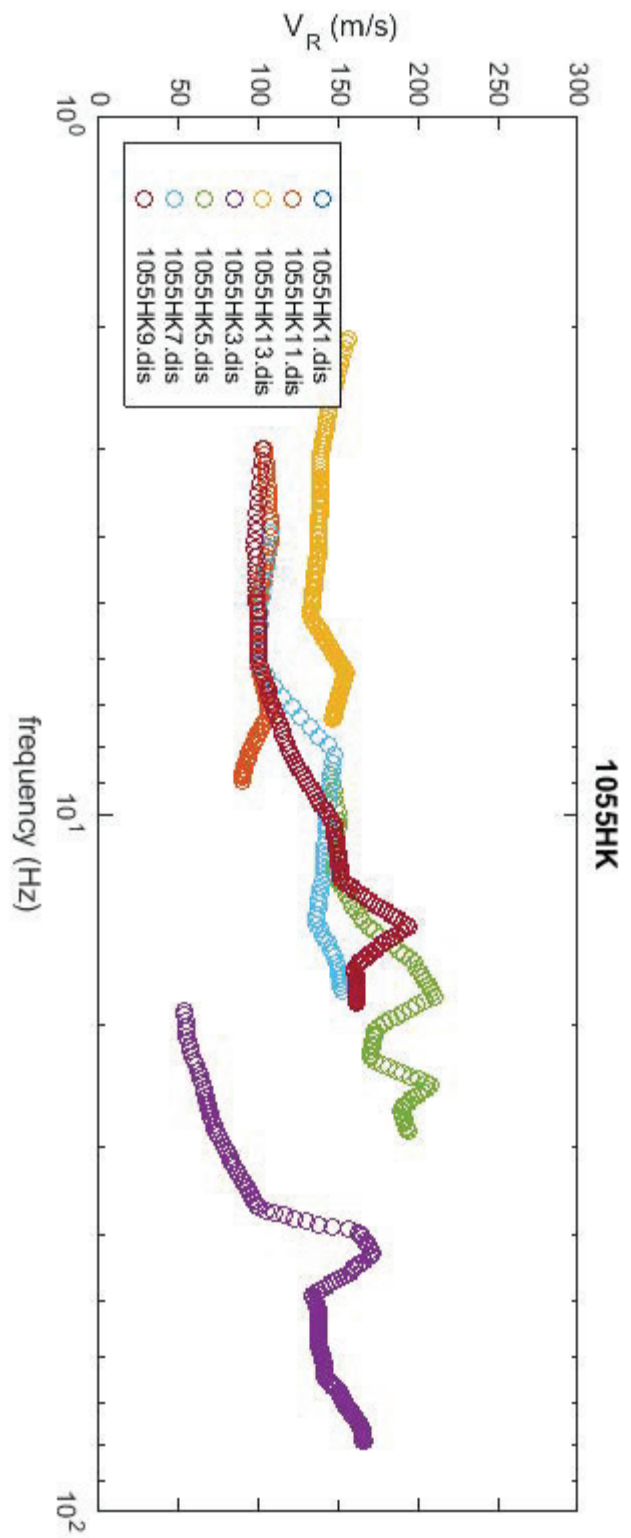




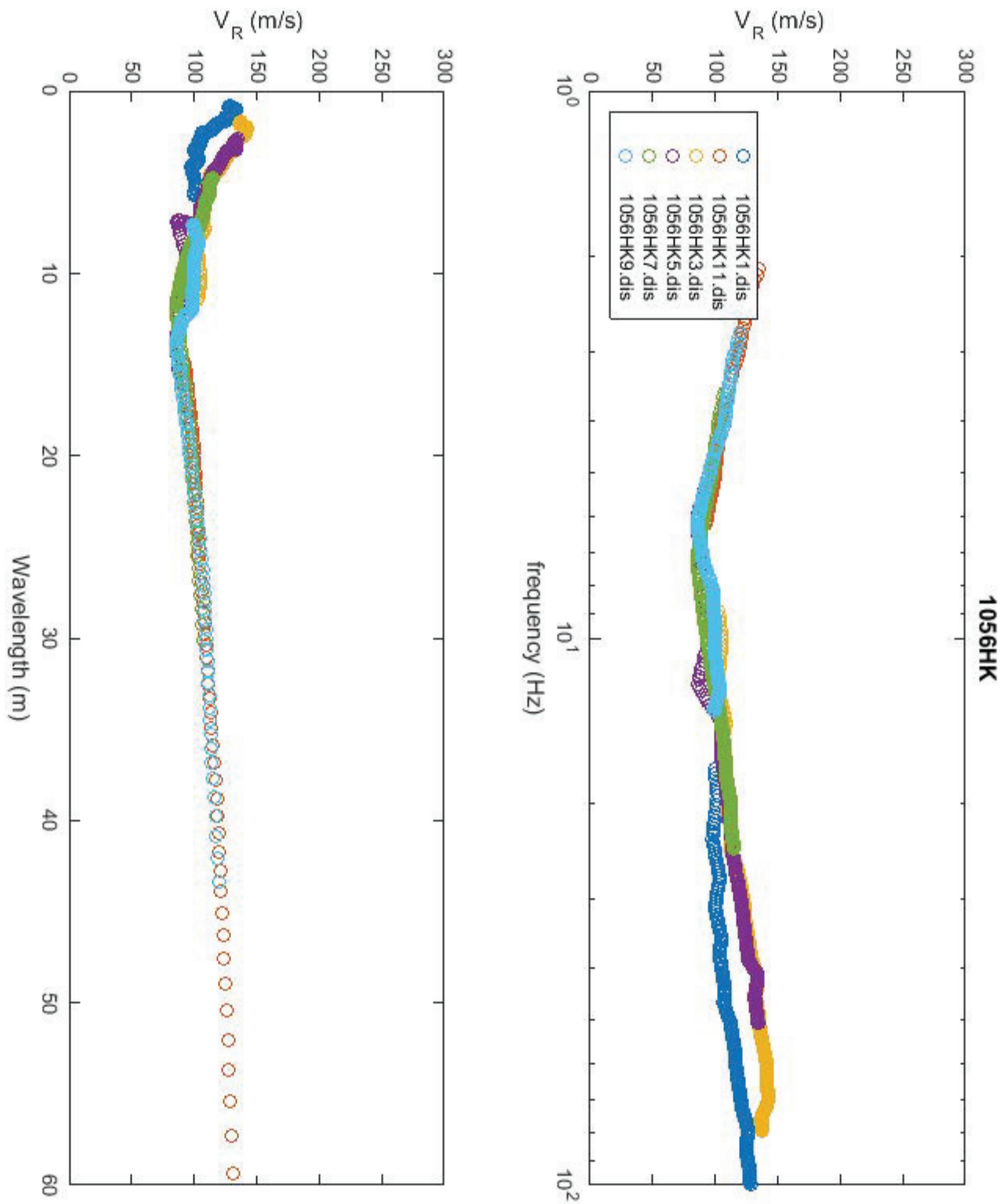


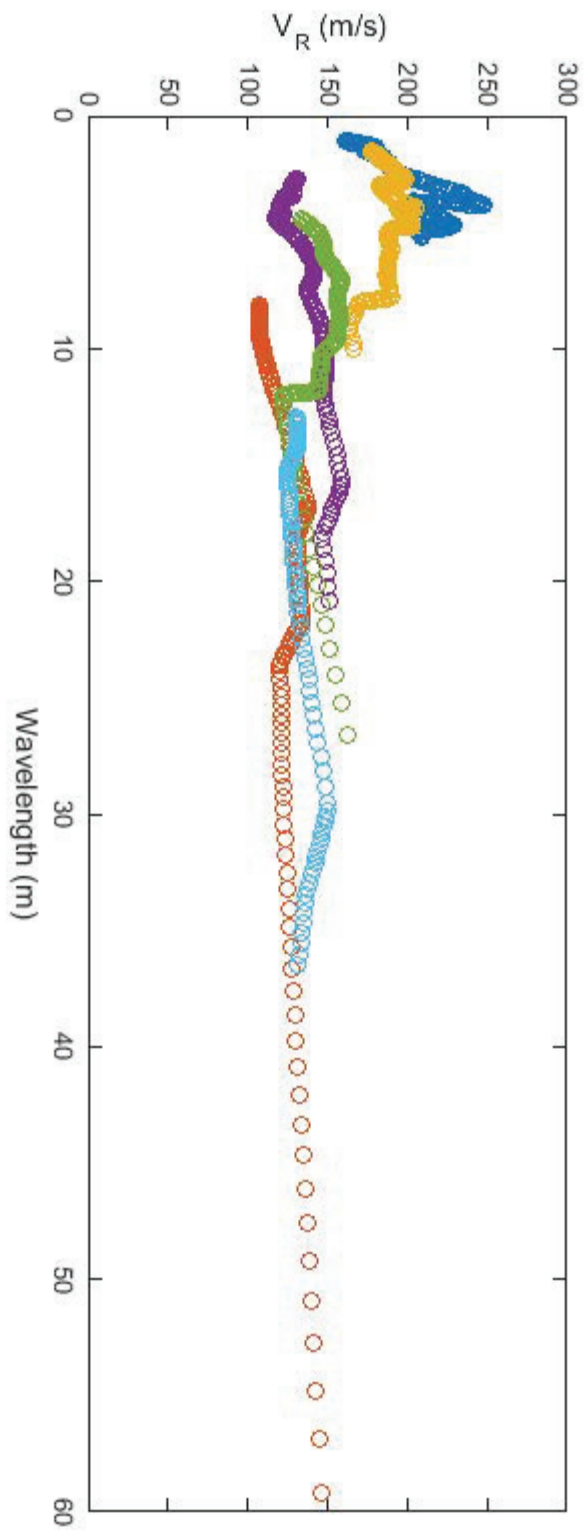
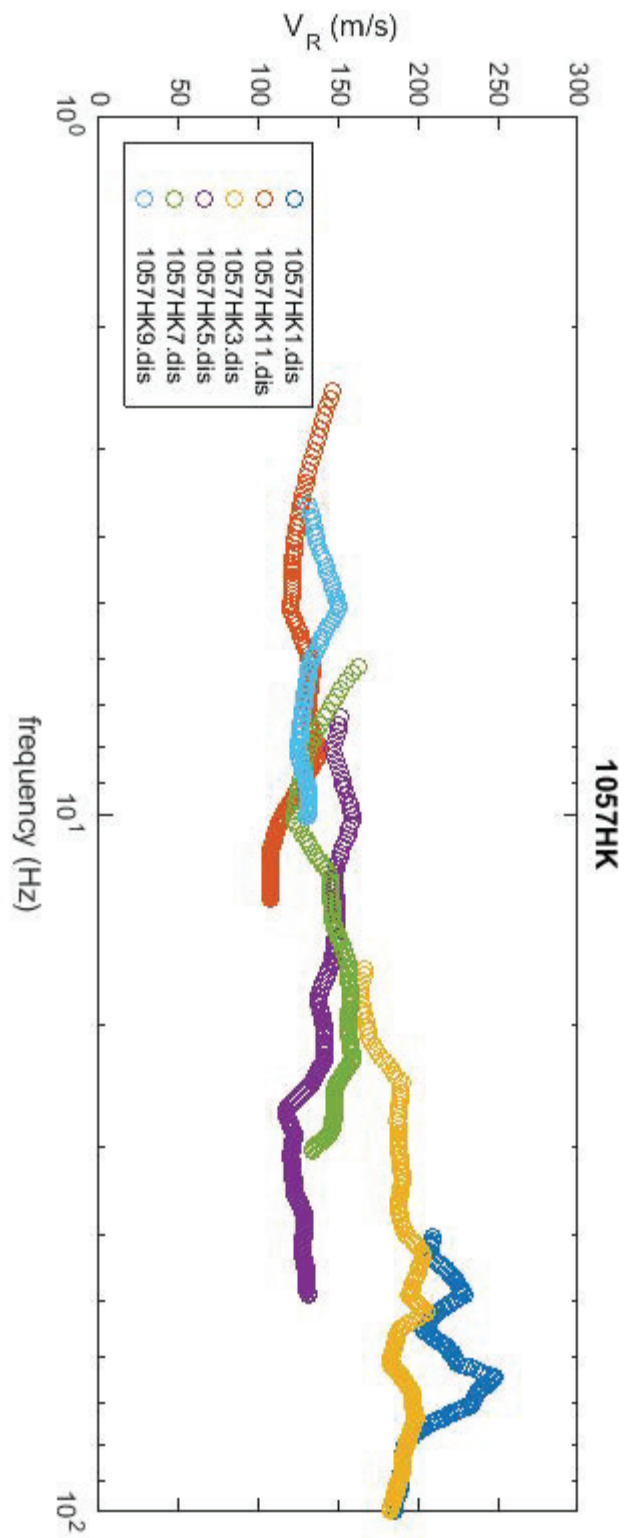


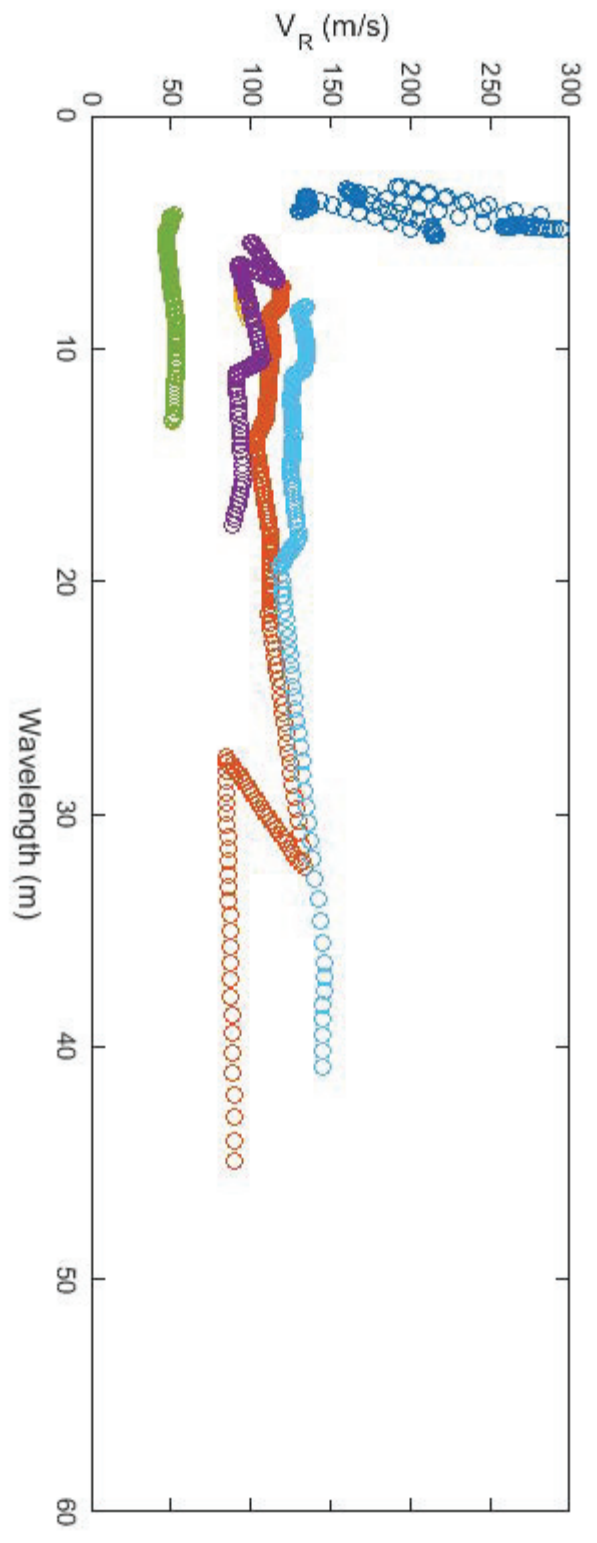
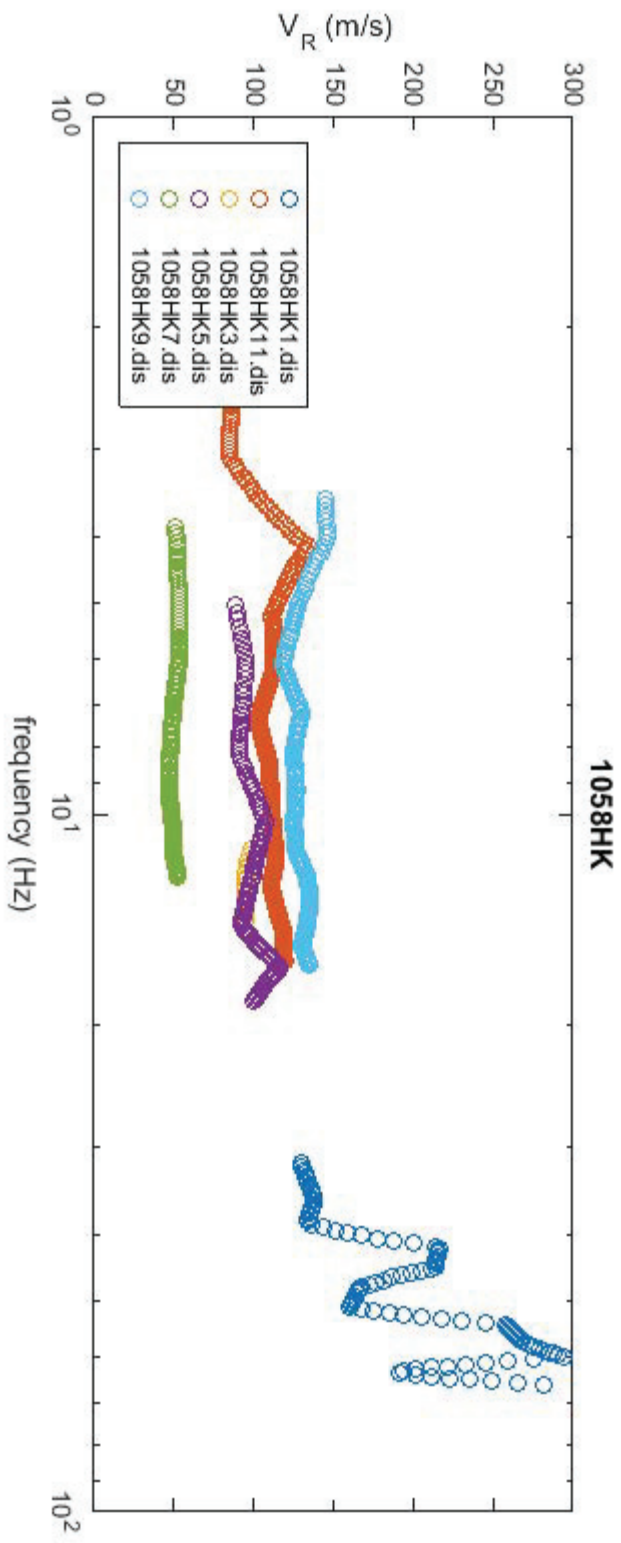


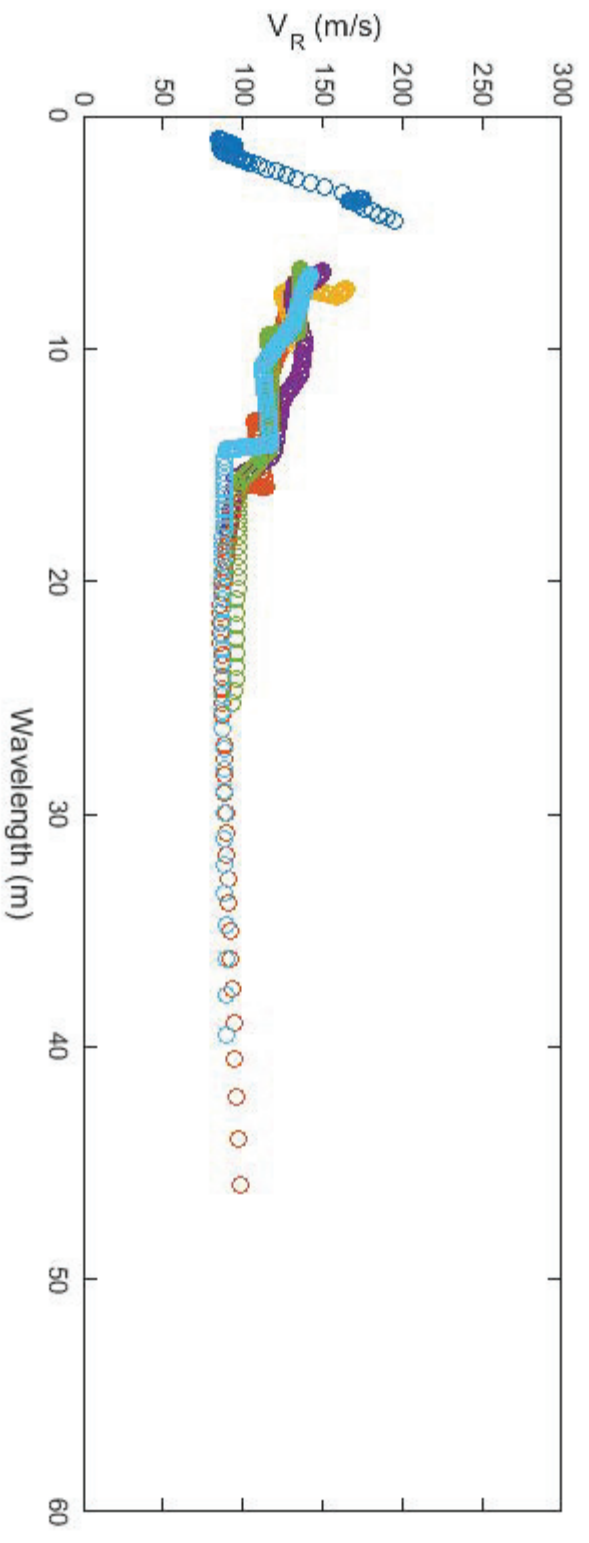
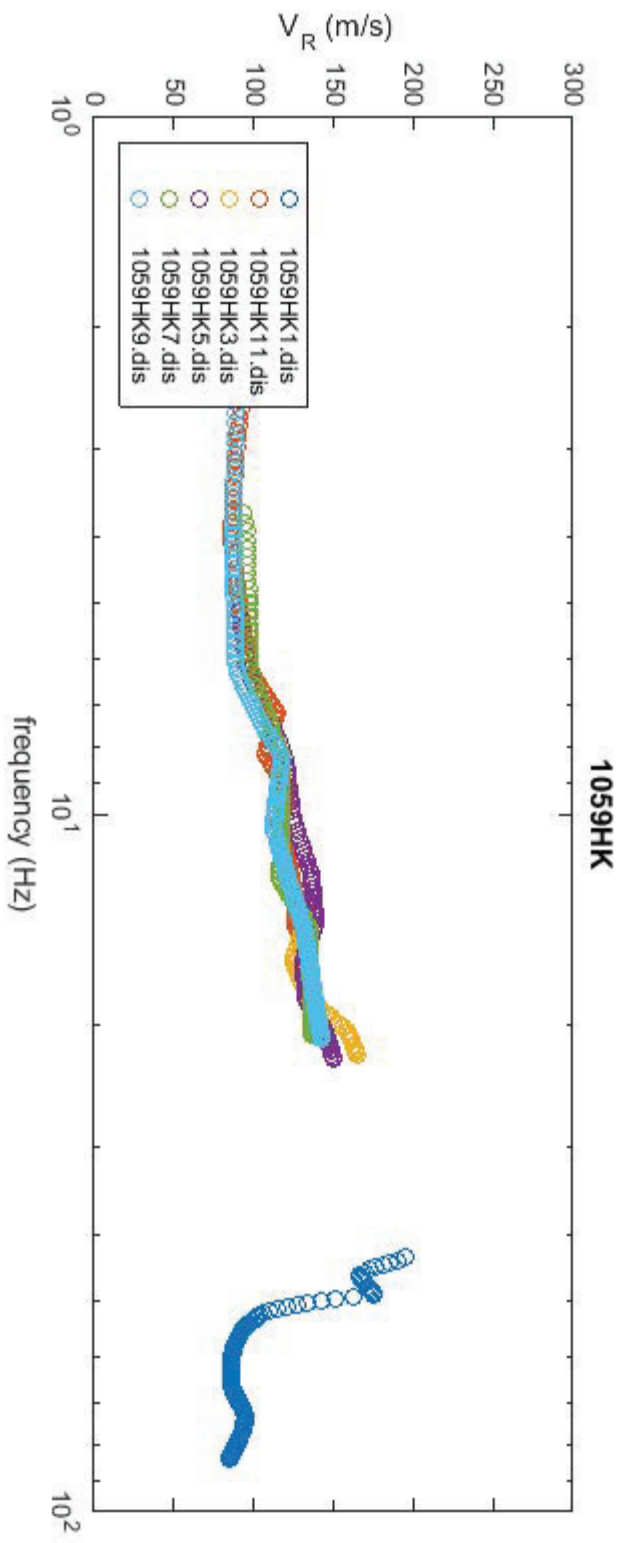


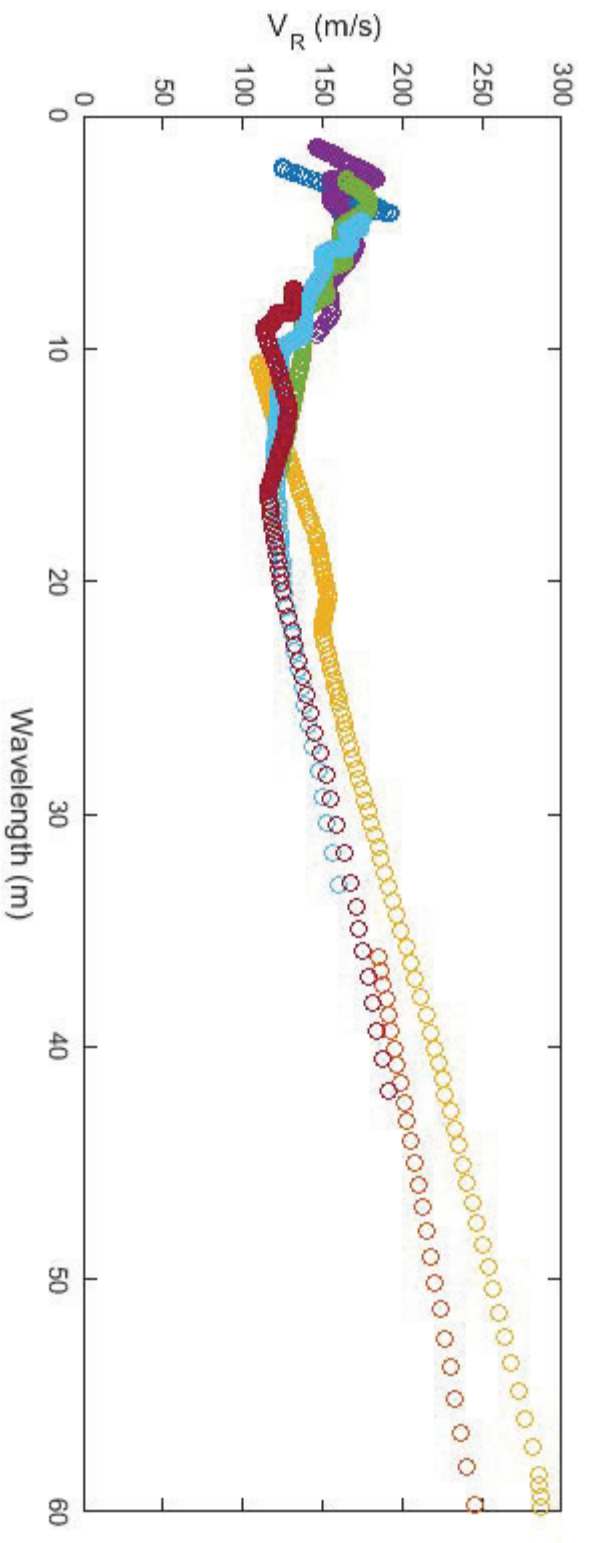
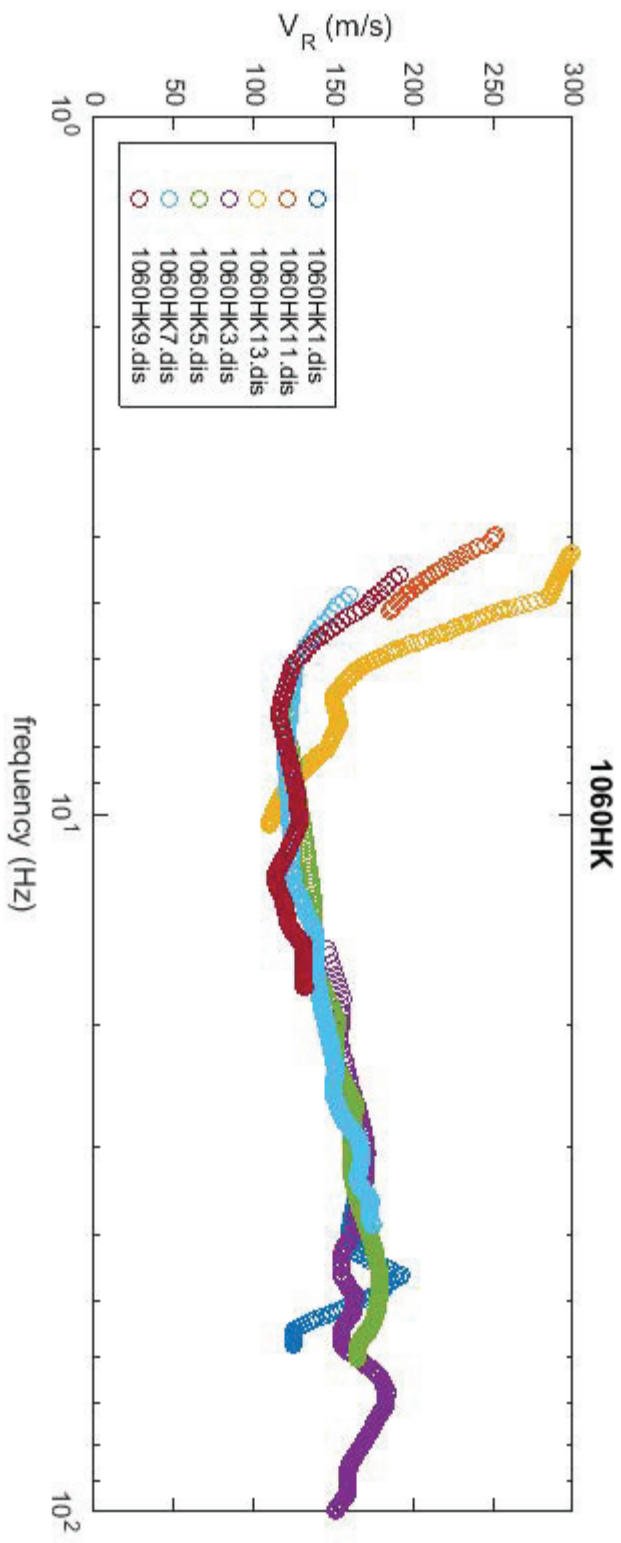


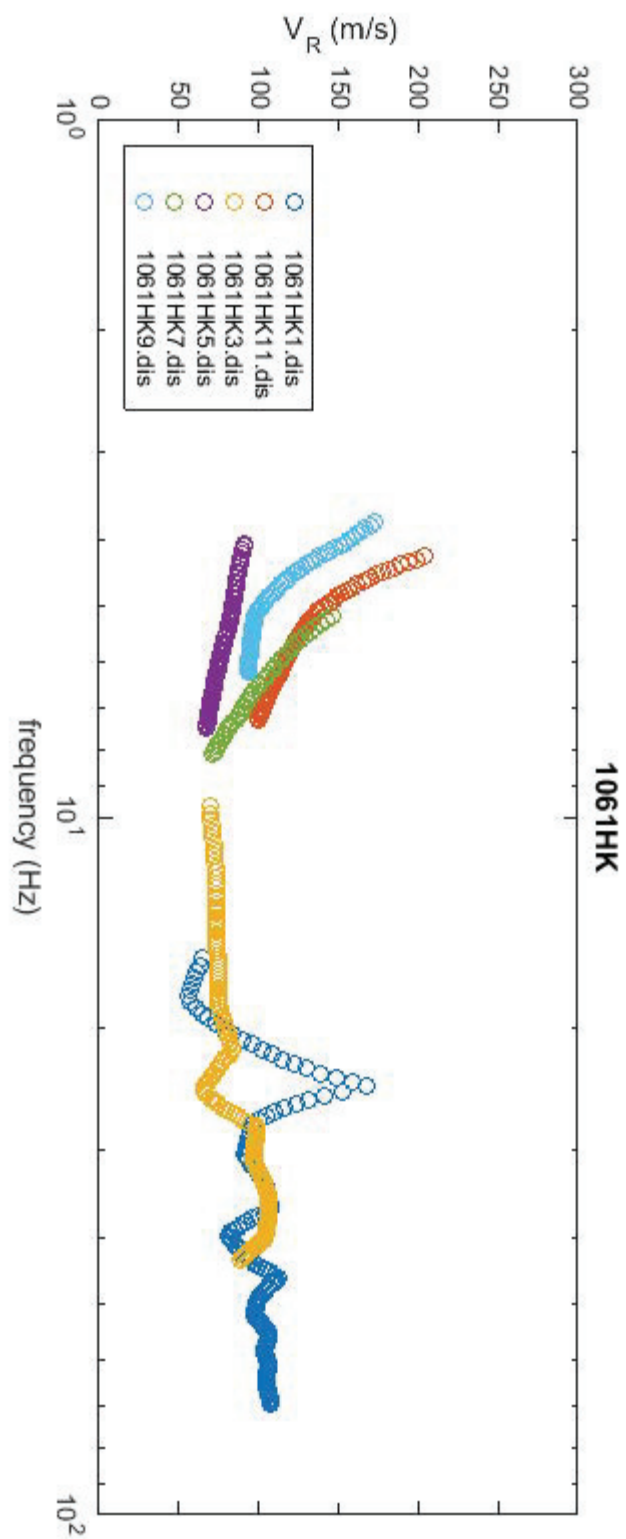
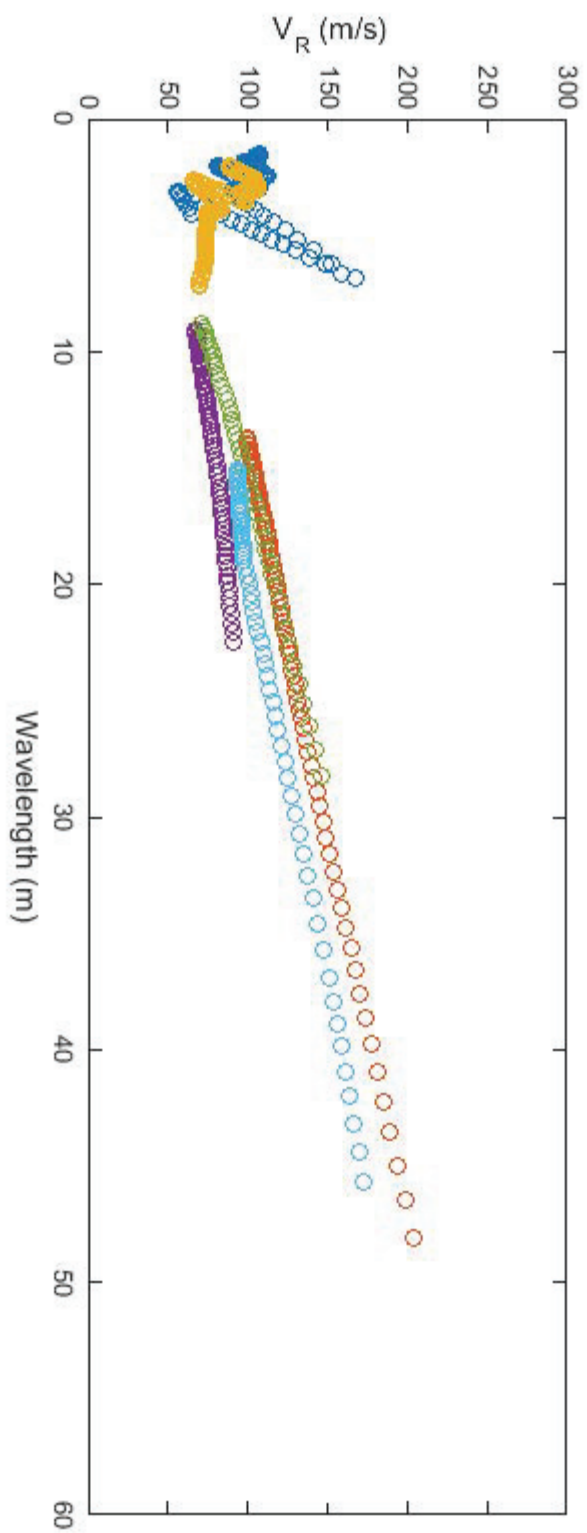


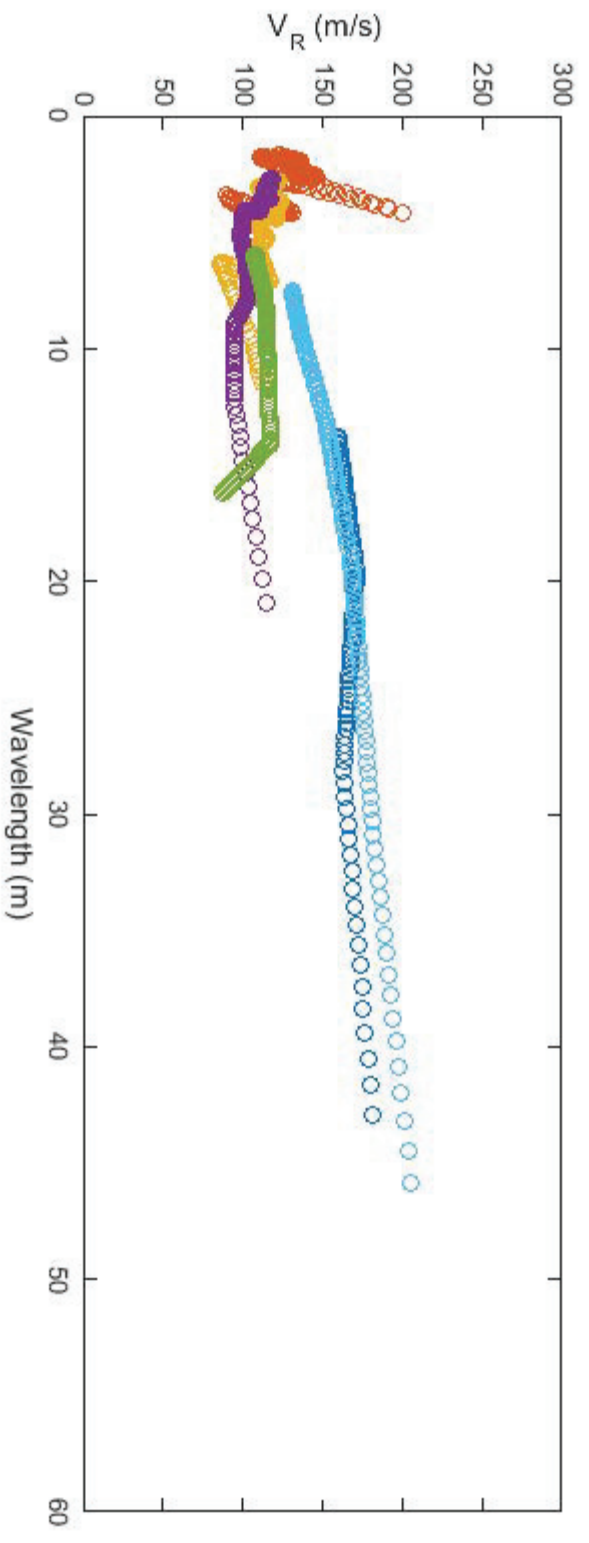
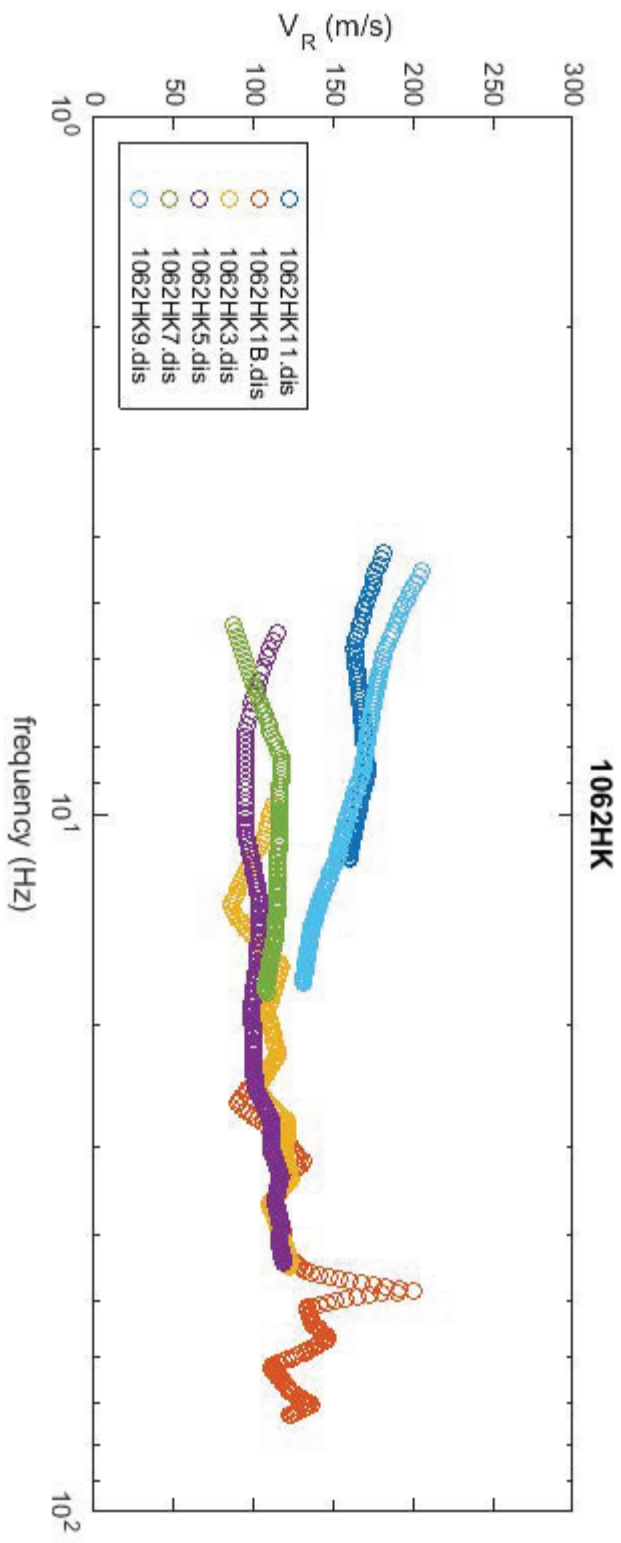


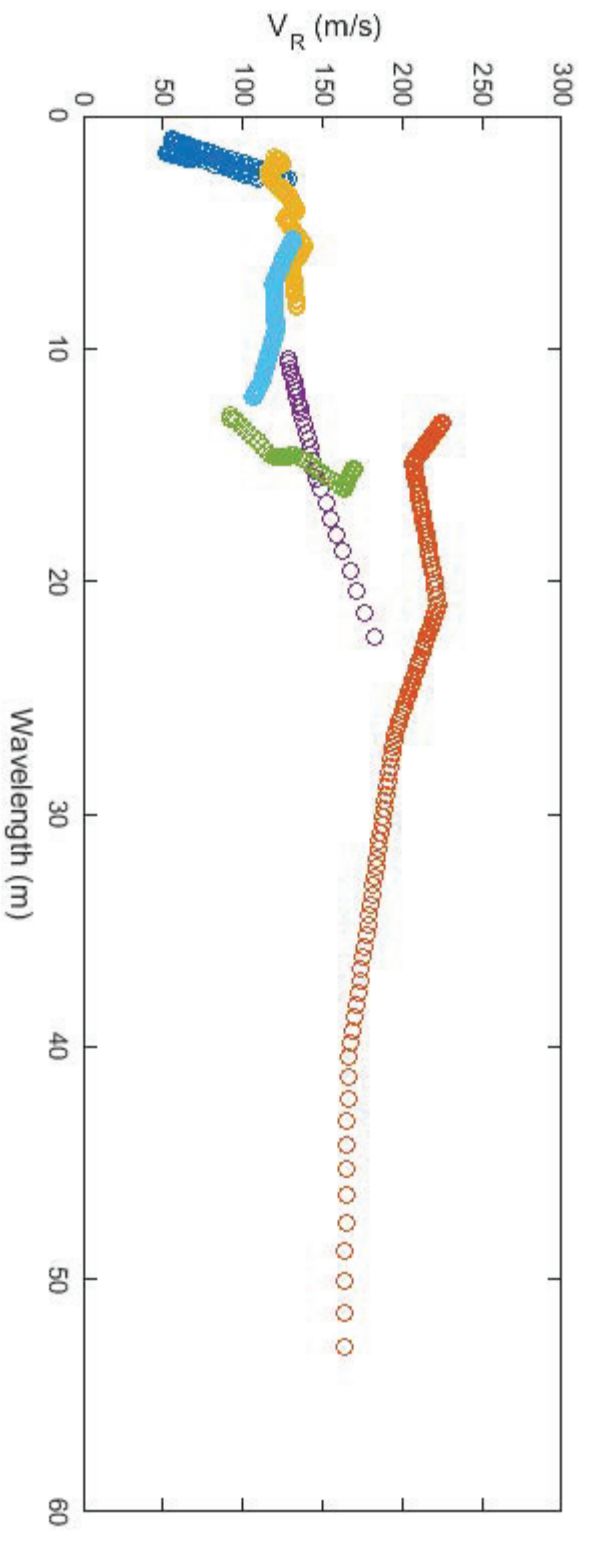
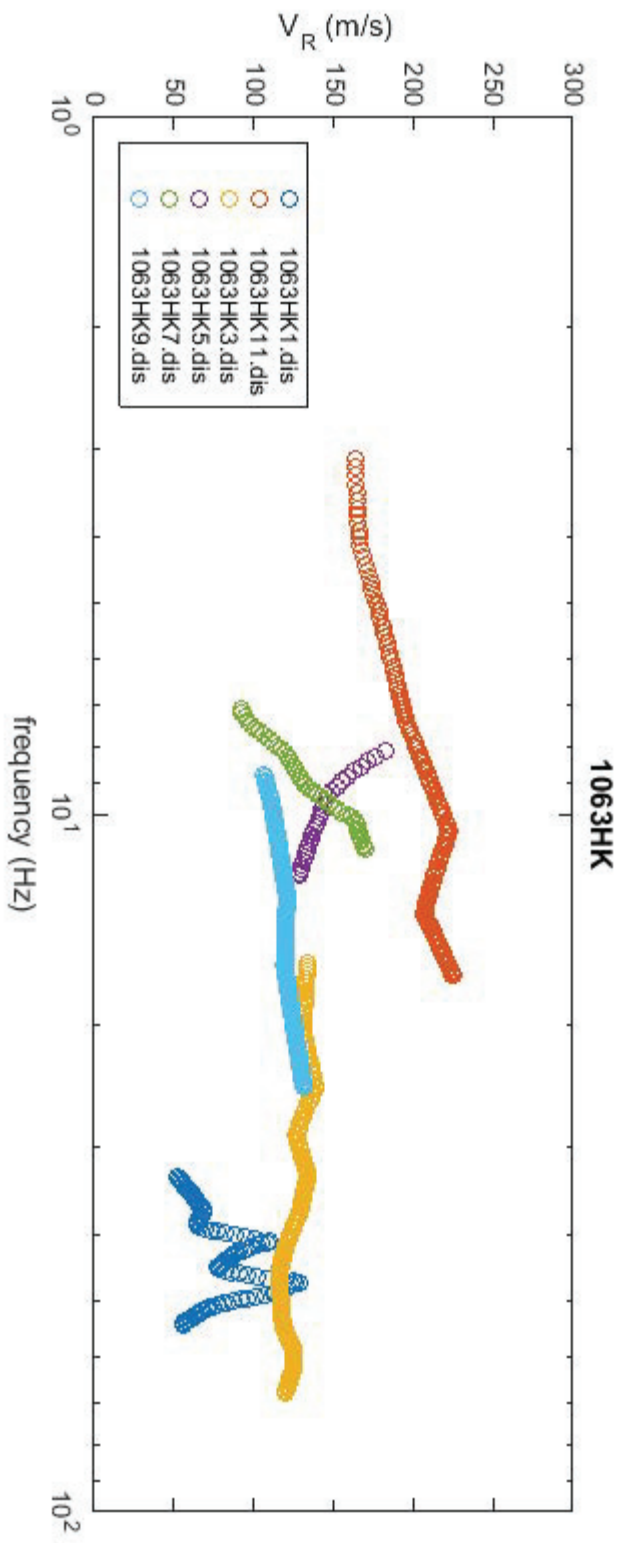




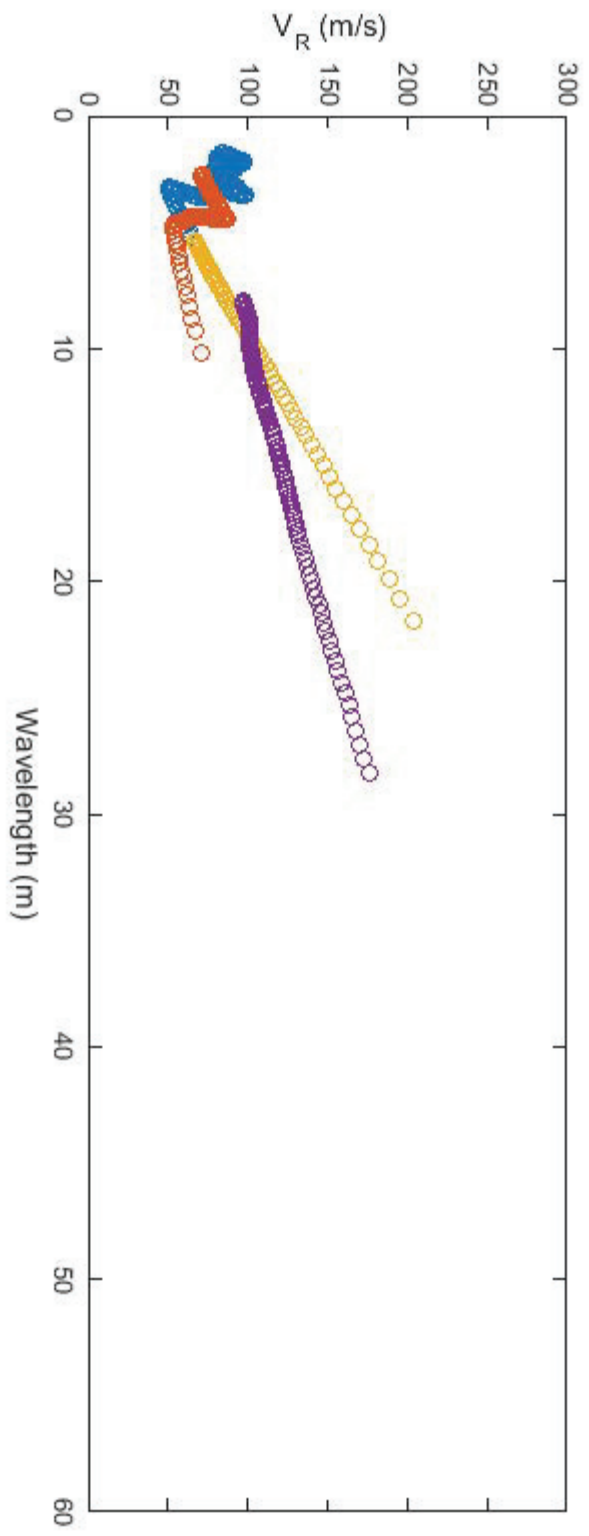
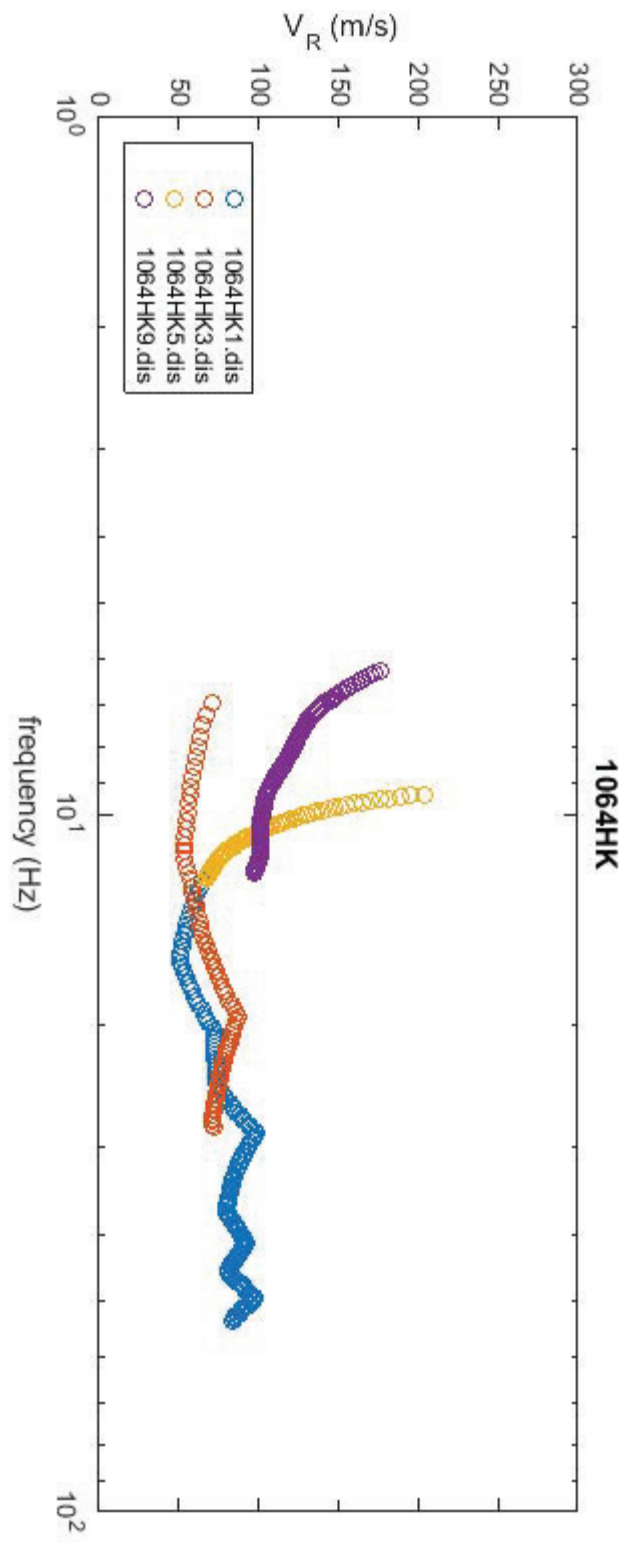


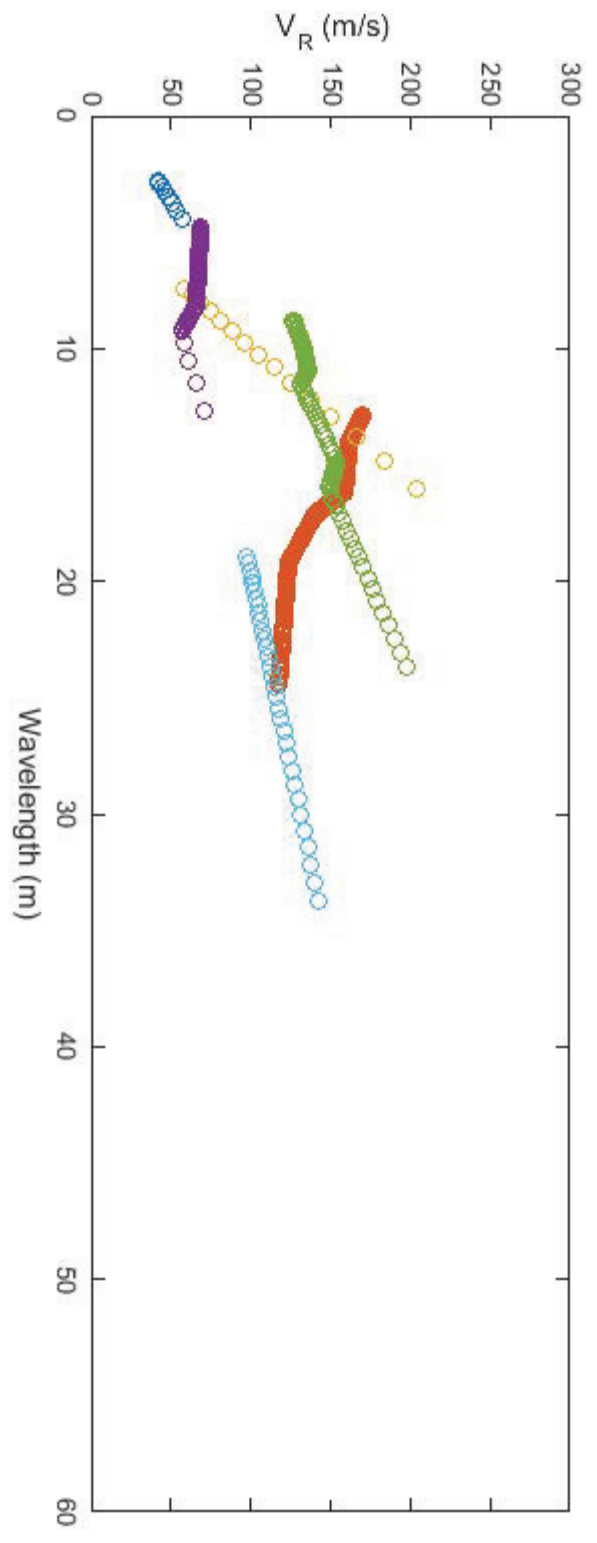
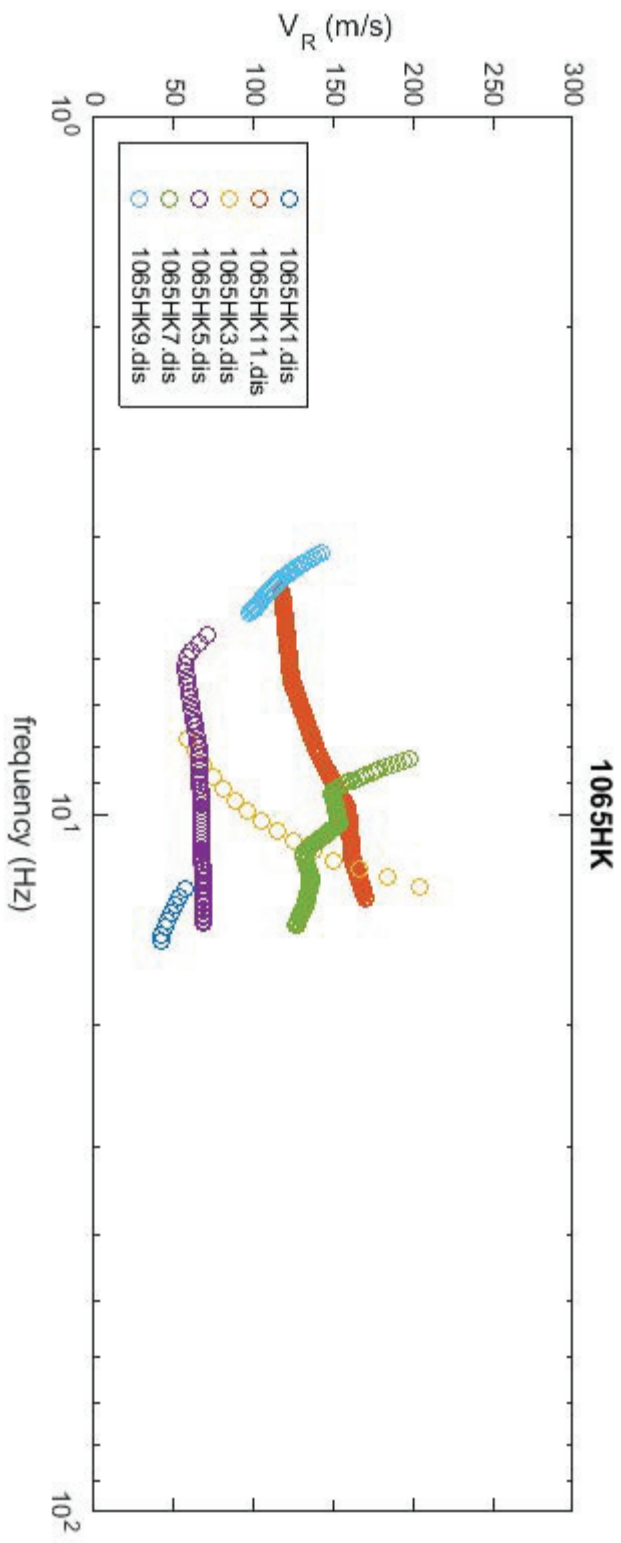


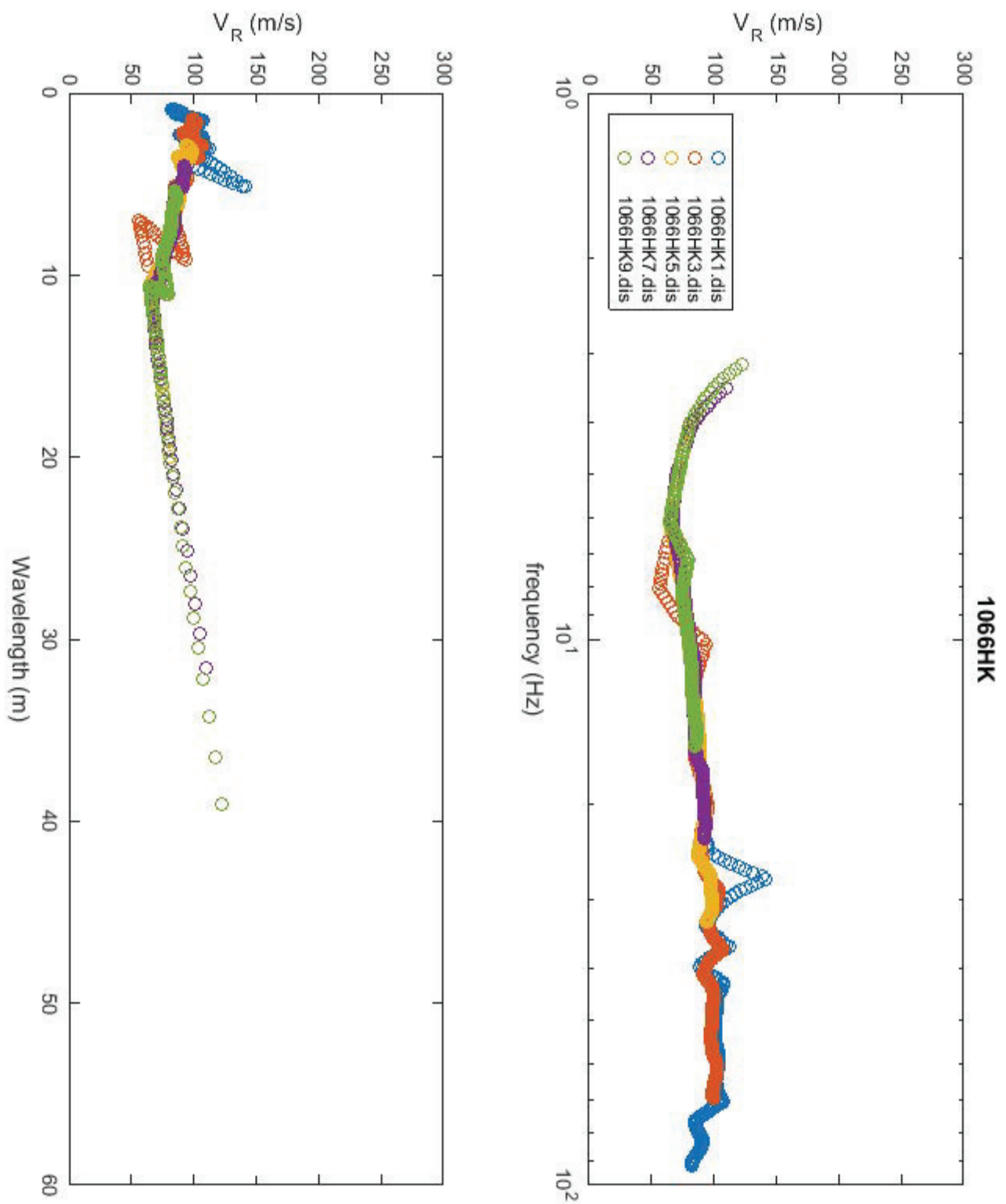


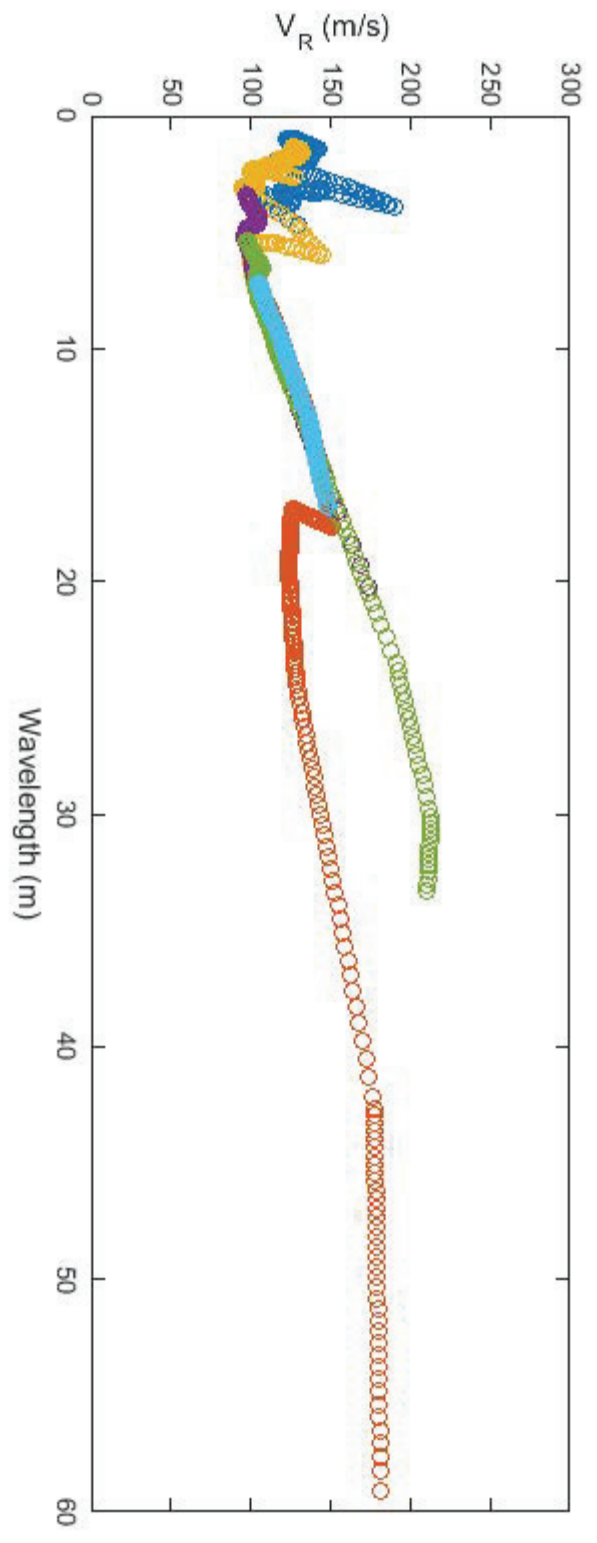
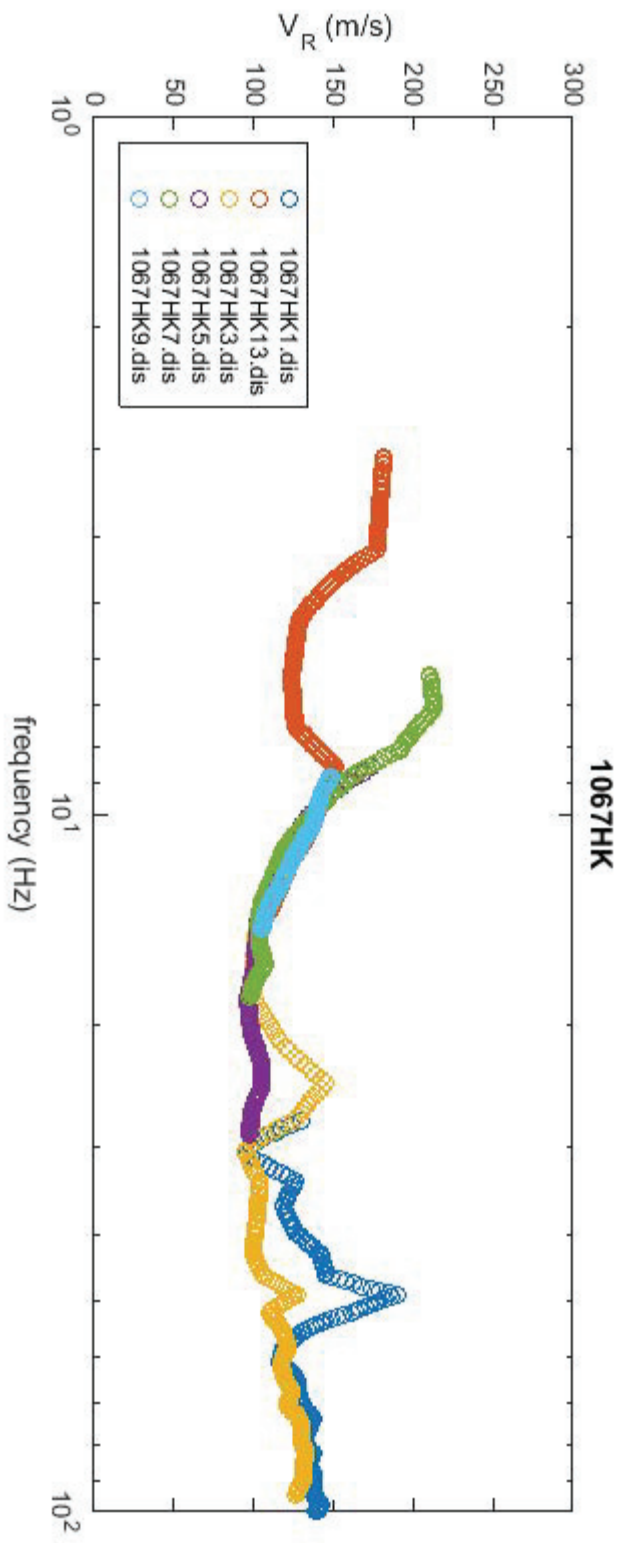


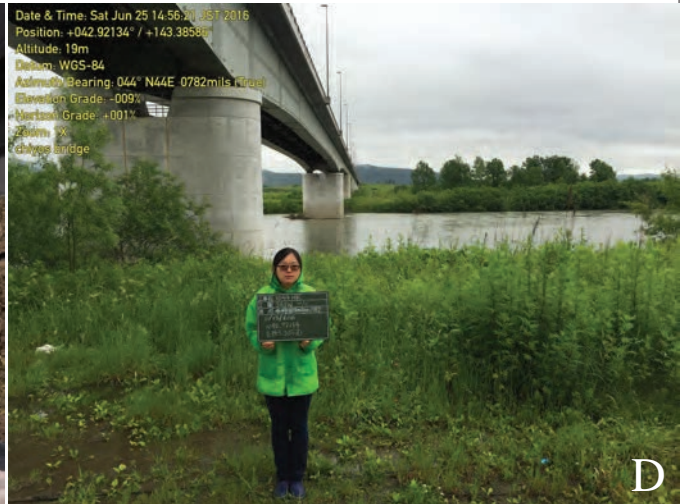
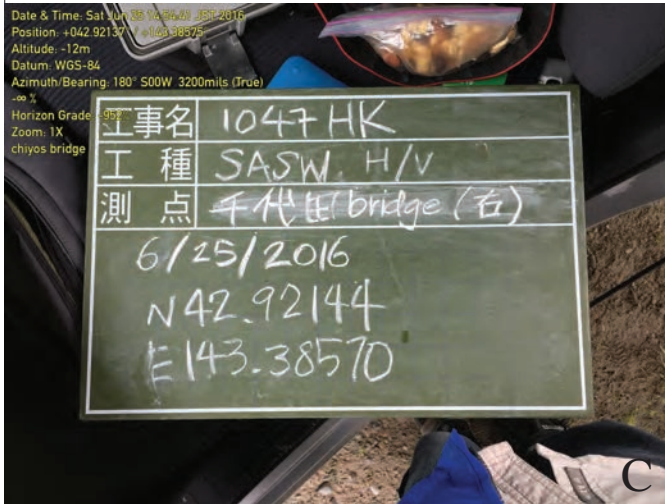




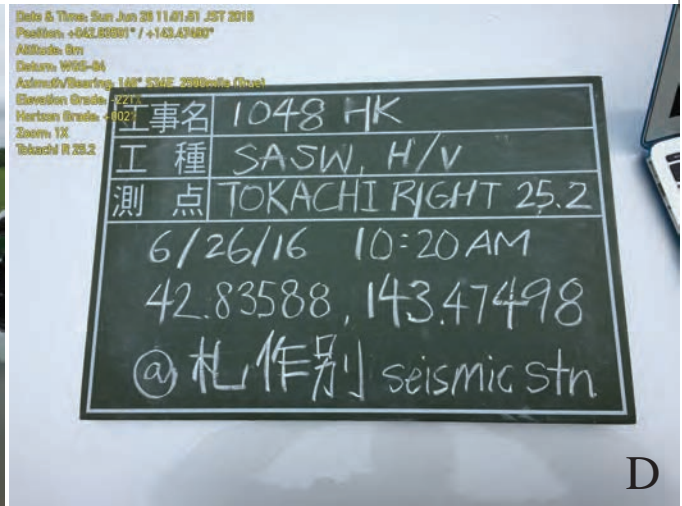




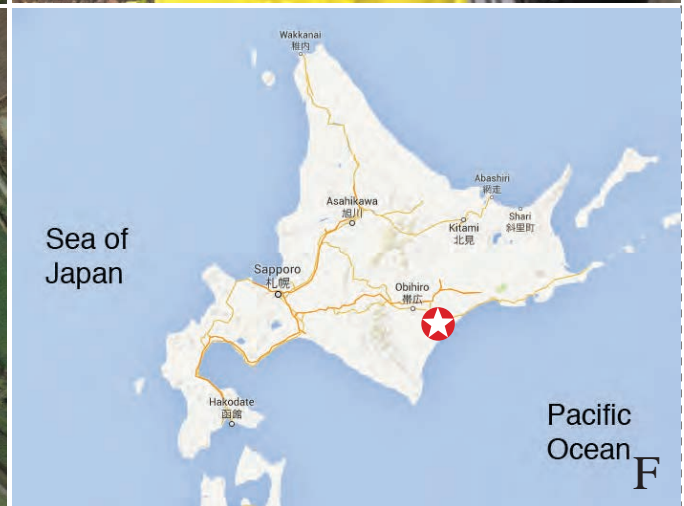
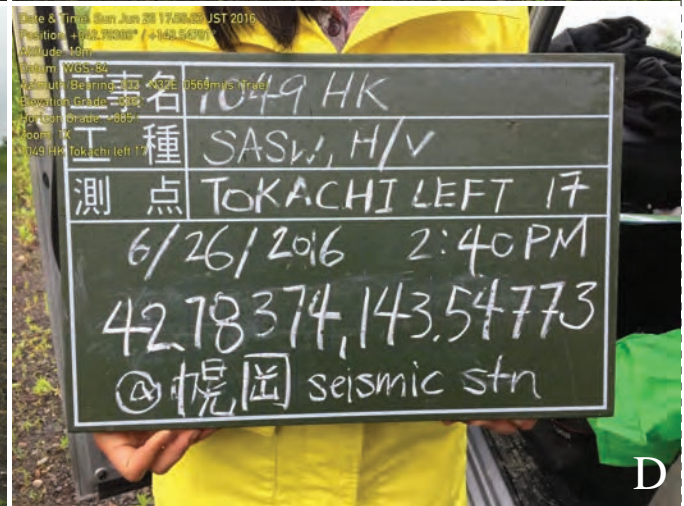
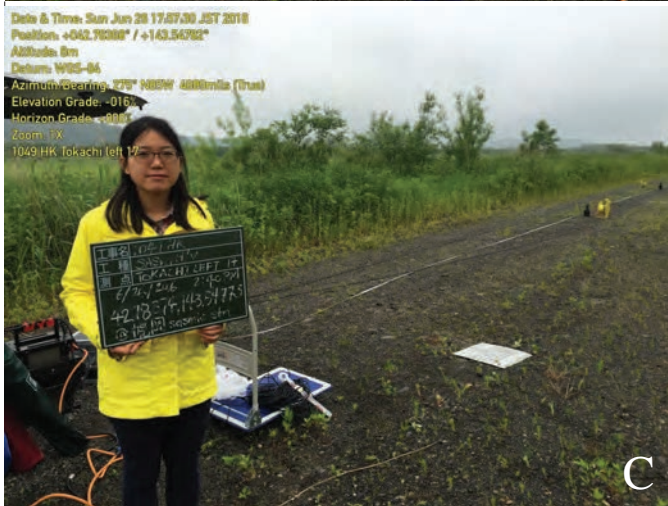
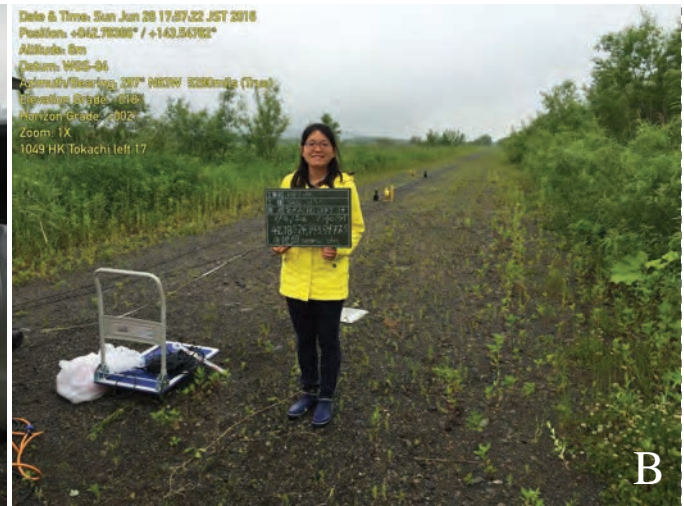




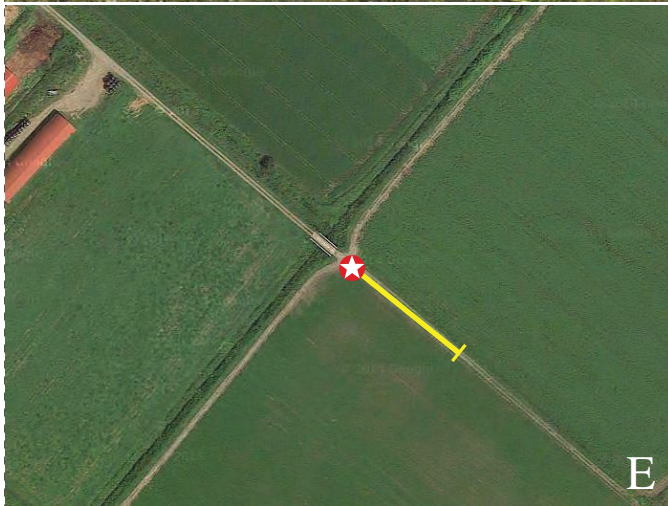
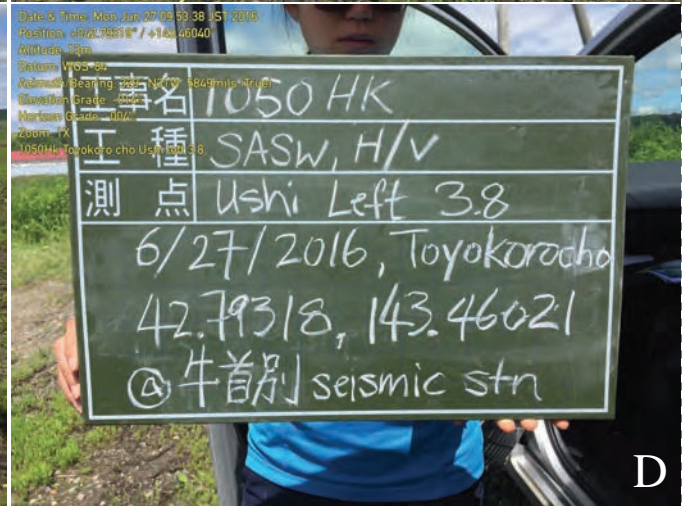
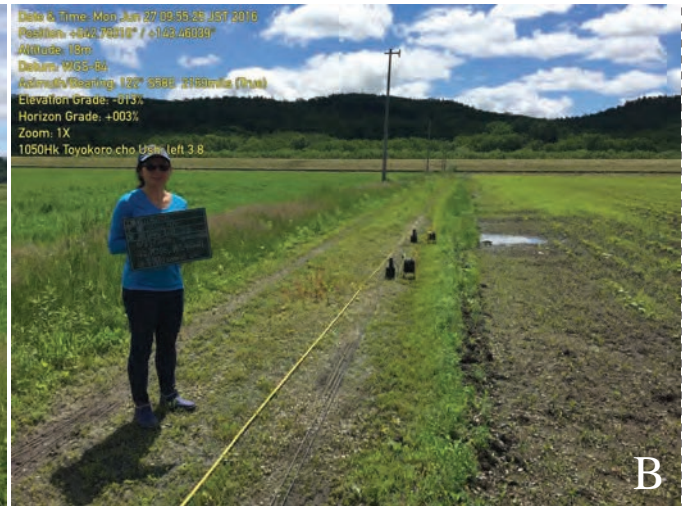
Surface wave test site 1047HK located on the SW bank of the Tokachi River 16 km east of Obihiro, Hokkaido, Japan (lat 42.92140, long 143.3858). A) view northwest from the shaker; B) view southeast toward the seismometer array; C) site information; D) view to the northeast from the test site; E) satellite view of the local site, yellow bar is seismometer array; F) site location near Obihiro, Hokkaido, Japan.



Surface wave test site 1048HK located on the right bank Tokachi River dike 22 km SE of Obihiro, Hokkaido, Japan (lat 42.8359, long 143.47497). A) view southeast to seismometer array on dike crest; B) view northwest on the dike from near the shaker; C) another view northwest; D) site information; E) satellite view of the local site, yellow bar is seismometer array; F) site location near Obihiro, Hokkaido, Japan.

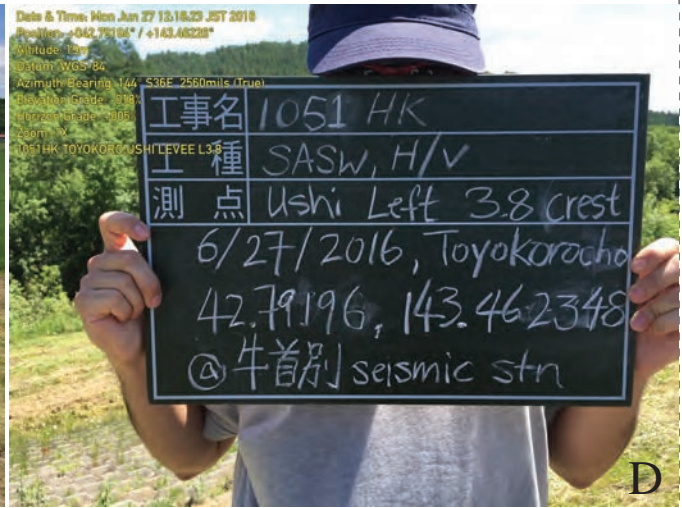
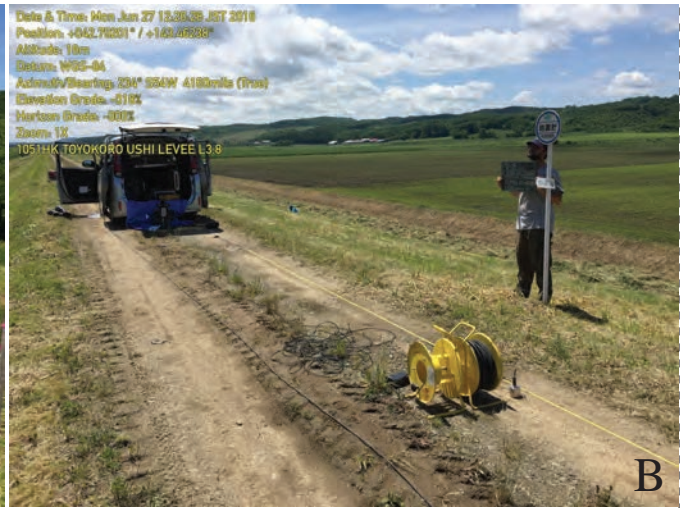


Surface wave test site 1049HK located on the inside of the left bank dike of the Tokachi River, location L17, 30 km SW of Obihiro, Hokkaido, Japan (lat 42.78367, long 143.54781). A) view southeast from near the shaker to seismometer array; B) view northwestward from the shaker; C) view westward from the shaker; D) site information; E) satellite view of the local site, yellow bar is seismometer array; F) site location near Obihiro, Hokkaido, Japan.

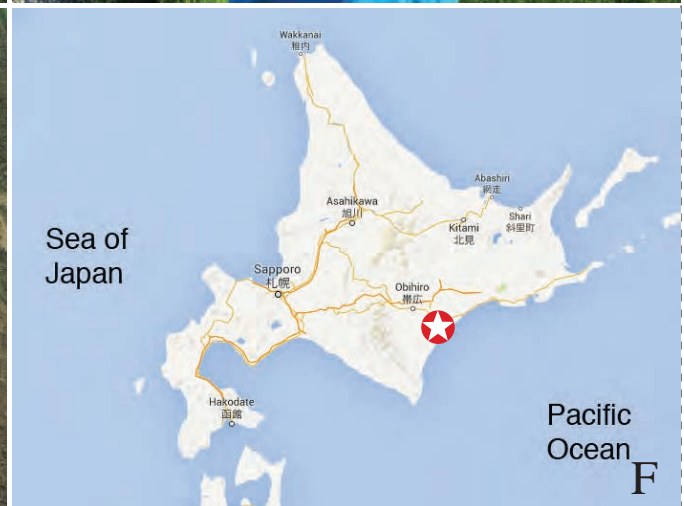
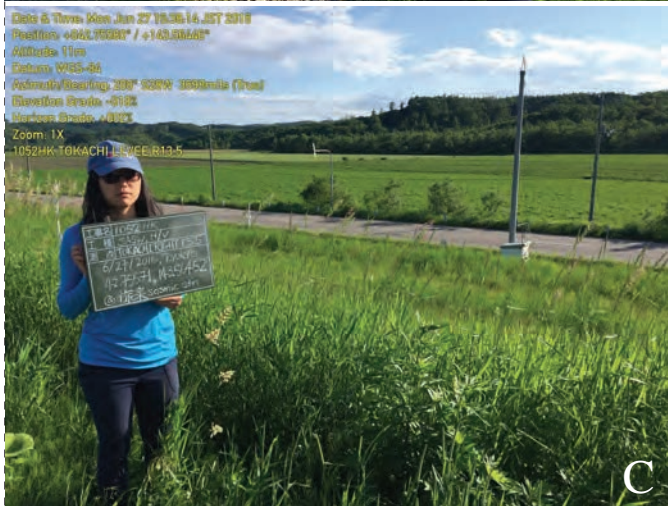


Surface wave test site 1050HK located 24 km SE of Obihiro, Hokkaido, Japan (lat 42.7931, long 143.46039). A) view northwest along the seismometer array toward the shaker; B) view southeast along the seismometer array; C) view southwestward along the seismometer array; D) site information; E) satellite view of the local site, yellow bar is seismometer array; F) site location near Obihiro, Hokkaido, Hokkaido, Japan.

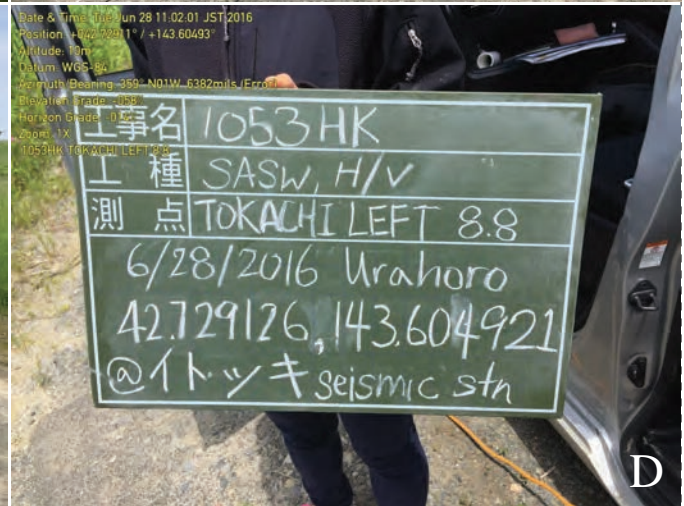




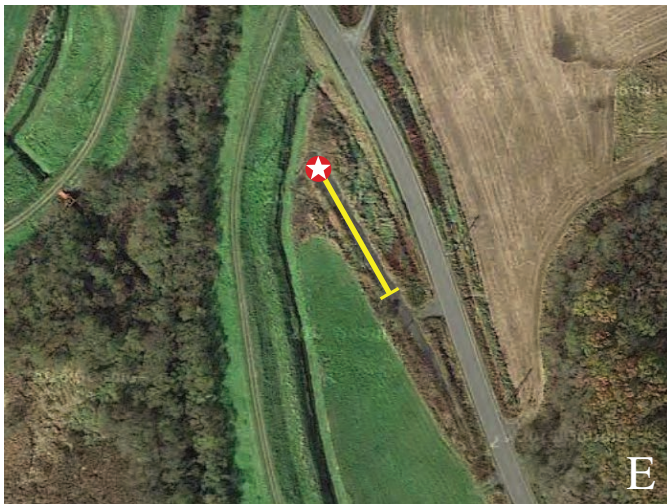
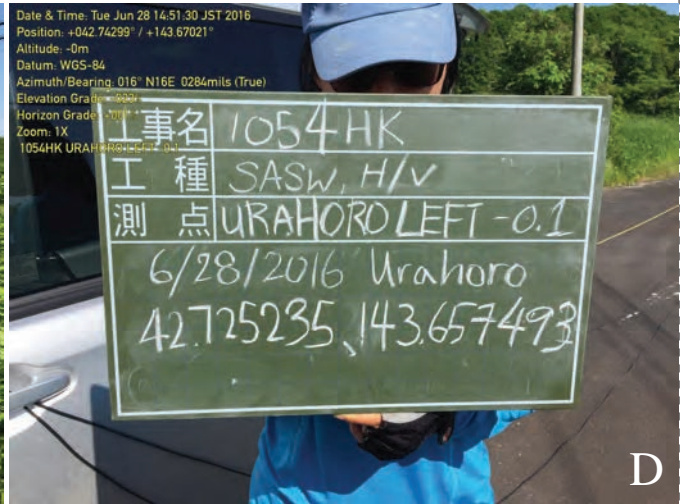
Surface wave test site 1051HK located 23 km SE of Obihiro, Hokkaido, Japan (lat 42.79196, long 143.462348). A) view northeast from the shaker to the seismometer array; B) view southwest toward the shaker; C) view to the west from the test site; D) site information; E) satellite view of the local site, yellow bar is seismometer array; F) site location near Obihiro, Hokkaido, Japan.



Surface wave test site 1052HK located on the Tokachi River right bank levee, location 13.5, 33 km SE of Obihiro, Hokkaido, Japan (lat 42.75571, long 143.56452). A) view southeast from the shaker to the seismometer array; B) another view southeast toward the shaker; C) view southwest from the test site; D) site information; E) satellite view of the local site, yellow bar is seismometer array; F) site location near Obihiro, Hokkaido, Japan.



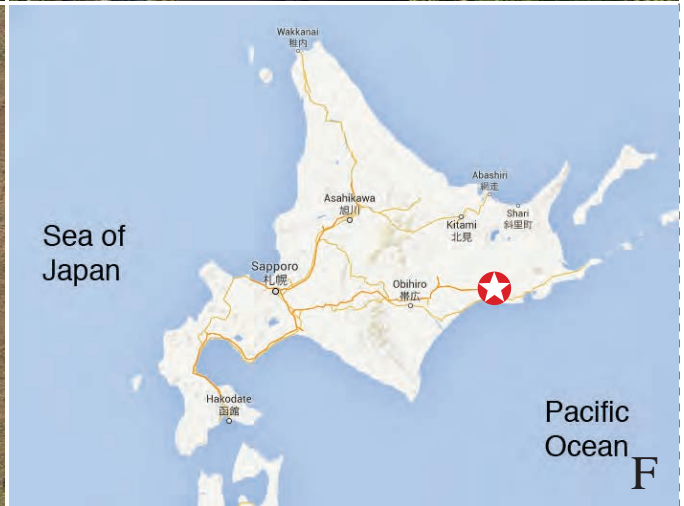
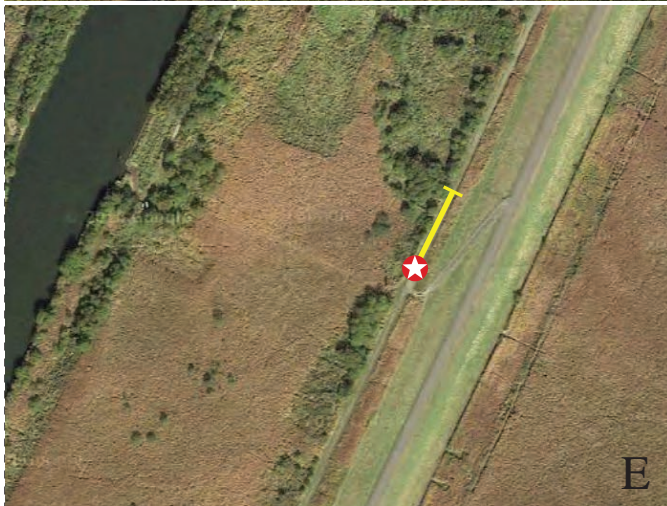
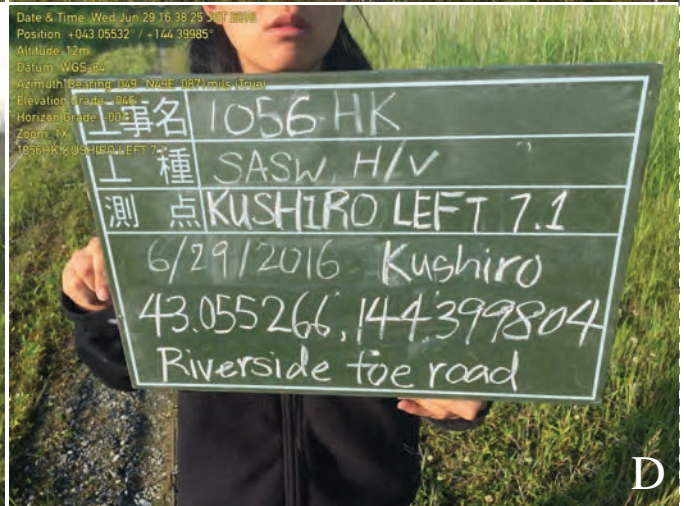
Surface wave test site 1053HK located inside the Tokachi River left bank levee, location L8.8, 37 km SE of Obihiro, Hokkaido, Japan (lat 42.72905, long 143.60495). A) view southward from the shaker to the seismometer array; B) view northward toward the shaker; C) view to the north from the shaker; D) site information; E) satellite view of the local site, yellow bar is seismometer array; F) site location near Obihiro, Hokkaido, Japan.



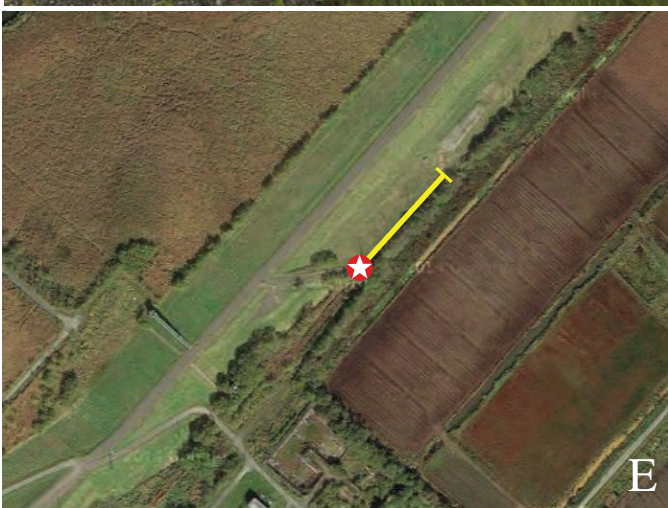
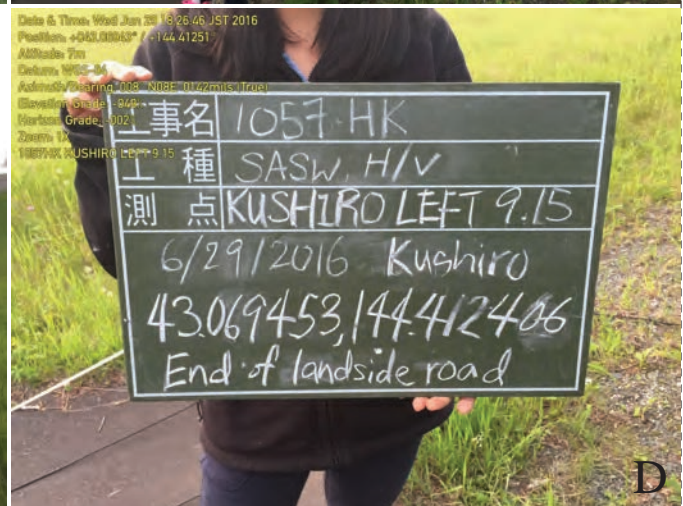
Surface wave test site 1054HK located outside the Urahoro left bank levee, location L -0.2, 41 km SE of Obihiro (lat 42.743, long 143.67023). A) view southeast from the shaker to the seismometer array; B) view north from the shaker location; C) another view southeast from the shaker; D) site information; E) satellite view of the local site, yellow bar is seismometer array; F) site location near Obihiro, Hokkaido, Japan.



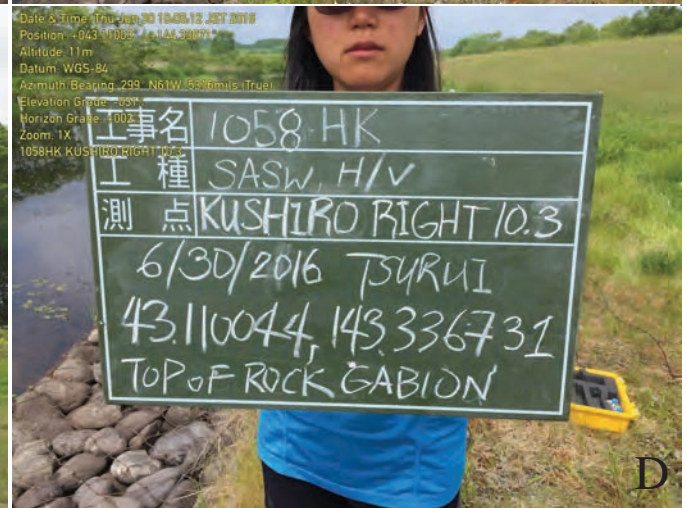
Surface wave test site 1055HK located 7 km north of Kushiro, Hokkaido, Japan (lat 43.08519, long 144.3782). A) view southeast from the shaker to the seismometer array; B) view northwest from the shaker location; C) another view northwest from the shaker; D) site information; E) satellite view of the local site, yellow bar is seismometer array; F) site location near Kushiro, Hokkaido, Japan.



Surface wave test site 1056HK located on the inside of 4 km north of Kushiro, Hokkaido, Japan (lat 43.05526, long144.39984). A) view northeast to the test site; B) view southwest toward the shaker location; C) another view southwest from the shaker; D) site information; E) satellite view of the local site, yellow bar is seismometer array; F) site location near Kushiro, Hokkaido, Japan.

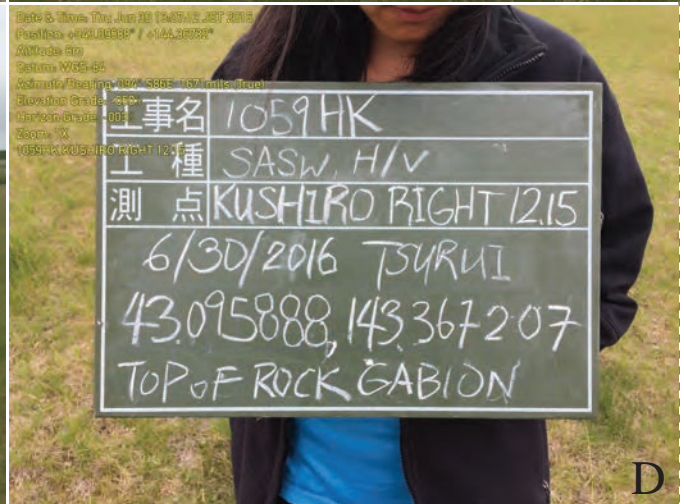


Surface wave test site 1057HK located outside the **xx** left bank dike 6 km NE of Kushiro, Hokkaido, Japan (lat 43.069453, long 144.412406). A) view northeast from the shaker to seismometer array; B) view north to the seismometer array; C) view southwest to the shaker location; D) site information; E) satellite view of the local site, yellow bar is seismometer array; F) site location near Kushiro, Hokkaido, Japan.

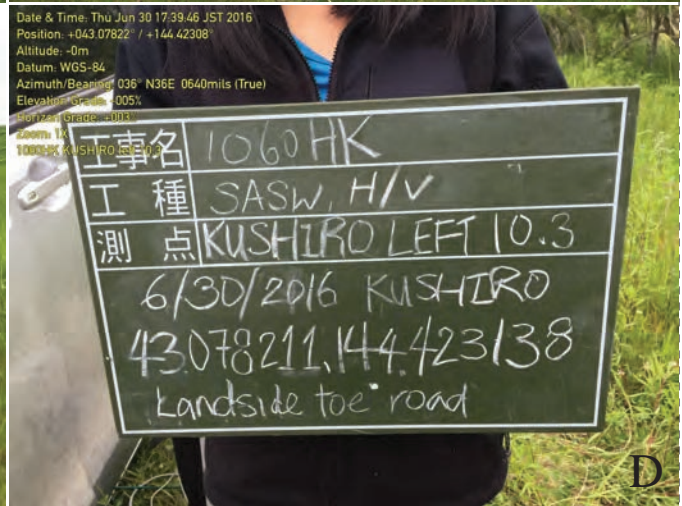


Surface wave test site 1058HK located 10 km north of Kushiro, Hokkaido, Japan (lat 43.11004, long 144.33671). A) view northwest to the shaker location; B) view southeast from near the shaker; C) view southward across the test site; D) site information; E) satellite view of the local site, yellow bar is seismometer array; F) site location near Kushiro, Hokkaido, Japan.

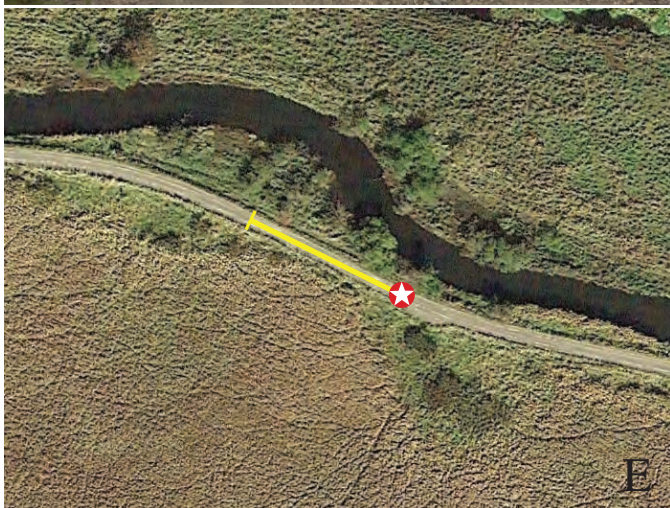




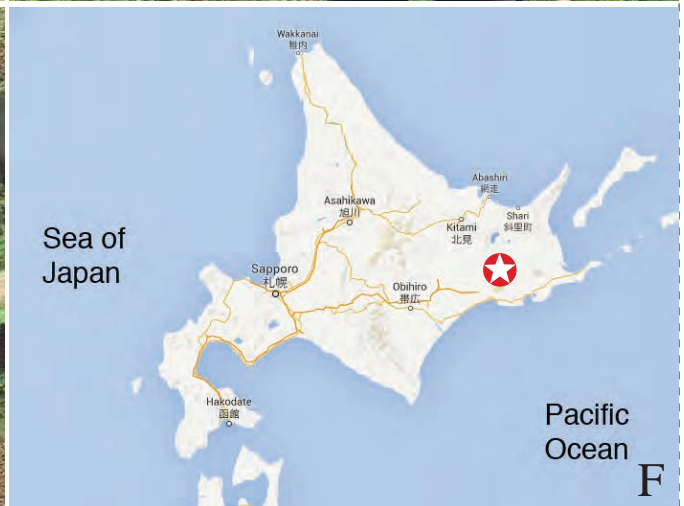
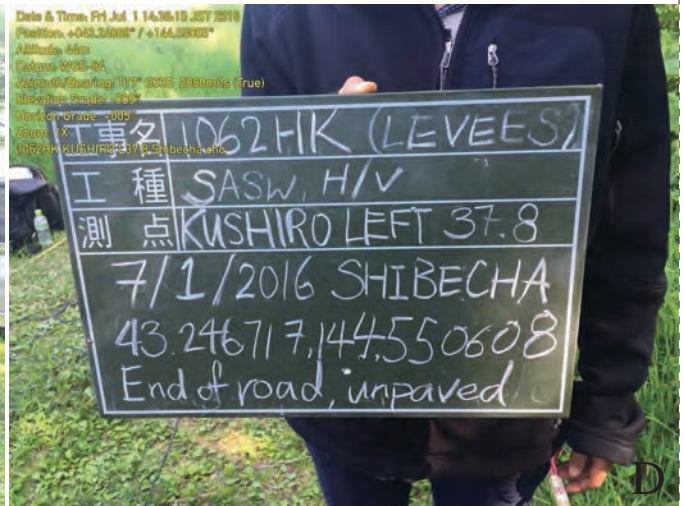
Surface wave test site 1059HK located 8 km north of Kushiro, Hokkaido, Japan (lat 43.09583, long 144.36730). A) view southeast from the shaker; B) view northwest toward the seismometer array; C) view west across the test site; D) site information; E) satellite view of the local site, yellow bar is seismometer array; F) site location near Kushiro, Hokkaido, Japan.



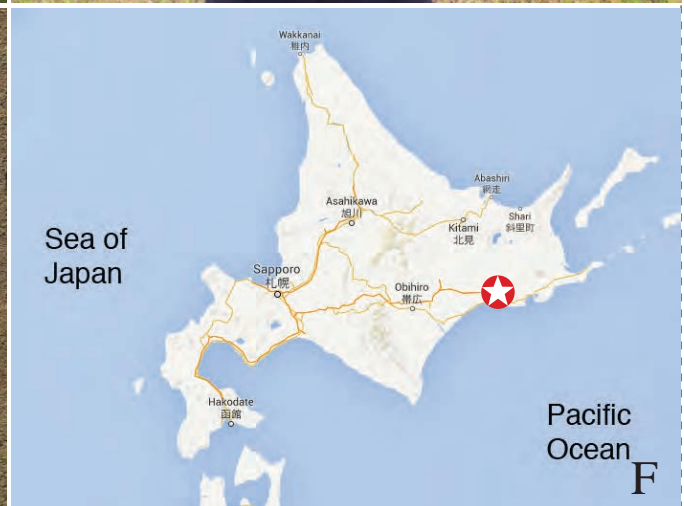
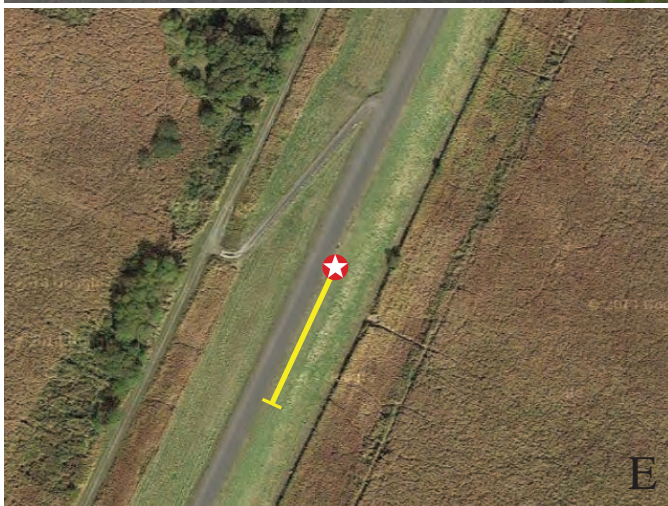
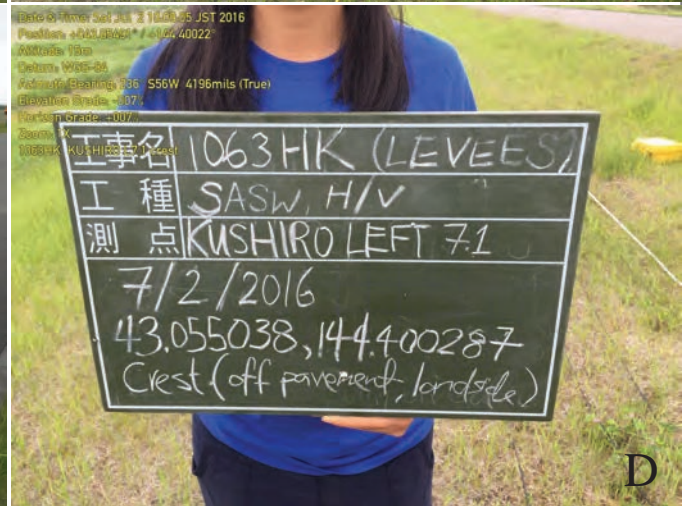
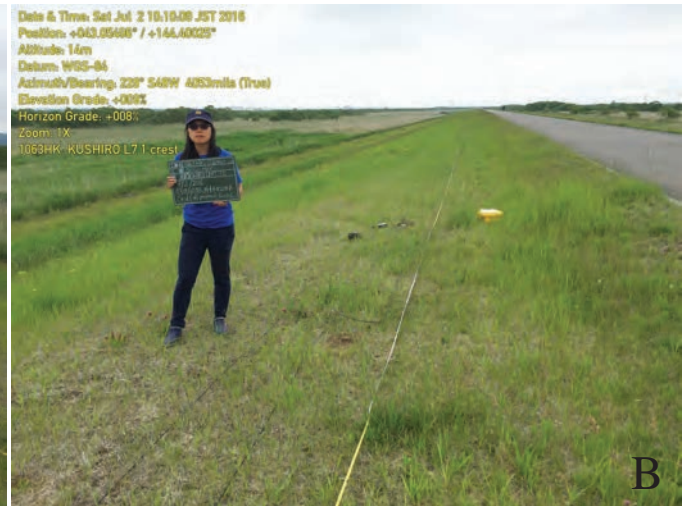
Surface wave test site 1060HK located about 6 km north of Kushiro, Hokkaido, Japan (lat 42.07822, long 144.4231). A) view northeast from the shaker; B) view southwestward toward the shaker; C) another view southwest toward the shaker; D) site information; E) satellite view of the local site, yellow bar is seismometer array; F) site location near Kushiro, Hokkaido, Japan.



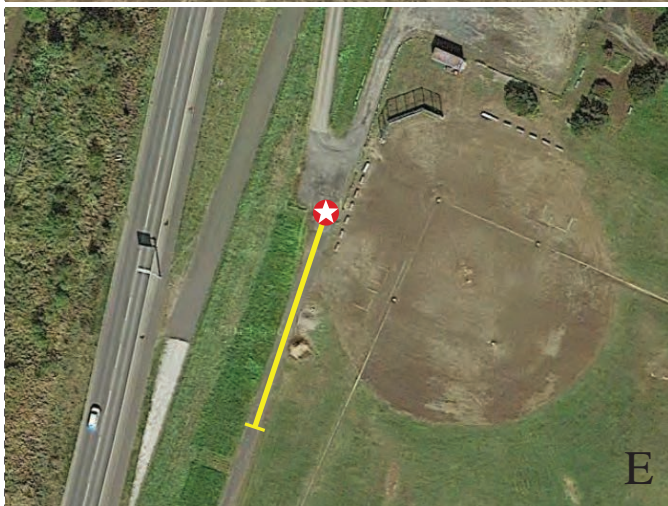
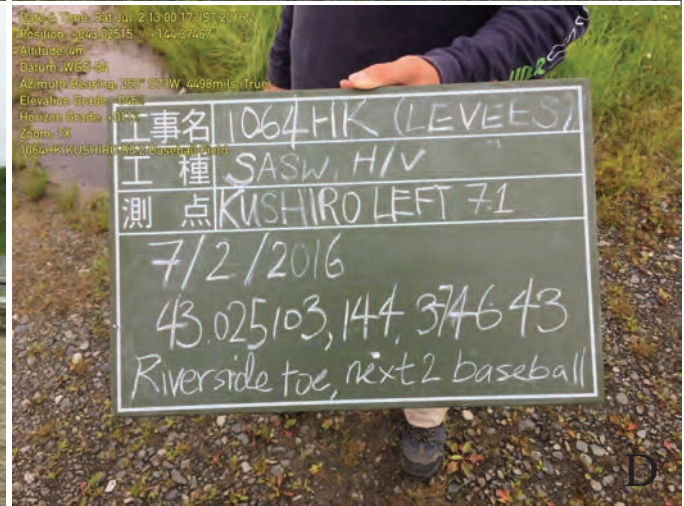
Surface wave test site 1061HK located 5 km north of Kushiro, Hokkaido, Japan (lat 43.073835, long 144.396618). A) view northwest from the shaker toward the seismometer array; B) view eastward from near the shaker; C) another view northwestward to the test site; D) site information; E) satellite view of the local site, yellow bar is seismometer array; F) site location near Kushiro, Hokkaido, Japan.



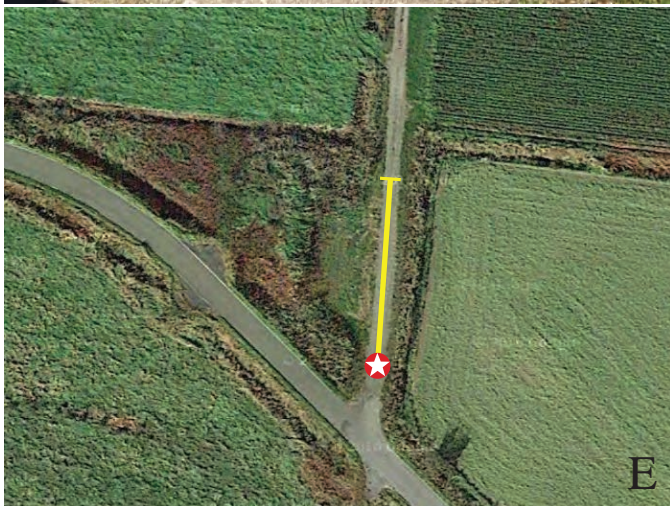
Surface wave test site 1062HK located 28 km NE of Kushiro, Hokkaido, Japan (lat 43.24672, long 144.55061). A) view northwest toward the shaker; B) view southeast from near the shaker; C) another view northwest at the test site; D) site information; E) satellite view of the local site, yellow bar is seismometer array; F) site location near Kushiro, Hokkaido, Japan.



Surface wave test site 1063HK located 3 km north of Kushiro, Hokkaido, Japan (lat 43.05511, long 144.40033). A) view southwest toward the shaker; B) view northeast from the the shaker; C) view northward from the test site; D) site information; E) satellite view of the local site, yellow bar is seismometer array; F) site location near Kushiro, Hokkaido, Japan.



Surface wave test site 1064HK located at northern Kurshiro, Hokkaido, Japan (lat 43.025103, long 144.374643). A) view north to the shaker; B) view south toward the seismometer array; C) view southwest to the test site; D) site information; E) satellite view of the local site, yellow bar is seismometer array; F) site location in Kushiro, Hokkaido, Japan.

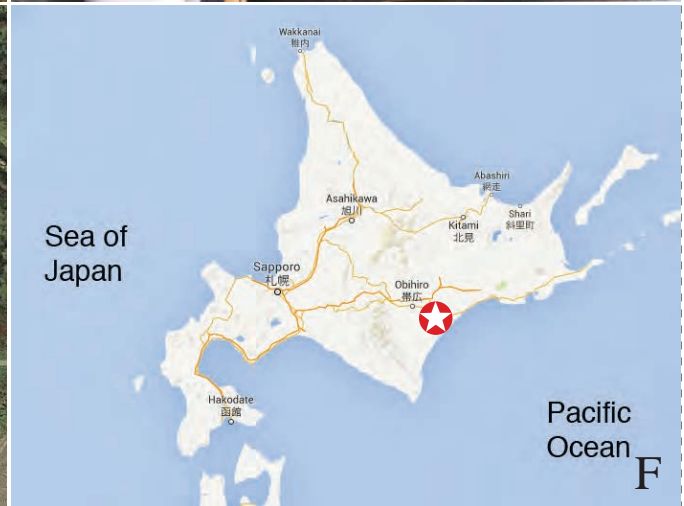
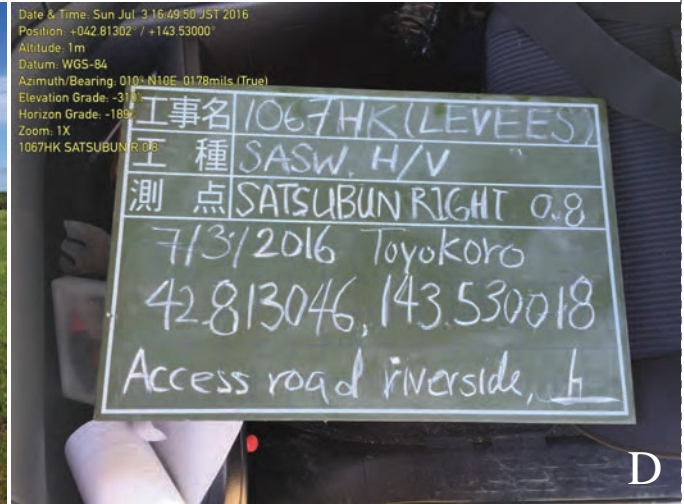


Surface wave test site 1065HK located 7 km SW of Urahoro, Hokkaido, Japan (lat 42.75003, long 143.60518). A) view south toward the shaker; B) view north toward the seismometer array; C) another view north from the shaker location; D) site information; E) satellite view of the local site, yellow bar is seismometer array; F) site location near Urahoro, Hokkaido, Japan.



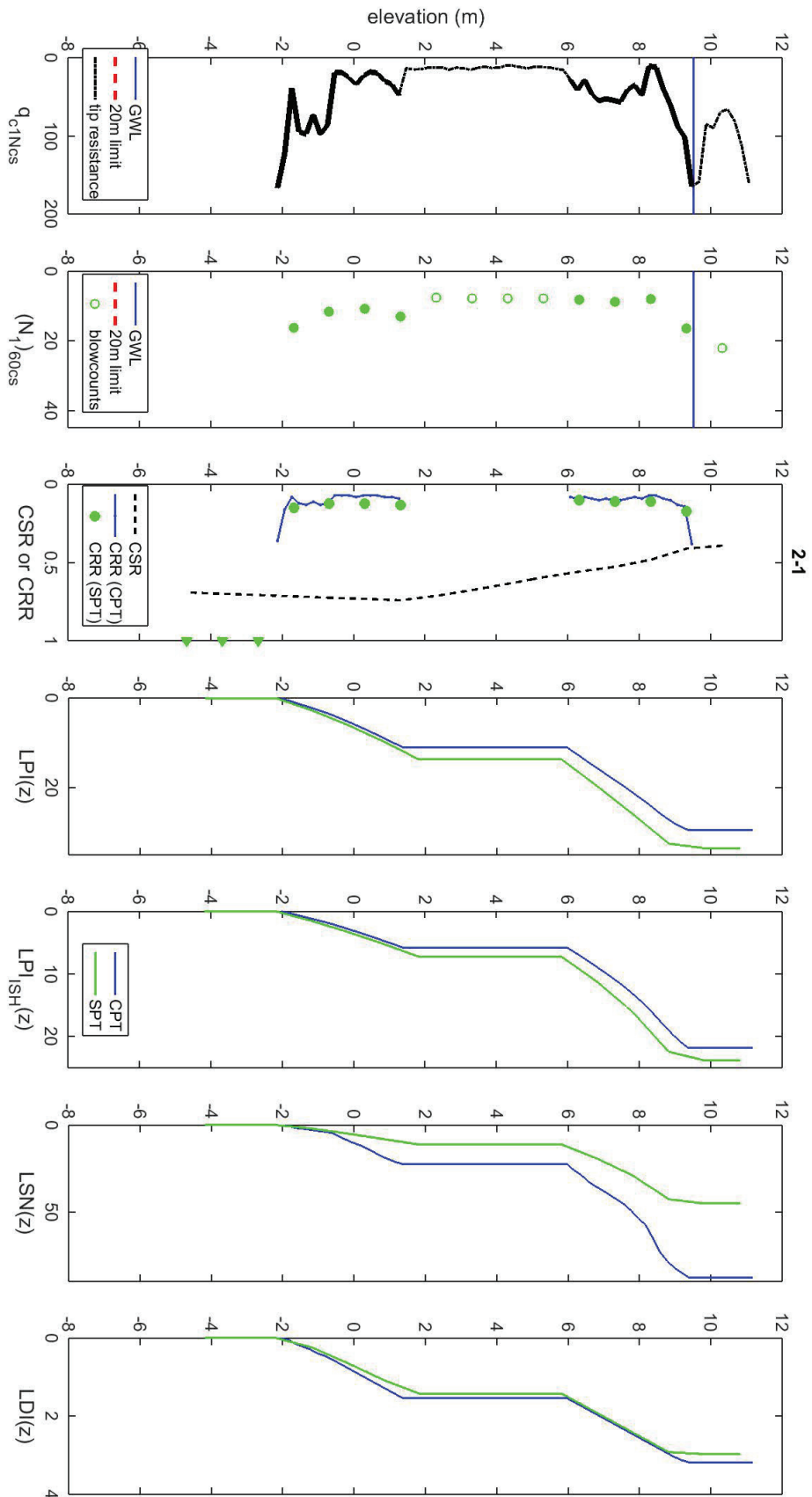
Surface wave test site 1066HK located inside the left bank levee of the Tokachi River near its mouth 11 km SW of Urahoro, Hokkaido, Japan (lat 42.70503, long 143.61595). A) view northwest from the shaker; B) view southeast toward the seismometer array; C) view north from the test site; D) site information; E) satellite view of the local site, yellow bar is seismometer array; F) site location near Urahoro, Hokkaido, Japan.

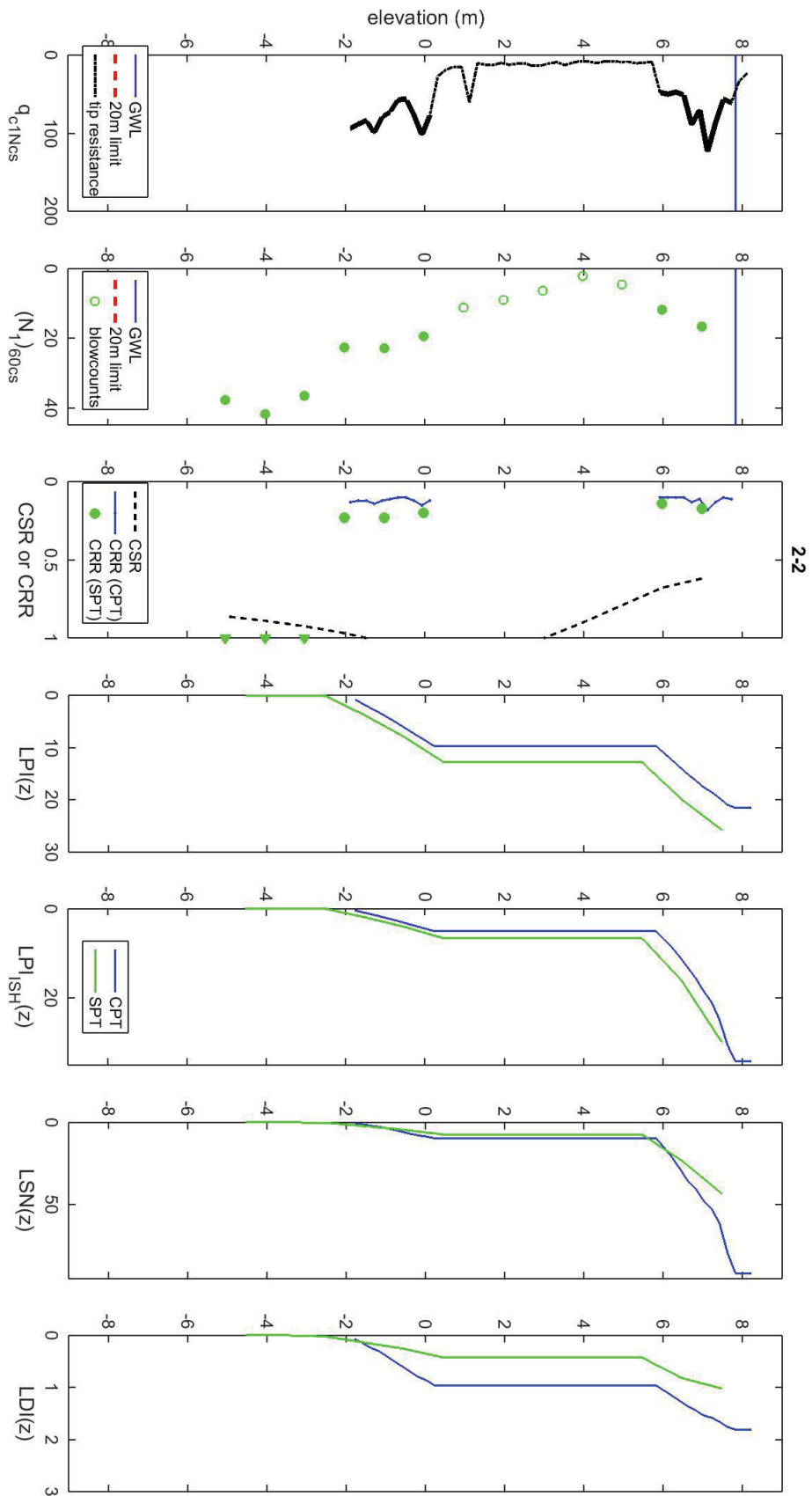


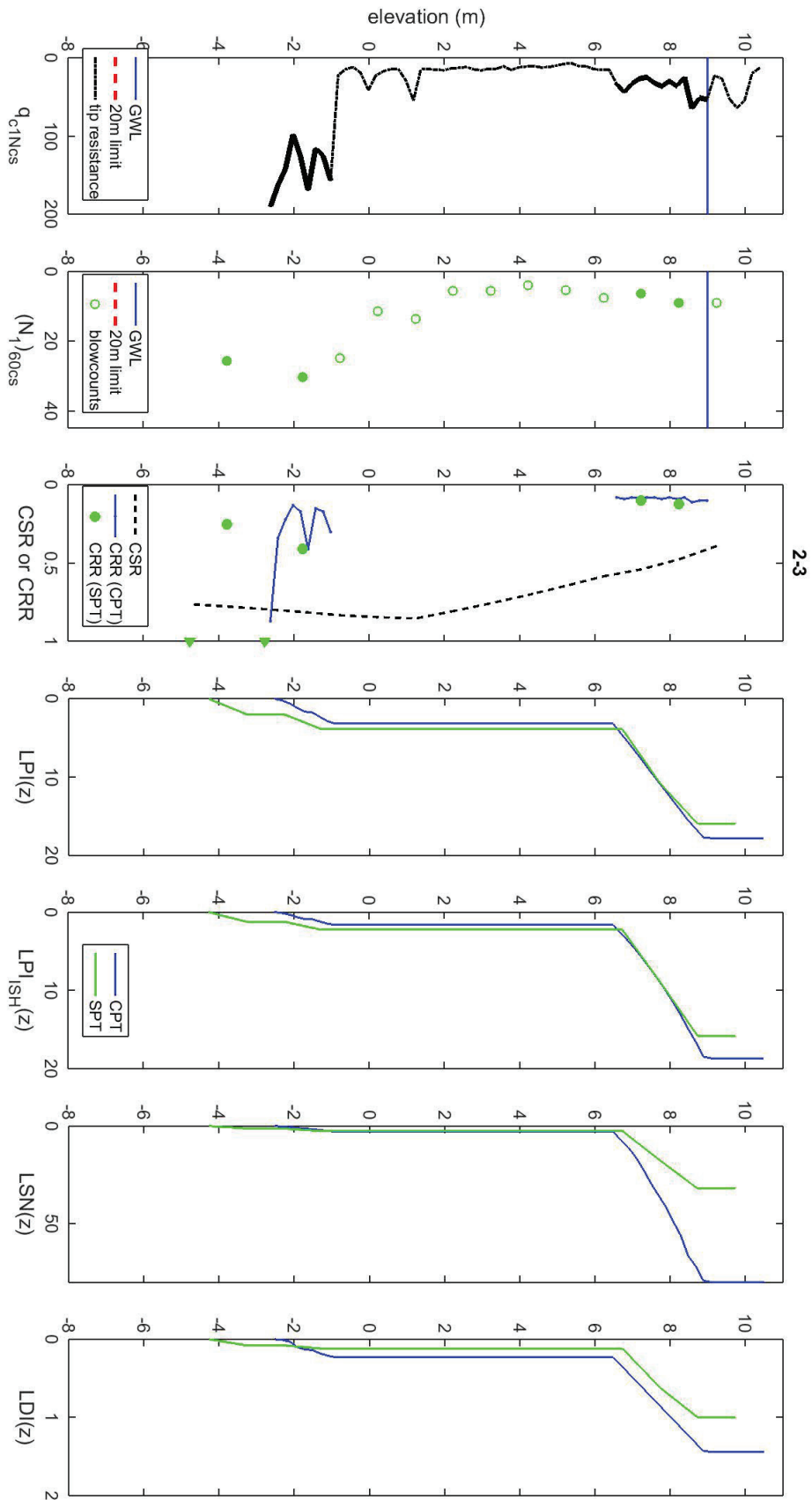


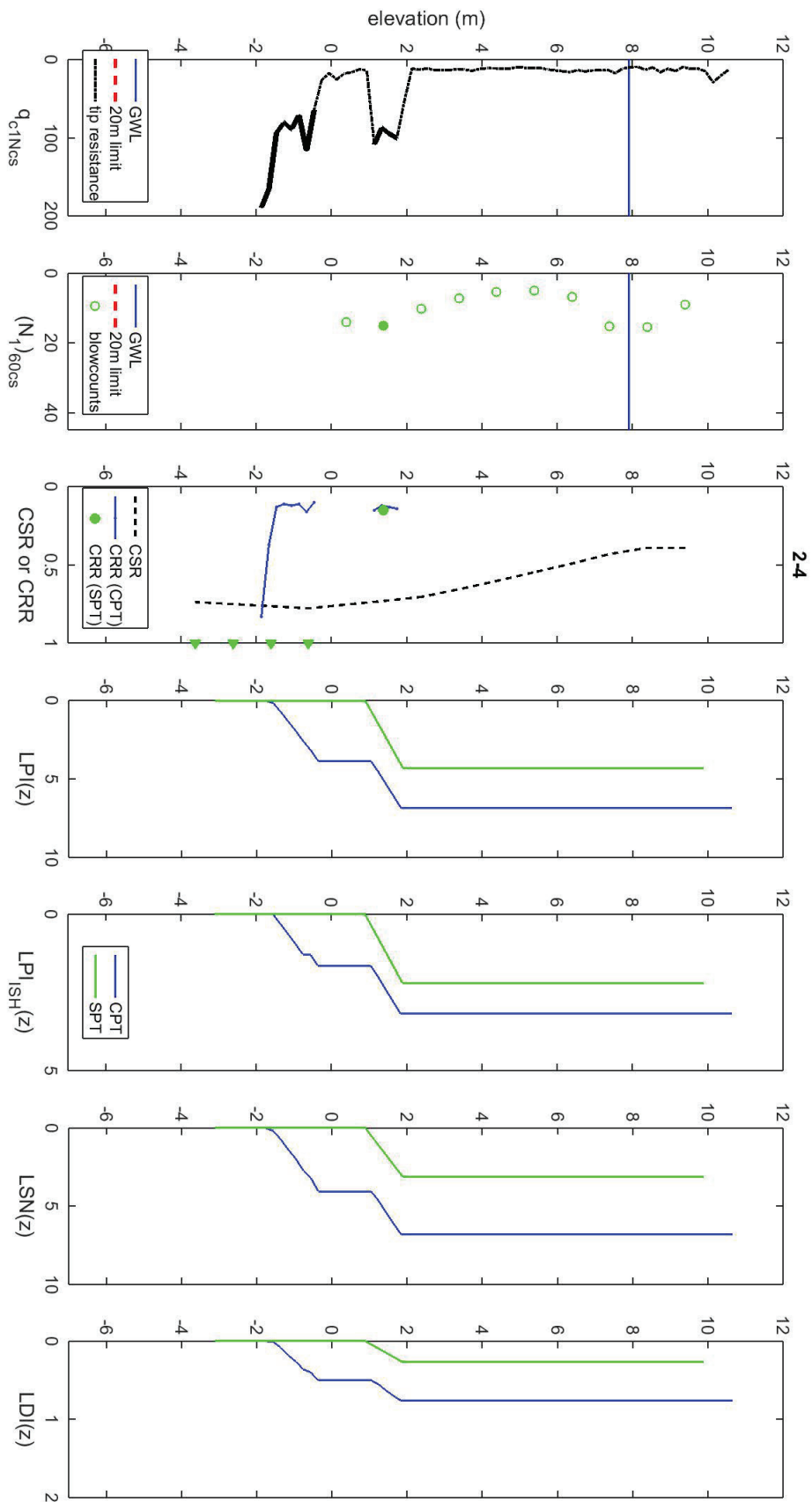
Surface wave test site 1067HK located 10 km west of Urahoro, Hokkaido, Japan (lat 42.81302, long 143.52979). A) view southeast from the shaker to the seismometer array; B) view northwest toward the shaker; C) another view southeast across the test site; D) site information; E) satellite view of the local site, yellow bar is seismometer array; F) site location near Urahoro, Hokkaido, Japan.

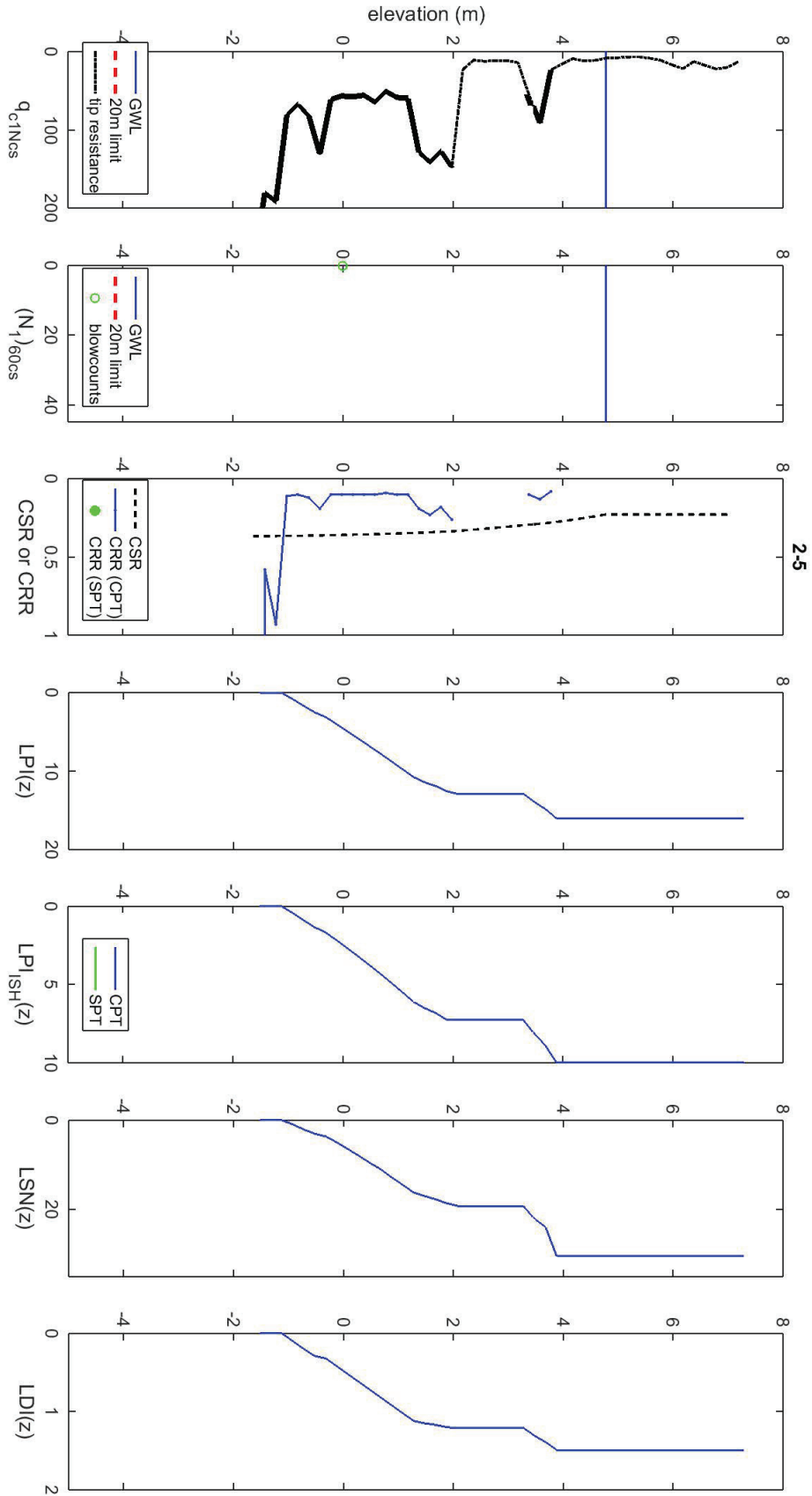
## **APPENDIX B: LIQUEFACTION SEVERITY INDICES AND 2-D MODELS**

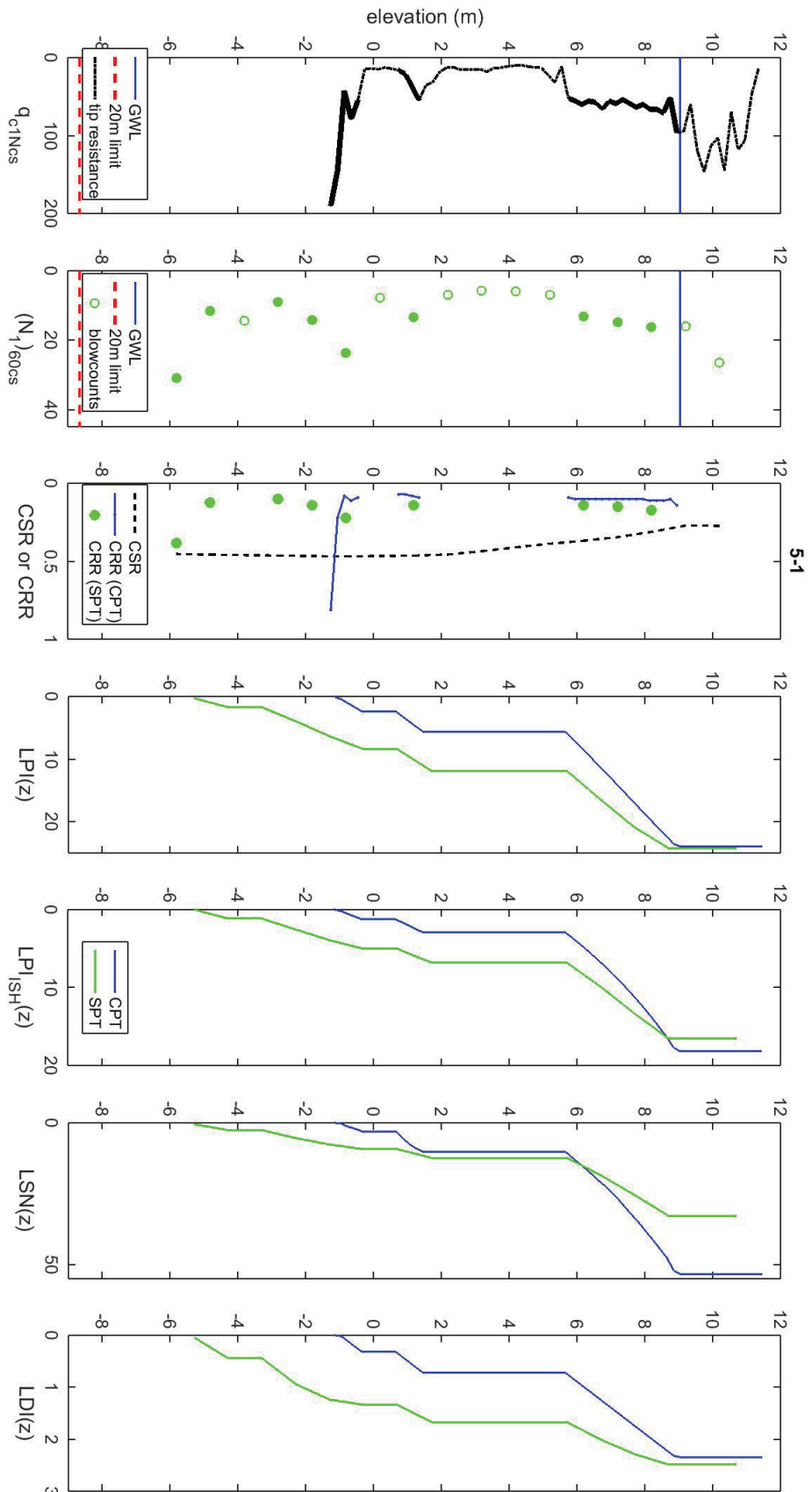




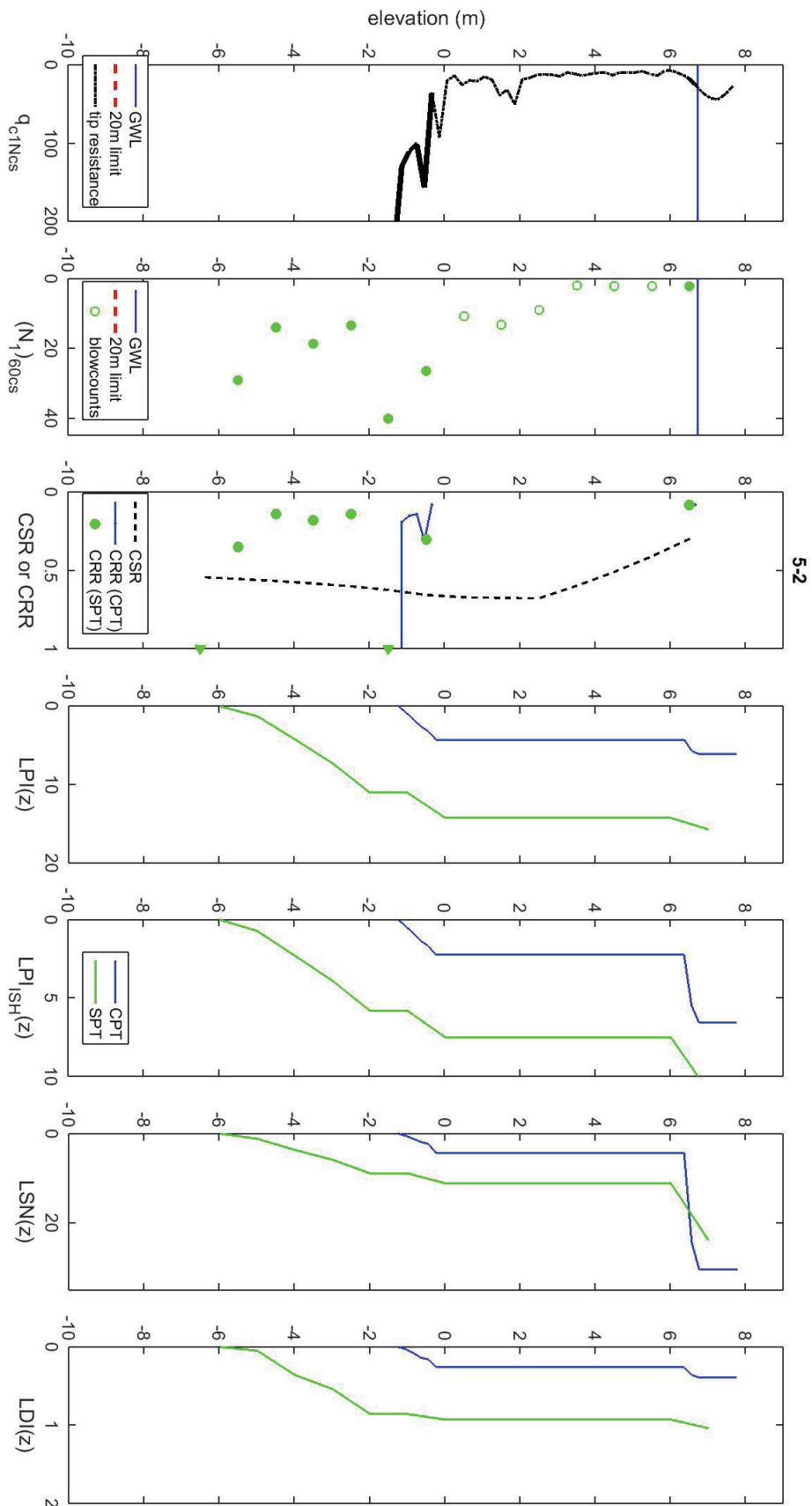




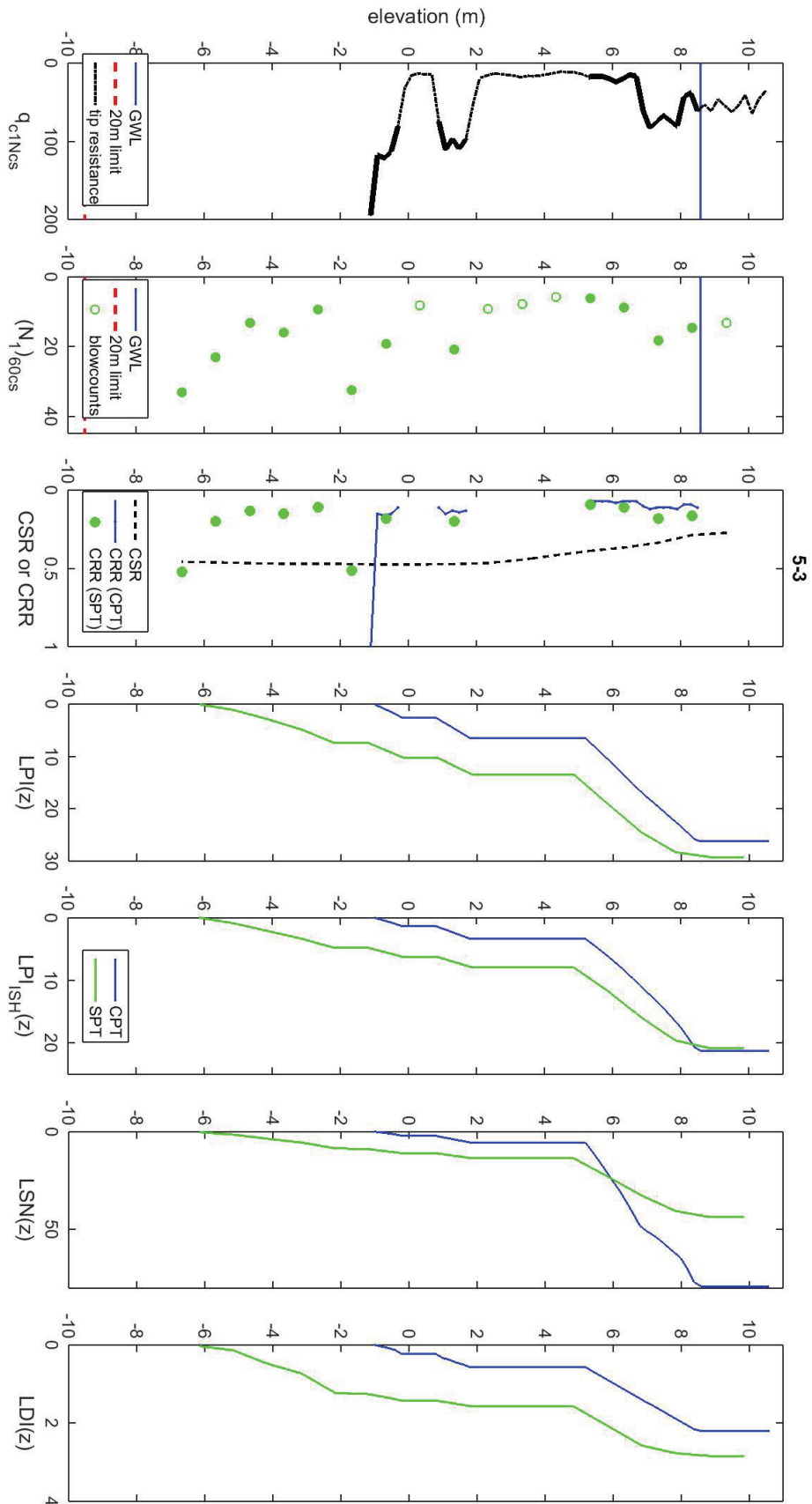




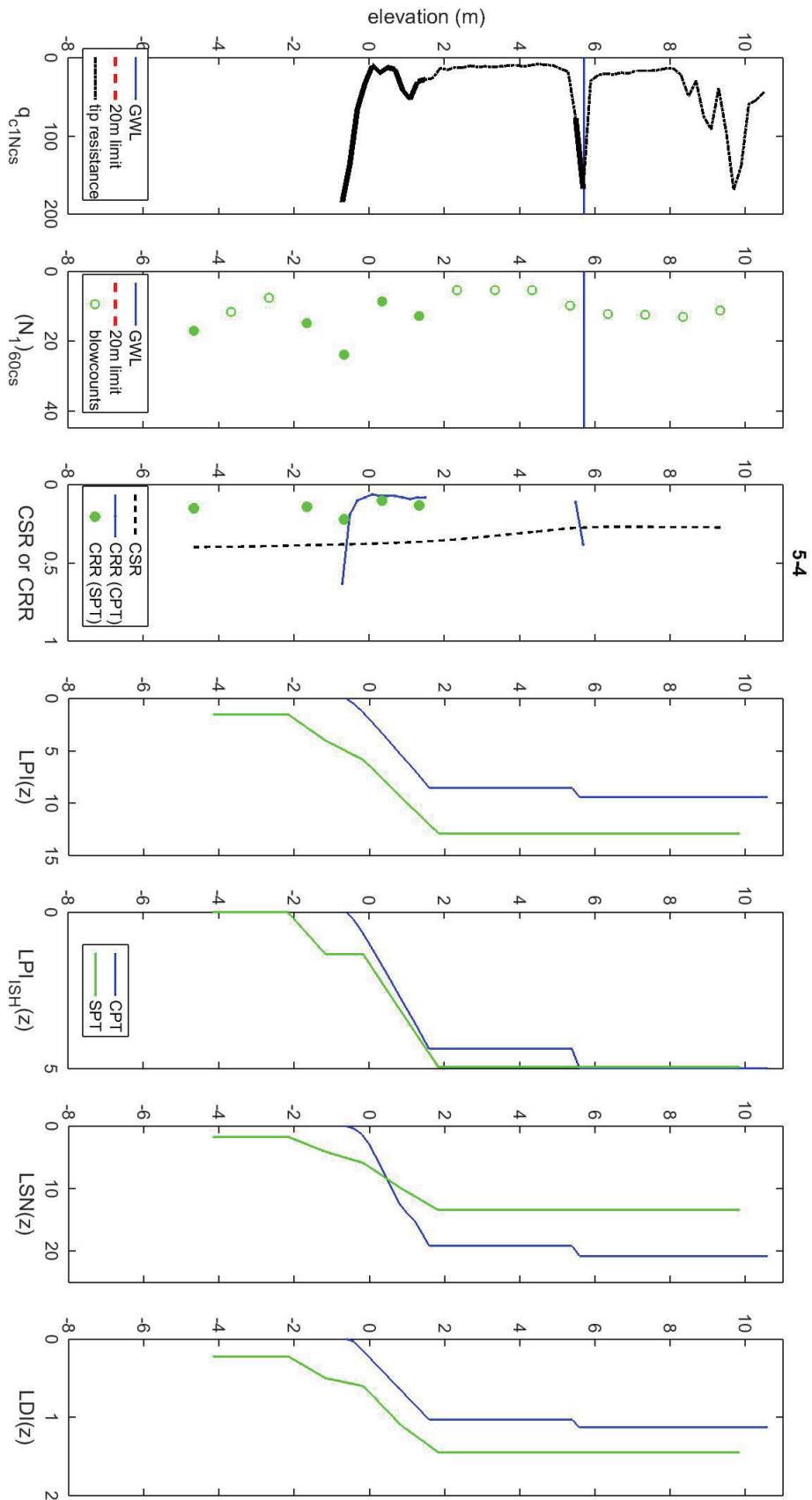




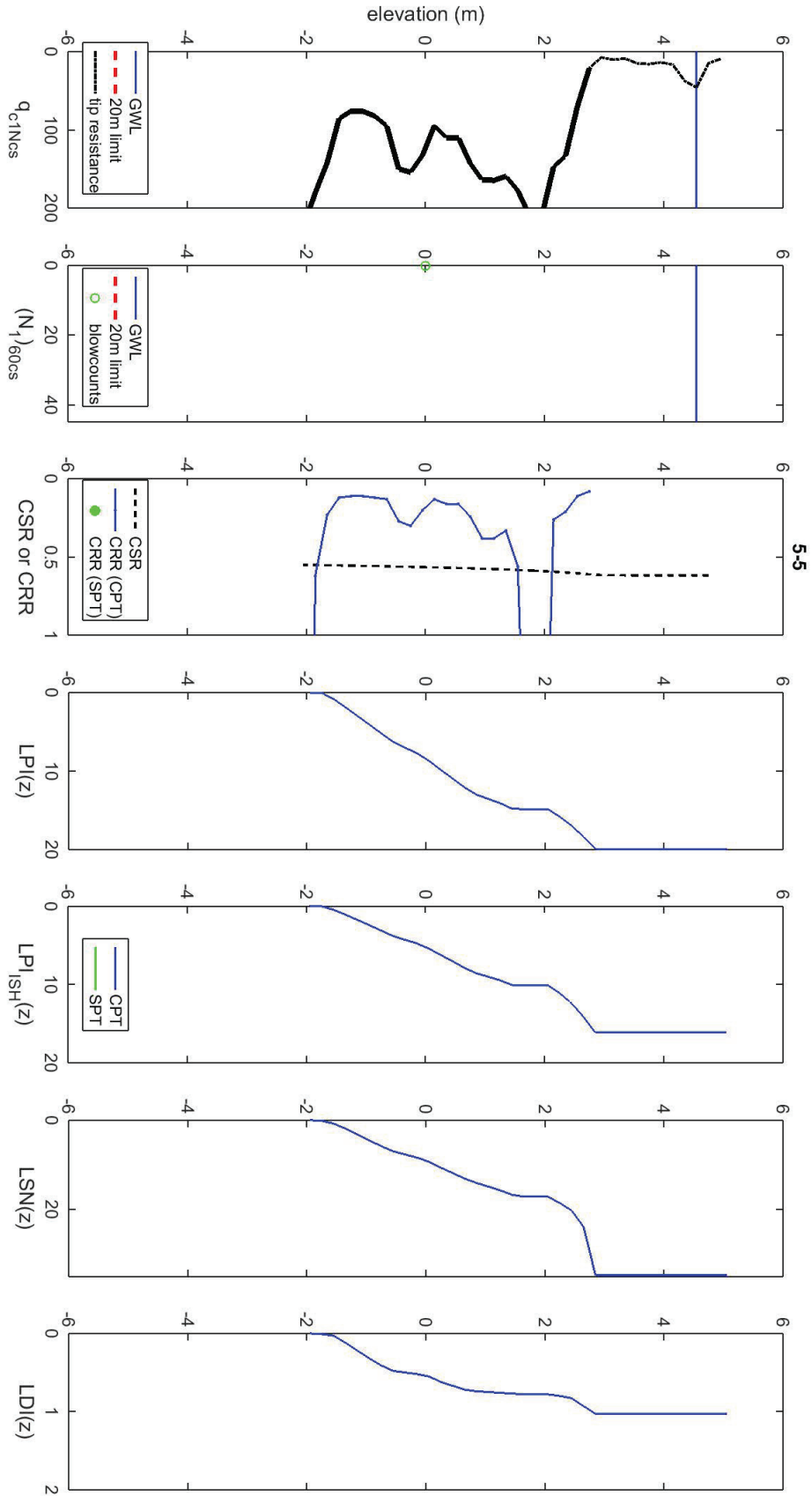
5-2

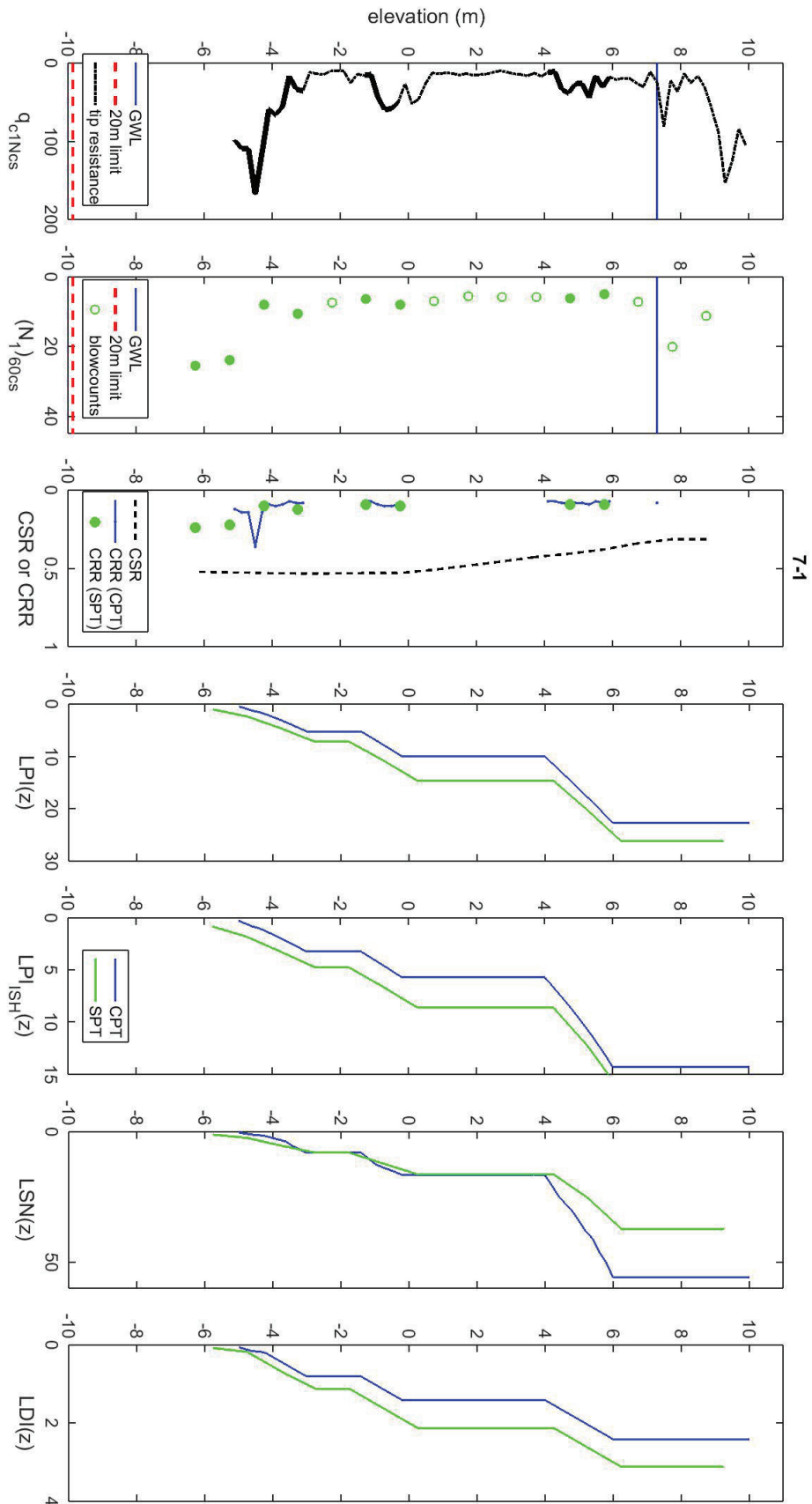


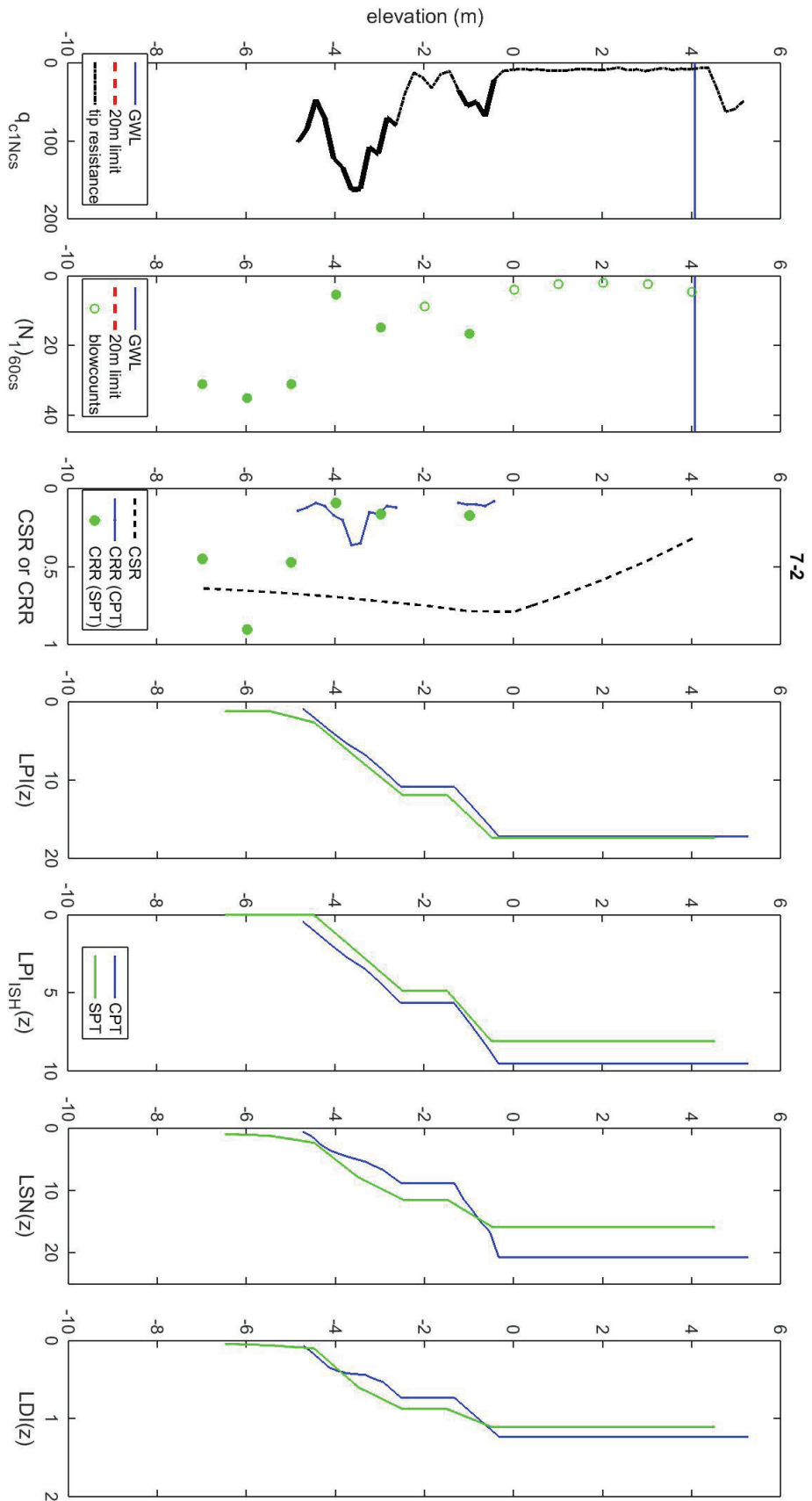
5-3

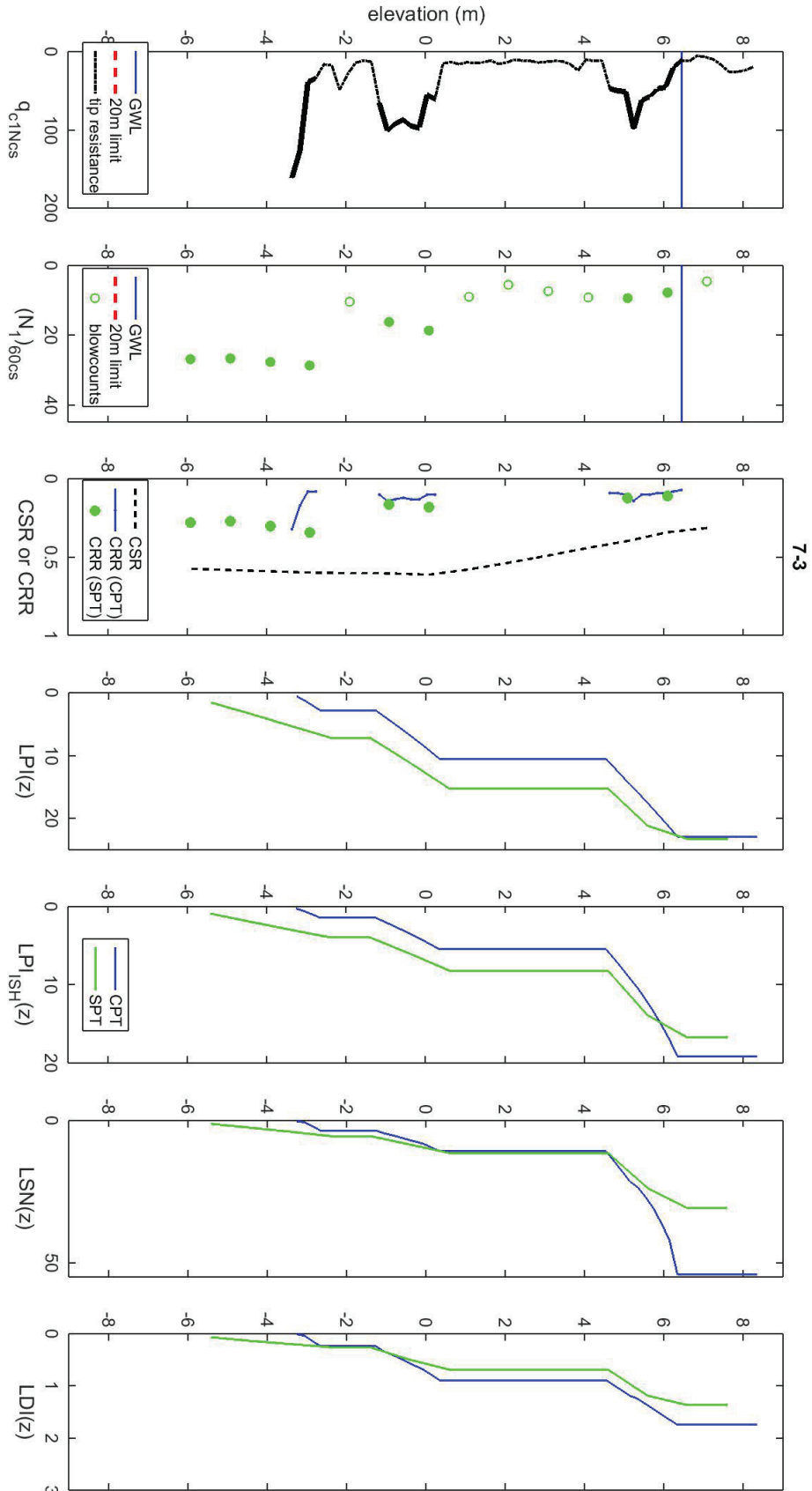


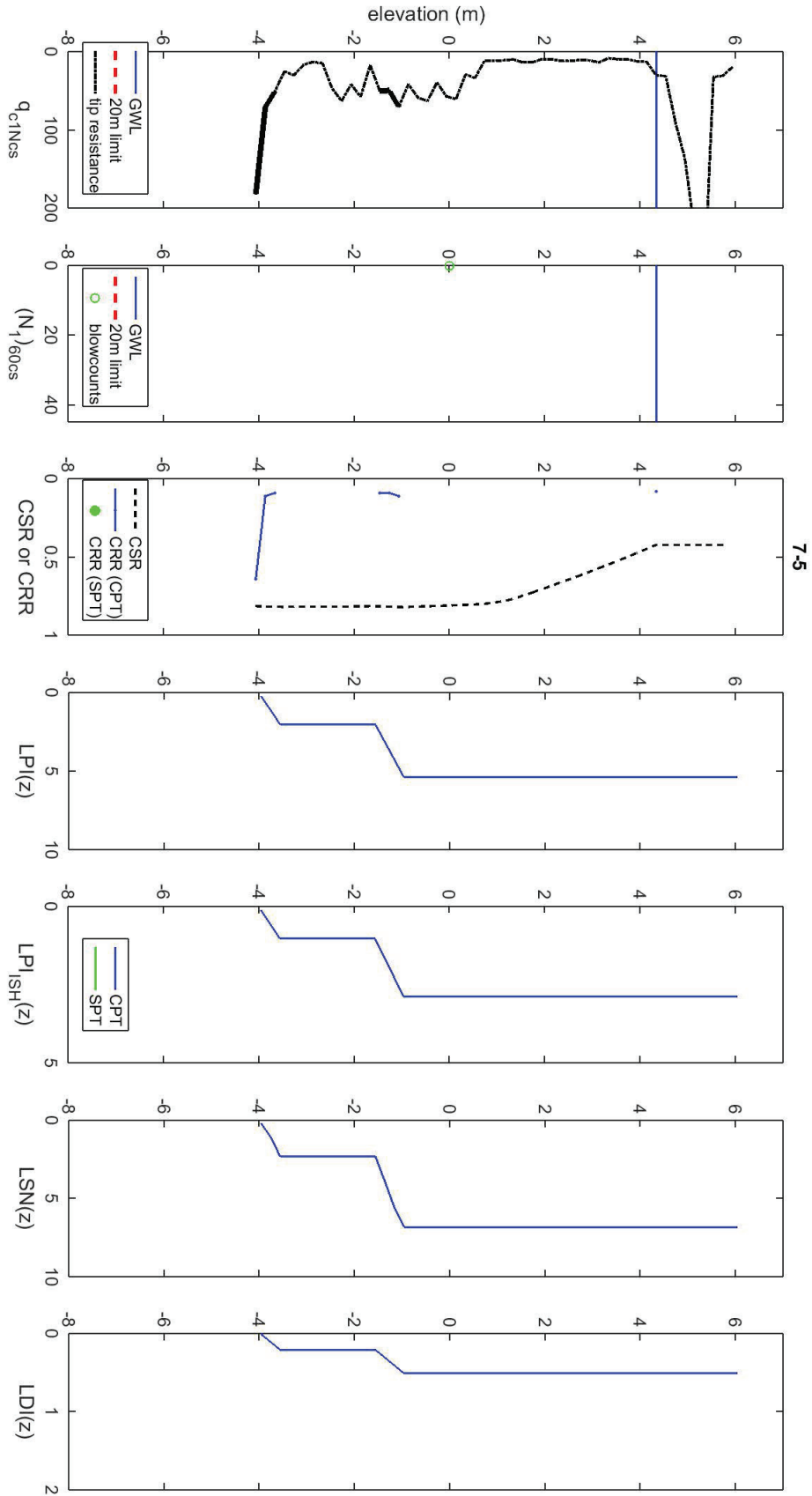
5-4



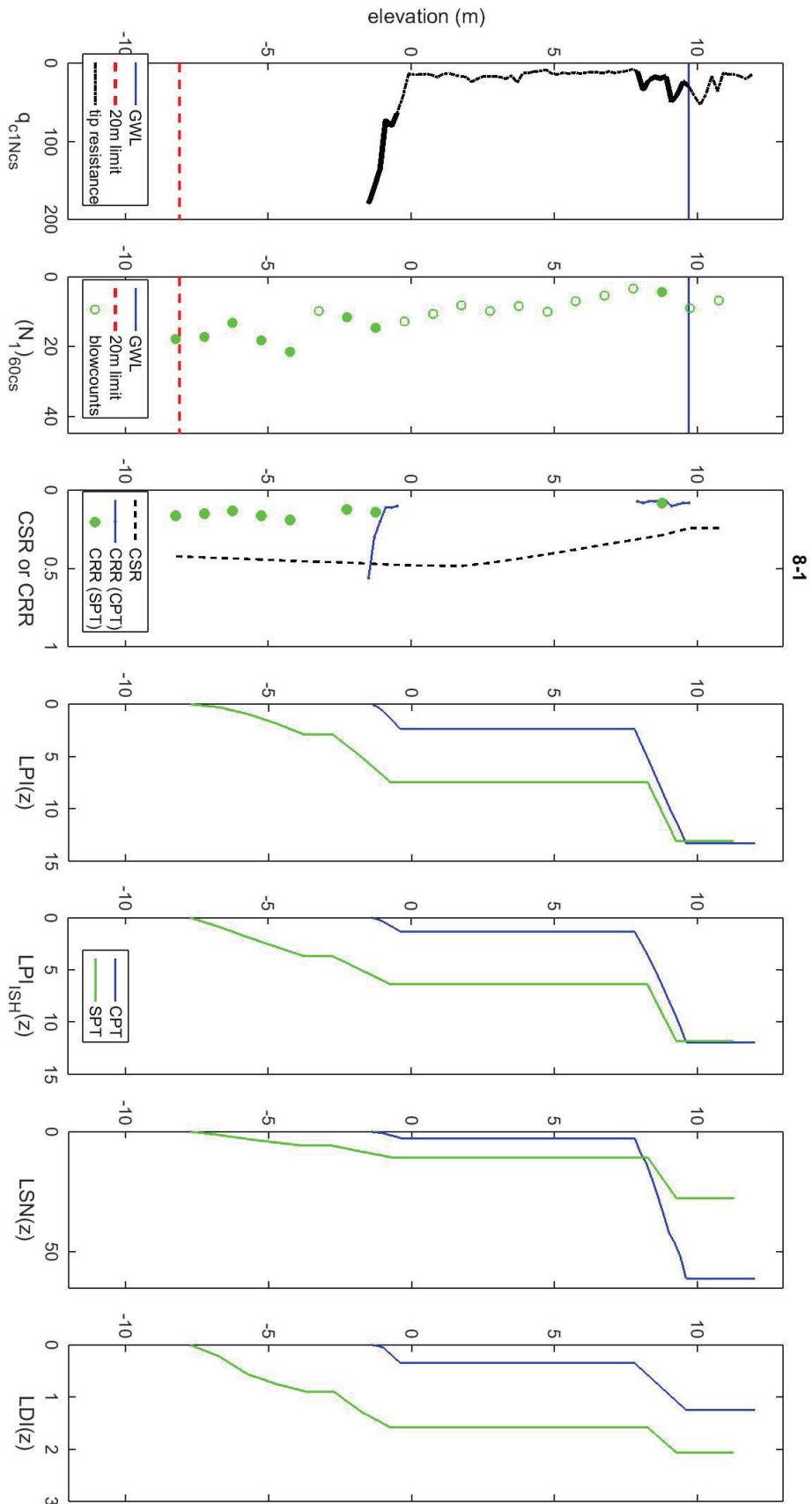


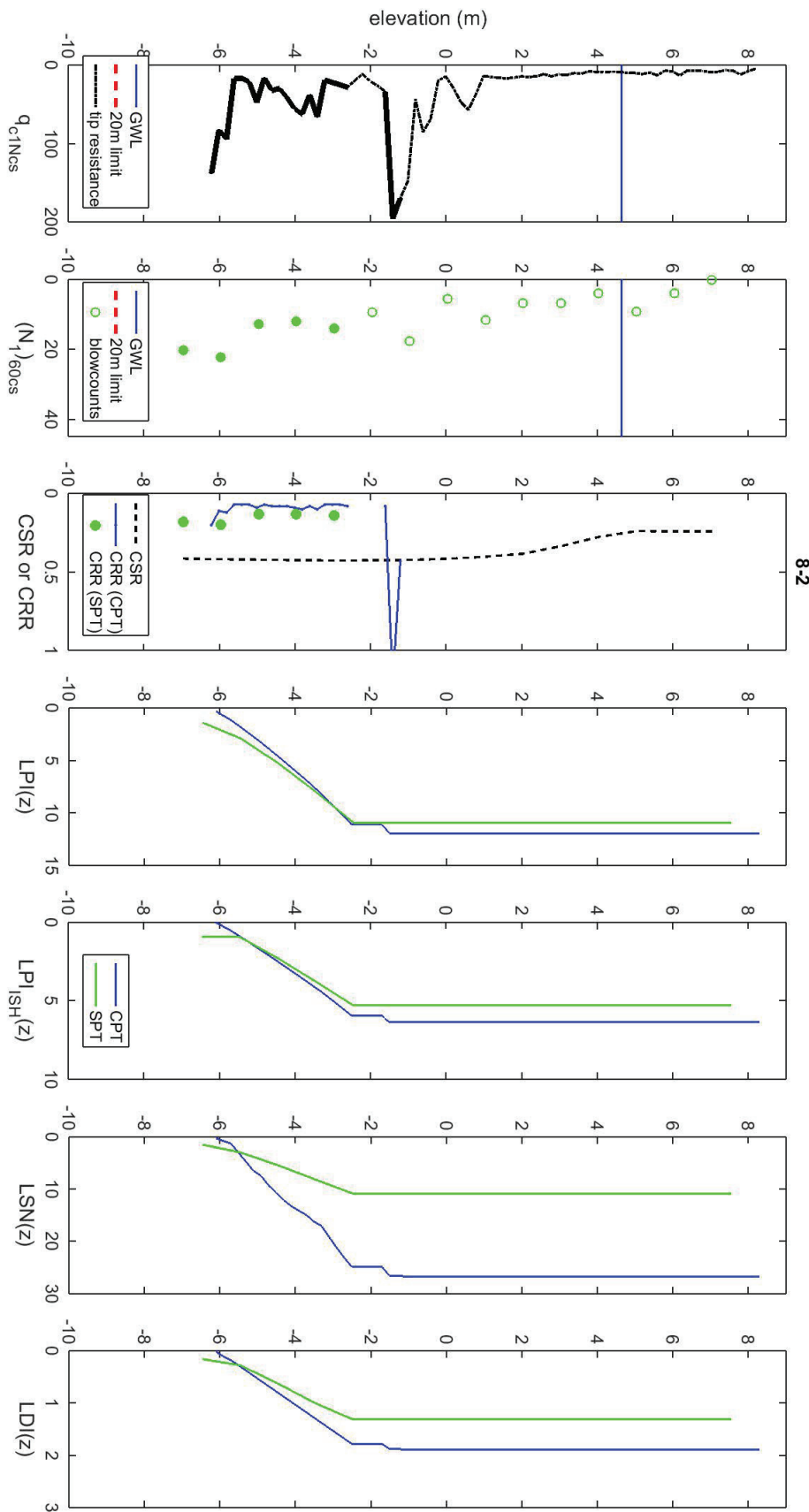




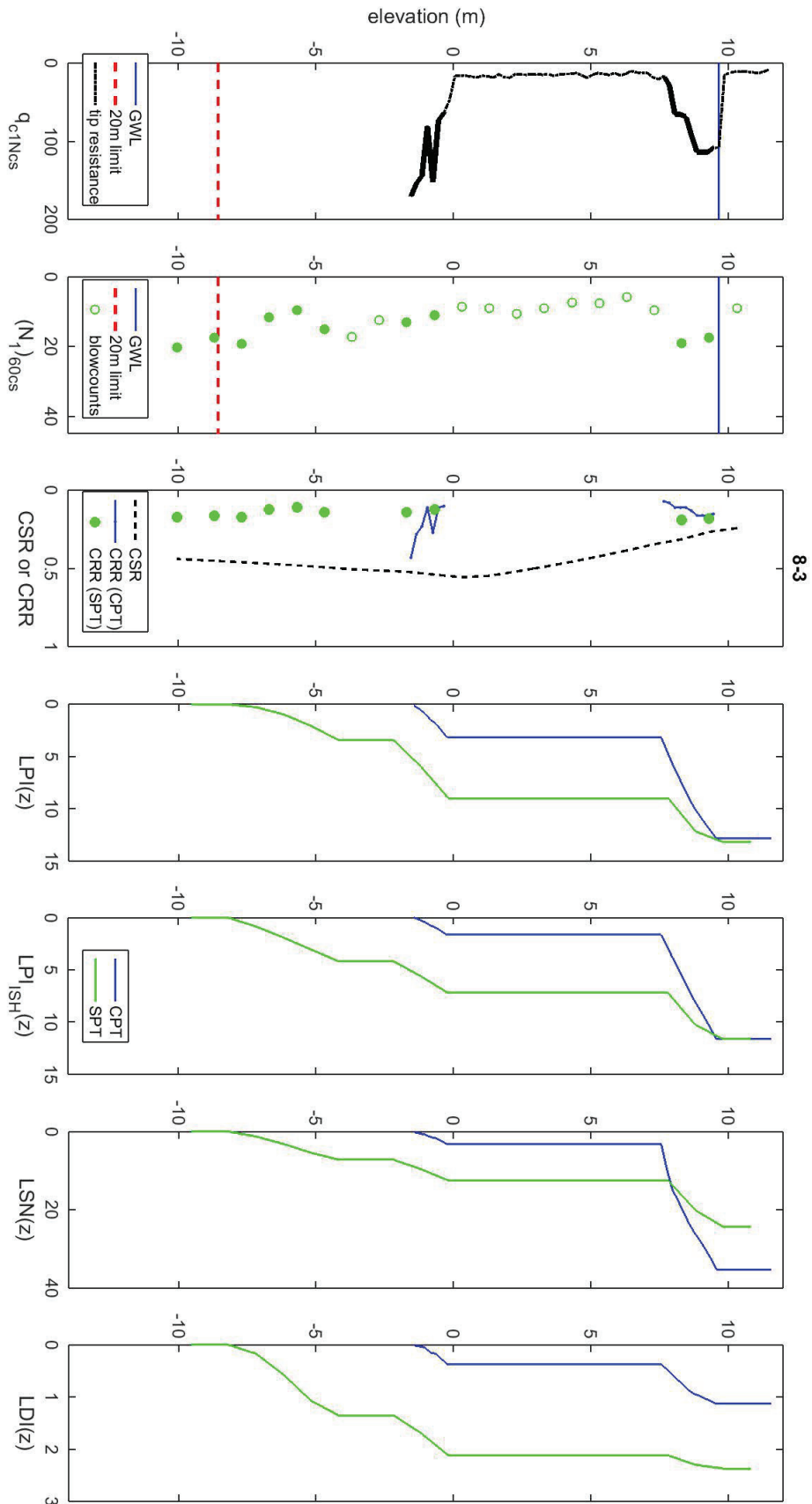


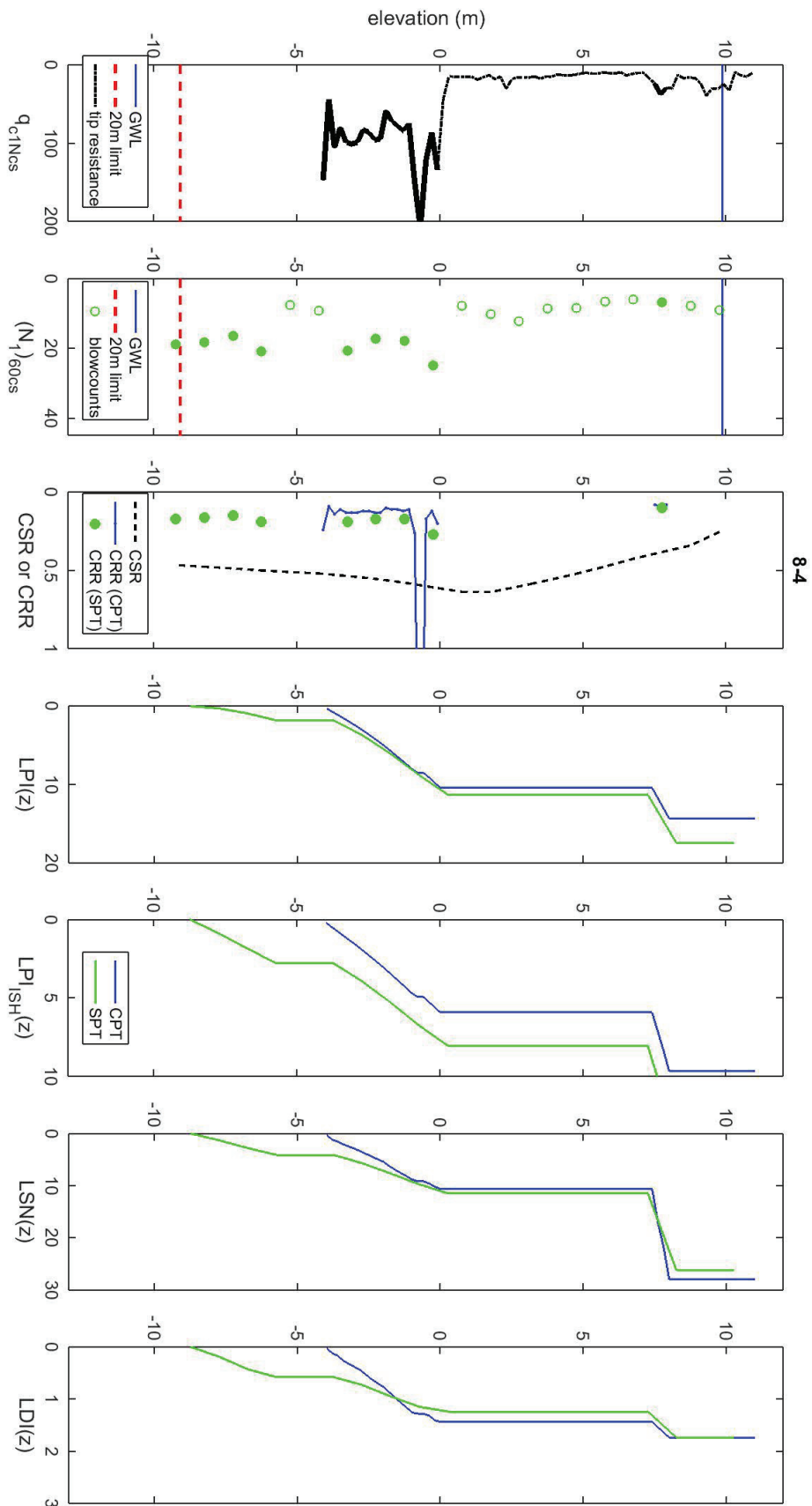


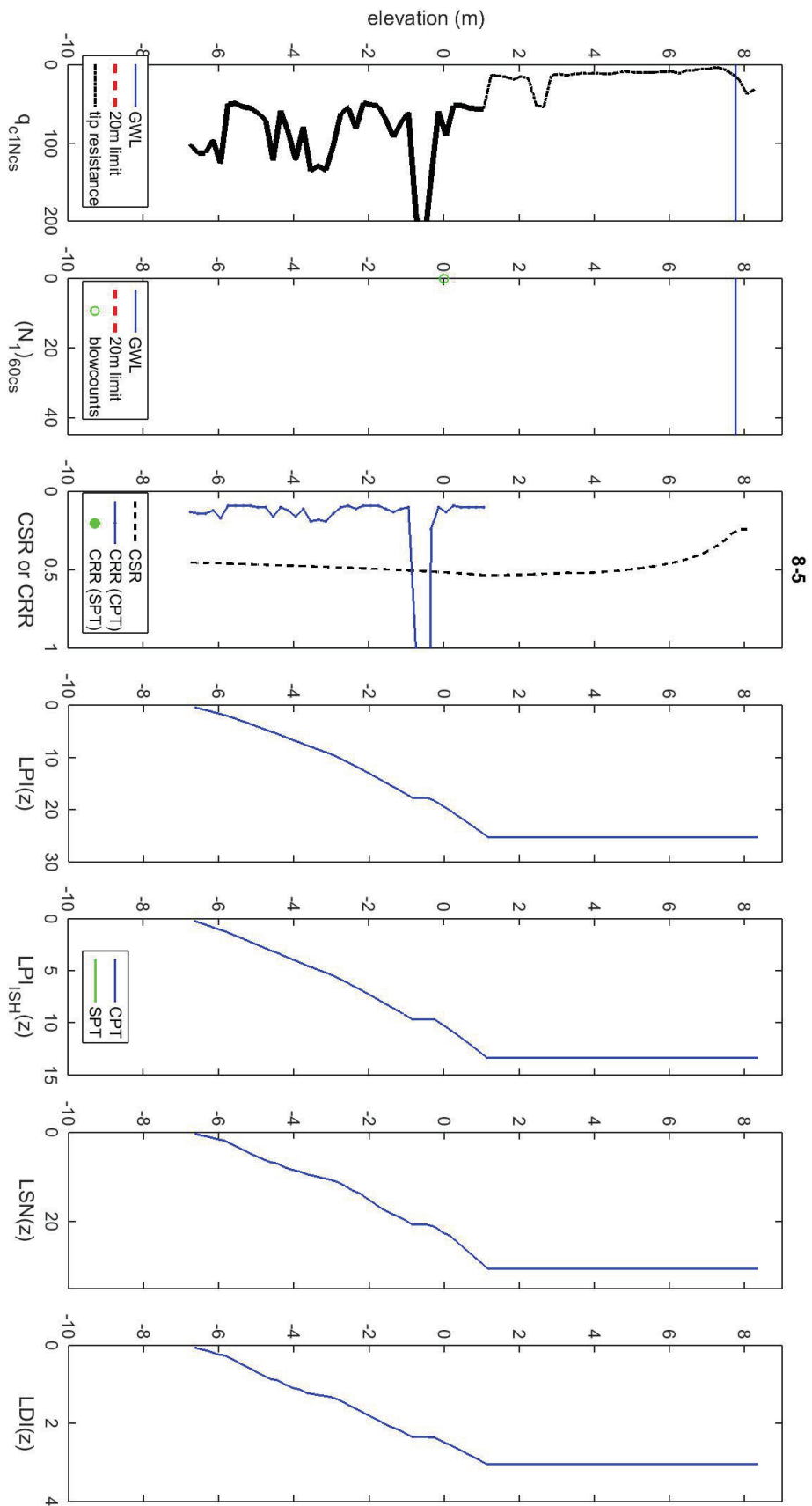


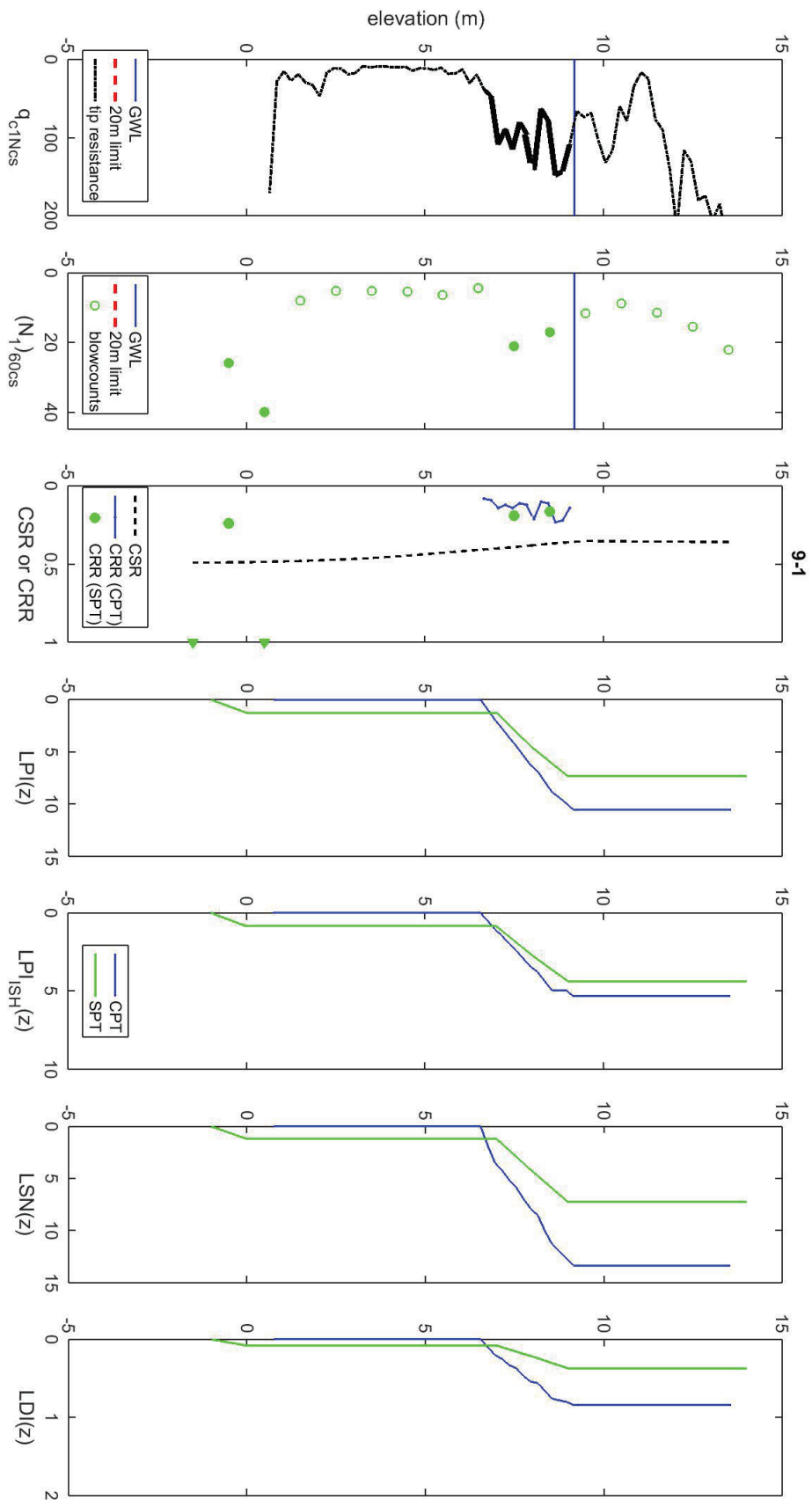


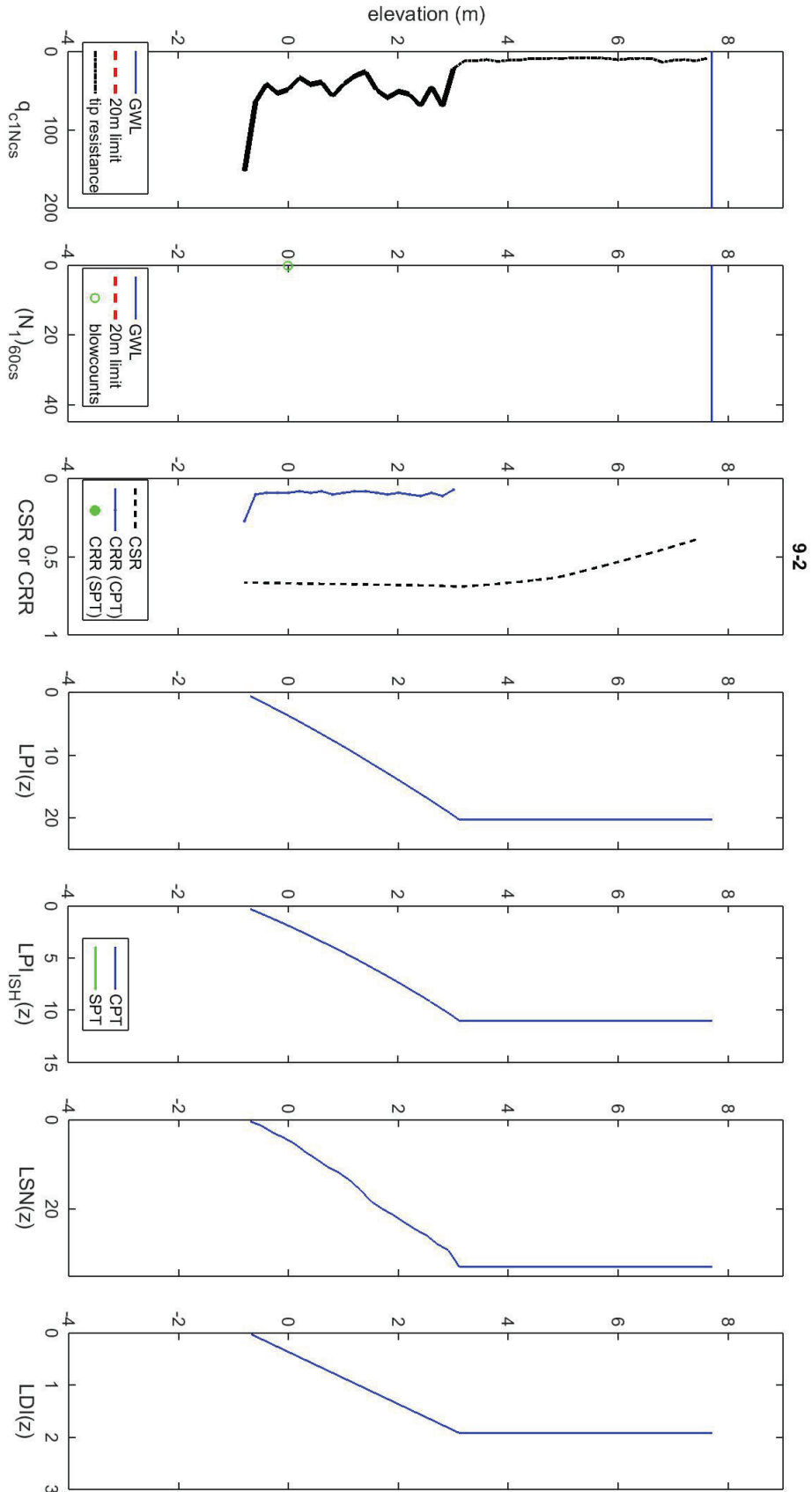
8-2

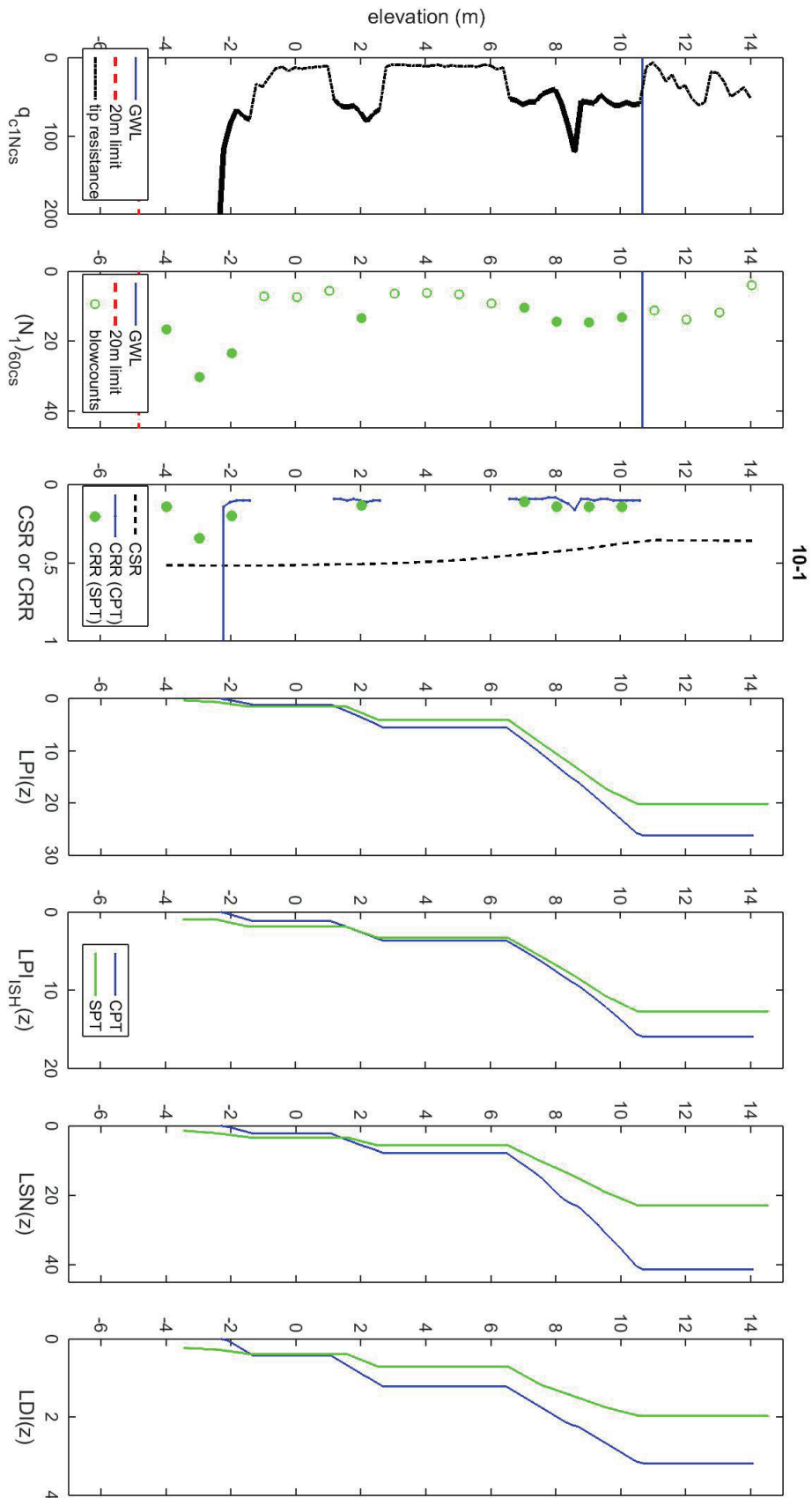




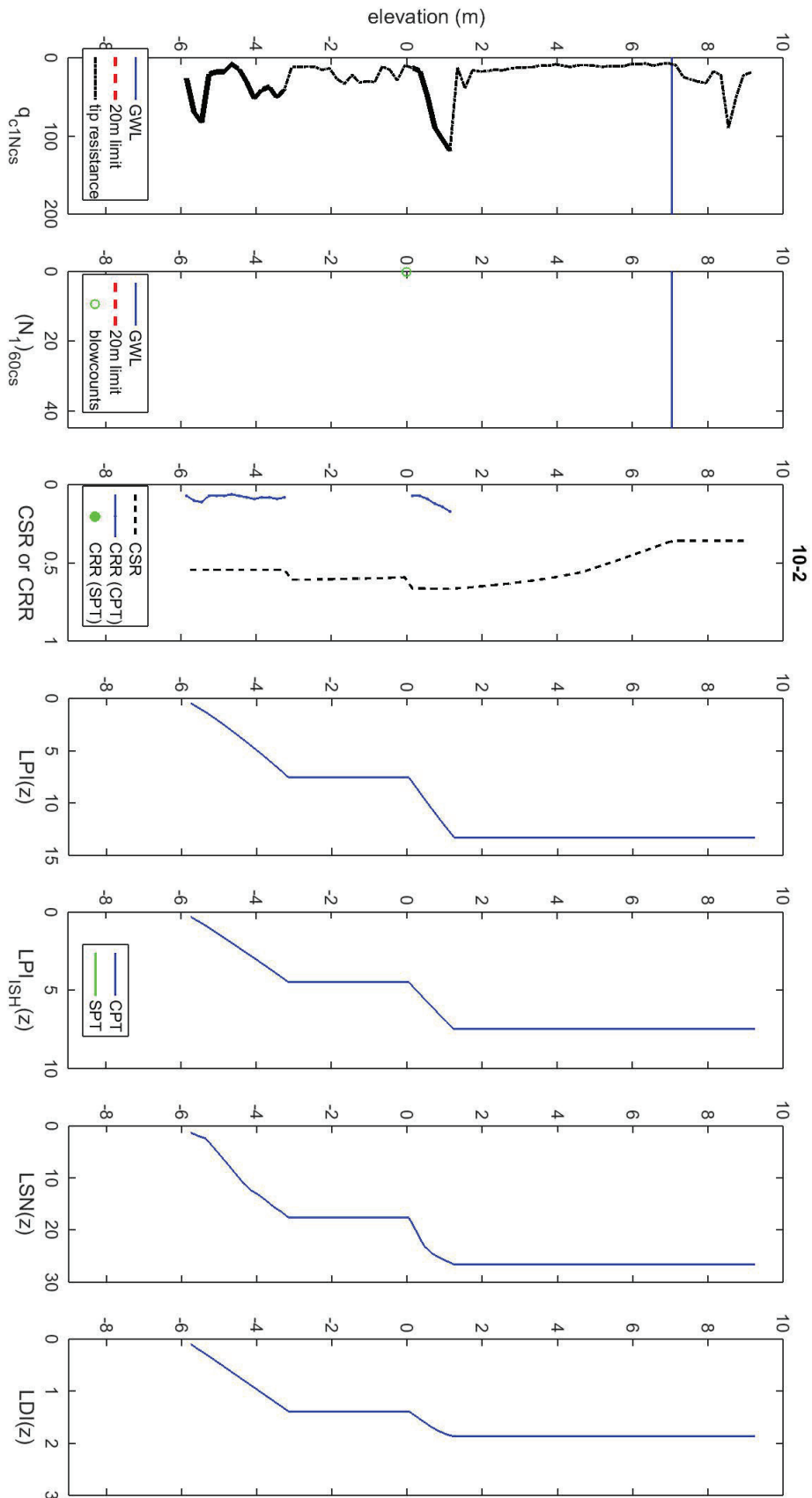


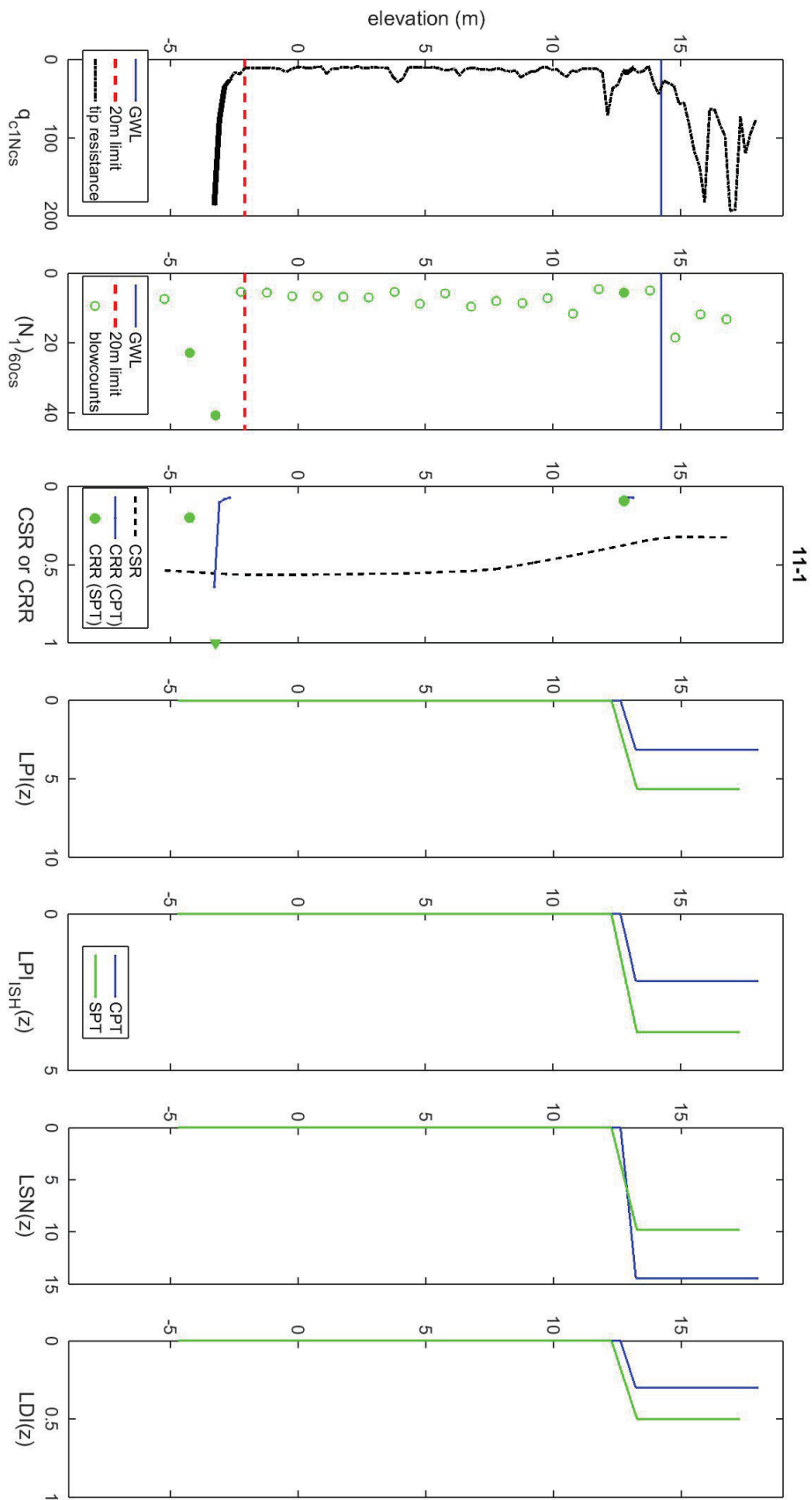


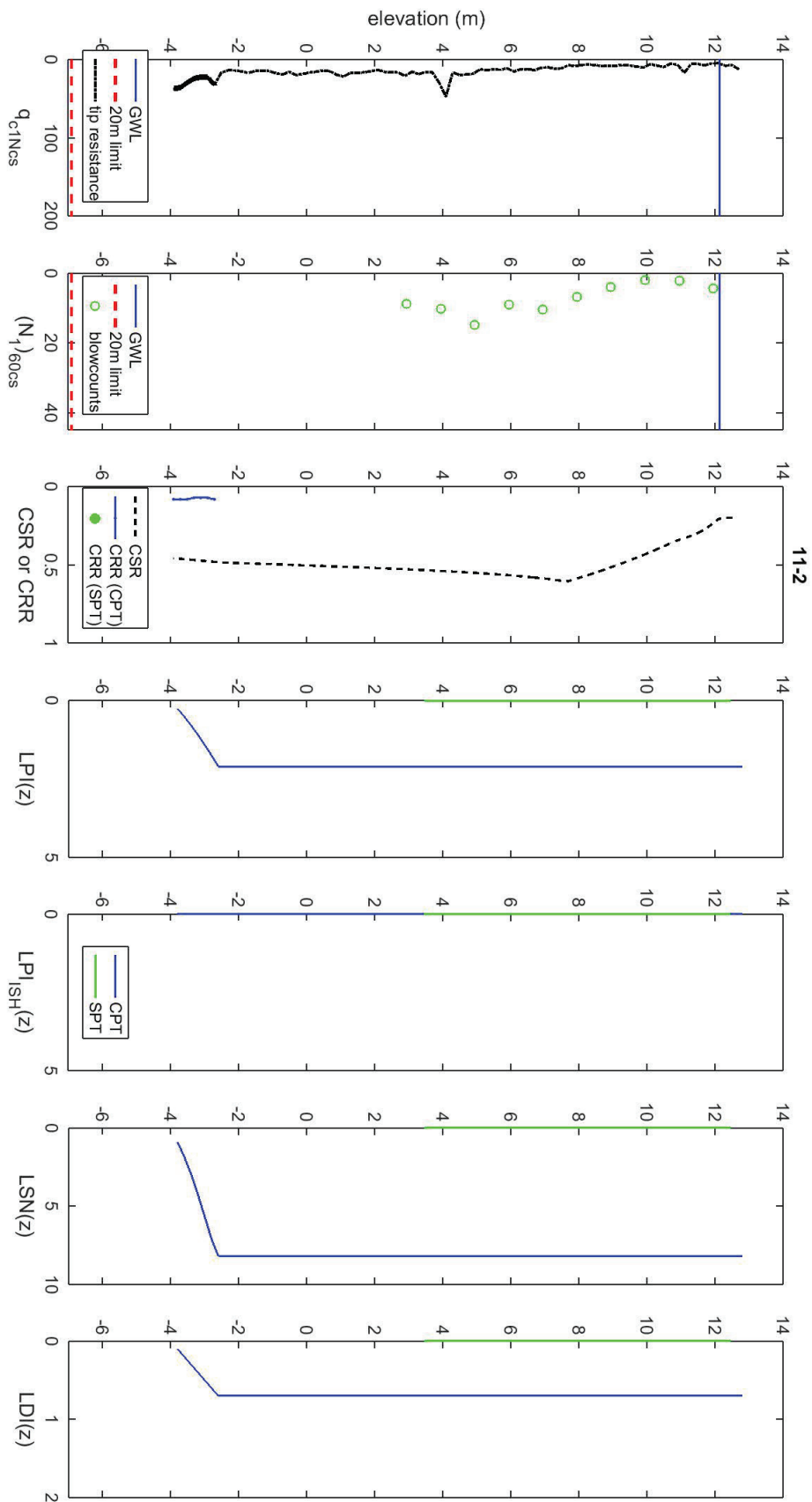


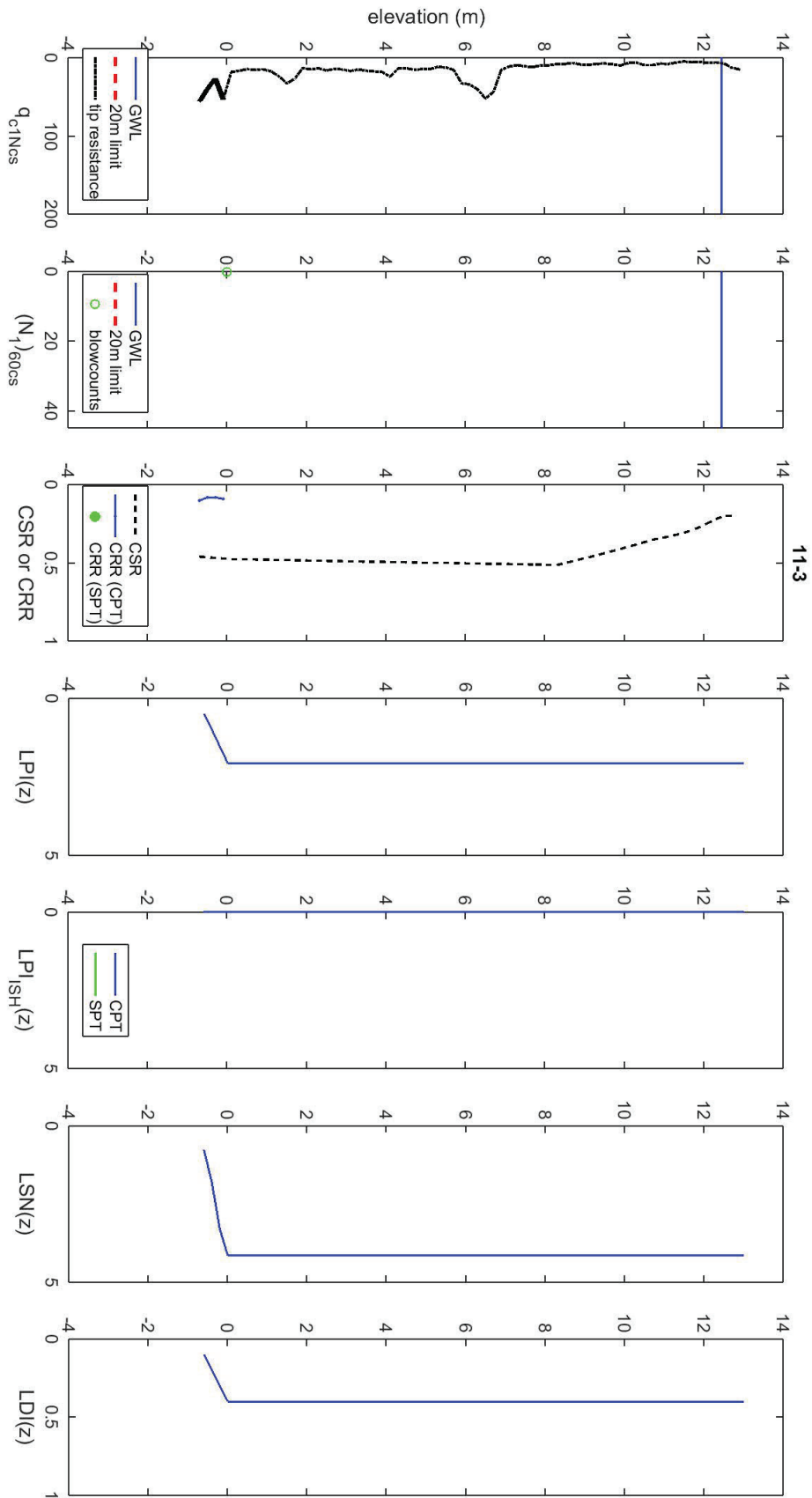


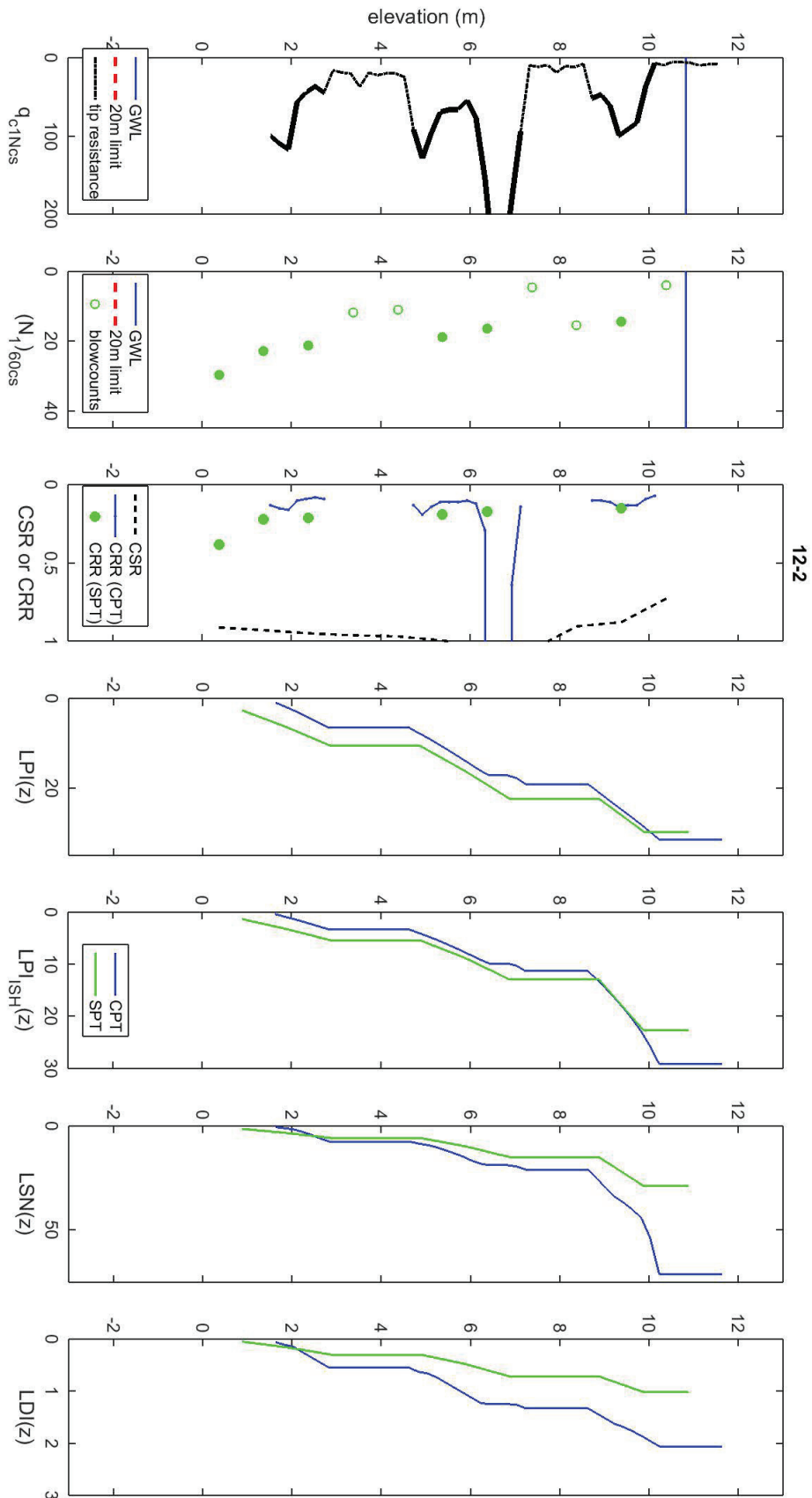


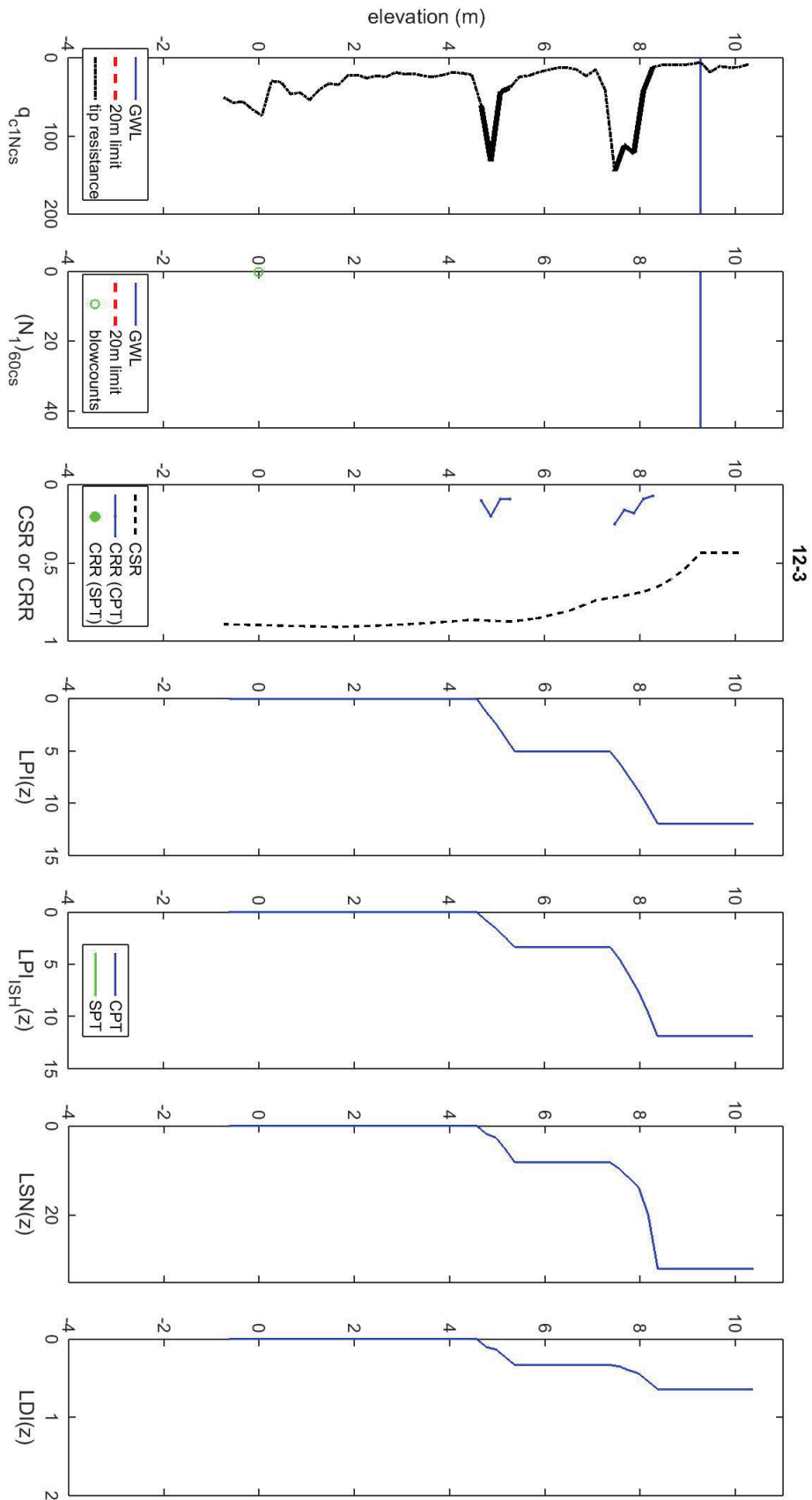


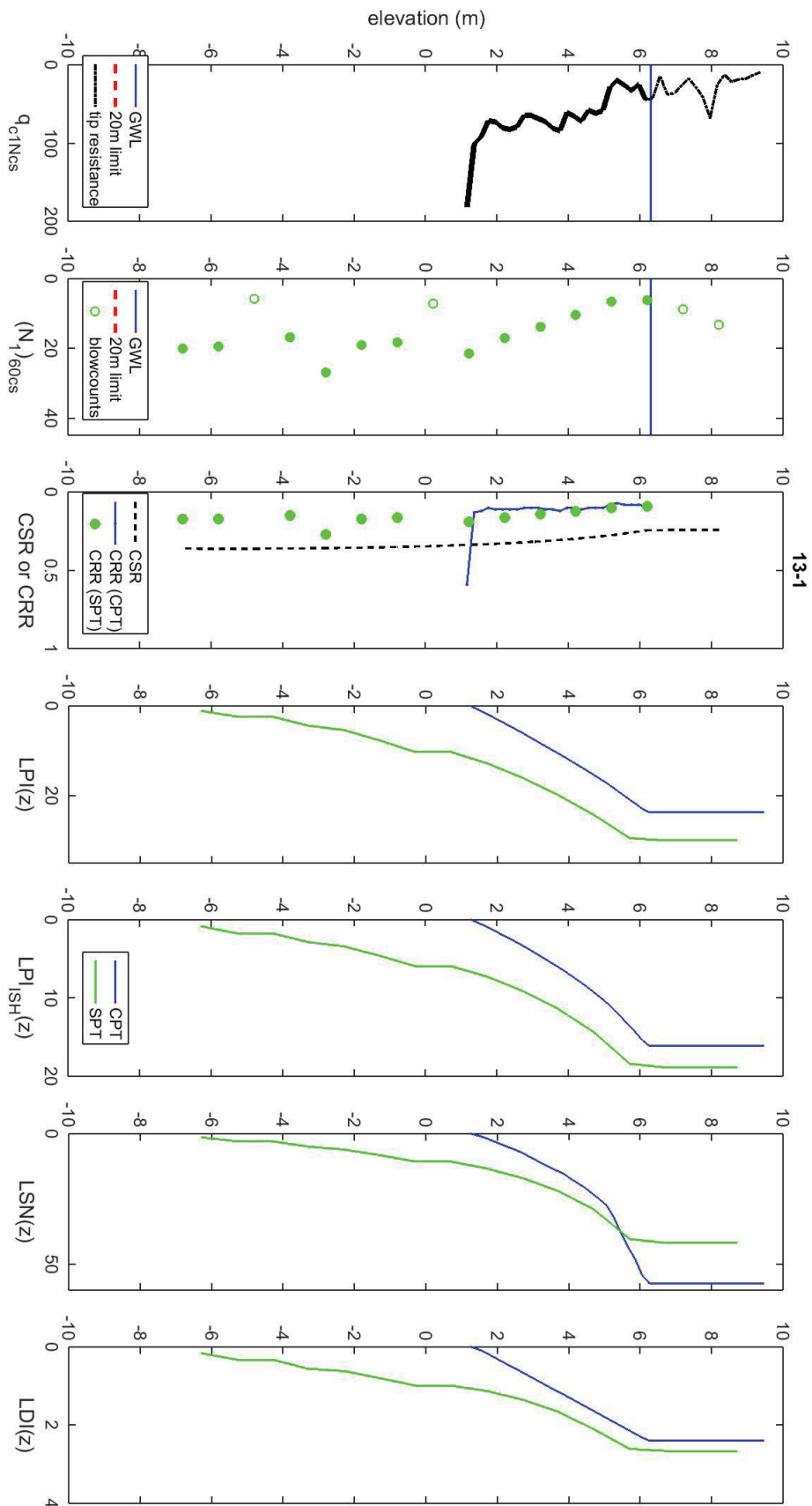


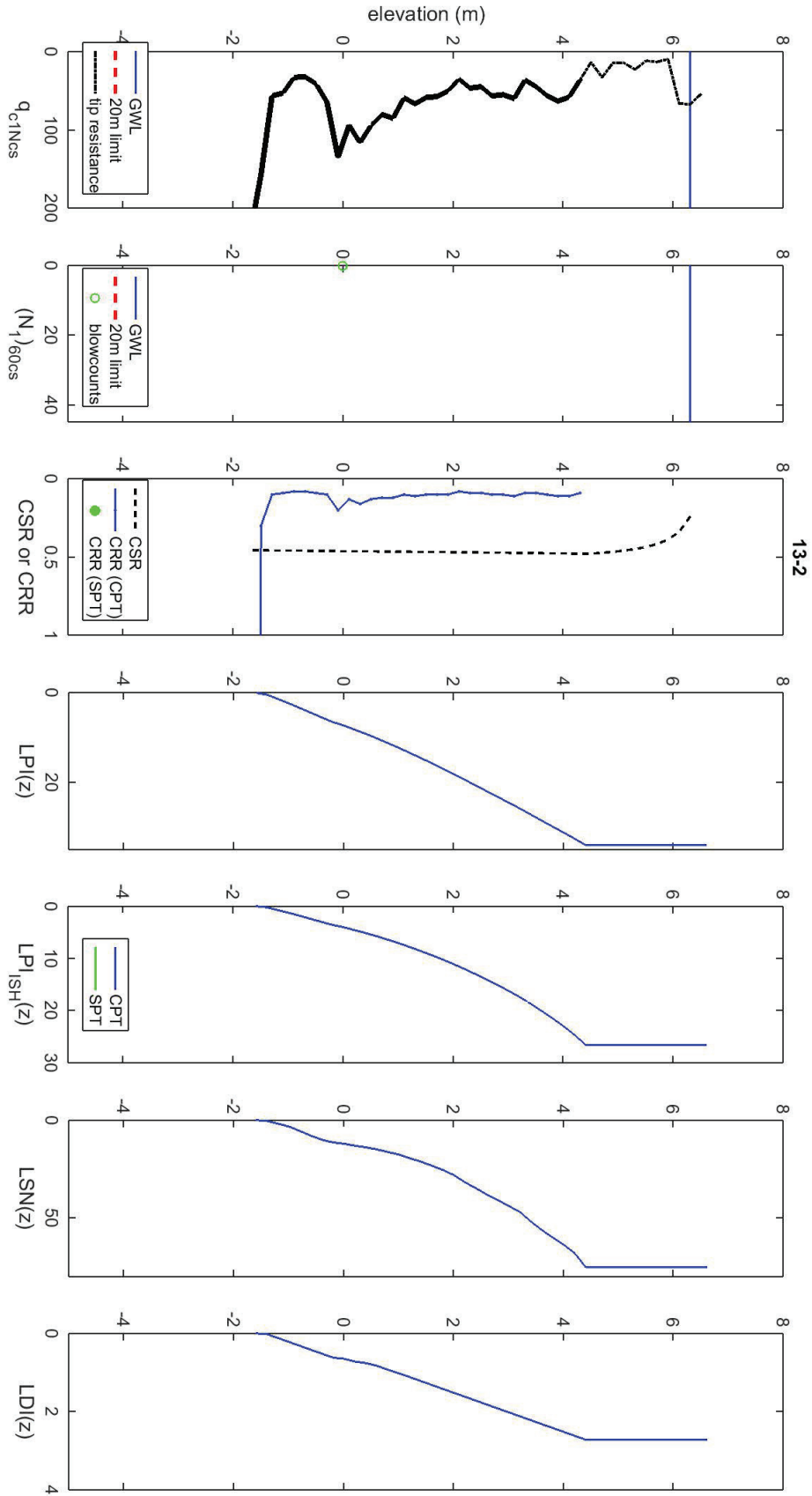




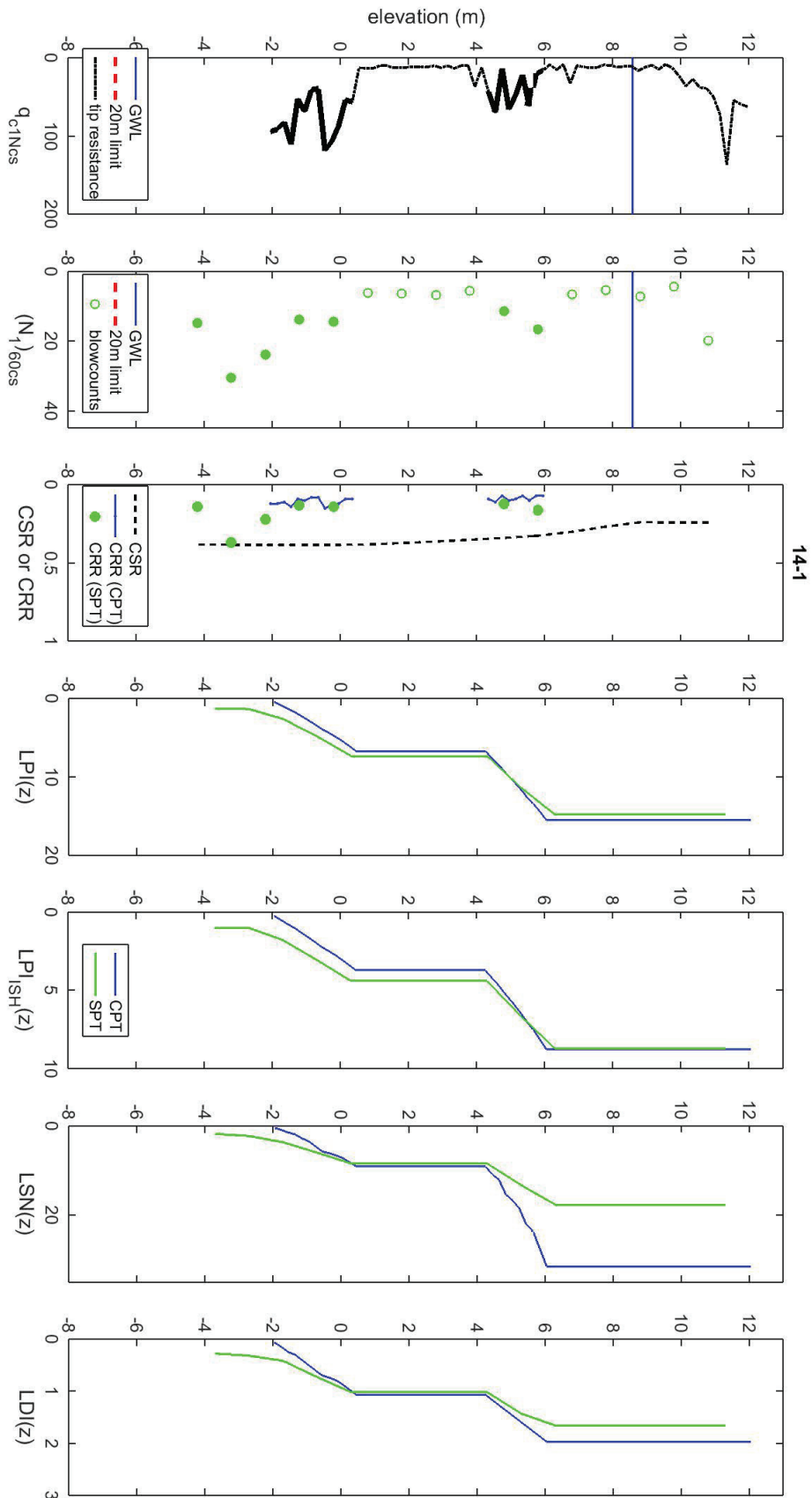


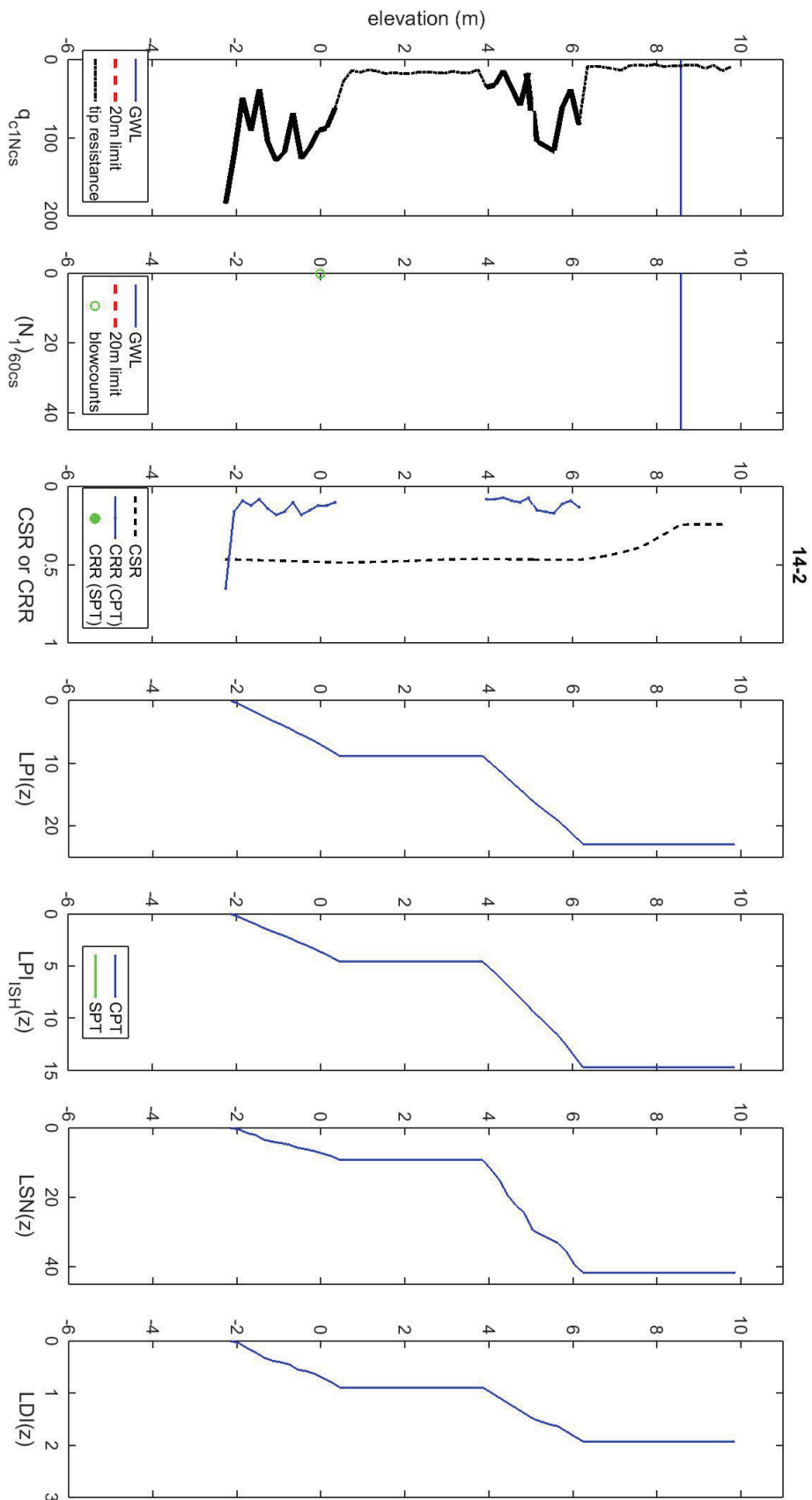




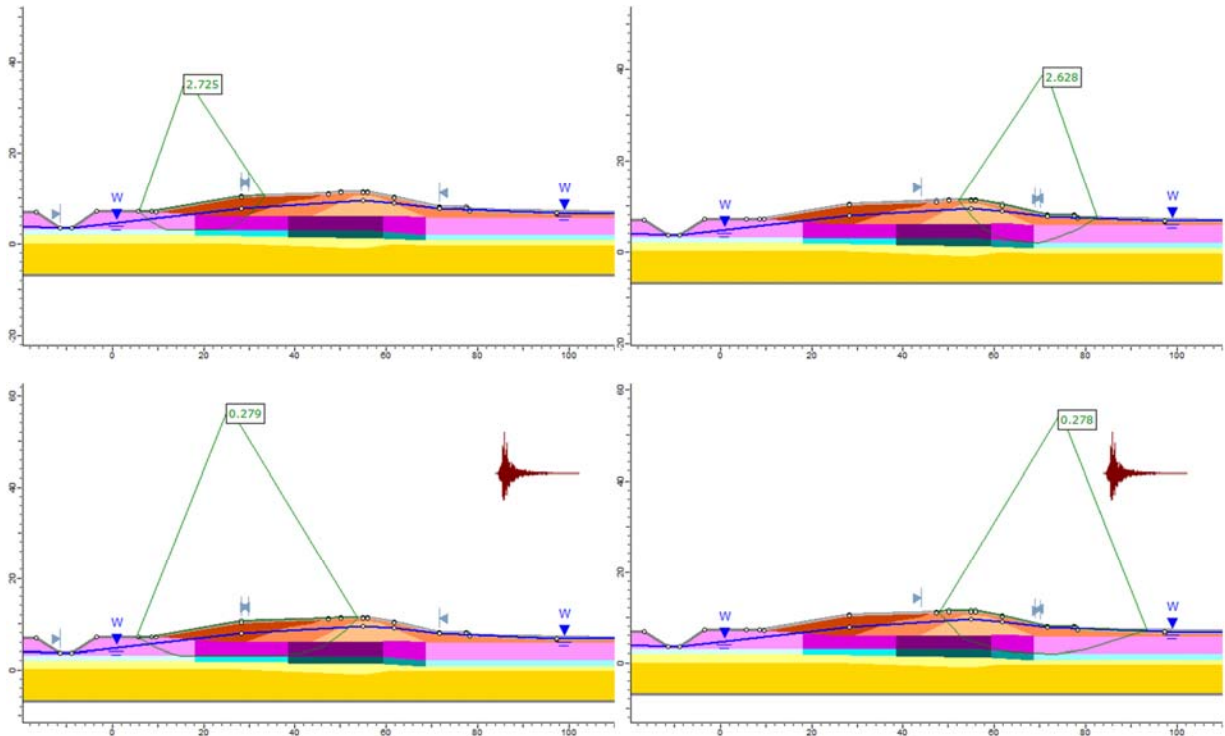






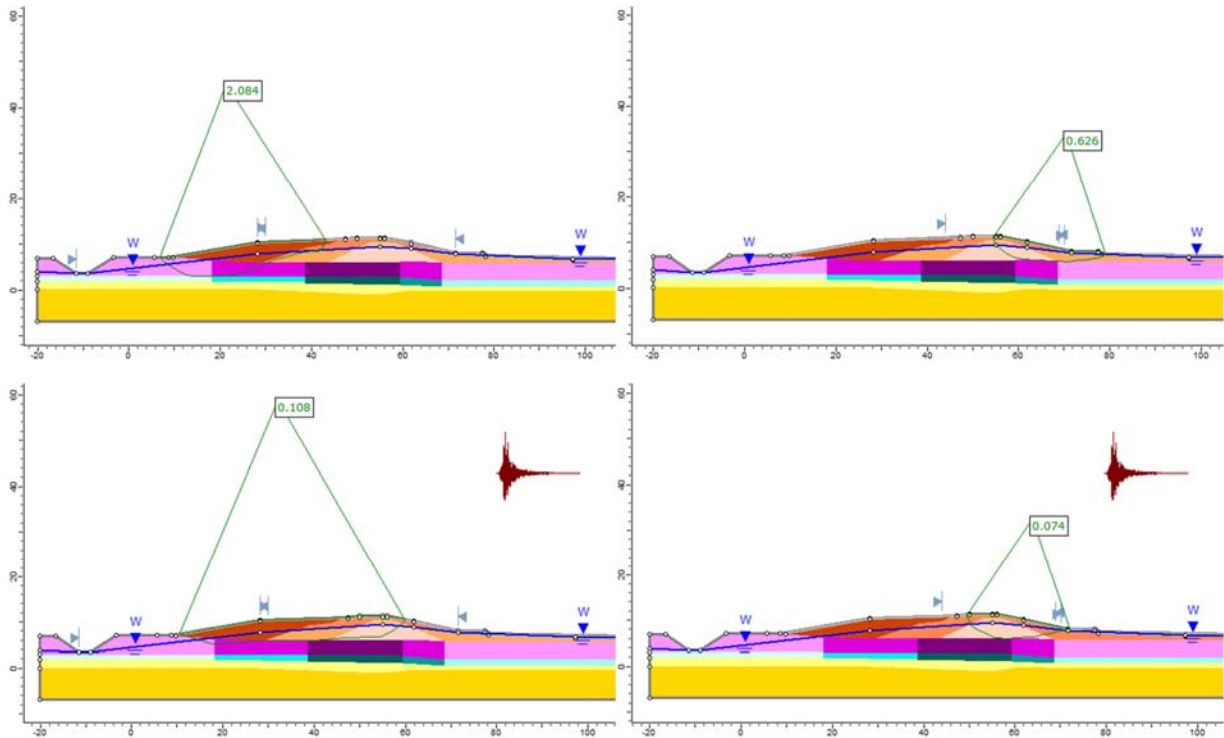


## Section 2 – Pre-earthquake



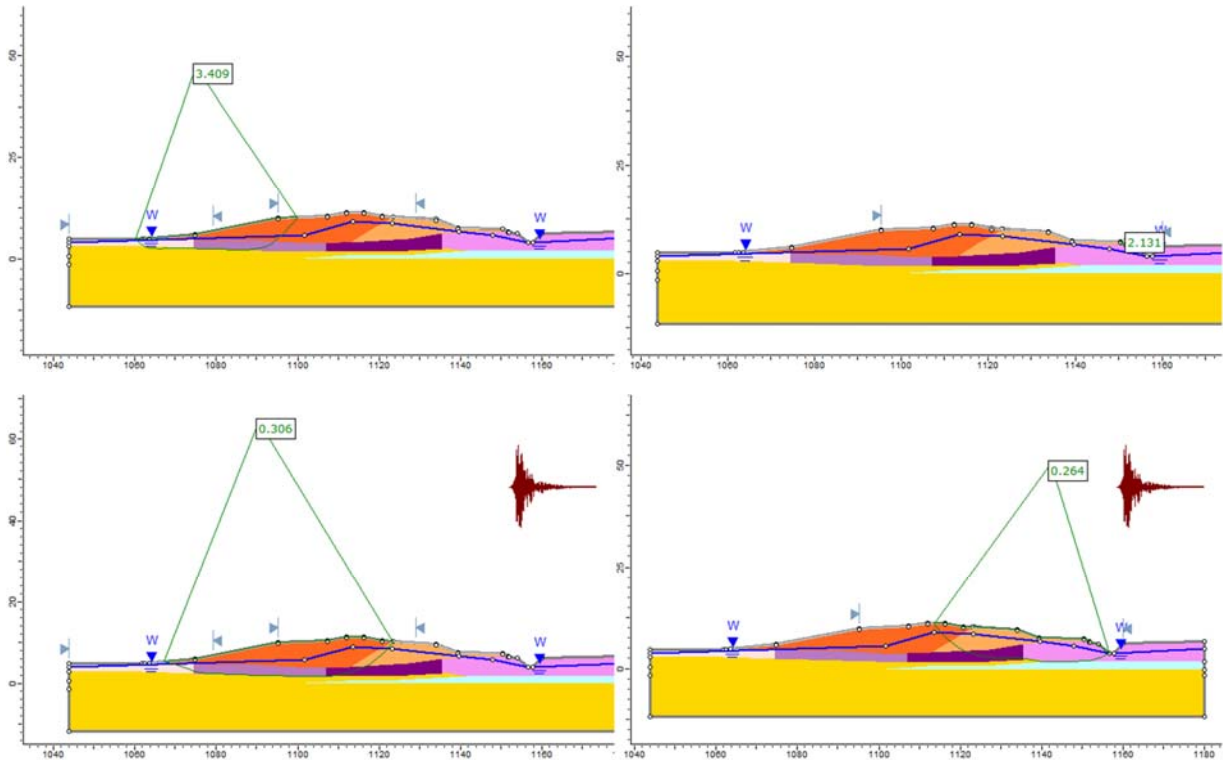
Material Name	Color	Unit Weight (kN/m <sup>3</sup> )	Sat. Unit Weight (kN/m <sup>3</sup> )	Strength Type	Cohesion (kPa)	Phi (deg)	Cohesion Type	Water Surface	Hu Type	Hu
Fill 1	<span style="color: #8B4513;">■</span>	19	20	Mohr-Coulomb	1	44		Water Surface	Custom	1
Fill 2	<span style="color: #FF8C00;">■</span>	19	20	Mohr-Coulomb	1	44		Water Surface	Custom	1
Fill 3	<span style="color: #FFD700;">■</span>	19	20	Mohr-Coulomb	1	38		Water Surface	Custom	1
Peat 1	<span style="color: #800080;">■</span>	10	11	Undrained	42.1		Constant	Water Surface	Custom	1
Peat 2	<span style="color: #FF00FF;">■</span>	10	11	Undrained	31.4		Constant	Water Surface	Custom	1
Peat 3	<span style="color: #FFB6C1;">■</span>	10	11	Undrained	23.6		Constant	Water Surface	Custom	1
Clay 1	<span style="color: #008080;">■</span>	14	16	Undrained	59		Constant	Water Surface	Custom	1
Clay 2A	<span style="color: #00CED1;">■</span>	14	16	Undrained	55.6		Constant	Water Surface	Custom	1
Clay 2B	<span style="color: #00FFFF;">■</span>	14	16	Undrained	49.3		Constant	Water Surface	Custom	1
Clay 3A	<span style="color: #ADD8E6;">■</span>	14	16	Undrained	58.2		Constant	Water Surface	Custom	1
Clay 3B	<span style="color: #ADD8E6;">■</span>	14	16	Undrained	42		Constant	Water Surface	Custom	1
Sand 1	<span style="color: #FFFF00;">■</span>	19	20	Mohr-Coulomb	1	41		Water Surface	Custom	1
Sand 2	<span style="color: #FFD700;">■</span>	19	20	Mohr-Coulomb	1	48		Water Surface	Custom	1

## Section 2 – Post-earthquake



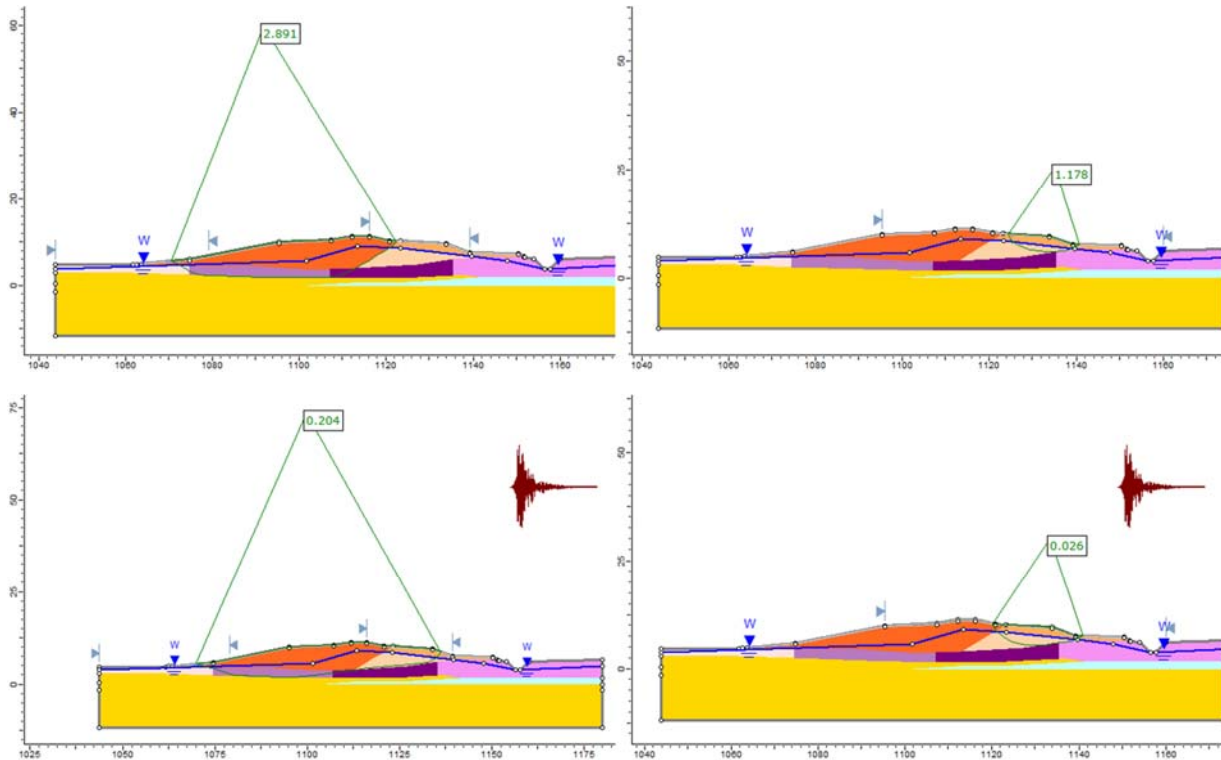
Material Name	Color	Unit Weight (kN/m <sup>3</sup> )	Sat. Unit Weight (kN/m <sup>3</sup> )	Strength Type	Cohesion (kPa)	Phi (deg)	Cohesion Type	Water Surface	Hu Type	Hu
Fill 1	<span style="color: #C85130;">■</span>	19	20	Mohr-Coulomb	1	44		Water Surface	Custom	1
Fill 2	<span style="color: #E69A00;">■</span>	19	20	Mohr-Coulomb	1	44		Water Surface	Custom	1
Fill 3	<span style="color: #F4C400;">■</span>	19	20	Mohr-Coulomb	1	38		Water Surface	Custom	1
Peat 1 (soften)	<span style="color: #6A329F;">■</span>	10	11	Undrained	37.9		Constant	Water Surface	Custom	1
Peat 2 (soften)	<span style="color: #E91E63;">■</span>	10	11	Undrained	28.3		Constant	Water Surface	Custom	1
Peat 3	<span style="color: #F080F0;">■</span>	10	11	Undrained	23.6		Constant	Water Surface	Custom	1
Clay 1	<span style="color: #006400;">■</span>	14	16	Undrained	59		Constant	Water Surface	Custom	1
Clay 2A	<span style="color: #008080;">■</span>	14	16	Undrained	55.6		Constant	Water Surface	Custom	1
Clay 2B	<span style="color: #00CED1;">■</span>	14	16	Undrained	49.3		Constant	Water Surface	Custom	1
Clay 3A	<span style="color: #ADD8E6;">■</span>	14	16	Undrained	58.2		Constant	Water Surface	Custom	1
Clay 3B	<span style="color: #ADD8E6;">■</span>	14	16	Undrained	42		Constant	Water Surface	Custom	1
Sand 1	<span style="color: #FFFF00;">■</span>	19	20	Mohr-Coulomb	1	41		Water Surface	Custom	1
Sand 2	<span style="color: #FFD700;">■</span>	19	20	Mohr-Coulomb	1	48		Water Surface	Custom	1
S29-37 (liq)	<span style="color: #FFDAB9;">■</span>	19	20	Undrained	5.4		Constant	Water Surface	Custom	1

## Section 5 – Pre-earthquake



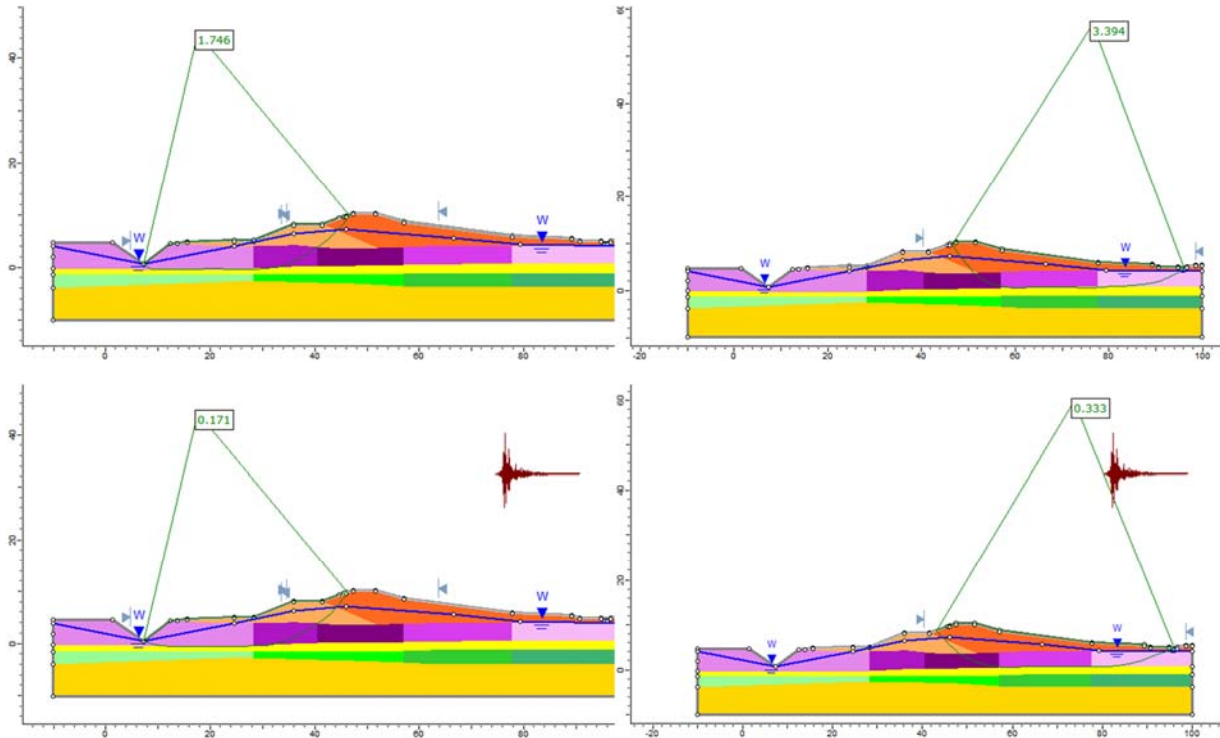
Material Name	Color	Unit Weight (kN/m <sup>3</sup> )	Sat. Unit Weight (kN/m <sup>3</sup> )	Strength Type	Cohesion (kPa)	Phi (deg)	Cohesion Type	Water Surface	Hu Type	Hu
Fill 1		19	20	Mohr-Coulomb	1	42		Water Surface	Custom	1
Fill 2		19	20	Mohr-Coulomb	1	37		Water Surface	Custom	1
Peat 1		10	11	Undrained	43.9		Constant	Water Surface	Custom	1
Peat 2		10	11	Undrained	41.3		Constant	Water Surface	Custom	1
Peat 3R		10	11	Undrained	25.3		Constant	Water Surface	Custom	1
Peat 3L		10	11	Undrained	31.3		Constant	Water Surface	Custom	1
Clay 3		14	16	Undrained	69		Constant	Water Surface	Custom	1
Sand 1		19	20	Mohr-Coulomb	1	41		Water Surface	Custom	1

### Section 5 – Post-earthquake



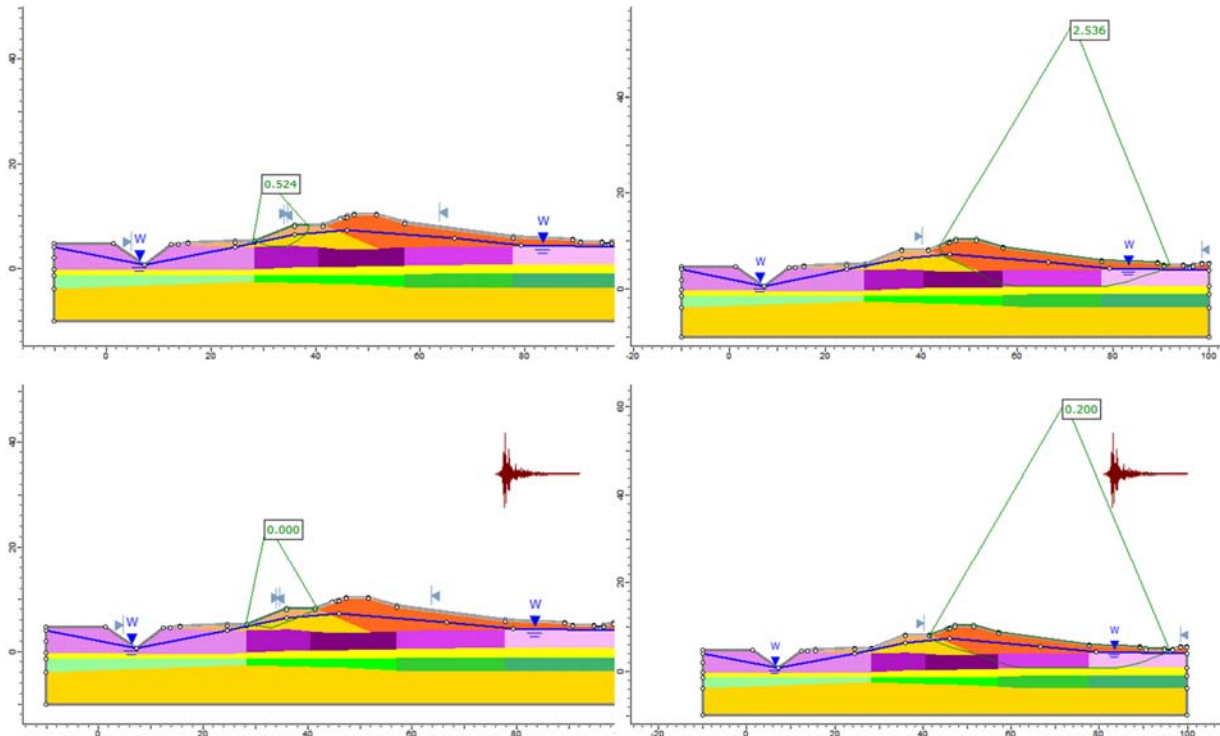
Material Name	Color	Unit Weight (kN/m <sup>3</sup> )	Sat. Unit Weight (kN/m <sup>3</sup> )	Strength Type	Cohesion (kPa)	Phi (deg)	Cohesion Type	Water Surface	Hu Type	Hu
Fill 1	Orange	19	20	Mohr-Coulomb	1	42		Water Surface	Custom	1
Fill 2	Light Orange	19	20	Mohr-Coulomb	1	37		Water Surface	Custom	1
Peat 1 (soften)	Dark Purple	10	11	Undrained	39.5		Constant	Water Surface	Custom	1
Peat 2 (soften)	Purple	10	11	Undrained	37.2		Constant	Water Surface	Custom	1
Peat 3R(soften)	Pink	10	11	Undrained	22.8		Constant	Water Surface	Custom	1
Peat 3L(soften)	Light Pink	10	11	Undrained	31.3		Constant	Water Surface	Custom	1
Clay 3	Light Blue	14	16	Undrained	69		Constant	Water Surface	Custom	1
Sand 1	Yellow	19	20	Mohr-Coulomb	1	41		Water Surface	Custom	1
Fill 2 (liquefied)	Light Orange	19	20	Undrained	6.1		Constant	Water Surface	Custom	1

## Section 7 – Pre-earthquake



Material Name	Color	Unit Weight (kN/m <sup>3</sup> )	Sat. Unit Weight (kN/m <sup>3</sup> )	Strength Type	Cohesion (kPa)	Phi (deg)	Water Surface	Hu Type	Hu
Fill1	<span style="color: orange;">■</span>	19	20	Mohr-Coulomb	1	42	Water Surface	Custom	1
Fill 2	<span style="color: #FFA500;">■</span>	19	20	Mohr-Coulomb	1	38	Water Surface	Custom	1
Peat 1	<span style="color: purple;">■</span>	10	11	Mohr-Coulomb	51.7	0	Water Surface	Custom	1
Peat 2L	<span style="color: #800080;">■</span>	10	11	Mohr-Coulomb	31.3	0	Water Surface	Custom	1
Peat 2R	<span style="color: #E066FF;">■</span>	10	11	Mohr-Coulomb	38.9	0	Water Surface	Custom	1
Peat 3L	<span style="color: #DDA0DD;">■</span>	10	11	Mohr-Coulomb	21.3	0	Water Surface	Custom	1
Peat 3R	<span style="color: #F0E6FF;">■</span>	10	11	Mohr-Coulomb	26	0	Water Surface	Custom	1
Ac 1	<span style="color: #00FF00;">■</span>	16	18	Mohr-Coulomb	83.1	0	Water Surface	Custom	1
Ac 2R	<span style="color: #32CD32;">■</span>	16	18	Mohr-Coulomb	93.9	0	Water Surface	Custom	1
Ac 3R	<span style="color: #2ECC71;">■</span>	16	18	Mohr-Coulomb	104.9	0	Water Surface	Custom	1
Ac 3L	<span style="color: #90EE90;">■</span>	16	18	Mohr-Coulomb	60.5	0	Water Surface	Custom	1
As1	<span style="color: #FFFF00;">■</span>	19	20	Mohr-Coulomb	1	38	Water Surface	Custom	1
As2	<span style="color: #FFD700;">■</span>	19	20	Mohr-Coulomb	1	43	Water Surface	Custom	1

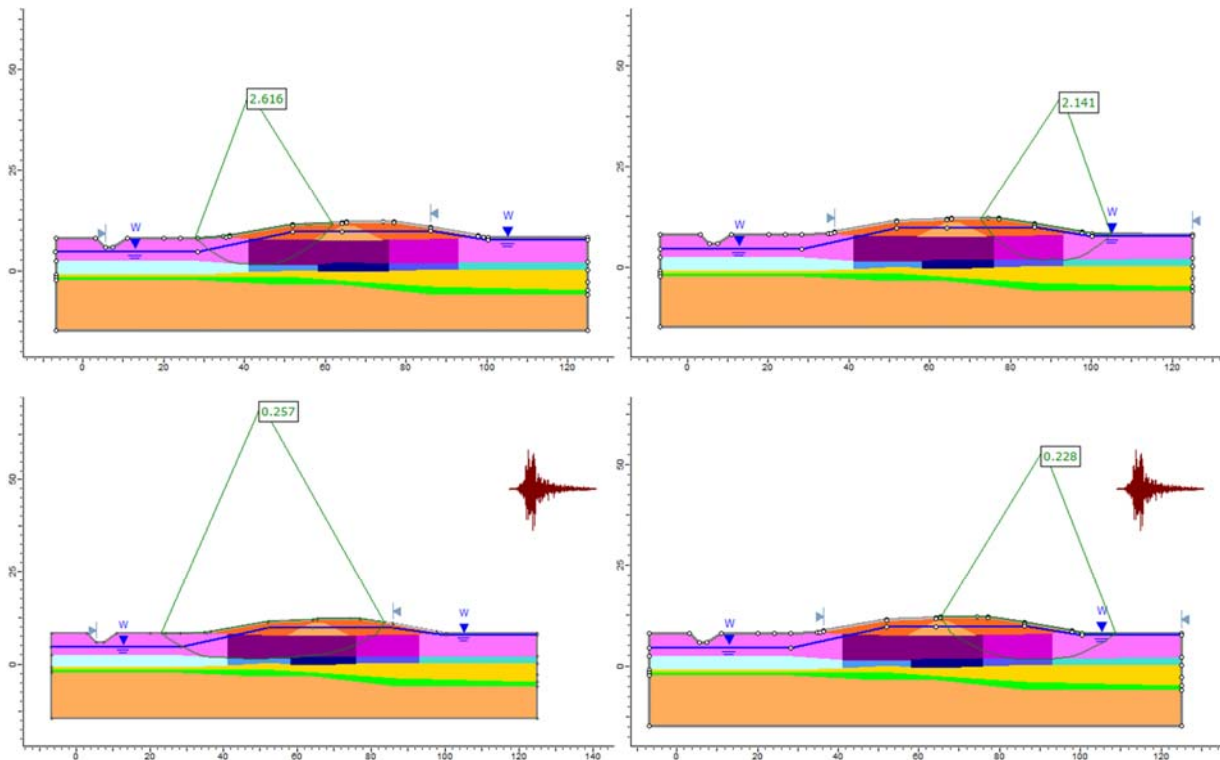
## Section 7 – Post-earthquake



Material Name	Color	Unit Weight (kN/m <sup>3</sup> )	Sat. Unit Weight (kN/m <sup>3</sup> )	Strength Type	Cohesion (kPa)	Phi (deg)	Cohesion Type	Water Surface	Hu Type	Hu
Fill1	<span style="color: orange;">■</span>	19	20	Mohr-Coulomb	1	42		Water Surface	Custom	1
Fill 2	<span style="color: lightorange;">■</span>	19	20	Mohr-Coulomb	1	38		Water Surface	Custom	1
Peat 1 (soften)	<span style="color: purple;">■</span>	10	11	Undrained	41.4		Constant	Water Surface	Custom	1
Peat 2L (soften)	<span style="color: magenta;">■</span>	10	11	Undrained	25		Constant	Water Surface	Custom	1
Peat 2R (soften)	<span style="color: pink;">■</span>	10	11	Undrained	31.1		Constant	Water Surface	Custom	1
Peat 3L (soften)	<span style="color: lightpink;">■</span>	10	11	Undrained	17		Constant	Water Surface	Custom	1
Peat 3R (soften)	<span style="color: lightpink;">■</span>	10	11	Undrained	20.8		Constant	Water Surface	Custom	1
Ac 1 (soften)	<span style="color: green;">■</span>	16	18	Undrained	74.7		Constant	Water Surface	Custom	1
Ac 2R (soften)	<span style="color: green;">■</span>	16	18	Undrained	84.5		Constant	Water Surface	Custom	1
Ac 3R	<span style="color: teal;">■</span>	16	18	Undrained	104.9		Constant	Water Surface	Custom	1
Ac 3L	<span style="color: lightgreen;">■</span>	16	18	Undrained	54.5		Constant	Water Surface	Custom	1
As1	<span style="color: yellow;">■</span>	19	20	Mohr-Coulomb	1	38		Water Surface	Custom	1
As2	<span style="color: orangeyellow;">■</span>	19	20	Mohr-Coulomb	1	43		Water Surface	Custom	1
Fill 2 (liq)	<span style="color: yellow;">■</span>	19	20	Mohr-Coulomb	4.1	0		Water Surface	Custom	1

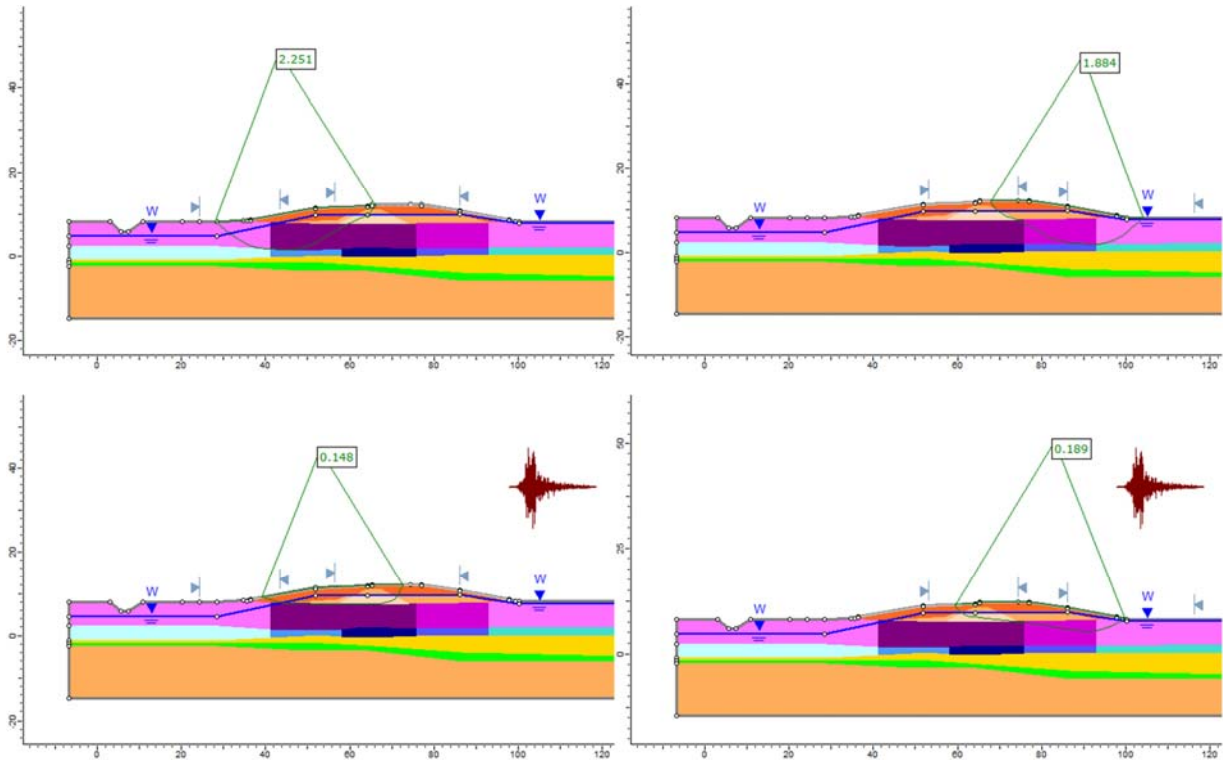


## Section 8 – Pre-earthquake



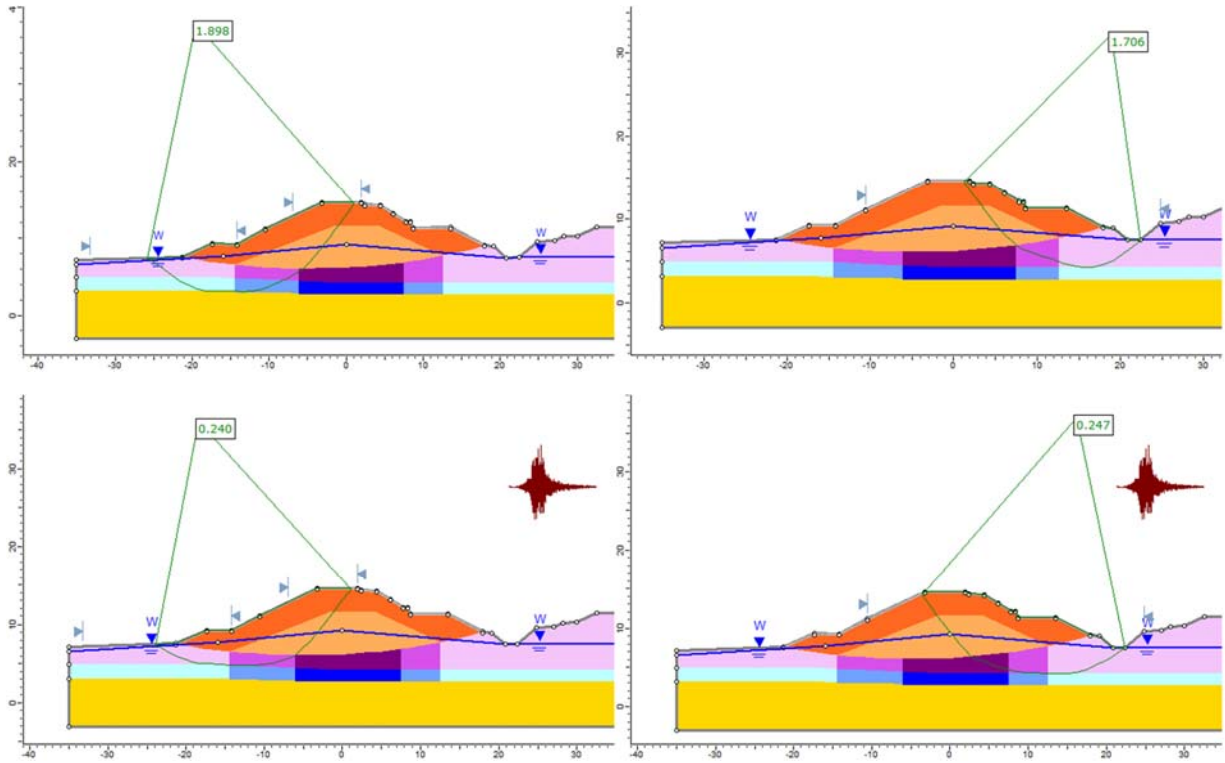
Material Name	Color	Unit Weight (kN/m <sup>3</sup> )	Sat. Unit Weight (kN/m <sup>3</sup> )	Strength Type	Cohesion (kPa)	Phi (deg)	Cohesion Type	Water Surface	Hu Type	Hu
Fill 1	<span style="color: orange;">■</span>	19	20	Mohr-Coulomb	1	40		Water Surface	Custom	1
Fill 2	<span style="color: #f4a460;">■</span>	19	20	Mohr-Coulomb	1	37		Water Surface	Custom	1
Peat 1	<span style="color: purple;">■</span>	10	11	Undrained	37		Constant	Water Surface	Custom	1
Peat 2	<span style="color: magenta;">■</span>	10	11	Undrained	28.2		Constant	Water Surface	Custom	1
Peat 3	<span style="color: pink;">■</span>	10	11	Undrained	22.9		Constant	Water Surface	Custom	1
Sand 1	<span style="color: yellow;">■</span>	19	20	Mohr-Coulomb	1	38		Water Surface	Custom	1
Sandy Silt	<span style="color: green;">■</span>	16	18	Mohr-Coulomb	1	35		Water Surface	Custom	1
Clay 1	<span style="color: darkblue;">■</span>	16	18	Undrained	86.1		Constant	Water Surface	Custom	1
Clay 2L	<span style="color: lightblue;">■</span>	16	18	Undrained	80.8		Constant	Water Surface	Custom	1
Clay 2R	<span style="color: blue;">■</span>	16	18	Undrained	72.3		Constant	Water Surface	Custom	1
Clay 3L	<span style="color: cyan;">■</span>	16	18	Undrained	73.7		Constant	Water Surface	Custom	1
Clay 3R	<span style="color: teal;">■</span>	16	18	Undrained	59.7		Constant	Water Surface	Custom	1
Sand 2	<span style="color: #f4a460;">■</span>	19	20	Mohr-Coulomb	1	41		Water Surface	Custom	1








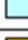

## Section 8 – Post-earthquake



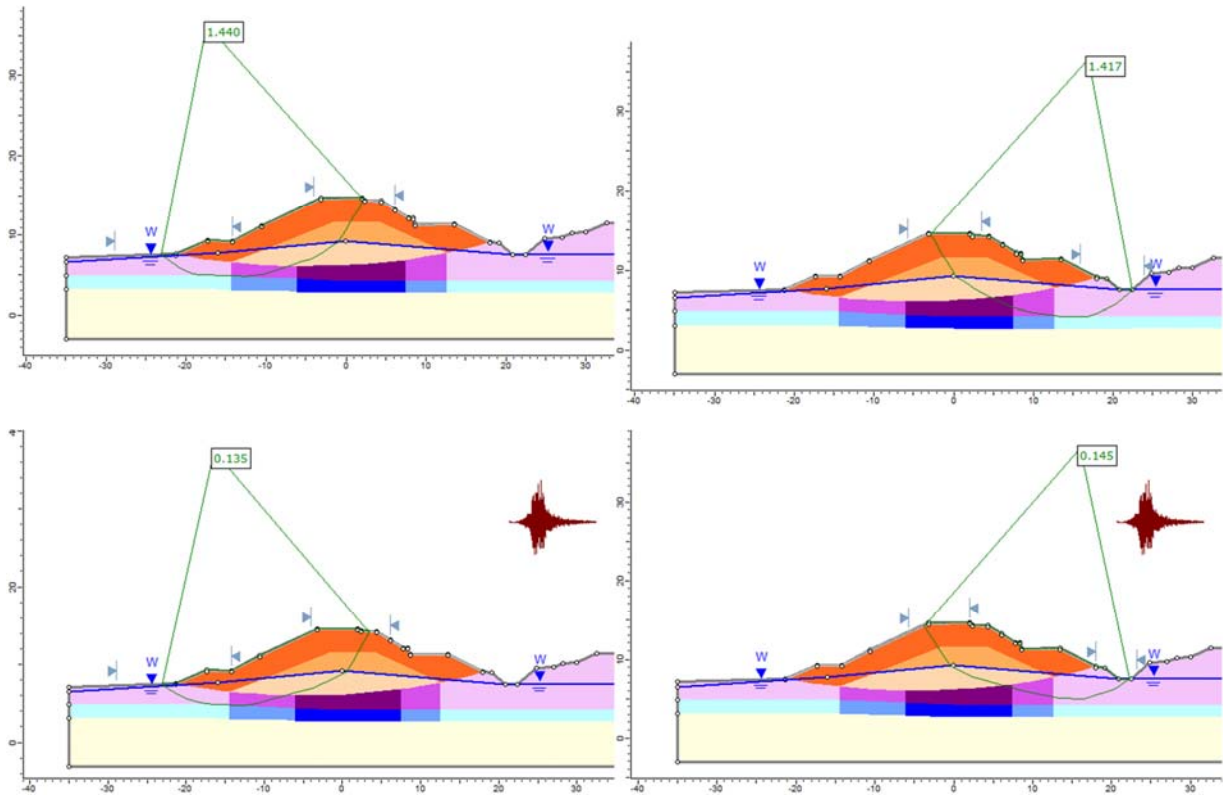
Material Name	Color	Unit Weight (kN/m <sup>3</sup> )	Sat. Unit Weight (kN/m <sup>3</sup> )	Strength Type	Cohesion (kPa)	Phi (deg)	Cohesion Type	Water Surface	Hu Type	Hu
Fill 1	Orange	19	20	Mohr-Coulomb	1	40		Water Surface	Custom	1
Fill 2	Light Orange	19	20	Mohr-Coulomb	1	37		Water Surface	Custom	1
Peat 1 (soften)	Dark Purple	10	11	Undrained	33.3		Constant	Water Surface	Custom	1
Peat 2 (soften)	Magenta	10	11	Undrained	25.4		Constant	Water Surface	Custom	1
Peat 3	Pink	10	11	Undrained	22.9		Constant	Water Surface	Custom	1
Sand 1	Yellow	19	20	Mohr-Coulomb	1	38		Water Surface	Custom	1
Sandy Silt	Green	16	18	Mohr-Coulomb	1	35		Water Surface	Custom	1
Fill S27 (liq)	Light Orange	19	20	Undrained	3.5		Constant	Water Surface	Custom	1
Fill S53 (liq)	Light Orange	19	20	Undrained	15.7		Constant	Water Surface	Custom	1
Clay 1	Dark Blue	16	18	Undrained	86.1		Constant	Water Surface	Custom	1
Clay 2L	Blue	16	18	Undrained	80.8		Constant	Water Surface	Custom	1
Clay 2R	Blue	16	18	Undrained	72.3		Constant	Water Surface	Custom	1
Clay 3L	Light Blue	16	18	Undrained	73.7		Constant	Water Surface	Custom	1
Clay 3R	Cyan	16	18	Undrained	59.7		Constant	Water Surface	Custom	1
Sand 2	Orange	19	20	Mohr-Coulomb	1	41		Water Surface	Custom	1

### Section 9 – Pre-earthquake



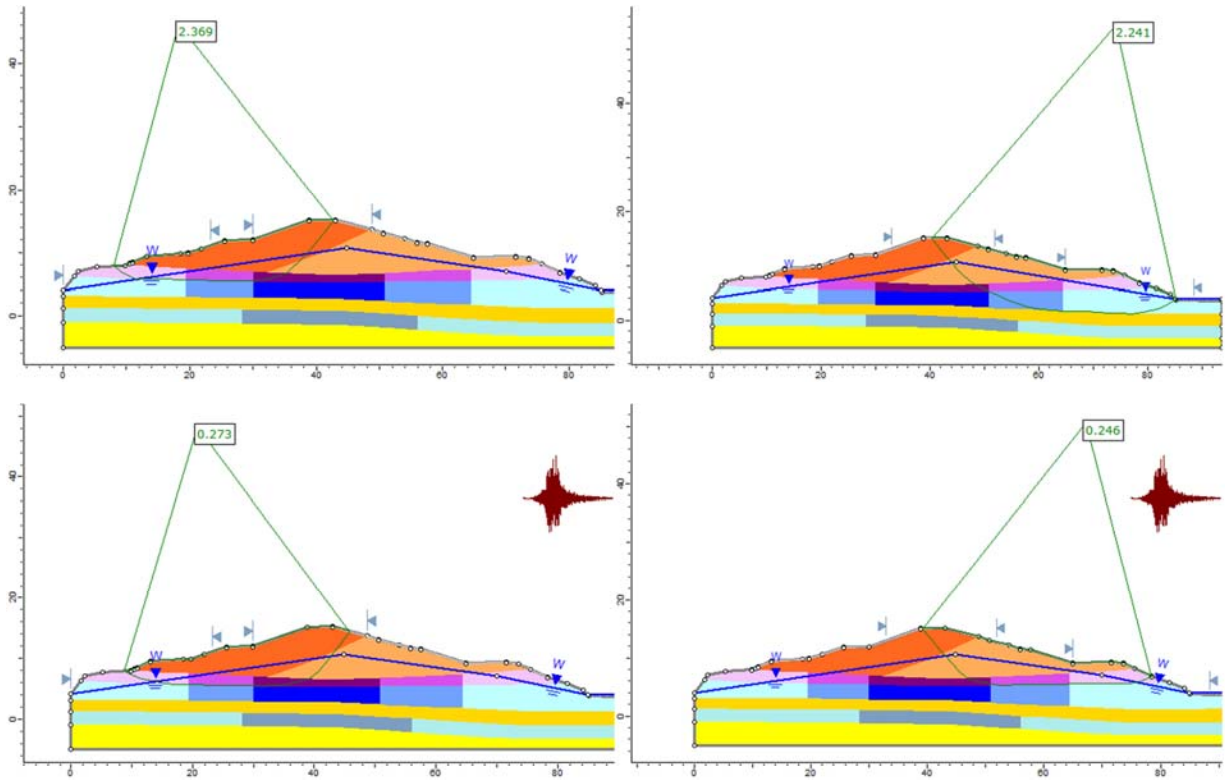
Material Name	Color	Unit Weight (kN/m <sup>3</sup> )	Sat. Unit Weight (kN/m <sup>3</sup> )	Strength Type	Cohesion (kPa)	Phi (deg)	Cohesion Type	Water Surface	Hu Type	Hu
Fill 1		19	20	Mohr-Coulomb	1	44		Water Surface	Custom	1
Fill 2		19	20	Mohr-Coulomb	1	40		Water Surface	Custom	1
Peat 1		10	11	Undrained	61.3		Constant	Water Surface	Custom	1
Peat 2		10	11	Undrained	41.8		Constant	Water Surface	Custom	1
Peat 3		10	11	Undrained	22.3		Constant	Water Surface	Custom	1
Clay 1		14	16	Undrained	70.8		Constant	Water Surface	Custom	1
Clay 2		14	16	Undrained	52.1		Constant	Water Surface	Custom	1
Clay 3		14	16	Undrained	33.3		Constant	Water Surface	Custom	1
Sand 1		20	21	Mohr-Coulomb	1	46		Water Surface	Custom	1













## Section 9 – Post-earthquake



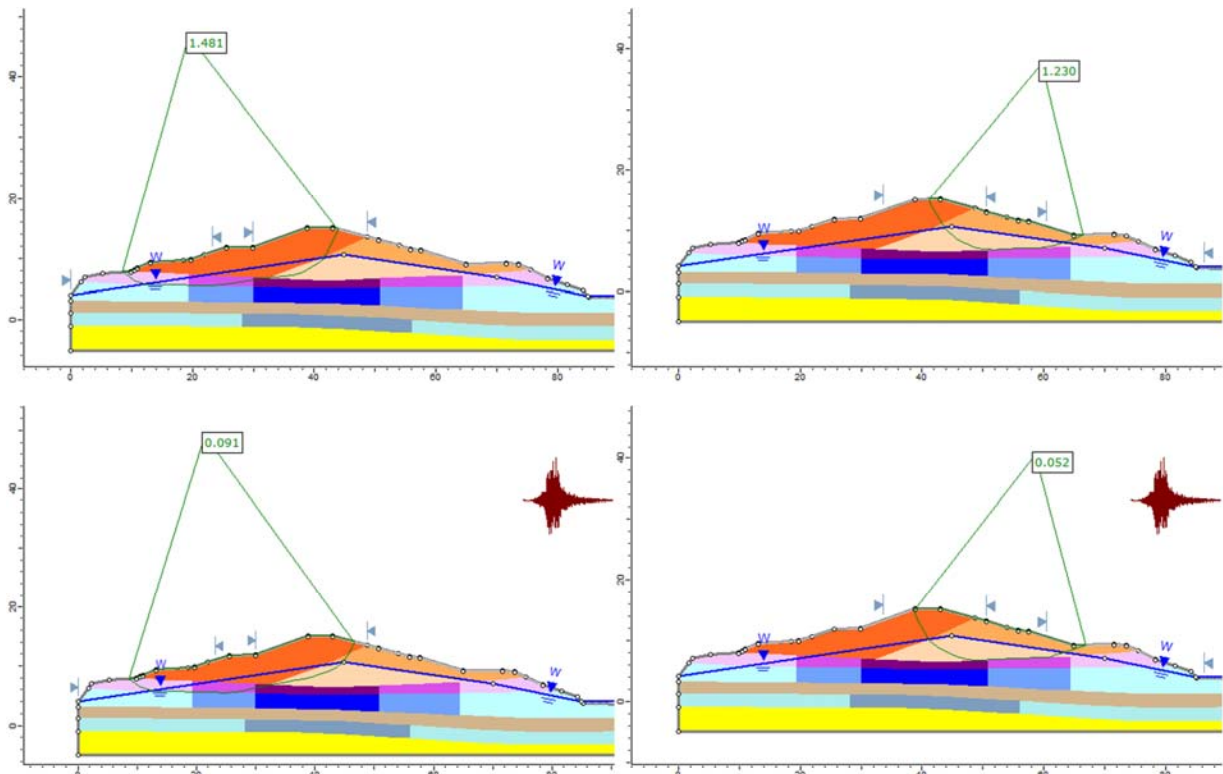
Material Name	Color	Unit Weight (kN/m <sup>3</sup> )	Sat. Unit Weight (kN/m <sup>3</sup> )	Strength Type	Cohesion (kPa)	Phi (deg)	Cohesion Type	Water Surface	Hu Type	Hu
Fill 1	<span style="color: orange;">■</span>	19	20	Mohr-Coulomb	1	44		Water Surface	Custom	1
Fill 2	<span style="color: lightorange;">■</span>	19	20	Mohr-Coulomb	1	40		Water Surface	Custom	1
Peat 1 (soften)	<span style="color: purple;">■</span>	10	11	Undrained	49		Constant	Water Surface	Custom	1
Peat 2	<span style="color: magenta;">■</span>	10	11	Undrained	41.8		Constant	Water Surface	Custom	1
Peat 3	<span style="color: pink;">■</span>	10	11	Undrained	22.3		Constant	Water Surface	Custom	1
Clay 1 (soften)	<span style="color: blue;">■</span>	14	16	Undrained	56.6		Constant	Water Surface	Custom	1
Clay 2	<span style="color: lightblue;">■</span>	14	16	Undrained	52.1		Constant	Water Surface	Custom	1
Clay 3	<span style="color: cyan;">■</span>	14	16	Undrained	33.3		Constant	Water Surface	Custom	1
Fill 2 (liq)	<span style="color: peachpuff;">■</span>	19	20	Undrained	24		Constant	Water Surface	Custom	1
Sand 2 (liq)	<span style="color: yellow;">■</span>	19	20	Undrained	104		Constant	Water Surface	Custom	1

### Section 10 – Pre-earthquake



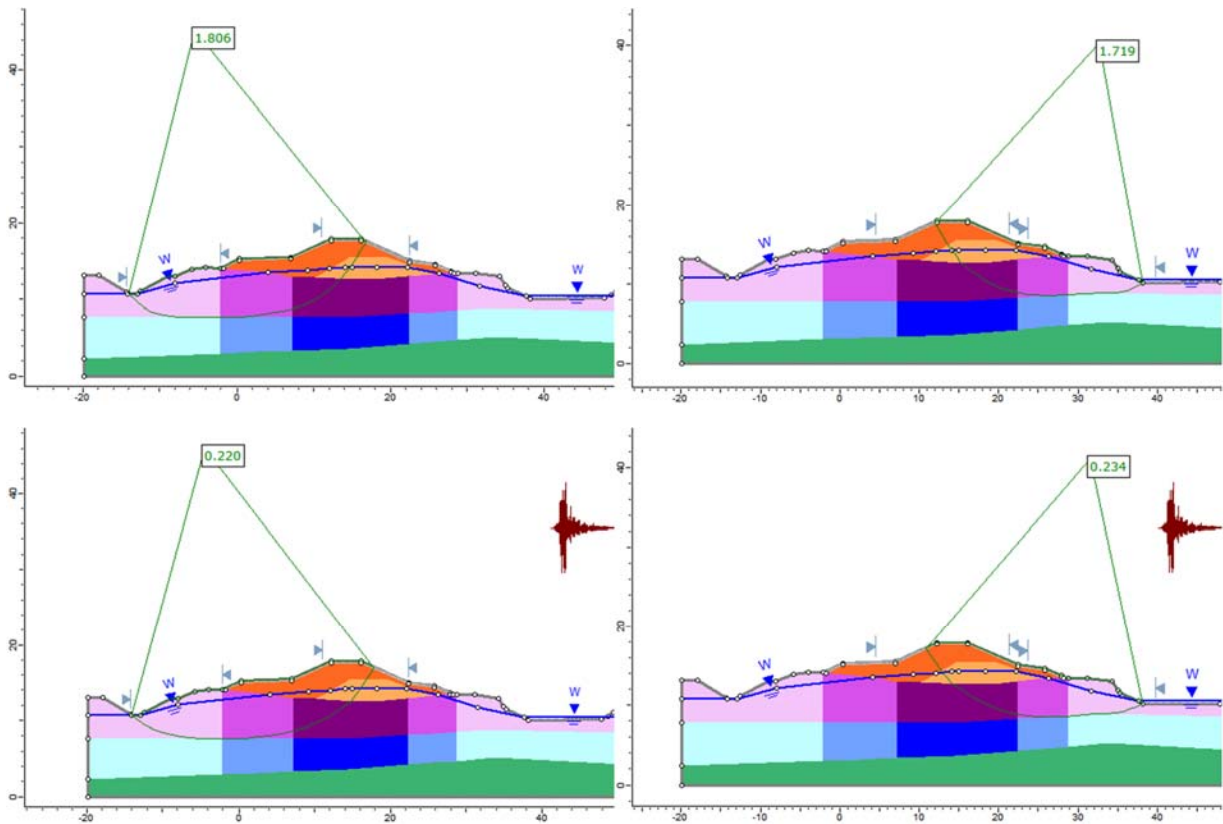
Material Name	Color	Unit Weight (kN/m <sup>3</sup> )	Sat. Unit Weight (kN/m <sup>3</sup> )	Strength Type	Cohesion (kPa)	Phi (deg)	Cohesion Type	Water Surface	Hu Type
Fill 1		19	20	Mohr-Coulomb	1	40		Water Surface	Custom
Fill 2		19	20	Mohr-Coulomb	1	40		Water Surface	Custom
Peat 1		10	11	Undrained	50.7		Constant	Water Surface	Custom
Peat 2		10	11	Undrained	35.8		Constant	Water Surface	Custom
Peat 3		10	11	Undrained	20.8		Constant	Water Surface	Custom
Clay 1A		14	16	Undrained	85.6		Constant	Water Surface	Custom
Clay 1B		14	16	Undrained	63.3		Constant	Water Surface	Custom
Clay 1C		14	16	Undrained	40.9		Constant	Water Surface	Custom
Sand 1		20	21	Mohr-Coulomb	1	46		Water Surface	Custom
Sand 2		19	20	Mohr-Coulomb	1	38		Water Surface	Custom
Clay 2A		14	16	Mohr-Coulomb	113.3	0		Water Surface	Custom
Clay 2B		14	16	Mohr-Coulomb	102.7	0		Water Surface	Custom

## Section 10 – Post-earthquake



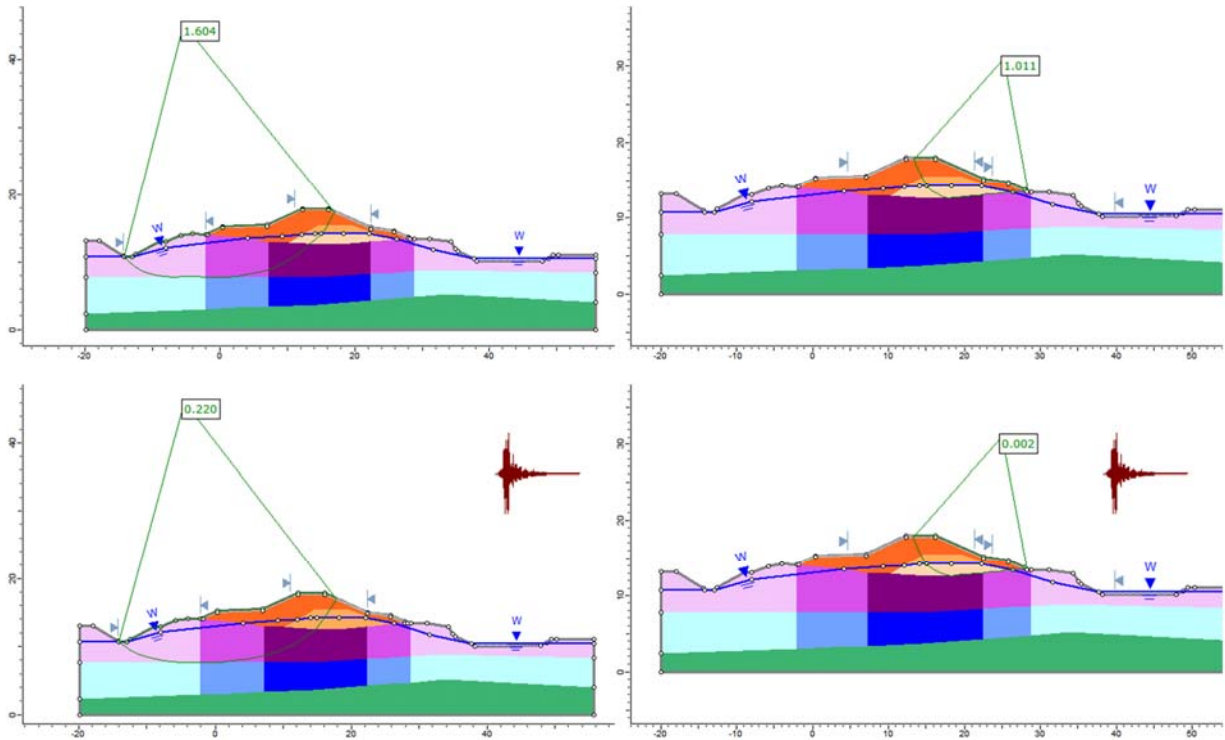
Material Name	Color	Unit Weight (kN/m <sup>3</sup> )	Sat. Unit Weight (kN/m <sup>3</sup> )	Strength Type	Cohesion (kPa)	Phi (deg)	Cohesion Type	Water Surface	Hu Type	Hu
Fill 1	<span style="color: orange;">■</span>	19	20	Mohr-Coulomb	1	40		Water Surface	Custom	1
Fill 2	<span style="color: lightorange;">■</span>	19	20	Mohr-Coulomb	1	40		Water Surface	Custom	1
Peat 1 (soften)	<span style="color: purple;">■</span>	10	11	Undrained	40.6		Constant	Water Surface	Custom	1
Peat 2 (soften)	<span style="color: magenta;">■</span>	10	11	Undrained	28.6		Constant	Water Surface	Custom	1
Peat 3 (soften)	<span style="color: pink;">■</span>	10	11	Undrained	16.6		Constant	Water Surface	Custom	1
Clay 1A (soften)	<span style="color: blue;">■</span>	14	16	Undrained	77		Constant	Water Surface	Custom	1
Clay 1B (soften)	<span style="color: lightblue;">■</span>	14	16	Undrained	56.9		Constant	Water Surface	Custom	1
Clay 1C (soften)	<span style="color: cyan;">■</span>	14	16	Undrained	36.8		Constant	Water Surface	Custom	1
Sand 2	<span style="color: yellow;">■</span>	19	20	Mohr-Coulomb	1	38		Water Surface	Custom	1
Fill 2 (liq)	<span style="color: lightorange;">■</span>	19	20	Undrained	14.4		Constant	Water Surface	Custom	1
Sand 1 (liq)	<span style="color: tan;">■</span>	19	20	Undrained	104.4		Constant	Water Surface	Custom	1
Clay 2A (soften)	<span style="color: grey;">■</span>	14	16	Undrained	102		Constant	Water Surface	Custom	1
Clay 2B	<span style="color: cyan;">■</span>	14	16	Mohr-Coulomb	102.7	0		Water Surface	Custom	1

### Section 11 – Pre-earthquake



Material Name	Color	Unit Weight (kN/m <sup>3</sup> )	Sat. Unit Weight (kN/m <sup>3</sup> )	Strength Type	Cohesion (kPa)	Phi (deg)	Cohesion Type	Water Surface	Hu Type	Hu
Fill 1	Orange	19	20	Mohr-Coulomb	1	42		Water Surface	Custom	1
Fill 2	Light Orange	19	20	Mohr-Coulomb	1	38		Water Surface	Custom	1
Peat 1	Dark Purple	10	11	Undrained	44.6		Constant	Water Surface	Custom	1
Peat 2	Medium Purple	10	11	Undrained	30.5		Constant	Water Surface	Custom	1
Peat 3	Light Purple	10	11	Undrained	16.4		Constant	Water Surface	Custom	1
Silty Clay	Green	14	16	Undrained	63		Constant	Water Surface	Custom	1
Clay 1	Dark Blue	14	16	Undrained	58.3		Constant	Water Surface	Custom	1
Clay 2	Medium Blue	14	16	Undrained	50.2		Constant	Water Surface	Custom	1
Clay 3	Light Blue	14	16	Undrained	42.1		Constant	Water Surface	Custom	1

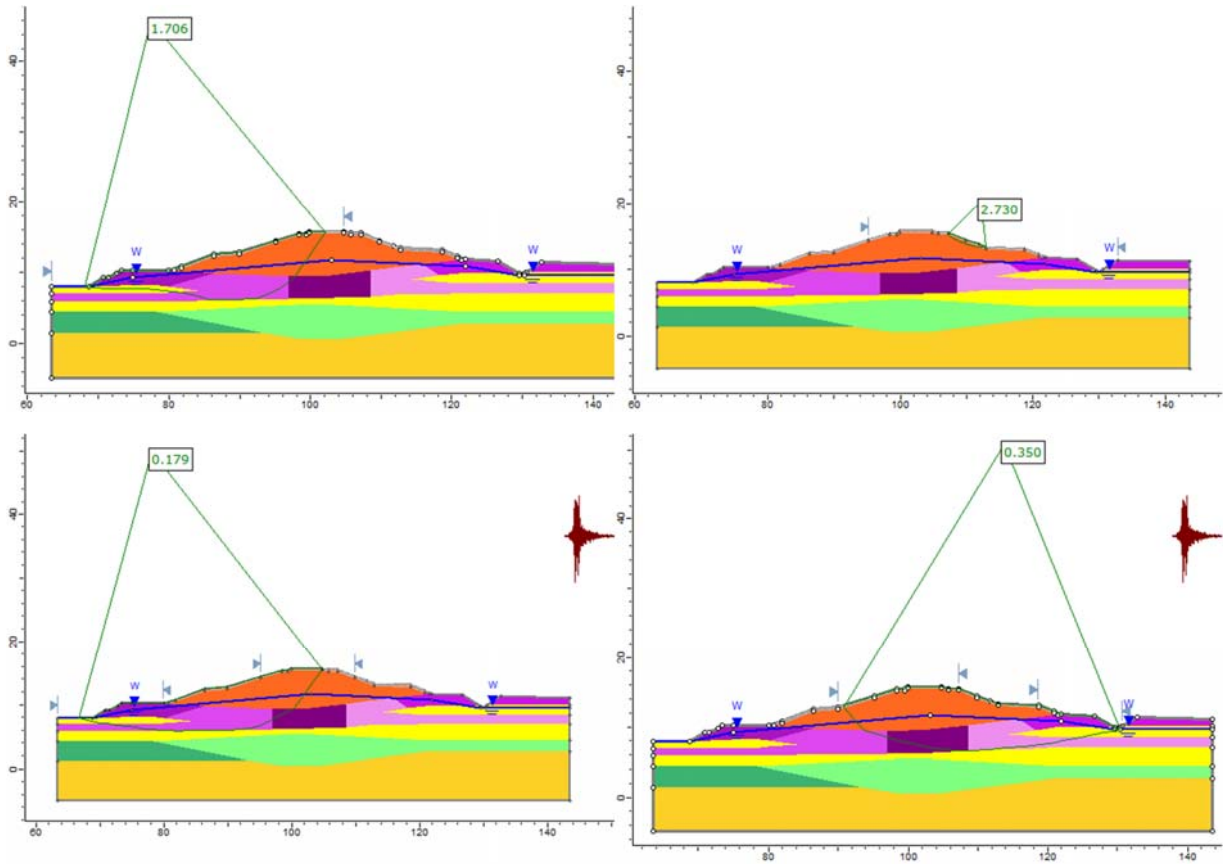
## Section 11 – Post-earthquake



Material Name	Color	Unit Weight (kN/m <sup>3</sup> )	Sat. Unit Weight (kN/m <sup>3</sup> )	Strength Type	Cohesion (kPa)	Phi (deg)	Cohesion Type	Water Surface	Hu Type	Hu
Fill 1	<span style="color: orange;">█</span>	19	20	Mohr-Coulomb	1	42		Water Surface	Custom	1
Fill 2	<span style="color: lightorange;">█</span>	19	20	Mohr-Coulomb	1	38		Water Surface	Custom	1
Fill 2 (liq)	<span style="color: peachpuff;">█</span>	19	20	Mohr-Coulomb	6.1	0		Water Surface	Custom	1
Peat 1	<span style="color: purple;">█</span>	10	11	Mohr-Coulomb	44.6	0		Water Surface	Custom	1
Peat 2 (soften)	<span style="color: magenta;">█</span>	10	11	Undrained	28.5		Constant	Water Surface	Custom	0
Peat 3 (soften)	<span style="color: pink;">█</span>	10	11	Undrained	15.2		Constant	Water Surface	Custom	0
Silty Clay	<span style="color: green;">█</span>	14	16	Undrained	63		Constant	Water Surface	Custom	0
Clay 1	<span style="color: blue;">█</span>	14	16	Undrained	58.3		Constant	Water Surface	Custom	0
Clay 2	<span style="color: lightblue;">█</span>	14	16	Undrained	50.2		Constant	Water Surface	Custom	0
Clay 3	<span style="color: cyan;">█</span>	14	16	Undrained	42.1		Constant	Water Surface	Custom	0

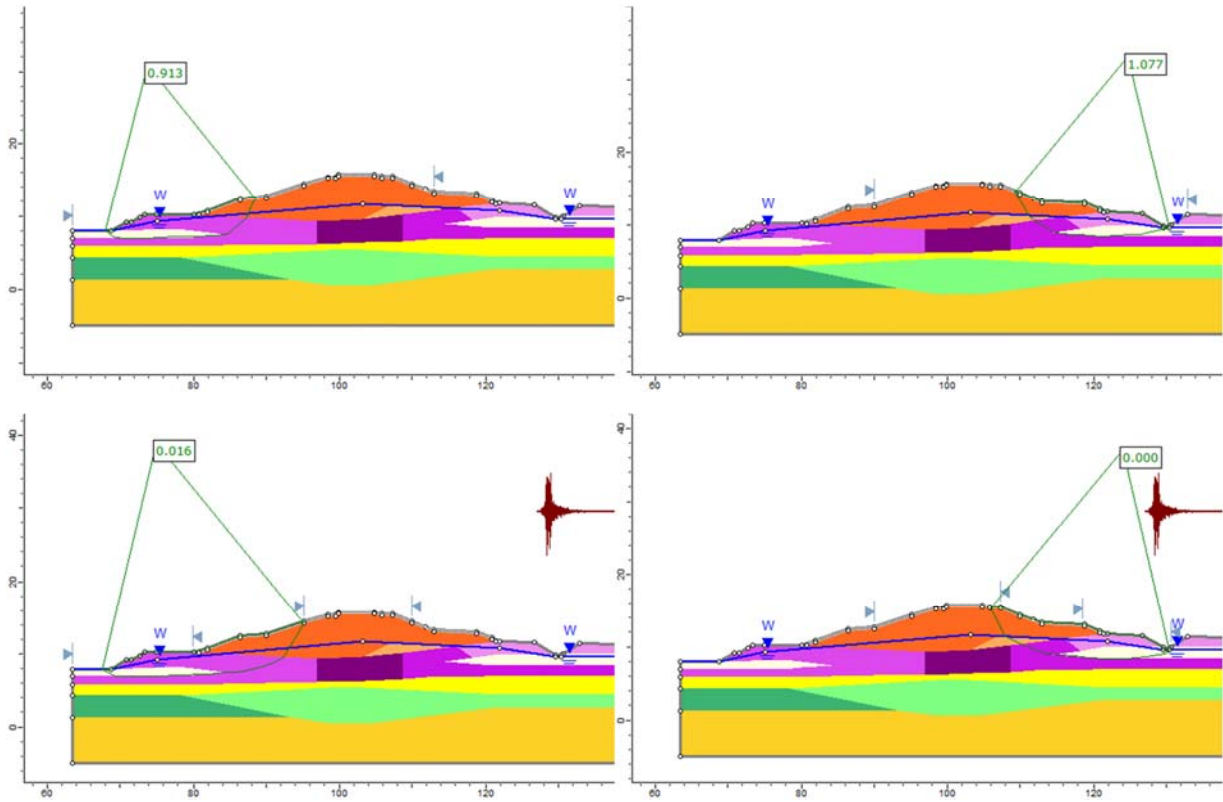


## Section 12 – Pre-earthquake



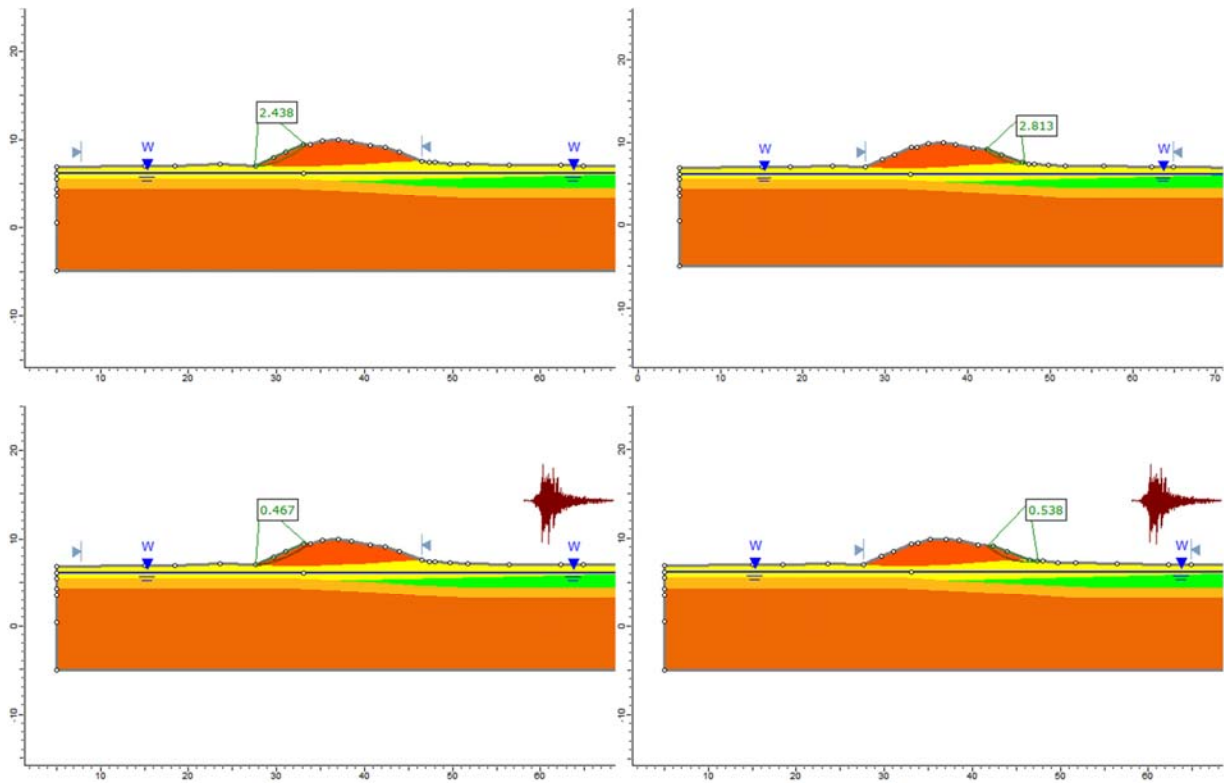
Material Name	Color	Unit Weight (kN/m <sup>3</sup> )	Sat. Unit Weight (kN/m <sup>3</sup> )	Strength Type	Cohesion (kPa)	Phi (deg)	Cohesion Type	Water Surface	Hu Type	Hu
Fill 1	<span style="color: orange;">■</span>	19	20	Mohr-Coulomb	1	40		Water Surface	Custom	1
Peat 1	<span style="color: purple;">■</span>	10	11	Undrained	40		Constant	Water Surface	Custom	0
Peat 1L	<span style="color: purple;">■</span>	10	11	Undrained	17.9		Constant	Water Surface	Custom	0
Peat 1R	<span style="color: purple;">■</span>	10	11	Undrained	30.3		Constant	Water Surface	Custom	0
Peat 2L	<span style="color: purple;">■</span>	10	11	Undrained	25.1		Constant	Water Surface	Custom	0
Peat 2R	<span style="color: purple;">■</span>	10	11	Undrained	39.6		Constant	Water Surface	Custom	0
Silty Clay	<span style="color: green;">■</span>	14	16	Undrained	78.6		Constant	Water Surface	Custom	0
Sandy Silt	<span style="color: green;">■</span>	16	18	Undrained	94.6		Constant	Water Surface	Custom	0
Sand 1	<span style="color: yellow;">■</span>	19	20	Mohr-Coulomb	1	40		Water Surface	Custom	1
Sand 2	<span style="color: orange;">■</span>	19	20	Mohr-Coulomb	1	44		Water Surface	Custom	1

## Section 12 – Post-earthquake



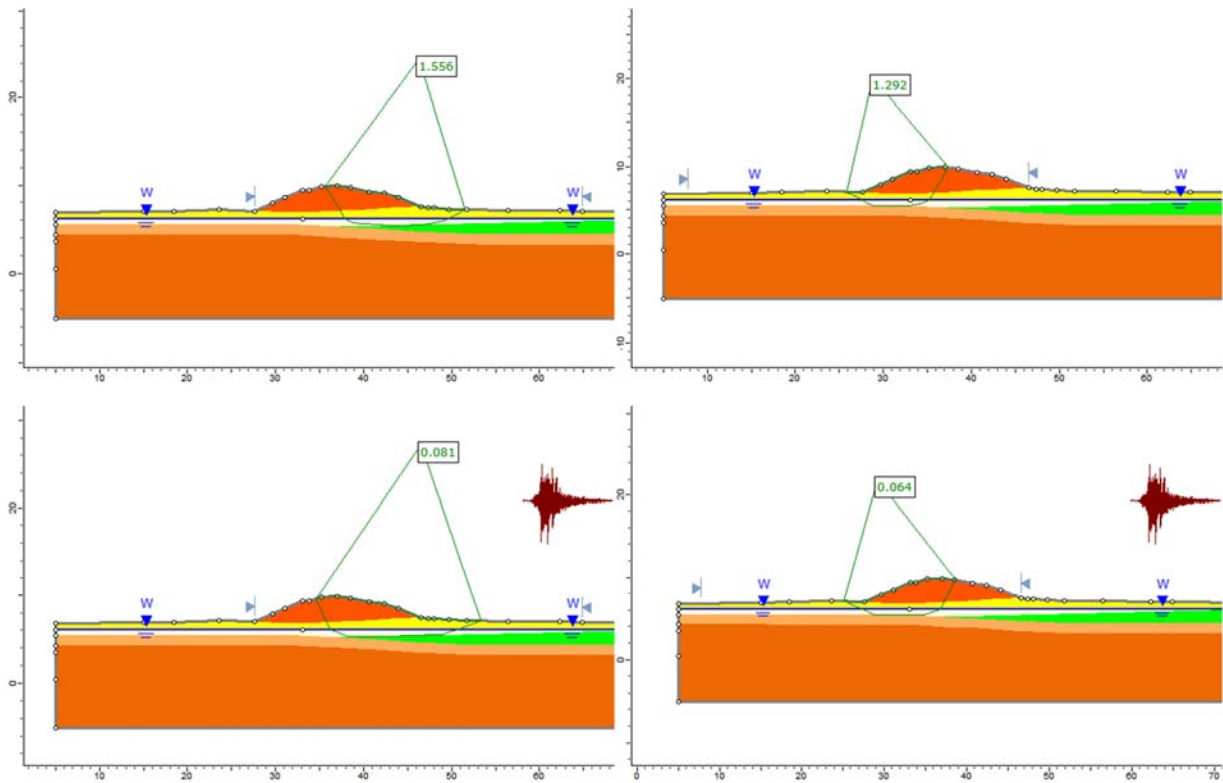
Material Name	Color	Unit Weight (kN/m <sup>3</sup> )	Sat. Unit Weight (kN/m <sup>3</sup> )	Strength Type	Cohesion (kPa)	Phi (deg)	Cohesion Type	Water Surface	Hu Type	Hu
Fill 1	Orange	19	20	Mohr-Coulomb	1	40		Water Surface	Custom	1
Fill (liq)	Light Orange	19	20	Mohr-Coulomb	9.1	0		Water Surface	Custom	1
Peat 1	Dark Purple	10	11	Undrained	40		Constant	Water Surface	Custom	0
Peat 1R	Magenta	10	11	Undrained	30.3		Constant	Water Surface	Custom	0
Peat 2L (soften)	Pink	10	11	Undrained	20.1		Constant	Water Surface	Custom	1
Peat 2R	Light Pink	10	11	Undrained	39.6		Constant	Water Surface	Custom	0
As1 (liq)	Light Yellow	19	20	Undrained	2.7		Constant	Water Surface	Custom	1
Silty Clay	Green	14	16	Undrained	78.6		Constant	Water Surface	Custom	0
Sandy Silt	Light Green	16	18	Undrained	94.6		Constant	Water Surface	Custom	0
Sand 1	Yellow	19	20	Mohr-Coulomb	1	40		Water Surface	Custom	1
Sand 2	Orange-Yellow	19	20	Mohr-Coulomb	1	44		Water Surface	Custom	1

### Section 13 – Pre-earthquake



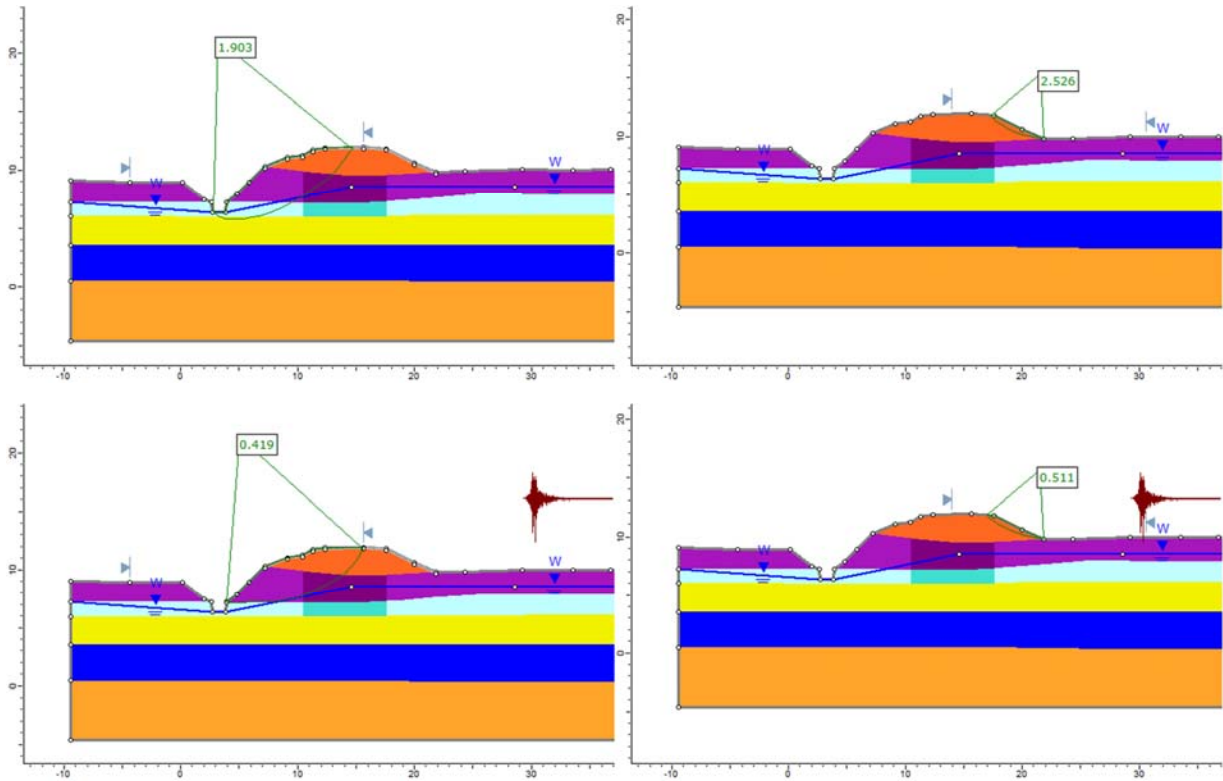
Material Name	Color	Unit Weight (kN/m <sup>3</sup> )	Sat. Unit Weight (kN/m <sup>3</sup> )	Strength Type	Cohesion (kPa)	Phi (deg)	Cohesion Type	Water Surface	Hu Type	Hu
Fill 1	Orange	19	20	Mohr-Coulomb	1	41		Water Surface	Custom	1
Sandy Silt	Green	16	18	Undrained	67		Constant	Water Surface	Custom	0
Sand 1	Yellow	19	20	Mohr-Coulomb	1	37.1		Water Surface	Custom	1
Sand 2	Light Orange	14	16	Mohr-Coulomb	1	39.4		Water Surface	Custom	1
Sand 3	Dark Orange	16	18	Mohr-Coulomb	1	40		Water Surface	Custom	1

### Section 13 – Post-earthquake



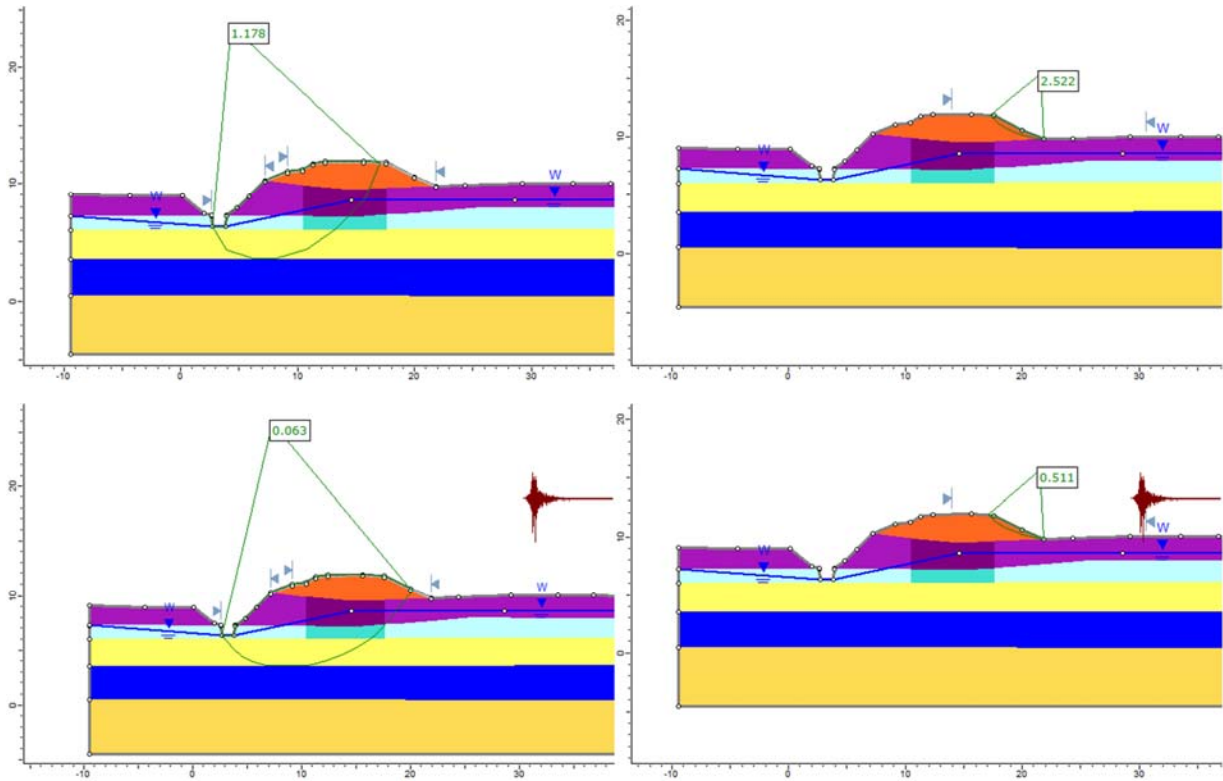
Material Name	Color	Unit Weight (kN/m <sup>3</sup> )	Sat. Unit Weight (kN/m <sup>3</sup> )	Strength Type	Cohesion (kPa)	Phi (deg)	Cohesion Type	Water Surface	Hu Type	Hu
Fill 1	Orange	19	20	Mohr-Coulomb	1	41		Water Surface	Custom	1
Sandy Silt	Green	16	18	Undrained	67		Constant	Water Surface	Custom	0
Sand 1	Yellow	19	20	Mohr-Coulomb	1	37.1		Water Surface	Custom	1
Sand 3	Orange	16	18	Mohr-Coulomb	1	40		Water Surface	Custom	1
Sand 1 (liq)	White	19	20	Mohr-Coulomb	5.2	0		Water Surface	Custom	1
Sand 2A (liq)	Light Orange	19	20	Mohr-Coulomb	11.8	0		Water Surface	Custom	1

### Section 14 – Pre-earthquake



Material Name	Color	Unit Weight (kN/m <sup>3</sup> )	Sat. Unit Weight (kN/m <sup>3</sup> )	Strength Type	Cohesion (kPa)	Phi (deg)	Water Surface	Hu Type	Hu
Fill 1	<span style="color: orange;">■</span>	19	20	Mohr-Coulomb	1	43	Water Surface	Custom	1
Peat 1	<span style="color: purple;">■</span>	10	11	Undrained	31.2		Water Surface	Custom	1
Peat 2	<span style="color: magenta;">■</span>	10	11	Undrained	20.1		Water Surface	Custom	1
Clay 1A	<span style="color: cyan;">■</span>	14	16	Undrained	39.4		Water Surface	Custom	1
Clay 1B	<span style="color: lightblue;">■</span>	14	16	Undrained	31.1		Water Surface	Custom	1
Clay 2	<span style="color: blue;">■</span>	14	16	Undrained	64.7		Water Surface	Custom	1
Sand 1	<span style="color: yellow;">■</span>	19	20	Mohr-Coulomb	1	40	Water Surface	Custom	1
Sand 2	<span style="color: orange;">■</span>	19	20	Mohr-Coulomb	1	40	Water Surface	Custom	1

### Section 14 – Post-earthquake



Material Name	Color	Unit Weight (kN/m3)	Sat. Unit Weight (kN/m3)	Strength Type	Cohesion (kPa)	Phi (deg)	Water Surface	Hu Type	Hu
Fill 1	Orange	19	20	Mohr-Coulomb	1	43	Water Surface	Custom	1
Peat 1	Purple	10	11	Undrained	31.2		Water Surface	Custom	1
Peat 2	Magenta	10	11	Undrained	20.1		Water Surface	Custom	1
Clay 1A	Cyan	14	16	Undrained	39.4		Water Surface	Custom	1
Clay 1B	Light Blue	14	16	Undrained	31.1		Water Surface	Custom	1
Clay 2	Dark Blue	14	16	Undrained	64.7		Water Surface	Custom	1
Sand 1 (liq)	Yellow	19	20	Mohr-Coulomb	12.7	0	Water Surface	Custom	1
Sand 2 (liq)	Tan	19	20	Mohr-Coulomb	18.4	0	Water Surface	Custom	1

## REFERENCES

- Abrahamson, N., Kuehn, N., Gulerce, Z., Gregor, N., Bozorgnia, Y., Parker, G., Stewart, J., Chiou, B., Idriss, I.M., Campbell, K., Youngs, R. Update of the BC Hydro Subduction Ground-Motion Model using the NGA-Subduction Dataset. 2018. *Pacific Earthquake Engineering Research Center*, June. Volume 02.
- Ahdi, S.K., Stewart, J.P., Ancheta, T.D., Kwak, D.Y., Mitra, D., 2017. Development of *VS* profile database and proxy-based models for *VS30* prediction in the Pacific Northwest region of North America. *Bulletin of the Seismological Society of America*, Volume 107, pp. 1781-1801.
- Al Atik, L., 2015. NGA-East: Ground-Motion Standard Deviation Models for Central and Eastern North America. *Pacific Earthquake Engineering Research Center*, June. Volume 07.
- Ancheta, T.D., Darragh, R.B., Stewart, J.P., Seyhan E., Silva, W.J., Chiou B. S.-J., Wooddell, K.E., Graves, R. W., Kottke, A. R., Boore, D. M., Kishida, T., Donahue, J. L., 2014. NGA-West2 Database. *Earthquake Spectra*, August. 30(3), pp. 989-1005.
- Baker, J.W., 2015. Efficient analytical fragility function fitting using dynamic structural analysis. *Earthquake Spectra*, 31(1), pp.579–599.
- Baker, J.W., Lin, T. & Shahi, S.K., 2011. New Ground Motion Selection Procedures and Selected Motions for the PEER Transportation Research Program *Pacific Earthquake Engineering Research Center*, March, Volume 03.
- Van Ballegooy, S., Malan, P., Lacrosse, V., Jacka, M.E., Cubrinovski, M., Bray, J.D., O'Rourke, T.D., Crawford, S.A., Cowan, H., 2014. Assessment of liquefaction-induced land damage for residential Christchurch. *Earthquake Spectra*.
- Bolton M.D. (1986). The strength and dilatancy of sands, *Géotechnique*, 36(1): 65-78.
- Bonilla, L. F., Steidl, J.H., Gariel, J.-C., Archuleta, R.J., 2002. Borehole Response Studies at the Garner Valley Downhole Array, Southern California. *Bulletin of the Seismological Society of America*, 92(8), pp. 3165-3179.
- Boore, D. M., 2010. Orientation-Independent, Nongeometric-Mean Measures of Seismic Intensity from Two Horizontal Components of Motion. *Bulletin of the Seismological Society of America*, August, 100(4), pp. 1830-1835.

- Boore, D.M., Stewart, J.P., Seyhan, E., Atkinson, G. M., 2014. NGA-West2 Equations for Predicting PGA, PGV, and 5% Damped PSA for Shallow Crustal Earthquakes. *Earthquake Spectra*, 30(3), pp. 1057-1085.
- Boulanger, R.W. & Idriss, I.M., 2006. Liquefaction Susceptibility Criteria for Silts and Clays. *Journal of Geotechnical and Geoenvironmental Engineering*, 132(11), pp.1413–1426.
- Boulanger, R.W. & Idriss, I.M., 2007. Evaluation of Cyclic Softening in Silts and Clays. *Journal of Geotechnical and Geoenvironmental Engineering*, 133(6), pp.641–652.
- Boulanger, R.W., and Idriss, I. M. 2016. “CPT-based liquefaction triggering procedure.” *Journal of Geotechnical and Geoenvironmental Engineering*, ASCE, 04015065, 10.1061/(ASCE)GT.1943-5606.0001388.
- Boulanger, R.W., Wilson, D.W. & Idriss, I.M., 2012. Examination and Re-evaluation of SPT-Based Liquefaction Triggering Case Histories, *Journal of Geotechnical and Geoenvironmental Engineering*, 138(8), pp 898-909.
- Cadet, H., Bard, P.-Y., Duval, A.-M., Bertrand, E., 2012. Site effect assessment using KiK-net data: part 2—site amplification prediction equation based on  $f_0$  and  $V_{sz}$ . *Bulletin of Earthquake Engineering*, April, 10(2), pp. 451-489.
- Cook, R.D., and Weiberg, S., 1999. Applied regression including computing and graphics. *Wiley & Sons*, New York.
- Darendeli, M., 2001. Development of a new family of normalized modulus reduction and material damping curves. Ph.D. Thesis, Department of Civil Engineering, University of Texas, Austin.
- Duncan, M., Wright, S. & Brandon, T., 2014. Soils Strength and Slope Stability. John Wiley and Sons Inc.
- Eslami, M., 2017. Experimental Mapping of Elastoplastic Surfaces for Sand and Cyclic Failure of Low- Plasticity Fine-Grained Soils. Ph.D Thesis, Department of Civil and Environmental Engineering, University of California - Los Angeles.
- Ghofrani, H., Atkinson, G., 2011. Forearc versus backarc attenuation of earthquake ground motion. *Bulletin of the Seismological Society of America*, December, 101(6), pp. 3032-3045.
- Ghofrani, H., Atkinson, G.M., Goda, K., 2013. Implications of the 2011 M9.0 Tohoku Japan earthquake for the treatment of site effects in large earthquakes. *Bulletin of Earthquake Engineering*, January, 11(1), pp. 171-203.



- Ghofrani, H., Atkinson, G. M., 2014. Site condition evaluation using horizontal-to-vertical response spectral ratios of earthquakes in the NGA-West 2 and Japanese databases. *Soil Dynamics and Earthquake Engineering*, Volume 67, pp. 30–43.
- Groholski, D.R. et al., 2016. Simplified Model for Small-Strain Nonlinearity and Strength in 1D Seismic Site Response Analysis. *Journal of Geotechnical and Geoenvironmental Engineering*, 142(9),
- Hashash, Y.M.A. et al., 2016. DEEPSOIL V6.1, User Manual, Urbana, IL: Board of Trustees of University of Illinois at Urbana-Champaign.
- Hassani, B., Atkinson, G.M., 2018a. Site-effects model for Central and Eastern North America based on peak frequency and average shear-wave velocity. *Bulletin of the Seismological Society of America*, Volume 108.
- Hassani, B., Atkinson, G.M., 2018b. Application of a site-effects model based on peak frequency and average shear-wave velocity to California. *Bulletin of the Seismological Society of America*, Volume 108.
- Hayashi, H. Yamanashi, T., Hashimoto, H., Yamaki, M., 2018. Shear Modulus and Damping Ratio for Normally Consolidated Peat and Organic Clay in Hokkaido Area. *Geotechnical and Geological Engineering*.
- Hayashi, H. & Hayashi, T., 1991. Estimation of undrained shear strength for peat using CPT, pp.1159–1160. *Australian Geomechanics Society, Sydney, Australia. (ISBN 978-0-9946261-2-7)*
- Hokkaido River Disaster Prevention Research Center, 2004. H15 Tokachi-Okii River Disaster Investigation Report [Japanese]
- Hokkaido River Disaster Prevention Research Center, 2005. H16 Tokachi-Okii River Disaster Investigation Report [Japanese]
- Ide, S. & Minoru, T., 1996. The dynamic rupture process of the 1993 Kushiro-oki earthquake. *Journal of Geophysical Research*, 101, pp.5661–5675.
- Idriss, I. M., 2011. Use of VS30 to represent local site conditions. *4<sup>th</sup> LASPEI/IAEE International Symposium Effects of Surface Geology on Strong Ground Motions*, Santa Barbara, CA.
- Idriss, I.M. & Boulanger, R.W., 2007. Residual shear strength of liquefied soils. USSD 2007 Modernization and Optimization of Existing Dams and Reservoirs.

- Idriss, I.M. & Boulanger, R.W., 2008. Soil liquefaction during earthquakes. *Earthquake Engineering Research Institute*, 136(6), p.755.
- Ishihara, K., 1985a. Stability of natural deposits during earthquakes. In Proceedings of the Eleventh International Conference on Soil Mechanics and Foundation Engineering.
- Ishihara, K. & Yoshimine, M., 1992. Evaluation of Settlements In Sand Deposits Following Liquefaction During Earthquakes. *Soils and Foundations*.
- Jaky, J., 1948. Pressure in silos. In Proceedings of the 2nd International Conference on Soil Mechanics and Foundation Engineering. pp. 103–107.
- Japan Highway Public Corporation (JHPC), 2005. Guidelines for Electronic Delivery of Surveys: Appendix of Geological Survey Part [Japanese].
- Jayaram, N. & Baker, J., 2009. Correlation model for spatially distributed ground-motion intensities. *Earthquake Engineering & Structural Dynamics*.
- Kawase, H., Sánchez-Sesma, F. J., Matsushima, S., 2011. The Optimal Use of Horizontal-to-Vertical Spectral Ratios of Earthquake Motions for Velocity Inversions Based on Diffuse-Field Theory for Plane Waves. *Bulletin of the Seismological Society of America*, 101(5), pp. 2001-2014.
- Kayen, R. Moss, R. E. S., Thompson, E. M., Seed, R. B., Cetin, K. O., Der Kiureghian, A., Tanaka, Y., Tokimatsu, K., 2004. Global Shear Wave Velocity Database for Probabilistic Assessment of the Initiation of Seismic-soil Liquefaction. Proc. 11th International Conference on Soil Dynamics & Earthquake Engineering, pp.506–512.
- Kim, B., Hashash, Y.M.A., Stewart, J.P., Rathje, E.M., Harmon, J.A., Musgrove, M.I., Campbell, K. W., Silva, W.J., 2016. Relative differences between nonlinear and equivalent-linear 1-D site response analyses. *Earthquake Spectra*, 32(3), pp. 1845-1865.
- Kishida, T., Boulanger, R.W., Abrahamson, N.A., Wehling, T. M., Driller, M. W., 2009. Regression Models for Dynamic Properties of Highly Organic Soils. *Journal of Geotechnical and Geoenvironmental Engineering*, 135(4), pp.533–543.
- Kishida, T., Boulanger, R.W., Abrahamson, N.A., Driller, M.W., Wehling, T.M. et al., 2009. Seismic response of levees in the Sacramento-San Joaquin Delta. *Earthquake Spectra*, 25(3), pp.557–582.

- Kishida, T., Bozorogina, Y., Abrahamson, N.A., Ahdi, S.K., Ancheta, T.D., Boore, D.M., Campbell, K.W., Darragh, R.B., Magistrale, H., Stewart, J.P., 2017. Development of the NGA-Subduction Database. *Proc. 16th World Conf. on Earthquake Eng.*, Santiago, Chile (Paper No. 3452).
- Koketsu, K., Hikima, K., Miyazaki, S., Ide, S., 2004. Joint inversion of strong motion and geodetic data for the source process of the 2003 Tokachi-oki, Hokkaido, earthquake. *Earth, Planets and Space*, 56(3), pp.329–334.
- Konno, K., & Ohmachi, T., 1998. Ground-motion characteristics estimated from spectral ratio between horizontal and vertical components of microtremor. *Bulletin of the Seismological Society of America*, Volume 88, pp. 228–241.
- Kramer, S.L. & Wang, C.-H., 2015. Empirical Model for Estimation of the Residual Strength of Liquefied Soil. *Journal of Geotechnical and Geoenvironmental Engineering*.
- Kwak, D.Y., Stewart, J.P., Brandenburg, S.J., Mikami, A., 2016. Characterization of Seismic Levee Fragility using Field Performance Data. *Earthquake Spectra*, 32(1), pp.193–215.
- Kwak, D.Y., Stewart, J.P., Mandokhail, S.-J., Park, D., 2017. Supplementing *VS30* with H/V Spectral Ratios for Predicting Site Effects. *Bulletin of the Seismological Society of America*, October, 107(5), pp. 2028-2042
- Kwak, D.Y., Brandenburg, S.J., Mikami, 2015. Prediction Equations for Estimating Shear Wave Velocity from Combined Geotechnical and Geomorphic Indexes Based on Japanese Data Set. *Bulletin of the Seismological Society of America*, 105(4), pp.1919–1930.
- Lachet, C., Hatzfeld, D., Bard, P.-Y., Theodulidis, N., Papaioannou, C., Savvaidis, A., 1996. Site effects and microzonation in the city of Thessaloniki (Greece) comparison of different approaches. *Bulletin of the Seismological Society of America*, 86(6), pp. 1692-1703.
- Ladd, C.C., 1991. Stability Evaluation during Staged Construction. *Journal of Geotechnical Engineering*.
- Lermo, J. & Chávez-García, F. J., 1993. Site effect evaluation using spectral ratios with only one station. *Bulletin of the Seismological Society of America*, 83(5), pp. 1574-1594.
- Lunne, T., Christoffersen, H.P. & Tjelta, T.I., 1985. Engineering Use of Piezocone Data in North Sea Clays. In *Proc. ICSMFE-11*. pp. 907–912.

- Maurer, B.W., Green, R.A. & Oliver-Denzil, S.T., 2015. Moving towards an improved index for assessing liquefaction hazard: Lessons from historical data. *Soils and Foundations*, 55(4), pp.778–787.
- Mayne, P.W. & Kulhawy, F.H., 1982. K-OCR relationships in soil. *Journal of the Geotechnical Engineering Division*.
- Menq, F.Y. (2003). *Dynamic properties of sandy and gravelly soils*. Ph.D. Dissertation, Department of Civil Engineering, University of Texas, Austin.
- Midorikawa, S. & Nogi, Y., 2015. Estimation of  $V_{S30}$  from Shallow Velocity Profile (in Japanese). *Journal of Japan Association of Earthquake Engineering*, 15(2), pp.91–96.
- Moehle, J. & Deierlein, G.G., 2004. A framework for performance-based earthquake engineering. In 13th World Conference on Earthquake Engineering. Vancouver, B.C., Canada.
- Montgomery, J. & Boulanger, R.W., 2017. Effects of Spatial Variability on Liquefaction-Induced Settlement and Lateral Spreading. *Journal of Geotechnical and Geoenvironmental Engineering*, 143(1)
- National Research Institute for Earth Science and Disaster Prevention (NIED), 2018. (Japan Seismic Hazard Information Station (J-SHIS)). Available at: <http://www.j-shis.bosai.go.jp/en/> [Accessed December 4, 2018].
- Negussey, D., Wijewickreme, W.K.D. & Vaid, Y.P., 1988. Constant-volume friction angle of granular materials. *Canadian Geotechnical Journal*, 25(1), pp.50–55.
- Newmark, N.M., 1965. Effects of Earthquakes on Dams and Embankments. *Géotechnique*, 15(2), pp.139–160.
- Olson, S.M. & Stark, T.D., 2002. Liquefied strength ratio from liquefaction flow failure case histories. *Canadian Geotechnical Journal*.
- Pelekis, P.C. & Athanasopoulos, G.A., 2011. An overview of surface wave methods and a reliability study of a simplified inversion technique. *Soil Dynamics and Earthquake Engineering*, 31(12), pp.1654–1668.
- Porter, K., Kennedy, R. & Bachman, R., 2007. Creating fragility functions for performance-based earthquake engineering. *Earthquake Spectra*, 23(2), pp.471–489.

- Rocscience Inc. 2017, *Slide 7.0 - 2D Limit Equilibrium Slope Stability Analysis*. www.rocscience.com, Toronto, Ontario, Canada.
- Rodriguez-Marek, A., Montalva, G.A., Cotton, F., Bonilla, F., 2011. Analysis of Single-Station standard deviation using the KiK-net Data. *Bulletin of the Seismological Society of America*, 101(3), pp. 1242-1258.
- Sasaki, Y., 2009. River dike failures during the 1993 Koshiro-oki earthquake and the 2003 Tokachi-oki earthquake. *Earthquake Geotechnical Case Histories for Performance-based Design*, pp.131–157.
- Seyhan, E. & Stewart, J.P., 2014. Semi-Empirical nonlinear site amplification from NGA-West2 data and simulations. *Earthquake Spectra*, August, 30(3), pp. 1241-1256.
- Shafiee, A., 2016. Cyclic and Post-Cyclic Behavior of Sherman Island Peat. Ph.D Dissertation, University of California - Los Angeles.
- Sheahan, T.C., Ladd, C.C. & Germaine, J.T., 1996. Rate-Dependent Undrained Shear Behavior of Saturated Clay. *Journal of Geotechnical Engineering*.
- Stewart, J.P., Afshari, K. & Hashash, Y.M.A., 2014. Guidelines for Performing Hazard-Consistent One-Dimensional Ground Response Analysis for Ground Motion Prediction. *Pacific Earthquake Engineering Research Center*, October. Volume 16
- Stewart, J.P., Afshari, K. & Goulet, C.A., 2017. Non-Ergodic Site Response in Seismic Hazard Analysis. *Earthquake Spectra*, November, 33(4), pp. 1385-1414.
- Stewart, J.P., Liu, A.H., & Choi, Y., 2003. Amplification factors for spectral acceleration in tectonically active regions. *Bulletin of the Seismological Society of America*, 93(1), pp. 332-352.
- Terronez, A., 2017. Non-Linear Ground Motion Amplification Functions for Fine Grained and Highly Organic Soils. M.S. Thesis, University of California - Los Angeles.
- Theodulidis, N., Bard, P.-Y., Archuleta, R. & Bouchon, M., 1996. Horizontal-to-vertical spectral ratio and geological conditions: The case of Garner Valley Downhole Array in southern California. *Bulletin of the Seismological Society of America*, 86(2), pp. 306-319.
- Tokimatsu, K. & Sekiguchi, T., 2006. Effects of nonlinear properties of surface soils on strong ground motions recorded in Ojiya during 2004 Mid Niigata Prefecture Earthquake. *Soils and Foundations*, 46(6), pp.765–775.

- Vorogushyn, S., Merz, B. & Apel, H., 2009. Development of dike fragility curves for piping and micro-instability breach mechanisms. *Natural Hazards and Earth System Science*, 9(4), pp.1383–1401.
- Wakamatsu, K. & Matsuoka, M., 2011. Developing a 7.5-sec site-condition map for Japan based on geomorphologic classification. *WIT Transactions on the Built Environment*, 120, pp.101–112.
- Wakamatsu, K. & Matsuoka, M., 2013. Nationwide 7.5-arc-second Japan engineering geomorphologic classification map and VS30 zoning. *Journal of Disaster Research*, 8(5), pp.904–911.
- Wang, P., Stewart, J.P., Bozorgnia, Y., Boore, D.M., Kishida, T., 2017. “R” Package for Computation of Earthquake Ground-Motion Response Spectra. *Pacific Earthquake Engineering Research Center*, Volume 9.
- Wehling, T.M. Boulanger, R.W., Arulnathan, R., Harder Jr, L.F., Driller, M.W., 2003. Nonlinear Dynamic Properties of a Fibrous Organic Soil. *Journal of Geotechnical and Geoenvironmental Engineering*, 129(10), pp.929–939.
- Yasuhara, K., 1994. Postcyclic Undrained Strength for Cohesive Soils. *Journal of Geotechnical Engineering*, 120(11), pp.1961–1979.
- Yoshimine, M. Nishizaki, H., Amano, K., Hosono, Y., 2006. Flow deformation of liquefied sand under constant shear load and its application to analysis of flow slide of infinite slope. *Soil Dynamics and Earthquake Engineering*, 26(2–4 SPEC. ISS.), pp.253–264.
- Zhao, J.X. & Hua, X., 2013. A Comparison of VS30 and Site Period as Site-Effect Parameters in Response Spectral Ground-Motion Prediction Equations. *Bulletin of the Seismological Society of America*, 103(1), pp. 1-18.
- Zhao, J.X. Liang, X., Jiang, F., Xing, H., Zhu, M., Hou, R., Zhang, Y., Lan, X., Rhoades, D.A., Irikura, K., Fukushima, Y., Somerville, P.G., 2016a. Ground-Motion Prediction Equations for Subduction Interface Earthquakes in Japan Using Site Class and Simple Geometric Attenuation Functions. *Bulletin of the Seismological Society of America*, August, 106(4), pp. 1518-1534.
- Zhao, J. X. Jiang, F., Shi, P., Xing, H., Huang, H., Hou, R., Zhang, Y., Yu, P., Lan, X., Rhoades, D.A., Somerville, P.G., Irikura, K., Fukushima, Y., 2016b. Ground-Motion Prediction Equations for Subduction Slab Earthquakes in Japan Using Site Class and Simple Geometric Attenuation Functions. *Bulletin of the Seismological Society of America*, August, 106(4), pp. 1535-1551